231A

Proceedings of the

Sea Ice Mechanics and Arctic Modeling Workshop

April 25-28, 1995, Hilton Hotel, Anchorage, Alaska

Volume 1

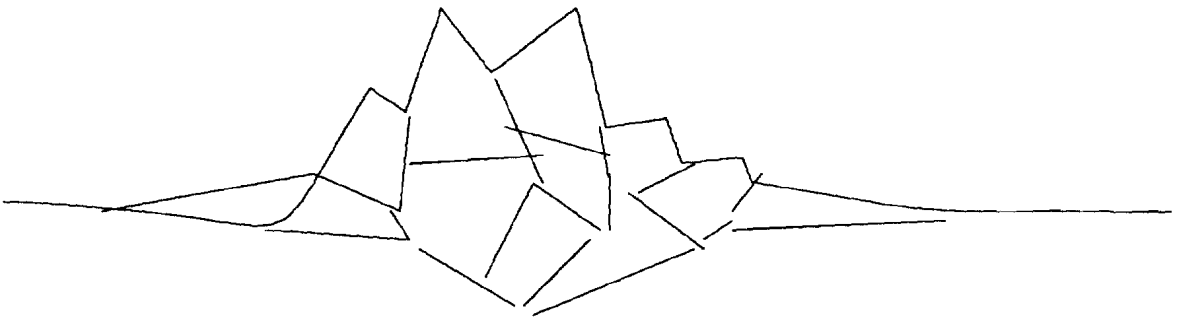

Sponsored by

U.S. Minerals Management Service,
U.S. Navy Office of Naval Research,
Canadian National Energy Board,
and Participating Members of the Oil Industry:
Amoco, Arco, Chevron, and Mobil

Organized by Northwest Research Associates, Inc.
Bellevue, WA

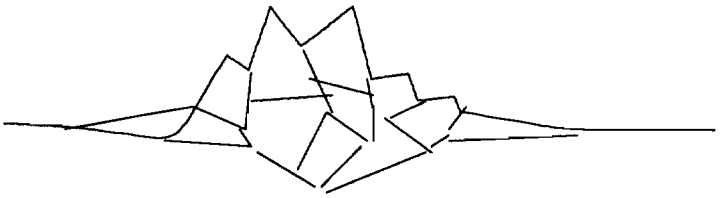

Sea Ice Mechanics and Arctic Modeling Workshop
Volume 1

Table of Contents

Front cover: A first-year ridge in the Beaufort Sea near the SIMI East Camp (photo by M. Coon)

Rear cover: Site of ice fracture tests near the SIMI East Camp (photo by S. Echert)

1. INTRODUCTION

The Sea Ice Mechanics and Arctic Modeling Workshop to be held in Anchorage, Alaska, April 25-28, 1995, will focus on current state of the practice and future research needs relative to offshore oil and gas facilities and will also review the results of the U.S. Navy's Office of Naval Research (ONR) Sea Ice Mechanics Initiative (SIMI). SIMI is a continuing ONR program running from October 1992 through September 1996, with sea ice mechanics and Arctic acoustics field programs, laboratory studies, and modeling work. The SIMI goals are to understand sea ice constitutive laws and fracture mechanics over the full range of geophysical scales, to determine the scaled responses to applied external forces, and to develop physically based constitutive and fracture models. The goals were established at a SIMI planning meeting held at Airlie, Virginia, in November 1990. The report from that meeting is included as Appendix A. The main field experiments were defined at a second SIMI planning meeting held at Sidney, British Columbia, in August 1993 and are described in the Summary Plan included as Appendix B. The main field experiments were conducted in the Beaufort Sea during 1993 and 1994.

Volume 1 has four major parts:

1. Four ice maps: the fall and spring SIMI camps at 2-km and 10-km scales (included in this section).
2. Summaries of poster presentations by the SIMI Principal Investigators of their findings to date, their model developments, their data sets, and their upcoming publications. These are divided into five sections focusing on broad topics. Each section begins with a list of the papers in the section and a list referring the reader to papers in other sections containing information on the same subject.
3. Proceedings of the first SIMI planning meeting (as Appendix A).
4. The SIMI Summary Plan (as Appendix B).

After the workshop, NWRA will publish the invited lectures and working-group summary presentations and recommendations in Volume 2.

Volume 1 is organized as follows. Section 2 includes the summary papers on Arctic acoustic experiments. Sea ice fracture mechanics papers are in Section 3. Laboratory and field studies of sea ice properties are in Section 4. Section 5 presents investigations of pack ice stress, ice strain, and other observations, such as CTD casts. Section 6 includes the various sea ice modeling studies. There is a cross-reference list of papers at the beginning of each section.

Map 1. Vicinity of SIMI West Camp, September 1993.

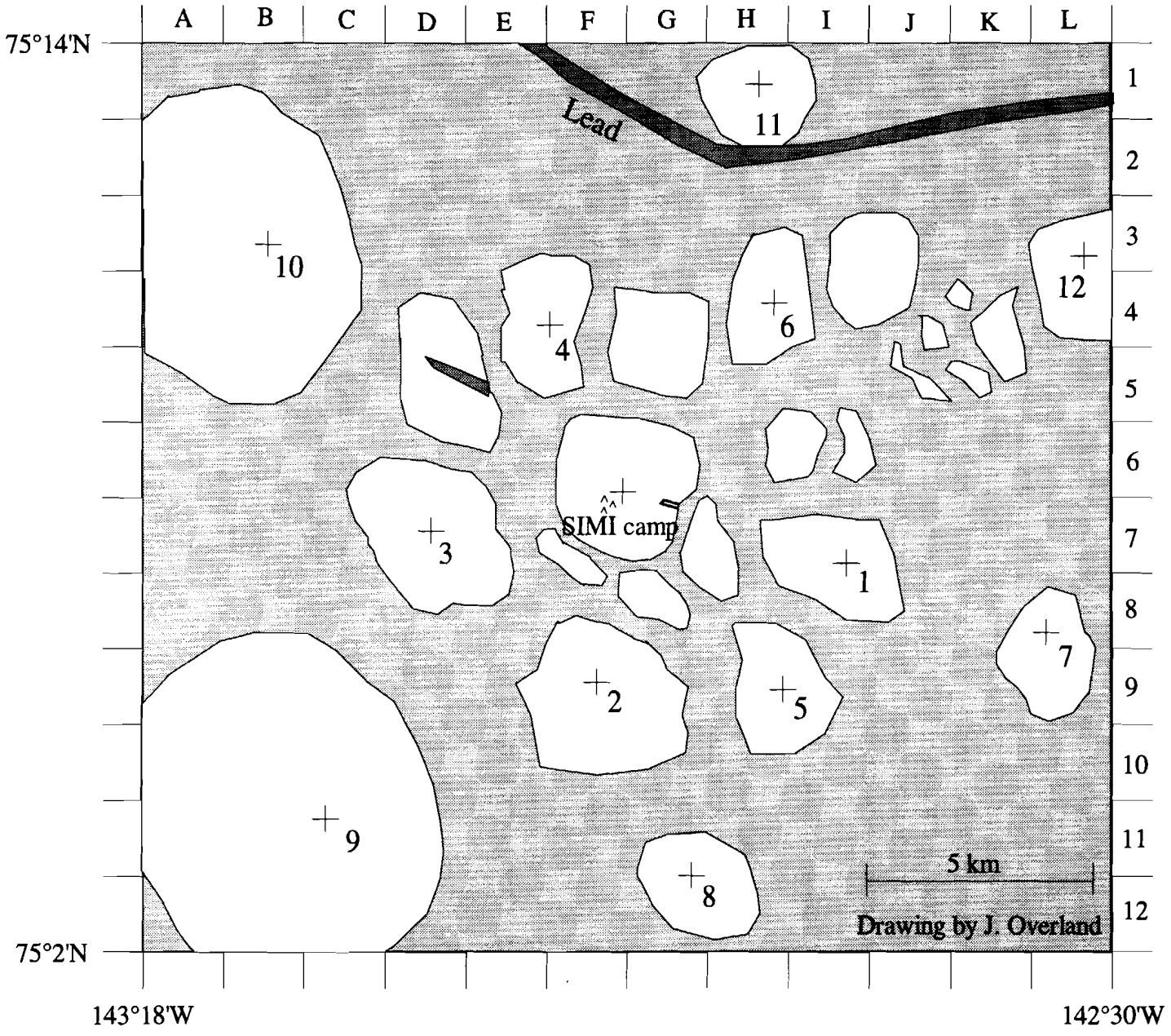

Map 2. SIMI West Camp, November 1993.

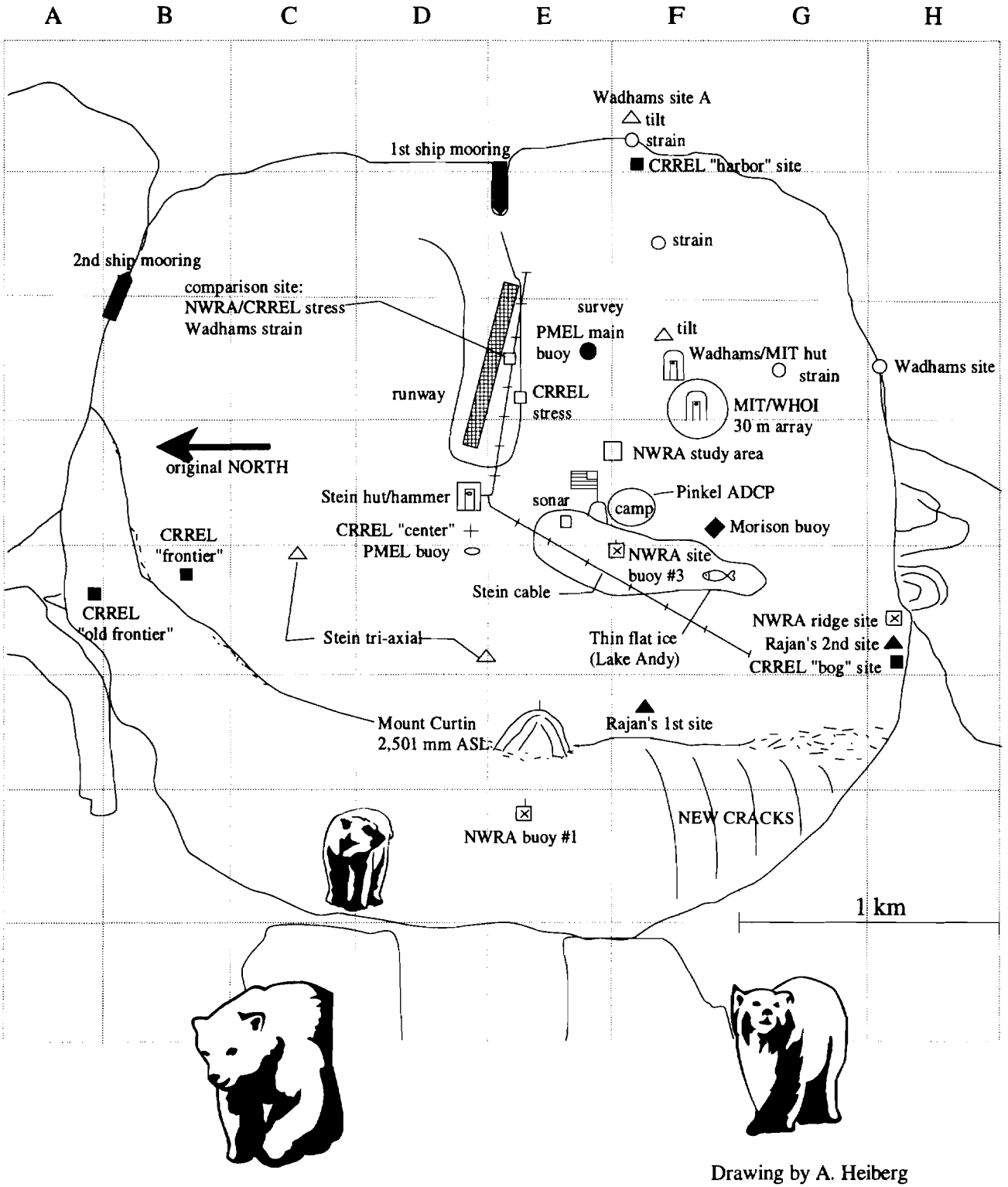

Drawing by A. Heiberg

Map 3. Vicinity of SIMI East Camp, April 1994.

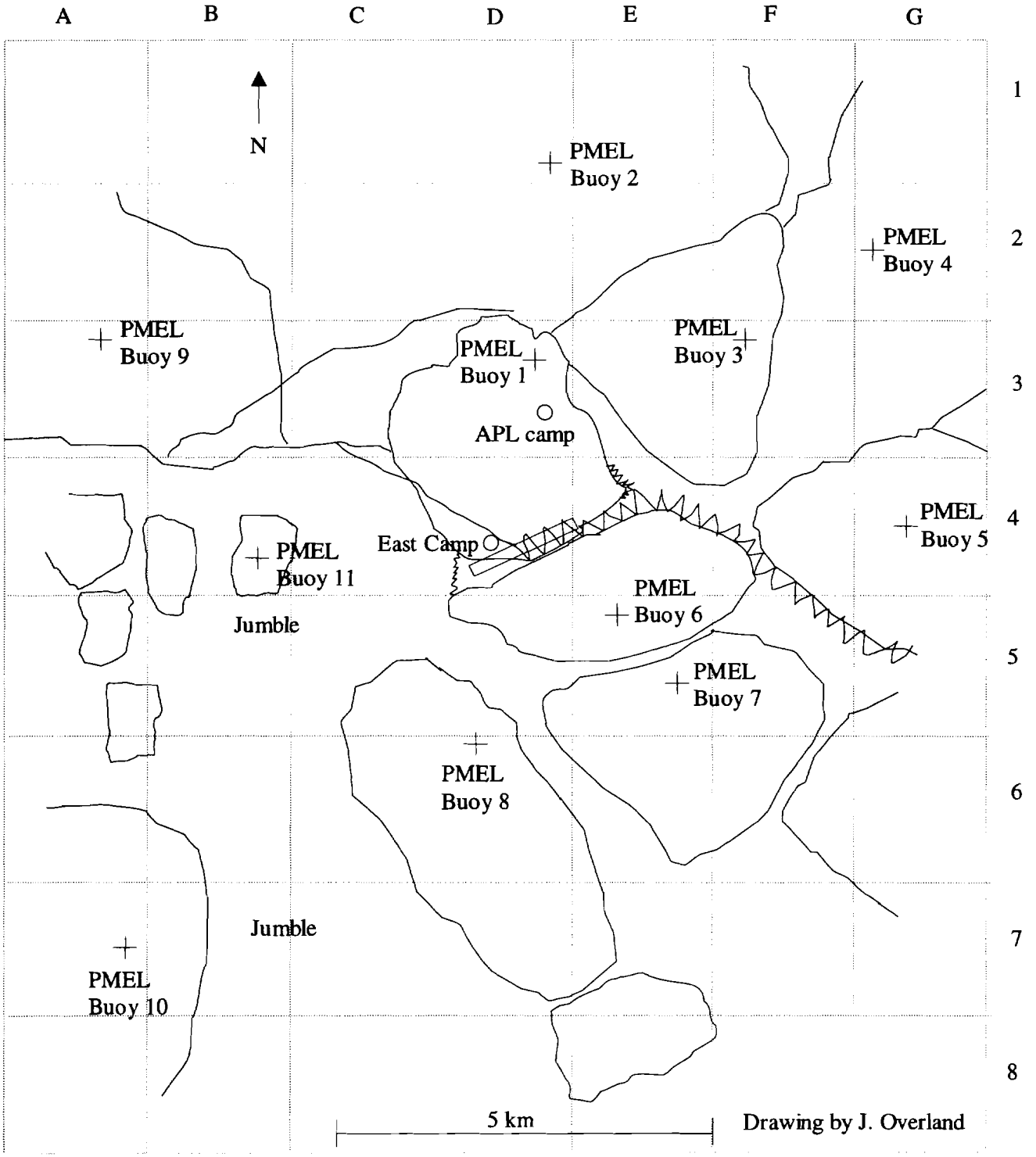

Map 4. SIMI East Camp, April 1994.

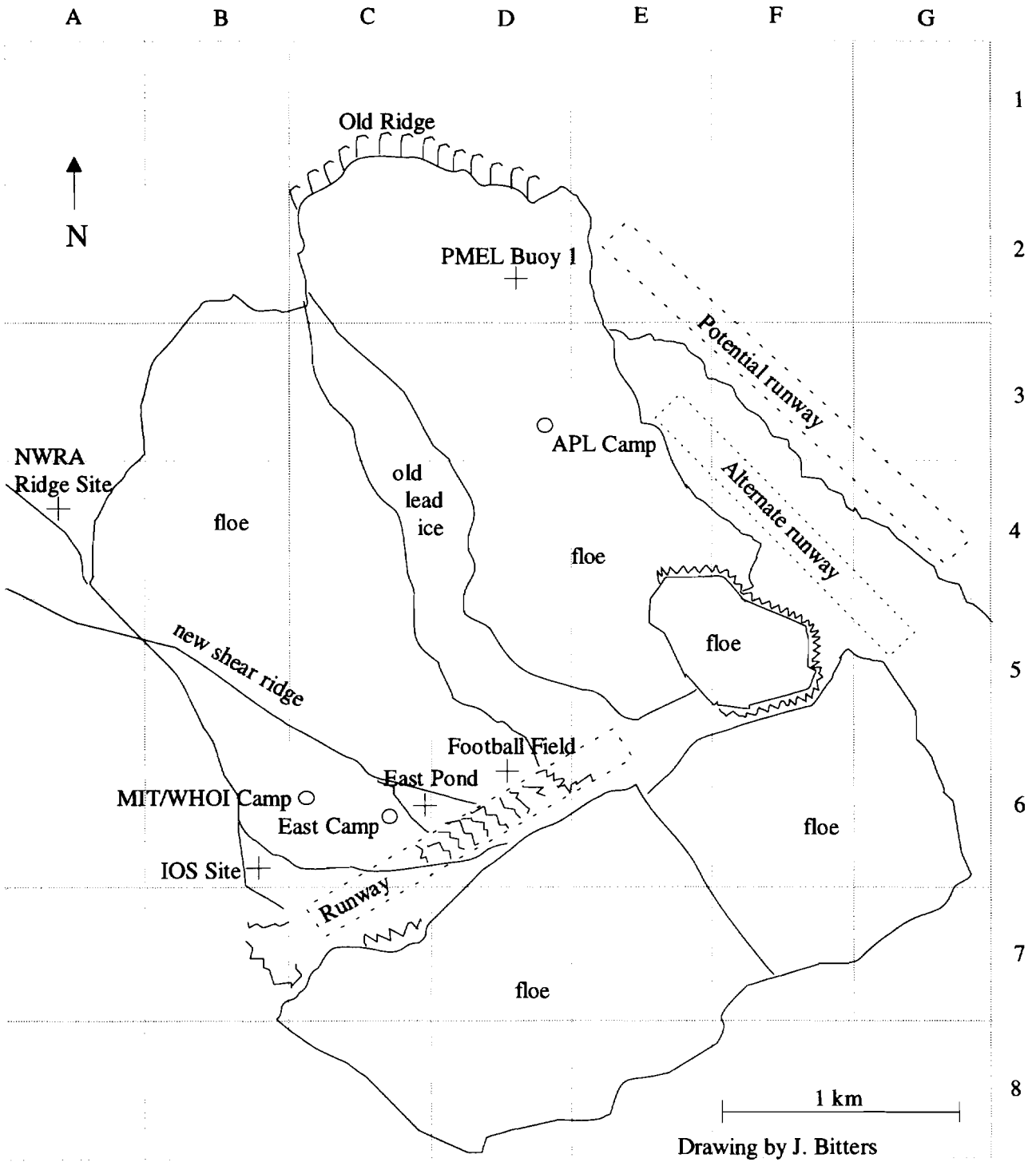

2. ACOUSTICS

Papers included in this section are the following:

"Acoustic and Seismic Studies of Ice Mechanics," by Dr. David Farmer (P.I.) and Dr. Yunbo Xie of the Institute of Ocean Sciences

"Transarctic Acoustic Propagation," by Peter Mikhalevsky of Science Applications International Corp., Arthur B. Baggeroer and Henrik Schmidt of the Massachusetts Institute of Technology, Keith von der Heydt and Edward K. Sheer of Woods Hole Oceanographic Institute, and Alexander Gavrilov of AcoustInform Ltd. Co.

"Sea Ice Failure Mechanisms," by Robert S. Pritchard of IceCasting, Inc.

"Sea Ice Mechanics Research: Tomographic Imaging of Wave Speeds and Acoustic Emission Event Localization," by Subramaniam D. Rajan of Woods Hole Oceanographic Institution

"Seismo-Acoustic Remote Sensing of Ice-Mechanical Processes in the Arctic," by Henrik Schmidt, Arthur B. Baggeroer, and Ira Dyer of the Massachusetts Institute of Technology and Keith von der Heydt and Edward K. Scheer of Woods Hole Oceanographic Institution

"SIMI Winter-Over Geophone/Hydrophone System," by Dr. Peter J. Stein (P.I.), Mr. Douglas W. Andersen, Mr. Armen Bahlavouni, and Mr. Steven E. Euerle of Scientific Solutions, Inc. and Mr. Gerald M. Santos and Mr. Richard K. Menoche of the Naval Undersea Warfare Center Division Newport

Papers with additional information on acoustics in Section 6, Modeling:

"Sea Ice Mechanics Related to Thermally Induced Stresses and Fracturing of Pack Ice," by Dr. James K. Lewis of Ocean Physics Res. & Dev. and Dr. Peter J. Stein of Scientific Solutions Inc.

Acoustic and Seismic Studies of Ice Mechanics

Dr. David Farmer (P.I.), Dr. Yunbo Xie, Institute of Ocean Sciences, Sidney, BC, Canada

Scope of Model and/or Data Set

The geo-hydrophone array (the main system) used in SIMI experiment consisted of five hydrophones and five geophones. The maximum spacing of the array was 200 meters forming a cross configuration (Figure 1). The maximum hydrophone depth was 20 meters. Geophones in all deployments were frozen into the ice making secure contact with the surface.

Given the uncertain nature of natural ice events (both in location and time), a portable recording system was also brought to the camp site. This system had two hydrophones and could be flown on a helicopter to an active site to observe on-going events. All the hydrophone and geophone signals were digitally recorded on VHS tapes. Both systems digitized the data at a rate of 176 kilo-bytes per second. This rate translated into various sampling frequencies for hydrophone and geophone channels depending on multiplexing modes. Table 1 summarizes features of all the sensors:

Table 1: Summary of Sensors of the two Systems

Sensor(s)	Make	Sampling Freq.	System
H_{1-5}	MetOcean MH5092	11025 Hz	Main
G_1	OYO HS1-LP3D	5600 Hz	Main
G_{2-5}	Mark L-28D	680 Hz	Main
Ha, Hb	MetOcean MH5091	44100 Hz	Portable

Although our main goal in SIMI was to observe active ice events, the uncertain nature of these events limited our chances. The relatively short camp time allocated to us (2 weeks) and logistical difficulties in deploying the main system beyond distances reachable by snowmobiles also hindered our efforts. To ensure the best use of the main system, before finalizing the deployment site, we had utilized the geo-hydrophone array for monitoring a number of mechanical tests on ice samples conducted by the SIMI ice mechanics groups led respectively by Max Coon, Robert Pritchard and John Dempsey. These tests were carried out at sites within walking distances from the ice camp. They simulated various mechanical failure modes associated with ridging and lead formation processes. The geo-hydrophone array system was deployed 3 times at 3 different sites near the main camp for the entire experimental period.

The mechanical testing of ice samples and seismic-acoustic sensing of sound radiated from these tests formed the basis for collaborations between the IOS and other ice mechanics groups at the camp. Such collaborations allowed us to focus

on investigations of acoustic and seismic emissions from failure modes controlled by the tests. These controlled tests represented idealization of natural failure processes. Nevertheless they allowed observation of radiated signals from known sources. Therefore, relationships can be established between a particular failure mode and its acoustic and seismic emissions.

The geo-hydrophone system was used in continuous listening mode for most of the time after being deployed at its permanent site. The system recorded many naturally-occurring events near the camp although most of these were due to thermal forcing. To acquire acoustic signals from active ice events occurring at remote areas from the camp, the portable ambient sound recording system was set at a standby mode, ready to be flown to an active site by the camp helicopter on a short notice. On April 16 and 19, active ice events were observed in an ice field about 90 nautical miles south of main camp. The system was promptly brought to the site and deployed beside a refrozen lead where several hours of ice rafting, stick-slipping and rubbing acoustical data were obtained. Part of the scenario was also simultaneously filmed.

Observations of Acoustic and Seismic Radiation in Simulated Ice Interaction Tests: collaborative work with Coon and Pritchard

On April 8, we deployed our geo-hydrophone system at a test site near the camp where Max Coon and Robert Pritchard conducted an ice failure simulation experiment. The test was carried out on a smooth first-year ice field adjacent to a rough multi-year floe. Small ice samples with individual volumes less than $1m^3$ were taken from the field. These samples were then used for simulating various failure modes associated with a ridging process. The simulation included flip-flopping and dropping of these samples onto the first-year ice surface, dragging them on dry, wet and snow-covered areas and rafting against rough surfaces. The testing area was encompassed by our geo-hydrophone array. Both seismic and acoustic signals were recorded by our system. Figures 2 and 3 are two examples of signals due to flip-flopping and dragging on a dry surface, respectively. As expected flip-flopping generated strong flexural waves on geophone channels. We found that ice-dragging on the dry surface induced intermittent pulsing signals which best simulated the stick-slip process. This becomes evident when the signal is compared later with stick-slipping acoustical pulses induced by natural events. Also, the signal-to-noise ratio for these pulsed signals is much higher on the hydrophone channels than on the geophones (see Figure 3). This again confirms that acoustic emission due to failure suffers relatively minor alteration if propagating through acoustical channels beneath the ice. Thus, hydrophone signals are superior to seismic signals for inversion of failure mechanisms. Similar tests were also conducted at the permanent array site.

Observations of Acoustic and Seismic Radiation in Large-scale Ice Fracture Experiment: collaborative work with Dempsey

The simulation of ice fracturing process at scales of meters to tens of meters is more relevant to the study of large-scale floe failure under natural forces. Previous field collaborations between the IOS acoustical group and Dempsey's ice fracture mechanics group have yielded valuable acoustic data from controlled fracture tests (see Xie and Farmer 1993). The SIMI program brought our two teams together again. This provided another opportunity for simultaneous observations of large-scale fracture tests on field ice using both mechanical means and the geo-hydrophone array.

The test site was located adjacent to the SIMI main camp where a multi-year ice field had recently broken up. This created a few large multi-year floes around the camp. One of these floes was approximately 80m across. This thick floe ($4 \sim 5$ meters) covered with packed uneven snow, was surrounded by a layer of newly formed ice (less than 2 meter thick). The floe was chosen for the large-scale fracture test by Dempsey. The purpose of the test was to use a controlled tensile load to split the floe. The method was similar to that used in a previous fracture experiment (see Xie and Farmer, 1993 for detailed description). A 20-meter long slit was cut through the floe from its edge. A few flatjacks were inserted into the slit, which were then inflated with air under pressure, applying tensile loads throughout the entire ice thickness. At tip of the slit (or crack) a sensor was deployed across the open crack to measure the crack tip opening displacement (CTOD). Both the loading and CTOD output were controlled and monitored, respectively by Dempsey's system.

The deployed geo-hydrophone array system consisted of 5 hydrophones and 5 geophones. Hydrophones were deployed at 20m beneath the new ice around the multi-year floe, and geophones were deployed at cleared areas on the floe surface. Figure 4 shows the geometry of the geo-hydrophone array. The maximum spacing between hydrophones was approximately 90 meters. This array was more sophisticated than the one used in our 1993 Resolute Bay Experiment (which had only two hydrophones, and, therefore, could not independently position the fracture trajectory). The present array constituted an over-determined system for tracking the crack positions although it turned out that reliable correlation analyses could only be obtained through data recorded on the H1, H2 and H5 channels during the early stage of the fracturing test. This is because prior to the final fracturing, most cracks occurred at or near the slit tip resulting in higher signal-to-noise ratios on channels of the three nearby hydrophones. Figure 5 shows an example of tip cracking acoustic signals detected by the 5 hydrophones: H3 and H4 sensed small signals. Apart from the range effect, weak signals on H3 and H4 channels might also result from radiation patterns of such tensile cracking sound which might show maximum radiation normal to the fault planes (in this case more

or less perpendicular to the slit). It is also apparent that most detected cracking signals are milli-second long exponentially decaying sine waves.

The fracture test lasted about 40 minutes during which 7 tensile loadings were applied cyclically to the floe. Figure 10 show the CTOD records (provided by Dempsey) for the entire experiment. The corresponding loading history looks very similar to the CTOD record (Dempsey, personal communications). From these results, it is evident that the floe was fractured to some extent by the loading, and considerable cracking occurred near the tip of the pre-cut slit. Based on the raw acoustic signals recorded on H1, we calculated the corresponding root-mean-square sound level, and presented the results in Figure 7. These *rms* values were based on statistics of raw data sliced by a 2.5-second long window. A large amount of noise from other activities at the site contaminated the signals, especially the small cracking sounds. These activities included walking and snowmobile maneuvering on the snow. Nevertheless, one can still identify the two major cracking events in Figure 7. To extract cracking signals from the raw data, a digital filter was imposed to hi-pass filter the acoustic data at a cut-off frequency of 2 kHz. This certainly reduced but did not eliminate the noise. To further avoid the noise problem, we carefully scanned the audible acoustic recordings and successfully identified sections of data that contained cracking signals. A more detailed records of *rms* sound level (based on windows of 185-ms long hi-pass filtered data) was obtained for these selected data sets. The results are shown in Figure 8 together with the CTOD records. It is seen that most cracks result from loading though maximum cracking activities occur prior to the maximum openings or loadings.

To evaluate the cracking activity and its relationship to CTOD, we used the same selected hydrophone data sets to estimate the cracking rate, i.e., number of individual cracks per second. The procedures involved identifying individual cracks from the raw data. Since most cracks generated milli-second long pulses, these pulses can cause sudden increases of under-ice acoustic power at milli-second time scales. Thus, an 11-millisecond long window was chosen to segment the data. The *rms* values of these data segments were then calculated. A cracking event is identified if the *rms* value of the data segment is greater than that of the previous segment by 2. This threshold was chosen based on many test runs, and proved reasonably robust in identifying cracks. Cracking rates were estimated for the two major fracturing processes observed in both CTOD and under-ice sound level records. Figures 9 and 10 present the 2 cracking rates as a function of time, and corresponding CTOD records.

From these results, we see that the first major fracturing process lasted about 40 seconds with a total of 784 identified individual cracks, and the final fracturing took only 10 seconds with less than 200 cracks. Both processes indicated that

cracking intensified as the load increased. However, cracking rates reached their maxima prior to loading peaks.

The attempt to split the floe during the first 30 minutes of cyclic loadings did not succeed even though a large number of cracks were detected (see Figure 8). The last attempt to raise loads resulted in destruction of the flatjack. At that point, there were still no traceable surface fractures to confirm whether the floe had been split. The thick and uneven snow layers on the floe surface further hindered *in situ* investigation of fracturing consequences through mechanical means. Therefore, the revelation of fracture development (cracking trajectories) can only be achieved through analyses of acoustic emissions from induced cracks. To track the locations of these cracks, cracking signals received by 3 hydrophones (H1, H2 and H5) were cross-correlated using H5 as a reference channel. Data were hi-pass filtered (at 100 Hz) and segmented by a 90-millisecond window before performing correlation analyses. Peaks from each correlation results were used to estimate delays between time arrivals among the cracks detected on the three hydrophone channels. Figure 11 shows 2 sets of correlation peaks for the first major fracturing scenario with positive values corresponding to delays between signals recorded on H1 and H5, and negative values between H2 and H5. Due to the intermittent nature of the cracking process and spatially sensitive signal strengths of cracking sounds, we found it necessary to interpolate these data points in Figure 11 in order to obtain coherent delay trends. A spline-fit model was implemented to extract the trends (indicated by lines in Figure 11). The fitting curves were then used to infer fracture development as a function of time. Based on array geometry and floe size, an iteration routine was developed to search for crack positions for any given delays on the curves. This method allowed successful inference of crack locations as a function of time, in other words the fracture history.

Figure 12 displays the crack trajectory during the first major fracturing. The result was based on a 20-second long acoustic recording during the fracturing. Crack positions were inferred at a 20-ms time interval. Development of the crack, referenced to the location of H1, is given in Figure 12b as a function of time. It is apparent that the fracture did not advance too far from the tip of the pre-cut slit. Therefore, we conclude that as of this time (30 minutes into the experiment) the floe remained unfractured.

To see if the last attempt was able to fracture the floe, similar correlation analyses were carried out for a 10-second data set recorded during the last loading. Figure 13 shows the correlation peaks and their interpolated trends which exhibit much larger variations than that in Figure 11. Figure 14a shows the corresponding trajectory. The crack locations were estimated in a 10-ms time interval. The corresponding crack advance is given in Figure 14b as a function of time. No significant crack growth (with respect to the slit tip) was observed up to the first 7 seconds when suddenly the cracking accelerated: in less than 1 second the crack tip advanced more than 10 meters.

Observations of Acoustic and Seismic Radiation from Natural Ice Rafting Events.

On April 16, a lead of open water was spotted from the air. The site location was approximately 90 nautical miles south of the main camp. Part of the open water had refrozen forming a layer of smooth thin ice which was only a few centimeter thick. Figure 5 is an aerial view of the site. A camp was established near the lead and it was observed that the lead started to close in causing active ice movements. Audible sounds were heard in the field which were related to natural ice rubbing, rafting and stick-slipping processes.

To record these signals, the portable ambient sound system was promptly flown to the site and the two hydrophones were deployed at the 5-m water depth through the lead ice. The horizontal spacing of the array was about 40 meters. A total of 3 hours of exceptional acoustical signals were acquired from April 16-19. These sounds were later correlated with various ice movements filmed with a video camera by Coon's group at close ranges from the sources. Although the camera and our ambient sound recording system were not synchronized, the strikingly similar acoustic signatures recorded by the camera's built-in microphone and our hydrophones allowed us to correlate some of the hydrophone data with visually detected ice events. The best example was a stick-slip process that occurred between two sliding ice sheets approximately 5-cm thick. The surfaces of the ice were dry and covered with frost. The sliding was in a stick-slip manner. The slipping frequencies and individual sliding distances were observed to be $1 \sim 2$ Hz, and a few centimeters, respectively. A 100-ms long stick-slip acoustic pressure signal is given in Figure 15.

There are two unique features. First, the signal consists of many similar pulses with semi-regular pulse-intervals, or using the seismological term the *recurrence time*. However, the recurrence time does vary from 2 *ms* to 6 *ms*. Second, there is a strong correlation between pulse amplitude and recurrence time: the larger the pulse, the longer the recurrence time. This correlation is illustrated in Figure 16 where the recurrence time (obtained through auto-correlation analysis of the stick-slip acoustic signal), and pulse-peak are plotted on a common time base. Such features are consistent with earthquake faulting theory: large earthquakes result from large area faulting caused by the release of a large amount of stress which has accumulated over a longer period, thus leading to a larger signal. According to the seismic inversion theory of faulting processes, the width of individual pulses is directly related to the slipping speed or distance. The inferred slipping distance is associated with the smallest slipping scales that can be resolved by the recording system. Figure 17 shows both temporal and spectral structures of a stick-slip acoustic pulse. The pulse is about 0.5 milli-second long, and its corner frequency is of order a few kilo-hertz.

The observed stick-slip process consisted of many spatial scales which resulted in multi-scale temporal structures in its emitted acoustic signals. Figure 18 is a 14-second long time series of sound pressure due to a stick-slip process.

The signal is composed of groups of pulses, and the recurrence times between these pulse groups range from 200 to 500 milli-seconds which are much longer than that between individual pulses. Such time scales are associated with the overall sliding distance from each slip which was estimated from the video recording to be of order centimeters. The acoustic emission reveals another interesting feature of stick-slip processes: the transition from stick-slipping to stable sliding. The sliding caused acoustic emission of multi-frequency bands at approximately 700 and 1500 Hz respectively. Rather than centering at these frequencies, the two bands fluctuated, which probably indicates the onset of a nonlinear vibration mode in the sliding ice.

Analysis and Publication Plans

The preliminary data analyses of SIMI data show that fracturing ice radiates acoustic and seismic energy into the water and surrounding ice field. Although these signals account for very small fractions of the total energy dissipated in the fracturing process, they provide an opportunity to use the seismic-acoustic sensing technique for tracking crack development and detailed failure processes. Using appropriate models, one can interpret observed acoustic and seismic features in terms of various parameters describing the faulting process. These include failure scales, cracking velocity, failure recurrence time, cracking energy, etc.

Further analysis will follow these preliminary findings:

1. The mechanical simulation of ice failure process is intriguing. Based on acoustic emissions from both simulation tests and natural events, it was found that ice rafting and dragging on dry surface best simulated the stick-slip process commonly observed in natural ridging and leading processes.

2. The large-scale floe fracturing experiment showed an average fracturing speed of approximately $50 m \cdot s^{-1}$. This value is similar to that observed in 1993 Resolute Bay experiment (Xie and Farmer, 1993). Maximum failures are usually *preceded* by maximum cracking activities.

3. Stick-slip processes generate unique acoustic pulses. These pulses show recurrence times ranging from milli-seconds to tens of milli-seconds. In some cases, it is observed that the pulse peak increases as the recurrence time increases. Stick-slip sounds also exhibit signal structures of multiple time scales ranging from milli-seconds to seconds. These time scales are related to various sliding scales.

Publication is planned for each of these three components of our contribution to SIMI.

References

Farmer, D, J. K. Lewis, P. Stein, W. B. Tucker and Y. Xie, *Ice mechanics-acoustics experiment, Allen Bay , March 1992* A report to the Office of Naval Research, published at Institute of Ocean Sciences, Sidney, BC, Canada, April, 1992.

Rottier, P., *Floe pair interaction event rates in the marginal ice zone* J. Geophy. Res. Vol. 97, No. C6, pp. 9391-9400, 1992.

Stein, P. J, *Interpretation of a few ice event transients* J. Acoust. Soc. Am., 83, pp. 617-622, 1988.

Xie, Y and D. M. Farmer, *Acoustical radiation from thermally stressed sea ice* J. Acoust. Soc. Am., 89(5), pp. 2215-2231, 1991.

Xie, Y and D. Farmer, *The sound of ice fracturing due to propagating tensile failure* A report to the Office of Naval Research, published at Institute of Ocean Sciences, Sidney, BC, Canada, July, 1993.

Xie, Y , *Acoustical tracking of ice failure processes* Presented at 3rd Conference on *Sea Surface Sound* March 7-12, 1994, UCLA.

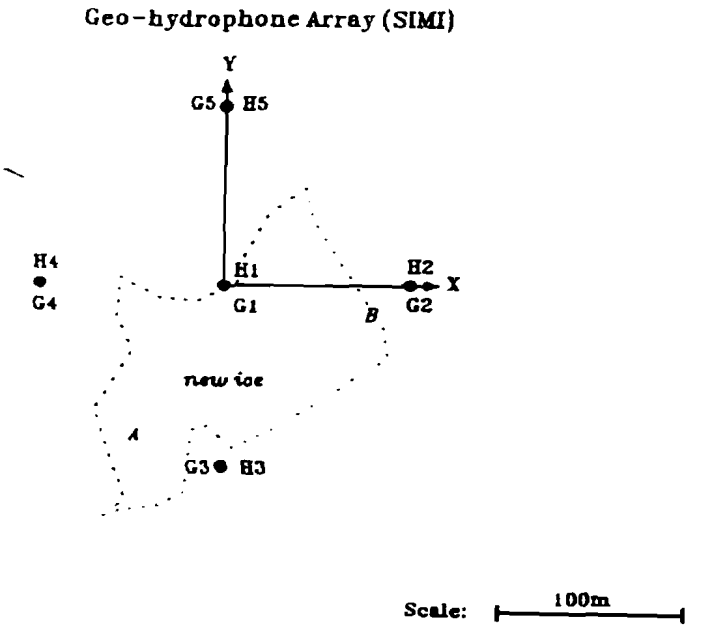

Figure 1. Configuration of a geo-hydrophone array deployed at SIMI permanent site. $H_{1,2,3,4,5}$ represent five hydrophones forming a 200 m × 200 m horizontal array at 20 m depth. The 5 tri-axial,geophones ($G_{1,2,3,4,5}$) were deployed on the ice surface. The dashed line (obtained via acoustical approach) outlines an area of new ice.

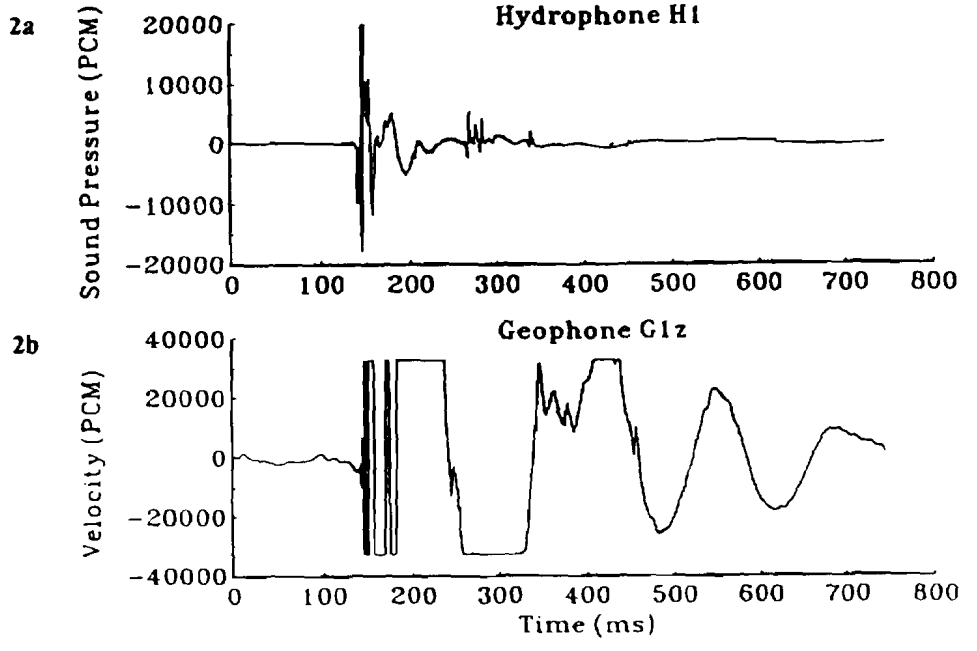

Figure 2. Acoustic and seismic signals (presented respectively in Figs. 2a and 2b) due to the flopping of an ice sample onto the surface of an ice field. The signals are measured in terms of digital counts by a Pulse-Coded-Modulator (PCM). The strong seismic wave saturates the vertical channel of geophone G_1.

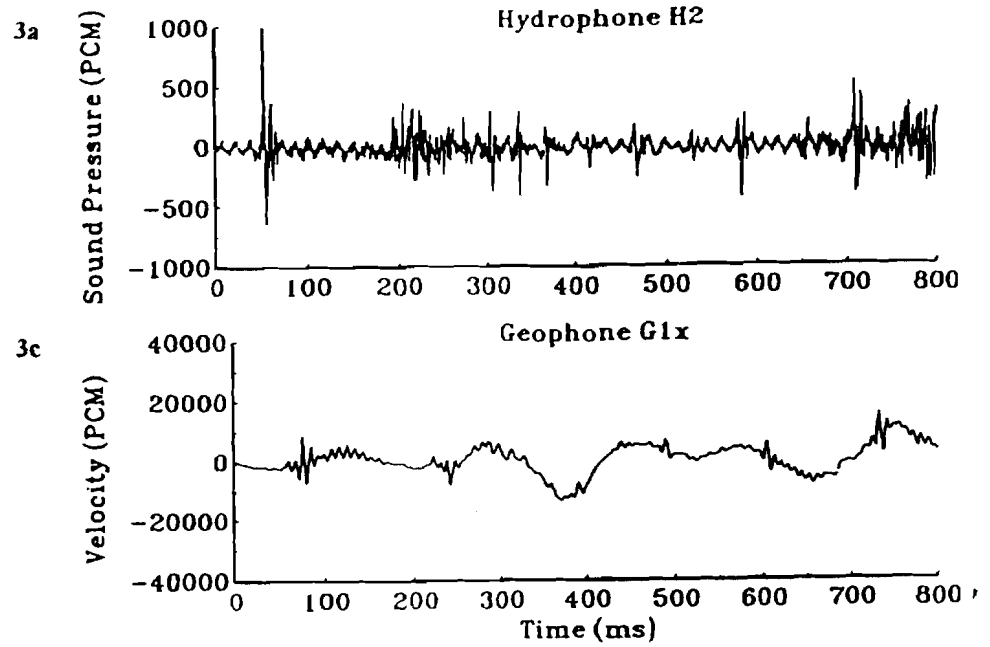

Figure 3. Acoustic and seismic signals (presented respectively in Figs. 3a and 3b) due to dragging of an ice sample on a dry ice surface. The pulsing signals recorded on the hydrophone channel resemble that due to a natural stick-slipping process.

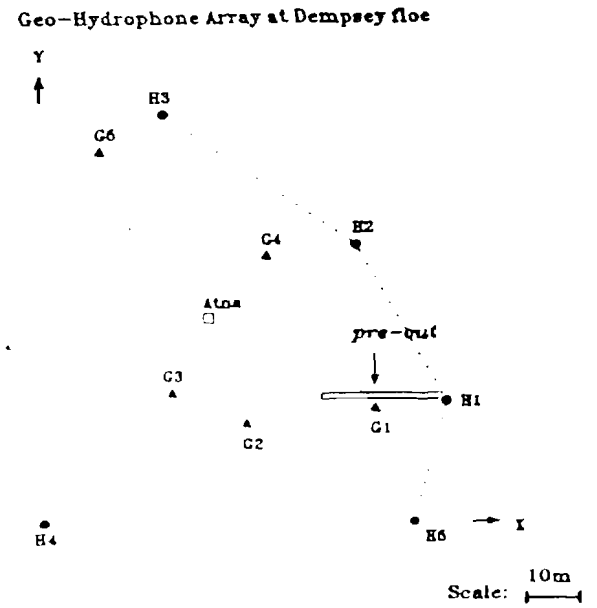

Figure 4. Configuration of the geo-hydrophone array deployed at Dempsey site. Also shown are the geometry and location of the pre-cut slit.

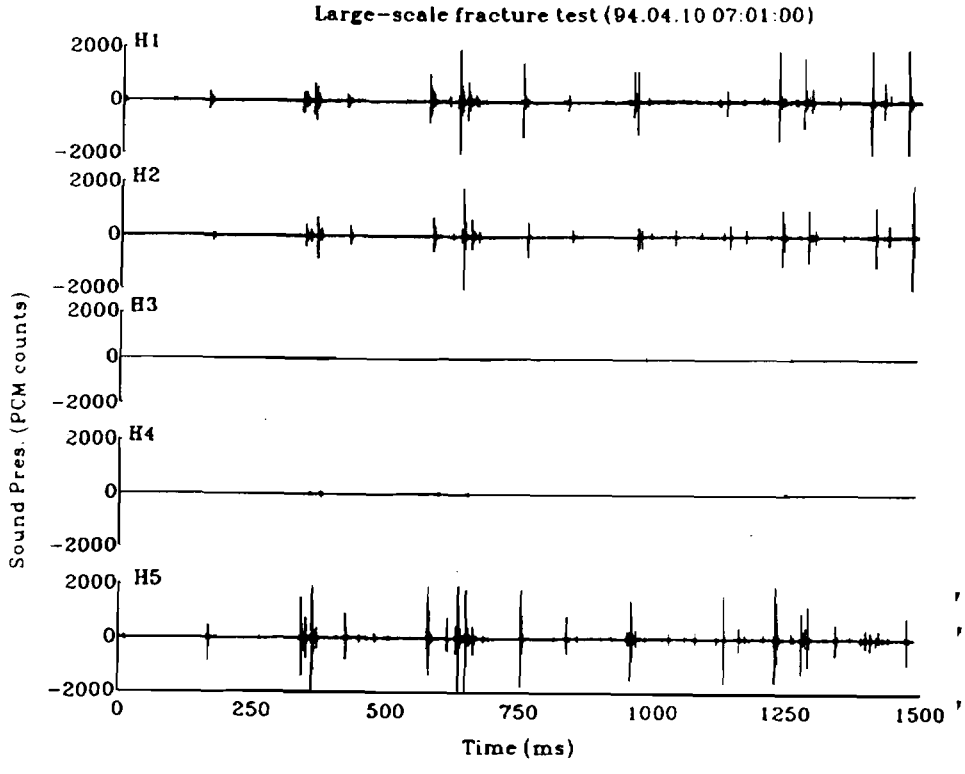

Figure 5. Acoustic signals due to tip cracking of the slit under controlled loads. Note similar signal strengths on $H_{1,2,5}$ channels and weak signals on H_3 and H_4.

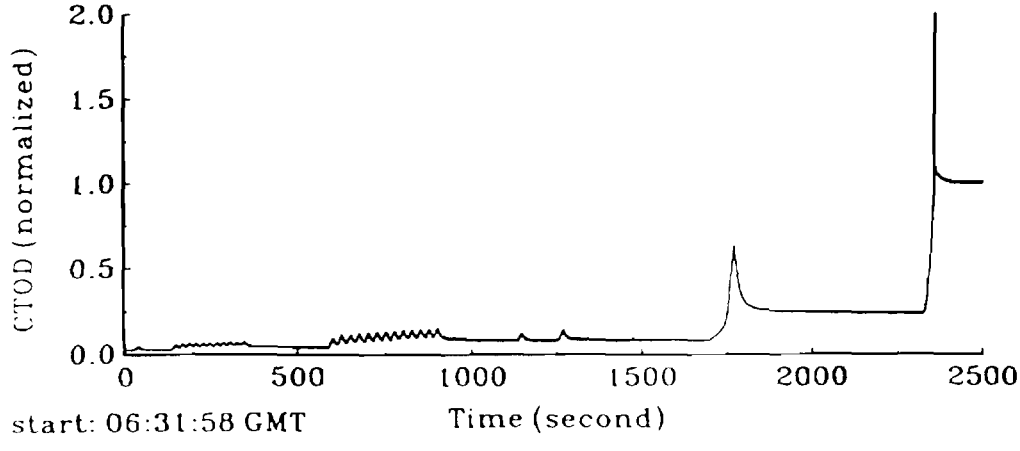

Figure 6. Crack tip opening displacement record for the entire fracture experiment (Courtesy of John Dempsey). A total of 7 groups of events were detected by the CTOD sensor. The data have been normalized.

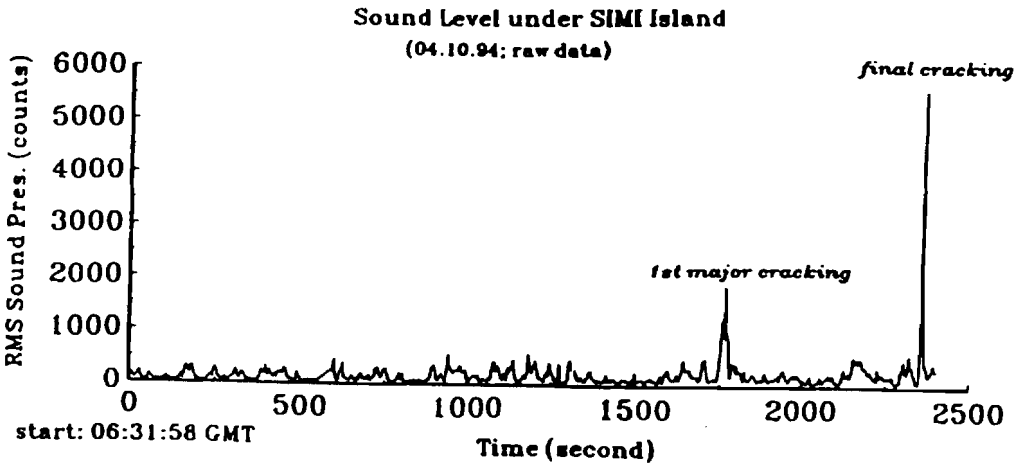

Figure 7. Root-mean-square sound level based on the raw data recorded on Hi channel for the entire fracture experiment. The 2 major cracking events are clearly identified but small cracking signals are masked by on-site artificial noise and cannot be unveiled.

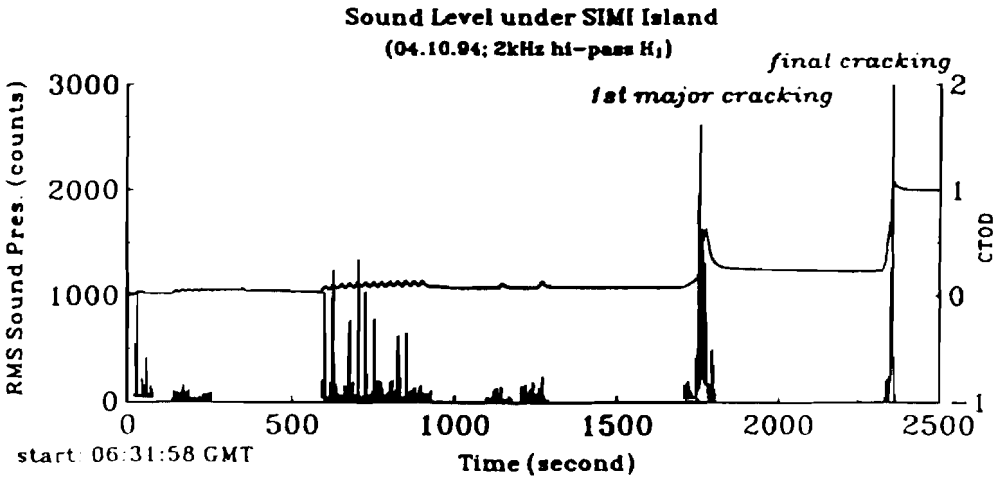

Figure 8. Root-mean-square sound level based on 2-kHz hi-pass data recorded on Hi channel for the entire fracture experiment. Apart from being filtered, the data have been carefully scanned for audible cracking signals. Clearly identified are not only the 2 major cracking events but also small cracking signals. These acoustical events correlate very well with the CTOD record.

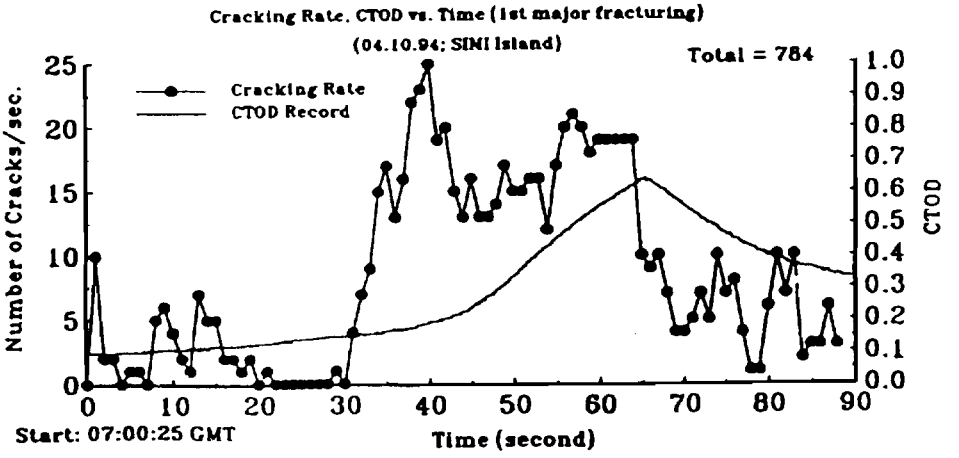

Figure 9. Cracking rate versus time during 1st major fracturing (identified in Figure 8). Also plotted is the CTOD record for the same period. A total of 784 cracks are identified over a 90-second period.

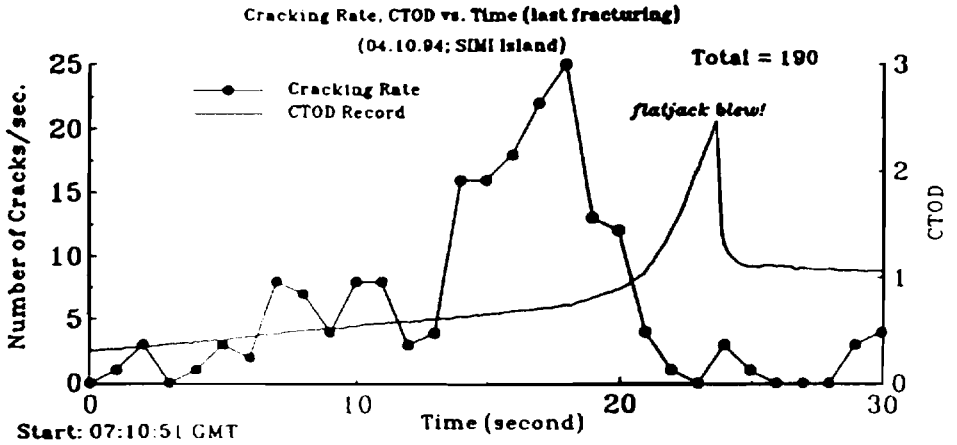

Figure 10. Cracking rate versus time during the last fracturing (identified in Figure 8). Also plotted is the CTOD record for the same period. A total of 190 cracks identified over a 30-second period.

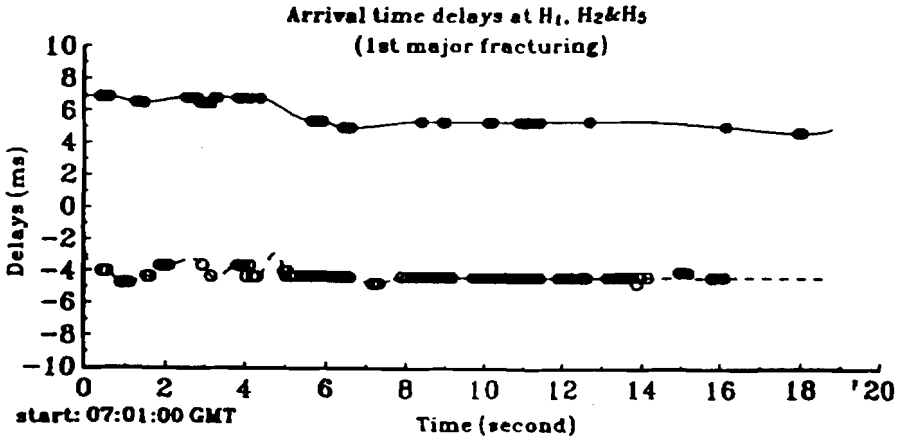

Figure 11. Delay relationships between arrival times of cracking sound at H1 (solid line) and H2 (dashed line) for 1st major fracturing process (using arrival times at H5 as reference). Empty and solid circles are delay estimates based on cross-correlations among acoustic recordings (sliced by a 90-ms window) on the 3 hydrophone channels. These estimated delay values are interpolated giving delay relationships as a continuous function of time.

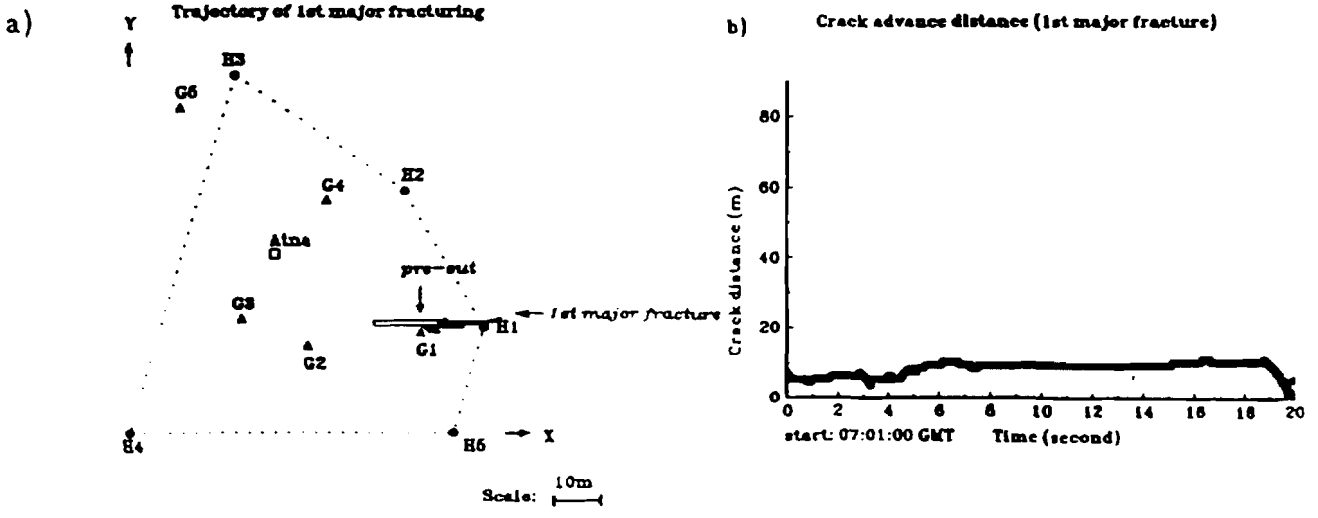

Figure 12. Fracture development during 1st major fracturing. a) Crack positions on the array frame; b) Cracking distance as a function of time using H1 location as reference.

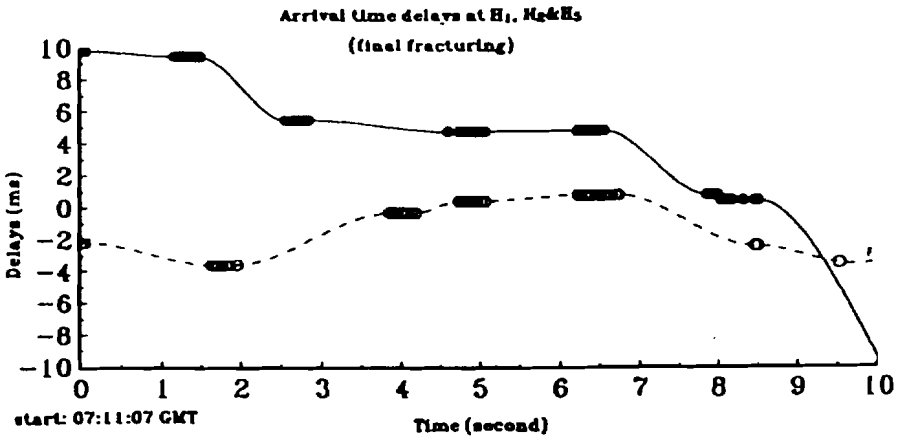

Figure 13. Delay relationships between arrival times of cracking sound at H1 (solid line) and H2 (dashed line) for the last fracturing process (using arrival times at H5 as reference).

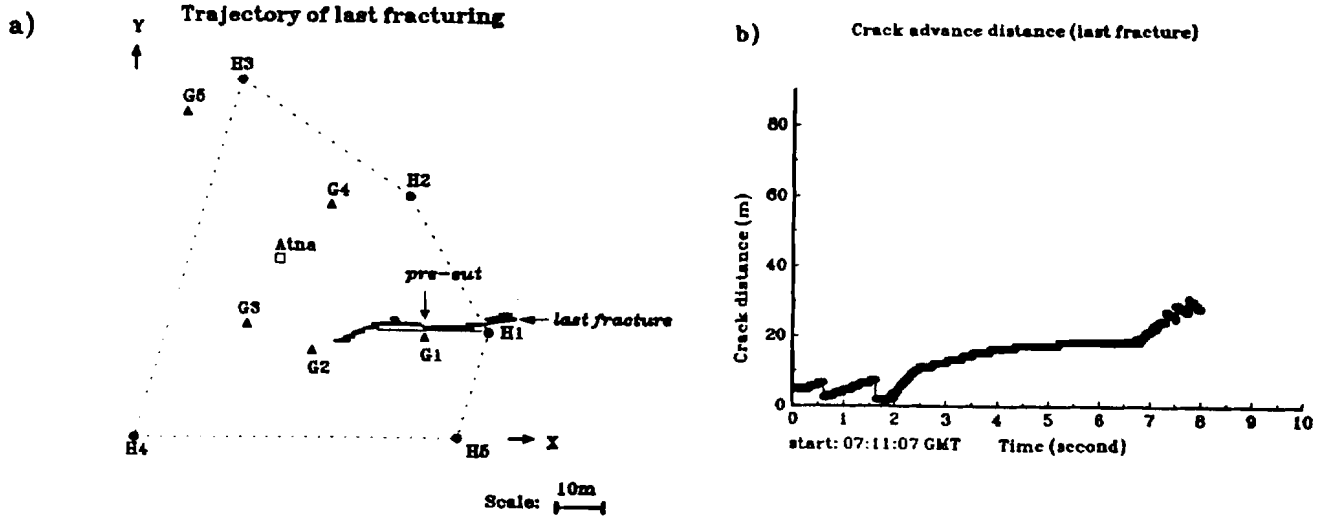

Figure 14. Fracture development during last fracturing. a) Crack positions on the array frame. b) Cracking distance as a function of time using H1 location as reference.

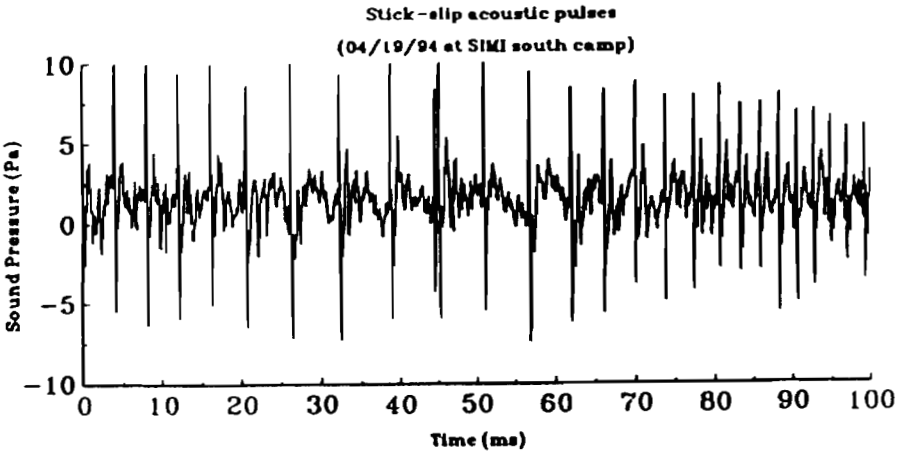

Figure 15. Time series of under-ice acoustic pressure due to stick-slip ice movements.

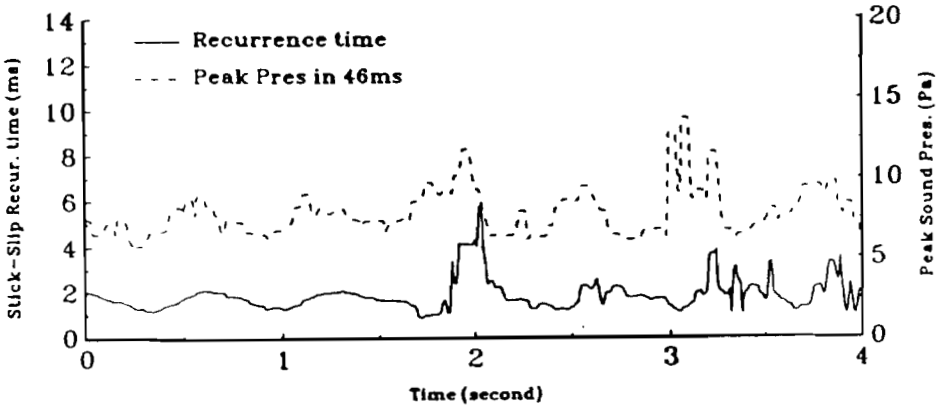

Figure 16. Recurrence time and peak pressure as a function of time of the stick-slip pulses shown in Figure 15. Note the two curves show similar phase variations.

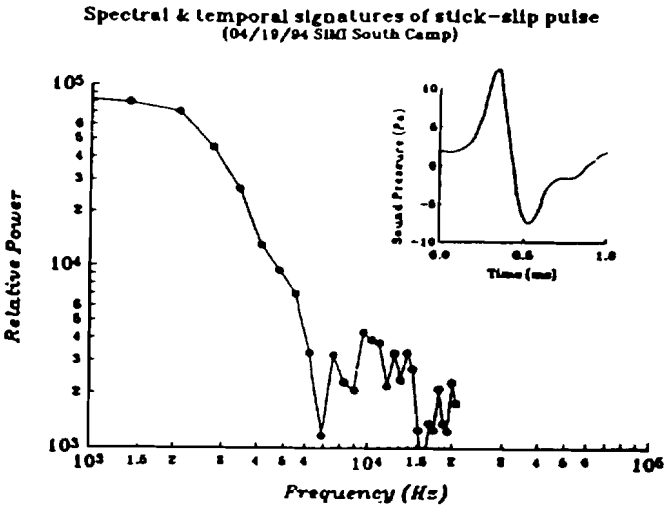

Figure 17. Power spectrum and temporal structure of an individual stick-slip acoustic pulse.

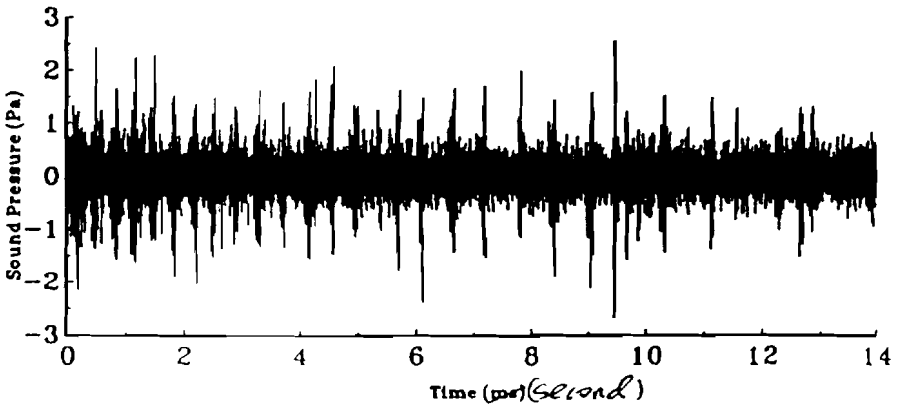

Figure 18. Time series of a stick-slip acoustic signal showing longer temporal structures.

TRANSARCTIC ACOUSTIC PROPAGATION

PETER MIKHALEVSKY
Science Applications International Corp.

ARTHUR B. BAGGEROER and HENRIK SCHMIDT
Massachusetts Institute of Technology

KEITH VON DER HEYDT and EDWARD K. SCHEER
Woods Hole Oceanographic Institution

and

ALEXANDER GAVRILOV
AcoustInform Ltd. Co., Moscow

Scope of Model and/or Data Set

OBJECTIVES

The objective of the Transarctic Acoustic Propagation (TAP) experiment was to test the feasibility of using long-range, low frequency acoustic thermometry for climate study work in the Arctic [1, 2, 3]. Since trans-basin propagation had never been attempted before in the Arctic there were several fundamental issues that needed to be resolved; (1) how much propagation loss would there be at 20 Hz, and would there be enough useful received energy, (2) would the continuous wave (CW) and maximal length sequences (MLS) remain coherent enough to achieve sufficient narrowband processing gain, and pulse compression gain respectively, and (3) would there be a repeatable and predictable mode/ray arrival structure? All of these issues were resolved successfully in the affirmative. In addition the measured modal arrival times indicate faster propagation speeds than predicted using historical climatology. The reason for this discrepancy could be warmer water in the Arctic as reported during recent icebreaker CTD measurements in the Arctic [5, 6]. This will be one of the important issues of the on-going research.

TURPAN CAMP SOURCE

Ice camp Turpan was established on April 9, 1994 at 83x 26 N and 27x 10 E by a joint U.S. and Russian team. An acoustic source built by the Institute of Applied Physics in Nizhny Novgorod for this experiment was deployed at Turpan. The acoustic source was based on a well tested electromagnetic design [7]. The source level transmitted was 195 dB re 1 fPa or 250 watts acoustic. Acoustic transmissions were started at 0900Z on April 17 after a day of testing and continued through 1400Z on April 22. Forty-three (31 CW and 12 MLS) transmissions centered at 19.6 Hz each of one hour duration (except for two half-hour transmissions at 17.6 Hz and 21.6 Hz) were successfully completed (Table). Receiving

TRANSARCTIC ACOUSTIC PROPAGATION EXPERIMENT

April 1994

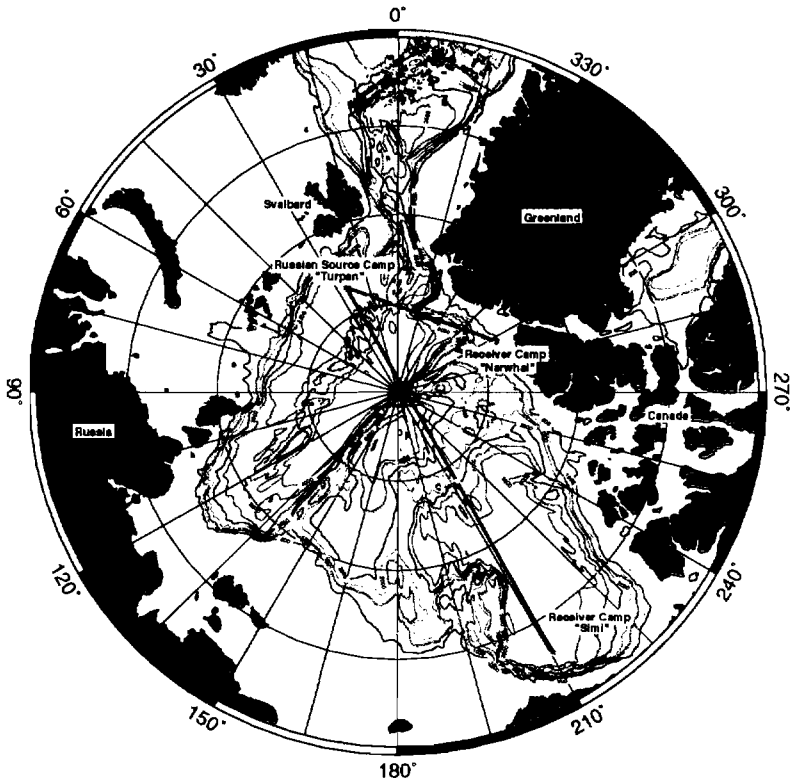

Src Camp "Turpan": 83 30.0' N, 26 0.0' E (North of Svalbard)
Rcvr Camp "Narwhal": 83 52.5' N, 62 52.9' W (Lincoln Sea)
Rcvr Camp "Simi": 72 59.9' N, 149 35.8' W (Beaufort Sea)

FIGURE 1. Geographical locations of the source and receiver camps during the TAP experiment

acoustic arrays were located in the Lincoln Sea at ice camp Narwhal, and in the Beaufort Sea at ice camp SIMI (Sea Ice Mechanics Initiative) (see following section). A 19 element vertical array was deployed at Narwhal with the elements spaced at approximately every 30m. The locations of the source- and receiver camps are shown in Fig. 1.

SIMI CAMP RECEIVING ARRAYS

With the primary objective of monitoring and localizing ice activity during the Spring SIMI field experiment, MIT/WHOI deployed 2 hydrophone arrays, approximately 300m from the main East Camp area, both of which were also used for recording the TAP transmissions in the period Apr.17–22, 1995. A vertical line array (VLA) of hydrophones, having 32 sensors

"TURPAN" transmissions. All transmissions on "regular schedule" except where noted. Start times shown, one hour transmission.

Date - 0900z, 1100z, 1300z, 1500z, 1700z (day schedule)
1900z, 2200z, 0100z, 0400z, 0700z (night schedule)

4/15 - Source testing in air and @ 6m depth
4/16 - Source testing at 6m, 20m, 30m, 40m, 50m, 60m depth
1930-2030z 19.60746Hz @ 190 dB
4/17 - CW, CW, M255(note 1), CW, M511(note 1)
CW, CW, CW, CW, CW

All M-sequences on and after 4/18 are 12.5 cycles/digit

4/18 - CW(note 2), CW(note 2), M255

- Secured transmissions -

4/19 - 1500z-1630z intermittent source testing
1630z-1700z CW @ 21.6 Hz
1900z-2000z CW @ 19.6 Hz
2040z-2100z CW @ 17.6 Hz
2200z-2300z M255

CW(note 3), M255, CW (regular night schedule starting @0100z)

4/20 - CW, CW, M255, CW, M511(note 4)
CW, CW(note 5), CW, CW(note 7), CW
4/21 - M127, CW, M1023, CW(note 6), M511(note 8)
CW, CW, CW, CW, CW
4/22 - M127, CW, M255(note 9)

- End of experiment -

Notes: 1: 25 cycles/digit +/-pi/4 modulation
2: generator (and rubidium clock) turned off after transmission

3: this CW and all following CW's @ 19.6Hz
4: this sequence had problems during transmission, source unable to make phase transitions cleanly
5: CW signal went off and then on at ~2226z
6: tone went off and on again twice around 1514z
7: signal went off @ 0458z erratic until 0500z
8: pi/2 phase shifts observed ~1730z
9: waveform distorted possible mechanical problem

linearly spaced from a depth 62 to 279 meters was deployed at the APEX site shown in Fig. 2. Surrounding this APEX was a horizontal array consisting of a 12 hydrophone circular deployment augmented by 12 additional sensors on nominal north-south and east-west legs 240m in length. Prior to the Transarctic Acoustic Propagation receptions, 8 more hydrophones were deployed for a total of 32 in the horizontal array (HA), all at a depth of 60 m. Fig. 2 labels nominally indicate the direction and range in meters of sensors as surveyed relative to the APEX. The sensitivities of the HA and VLA sensors was -160dBV

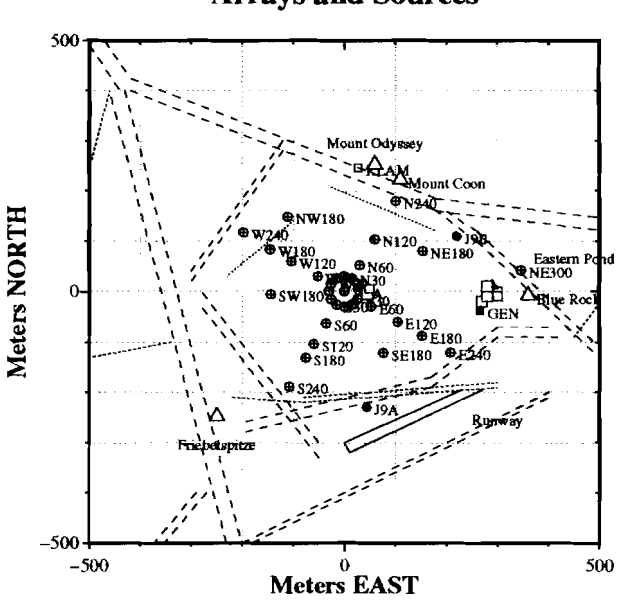

FIGURE 2. Seismo-Acoustic arrays deployed by MIT/WHOI on and around the East Camp floe. A total of 32 hydrophones were deployed in the horizontal array in a combined circular/cross configuration. A 32 element vertical array was deployed at the horizontal array apex. Two J-9 acoustic sources (J9A and J9B) were deployed for sensor tracking.

and -175dBV μPa/ $\sqrt{Hz}$ respectively.

With the exception of breaks for generator maintenance, data were acquired and stored continuously on 8mm tape (Exabyte), from a set of these sensors according to the table below.

DATE(Apr)	#data ch	BW(Hz)	time/tape	tape #s	QTY data
4 - 13	24 HA	300	26 hr	1,3 - 14	42 GB
14	32 HA,16 VLA	300	10 hr	15	3.5
15	32 HA,18 VLA	300	10 hr	16	3.5
16 - 18	32 HA,25 VLA	300	10 hr	17 - 22	23
18 - 23	32 HA,32 VLA	300	10 hr	23 - 33	45
23	32 HA	2700	2.5 hr	34 - 37	16

Two USRD J9 acoustic sources were deployed and each driven with a dual tone signal for use in localizing the VLA channels. Consequently, during the period 15-23 April, tonals in the 64 to 76 Hz region are evident.

Findings to Date

MIT/WHOI MODELING AND ANALYSIS

In parallel to their SIMI analysis work, MIT/WHOI has devoted a significant part of their effort to understanding the long-range Arctic acoustic environment. Existing propagation models in combination with new ice scattering theories are used to isolate the significance of individual acoustic signatures as indicators of climate-related changes in the ice cover and the oceanography. Also, with the effect of TAP experiments on marine mammals being an important environmental concern, MIT/WHOI has been investigating the feasibility of

using large-aperture acoustic arrays for tracking whales, in turn allowing for monitoring behavioral changes associated with deployment of tomgraphy sources.

Resolution Analysis

An area where the MIT group has achieved significant progress in the past couple of years, and which is of direct relevance to the TAP effort, is the development of models representing the theoretical resolution properties of ocean acoustic tomography. The cornerstone of this work, which builds on the pioneering MIT/WHOI work in matched field processing [8, 10], is a theoretical representation of the optimal resolution a particular sensor system can achieve in any relevant parameter. This modeling work is described in several publication [15, 16, 21, 22].

Comparison of ice scattering theories

Scattering theories developed at MIT by LePage & Schmidt [11, 14] and Kudryashov [23] have been used to predict long-range transmission loss in the Arctic. Kudryashov's method is based on perturbing an impedance boundary condition at the interface, while LePage & Schmidt's method uses a boundary operator approach to perturb all boundary conditions at the rough interface. Earlier comparisons showed very close agreement between the approaches [24], but this apparent agreement was seen because the MIT group had not included the effects of attenuation in the ice. Fig. 3 shows mode attenuation coefficients for scattering from the ice sheet calculated using the two methods, using a historical sound speed profile (GDEM) and typical ice parameters. The results in Fig. 3 were obtained assuming top and bottom of the ice to be rough, with identical but uncorrelated roughness statistics. Expressions from Kudryashov's paper, including ice attenuation, give nearly identical results to the MIT approach with zero ice attenuation. When attenuation is included, i.e with the two approaches modeling the same physical scenario, the boundary operator approach yields much higher mode attenuations as is evident from Fig. 3. Both approaches predict lower loss if the ice surface more realistically is assumed to be less rough than the bottom, but also in that case the MIT approach yields significantly higher losses than Kudryashov's approach.

This disagreement can be understood by considering scattering from a rough fluid-fluid interface. The boundary operator approach ensures that both the mean and scattered fields satisfy the two boundary conditions at the rough interface. The impedance boundary condition, however, is only a single boundary condition based on the the unperturbed reflection coefficient. As a result an expression for the scattered field derived from the impedance condition alone cannot satisfy both boundary conditions at the rough interface.

Sensitivity to ice parameters

LePage & Schmidt's [14] model can be used to study the sensitivity of modal attenuations and group speeds on parameters of the ice cover. Based on ice measurements it is assumed that ice thickness and roughness are correlated. Preliminary results show propagation has the highest sensitivity to ice thickness/roughness and roughness correlation length (each gives $\approx \pm$ 0.008 dB/km attenuation changes and $\approx \pm$ 0.1 m/s group velocity changes for mode 1 over the parameter range studied), less sensitivity to shear attenuation, and very little sensitivity to wave speeds or compressional attenuation in the ice. These results are qualitatively similar to the results obtained using the impedance scattering theory [25], but the MIT approach predicts a greater effect due to changing thickness.

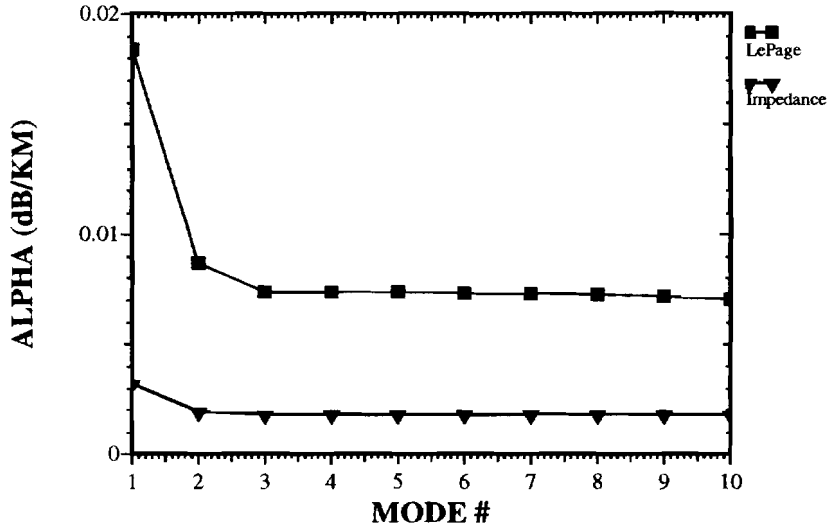

FIGURE 3. Mode attenuation comparisons. Both surface and bottom of ice cover are rough. Mean ice thickness H = 4 m., RMS roughness σ = 2 m., correlation length L = 22 m. Triangles represent Kudryashov's approach while the MIT approach yields results marked with squares.

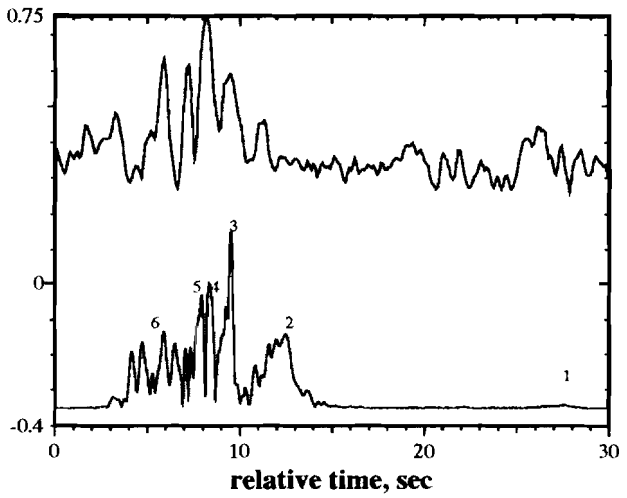

FIGURE 4. Data–model comparison. Top: VLA data, channel 27 Bottom: Coupled mode simulation

Time-series modeling

The mode code KRAKEN is used to generate time series simulations for the TAP scenario, with LePage's SELFCON code used to specify the boundary condition at the ice. Historical sound speed profiles (GDEM) are used for the modeling. Our results show that higher modes are strongly affected by mode coupling at the Lomonosov ridge. We also note that the sound speed profiles change gradually between the warmer Atlantic water and the cooler water in the Canadian basin. Gavrilov *et al* [25] report strong inter-annual variations in the penetration of the Atlantic water into the Arctic. Since mode arrival times are much more strongly affected by the front location than by any ice parameters, knowledge or estimation of the oceanography is quite important.

Figure 4 compares a pulse compressed arrival on the SIMI array at a depth of 272 m with a coupled-mode calculation for propagation of a Gaussian pulse, plotted vs. relative

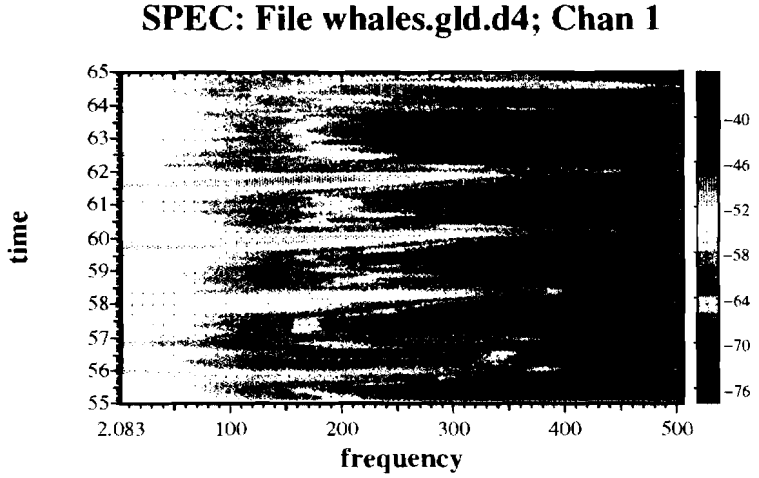

FIGURE 5. "Waterfall" display of whale calls recorded in the Fram Straits during CEAREX-89

arrival time. Individual modal arrivals are identified on the simulation result (lower trace). Although dispersion of the Gaussian pulse complicates the comparison, such simulations are used to identify modal arrivals in the data. We can explain differences in the detailed, relative modal arrival times by assuming that the warm Atlantic water penetrated deeper into the Arctic during the experiment than is shown in the historical sound speed data. If the front is shifted 500 km further along the path then the mode 2 - mode 3 separation largely disappears and the other modes shift slightly, giving even better agreement with the data.

Marine Mammal Tracking

The amount of marine mammals detected in the SIMI experiments were extremely sparse, both at the source and the receiver camps. This observation is consistent with the experience of the MIT/WHOI group that apart from the immidiate vicinity of the ice edge, the Arctic Ocean is extremely sparse in marine mammal population, whales in particular. This is an encouraging result since it hopefully will make it less likely that mammal protection issues become an obstacle to future TAP experiments.

To address the feasibility of using large aperture arrays for tracking the whales, MIT/WHOI has been analysing the CEAREX data, very rich in mammal sounds due to the fact that this data were recorded very close to the ice edge in the Fram Straits. The digital data collected from the full array had insufficient bandwidth for this analysis, and instead the analog data recorded over a wide band on 12 sensors have been scanned for mammal sounds and digitized. Windowed frequency analysis has been applied to this data to generate the "waterfall" displays usually used by marine biologists for identification. Fig. 5 shows an example. Spectral-coherent focused array processing is currently being applied to track this and other whales identified in the data set. This work is performed in coordination with marine biologists at WHOI (K. Fristrup).

SAIC/RUSSIAN MODELING AND ANALYSIS

The SAIC group is working closely with Russian groups in Moscow, Nizhny Novgorod and St. Petersburg. Russian propagation codes referred to earlier [24] have been used to model

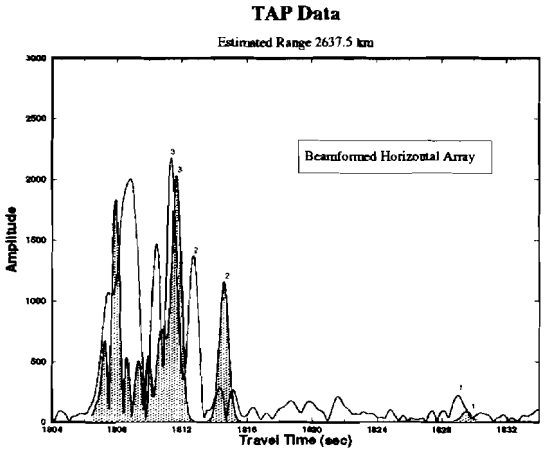

FIGURE 6. Pulse compression response of 255 digit MLS showing distinct mode arrivals.

the TAP transmissions and have been compared to SAIC developed codes for fully coupled bottom interacting normal mode propagation [28, 29]. Figure6 shows the result of pulse compression processing of a 255 digit MLS signal from April 20 at 1300Z plotted with the modelled result. Comparison of these results with the MIT group results is very favorable. Note the difference in the travel time especially for mode 2. It is this difference that could be attributed to warmer water in the Atlantic Intermediate layer (AIW) which is consistent with preliminary modelling results, and the reported warming from the ice breaker cruises in 1993 and 1994. These results indicate a that warmer AIW is extending further into the Arctic Ocean towards the Lomonosov Ridge extending the shallow surface duct common in the Eastern Arctic further west. This increases the decoupling of mode 2 from the surface causing less ice loss, less dispersion, and a faster travel time.

Exceptional stability and coherence of the CW and MLS data has permitted optimal signal processing gains. Since all of the MLS signals were modulated at $\pm\pi/4$ half of the energy was in the carrier at 19.6 Hz. A complete phase history during the TAP experiment has been calculated using the CW and MLS sequences. The phase changes track the GPS navigation very closely. RMS phase noise is very small, in the range of a hundredth of a cycle at 19.6 Hz. This corresponds to an integrated temperature change along the acoustic path of approximately .0001 degrees C. The precision afforded by the phase detection looks very promising for phase tomography which relies on vertical array modal beamforming for separating the modal arrivals. This approach as compared to the conventional time domain MLS tomography will be part of the on- going research effort.

Analysis and Publication Plans

The MIT group will continue the development of more complete models of propagation and scattering in and below the Arctic ice cover. We have established a world leadership in this area, and several publications are in the publishing pipeline [18, 19, 20]. A Ph.D thesis presenting an integrated scattering formulation for waveguides, including volume and rough interface scattering, will be finished in 1995. This thesis will have a specific section on the TAP modeling effort. Another thesis is expected to be finished early 1996, describing a new spectral approach to seismo-acoustic modeling in range-dependent, fluid-elastic waveguides.

This work extends the fluid formulation described in Ref. [20].

The theoretical work at MIT on the resolution of acoustic tomography will be presented at a couple of international conferences in 1995 [21, 22], and a journal paper is in preparation.

The SAIC group and the Russian group will continue to work on the implications for climate monitoring using acoustic thermometry in the Arctic. Preliminary results with have been presented at several ASA meetings, the Scientific Committee for Ocean Research (SCOR) meetings and the upcoming ICA 1995 [30, 31, 32, 33] Our Russian colleagues have prepared numerous reports [24, 25, 26]. In addition to the analysis plans reported above, we intend to pursue the issue of Acoustic Intensity Tomography to invert changes in intensity along propagation paths to determine changes in ice thickness and roughness which is one of the most important elements of acoustic monitoring in the Arctic. We expect to work closely with the MIT group on this effort. An article for EOS will be submitted in March 1995 on the TAP experiment and preliminary results. An article for Nature is being prepared now and may be published as a companion paper with the ice breaker results. Papers will be presented at the upcoming ASA in May 1995 and Oceans 95.

Publications

1. Mikhalevsky, P.N., R.Muench, F.R.DiNapoli,"Arctic Ocean warming; Can we measure it acoustically?", 2nd Meeting of the Oceanographic Society, St. Petersburg, FL., March 1991.
2. Mikhalevsky, P.N., R.Muench, F.R.DiNapoli,"Acoustic measurement of Arctic Ocean warming, Proposal submitted to the National Science Foundation, April 1990, revised and resubmitted, March 1991.
3. Mikhalevsky, P.N.,"Feasibility of acoustic thermometry of Arctic Ocean climate change", J. Acoust. Soc. Am., 94(3 Pt. 2), Sept. 1993.
4. Mikhalevsky, P.N., R. Muench, and A.B.Baggeroer,"Acoustic thermometry for Arctic Ocean climate", Proceedings Oceans '93, Vol. I, Victoria, B.C., Oct. 18-21, 1993.
5. Carmack, E.C., R.W.Macdonald, R.G.Perkin, F.A.McLaughlin, and R.J. Pearson,"Evidence for warming of Atlantic Water in the Southern Canadian Basin of the Arctic Ocean: Results from the Larsen-93 Expedition", Geoph. Res. Let., submitted Oct. 1994.
6. Aagaard, K., and E.C. Carmack, quoted in Science, 266, December 23, 1994.
7. Slavinsky, M., B. Bogolubov, I. Alelekov, K. Pigalov, J.L.Spiesberger, and P. Boutin, "Evaluation of electromagnetic source for ocean climate acoustic thermometry at Lake Seneca", WHOI Technical Report, No. WHOI-93-09.
8. A.B. Baggeroer, W.A. Kuperman and H. Schmidt, "Matched field processing: Source localization in correlated noise as an optimum parameter estimation problem," *J. Acoust. Soc. Am.*, 83(2), 571-587, 1988.
9. W.A. Kuperman and H. Schmidt, "Self-consistent perturbation approach to rough surface scattering in stratified elastic media," *J. Acoust. Soc. Am.*, 86, 1511-1522, 1989.
10. H. Schmidt, A.B. Baggeroer, W.A. Kuperman, and E.K. Scheer, "Environmentally tolerant beamforming for high resolution matched field processing: Deterministic mismatch," *J. Acoust. Soc. Am.*, **88**, 1851-1862, 1990.
11. K.D. LePage. *Elastic scattering in oceanic waveguides.* PhD thesis, Massachusetts Institute of Technology, September 1992.
12. J.-Y. Liu, "Seismo-acoustic interface scattering of surface-generated ambient noise in a stratified ocean," PhD thesis, Massachusetts Institute of Technology, October 1992.
13. F.B. Jensen, W.A. Kuperman, M. Porter, and H. Schmidt, *Computational Ocean Acoustics*," American Institute of Physics, 1994.
14. K. Lepage and H. Schmidt, "Modeling of low frequency transmission loss in the Central Arctic," *J. Acoust. Soc. Am.* 96(3), 1783–1795, 1994.
15. A.B.Baggeroer and H. Schmidt, "Parameter estimation bounds and the accuracy of full field inversions." In O. Diachok, et al, editor, *Full field inversion methods in ocean and seismic acoustics*, Kluwer Academic Publishers, Dordrecht, The Netherlands, 1994.

16. H. Schmidt and A.B.Baggeroer. "Physics-imposed resolution and robustness issues in seismo-acoustic parameter inversion". In O.Diachok, et al, editor, *Full field inversion methods in ocean and seismic acoustics*, Kluwer Academic Publishers, Dordrecht, The Netherlands, 1994.
17. H. Schmidt, "Seismo-acoustics of the Arctic ice cover." In L. Bjørnø, editor, *Underwater acoustics*, European Commission, Luxembourg, 1994.
18. K. LePage and H. Schmidt, "Analysis of spatial reverberation statistics in the Central Arctic", *J. Acoust. Soc. Am.*, In Press, 1995.
19. H. Schmidt and W. A. Kuperman, "Spectral representations of rough interface reverberation in stratified ocean waveguides," *J. Acoust. Soc. Am.*, In Press: 1995.
20. H. Schmidt, W. Seong, and J.T. Goh, "Spectral super-element approach to range-dependent ocean acoustic modeling," *J. Acoust. Soc. Am.*, In Press: 1995.
21. A.B. Baggeroer and H. Schmidt, "Cramer-Rao bounds for matched field tomography and ocean acoustic tomography," Proc. IEEE ICASSP '95, 1995.
22. A.B. Baggeroer and H. Schmidt, "A comparison of matched field tomography and ocean acoustic tomography using Cramer-Rao parameter estimation bounds," Proc. International Congress of Acoustics, Trondheim, Norway, June 1995.
23. V.M. Kudryashov. Influence of shear elasticity on the scattering of sound by a plate with statistically rough boundaries. *Sov. Phys. Acoust.*, 33(6):625–627, Nov.-Dec. 1988.
24. A.N. Gavrilov and V.M. Kudryashov, Numerical modeling of low-frequency sound propagation in horizontally stratified arctic waveguide. *AcoustInform Ltd.*, March 1994.
25. A.N. Gavrilov, Acoustic monitoring of arctic ocean climate: feasibility research and modeling. *AcoustInform Ltd.*, Aug. 1994.
26. A.N. Gavrilov, Modeling acoustic response on long-term variation and climatic change of the water and ice cover characteristics on trans-Arctic paths, *AcoustInform Report*, Vol 2, Contract No. 002-1, Aug. 1994.
27. Mikhalevsky, P.N., Characteristics of CW signals propagated under the ice in the Arctic, *J. Acoust. Soc. Am.*, 70(6), Dec. 1981.
28. Evans, R.B., A coupled mode solution for acoustic propagation in a waveguide with stepwise depth variations of a penetrable bottom, *J. Acoust. Soc. Am.*, 74, 1983.
29. Freese, H., Use of simplified coupled mode propagation for prediction of impulse responses of megameter trans-Arctic propagation paths, *J. Acoust. Soc. Am.* Submitted: Jan. 1995.
30. Mikhalevsky, P.N., Special techniques required for the application of acoustic thermometry in the Arctic, Scientific Committee for Ocean Research (WG 96) Meeting, Hawaii, Oct. 1994.
31. Mikhalevsky, P.N., Trans-Arctic propagation for ocean climate studies, *J. Acoust. Soc. Am.*, 95(5 Pt. 2), May 1994.
32. Mikhalevsky, P.N., A.B.Baggeroer, A.Gavrilov, and M.Slavinsky, CW and M-Sequence transmissions across the Arctic, *J. Acoust. Soc. Am.*, 96(5 Pt. 2), Nov. 1994.
33. Mikhalevsky, P.N., A.B.Baggeroer, A.Gavrilov, M. Slavinsky, Transarctic Acoustic Propagation (TAP) Feasibility Experiment, Proc. International Congress on Acoustics, Trondheim, Norway, June 1995.

Sea Ice Failure Mechanisms

Robert S. Pritchard
IceCasting, Inc. (ICI)
11042 Sand Point Way N.E.
Seattle, WA 98125-5846
Tel/fax: (206)363-3394
E-mail: rsp@halcyon.com

Scope of Model and/or Data

The goal of ICI's research is to understand the mechanical behavior of sea ice on structural, meso, and geophysical scales and to develop models that accurately describe both the dynamical and acoustical behavior. We now have the ability to describe the presence of individual ridges, rafts, and leads in larger scale models by describing ice behavior as an anisotropic elastic plastic material [*Coon, et al.*, 1992]. Thus, our attention can focus on estimating failure loads and acoustical sources of individual processes.

Controlled-load Tests -- This task focused on conducting tests that isolate individual failure mechanisms that contribute to ridging and rafting. ICI studied rafting, over-ride, under-ride, beam bending, block dropping, flopping, and splashing jointly with Dr. M. D. Coon and other NWRA investigators. Each experiment approximated the behavior of *in situ* sea ice, except that the process was isolated and the loading was applied artificially. Acoustic emissions for the tests were determined jointly with Drs. D. M. Farmer and Y. Xie (IOS) and Dr. H. Schmidt (MIT).

We conducted over thirty tow tests and forty other tests (see the Coon, Echert, and Knoke paper in this volume for another description). These tests were conducted at the Football field (Map 4, D6), East Pond (Map 4, C6), South Camp (about 18 km south of East Camp), and the IOS site (Map 4, B6).

Finger Rafting -- This task attempts to identify the conditions that control whether ice fails in simple or finger rafting. Rafting, in general, has received less attention than ridging, perhaps because its behavior appears to be less complicated and because it occurs most frequently in thin ice. However, since vertical heat transfer rates are much larger through open water and thin ice, the mechanisms that affect rafting could be important in describing the distribution of open water and thin ice, which is important to climate dynamics.

Plate Bending -- Static and dynamic plate bending tests were conducted on thin ice. Our goal was to estimate elastic properties and characteristic lengths directly from deflections of the plate.

Thicknesses ranged over about 6-16 cm. At least the bottom half of each ice plate was

porous, dendritic growth with no appreciable strength. These results will provide information that may help to gain understanding of finger rafting. ICI studied plate bending jointly with Dr. T. B. Curtin, ONR.

Characteristics and Leads -- This task has the goal of learning if the characteristic directions of a plasticity model can describe the lead patterns observed in imagery. This idea has been of interest for about two decades. Some investigators have assumed that classical plasticity models with a Coulomb yield surface explain observed behavior. I am less certain, and wish to learn if and under what conditions such a relationship exists.

Findings to Date

Controlled-load Tests -- The drop tests have been analyzed to estimate the acoustic emissions. These results will appear in *Pritchard, et al.*, [1995]. This work was performed jointly with NWRA and IOS. The acoustic signal generated by the first impact is isolated from the flexural wave (see Figure 1). The flexural wave is confined near to the surface and is dispersed by irregularities in the ice sheet and therefore does not propagate to the far field. The acoustic signal is approximated as a dipole source. We have found that the ratio of total radiated acoustic energy to the kinetic energy at impact is about 10×10^{-6} when the ice sheet is bare (Figure 2). This is true when blocks are dropped flat, at an angle, or tipped from standing on edge. The ratio is reduced to about 2×10^{-6} if the ice sheet is covered by 1 cm of snow. The acoustic spectrum of a block tipped over and flopped onto a snow-covered ice sheet is shown in Figure 1. The first impact acoustic emission and the flexural seismic signal are shown separately here. When the ice sheet is bare, the spectrum above 200 Hz increases by about 10 dB.

Results of one over-ride test have been analyzed. Stick-slip behavior is observed, as with other sliding tests. The force and noise histories are shown in Figure 3. This figure was prepared by Dr. Y. Xie and will appear in *Pritchard, et al.* [1995]. Please see the Coon, Echert, and Knoke paper in this volume for another description.

A simple dynamic model of the stick-slip motion of a block pulled by a flexible cable and restrained by Coulomb friction is being analyzed. The model will be useful for estimating static and dynamic friction coefficients and the spring constant of the cable. This analysis will also show which parameters affect the time between slippage. This result will provide information on the flexibility of the ice cover because we have such data from noise observations during rafting events at South Camp.

Finger Rafting -- Prior to this study, ICI proposed that finger rafting might be explained by considering the two dimensional bending of a semi-infinite elastic plate. The idea is that fundamental solutions of an elastic flat plate vary in two directions, and these variations are coupled in specific and known ways. If the edge of the semi-infinite flat plate is loaded, variations along the edge may be expanded in a Fourier series. The hills and valleys along this

edge, when compressed by other ice, can easily be penetrated, forming fingers. For each of the higher modes, finger width is determined as a function of ice thickness, elastic properties, and buoyancy. The zeroeth mode has no variation in the *y* direction so that its behavior is analogous to deflection and bending of a beam. This mode can help explain simple rafting. Half-wavelengths for the n-*th* mode are

$$L_n = \frac{1}{2n}\left(\frac{Eh^3}{12(1-\nu^2)\rho_w g}\right)^{1/4} \qquad (1)$$

First mode ($n = 1$) finger widths are shown in Figure 4 for nominal material property values: $\rho_w = 1026$ kg/m^3, $E = 3$ GPa, and $\nu = .3$.

Several data points were obtained previously from LEADEX (courtesy of Dr. J. Morison) and the SIMI Pilot Experiment (courtesy of Dr. M. Coon). Two additional points were measured during SIMI.

The observed finger widths do not agree with the modeled finger widths, unless the Young's modulus is increased by nearly two orders of magnitude, or the thickness is roughly tripled. The effective thickness (if the porous, dendritic skeleton were neglected) would be smaller than the nominal thickness used in the plot, which would cause the comparison to be even worse. Also, while the elastic constants are not well-known for very thin ice, they cannot be so different for 20 cm-thick ice. Therefore, I must conclude that the elastic plate model does not explain finger rafting. The bending experiments described in the next paragraph were designed to help provide new information on finger rafting.

A finger raft of very thick ice (1.4-1.6 m) was observed. The feature was named Jay's Fingers. We were surprised to find that ice of this thickness rafted and even more surprised that it formed fingers. It is generally thought that only thin ice can form finger rafts. It had finger widths of about 100 m. We drilled this feature to determine ice thickness and to confirm that it was a finger raft rather than a sinewy ridge. It was. A photograph of the area is presented in Figure 5.

Plate Bending -- Our first static bending test of 9.5 cm-thick ice (of which about half was porous, dendritic growth without strength) did not deflect according as an elastic material. The nearest measurement was about 1.5 m from the load (a ring load having diameter 0.6 m) and no deflection was observed beyond this radius. It is likely that a plastic hinge formed somewhere within this radius.

Characteristics and Leads -- Large scale flaws can form along characteristics if boundary geometry and forcing by wind and current combine to cause a discontinuity in the velocity field [*Pritchard*, 1988, 1991, 1992]. These flaws might not be noticed until a later time when divergence occurs. A series of flaws can be created as the ice moves past the location where

the velocity discontinuity is located. When uniaxial opening or pure shearing occurs, leads are observed to be perpendicular to the direction of maximum opening. When not aligned with the original directions of the flaws, the opening first appears as jagged lines. The original characteristic directions remain apparent until continued opening makes the single principal direction dominant. When pure opening occurs, the original characteristic directions remain apparent.

Analysis and Publication Plans

- Mechanical Behavior of Ice during Rafting
- The Range of Acoustical Emissions from Ice during Rafting
- An Example of Finger Rafting of Thick Ice -- Jay's Fingers
- Bending of Thin Ice Sheets
- Sea Ice Leads and Characteristics

References

Coon, M. D., Echert, D. C., and Knoke, G. S. "Pack Ice Anisotropic Constitutive Model," in *IAHR 92, Proceedings of the 11th International Ice Symposium*, Banff, Alberta, June 15-19, 1992.

Pritchard, R. S. (1988) "Mathematical Characteristics of Sea Ice Dynamics Models," *J. Geophys. Res.*, vol.93, no. C12, pp.15609-15618.

Pritchard, R. S. (1991) "Large-Scale Lead Patterns in Sea Ice," in *Proceedings of the First Soviet-American Workshop on Ice Mechanics and its Applications*, 16-26 June, 1991, Institute for Problems in Mechanics, Moscow.

Pritchard, R. S. (1992) "Sea Ice Leads and Characteristics," in *IAHR 92, Proceedings of the 11th International Symposium on* Ice, 15-19 June, 1992, Banff, Alberta, pp. 1176-1187.

Pritchard, R. S., Xie, Y, Farmer, D. M., Coon, M. D., Knoke, G. S., and Echert, D. C. (1995) "Acoustic Signatures of Small-Scale Processes Associated with Ridging," to appear in ICE MECHANICS -- 1995, ASME.

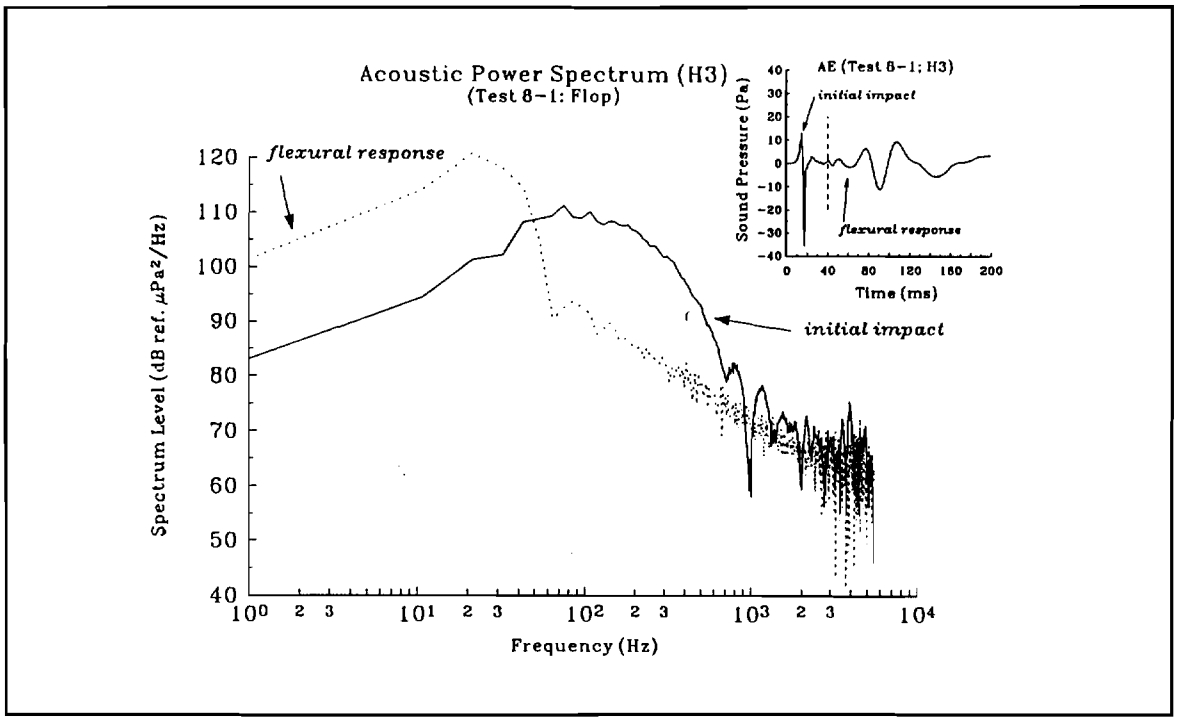

Figure 1. Spectrum of block of ice tipped over and flopped onto the ice sheet. The insert shows the acoustic pressure time history.

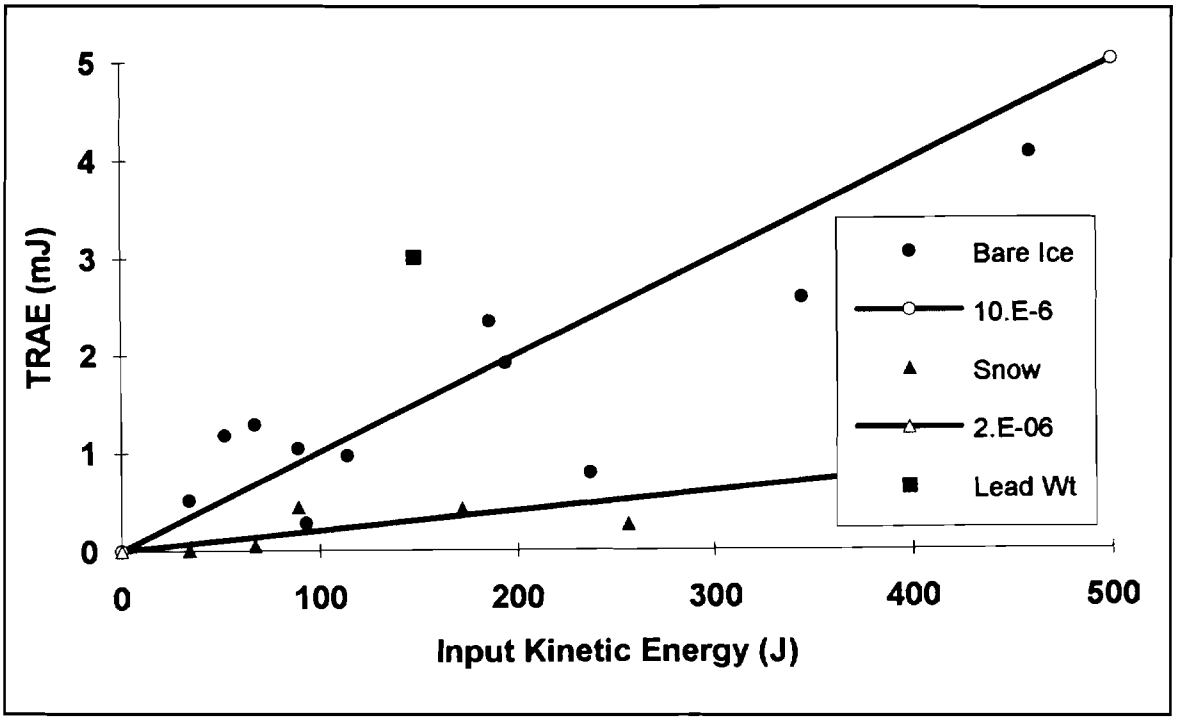

Figure 2. Comparison between total radiated acoustic energy and impact kinetic energy for 16 Drop Tests.

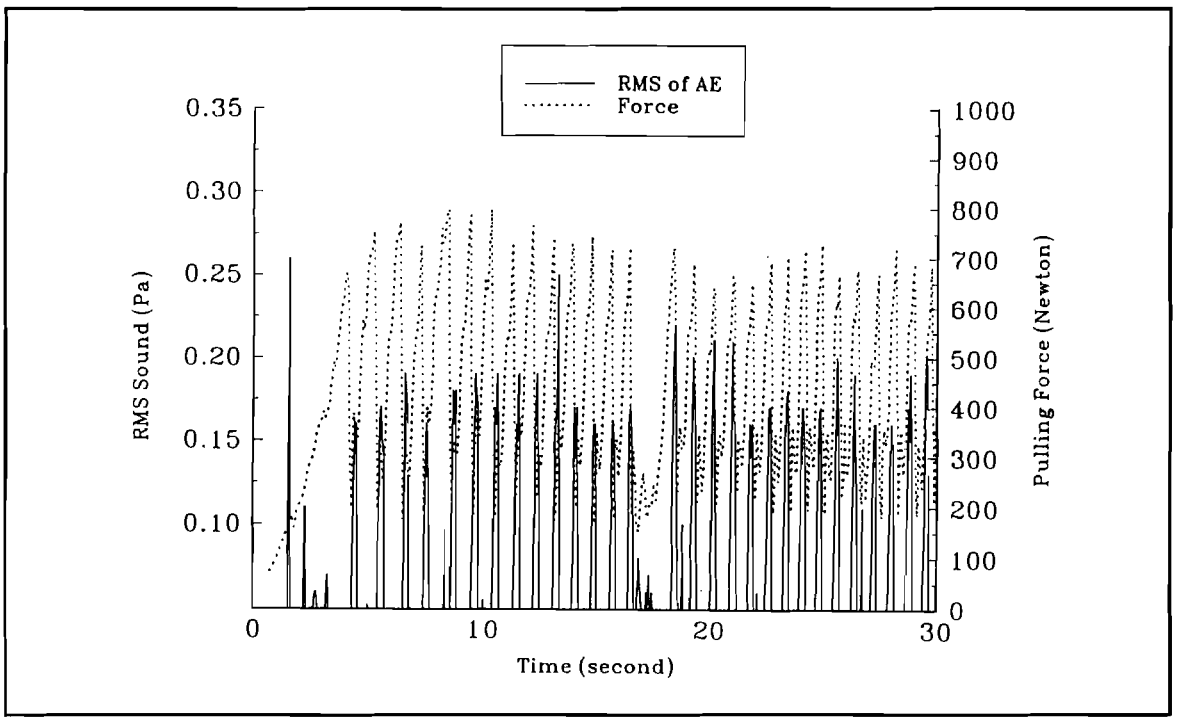

Figure 3. Stick-slip behavior an ice block over-riding the ice cover for Test 8-13. Towing force and acoustic emission are shown.

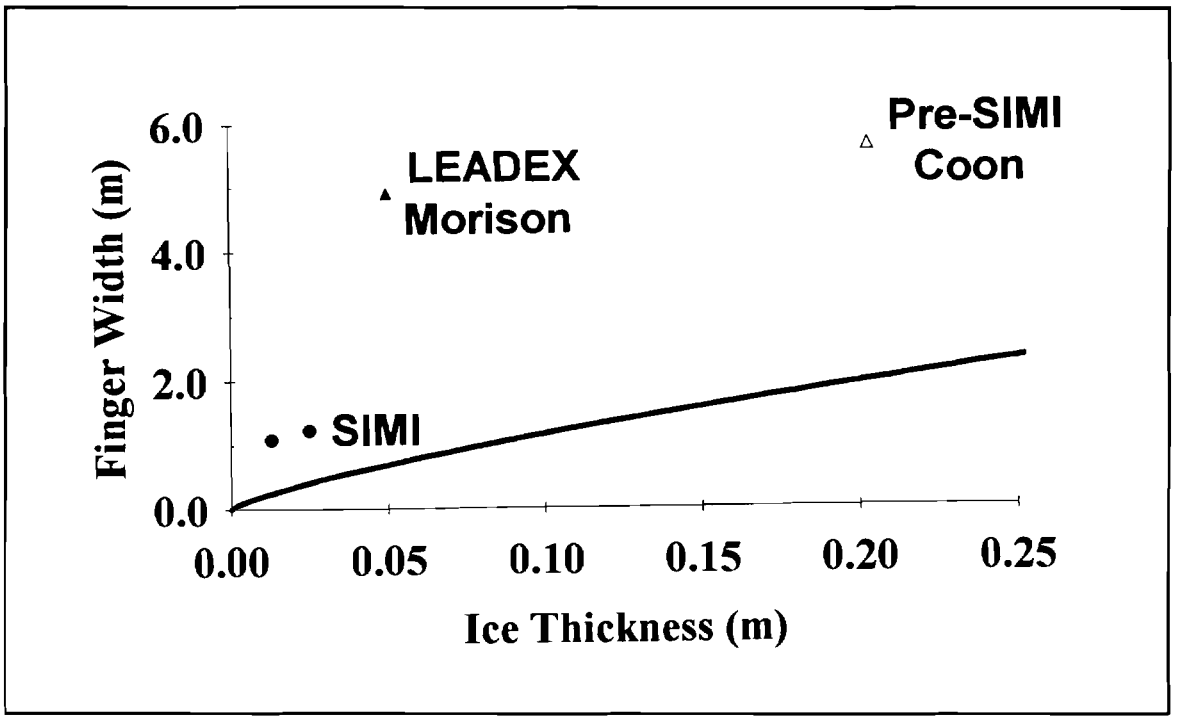

Figure 4.Comparison between characteristic width of first mode bending of a semi-infinite elastic plate and observed widths of finger rafts.

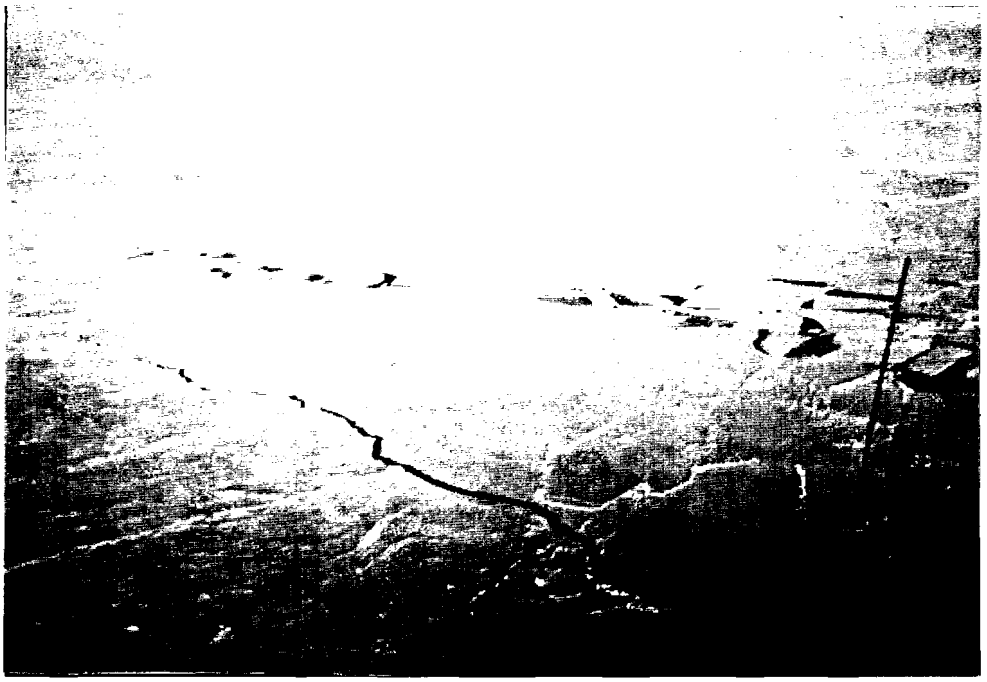

Figure 5. Photograph of Jay's Fingers. Thick ice (1.4-1.6 m) was rafted into 100 m-wide fingers.

Sea Ice Mechanics Research: Tomographic imaging of wave speeds and acoustic emission event localization

Subramaniam D. Rajan, Woods Hole Oceanographic Institute, Woods Hole, MA 02543.

Description of experiment

The objectives of the experiment are as follows.

- Determine the evolution of wave speeds in sea ice in a region close to a ridge and investigate relationships between changes in wave speed structure to activities in the ridge.
- Monitor acoustic emission events caused by ice cracking or other events with a view to classify and localize the events and study the correlation between the type of event and its location.

The field experiment, therefore, consists of two components i.e., (i) an active (tomography) system and (ii) a passive (acoustic emission) system. The tomography experiment is designed to investigate the evolution of wave speeds in sea ice. The passive system monitors acoustic emission events caused by cracking or other processes taking place in the ice. Further, the location of the acoustic emission events will be determined by combining the wave speed information obtained from the tomography experiment and the arrival time of acoustic emission signals. The experimental site is marked Rajan's site 2 in Map 2(G5).

The layout of the arrays for the active and passive systems is shown in Figure 1. The tomography (active) system consists of two separate sets of arrays deployed one on either side of the ridge. The ridge feature separates the main floe from a re-frozen lead region. The vertical arrays, which can either be a transmitter or a receiver array, comprise nine elements. The first six elements are 0.5 m apart with the rest at 2 m spacing. In addition to the vertical arrays, horizontal arrays are deployed near the top surface of the ice as shown in Figure 1. These elements are placed 0.5 m from the ice surface and the arrays consist of transmitters and receivers placed alternately. Note that arrays whose label starts with the letter T are transmitter arrays and those with R are receiver arrays. The passive system consists of six receivers PL1 through PL6

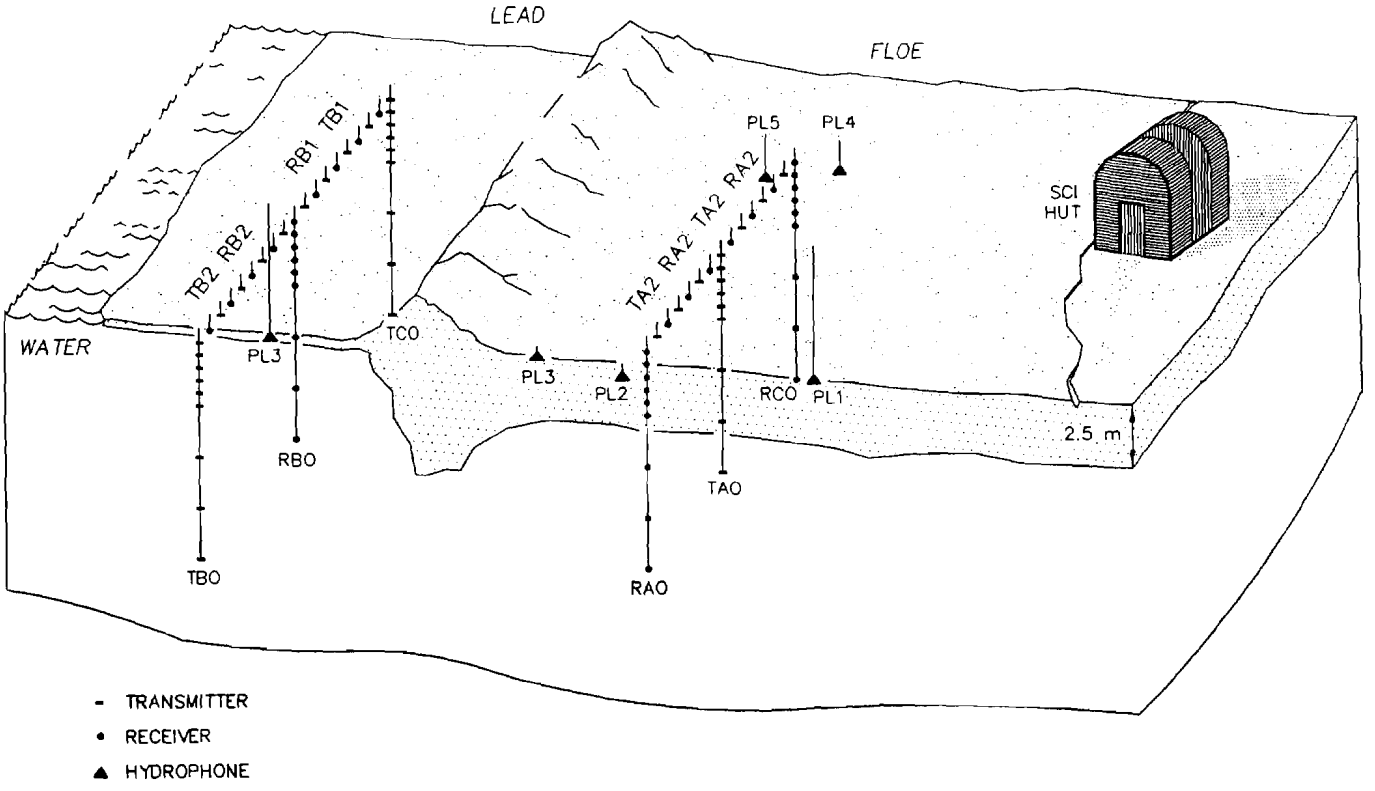

SEA ICE MECHANICS INITIATIVE
Oct.–Dec. 1993

Figure 1: Layout of active and passive system arrays

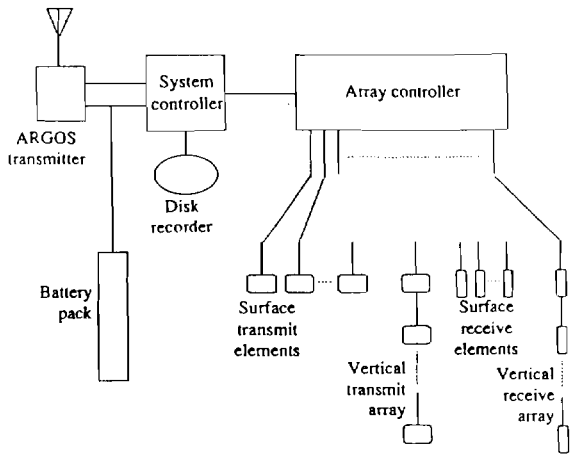

Figure 2: Block diagram of system modules

deployed in the region close to the arrays as shown in Figure 1. Of the six receivers, two are in the water column and the rest are placed in the ice sheet. All the elements in the ice sheet (belonging to both the systems) are frozen in.

A. Active system operation

The system performs experiments repeatedly and the time interval between experiment can be preset. An experiment is defined as the sequential excitation of each transmitter with a 12 KHz ping with synchronized time series acquisition of the received signal by all receivers one at a time. When all transmit-receive paths have been excited and all corresponding data recorded, the experiment is complete and the system is shut down until it is time for the next experiment.

The block diagram (Figure 2) shows the modules required to perform these functions. The main functions of the array and system controller are as follows.

Array controller: Connects the selected transmitter to the transmit circuitry, and connects the selected receiver to the front end and digitizer circuitry. Performs automatic gain control and collects the data.

System controller: Determines the sequence of array pairs to be used. Communicates with the array controller, collects the acquired data from the array controller and sends it the disk recorder. A subset of the data is sent to the ARGOS for transmission. At the end of the experiment, turns off system power except for the timer circuit.

A more complete description of the system is given in Reference 1.

B. Passive system operation

The passive system comes into operation when the active system shuts down between experiments. During this period the phones which comprise the passive system are in a listening mode. The signal received by PL1 is used to decide whether an acoustic emission event has occured. This decision is based on short and long time averages. Once an event is detected, the signal at all six hydrophones for a specified time interval before and after the event are acquired. In order to prevent the logger from filling up with data over a short period of time, only a specified number of events is allowed per hour. This limit is preset. If the number of events during the time interval exceeds this limit, events in excess of this limit will be ignored. On the other hand if the number of events is less than the specified number then the allowable number of events for the next time period is augmented by this shortfall. The signals at each of the hydrophones are digitized at a sampling rate of 15 KHz per channel and recorded on a data logger separate from the one used for the active system. The logger is also housed along with the active system electronics.

Data

Both the active and the passive systems were deployed during November 2 - 11, 1993. The system went into autonomous operation on November 12, 1993.

Around November 30, 1993 the region near our site became very active with large cracks occuring at a number of locations. Since there was the possibility of losing the system and the data logger, the decision was made to remove the electronics package from its housing before the region became unapproachable. The system was therefore recovered on December 4, 1993. The available data pertains to the short time period of about 20 days.

A. Active system

The data of the tomography system are the signals acquired at each of the receivers. The signal acquired by the receivers in the vertical array RC0 for a pulse transmitted

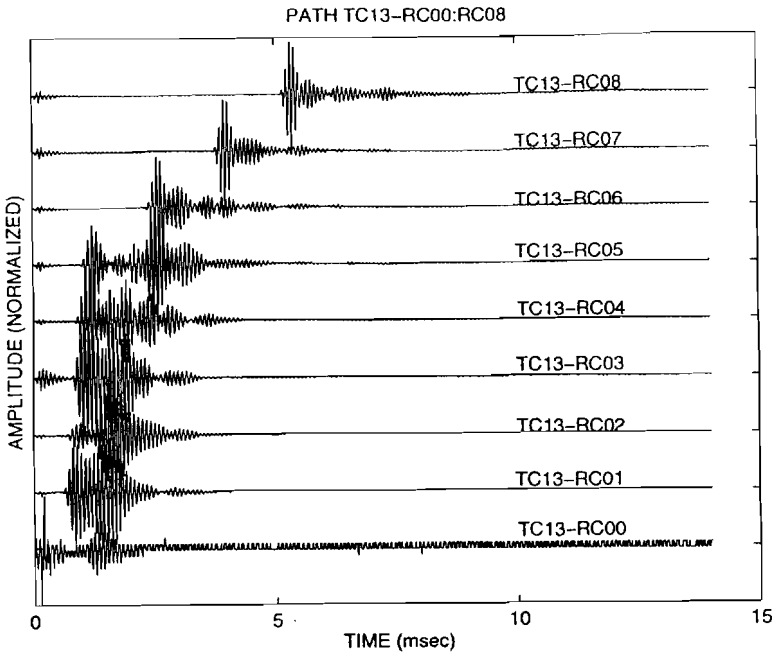

Figure 3: Signals acquired at array RC0. Transmitter TC13

by transmitter TC13 in the horizontal array TC1 is shown in Figure 3. The data for each experiment consists of data from 1595 source/receiver combinations. The time interval between experiments was preset to be 3 days. However, due to some defect yet unidentified, the actual interval between experiments was 6 days. Therefore the data collected correspond to experiments performed on November 12, 18, 24 and 30, 1993.

B. Passive listening experiment

As described earlier, the acoustic emission data are collected at each of the six receivers comprising the system. An example of an data for an acoustic emission event is shown in Figure 4. During the period the system was in operation a total of 370 events were detected.

Analysis of data

A. Active system data

The time taken by an acoustic pulse to travel from a source to a receiver is determined from data. This travel time (t) is related to the bulk wave speed in the medium by the ray equation

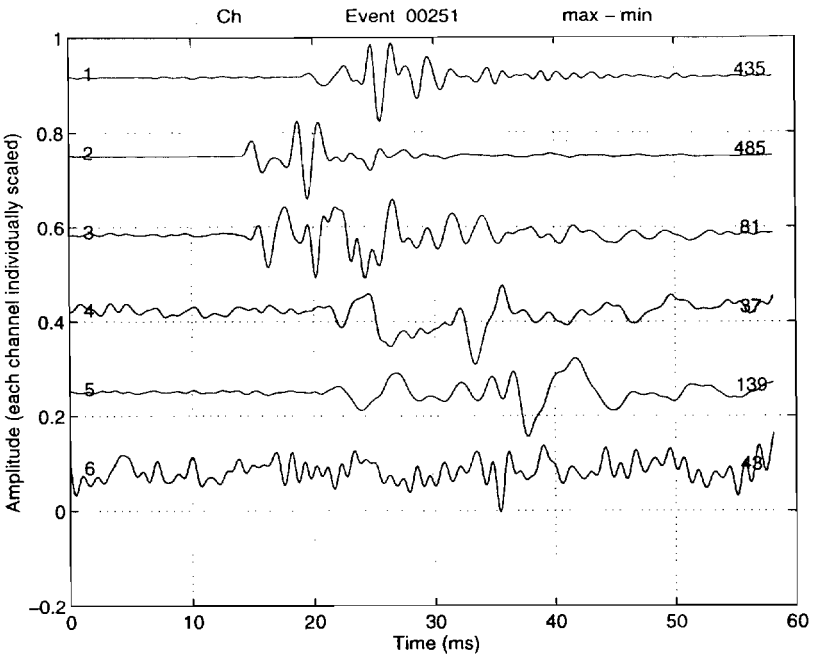

Figure 4: Data acquired by passive system. (Event 251)

$$t = \int \frac{dl}{C(\bar{x})}, \tag{1}$$

where dl is the differential length along the ray path and $C(\bar{x})$ is the wave speed as a function of its spatial coordinates $\bar{x}$. By using a combination of sources and receivers, the entire region between the vertical arrays is covered by a matrix of rays, and the travel times for the pulses to travel along different ray paths are obtained. Using this travel time information one can estimate the wave speeds in the region between the vertical arrays. Details of the inversion procedure are given in [2].

It was observed from trial transmissions done prior to November 12, 1993 that the SNR of signals for paths across vertical arrays was low when the paths were through ice. This was because of the high attenuation of the signals during their passage through the ice and we attributed this to the condition of the ice. We had hoped that during the winter, the condition of the ice would improve resulting in a higher SNR for paths through the ice. Since the system was recovered in early December such improvements did not take place. The data acquired has very low signal to noise ratio for ice paths between elements in the vertical arrays making it difficult to determine the travel time for these paths. This restricts the number of paths that can be used

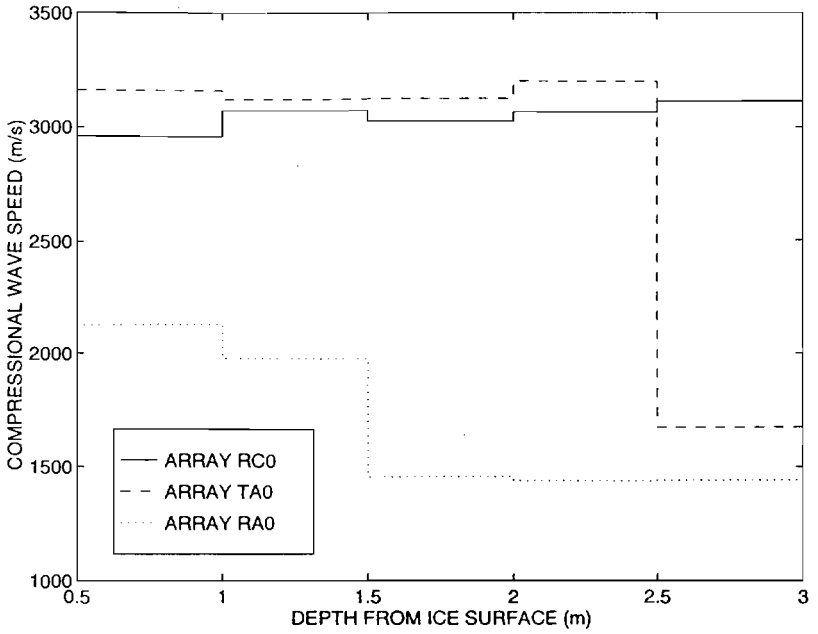

Figure 5: Compressional wave speed profiles at arrays TA0, RA0 and RC0

in the inversion. However we notice that for paths between elements on the horizontal array and the vertical array adjacent to it the SNR is high and therefore one can use VSP geometry to determine the compressional wave speed profiles at the vertical arrays. The compressional wave speed profiles at the vertical arrays TA0, RA0 and RC0 obtained using the VSP approach from November 12, 1993 tomography experiment data are shown in Figure 5. We note that the compressional wave speed in the ice at the location of arrays TA0 and RC0 is practically constant. An examination of the temperature structure in the ice reveals that it is almost isothermal with temperature of -1.5° C for the bulk of the ice with a 0.5 m layer at the top surface of temperature -3.0° C. Further the we note that at the array RA0 the ice is thin with the wave speed much lower. This reduced wave speed is because of the presence of under-ice melt ponds in this region.

B. Passive system data

Classification of signals

It is known that the acoustic emission signal characteristics are related to the mechanisms that caused it. Examination of about 100 events recorded during this experiment

yielded six types of signals. These types together with their spectrogram are shown in Figure 6. All the signals were acquired by PL1, the phone which is located in the water column. It may be seen that the spectral characteristics of each of these signals are different. It is possible therefore to use the spectral characteristics of the signal to classify the signals. Schemes for classifying short duration signals that make use of spectral information as well as other information such as signal duration, bandwidth, AR model coefficients have been proposed [3].

Acoustic emission source location

The signal to each of the PL element arrives at different times depending on the location of the source as seen in Figure 4. The arrival time information together with the wave speed information obtained from tomography experiment can be used to determine the location of the source. This problem has been well studied and a number of algorithms proposed to determine the source location[4-6].

Proposed analysis

The data obtained will be analyzed to obtain the following.

1. Compressional wave speed profiles in the ice. Since the transmission in the horizontal across arrays has very low SNR, the data which correspond to paths in the vertical will be used and the compressional wave speed as a function of depth will be inferred.

2. The acoustic emission data will be analyzed and the signals classified. Techniques used in other areas for classification of signals will be used to identify and classify the signals.

3. The location of various emission events will be determined and the correlation between the type of event and its location will be studied.

4. Efforts will also be made to study the inverse problem of determining the source signature from the signal recorded at the passive system hydrophones.

It is proposed to publish the results of the analysis in journals such as the Journal of the Acoustical Society of America and Journal of the Geophysical Research.

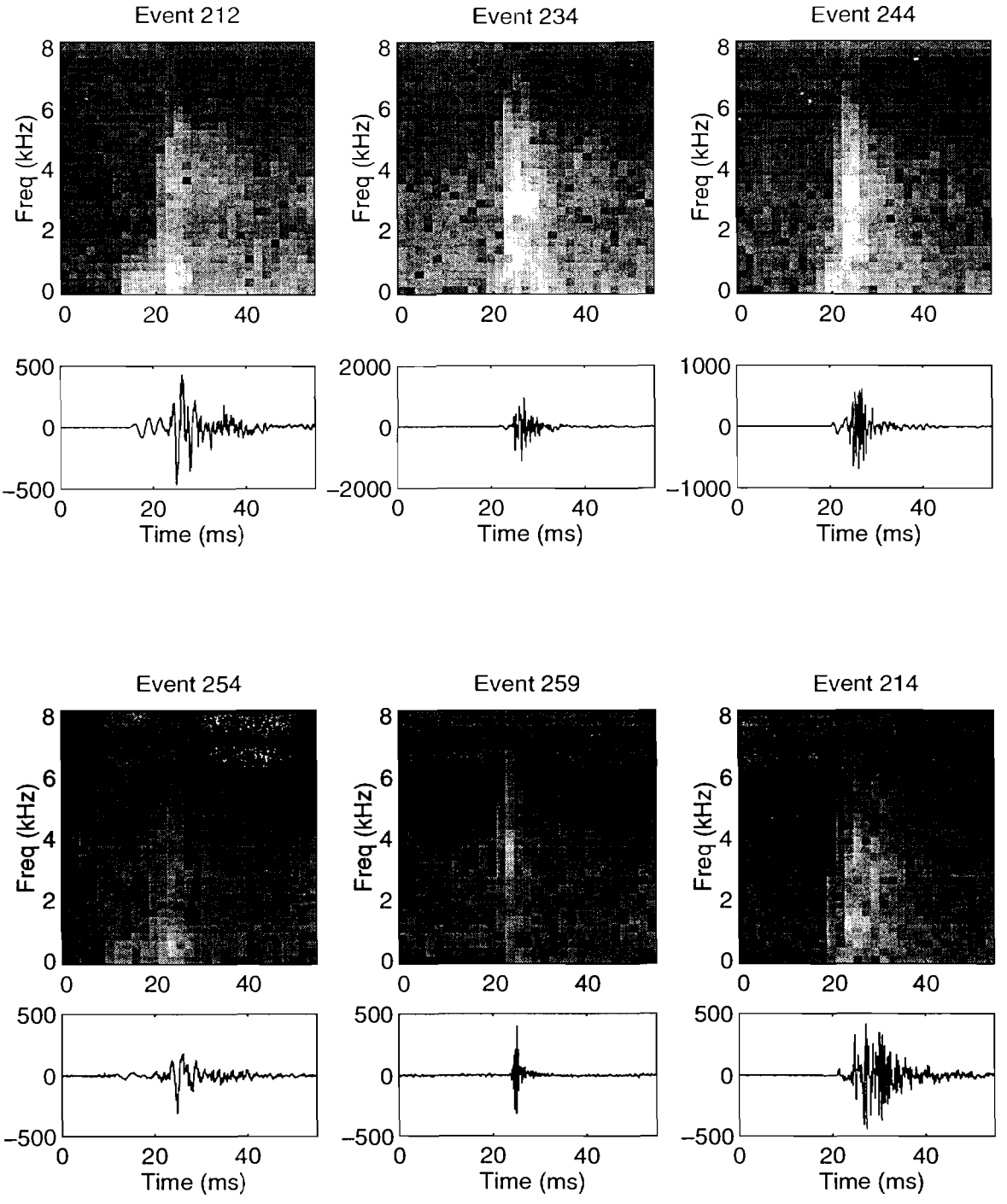

Figure 6: Spectral content of six types of acoustic emission signals

References

1. "Multi-season acoustic tomography experiment in the Arctic," Kenneth R. Peal, Subramaniam D. Rajan, and George V. Frisk, Proceedings of the IEEE Oceans Conference, II-41 - II-46, Victoria, British Columbia, Canada (October, 1993).

2. " Determination of compressional and shear wave speed profiles in sea ice by cross-hole tomography - Theory and experiment,", Subramaniam D. Rajan, George V. Frisk, James A. Doutt, and Cinthia J. Sellers, J. Acoust. Soc. America, 93(2), 721-738, 1993.

3. " A neural network based hybrid system for detection, characterization and classification of short duration oceanic signals, " J. Gosh, L. M. Deuser, and S. D. Beck, IEEE Journal of Oceanic Engineering, 351 - 363, 1992.

4. " Simultaneous acoustic emission and ultrasonic tomographic imaging in anisotropic polymer composite material," T. M. Chow, D. A. Hutchins, and J. T. Mottram, J. Acoust. Soc. Am., 94(2), 944 - 953, 1993.

5. " Non-linear earthquake location: Theory and example," C. H. Thurber, Bulletin of the Seismological Society of America, 75(3), 779 - 790, 1985.

6. " Three dimensional AE source location in metals," K. H. Kim and T. Kishi, Non-destructive testing communications, 3, 75 -88, 1987.

SEISMO-ACOUSTIC REMOTE SENSING OF ICE-MECHANICAL PROCESSES IN THE ARCTIC

HENRIK SCHMIDT, ARTHUR B. BAGGEROER and IRA DYER
Massachusetts Institute of Technology

and

KEITH VON DER HEYDT and EDWARD K. SCHEER
Woods Hole Oceanographic Institution

Scope of Model and/or Data Set

The primary objective of the Sea Ice Mechanics ARI is to develop a fundamental understanding of the mechanical behavior of sea ice undergoing environmental forcing due to currents, wind and heat flux. The several Arctic acoustics experiments of the past have made it clear that ice fracturing is the dominant source of ambient noise, in turn suggesting that this forms the major component of the physical processes leading from environmental forcing to the development of macroscopic ice features such as ridges, leads and raftings. On this background, the specific objective of the MIT/WHOI effort is to develop a basic understanding of these ice fracturing processes and their relation to the environmental forcing, in particular in terms of their role in the ridge building process.

Ice interaction is a dominant factor in Arctic acoustics and another objective is to use the data recorded during SIMI from both artificial sources and natural sources such as ice events and mammal sounds to improve the understanding of this interaction, in particular in terms of coupling into seismic waves in the ice cover.

SIMI-94 EXPERIMENTAL EFFORT

Surveillance Hydrophone Array

As a mechanism for monitoring and localizing ice activity during the Spring SIMI field experiment, MIT/WHOI deployed 2 hydrophone arrays, comprising an icemicity "surveillance" capability approximately 300m from the main camp area. A vertical line array (VLA) of hydrophones, having 32 sensors linearly spaced from a depth 62 to 279 meters was deployed at the APEX site shown in Fig. 1. Surrounding this APEX was a horizontal array consisting of a 12 hydrophone circular deployment augmented by 12 additional sensors on nominal north-south and east-west legs 240m in length. Prior to the Trans Arctic Propagation receptions, 8 more hydrophones were deployed for a total of 32 in the horizontal array (HA), all at a depth of 60 m. Fig. 1 labels nominally indicate the direction and range in meters of sensors as surveyed relative to the APEX. The sensitivities of the HA and VLA sensors was -160dBV and -175dBV μPa/ $\sqrt{Hz}$ respectively.

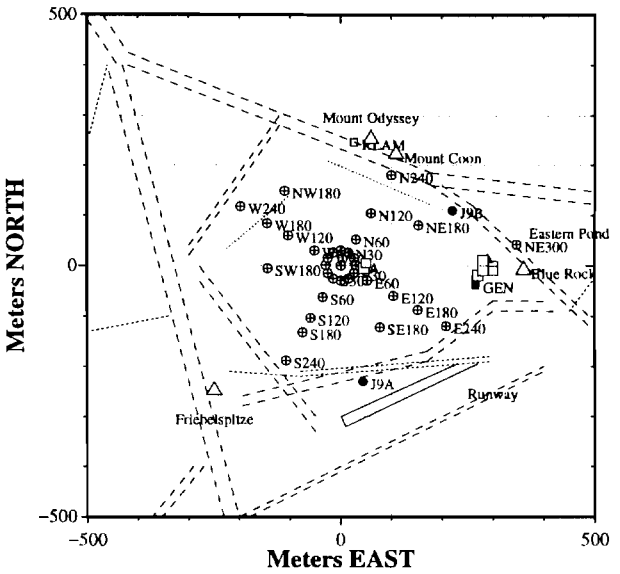

FIGURE 1. Seismo-Acoustic arrays deployed by MIT/WHOI on and around the East Camp floe. A total of 32 hydrophones were deployed in the horizontal array in a combined circular/cross configuration. A 32 element vertical array was deployed at the horizontal array apex. Two J-9 acoustic sources (J9A and J9B) were deployed for sensor tracking. RLAM's were deployed N of Mt. Odyssey and on East Pond, in addition to more remote deploments.

With the exception of breaks for generator maintenance, data were acquired and stored continuously on 8mm tape (Exabyte), from a set of these sensors according to the table below.

DATE(Apr)	#data ch	BW(hz)	time/tape	tape #s	QTY data
4 - 13	24 HA	300	26 hr	1,3 - 14	42 GB
14	32 HA,16 VLA	300	10 hr	15	3.5
15	32 HA,18 VLA	300	10 hr	16	3.5
16 - 18	32 HA,25 VLA	300	10 hr	17 - 22	23
18 - 23	32 HA,32 VLA	300	10 hr	23 - 33	45
23	32 HA	2700	2.5 hr	34 - 37	16

A subset of the recorded data were processed in realtime to develop a series of displays, Fig. 3 is an example, indicating the level and region of local ice activity. These results were used to select sites for deploying autonomous Radio LAN Acquisition Modules, (RLAMs) that acquired geophone data in the near-field of apparently active sites.

Two USRD J9 acoustic sources were deployed and each driven with a dual tone signal for use in localizing the VLA channels. Consequently, during the period 15-23 April, tonals in the 64 to 76 Hz region are evident in the recorded data.

Geophone Clusters

Ice motion, either as a result of natural activity or induced events, was measured directly by portable RLAM systems, each equipped with 5 - 3 axis geophones and 1 hydrophone. These systems were deployed at 8 sites in the vicinity of the SIMI-94 East Camp for varying times throughout the experiment. Data was telemetered via a radio local area network to a

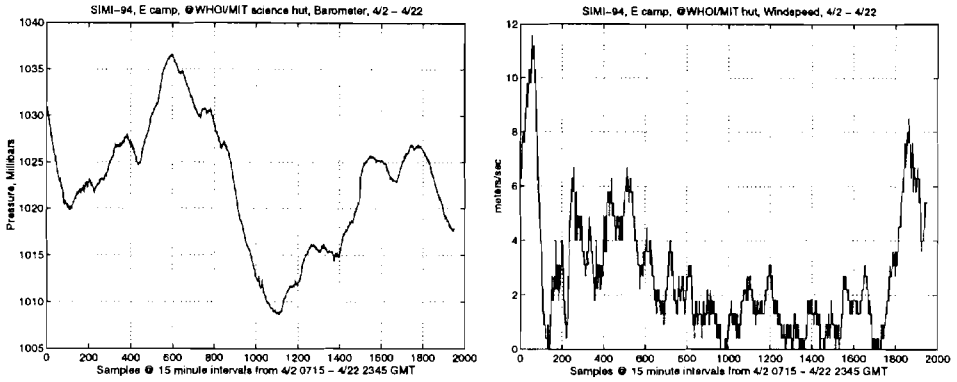

FIGURE 2. Barometric pressure and wind speed recorded during SIMI-94 experiment.

receiving system located at the MIT/WHOI science hut at the SIMI-94 East camp where it was stored on 8mm tape in a format similar to the "surveillance" system. The data bandwidth varied from 400 to 1600 Hz depending on whether 1, 2 or 3 RLAM units were operating simultaneously.

Data was acquired during selected times from 7 April through 18 April depending on the schedules of other experiments, such as induced fracturing and ice block drops as well as the detection of natural events. During the remainder of the experiment through 23 April, 3 RLAM units were kept in continuous operation near Mt. Odyssey, Ewart's site, the large lead just to the north of camp or the RLAM site 4km to the east. Data acquired from RLAM systems totals over 100 GB.

During the first week of RLAM use from 7 to 13 April, technical problems were experienced which compromised data quality because of electronic noise and/or unintentional scrambling of channels in the archived data. The latter problem is correctable and the former problem can at least be reduced with appropriate filtering.

Meteorology

During the 1993 and the 1994 SIMI field programs, the WHOI/MIT group collected basic meteorology data using an inexpensive package from Davis Instruments. Vector wind, air temperature at 1 point about 10 feet off the ice, barometric pressure, humidity and the temperature was acquired continuously from 2 to 23 April at 15 minute intervals. Figure 2 shows examples of the recorded data throughout the duration of the MIT/WHOI experiment, with Fig. 2(a) showing the barometric pressure and Fig. 2(b) ahowing the associated wind speeds. The wind speeds are consistent with the fact that very little ice activity occured in the East Camp area during the experiment.

High-Frequency Propagation

As part of our collaboration with MIT Sea Grant on the development of a robust and accurate Very Long BaseLine (VLBL) navigation system for AUV survey missions in the Arctic, we performed a series of high-frequency propagation experiments designed by Max Deffenbaugh to verify the performance of the navigation algorithms. A short vertical array was deployed in the hydrohole in East Camp, at depths of 15, 30, and 60 meters. A beacon was deployed for 24 hours at each of 3 positions, one at approximately 2 km range, one at 4 km, and one at 10 km range, all in the NE direction from camp.

Findings to Date

RADIO LAN AQUISITION MODULE (RLAM)

A major result of our SIMI effort is the development of a portable data acquisition system (Radio LAN Acquisition Module, RLAM). In particular, there are 2 new developments. The first consists of a board, designed for the ISA PC bus incorporating 8 - 24 bit sigma-delta analog-to-digital converter (ADC) channels with 20 bit rms dynamic range. Among the features are programmable bandwidth to 1500 Hz, low power dissipation, digital anti-alias filtering, and a "floating point" mode resulting in a 16 bit word. Secondly, since the telemetry of data at continuous rates in excess of 100 Kbytes/s was required, hardware and software was developed to use a wireless LAN to network 3 sites up to 5 km distant from the data recording system. Details of the system along with test data are described in Ref. [25].

The RLAM

Each RLAM system was deployed in an insulated polypropylene packing case sized to snugly hold the RLAM electronics chassis and a pair of battery packs for 1 week operation. Two alkaline battery packs situated above the electronics chassis were warmed by the approximately 26 watt system. RLAMs were configured to acquire data from 16 channels at a common selected rate according to one of 4 different configurations:

RLAM's	SAMPLE RATE	REC LEN ON TAPE	PTS/REC	RLAM TX SIZE	NET DATA RATE
1	3906 Hz	1009 KB	32256	1032192 bytes	125,000 bytes/s
2	1953	993	15872	507904	125,000
3	1953	1009	10752	344064	187,500
3	976	1009	10752	344064	93,750

Fifteen channels were devoted to 5 - 3 axis geophones. An omni directional broadband hydrophone was connected to the 16th input on each RLAM. The input amplifier, an Analog Devices AD620, is an instrumentation design and can be configured to receive a voltage or current mode signal. It is possible to supply power to a sensor such as a hydrophone or simply connect an unpowered sensor such as a geophone directly. This design emphasized rejection of signal crosstalk through 20 KHz with signals on long unshielded twisted pairs.

Telemetry

Two radio systems were used. The data telemetry link was a commercial "wireless" Ethernet LAN adapter for the ISA bus (WaveLAN) operating in the 902-928 MHz Industrial Scientific and Medical (ISM) band. It is a 250mw, spread spectrum link specified to have a maximum throughput of 2 Mbits/sec.

A second "survival" radio link was implemented with a UHF (455 Mhz) FM radio with bandwidth of about 3 kHz. This was operated at each RLAM in a receive only mode, allowing simple DTMF codes from a transmitter at the main camp to power and unpower RLAM's remotely. In addition to providing a failsafe reset method for the RLAM computer, the UHF radio was used to supply RLAM's with IRIG-B timecode. Consequently, all RLAM's were synchronized to a common absolute time source (GPS time) as were the acquistion systems at the camp for the horizontal and vertical arrays.

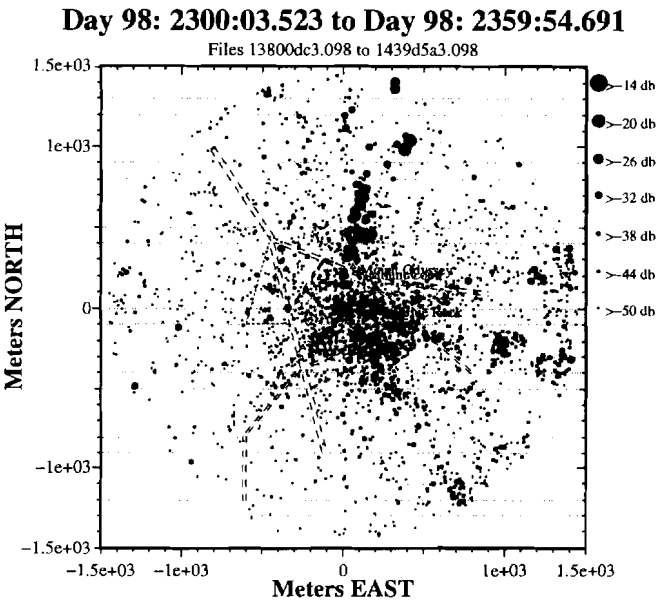

FIGURE 3. Ice events located by real-time beamforming on horizontal hydrophone array between 098:23.00Z and 098:23.59Z, including major events associated with existing crack immediately N of new shear ridge (Mount Odyssey)

REAL-TIME LOCALIZATION OF ICE EVENTS

During the SIMI 94 experiment in East Camp we recorded a total of more than 100Gb of data from the horizontal and vertical hydrophone arrays. The data were passed through the real-time beamformer, and hourly event maps were generated. As an example, Fig. 3 shows events detected between 098:23.00Z and 098:23.59Z, including major events associated with existing crack immediately N of new shear ridge (Mount Odyssey). The size of the markers indicate the estimated source levels of the individual events. As a result of this detection, one of the RLAM geophone clusters were deployed in vicinity of the crack and were recording the continued seismicity for several days following. This data has not yet been processed.

ANALYSIS OF GEOPHONE CLUSTER DATA

With the total of 100Gb+ data recorded during the various deployments of the RLAM units, only a small fraction has been analyzed sofar. Examples of events recorded, but not yet processed in detail, are given in Fig. 4.

Figure 4(a) shows a characteristic example of strong long-duration events recorded near the new NW–SE lead opened up NE of the Ewart camp, 1.9 km from Main Camp. We are yet to analyze these events in detail, but the strong polarization parallel to the lead suggest that they are associated with "edge waves" traveling along the lead. The strong hydrophone response suggests strong radiation into the water column from these waves.

Figure 4(b) shows an example of data recorded by an RLAM cluster deployed in the East Pond for monitoring the seismo-acoustic field produced by the various ice-mechanical sources simulated by Pritchard. The particular source is the socalled "splash" generated by an ice block falling into open water in a hydrohole. The geophone signals have much higher frequency content than the hydrophone signal, and clearly show contributions from the

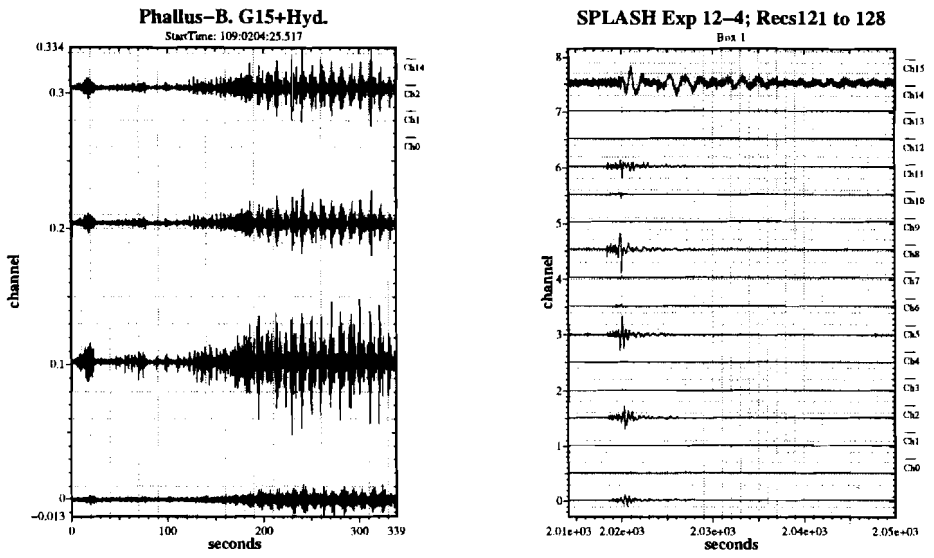

FIGURE 4. Examples of ice-mechanical events recorded by RLAM clusters. (a) RLAM cluster deployed at new lead 2 km NE of West Camp at 109:02.04Z. The uppermost trace represents a hydrophone, while the lower 3 traces represent two horizontal and a vertical geophone. The highest amplitudes were recorded on the geophone parallel to the lead. (b) RLAM cluster deployed on East Pond during "Splash" experiment 12-4 performed by Pritchard. Channels 0,2,5,8, and 11 are verticale geophones, Channel 15 is a hydrophone, and the remaining channels are horizontal geophones.

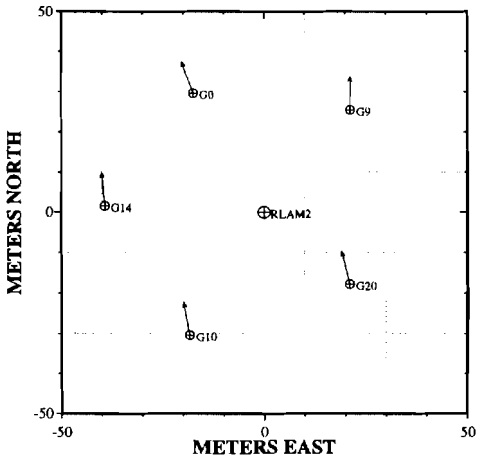

FIGURE 5. RLAM geophone array with X-component orientation

fast longitudinal waves and the slow flexural waves, in addition to the strong waterborne component.

Sofar our event analysis has focused on data recorded on a small ice floe 4 km E (93°7′) of East Camp. The geometry of the deployed geophone array is shown in Fig.5. Fig. 6 shows the high-pass filtered data recorded on the five vertical geophones, and their associated frequency spectra for an ice event. The different arrival times are evident in the filtered data, allowing for localization of the source by cross-correlation, yielding an estimated source

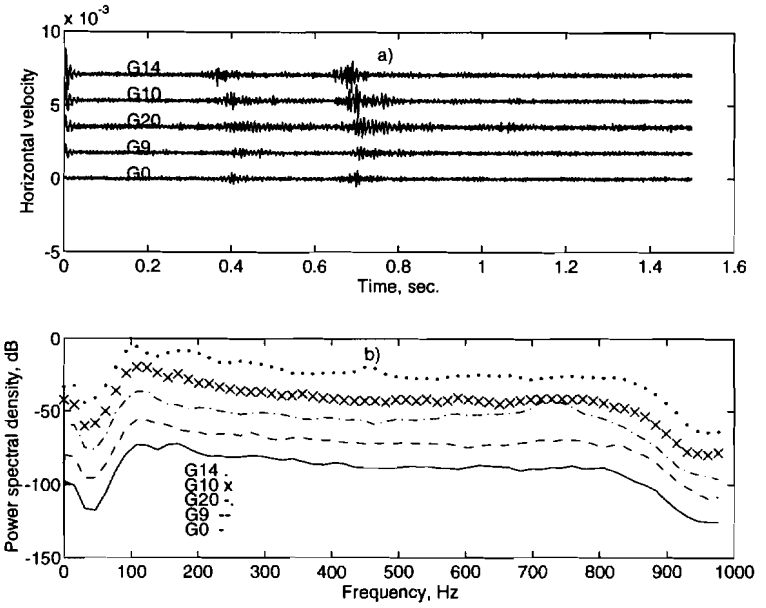

FIGURE 6. Timeseries and frequency spectra for event recorded on vertical geophones on ice floe 4 km NE of East Camp.

position 70 m SW of the array center. Also, significant differences are observed between the various geophone timeseries and spectra, both qualitatively and quantitatively, reflecting the horizontal inhomogeneity of the radiation pattern.

SEISMO-ACOUSTIC MODELING

We have been continuing our development of mathematical and numerical models of the seismo-acoustic field produced by ice cracks. A new such model combines a seismic moment representation with an efficient solution technique for stratified fluid-elastic representations, and a transformation reflecting the source dynamics [15]. Figure 7 shows an example of modeled geophone response to a propagating thermal crack in an Arctic ice cover. A tensile (e.g. thermal) crack is initiated at time t=0 s and propagates with a constant speed of 800 m/s for a total period of 20 ms, yielding a final crack length of 16 m. The acoustic emission is recorded by 3 vertical geophones, denoted G1, G2 and G3, placed at a range of 200 m from the crack initiation point, at bearings 120°, 90° and 60°, respectively, relative to the fracture propagation direction.

Figure 7(a) shows the modeled timeseries for geophones G1 (solid curve) and G2 (dashed curve). The crack tip is moving away from the receiver at a projected speed of 400 m/s, whereas the projected radial speed vanishes for geophone G2. A comparison of the two responses in Fig. 7(a) shows the expected frequency doppler shifts, both for the fundamental *compressional mode* arriving at $t = 0.06$ seconds, but much more clearly for the highly dispersive and slow fundamental *flexural mode* between $t = 0.12$ and $t = 0.5$ seconds. Another effect is a decrease in the observed amplitudes, primarily due to the longer mean range for geophone G1.

Similarly, Fig. 7(b) shows a comparison of the response of geophones G3 (solid curve) and G2 (dashed curve). For geophone G3 the crack tip is approaching with a projected

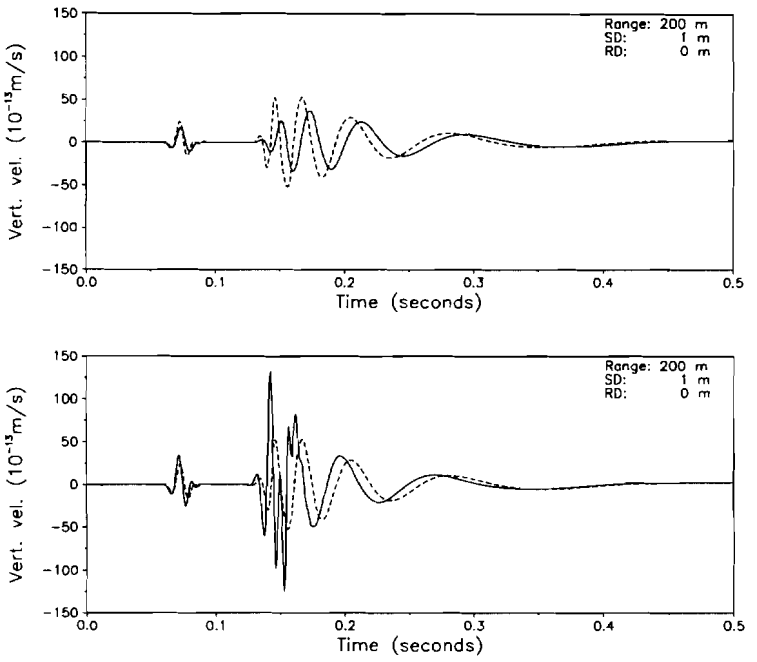

FIGURE 7. Comparison of modeled geophone signals from propagating thermal crack. **(a)** Signals received on geophone G1 (solid curve) and geophone G2 (dashed curve). Relative to the receiver, the source is receding with radial velocity $v_s \cos\theta_s = -400$ m/s for G1, and 0 m/s for G2. **(b)** Signals received on geophone G3 (solid curve) and geophone G2 (dashed curve). Relative to the receiver, the source is approaching with radial velocity $v_s \cos\theta_s = 400$ m/s for G3, and 0 m/s for G2.

speed of 400 m/s. and here the differences is obviously much more dramatic than for G1, with a distinct high-frequency arrival interfering with the initial phase of the fundamental flexural wave. This is due to the excitation of a higher order mode in the ice [15].

Other new model development associated with SIMI is described in Refs.[6] – [21].

An area where we have achieved significant progress in the past couple of years, and which is of direct relevance to our SIMI effort, is the development of models representing the theoretical resolution properties of ocean acoustic tomography, and other inverse problems such as the fracture plane analysis. The cornerstone of this work, which builds on the pioneering MIT/WHOI work in matched field processing [1, 3], is a theoretical representation of the optimal resolution a particular sensor system can achieve in any relevant parameter. This modeling work is described in several publication [16, 17, 26, 27].

SEISMO-ACOUSTIC ICE PROPERTY INVERSION

We have been continuing the development of inversion procedures for infering ice-mechanical properties from plate wave experimental data. This work combines the geophone data analysis of Miller and Schmidt [5] with the high-resolution matched field parameter estimation approaches developed in the past by MIT/WHOI [1, 3]. Specifically we have the past year been developing a wavelet-transform based inversion approach for the thickness, and compressional and shear speeds of the ice cover. A high resolution estimate of the group velocity of the ice modes is obtained through a wavelet transform, and subsequently matched using

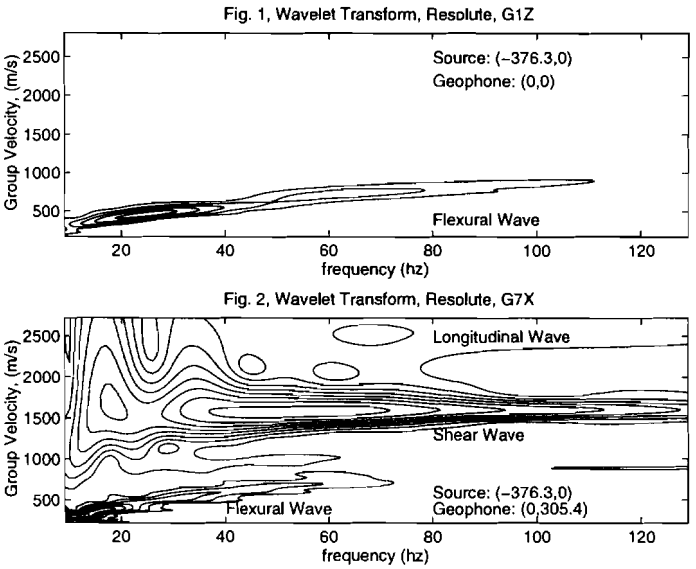

FIGURE 8. Dispersion characteristics of seismic modes in the ice cover, obtained using a wavelet transform approach. (a) Vertical geophone component. (b) Horizontal geophone component.

a numerical model. The method has been applied to the Resolute data, collected by Peter Stein, to invert for the physical parameters of the ice. The experiment was conducted in a smooth ice floe using a vertical hammer strike as the source and the data were recorded by geophones. With the traditional short-time Fourier transform (STFT), once a window has been chosen, the time-frequency resolution is fixed over the entire time-frequency plane. In comparison with the STFT, the wavelet transform lets the time and frequency resolutions vary in the time-frequency plane in order to obtain a multi-resolution analysis, so that the time resolution becomes arbitrarily good at high frequencies while the frequency resolution becomes arbitrarily good at low frequencies. Hence, the wavelet transform yields better parameter estimates than the STFT, especially for dispersive waves. Fig. 8(a) shows the result of the wavelet transform of a vertical geophone component, with the positive dispersion characteristics of the flexural wave being evident. Fig. 8(b) shows the wavelet transform of a horizontal geophone component, yielding high-resolution estimates of the dispersion characteristics of both the flexural wave, the horizontally polarized shear wave (SH), and the longitudinal wave.

Analysis and Publication Plans

The debugging and fine tuning of the RLAM units have been continued after the SIMI experiments, and the development is now considered complete. A final report describing the RLAM is in its final preparation stage and will be published in the Spring of 1995 [25].

Our analysis of the hydrophone array data will be continued with particular focus on the event statistics. This work is expected to lead to a Ph.D. Thesis (1997) and one or more journal papers.

The analysis of the geophone data is expected to lead to a Ph.D. thesis in 1997, and several journal papers before that, focusing on the fracture plane inversion. The dataset is so rich in event variety, that more theses are anticipated to result from this analysis in

the future. A particularly interesting component is the analysis of the long-duration events recorded along the new lead, as shown in Fig. 4. Our progress on fracture plane analysis will be presented in an invited paper at the ASME Ice Mechanics Workshop at UCLA, June 28-30, 1995.

The use of wavelet analysis for ice property inversion is currently being combined with an efficient search algorithm to yield a robust and reliable inversion procedure for ice properties and roughness characteristics. The algorithm will be used on the hammer-blow data collected by Peter Stein in West Camp in the Fall of 1993. This work is expected to lead to a Ph.D. thesis in the Fall of 1995.

Another Ph.D. thesis to be finished in the Spring of 1995 describes the analysis of short-range reverberation data collected in CEAREX 89. Two journal papers are currently being reviewed [22, 23], and one more is in preparation [24].

In addition we will continue our development of more complete models of propagation and scattering in and below the Arctic ice cover. We have established a world leadership in this area, and several publications are in the publishing pipeline [19, 20, 21]

Our inversion resolution work will be presented at a couple of international conferences in 1995 [26, 27], and a journal paper is in preparation.

Publications

1. A.B. Baggeroer, W.A. Kuperman and H. Schmidt, "Matched field processing: Source localization in correlated noise as an optimum parameter estimation problem," *J. Acoust. Soc. Am.*, 83(2), 571-587, 1988.
2. W.A. Kuperman and H. Schmidt, "Self-consistent perturbation approach to rough surface scattering in stratified elastic media," *J. Acoust. Soc. Am.*, 86, 1511-1522, 1989.
3. H. Schmidt, A.B. Baggeroer, W.A. Kuperman, and E.K. Scheer, "Environmentally tolerant beamforming for high resolution matched field processing: Deterministic mismatch," *J. Acoust. Soc. Am.*, **88**, 1851-1862, 1990.
4. P. Gerstoft and H. Schmidt, "A boundary element approach to ocean seismo-acoustic facet reverberation," *J. Acoust.Soc. Am.*, 89, 1629-1642, 1991.
5. B.E. Miller and H. Schmidt, "Observation and inversion of seismo-acoustic waves in a complex Arctic ice environment," *J. Acoust. Soc. Am.*, 89, 1668-1685, 1991.
6. K.D. LePage. *Elastic scattering in oceanic waveguides.* PhD thesis, Massachusetts Institute of Technology, September 1992.
7. J.-Y. Liu, "Seismo-acoustic interface scattering of surface-generated ambient noise in a stratified ocean," PhD thesis, Massachusetts Institute of Technology, October 1992.
8. M. Deffenbaugh, H. Schmidt, and J. Bellingham, "Acoustic navigation for Arctic under-ice AUV missions," *Proc. Oceans '93* 1993.
9. F.B. Jensen, W.A. Kuperman, M. Porter, and H. Schmidt, *Computational Ocean Acoustics*," American Institute of Physics, 1994.
10. M. Deffenbaugh, "A matched field processing approach to long range acoustic navigation," MS Thesis, Massachusetts Institute of Technology, February 1994.
11. J.T. Goh and H. Schmidt, "Validity of spectral theories for weakly range-dependent ocean environments – Numerical results," *J. Acoust. Soc. Am.*, 95 (2), 727-732, 1994.
12. K.D. Rolt and H. Schmidt, "Effects of refraction on synthetic aperture sonar imaging," *J. Acoust. Soc. Am.*, 95 (6), 3424-3429, 1994.
13. K. Lepage and H. Schmidt, "Modeling of low frequency transmission loss in the Central Arctic," *J. Acoust. Soc. Am.* 96(3), 1783–1795, 1994.
14. K.D. Rolt, H. Schmidt, and G.H. Rolt, "Commentary on 'Effects of propagation on the operation of a synthetic aperture sonar' [J.Acoust.Soc.Am. 82(4), 1403-1408, Oct. 1987]," *J. Acoust. Soc. Am.*, 96 (4), 469–475, 1994.

15. H. Schmidt and W.A. Kuperman, "Spectral and modal representations of the Doppler shifted field in ocean waveguides," *J. Acoust. Soc. Am.*,96 (4), 386–395, 1994.
16. A.B.Baggeroer and H. Schmidt, "Parameter estimation bounds and the accuracy of full field inversions." In O. Diachok, et al, editor, *Full field inversion methods in ocean and seismic acoustics*, Kluwer Academic Publishers, Dordrecht, The Netherlands, 1994.
17. H. Schmidt and A.B.Baggeroer. "Physics-imposed resolution and robustness issues in seismo-acoustic parameter inversion". In O.Diachok, et al, editor, *Full field inversion methods in ocean and seismic acoustics*, Kluwer Academic Publishers, Dordrecht, The Netherlands, 1994.
18. H. Schmidt, "Seismo-acoustics of the Arctic ice cover." In L. Bjørnø, editor, *Underwater acoustics*, European Commission, Luxembourg, 1994.
19. K. LePage and H. Schmidt, "Analysis of spatial reverberation statistics in the Central Arctic", *J. Acoust. Soc. Am.*, In Press, 1995.
20. H. Schmidt and W. A. Kuperman, "Spectral representations of rough interface reverberation in stratified ocean waveguides," *J. Acoust. Soc. Am.*, In press: 1995.
21. H. Schmidt, W. Seong, and J.T. Goh, "Spectral super-element approach to range-dependent ocean acoustic modeling," *J. Acoust. Soc. Am.*, In Press: 1995.
22. T. Kapoor and H. Schmidt, "Spherical coordinate Green's functions for ring tractions in a solid unbounded elastic medium," *J. Acoust. Soc. Am.*, Submitted: 1995.
23. T. Kapoor and H. Schmidt, "Acoustic scattering from a three-dimensional protuberance on a thin infinite submerged elastic plate," *J. Acoust. Soc. Am.*, Submitted: 1995.
24. T. Kapoor and H. Schmidt, "Matched-field evaluation of low-frequency acoustic scattering from rough Arctic ice," *J. Acoust. Soc. Am.*, In preparation: 1995.
25. K. von der Heydt and C. Eck, "Radio LAN Acquisition Module (RLAM), Recent Developments for High Resolution Data Collection Systems as Implemented for the ONR Sea Ice Mechanics Experiment", WHOI Technical Report. In progress, Spring 1995.
26. A.B. Baggeroer and H. Schmidt, "Cramer-Rao bounds for matched field tomography and ocean acoustic tomography," Proc. IEEE ICASSP '95, 1995.
27. A.B. Baggeroer and H. Schmidt, "A comparison of matched field tomography and ocean acoustic tomography using Cramer-Rao parameter estimation bounds," Proc. International Congress of Acoustics, Trondheim, Norway, May 1995.

SIMI WINTER-OVER GEOPHONE/HYDROPHONE SYSTEM

Dr. Peter J. Stein (P.I.), Mr. Douglas W. Andersen, Mr. Armen Bahlavouni, and Mr. Steven E. Euerle of Scientific Solutions, Inc. (SSI) and Mr. Gerald M. Santos and Mr. Richard K. Menoche of the Naval Undersea Warfare Center Division Newport (NUWC).

Scope of the Data Set

Background - Similar to land-based seismology, geophones and hydrophones are paramount to researching the strength and growth of, and the mechanical failures (fractures) in sea ice. In April 1992, in support of the SIMI initiative, a 1-km aperture, 12-element, tri-axial geophone array was deployed on the ice off the coast of Resolute Bay, Canada. It was used to study thermal ice fracturing events and elastic wave propagation in ice. In addition, radiometer data and other pertinent meteorological data was collected. Some of the results from the Resolute experiment are described in a companion report (Lewis and Stein, "Sea Ice Mechanics Related to Thermally-Induces Stress and Fracturing In Pack Ice"). For the main SIMI field experiment, a more ambitious winter-over geophone/hydrophone system was deployed. The intent of this system was twofold: 1) to use an automated hammer blow source and the geophone array to characterize acoustic wave propagation in the ice, and to invert this data to get ice mechanical properties, and 2) to collect ambient noise data with the geophone/hydrophone system and relate this data to thermal fracturing. In this summary we will focus on this system and some preliminary data results.

Most acoustic/seismic measurements of elastic wave propagation in ice and of the fracturing of sea ice have been made in spring-time conditions, usually on relatively smooth first-year ice. In order to truly understand the physical mechanisms behind ice growth, stress, and fracturing, long-term and year-round measurements are required. One of the goals for the SIMI winter-over geophone array deployment was to deploy a geophone array in the fall on multi-year ice and study the elastic wave propagation and fracturing of ice throughout the winter. Another clear goal for the SIMI winter-over geophone system was to develop and test methods for deploying complex and often power-hungry seismoacoustic systems for long periods of times in the Arctic and automating the data collection methods.

During the fall SIMI field operation the SSI/NUWC team successfully deployed 20 tri-axial geophones and 4 hydrophones along with a data acquisition and power system designed to operate until recovery in the spring. In an overall sense the system was very successful in that a valuable data set was collected for studying wave propagation and fracturing under fall to early-winter conditions. Unfortunately, the data storage device failed on 16 December and no further data was collected until the system was revisited in the spring. However, almost all other components performed flawlessly and valuable lessons were learned. The ability to successfully deploy unmanned seismoacoustic systems in the Arctic for long periods of time was clearly demonstrated.

Winter-Over System Description - The array layout showing the deployed location of the geophones and hydrophones is shown in Figure 1. The legs of the array match the cable lines

extending from the "Stein" hut shown in Map 2 of the SIMI West Camp in November 1993. Two geophones were also deployed as outliers and are also shown on Map 2. Figure 2 is a schematic showing the general elements of the overall winter-over system. The tri-axial geophones are type LRS-1033 with a resonance frequency of 4.5 Hz. Differential preamplifiers (60 dB) for each tri-axial phone were located near the sensor. Each sensor was individually cabled back to the data acquisition system in the insulated "Stein" hut. The hydrophones were roughly 5" diameter by 7" long PZT cylinders with a nominal sensitivity of -182 dBV/μPa. These phones were deployed at a depth of 100 m and cabled to 60 dB preamplifiers in the hut. The signals from all sensors were then differential-to-single-end amplified, antialias filtered, and connected into a PC based ANALOGIC 200-kHz A/D board. The A/D board was controlled via the PC which contained a flash RAM disk for storing the operating system and data collection software and a RAM disk for temporary storage of the data. The computer hard drive and floppy drives were disconnected for unmanned operation to reduce power consumption. Data was stored as backup files on an Exabyte 50 GB stacker.

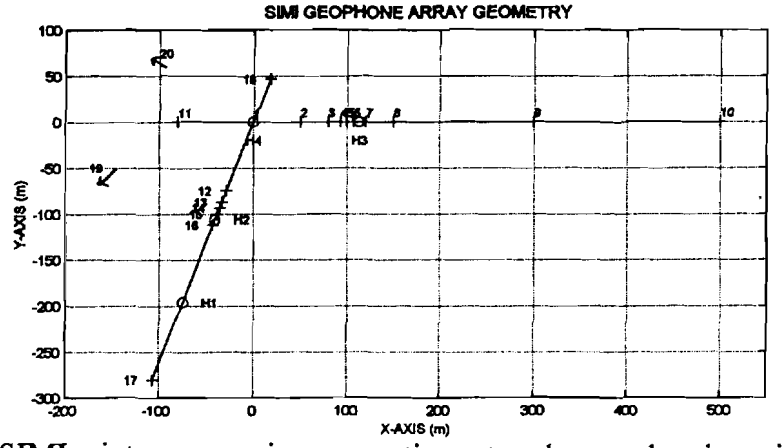

Figure 1. SIMI winter-over seismoacoustic system layout showing tri-axial geophone and hydrophone locations. Hydrophones were omnidirectional below 5 kHz and were deployed at a depth of 100 m.

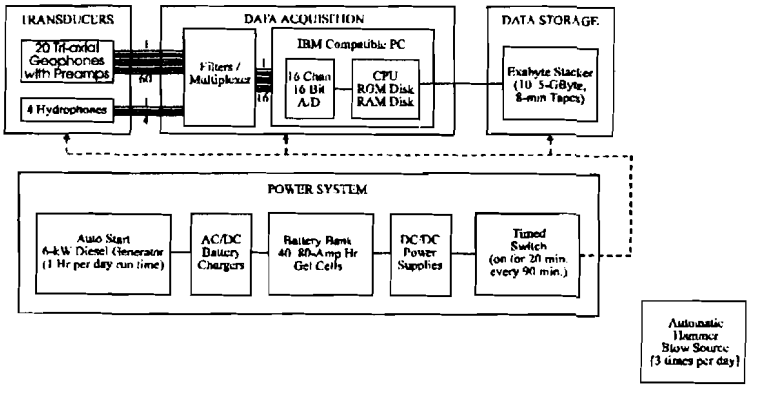

Figure 2. Schematic of the winter-over digital data acquisition system.

The power system consisted of forty 88-AH gel-cell batteries charged by an autostart diesel

generator. The batteries could keep the system operational for roughly 45 days should the generator have failed. The PC and all hardware were converted to operate off the batteries using DC-DC power supplies. In the unmanned phase the generator was started once per day and ran for 1 hour. This was sufficient to keep the batteries fully charged. Four 55 gallon drums of diesel fuel were connected to the generator through a single manifold. The generator was also equipped with an autofill oil reservoir. The generator and all power systems were operational when the camp was revisited in the spring.

The data acquired can be divided into three phases: fall manned, fall unmanned, and spring manned. All of the SIMI data was saved on 8-mm tapes using the Exabyte Stacker. Generally data was collected either at a low or high frequency mode. In the low-frequency mode, the data was antialias filtered at 100 Hz and digitized at 250 Hz and data was collected from all 20 tri-axial geophones (60 sensors) plus 3 of the hydrophones. In the high-frequency mode the data was antialias filtered at 5 kHz and digitized at 10 kHz, and data was collected from one of the tri-axial geophones (3 channels) and 3 hydrophones. In the unmanned phase a timer turned the system on approximately every 1.5 hours. Each time the system started, eighty five contiguous 5.1-second low frequency records were collected followed by fifty 1.0-second high frequency records. We had hoped to have the acquisition system powered at all times and data recording triggered by ice events. However, we were unable to get the triggering system operational in time for the field operations and thus went to timed acquisition.

A heating system in the hut consisting of a catalytic propane heater set on low connected via a manifold to propane cylinders was provided by the University of Washington (A. Heiberg). Substantial additional heat was provided by the diesel generator operation. The temperature in the hut was monitored for several days before departure. One hour of generator operation would warm the hut to above 25°C. Following this the temperature would fall slowly to about 0°C by the next days generator operation.

Figure 3 is a picture of the inside of the "Stein" hut just prior to leaving the system for unmanned operations.

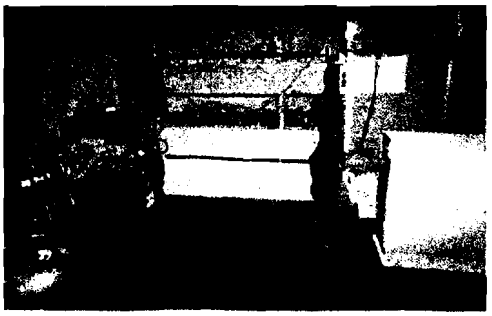

Figure 3. Picture showing the inside of the "Stein" hut as left for unmanned operation. Shown are the propane heater and generator system (left), the batteries (left center), the cable terminations box with antialias filter and amplifiers (right center), and the data acquisition system with Exabyte tape stacker (right). The gear was secured to prevent motion due to the generator vibrations.

Automated Hammer Blow Source - An automated hammer blow source was developed to provide a repeatable source signature for generating elastic waves in the ice during the unmanned operations. This device is shown in Figure 4 and it's source signature is shown in Figure 5. During the unmanned phase it was deployed at the apex of the geophone array and set to impact the ice approximately 3 times per day. When the hammer-blow system started it automatically turned on the data acquisition system and started the data recording. 50 automated hammer blows were successfully recorded during the unmanned phase. The hammer operated successfully beyond the time at which the acquisition system failed. Sometime before spring a crack ran close to the hammer and the bottom portion flooded with sea water. This caused the entire device to become covered with rust. In March the hammer was found with the weight stuck near the top due to the rust on the stainless steel shaft. However, the motor and chain drive were still operational.

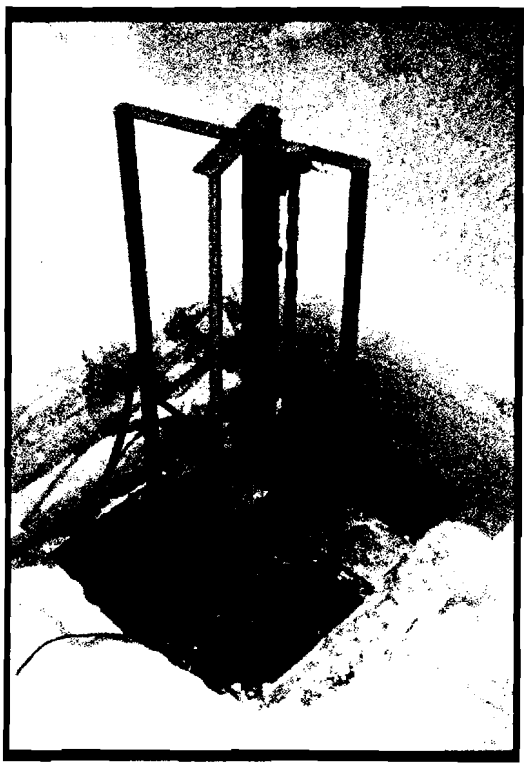

Figure 4. Picture showing the automated hammer blow source (a). A 45 kg weight was lifted 0.7 m and dropped. The base of the device is a 1.27 cm thick steel plate. The weight strikes an area which is covered with silicone rubber and a thin steel plate. The device was attached through the ice using ice screws inserted through holes in the base plate.

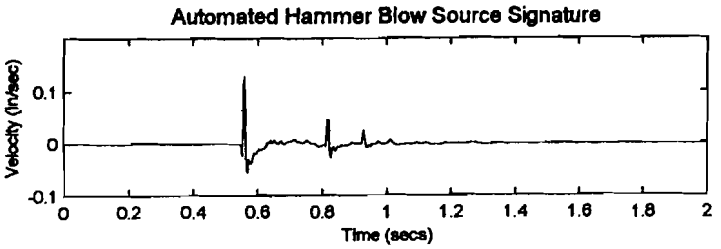

Figure 5. Time series of the hammer blow source on the vertical axis of a geophone 1 m away. It shows a "multiple strike" which added some complications to the data analysis.

Fall Manned Phase - Data Acquired - Over 4 GB of data was collected with the geophone/hydrophone system during the period of 16 to 28 November. This data consisted primarily of sledge hammer blows performed at several of the geophone locations, hammer blows using the automated source located at the array apex, and ambient data taken throughout the period. Also, data was taken during a "cleared snow-area test" on the night of 23 Nov 1993, in which a 7 by 7 meter area of ice was cleared of snow during extreme cooling conditions (falling temperatures, clear skies, calm winds). The cooling conditions resulted in a substantial amount of thermal fracturing that night. Removing the snow cover resulted in greatly increased thermally induced tensile stresses measured in the clearing. Also, long-wave radiometer data was collected during the period from 7 to 28 November (unmanned operation of radiometers is not yet feasible due to frosting of the domes - they must be cleaned periodically).

Fall Unmanned Phase - Data Acquired - Approximately 5 GB of data were collected with the geophone/hydrophone array during the time period between 28 November and 16 December. Data collection halted on December 16 when the Exabyte data storage device failed. This data represents a total of over 1600 minutes of low frequency (< 100 Hz) geophone data and 190 minutes of high frequency (<5 kHz) hydrophone data. Each data set consists of 7 minutes of geophone data and 50 seconds of hydrophone data collected every 90 minutes. The data also contains geophone recordings of the automated hammer blow source impacts approximately 3 times per day.

Spring Manned Phase - Data Acquired - After leaving on 28 November, the system was next revisited on 20 March. It was found that the tape backup failed on 16 December. The automated hammer blow failed at some later date due to being flooded by a nearby crack. It is likely that this occurred sometime in March, as the crack that resulted in the flooding was not present when the camp was checked in February. The primary purpose of the spring manned phase was to recover the system but some data was acquired. Data includes sledgehammer blows and ambient recordings during two overnight periods from 21 March to 23 March 1994. The totality of the data collected by the winter-over geophone system is summarized in Table 1.

Findings to Date

Cleared Snow Area Test - The cleared snow area test of 23 November 1994 was very successful. We chose a night which was expected to have intense thermal fracturing, with falling temperatures, clear skies, and calm winds to perform the cleared snow area test. The measured stresses at a depth of 25 cm at a CRREL stress sensor located in the center of the area are shown in Figure 6. Also shown in Figure 6 are the cleared snow area stresses from the Resolute Bay Experiment. Note the extreme increase in tensile stress after the snow was cleared (day 328). Also in both tests there was a temporary *increase* in compressive stress just when the snow was cleared. This phenomenon has not yet been explained. During the night an ice crack occurred which ran in an L shape across the cleared snow area. Indeed we see what appears to be a stress relief of around 20 kPa just before midnight Zulu on day 328. It is also clear that tensile cracking can occur at 10 m scale average stresses well below 50 kPa.

TABLE 1. SUMMARY OF DATA ACQUIRED BY WINTER-OVER GEOPHONE/HYDROPHONE SYSTEM

DATES	DATA TYPE	DATA SET* INTERVAL	COMMENTS
16 Nov 1993	Geophones	Once	Several sledge hammer blows collected at each of 8 geophone locations.
16-28 Nov 1993	Geophones and Hydrophones	Several to many sets per day	Camp noise contamination at times.
7-28 Nov 1993	Long wave and short wave radiometer	One sample every 5 min.	
23 Nov 1993	Geophones and Hydrophones	Every 38 min.	Cleared snow area; stress data collected by CRREL.
28 Nov-16 Dec 1993	Geophones and Hydrophones	Every 1.5 hours	Ambient.
28 Nov-16 Dec 1993	Geophones	Every 7 hours	Automated hammer blow.
21 Mar 1994	Geophones	Once	Several sledge hammer blows at each of 4 geophone locations.
21-23 Mar 1994	Geophone and Hydrophones		Overnight ambient.

* - 1 Data set consists of 85 nearly contiguous 5.1 sec records of geophone data sampled at 250 kHz followed by 50 nearly contiguous 1 sec records of hydrophone data sampled at 10 kHz.

The geophone/hydrophone data acquisition set up for that night collected data for approximately 8 minutes at 38 minute intervals throughout the night. The data showed intense thermal fracturing over the whole floe that night beginning roughly at 6 PM local and lasting through the night. Approximately two-thirds of the taped files of 250-Hz geophone data from this night have been transferred to optical disc and processed (none of the 10-kHz files from this period have been processed). The processing here involved searching all files over all geophone channels for "events" by using a threshold type peak detection scheme. Specifically, an "event" was detected if a data sample exceeded an rms average of the previous .25 seconds of data by the threshold. Events were generally categorized as "ice events" or hammer blows (the automated hammer blow source was also operating on this night). Several of the events found appear to have occurred in the general vicinity of the cleared snow area. However, we cannot yet isolate the particular event which gave the stress drop, and, since we had to revert to timed data acquisition instead of triggering on events, it is unlikely we would have caught it. A disproportionate number of the events were found on Geophone 19, the outlier near the Rajan camp, and might have been precursors to the succeeding ice breakup near this location. It seems evident that the thermal fracturing was a factor in the breakup which occurred soon after in this area.

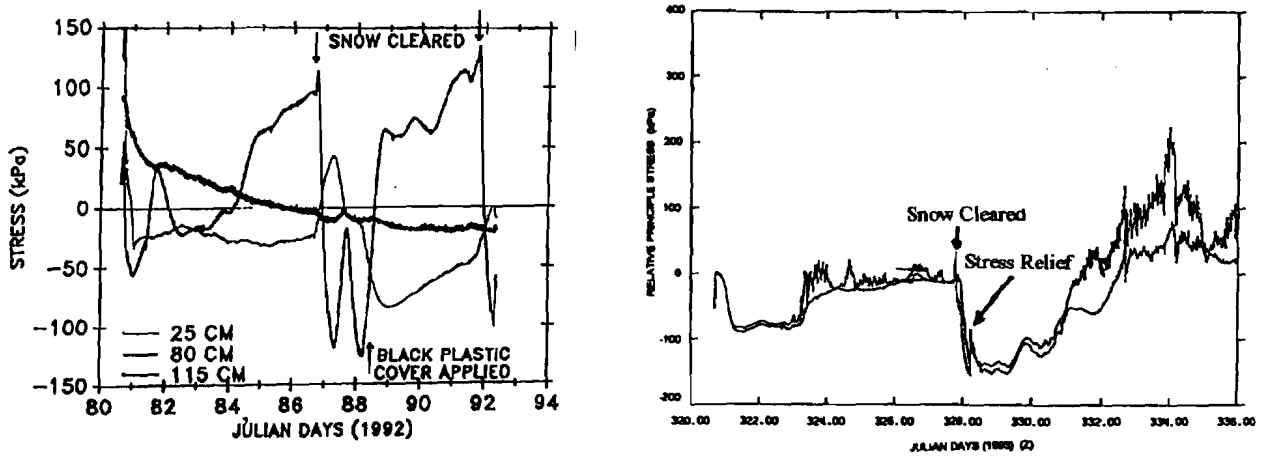

(a) (b)

Figure 6. Stress levels measured at by a shallow sensor in the middle of a roughly 7 m by 7 m cleared snow area. Plot (a) is from the Resolute Experiment conducted in Allen Bay in March 1993. Plot (b) is from SIMI and shows the relative and not absolute stress. The rapid increase in tensile stress is due to the snow being cleared off. Note the unexplained increase in compressive stress just when the snow was cleared and the stress relief likely due to a fracture which occurred during the night.

Ambient Geophone/Hydrophone Recordings -Data sets from the three days just before we left camp (Nov 25, 26, 27) were examined using the same search techniques as described above. No "ice events" were found on the few days following the night of intense thermal fracturing on the 23rd. We have processed all of the geophone and hydrophone data from the unmanned phase of the experiment 16 November - 16 December 1993 to pull out the automated hammer blows and determine episodes of high-thermal fracturing. Days on which many events were detected occurred on Julian days 339, 346-347, and 349. It seems certain that thermal fracturing, which has been shown to occur roughly every week in spring-time conditions, also occurs in the fall and into the winter. Thermal fracturing is likely a fundamental method for ensuring a structurally weak kilometer scale ice pack.

All hydrophone files for this period were processed by digitally filtering all data for Hydrophones 2 and 4 in one-third octave bands from 10 Hz to 4000 Hz and calculating average levels for the file in a one second window. A plot of the RMS pressure in one-third octave bands as a function of frequency and time is given in Figure 7. Note the overall high levels corresponding to Julian days 346 when many thermal events were detected on the geophones. It is hoped that this data will be useful in determining the frequency content of

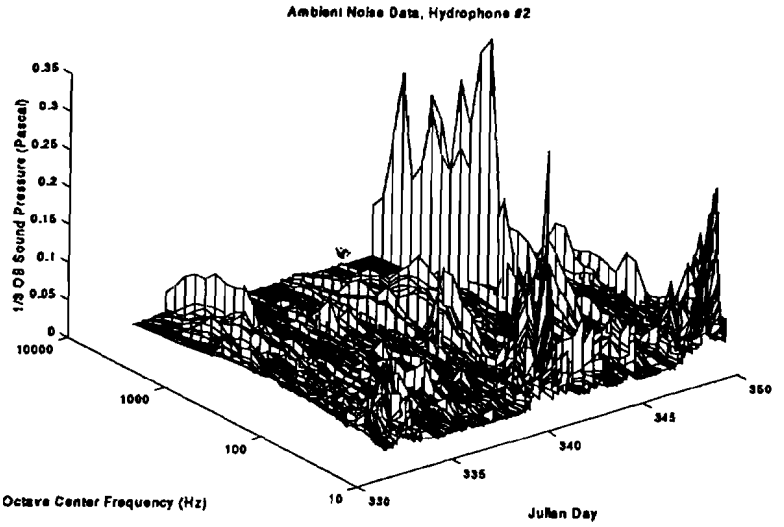

Figure 7. Ambient noise in RMS pressure in one-third octave bands averaged over 1 sec as a function of frequency and time.

Hammer Blow Data - An extensive set of hammer blow data in fall multi-year ice was collected. All hammer blows (sledge and automated) have been found in the data and are currently being processed. A major difficulty has been in working with the warm and highly variable multi-year ice which was common at the fall Simi camp. Another complication is that the hammer blow source has a multiple signature as a result of the bouncing of the weight (see Figure 5). For future tests the hammer blow source should be modified to avoid this double bounce.

For comparison, time series data from four hammer blows is shown in Figure 8, one from the Resolute test, a sledge hammer blow from the fall and spring Simi Experiment, and an automated hammer blow source drop. Note the clean longitudinal and shear wave arrivals in the Resolute data which are absent from the Simi data. There is also little transverse motion for the flexural wave at Resolute as would be expected for a flat plate. For the Simi data, the transverse motion is almost equal to the longitudinal motion, even at 80 meter range, which suggests a highly non-uniform propagation path. In the automated hammer blow data, versus the sledge hammer data, one can see the effects of the double bounce as a high frequency arrival overlapping the low frequency portion of the flexural wave. These complexities are currently being sorted out.

Even with the complexities we are able to estimate the flexural wave speed over the unmanned period and again in the spring using a frequency domain beamforming technique. This is given as Figure 9. Using measured flexural wave speed and the ratio of vertical to horizontal motion, we can determine an effective ice thickness for the ice around one of the geophones. This is plotted in Figure 10. We are currently working to determine the bending rigidity (Young's Modulus) as a function of time using the above estimate of thickness versus time, and an assumed ice density and Poisson's ratio. We are also working to compute these parameters using the data and a more appropriate vertical profile in the ice. These techniques demonstrate the use of easily deployable geophones to determine the average thickness and rigidity of the ice.

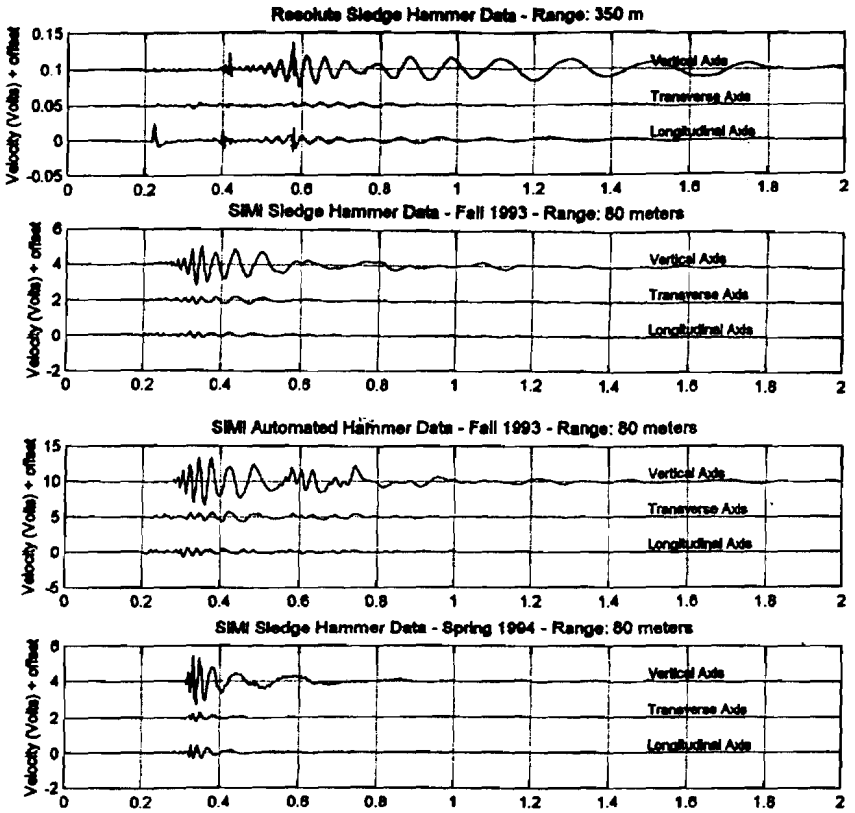

Figure 8. Vertical geophone hammer blow time series for a 4.5 kg sledge hammer at (a) Resolute Spring (94), (b) SIMI (Fall 93), (c) SIMI (Spring 94), and (d) the automated hammer blow at SIMI (Fall 93).

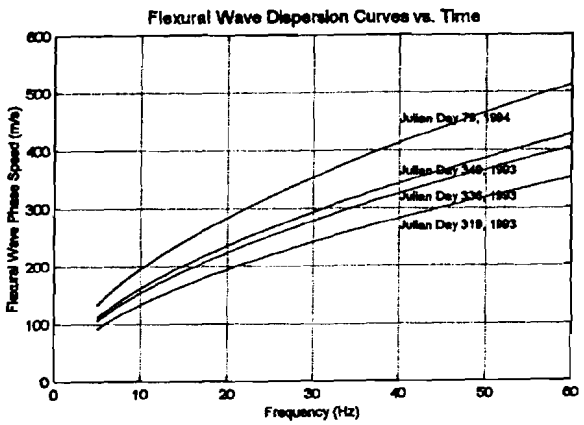

Figure 9. Flexural wave speed computed from the winter-over geophone system and automated hammer blow source using Geophones 3-7 on the runway leg. Wave speeds are computed by frequency domain beamforming and extrapolating using a known flexural wave dispersion curve.

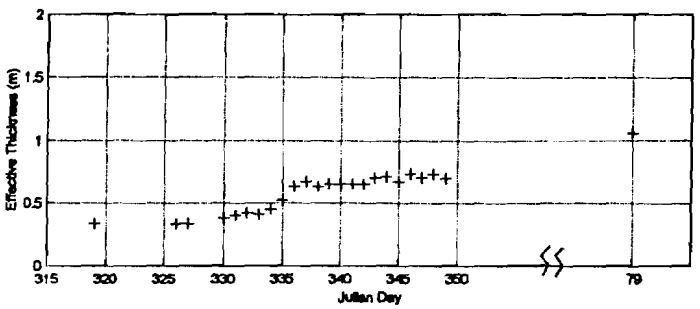

Figure 10. The effective average thickness around Geophone Number 3, computed by beamforming to get dispersion curves, using phase and amplitude relationships between vertical to longitudinal geophone motions.

Analysis and Publication Plans

Our first priority is to analyze the automated hammer blow data and invert the data for ice properties. We will also be looking at the ambient noise records to continue our effort with J. Lewis to formulate a predictive model for thermally induced ambient noise. Our focus for much of this work is to develop tools to help interpret and/or monitor the effects of climate change in the Arctic. We plan to publish papers and make presentations at AGU and ASA Conferences. A special session on Seismoacoustic Determination of Sea Ice Processes is planed for the Spring ASA meeting (31 May to 3 June 1995). The following is a list of potential papers and/or presentations resulting from our SIMI work:

- Determination of sea ice processes using geophone arrays
- Time variation of the thickness and modulus of sea ice measured using geophones
- A predictive model for thermally induced ambient noise in the Arctic
- On the importance of thermally induced stresses in Arctic Pack ice

The following is a list of publications and presentations resulting from our Simi work:

"Observations and modeling of thermally-induced stresses in first-year sea ice." J.K. Lewis, W.W. Tucker, and P.J. Stein, J. Geophys. Res, 99(C8), 16361-16371, 1994.

"Monitoring thermal fracturing on ice: The relation to ice stress and strength." J.K. Lewis, W.B. Tucker, and P.J. Stein, Acoust. Soc. Amer., 94(3) Pt. 2, September, 1993.

"Additional data on low-frequency elastic wave propagation in ice." P.J. Stein, Acoust. Soc. Amer., 92(4) Pt. 2, October, 1992.

"Distribution of Ice Events During High Thermal Ice Cracking Activity.", P.J. Stein, Amer. Geophys. Union Oceans Sciences Conference, January, 1992.

3. FRACTURE MECHANICS

Papers included in this section are the following:

"Effect of Size on Distributed Damage and Fracture of Sea Ice," by Prof. Zdeněk P. Bažant (P.I.), Dr. Ying-Neng Li, Dr. Milan Jirásek, Zhengzhi Li, and Jay-Jang Kim of Northwestern University

"Scale Effects on the Fracture and Constitutive Behavior of Sea Ice," by Dr. John Dempsey (P.I.) and Robert Adamson of Clarkson University

Papers with additional information on fracture mechanics in Section 2, Acoustics:

"Acoustic and Seismic Studies of Ice Mechanics," by Dr. David Farmer (P.I.) and Dr. Yunbo Xie of the Institute of Ocean Sciences

Papers with additional information on fracture mechanics in Section 4, Ice Properties:

"Crack Nucleation Mechanisms in Columnar Ice -- Recent Developments," by V. Gupta (co-P.I.), R. C. Picu, J. Bergström, and H. J. Frost (co-P.I.) of the Thayer School of Engineering, Dartmouth College

Papers with additional information on fracture mechanics in Section 6, Modeling:

"Sea Ice Mechanics Related to Thermally Induced Stresses and Fracturing of Pack Ice," by Dr. James K. Lewis of Ocean Physics Res. & Dev. and Dr. Peter J. Stein of Scientific Solutions, Inc.

"Measurements of Crack Velocity in Sea Ice Using Electromagnetic Techniques," by Dr. Victor Petrenko (P.I.) and Mr. Oleg Gluschenkov of the Thayer School of Engineering, Dartmouth College

"Constitutive Equations and Fracture Models for Sea Ice," by Dr. Gregory Rodin (co-P.I.), Dr. Richard Shapery (co-P.I.), Mr. Khaled Abdel-Tawab, and Ms. Lu Wang of the University of Texas

"Physically Based Constitutive Modeling of Ice: Damage and Failure," by Mao S. Wu (P.I.), J. Niu, Y. Zhang, and H. Zhou of the Department of Engineering Mechanics, University of Nebraska-Lincoln

Effect of Size on Distributed Damage and Fracture of Sea Ice

Prof. Zdeněk P. Bažant (P.I.), Dr. Ying-Neng Li, Dr. Milan Jirásek, Zhengzhi Li and Jay-Jang Kim of Northwestern University, Department of Civil Engineering, Evanston, Illinois, 60208.

Scope of Model, Objectives and Approach

(1) Develop a more accurate and realistic method for predicting load capacity and failure of floating sea ice plates in the Arctic and propagation of large scale fractures in these plates. (2) Establish the scaling law, determine the size effect (missing from previous models), and formulate a general fracture and damage model applicable to floating sea ice plates. The approach is theoretical and computational. The theory consists in the development of a mathematical model for fracture and damage of sea ice plates and study of its implications. Available field observations and laboratory evidence are used to calibrate the model. The computational approach uses finite element and discrete element methods.

Significant Findings to Date

Theory of Fracture Scaling -- Predictions of sea ice failure are needed for the assessment of: (1) vertical penetration of a submarine, (2) development and opening of large open water leads, (3) initiation and build up of pressure ridges, (4) ice breaking, and (5) navigation in the Arctic (Fig. 1). They have traditionally been made on the basis of strength theory, which assumes the ice to fail when the stress reaches a certain strength limit. This approach is in principle correct only for plastic materials which, after the strength limit is reached, yield at constant stress. When the material fractures, the stress that it transmits drops, and then the correct failure theory is fracture mechanics, which is obviously the case for ice. This theory has not been used in practice so far because evidence deemed to be contrary was previously found in small-scale laboratory tests of ice. Recently, however, it became clear this evidence merely proves inapplicability of linear elastic fracture mechanics to very small fractures. This is explained by the fact that sea ice, as well as other brittle heterogeneous materials develop, due to their heterogeneity, a relatively large damage zone around the crack tip. For large fractures, the size of this zone becomes small in comparison to the structure dimensions. By this argument it has been concluded that for large-scale fracture of ice, fracture mechanics is the only correct theory.

The basic difference between the strength theory of failure and fracture mechanics is in scaling. This is crucially important for extrapolating laboratory tests to real scale -- the basic problem for sea ice. The scaling is manifested by size effect. The size effect is understood as the dependence of the nominal strength of structure on the characteristic dimension D, when geometrically similar situations are compared. The nominal strength is defined as the failure load P divided by the square of D. According to the classical strength theory or plastic limit analysis, there is no size effect, that is, the nominal strength for geometrically similar situations is the same. In linear elastic fracture mechanics, the nominal strength decreases inversely to the square root of D. In the plot of logarithm of nominal strength versus $\log D$, the size effect is represented by a straight line of slope $-1/2$, as shown in Fig. 2c. The strength theory is in that plot represented by a horizontal line. The reason for this size effect is that, according to fracture mechanics, the strain energy released by the formation of fracture must be equal to the energy needed to create the fracture surfaces. The former increases as the square of fracture length a or structure size D, while the latter increases only in proportion to D. Since both must be equal for any characteristic size D, the nominal strength must decrease with D. This is

explained in Fig. 2a, b where the shaded area, which approximately represents the zone from which strain energy is released due to the fracture, is proportional to a^2 or to D^2.

For brittle heterogeneous materials such as sea ice (also called quasibrittle materials) the scaling and size effect are more complicated. In these materials, the fracture process zone at the fracture front is large, having dimension l that is not small compared to laboratory specimen size. In this zone the material undergoes distributed cracking which is approximately governed by strength theory. Therefore, the size effect represents a gradual transition from the strength theory, for which there is no size effect, to the so-called linear elastic fracture mechanics (LEFM), for which the size effect is as strong as possible (see Fig. 2c). As shown by Bažant, this transition can be approximately described by the simple law given in the figure (where D_0 and σ_0 are constants if geometrically similar situations are considered).

The aforementioned size effect, however, describes only fracture of sea ice plates due solely to in-plane horizontal forces, which are relatively rare. In most practical problems (see Fig. 1), the floating ice plate fractures by bending. For bending fracture (Fig. 2d), there is also size effect but, as found in this project, it is different and slightly weaker. It has been found that, in geometrically similar situations, the nominal bending strength is inversely proportional to the *3/8* power of sea ice thickness h. At first it may seem surprising that it is not proportional to the inverse square root of h. This may be understood by noting that formation of a bending fracture is equivalent to applying on the floating plate a bending moment opposite to that carried before (Fig. 2d). This produces deflections in the form of an exponentially decaying sinusoidal wave, shown (with exaggerated deflections) in Fig. 2d. The important point is that the distance between two inflection points, L, is not proportional to the plate thickness h but to $h^{3/4}$. The bending fracture releases the strain energy up to a certain fixed distance from the fracture, proportional to L (shaded area in Fig. 2f, *g*). Thus the energy release per unit length of the bending fracture (Fig. 2f) is proportional to $(\sigma_N h)\, h^{3/4}$, which must be equal to the energy required to create the crack surface, which is proportional to h. From this the *-3/8* power law follows. This law has been shown to be a general property of bending fractures of floating elastic plates. It applies not only to fractures caused by vertical loads, but also to fractures caused by temperature difference between the top and bottom of the floating plate. It also applies approximately to bending fractures in presence of in-plane compressive forces in the plate, which tend to cause buckling.

Vertical Penetration Through Floating Ice Plate -- The scaling law and size effect, however, are not the whole story. Complete fracture mechanics solutions have shown that the fracture patterns due to penetration of plates of different thicknesses are not exactly geometrically similar. A computer program has been written to solve the two-dimensional plate bending problem around a star-shaped system of cracks emanating from a small loaded circle (Fig. 3). The law for the growth of the star cracks as a function of the load-point displacement has been obtained and, as already known from experiments, it was found that the propagation of the radial star cracks is stable, with the load always increasing at increasing displacement. The maximum load, i.e., failure load, is obtained at the initiation of circumferential cracks at a certain distance from the loaded zone. The crack initiation, unlike crack propagation, is properly described by the strength theory, which has a different size effect, altering and mitigating the size effect associated with the radial crack growth.

Two additional phenomena further modifying the size effect have been identified. The number of radial cracks depends on the thickness of the plate, ice strength, elastic modulus and the energy that the material requires for fracture (Fig. 2c). The number of radial cracks strongly decreases with

increasing stiffness, and because in a thicker plate there are fewer cracks to absorb the released energy, the size effect is made stronger by this phenomenon. Finally, in practical problems the diameter of the loaded area is not proportional to the plate thickness, because the problem is to predict the penetration force for an object of a fixed size through plates of different thicknesses. The correction for the diameter of the loaded area also increases the size effect because the ratio of the diameter to the thickness of the plate gets smaller for thicker plates.

The combination of all these phenomena superimposed on the underlying *-3/8* power law produces a strong and complicated size effect (Fig. 3d, e), for which the calculation method has been developed.

Determination of the number n of radial star cracks, mentioned above, is not an elementary problem with a solution in the literature. The difficulty lies in the initiation of fracture propagation because the energy release rate of an infinitely short crack is zero. Of course, the initiation per se is governed by the strength theory, which must be combined with fracture mechanics. Analysis showed that once the strength criterion before the crack formation is reached, cracks of a certain spacings jump to a certain initial equilibrium length a_0. One needs three conditions to determine the initial equilibrium crack length, the crack spacing, and the load at which the initiation occurs. In addition to the strength criterion, these consist in the condition that after the initial jump the rate of release of energy from the structure must equal the energy release rate required for further fracture growth (Fig. 3), and that the total energy release during the initial jump must equal the total energy required to form the initial cracks. These conditions were used in conjunction with a finite element program for the bending of a plate on elastic foundation, and provided the number of initial star cracks.

Size Effect in Thermal Bending Fracture -- Stresses caused by thermal changes of weather (Fig. 4b), especially those due to cooling in the fall, can cause floating ice plates to fracture (Fig. 4a). In the past, this problem has been solved on the basis of strength theory. However, in view of the arguments already explained, the solution must be based on fracture mechanics to correctly capture the size effect. The problem of a stationary equilibrium propagation of a semi-infinite crack in an infinite plate has been solved in detail, and the *-3/8* power size effect (Fig. 4c) has been established, as one major new result of this project. Because of long duration of thermal stresses, the relaxation due to creep of ice, which is very pronounced, has been included in the analysis and it was shown that the *-3/8* power law is approximately applicable even in the presence of creep (Fig. 4c). The analysis showed that while a temperature drop of 25 °C is required to crack a plate 1 m thick, a drop of only 12 °C is required to crack a plate 6 m thick, provided that similar temperature profiles get established (which takes much longer for a thicker plate). This analysis provided a possible answer to an old puzzle, first stated by Assour: the new fractures suddenly forming in the Arctic Ocean and running for distances of many miles do not follow the path of the smallest thickness of ice, that is, around the individual floes of several miles in size, separated by thin refrozen water leads. Rather, they cut straight through the thick ice. The discovery of the size effect explains why. Formation of these fractures is important for understanding the mechanism of build-up of pressure ridges, rafting, and opening of water leads (this is important also for navigation, and for surfacing as well as non-detectibility of submarines); Fig. 1.

Part-Through Cracks and Dome Effect in Penetration -- The penetration solution just described has been obtained under the assumption that the bending crack cuts through the entire thickness of the ice plate all the way to the crack front. In reality, the bending crack opens gradually, that is, at the front there is a crack only to a portion of the plate thickness, and this portion increases with the

distance from the crack front, although closing of cracks may also occur due to compression forces. This requires a modification of the aforementioned solutions, which is important for not too long cracks. Furthermore, the rotation of crack faces in the opposite directions is opposed by contact stresses. Both phenomena, i.e., the part-through cracks and the contact stresses, produce in-plane compressive reactions from the ice plate, which oppose the bending fracture. They also shift vertically the location of the resultant of the in-plane forces, with the result that the penetration force is partially resisted not by plate bending but by a dome effect, the dome being represented by the surface of compression resultant location in the plate. Mathematically, this phenomenon causes a coupling between the plate bending problem and the in-plane elastic deformation of the plate. The problem has already been formulated mathematically and a solution, by means of finite elements, is in progress. In this solution, the part-through cracks are assumed to have a horizontal crack front within each finite element, propagating upwards. The propagation is based on a linear elastic fracture mechanics solution of the dependence of the in-plane normal force and bending moment across the cracked section on the additional in-plane displacement and bending rotation caused by the crack. This dependence has been obtained numerically. For initiating the vertical propagation of the crack in each element, a strength limit is assumed. A nonlinear optimization algorithm is used for solving the highly nonlinear equation system that arises, for each loading step. Fig. 5 shows examples of some results already obtained.

Nonlocal Damage and Random Particle Simulation -- Fracture mechanics is an idealized theory in which the fracture front is either a point or a line segment. All quasibrittle materials, including sea ice, have at fracture front a zone of distributed cracking. Its continuum-type modeling is possible but rather difficult. A simpler approach is to force a certain proper spacing of microcracks in the fracture process zone by assuming a suitable discrete micro-structure of the material in the fracture process zone. Such a micro-structure can be obtained by modeling the material as a system of particles. The spacing of the particles enforces a certain spacing of the cracks, as dictated by the preexisting inhomogeneities in ice (such as spacing of preexisting thermal cracks, effect of bottom roughness, spacing of warmer ice regions under snow drifts, spacing of larger brine pockets, etc.). The particles are considered to interact through central forces, whose law is selected so as to give correct elastic properties of the particle system, correct strength limit and correct fracture energy. A large computer program for particle simulation of large scale in-plane fracture of sea ice plate has been written. The program uses an explicit time step algorithm, which is very powerful and makes it possible to solve large systems (systems with over 120,000 degrees of freedom, and thousands of loading steps, have been handled on a desk-top work station).

Fig. 6 shows an application of this approach to the simulation of compression fracture caused by the impact of a large floe (several miles in size) traveling at various velocities and hitting a fixed obstacle. The obstacle can be an oil drilling platform or a bridge pier. There is one well recorded observation in which such an ice floe impacted a small island (Hans island, west of Greenland), having a vertical rock wall at its shore. The fracture sequence and pattern obtained in the particle simulation resembles well that observed in this event.

The particle simulation has also been used to study the size effect due to fracture mechanics. It was shown that the calculated maximum loads for specimens of various sizes follow the transitional curve in Fig. 2c and approach the asymptotic power law for large sizes.

Prediction of Fracture Characteristics by Micromechanical Analysis -- Experimental determination of the fracture energy and characteristic process zone size for large scale fracture of sea ice is difficult

because its direct measurement requires specimens of enormous sizes (over 10 m). Therefore, prediction or at least a crude estimation of the fracture characteristics from the properties of the microstructure would be extremely useful. To gain a better understanding of this problem and determine some basic relations, fracture of ice specimens of various sizes (such as those used recently by Dempsey's team in the Arctic) have been carried out by the random particle method (Fig. 7). The size effect curve shown in Fig. 2c has been simulated. The location of the final asymptote of this curve makes it possible to calculate the fracture energy, and the location of the intersection of the horizontal and inclined asymptotes makes it possible to determine the characteristic size of the process zone. An important point is the dependence of these characteristics on the fracture characteristics of the interparticle force interaction, particularly the microstrength limit for the inter particle force and the microductility number representing the ratio of the interparticle displacement at full break to the displacement at peak force (Fig. 8). It has been established that the macroscopic fracture energy decreases with an increasing coefficient of variation of the microstrength.

Simulation of Acoustic Emissions in Fracturing Sea Ice -- Recently, Dempsey's team conducted measurements of sea ice fracture properties on the Arctic Ocean near Resolute and Barrow. The size effect method, which has been developed by Bažant and is based on the size effect described by the curve in Fig. 2c, was one of the main approaches. Specimens of sizes ranging from less than 1 m up to 80 × 80 m and thickness 1.8 m have been broken in a controlled manner. Fracture patterns similar to those observed in these experiments have been achieved. The force and displacement data are not yet available for analysis, however, the acoustic records of fracture have already been made available (by Farmer and Xie). These acoustic data include the record of a hydrophone located in sea water beneath the advancing fracture. An innovative method of simulating the acoustic record has been developed, exploiting the existing program for random particle simulation of fracture. The interparticle breaks serve as microenergy releases and cause emission of acoustic waves. Analytical solutions of the wave propagation problem, including refraction at the plate-water interface, reflection from top of ice plate and from the sea bottom, and leaking of planar wave into sea water, have been incorporated in the random particle program. The acoustic records are being simulated; for example the record of power (energy) flux at the hydrophone (proportional to the square of pressure) versus time. The acoustic signals from the crack jumps in ice have been determined from a modified Farmer-Xie's acoustic model for shallow water in the frequency domain. The acoustic pressure time histories were synthesized by inverse Fourier transform. The synthesized acoustic signal shows statistical resemblance to the statistical record in the experiments (Fig. 9). A size effect has been detected in the acoustic emissions in the sense of a root-mean-square of the acoustic pressure (Fig. 9). This kind of size effect can be related to the energy released from the ice floe of various thicknesses and sizes. By inversion of the solution it may be possible to judge the size of the fracture from the received acoustic signal. This simulation demonstrates the possibility of varying the assumed microfracture characteristics so as to obtain a very similar record and thus determine which microfracture characteristics yield the correct results.

Statistical Weibull-Type Size Effect -- At the beginning of the project, the effect of randomness of material strength on the failure load has been studied. A detailed report would require a lengthy discussion. Suffice to say that the conclusion was that the statistical size effect is important only for failures that occur at fracture initiation but has only a minor influence on failures that occur after large stable crack growth. This comprises most, although not all, problems of sea ice fracture. A correction to the size effect law arising from these statistical effects has also been determined and was shown to be relatively minor under the aforementioned conditions.

PLANS AND FUTURE DIRECTIONS

In continuation of this program, the following problems should be solved: (1) Application of the present methods to the analysis of the experiments of Dempsey's team at Resolute and Barrow; (2) determination of the relations between macro- and micro- fracture characteristics; (3) fracture solutions for part-through cracks and cracks with large process zones; (4) generalization of fracture and failure models for sea ice to rate dependence; (5) determination of the relation between acoustic emission records and fracture process in sea ice; (6) enhancement of understanding of the size effect in sea ice, particularly with regard to the cohesive crack model; (7) formulation of a complete theory for crack initiation and crack spacing; (8) determination of the effect of creep and temperature on the evolution of ice fracture; (9) analysis of the possible role of fractal nature of crack surfaces in the size effect on sea ice fracture.

PUBLICATIONS

Main Papers in Refereed Journals

1. Bažant, Z.P. (1992). "Large-scale thermal bending fracture of sea ice plates." *J. of Geophysical Research*, 97(C11), 17,739-17,751.
2. Bažant, Z.P. (1993). "Scaling laws in mechanics of failure." *J. of Engrg. Mech.*, ASCE, 119(9), 1828-1844.
3. Bažant, Z.P., and Li, Y.-N. (1994). "Penetration fracture of sea ice plate: Simplified analysis and size effect." *J. of Engr. Mech.*, ASCE, 120(6), 1304-1321.
4. Li, Y.-N., and Bažant, Z.P. (1994). "Penetration fracture of sea ice plat: 2D analysis and size effect." *J. of Engr. Mech., ASME*, 116 (July), 256-259.
5. Bažant, Z.P., and Li, Y.-N. (1994). "Eigenvalue analysis of size effect for cohesive crack model." *Int. J. of Fracture*, 66, 213-226.
6. Bažant, Z.P., and Li, Y.-N. (1995). "Penetration fracture of sea ice plate." *Int. J. Solids Structures* 32, No. 3/4, 303-313.
7. Jirásek, M., and Bažant, Z.P. (1995). "Macroscopic fracture characteristics of random particle systems." *Int. J. of Fracture,* in press.
8. Jirásek, M., and Bažant, Z.P. (1995). "Particle model for quasibrittle fracture with application to sea ice." *J. of Engrg. Mech.*, in press.
9. Bažant, Z.P. (1995). "Can size effect in fracture be caused by fractal nature of crack surfaces?" *Int. J. of Fracture*, submitted to.
10. Bažant, Z.P. , and Li, Zhengzhi (1995). "Acoustic emissions in fracturing sea ice plate simulated by particle system." To be submitted to *J. of Engrg. Mech.*

Related Papers in Refereed Journals

11. Bažant, Z.P., Xi, Y., and Reid, S.G. (1991). "Statistical size effect in quasi-brittle structures: I. Is Weibull theory applicable?" *ASCE J. of Engrg. Mech.*, 117(11), 2609-2622.

12. Bažant, Z.P., and Xi, Y. (1991). "Statistical size effect in quasi-brittle structures: II. Nonlocal theory." *ASCE J. of Engrg. Mech.*, 117(11), 2623-2640.

13. Bažant, Z.P., and Beissel, S. (1994). "Smeared-tip superposition method for cohesive fracture with rate effect and creep." *Int. J. of Fracture* 65, 277-290.

14. Bažant, Z.P., and Li, Y.-N. (1994). "Cohesive crack model for geomaterials: stability analysis and rate effect." *Applied Mechanics Reviews 47*, (6, Part 2, June), pp. S91-S96.

15. Bažant, Z.P., and Jirásek, M. (1993). "R-curve modeling of rate and size effects in quasibrittle fracture." *Int. J. of Fracture*, 62, 355-373.

Proceedings Papers

16. Dempsey, J.P., Bažant, Z.P., Rajapakse, Y.D.S., and Shyam-Sunder, S., Editors (1993). *Ice Mechanics 1993* (Proc. of a Symposium as part of ASCE-ASME-SES Joint Mechanics Meeting held in Charlottesville, VA), AMD Vol. 163, Am. Soc. of Mech. Engrgs., New York, 1993.

17. Bažant, Z.P. (1992). "Large-scale fracture of sea ice plates." (Proc. *11th IAHR Ice Symposium*, Banff, Alberta), June (ed. by T.M. Hrudey, of Alberta, Edmonton), Vol. 2, pp. 991-1005.

18. Bažant, Z.P., and Gettu, R. (1991). "Size effects in the fracture of quasi-brittle materials." in *Cold Regions Engineering*, Proc., *6th ASCE International Specialty Conference* (held in Hanover, NH, 1991), ed. by D.S. Sodhi, ASCE, New York, 595-604.

19. Bažant, Z.P., and Li, Y.-N. (1993). "Fracture analysis of penetration through floating sea ice plate and size effect." Proc. *First Joint Mechanics Meeting of ASME-ASCE-SES (Meet'n'93)*, held in Charlottesville, VA, June, ed. by J.P. Dempsey, Z.P. Bažant, Y.D.S. Rajapakse and S. Shyam Sunder, 131-144.

20. Bažant, Z.P. (1991). "Penetration of arctic ice by submarines: Review of the current status of research." *Submarine Arctic Structures Review Panel.* Analysis and Technology, Inc., Arlington, VA.

21. Jirásek, M., and Bažant, Z.P. (1993). "Discrete element modeling of fracture and size effect in quasibrittle materials: Analysis of sea ice." Proc. held at M.I.T., *2nd Int. Conf. on Discrete Element Methods (DEM)*, March, ed. by J.R. Williams and G. G.W. Mustoe, IESL Publications, 357-368.

22. Bažant, Z.P., and Xi, Y. (1994). "Fracture of random quasibrittle materials: Markov process and Weibull-type models." *Structural Safety and Reliability* (Proc. of ICOSSAR '93-6th Intern. Conf. on Struct. Safety & Reliability, Innsbruck, Austria, Aug. 9-13, 1993), ed. by G.I.Schueller, M. Shinozuka, J.T.P. Yao, and A.A. Balkema, Rotterdam-Brookfield, 609-614.

BENDING FRACTURE OF SEA ICE

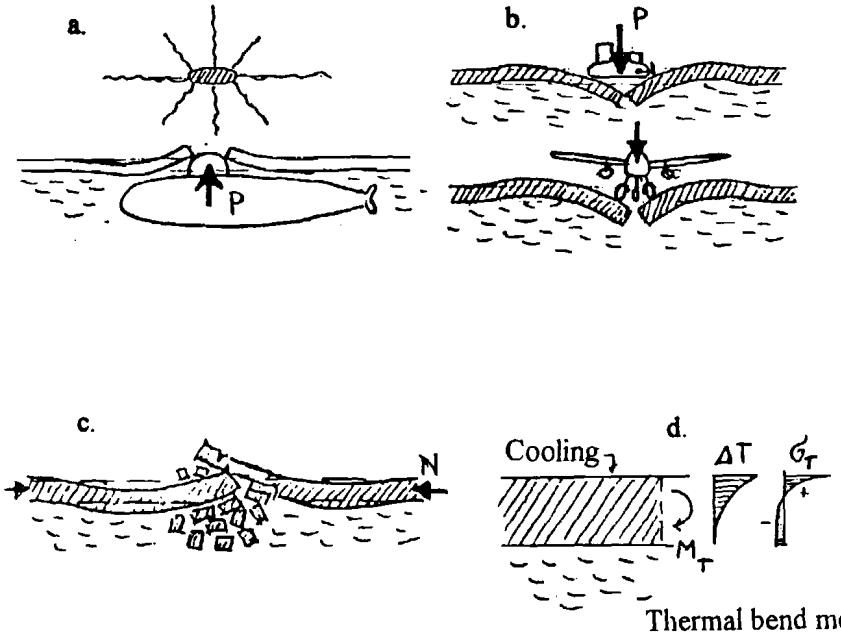

FIG. 1 Typical fracture problems for sea ice.

SCALING AND SIZE EFFECT IN FRACTURE

1) PLANE FRACTURE

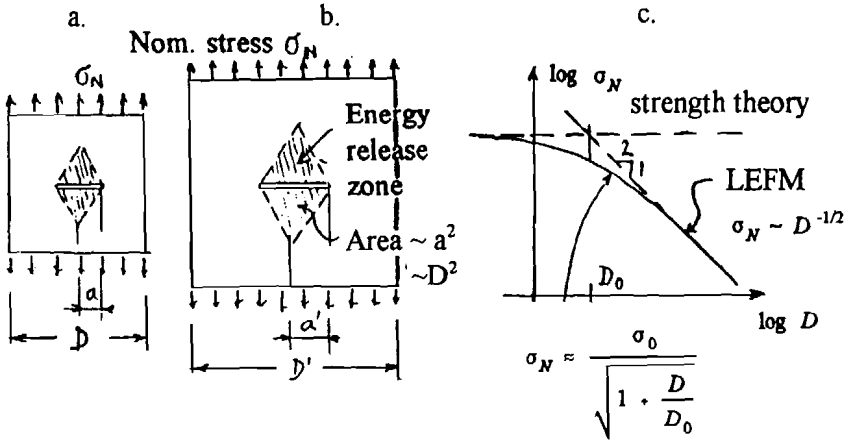

2) BENDING FRACTURE OF FLOATING PLATE

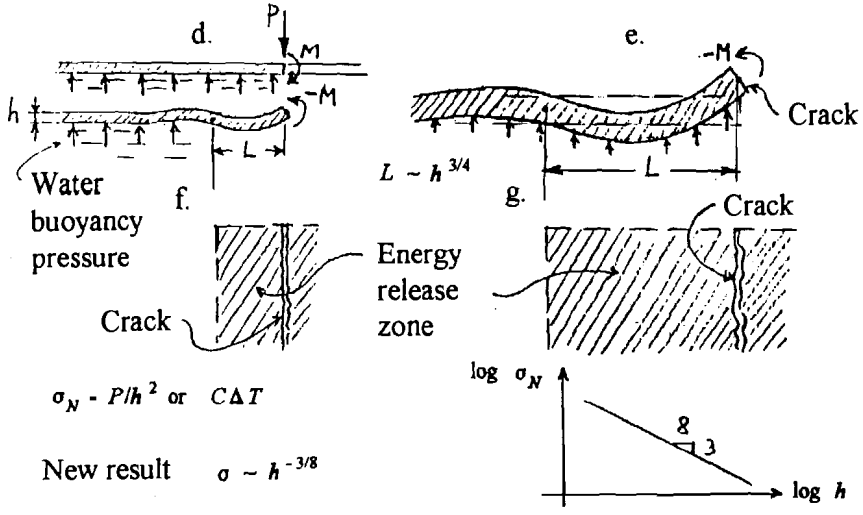

FIG. 2 Explanations of scaling and size effect for in-plane and bending fractures.

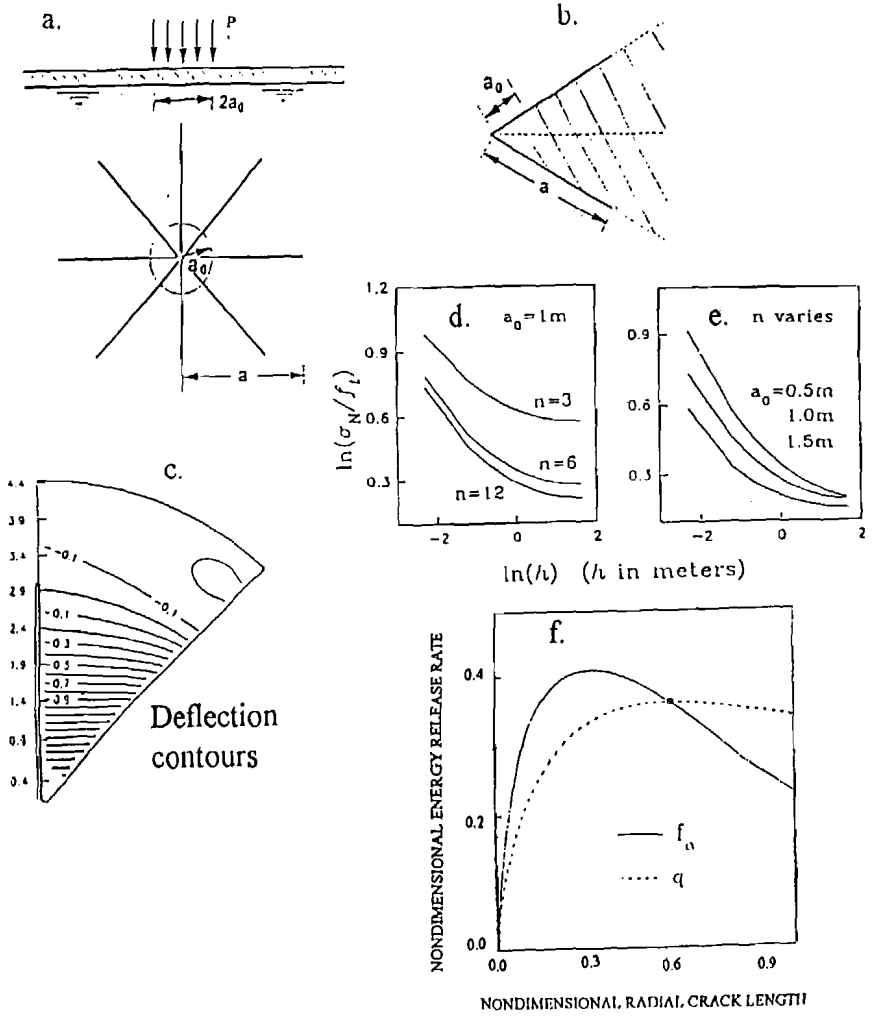

FIG. 3. Penetration fracture of sea ice plate under vertical load: (a) star-crack pattern, (b) plate wedge limited by two radial cracks, (c) typical calculated deflection contours of cracked plate, (d-e) decrease of nominal strength with plate thickness at constant loaded-area radius for various numbers of star cracks, and for various radii of loaded area and the most dangerous variation of the number of cracks, (f) diagrams of the incremental and average energy release rates, giving at their intersection and the initial crack length and the initial crack spacing.

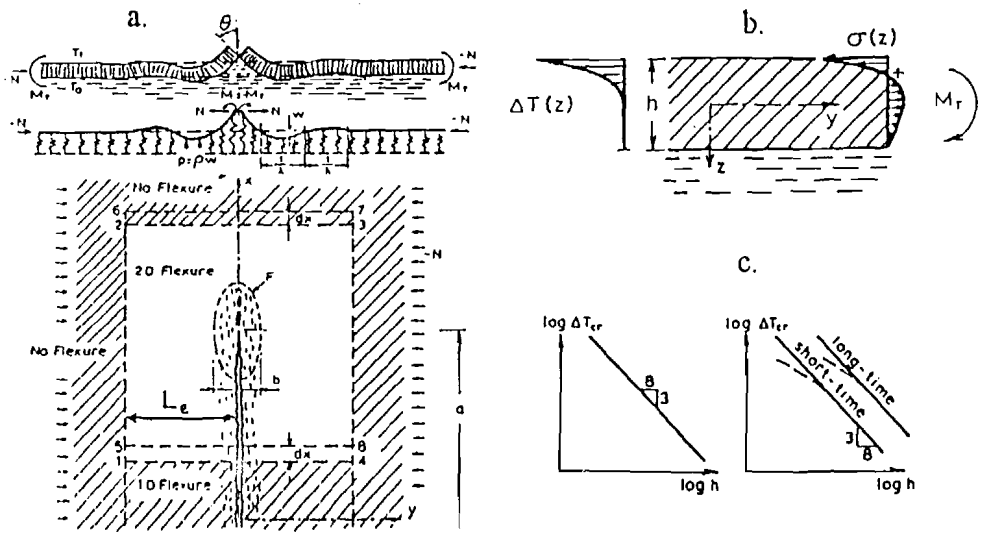

Fig. 4 Thermal bending fracture of floating ice plate: (a) Unloading that causes release of stored energy, (b) temperature and cooling stress profiles, and (c) effect of plate thickness *h* on critical temperature drop of short or long duration.

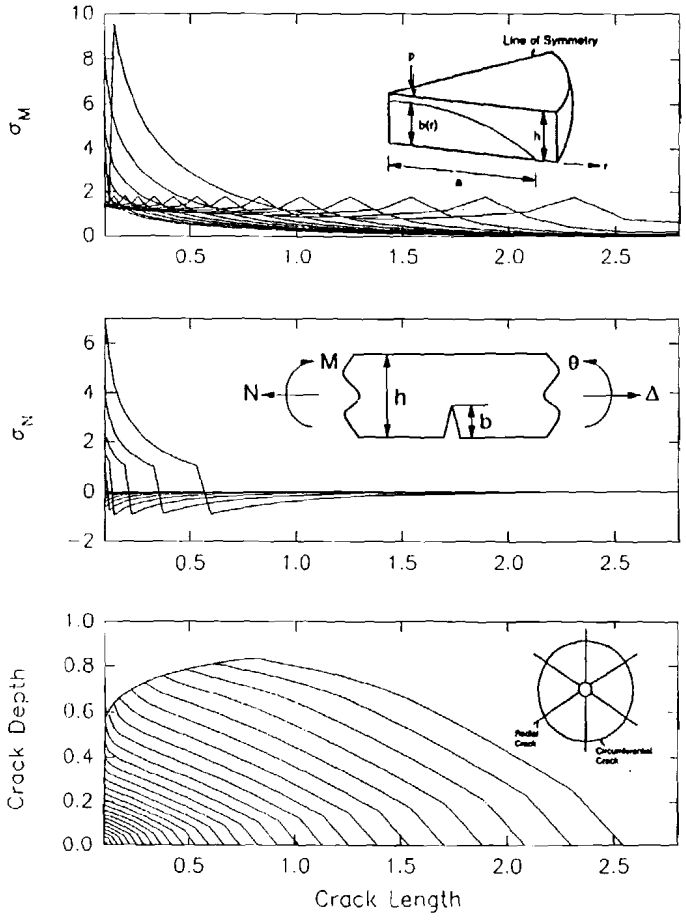

Fig. 5 (a) Distribution of bending stress along the crack length for crack tips at various locations; (b) distributions of the average normal stress along the crack length for crack tips at various locations; and (c) distributions of the vertical crack depth along the crack for crack tips at various locations. (Note that high compression stresses are transmitted across the partially cracked cross sections even far behind the crack tip.)

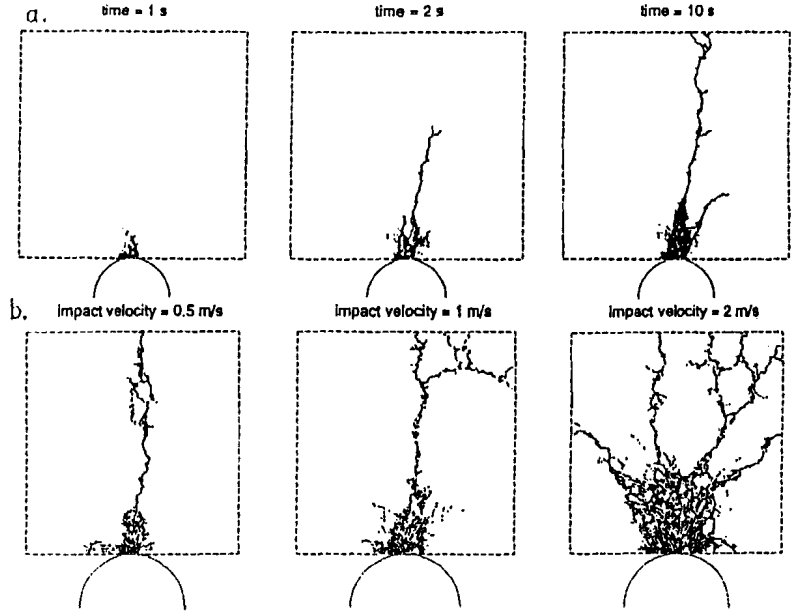

Fig. 6 Simulation of impact of ice floe on rigid circular obstacle by discrete element method. Top: fracture patterns at various times; botton: for various velocities.

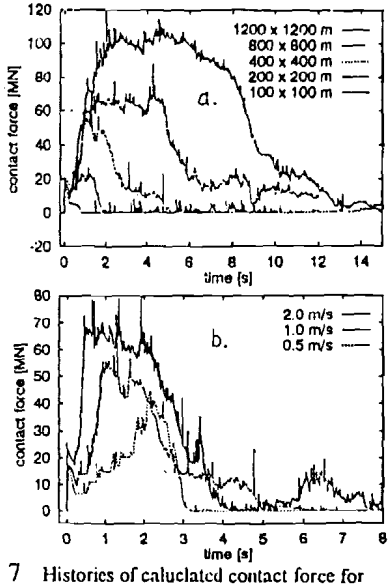

Fig. 7 Histories of caluclated contact force for Fig. 1, for various floe sizes and various impact velocities.

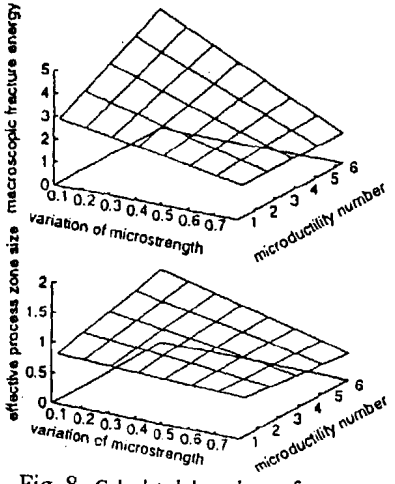

Fig. 8 Calculated dependence of macro-fracture energy and effective process-zone size on statistical coefficients of variation microstrength of ice and microductility.

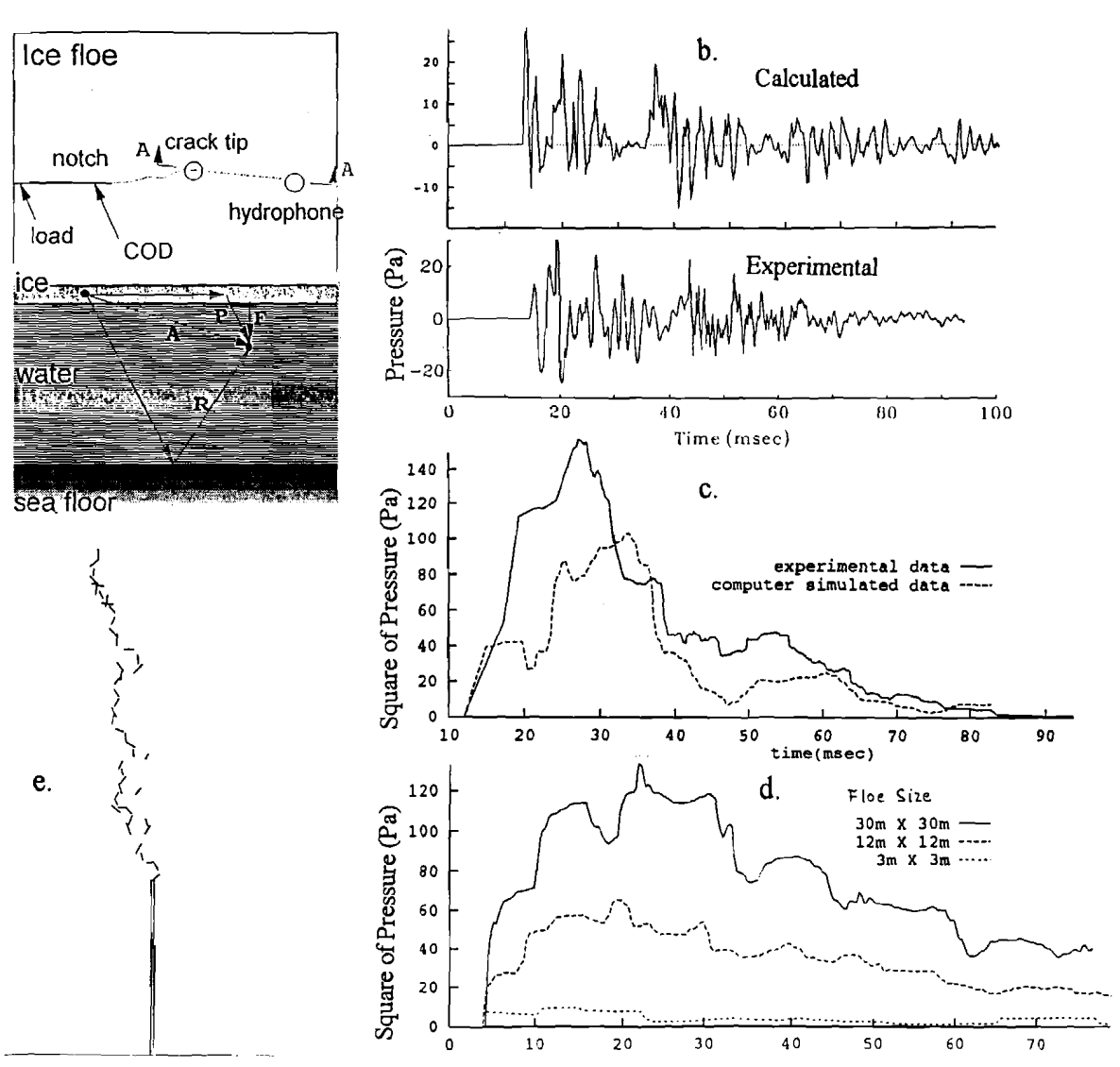

Fig. 9 Computers fracture simulation of acoustic signals obtained in Dempsey's tests at Resolute: (a) Plan view of ice specimen and acoustic paths in vertical section, (b) Calculated and recorded time history of pressure at geophone, (c) Calculated and recorded history of square of pressure, (d) Calculated histories of the square of pressure for fracturing of specimens of different sizes, and (e) Plan view of individual crack jumps causing acoustic emissions.

Scale Effects on the Fracture and Constitutive Behavior of Sea Ice

Dr. John Dempsey (PI), Robert Adamson of Clarkson University.

Scope of Large Scale Experiments

The P.I. has completed six field trips to the arctic over the last three years. These field trips were aimed at studying size and rate effects in sea ice. Large scale experiments coupled with small scale field and laboratory tests were completed to reach this goal. The experiments have yielded an abundance of information related to the fracture and constitutive behavior of sea ice. Table 1 summarizes the large-scale in-situ arctic experiments.

Table 1: **Summary of Large-Scale Experiments**

Date	Ice Type	Ice Thickness h(m)	Test Geometries	Size L(m)	Scale	# Tests
1/15-29, 1992 Canmore, Alberta	S1 fresh water ice	0.50	3pt[a] - FR[b] RT[c] - FR	0.50 0.34-28.64	**1:81**	4 9
4/17 - 5/7 1993 Resolute, N.W.T.	FY[d] sea ice slightly aligned	1.8	3pt - FR SQ[e] - FR SQ - FL[f]	3.0 0.5-80 3.0	**1:160**	1 15 2
11/9-19, 1993 Barrow, Alaska[1]	FY[a] sea ice Strongly aligned	0.30	SQ[b] R[g] RT[d] CORE[h]	2.5 2.5 1.0 0.36		5 1 2 4
3/9-20, 1994 Barrow, Alaska[1]	FY sea ice strongly aligned	1.5	SQ R SCB[i]	0.5-30 1.5-2.0 0.15	**1:60**	5 2 16
4/1-10, 1994 SIMI Floating Camp, Beaufort Sea[2]	FY sea ice slightly aligned	0.2-0.6 2<h<6	SQ MY Floe[j]	2-15 81	**1:7.5**	5 1
5/8-19,1994 Barrow Alaska[1]	FY sea ice strongly aligned	1.7	SQ R	0.25-30 8	**1:120** N/A	5 2

[1]Joint experiments with Cole, Petrenko, Shapiro and Weeks
[2]MY floe fracture experiment joint with Coon, Farmer, Pritchard and Xie
[a]3pt-Three point bend; [b]FR-Fracture; [c]RT-Reverse-tapered base-edge-cracked plates
[d]FY-First Year; [e]SQ-Square Plate (L×L); [f]FL-Flexure; [g]R-Rectangular Plate (L×2L)
[h]CORE - 0.2m diameter core, vertical, isothermal (small scale)
[i]SCB - Semi-Circular Bend Fracture/Flexure Geometry (small scale)
[j]MY Floe - Multi-Year floe

Detailed Summary of Large-Scale Experiments

Joint-Industry-Agency 'Large-Scale Ice Fracture Experiments:' A two-phase joint-industry-agency project (JIAP) was initiated in 1990 to calibrate a fracture theory for incorporation into probabalistic global ice load models. Phase I of the JIAP "Large-Scale Ice Fracture Experiments" was completed in January, 1992 near Calgary, Alberta. The primary goal of Phase I was to assess the feasibility of large-scale, full-thickness ice fracture measurements. Other objectives included: (1) Field experimentation of specimen cutting and scribing, loading systems, servo-control and instrumentation; (2) Determination of fracture toughness of full-thickness freshwater ice, global elastic modulus and scale effects.

Table 2: **Large Scale Ice Experiments @ Calgary, Alberta**

Test ID	Test Geometry	Dimensions (L x W) (m xm)	Crack Length (m)	Test Mode	Control	Ambient Air Temp. °C
GR1	Griffith	N/A	0.	gas	Load	-2.5
GR2	Griffith	N/A	0.	gas	Load	-3.0
B1	Beam	0.18x0.51	0.06	gas	Load	-2.4
B2	Beam	0.16x0.51	0.05	oil	CTOD	+5.3
B3	Beam	0.13x0.53	0.04	oil	CTOD	-1.6
B4	Beam	0.15x0.52	0.05	gas	Load	-2.1
RT1	Reversed-Taper	1.41x2.82	0.43	gas	Load	0
RT2	Reversed-Taper	0.41x0.82	0.14	gas	Load	-0.3
RT3	Reversed-Taper	4.42x8.82	1.23	gas	Load	-0.6
RT4	Reversed-Taper	0.34x0.68	0.95	gas	Load	+0.4
RT5	Reversed-Taper	1.04x2.08	0.39	gas	Load	+0
RT6	Reversed-Taper	10.36x20.72	3.12	gas	Load	+0
RT7	Reversed-Taper	3.18x6.36	0.99	oil	CTOD	0
RT8	Reversed-Taper	3.20x6.40	0.99	oil	NCTOD	-3
RT9	Reversed-Taper	28.64x57.28	8.98	gas	Load	+0
CM1	Cant. Beam	0.36x0.09	N/A	gas	Load	0
CM2	Cant. Beam	1.08x0.27	N/A	gas	Load	0

GR1,GR2,B1,B2: Bears Paw; B3,B4, All RT's, CM1,CM2: Spray Lakes.

The project began at the Bearspaw Reservoir near Calgary, Alberta. The Griffith tests and the first two beam tests were conducted there. Due to unseasonably warm temperatures, the test site was moved to Spray Lakes Reservoir in Canmore, Alberta. Ice conditions at the two sites were quite different in several respects. S2 freshwater ice existed at Bearspaw, whereas S1 columnar ice was found at Spray Lakes. Also, the ice at Bearspaw was highly fractured because of water level changes for hydropower needs. The ice at Spray Lakes had limited fractures and large areas with no visible cracks. The remaining experiments were conducted at the Spray Lakes site. Table 2 summarizes the experiments completed during Phase I of the project, at both Bearspaw and Spray Lakes.

Griffith Tests: Two Griffith experiments were performed at the Bears Paw Reservior (Figure

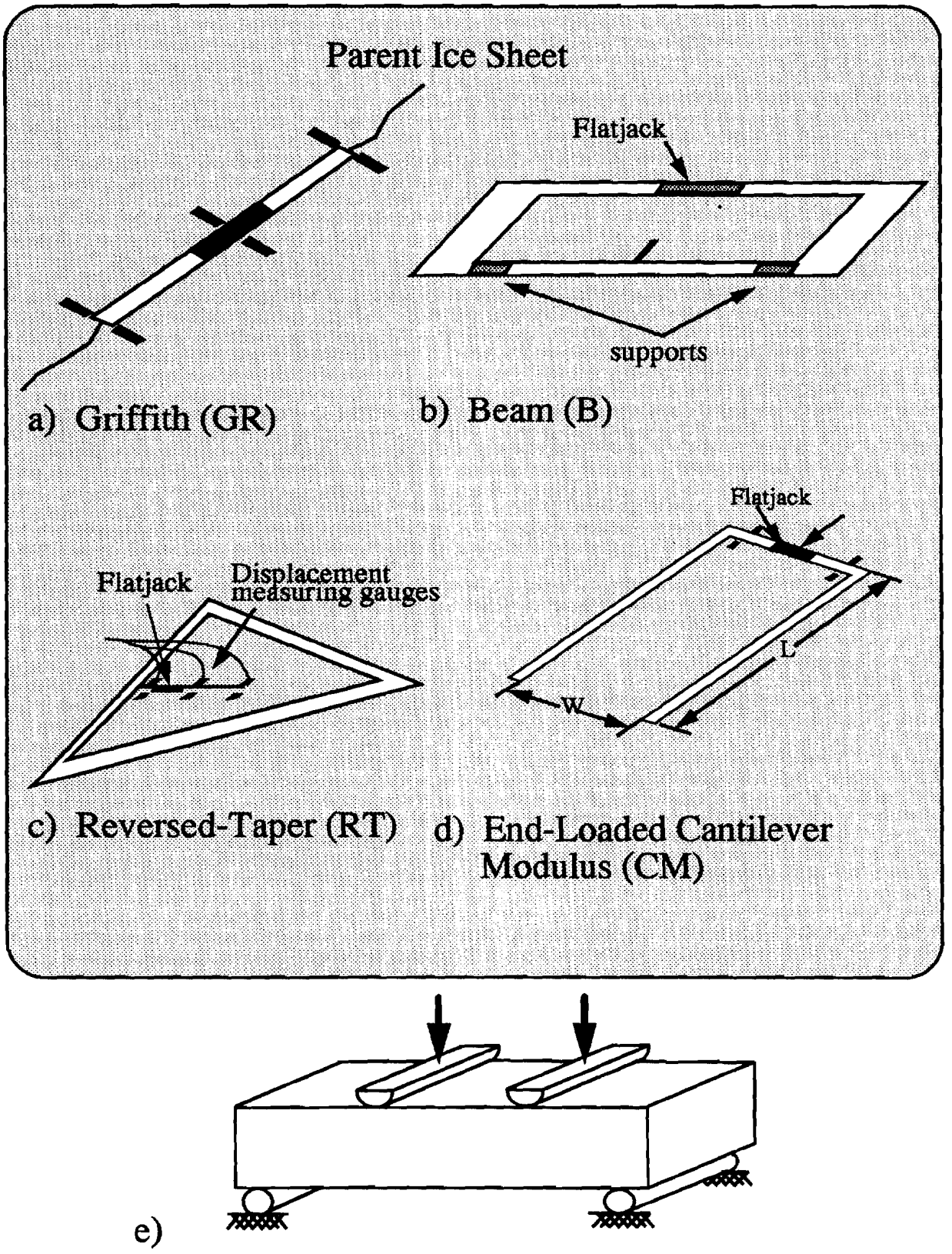

Figure 1: Test geometries: a) Griffith crack, b) Three-point-bend fracture test, c) Reversed-taper geometry, d) Cantilever beam experiment e) Small scale beam tests

1a). They consisted of simply cutting a notch in the ice sheet and inserting a flatjack. Displacement gauges were placed over the flatjack and at each of the crack tips. Stable cracking was achieved for about 3m from each crack tip.

Notched Bend Tests: The three point (3pt) bend fracture geometry shown in Figure 1b was used with the aim of investigating size effects on in–situ ice possessing a thermal gradient and a natural thermal crack density. Difficulties were encountered with the specimens freezing in place and with the sides melting – causing sloping sides unsuitable for use as loading faces. This behavior was evidenced especially in specimen B4 (Spray Lakes). Despite these problems, an initiated crack was arrested in specimen B2 (Bears Paw) by closed loop control of the servo-hydraulic system using feedback from a crack tip displacement gauge. Closed loop control of cracking had (at that time) never been performed in an ice fracture experiment in a laboratory which makes the occurrence of controlled cracking in a field experiment especially significant.

Reversed-Taper Geometry Experiments: Due to the difficulties encountered in preparing the notched bend tests, the reversed-taper geometry (RT) was adopted (Figure 1c). This geometry had been previously used for lab work at Clarkson University and proved to be very successful for promoting stable cracking (DeFranco and Dempsey, 1995). Nine RT tests, most with multiple loadings, yielded a scale range of 1:81 and included the then largest known controlled fracture test specimen (40.5 × 40.5 × 0.5m). Reducing the specimen width with increasing crack length a is conducive to slow crack extension through rapidly increasing compliance with crack extension. Tests performed with nitrogen gas generally resulted in unstable fracture. Most of the closed loop servo-controlled tests involved multiple loadings and stable crack propagation.

Cantilever Beam Experiments: An additional evaluation of specimen size on the elastic modulus was made using three in–situ cantilever beams as shown in Figure 1d. Several load/unload trials were performed on each experiment. Experiments CM1 and CM2 were successful. For CM3, the displacement gauges drifted due to the warm temperatures and wind; consequently, no useful data was obtained for this test.

Small Scale Tests: A set of small scale beam tests were completed by IMD of Canada at the site. These experiments help link the small scale lab tests with the large scale tests (Figure 1e).

Characterization: Due to the warm temperatures at the test site, no characterization could be done during the testing. A large block of the ice from Spray Lakes was shipped back to Clarkson University where detailed characterization of the ice was performed.

Phase II, Resolute Bay: Based on the success of Phase 1, large-scale fracture tests in full-thickness sea ice were conducted on Phase 2 in April, 1993 near Resolute, Northwest Territories (Kennedy et al., 1994). The tests in Resolute focused on the square plate geometry, with the successful completion of fifteen fracture and three flexure tests. Table 3 provides a summary of these experiments.

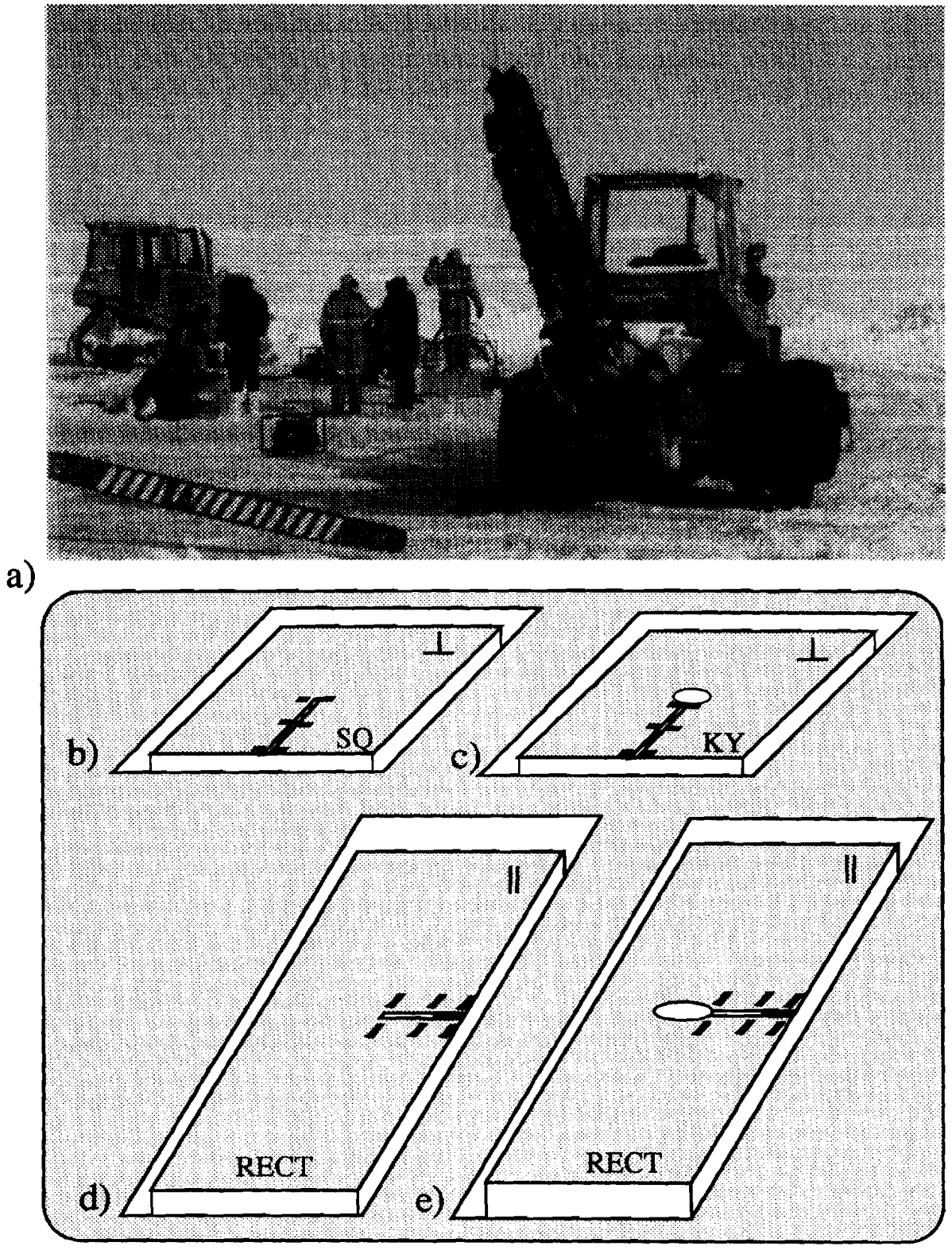

Figure 2: a) R-100 Ditchwitch for cutting out experiments; b) Square plate geometry; c) Square keyhole geometry; d) Rect. plate geometry; e) Rect. keyhole geometry

Table 3: **Large Scale Ice Experiments @ Resolute Bay**

Test ID	Test Geometry	Dimensions (L x W) (m xm)	Crack Length (m)	Test Mode	Control	Amb. Air Temp. °C
SQ1	Square	1.0x1.0	0.3	gas	Load	-9
SQ2	Square	0.9x0.9	0.28	gas	Load	-13
SQ3	Square	10.0x10.0	3.0	gas	Load	-13
SQ4	Square	10.0x10.0	5.02	gas	Load	-13
SQ5	Square	30.0x30.0	9.0	gas	Load	-13
SQ6	Square	30.0x30.0	9.0	gas	Load	-14
SQ7	Square	30.0x30.0	9.0	gas	Load	-15
SQ8	Square	3.0x3.0	0.9	gas	Load	-15
SQ9	Square	3.0x3.0	0.9	servo	CMOD	-3
SQ10	Square	0.5x0.5	0.26	gas	Load	-3
SQ11	Square	30.0x30.0	9.0	servo	NCTOD	-14
SQ12	Square	0.5x0.5	0.25	servo	CMOD	-14
SQ13	Square	80.0x80.0	24.0	gas	Load	-12
SQ14	Square	30.0x30.0	9.0	servo	NCTOD	-12
SQ15	Square	3.0x3.0	0.9	servo	CMOD	-17
FL1	Beam	1.0x0.25	no crack	gas	Load	-17
TE1	Keyhole	3.0x3.0	1.5	servo	Load	-6
TE2	Keyhole	3.0x3.0	1.5	servo	Load	-6

Square Plate Experiments: The square plates tested ranged from ($0.5 \times 0.5 \times 1.8$m) to ($80 \times 80 \times 1.8$m) covering a size range of 1:160. The ice was 1.8m thick so a large DitchWitch, shown in Figure 2a, was necessary to cut out the plates. It was able to create a 15 cm wide slot between the test piece and the parent ice sheet. This limited refreezing of the cut, providing the group time to clean the slush from the cut. A second smaller Ditchwitch was then used to cut the crack in the specimens. This machine cut a notch 1.6 cm wide, enough to insert the loading device, the flatjack. Because it was a narrow cut, it had to be constantly cleaned to prevent refreezing. Both rate and size effects were examined. The loading was achieved by means of a flatjack inserted into the precut crack in the specimen. On the surface of the specimen, the crack opening displacements were measured at three points: the crack mouth (CMOD), the crack tip (CTOD), and at a point in between (COD). At each point, two displacement gauges were used, an LVDT and a KAMAN non-contacting displacement gauge. The KAMAN gauge had a finer resolution, but went out of range much earlier. As the crack opened, the KAMAN gauge would go out of range and the LVDT continued measuring, providing a continuous record of the crack activity. This was necessary for capturing the unloading curve immediately following fracture. Figure 2b shows the test setup for a typical square plate fracture test. All gauges were connected to two different digital recording devices, two 486 computers. This method of two backups ensured that no data was lost. One 486 computer was used for real time viewing of the gauge responses and slow data acquisition. The other computer was devoted to high speed data aquisition.

The flatjack was pressurized by either a gas or servo-controlled oil system. The pressure in the flatjack was proportional to the pressure applied to the ice, and was calculated through lab calibration of the flatjack. When using air, the load applied to the ice was controlled. Typically, these were longer tests, running for at least five minutes. This system was capable of introducing prescribed unloadings at various times in the loading. The hysteresis loops in the Load vs COD plots provide constitutive information as well as information necessary to calculate internal friction values. Servo controlled tests used displacement feedback for control. These were faster tests, usually taking less than one minute to fracture.

Flexure Experiments: The testing of in-situ flexure beams proved to be a difficult task in Phase I. One flexure beam was tested in Phase II. The test was successful, but required an excessive amount of preparation. It was found that test specimens using self-equilibrated loading (the RT on Phase I and the square plate on Phase II) were inherently easier to setup, requiring minimal preparation. This provoked the use of the square plate keyhole geometry (Figure 2c). This was a flexure test similar to the square plate fracture tests, except that a 20cm hole was bored at the crack tip. The displacement gauges were placed at points on the crack, similar to the fracture tests.

High Speed Video: Bob Gagnon of CNRC filmed the cracking events in the large scale fracture tests.

Acoustics The acoustic signals resulting from the cracking events were recorded by Xie and Farmer from the Institute of Ocean Sciences. They deployed two hydrophones with a sampling frequency of 44.1kHz. These devices allowed acoustical measurements of propagation speeds of developing ruptures and acoustic radiation levels due to micro-cracking as the tensile load was increased.

Small Scale Tests: IMD/NRC of Canada carried out experiments on the flexural strength of the ice for different sizes, depths, and orientations (Figure 2d). A series of small scale fracture toughness measurements with a range of parameters similar to those of the strength tests were also performed.

Characterization: A tent was set up at the site with all the equipment necessary for the full characterization of the ice. Characterization of the full thickness of the ice sheet was completed as well as salinity and density profiles.

Sea Ice Mechanics Initiative (SIMI) - Barrow, AK: In order to track the seasonal evolution of the mechanical and physical properties of first year sea ice, three field trips were conducted at Barrow, Alaska: November 9–19, 1993, March 9–20 and May 8–19 of 1994. This was a joint effort including Weeks, Shapiro, and Byers from the University of Alaska at Fairbanks (UAF), Dave Cole from CRREL, New Hampshire, and our group from Clarkson University. A total of thirty large scale tests were completed covering a wide range of sizes, temperature profiles, and loading paths. Each set involved a large scale in-situ (full ice thickness) matrix of experiments and a complementary small scale (partial thickness) matrix of experiments. The ice conditions encountered at Barrow were very interesting; that is, the sea ice was strongly aligned, and thus, in addition to the salinity, grain size and thermal profile there was this additional important microstructural feature to incorporate. In all these experiments, a computer-controlled flatjack loading system was employed to load the ice along preset load paths recording both load and deformation. Issues examined included the effects of size, rate, load path (monotonic, cyclic and creep recovery) and geometrical test orientation vs c-axis alignment. Figure 3a shows the schematics of the various load paths. On each trip, detailed characterization and micrography was carried out by Cole

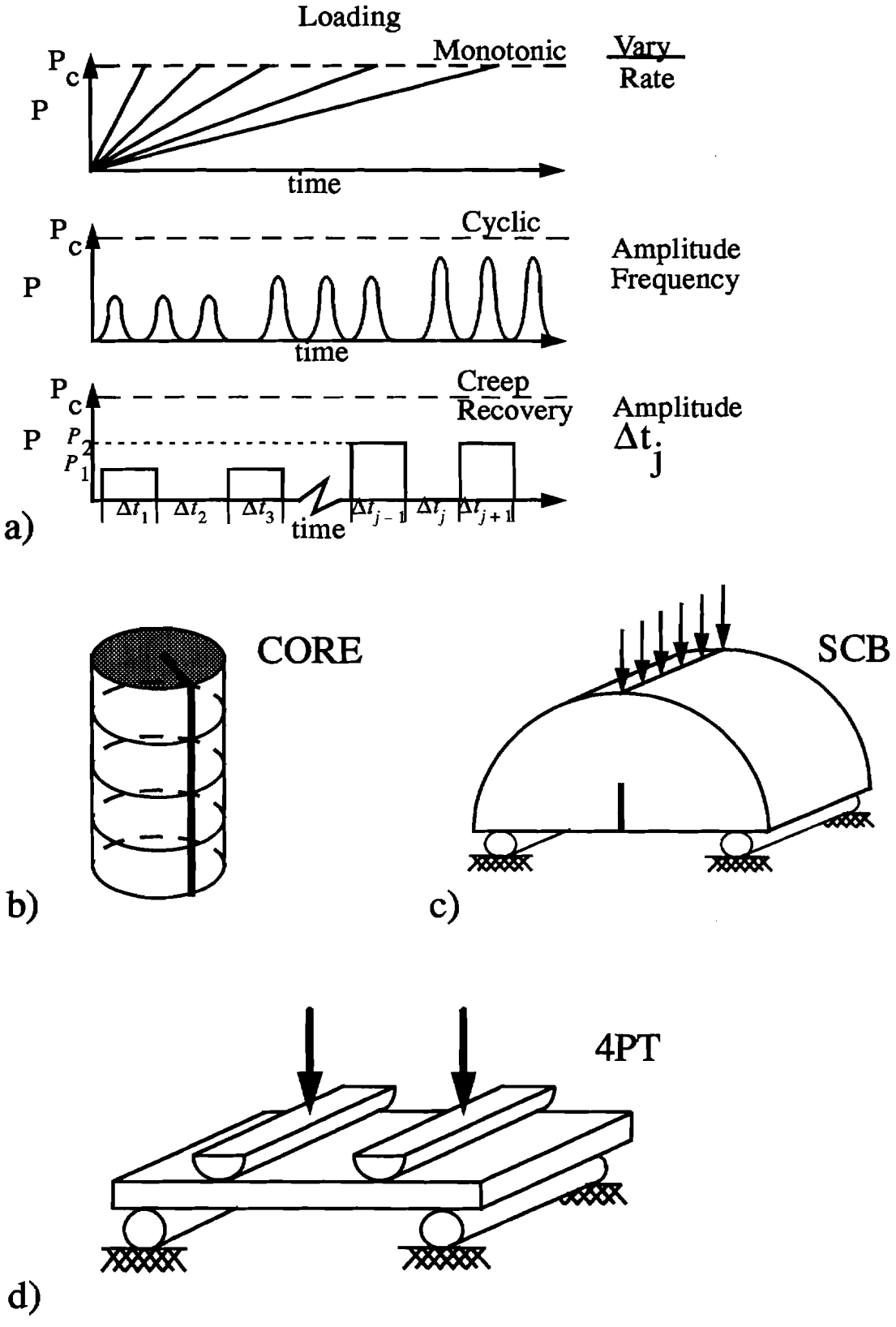

Figure 3: a) Schematic of various load paths b) Core geometry; c) SCB fracture geometry; d) Four-point-bend flexure geometry

Table 4: **Large Scale Ice Experiments @ Barrow, AK: November 9-19**

Test ID	Test Geometry	Dimensions (L x W) (m xm)	Crack Length (m)	Test Mode	Failure	Control
SPF1	Square	2.5mx2.5m	0.75	Fracture	Easy	Cyclic/Ramp
SPF2	Square	2.5mx2.5m	0.75	Fracture	Easy	Cyclic/Ramp
SPF3	Square	2.5mx2.5m	0.75	Fracture	Easy	CMOD-Ramp
SPF4	Square	2.5mx2.5m	0.75	Fracture	Hard	Cyclic/Ramp
SPF5	Rectangle	2.5mx5.0m	1.25	Flexure	Hard	Cyclic/Ramp
SPF6	Square	2.5mx2.5m	0.75	Flexure	Easy	Fast Ramp
SPF7	RT	1.0mx2.0m	0.3	Fracture	Easy	Fast Ramp
SPF8	RT	1.0mx2.0m	0.3	Fracture	Hard	Fast Ramp
CORE1	Core	0.36mx0.2mϕ	0.1	Fracture	Easy	Fast Ramp
CORE2	Core	0.36mx0.2mϕ	0.1	Fracture	Easy	Fast Ramp
CORE3	Core	0.36mx0.2mϕ	0.1	Fracture	Hard	Fast Ramp
CORE4	Core	0.36mx0.2mϕ	0.1	Fracture	Hard	Fast Ramp

Table 5: **Large Scale Ice Experiments @ Barrow, AK: March 9-20**

Test ID	Test Geometry	Dimensions (L x W) (m x m)	Crack Length (m)	Test Mode	Failure	Control
SQPL1	Square	1.5mx1.5m	0.45	Fract.	Easy	Ramp
SQPL2	Square	1.5mx1.5m	0.45	Fract.	Easy	Ramp
SQPL3	Rect.	3.0mx1.5m	0.45	Fract.	Hard	Ramp
SQPL4	Square	2.5mx2.5m	0.75	Fract.	Easy	Mono/Ramp
SQPL5	Square	2.0mx2.0m	0.6	Fract.	Easy	Ramp
SQPL6	Rect.	4.0mx2.0m	0.6	Fract.	Hard	Ramp
SQPL9	Square	30.0mx30.0m	9.0	Fract.	Easy	Cyc/CR/Ramp
SQPL10	Square	0.5mx0.5m	0.25	Fract.	Easy	Cyclic
SCB	SCB	0.15mx0.2mϕ	0.06	Fract.	H/E	Cyc/Ramp

Table 6: **Large Scale Ice Experiments @ Barrow, AK: May 8-19**

Test ID	Test Geometry	Dimensions (L x W) (m x m)	Crack Length (m)	Test Mode	Failure	Control
SQ1	Square	16.0x16.0	4.8	Fracture	Easy	CR/Ramp
SQ2	Square	4.0x4.0	1.2	Fracture	Easy	Cyclic/Ramp
SQ3	Rect	8.0x16.0	2.4	Fracture	Hard	CR/Cyc/Ramp
SQ4	Rect	8.0x16.0	3.0	Fracture	Hard	CR
SQ5	Square	1.0x1.0	0.29	Fracture	Easy	CR/Ramp
SQ6	Square	0.25x0.25	0.13	Fracture	Easy	CR
SQ7	Square	30.0x30.0	9.0	Fracture	Easy	Cyc/CR/Ramp

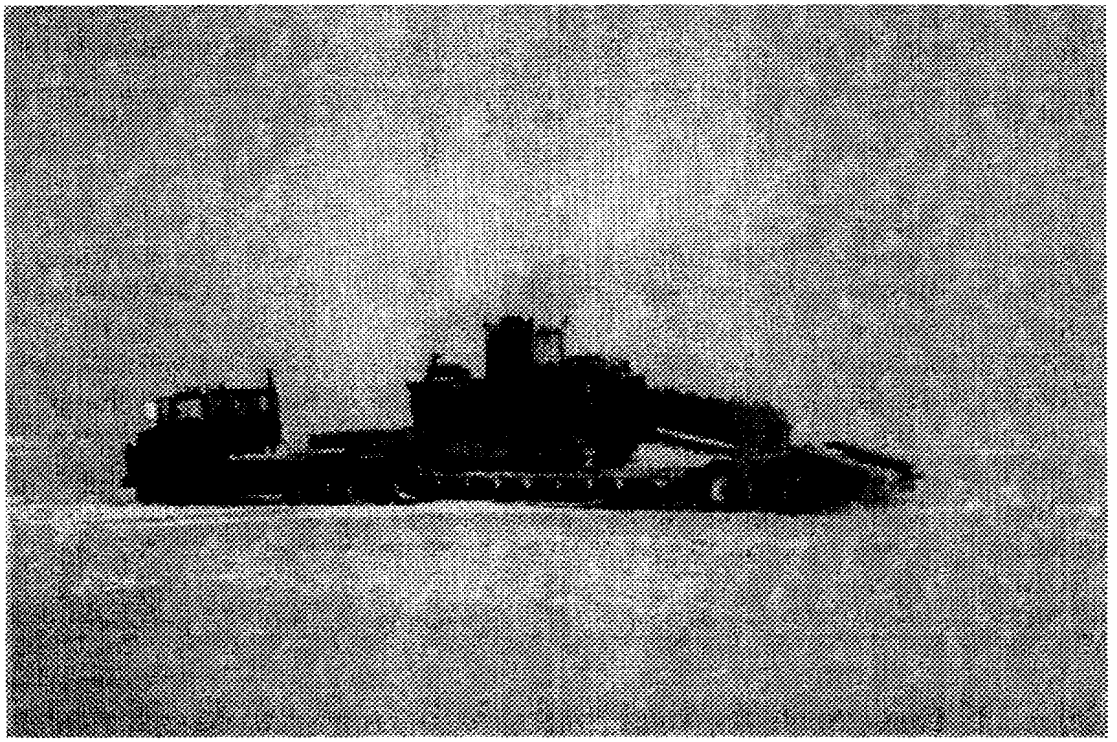

a)

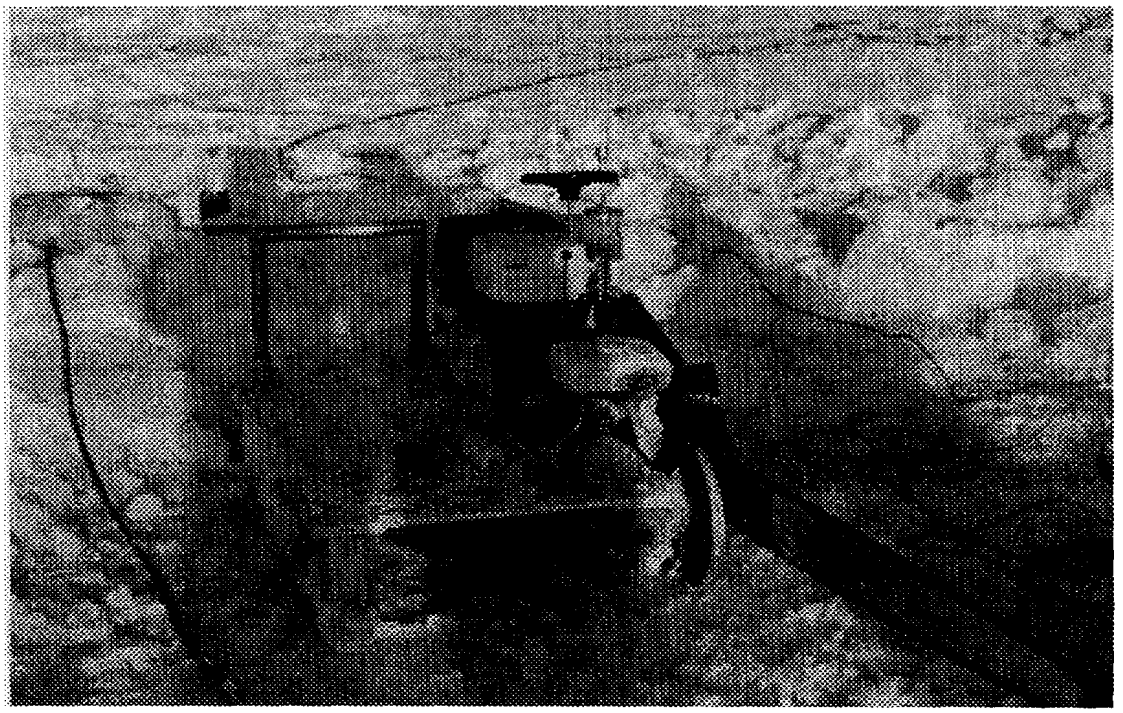

b)

Figure 4: Large-scale ice cutting machinery a) 30 ton Ditchwitch; b) Specially designed cutting machine

from CRREL in a cold room located near the test site.

November 9–19: At this time, the ice was about 30cm thick and showed a strong c-axis alignment. Because of the strong c-axis alignment, the test plan was modified and tests with the crack propagating parallel (hard fail, $\|$) and perpendicular (easy fail, $\perp$) to the c-axis were conducted. Table 4 presents the large scale tests completed on the first trip to Barrow, AK. Due to the success of the square plate geometry in Phase II, it was used again. Unfortunately when testing SPF4, a square plate with the precut crack in the hard fail direction, the crack still chose to propagate in the easy fail direction, resulting in a strength failure. To overcome this problem, a rectangular geometry was chosen, with a width twice that of the length. This geometry was tested in SPF5 and proved to be successful. The flexure tests were accomplished by drilling a hole at the tip of the crack which was precut in the square or rectangular sample. The RT geometry used in Phase I was also tested. This geometry was able to overcome the crack's tendency to propagate in the easy fail direction when testing in the hard fail plane. Petrenko from Dartmouth was present for these experiments to study the electromagnetic emissions from the fractures. Foil electrodes were placed on either side of the predicted crack path and were able to measure the velocity of the propagating cracks.

Small Scale Tests: Full depth cores were tested by cutting a crack from the side to the center of the core as shown in Figure 3b. A small flatjack was then put in the crack and the core was split in half. Each half was then used to make SCB specimens shown in Figure 3c. These tests show the variation in strength with respect to depth and orientation. Also, small plates subjected to four point bending were tested (Figure 3d). All small scale experiments were done under isothermal conditions by Shapiro and Weeks from UAF. These tests provided the link between large scale tests and small scale laboratory experiments.

March 9 to 20: At this time, the ice sheet was approximately 1.7m thick. The average air temperature was -25°C, creating a large temperature profile. Because of the ice thickness, the samples had to be cut with a ditchwitch (Figure 4a) and a specially designed saw (Figure 4b). To achieve similar aspect ratios (width to thickness) as compared to the first trip, larger samples were required. The tests conducted on the second trip are summarized in Table 5. A total of 10 tests were completed covering a size range of 1:30 with the largest being a 30m x 30m square plate. High speed measurements of the electromagnetic emissions (EME) were recorded providing quantitative information on the cracking dynamics.

Small Scale Tests: In addition to the large scale matrix, a set of small scale experiments were completed at the site. It consisted of sixteen semi-circular-bend (SCB) tests, 8 with the crack parallel to the c-axis (hard fail) and 8 with the crack parallel to the basal plane (easy fail). Each test was at a subsequently lower depth in the ice sheet, providing information on the strength relative to the depth. All of the SCB tests were conducted in a small field testing apparatus under isothermal conditions.

May 8 to 19: By this time in the season, the ice was still about 1.7m thick but had a near vertical temperature profile through the thickness. Again, the Ditchwitch and the special crack cutting machine were required. Table 6 presents the list of the tests conducted on the third trip. To compare with the largest size on the previous trip, another 30m x 30m plate was tested. Similar loading sequences were applied to both specimens in order to determine the effect of the temperature profile on the strength and cracking behavior. Schapery from the University of Texas visited the site and provided useful insight on applying load recovery sequences to determine the viscoelastic behavior of the sea ice. Cole from CRREL employed an acoustic emissions (AE) monitoring system on this trip. Two ultrasonic transducers were

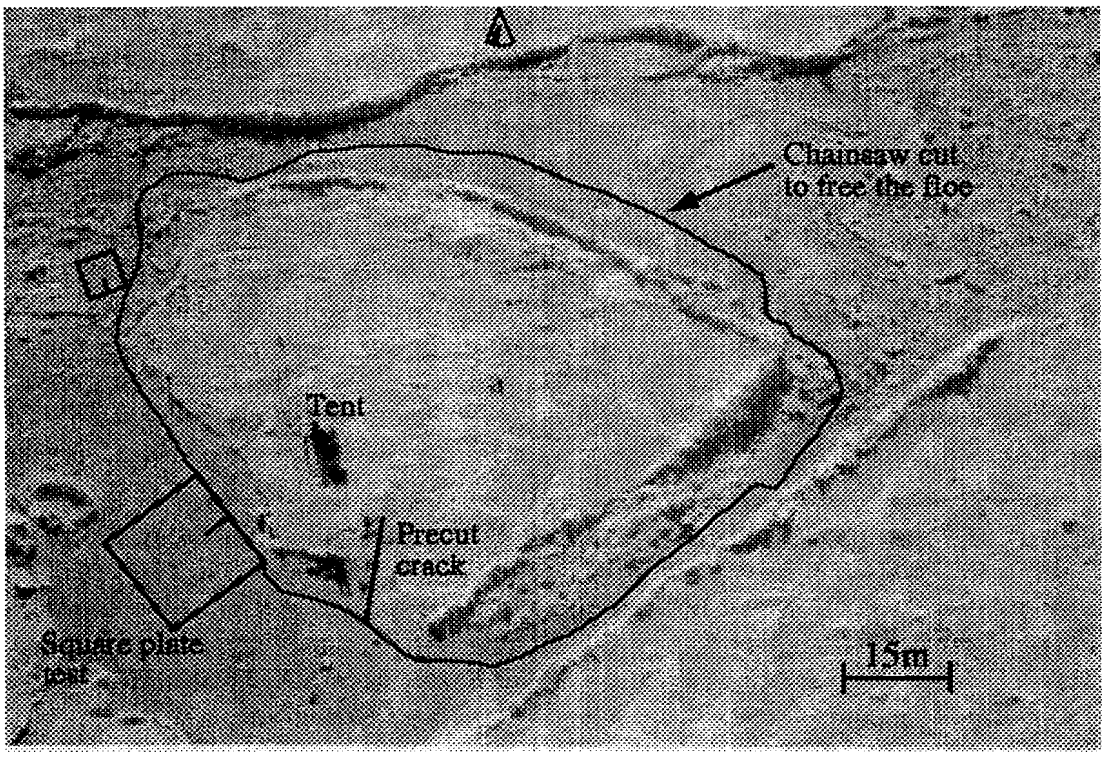

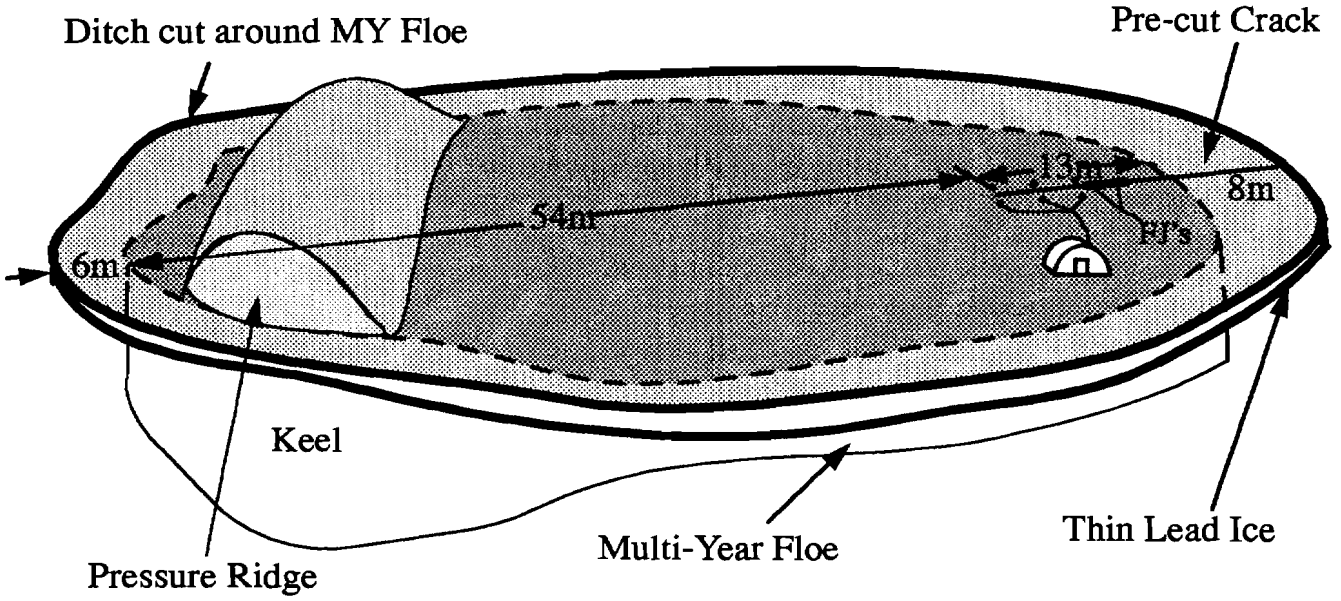

Figure 5: Multi-Year ice floe split at the SIMI Camp, Beaufort Sea

Table 7: **Large Scale Ice Experiments @ the Floating SIMI Camp, Beaufort Sea**

Test ID	Test Geometry	Dimensions (L x W) (m x m)	Crack Length (m)	Test Mode	Thickness (m)	Control
SQ1	Square	2.0x2.0	0.74	Fracture	0.20	Ramp
SQ2	Square	3.66x3.66	0.43	Fracture	0.20	Ramp
SQ3	Square	2.44x2.44	0.84	Fracture	0.60	Cyc/Ramp
SQ4	Square	4.88x4.88	0.84	Fracture	0.60	CR/Cyc/Ramp
SQ5	Square	15.0x15.0	3.29	Fracture	0.20	CR/Ramp
FLOE		80m dia.	9.0	Fracture	¿3.0	Cyc/Ramp

frozen to the surface slightly ahead and to either side of the crack tip. This system provided useful information on microcrack nucleation in the crack tip vicinity, giving a clear indication of the threshold load needed for the onset of microcracking activity.

Small Scale Tests: In addition to the large scale tests, lab sized specimens were tested at the site. SCB samples were tested as on the second trip. Three full depth cores were also shipped back to Clarkson University for continued testing at isothermal conditions. SCB as well as tension experiments were completed and a full characterization of the sheet was done to see if the ice morphology had changed.

FLOATING SIMI CAMP, BEAUFORT SEA: In the spring of 1994, the PI participated in a Sea Ice Mechanics Initiative (SIMI) project geared toward studying the mechanics of sea ice. A total of seven fracture tests were done at the SIMI floating camp in the Beaufort Sea. Table 7 has a summary of the experiments conducted at the camp.

Square Plate Tests on Lead Ice: Five square plate goemetry tests were completed on lead ice with thicknesses ranging from six inches to two feet. Most of the square plates were subjected to an extensive set of cyclic and creep recovery sequences at relatively low loadings. A controlled monotonic load ramp was applied to fracture the plates. As with previous field trips, displacement gauges were placed at chosen locations on the ice surface to measure the crack opening displacements. Blocks of ice from several of the experiments were shipped back to Clarkson University for full characterization.

Splitting of a Multi-Year Floe: The most significant field achievement of the PI was the successful splitting of a 80m diameter multi-year ice floe shown in Figure 5. The surrounding lead ice was double cut with chainsaws and the pieces were removed. This created about a one foot gap around the floe to ensure it was not subject to any confining forces. A crack about 10m long was then cut in the floe. Due to the limitations of the saw, the crack was only cut partially through the thickness. Low level cyclic loading was first applied to force the crack to propagate down through the thickness. The floe was then loaded to failure. Acoustic signals were recorded by Xie and Farmer and the MIT/WHOI group. Results from Xie and Farmer show the cracking as a function of time, verifying the splitting. In addition, crack velocities and crack paths were determined.

Findings to date

Phase I - Alberta, Canada: The in-situ experiments were all done at very warm temperatures, temperatures at which laboratory experiments are essentially impossible. A large size range was completed for very large macrocrystalline freshwater ice. It was very interesting to see that even short term loadings to failure exhibited nonlinearity. Through modelling efforts, the process zone was found to be very small for all sizes. Accordingly, the apparent size effect is due not to growth in the process zone size but rather specimen size vs. grain size (polycrystallinity effect).

Phase II - Resolute, Canada: A very large size range on thick (1.8m) slightly aligned first year sea ice was completed. Analysis of the experiments has shown a significant influence of bulk viscoelastic as well as rate dependent process zone behavior. It was also found that current size effect laws are not immediately applicable.

Barrow, Alaska: A large amount of data was collected for experments covering a large size range with variations in thickness, thermal profile, grain size and salinity. Cyclic as well as creep recovery loading sequences were applied to many of the experiments. This is very important for extracting the constitutive behavior of the sea ice necessary for modelling efforts. In addition, good fracture/electromagnetic information was obtained which is very useful for determining the cracking behavior. At present, little analysis of these experiments has been done.

SIMI Camp, Beaufort Sea: The cracking of a 80m diameter multi-year floe was a significant accomplishment on this trip. Xie and Farmer (1995) deployed a series of hydrophones around the floe, capable of tracking the cracking events. Interactions with Yunbo Xie have enabled us to correlate our load and displacement records with his record of the crack tip position. In addition to the floe, square plate tests were conducted on the thin lead ice. Although no analysis has been done, blocks of ice were shipped back to Clarkson University where a thorough characterization was done. It showed a slight alignment in the c-axis of the thin first year ice.

Analysis and Publication Plans

Analysis of the the field tests is underway at Clarkson University. In addition, characterization and testing of cores and blocks from the trips sent to Clarkson University is being done. Modeling efforts are in progress as well as checking the validity of various size effect laws. Interactions with Prof. Schapery (University of Texas, Austin) are underway for analyzing the creep recovery records as well as developing a constitutive model for sea ice incorporating a viscoelastic component. Interactions with Dave Cole include discussions related to sea ice micrography and implementation of his anelastic straining model. Interactions with Xie and Farmer and Petrenko will continue in an effort to relate their cracking information with our load and displacement records. Interactions with Shapiro and Weeks on the topics of small scale tests and ice characterization will continue. Following is a list of topics for future publications and collaborations related to results from the SIMI projects:

- Evaluation of existing size effect laws.
- Development of rate-independent process zone model.
- Development of rate-dependent process zone model.
- Development of process zone modeling incorporating bulk nonlinear viscoelastic de-

formation.

- Evaluation of stress-separation law dependencies on influences such as size and rate.
- Do the fracture properties at large scale differ significantly from those at small scale?
- Can laboratory-scale testing be used to predict properties at large scale?
- What particular problems are faced with large scale testing?
- Comparison of acoustic and electromagnetic crack position data with process zone modeling (Xie and Farmer, Petrenko).
- Comparison of acoustic energy signatures with process zone energy predictions (Xie and Farmer).
- Publish characteristics of small-scale and large scale data (Cole, Shapiro, Weeks)

Following is a list of related publications in print or to be submitted:

"Joint Sea Ice Experiments at Barrow, Alaska," D.M. Cole, J.P. Dempsey, R.M. Adamson, L.H. Shapiro, W. Weeks, C. Byers, V. Petrenko, O.V. Gluschenkov, in *ICE MECHANICS–1995*, ASME AMD-Vol. xxx (in preparation).

"Fracture analysis of semi-circular and semi-circular-bend geometries," R.M. Adamson, J.P. Dempsey and S.V. Mulmule, in *International Journal of Fracture* (submitted for publication, 1995).

"Large-scale ice fracture experiments in Alberta and at Resolute," J.P. Dempsey, R.M. Adamson, S.V. Mulmule, S.J. DeFranco and Y. Xie, in *ICE MECHANICS–1995*, ASME AMD-Vol. xxx (in preparation).

"Large-scale ice fracture experiments at Barrow and on the SIMI Camp," R.M. Adamson, J.P. Dempsey, S.V. Mulmule and Y. Xie, in *ICE MECHANICS–1995*, ASME AMD-Vol. xxx (in preparation).

J. P. Dempsey, Z. P. Bazant, Y. D. S. Rajapakse, S. S. Sunder, *ICE MECHANICS–1993*, ASME AMD-Vol. 163.

J. P. Dempsey and Y. D. S. Rajapakse, *ICE MECHANICS–1995*, ASME AMD-Vol. xxx (in preparation).

"Laboratory and field-scale fracture of an analogue quasi-brittle material: ice," J. P. Dempsey and S. J. DeFranco, in *Size Effect in Concrete Structures*, H. Mihashi, H. Okamura and Z. P. Bažant, E & FN SPON (Chapman and Hall) (1994) 151–158.

"Splitting of Ice Floes," J.P. Dempsey, S.J. DeFranco, D. Blanchet and A. Prodanovic, in *12th POAC Conference*, Vol. 1, 17–22, 1993.

"Large-Scale Ice Fracture Experiments," K.P. Kennedy, D. Blanchet, A. Prodanovic, J.P. Dempsey, S.J. DeFranco, P.A. Spencer and D. Masterson, in *12th POAC Conference*, Vol. 2, 527–536, 1993.

"Large-scale ice fracture experiments: Phase 2." K.P. Kennedy, K.J. Mamer, J.P. Dempsey, R.M. Adamson, P.A. Spencer and D.M. Masterson, in *IAHR 94: Proceedings of the 12th International Symposium on Ice*, Trondheim, Sweden, Vol. 1, pp 315-324, 1994.

"Fracture resistance determination of freshwater ice using a chevron notched tension specimen" L. M. Stehn, S. J. DeFranco and J. P. Dempsey, in *International Journal of Fracture* **65** 313–328, 1994.

"Specimen geometry effects on the fracture of warm pond (S1) ice," L.M. Stehn, S.J. DeFranco and J.P. Dempsey, in *ASCE Journal of Engineering Mechanics* **121**, 16–25, 1995.

"Orientation effects on the fracture of pond (S1) ice" L.M. Stehn, S.J. DeFranco and J.P. Dempsey, in *Engineering Fracture Mechanics* (in press).

"Fracture Analysis of base-edge-cracked reverse-tapered plates," J.P. Dempsey, R.M. Adamson and S.J. DeFranco, in *International Journal of Fracture*, (in press).

"A grain multiplication mechanism for the formation of transition zones in first year sea ice," Y. Wei, M. Johnston and J.P. Dempsey, in *Cold Regions Science and Technology* (in press).

4. ICE PROPERTIES

Papers included in this section are the following:

"Field and Laboratory Experiments and Modeling of the Constitutive Behavior of Sea Ice," by Dr. David M. Cole (P.I.) of the U.S. Army Cold Regions Research and Engineering Laboratory

"Crack Nucleation Mechanisms in Columnar Ice -- Recent Developments," by V. Gupta (co-P.I.), R. C. Picu, J. Bergström, and H. J. Frost (P.I.) of the Thayer School of Engineering, Dartmouth College

"Compressive Failure of Columnar Saline Ice under Multiaxial Loading," by Erland M. Schulson (P.I.) of the Thayer School of Engineering, Dartmouth College

"Studies of the Influence of Fabric and Structure on the Flexural Strength of Sea Ice and, of the Consolidation of First-Year Pressure Ridges," by Drs. Lewis H. Shapiro, Wilford F. Weeks, and William D. Harrison of the Geophysical Institute, University of Alaska Fairbanks

Papers with additional information on ice properties in Section 2, Acoustics:

"Sea Ice Failure Mechanisms," by Robert S. Pritchard of IceCasting, Inc.

Papers with additional information on ice properties in Section 5, Ice Stress, Ice Strain, and Ice Conditions:

"Pack Ice Stresses and their Relationship to Regional Deformation," Jacqueline A. Richter-Menge (P.I.), Bruce C. Elder, Walter B. Tucker III, and Dr. Donald K. Perovich of the U.S. Army Cold Regions Research and Engineering Laboratory

Field and Laboratory Experiments and Modeling of the Constitutive Behavior of Sea Ice

Dr. David M. Cole (P.I.) U.S. Army Cold Regions Research and Engineering Laboratory, Hanover, NH.

Scope of Model and/or Data Set

This line of research involves laboratory experiments and modeling of the mechanical properties of saline ice. Initially, the work focused on laboratory-grown ice subjected to reversed direct-stress (alternating uniaxial tension/compression) loading. The ability to perform this type of loading on ice was developed by the P.I. and his associates at CRREL, and the work previously focused on building a data base mapping out the effects of temperature, frequency, amplitude, microstructure and physical properties on the cyclic loading response of laboratory-grown ice. These findings, which primarily examined behavior at low strains (constant microstructural conditions) supported the development of a mechanistic model of the anelastic (time dependent recoverable) strain as described below. The effort was subsequently expanded to examine creep and creep recovery effects, employing the cyclic loading methodology to track compliance changes associated with the creep straining history. The physical properties of the laboratory-grown specimens were varied significantly to provide insight regarding the effects of salinity and porosity on compliance.

During FY94, the effort was expanded to address the behavior of naturally occurring sea ice, alignment and scale effects. This work is centered on a set of in-situ cyclic, creep and creep recovery field experiments conducted at Barrow, AK, in conjunction with J.P. Dempsey (Clarkson University), L. Shapiro and W. Weeks (University of Alaska, Fairbanks), under ONR's Sea Ice Mechanics Accelerated Research Initiative. The field experiments employed similar loading paths as the laboratory work and were repeated at three times during the growth season to relate the mechanical properties to the evolving physical properties of the sheet. The in-situ experiments were conducted in highly aligned ice in Elson Lagoon and cores were shipped to CRREL for detailed laboratory experiments which are currently in progress. In-situ cyclic, creep and creep recovery experiments were conducted on notched specimens over a range of physical scales from sub-meter to a maximum of 30×30 m^2. Applied frequency ranged from 5×10^{-3} to 1 Hz, which is bracketed by the frequency range applied in the laboratory experiments. The microcracking activity in the vicinity of the notch tip was monitored during the final set of field experiments employing the acoustic emissions monitoring technique. Ice sheet thickness for the three field trips was 0.3 m (November 1993), 1.38 m (March 1994) and 1.78 m (May 1995). Air and ice temperatures were monitored and eight salinity profiles were obtained for the test site during the growth season.

As an important aspect of this program is the linking of physical and mechanical properties of sea ice, a good deal of attention is being paid to characterizing physical properties in the field and in the laboratory specimens. In addition to the usual salinity, density and porosity determinations, photomicrography is being used extensively to help quantify the details of the microstructure. The ice saw developed for the field program provided a means to obtain thin slabs through the entire depth of the sheet. Under back lighting, it was possible to make unusually detailed observations of the brine drainage structures, which in turn are providing new insight into the development and geometric characteristics of these important sea ice features.

The cyclic loading response of sea ice is dominated by the elastic and anelastic (time-dependent but recoverable) components of deformation for many conditions of interest, and the associated theoretical effort has focused on identifying the underlying deformation mechanisms and developing a physically based model of the transient and steady-state viscoelastic behavior. With the availability of the results on field cores of aligned ice, the model is currently being expanded to address alignment effects. Additionally, since the temperatures observed in the in-situ experiments were relatively high ($T \geq -10°C$ for the November 1993 and May 1994 trips), the range of applicability of the model is currently being extended to higher temperatures ($T \leq -3°C$) on the basis of the laboratory results.

Findings to Date

The laboratory experiments have produced information on the effects of temperature, amplitude, frequency, microstructure, alignment and prestrain on the elastic and anelastic response of saline ice. Zero mean stress sinusoidal loading serves as the benchmark test in this program. The experiments have provided a means to examine saline ice as a material and to apply established methodologies to identify the operative deformational mechanisms. This is an important step toward one of the long-term goals of the work, which is to develop mechanistic links between the physical and mechanical properties of sea ice.

Experimental Observations on Laboratory-Grown Ice. Figure 1 shows typical cyclic loading behavior observed in the laboratory experiments. The hysteresis loops provide basic information on the transient and steady-state behavior, the internal friction, stress level and frequency effects. A study of the effect of creep prestrain (in the absence of microcrack damage) on compliance strongly indicated the operation of a dislocation-based mechanism for the dominant relaxation process. By producing specimens having a wide range in physical properties, it was possible to examine the relationship between physical and mechanical properties under well-controlled conditions. The experiments illustrated a direct link between total porosity and the magnitude of the anelastic straining at all the frequencies examined (Figure 2).

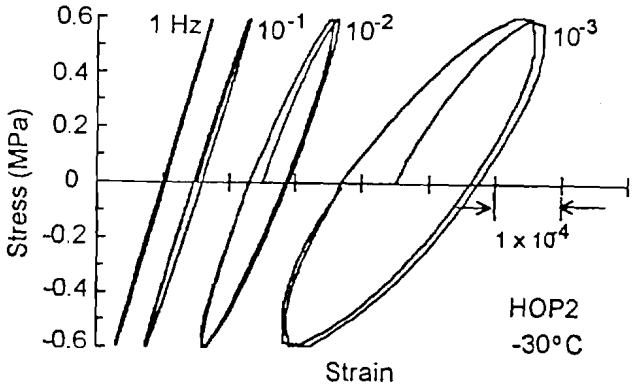

Figure 1. Typical hysteresis loops from laboratory-grown saline ice.

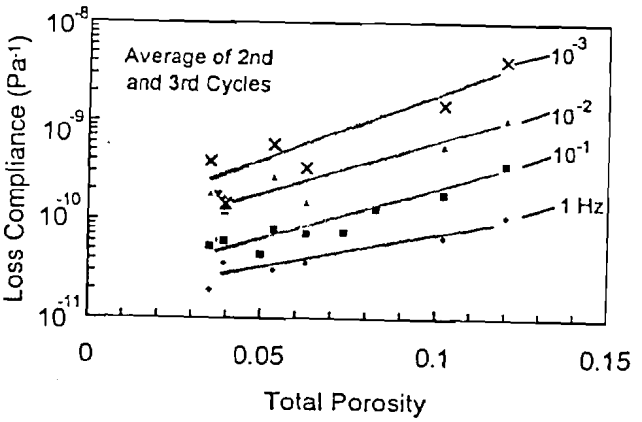

Figure 2. Compliance vs. porosity for several frequencies.

The study of temperature effects on the anelastic straining indicated that an activation energy $Q^d = 0.55$ eV adequately represents the dislocation relaxation for $T \leq -10°C$. The grain boundary relaxation is characterized by $Q^{gb} = 1.38$ eV.

Experimental Observations on Field Cores. Preliminary analysis of the field specimens indicates that the above-mentioned value of Q^d may be applicable to temperatures as high as -3°C, and work continues to verify this finding. Figure 3 shows the effective modulus at several frequencies as a function of temperature for $-3 \leq T \leq -10°C$. The response is characterized by a significant frequency effect and a surprisingly weak temperature dependence. Although at first surprising, the weak temperature dependence is taken to indicate near full relaxation with respect to the dislocation and grain boundary mechanisms under the prevailing conditions. The temperature dependence is similar to that observed for freshwater ice and are

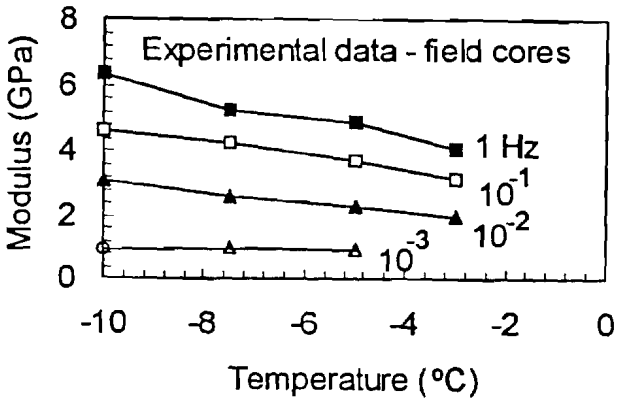

Figure 3. Effect of temperature on modulus several frequencies (45° orientation).

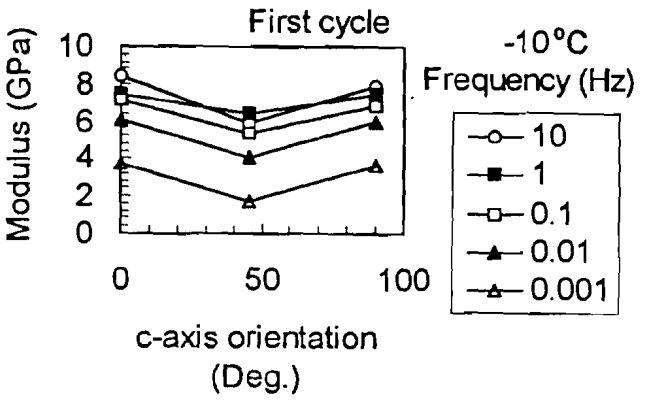

Figure 4. C-axis alignment effect for on modulus for several frequencies.

consistent with the model predictions as discussed below. Heretofore, alignment effects had been largely confined to examinations of compressive strength over a relatively narrow range of temperatures and loading rates. Figure 4 presents the c-axis orientation dependence of the effective modulus. The long axis of the cylindrical specimens fall along (0°), perpendicular to (90°) or at 45° to the preferred c-axis direction. The 0° and 90° orientations produce approximately the same effective modulus at the temperatures and frequencies examined. The values for the 45° orientation, which maximizes the resolved shear stress on the basal planes, consistently shows a lower modulus than the other two orientations.

Brine drainage networks and microstructure. Figure 5 gives an example of the unique observations that were made of the brine drainage networks through the entire depth of the ice sheet during the March, 1995, trip. The ice saw developed for the program by researchers at the University of Alaska, Fairbanks, made it possible to obtain smooth-sided, thin slabs that extended through the entire ice sheet. When photographed under back lighting, they provided an excellent view of the complex drainage networks. A photomicrography system was employed during the field work to document the details of the microstructure and inclusion geometry immediately after removal of the ice from the parent sheet (Figure 6). These serve as a basis of comparison for micrographs obtained from the cores shipped back for testing and provide useful insight regarding the in-situ characteristics of the ice.

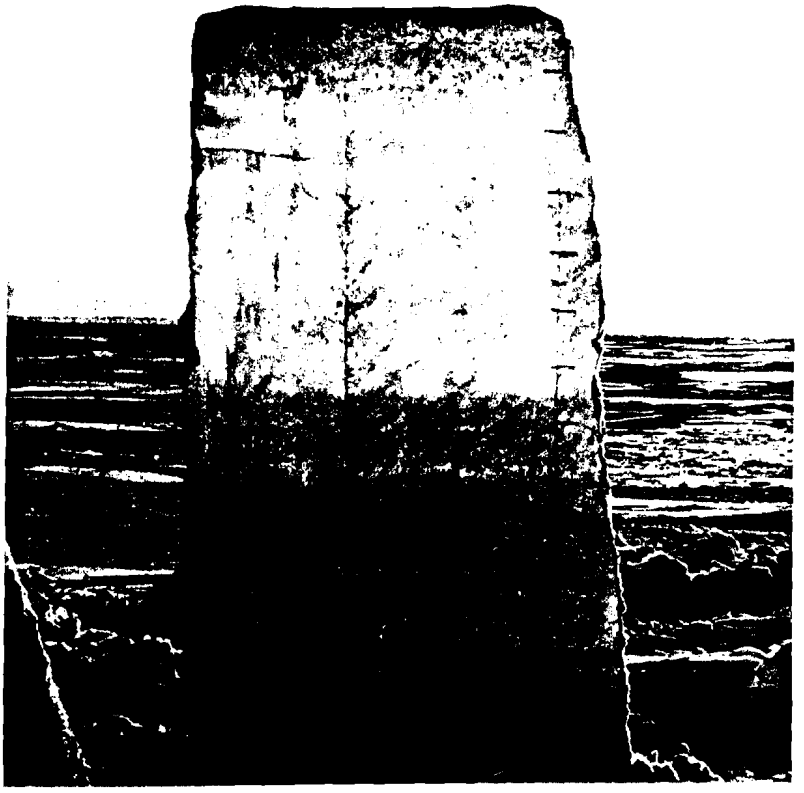

Figure 5. Brine drainage networks observed in March, 1995, at Elson Lagoon.

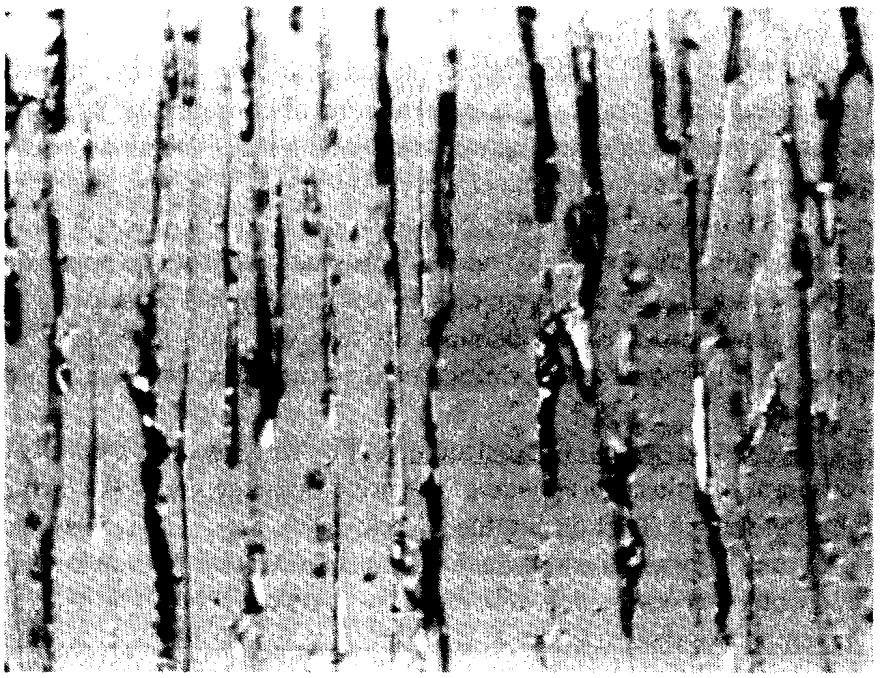

Figure 6. Typical sea ice micrograph obtained during the field experiments. Frame size is 10 ×15 mm^2.

Model of Cyclic Loading Response. Analysis of the laboratory experiments indicated that the anelastic behavior was due primarily to the operation of two distinct mechanisms: a dominant dislocation relaxation and a less significant grain boundary relaxation mechanism. Figure 7 illustrates a typical broad dislocation relaxation peak in terms of D_2 (out-of-phase or loss compliance) in the frequency-shifted data from a specimen examined at a number of temperatures, frequencies and stress levels. The curve shows the model predictions. The anelastic straining model (Cole, 1995) considers these two relaxations to be additive when no prestrain is involved, and Figure 8 shows the behavior of the model in terms of D_2, the 90°-out-of-phase (loss) compliance.

In the absence of deformation that would effectively lock the grain boundaries, $D_1 = D_1^d + D_1^{gb}$ and $D_2 = D_2^d + D_2^{gb}$, where:

$$D_1^d(\omega) = D_u^d + \delta D^d \left[1 - \frac{2}{\pi}\tan^{-1}\exp(\alpha^d s_i^d)\right]$$

$$D_2^d(\omega) = \alpha^d \delta D^d \frac{1}{\exp(\alpha^d s_i^d) + \exp(-\alpha^d s_i^d)} \qquad [1]$$

$$D_1^{gb}(\omega) = D_u^{gb} + \delta D^{gb} \left[1 - \frac{2}{\pi}\tan^{-1}\exp(\alpha^{gb} s_i^{gb})\right]$$

$$D_2^{gb}(\omega) = \alpha^{gb}\delta D^{gb}\frac{1}{\exp(\alpha^{gb}s_i^{gb}) + \exp(-\alpha^{gb}s_i^{gb})}$$

The superscripts d and gb indicate quantities pertaining to the dislocation and grain boundary relaxations, respectively; τ^j is a relaxation time, $s_i^d = \ln(\tau^d\omega)$ and $s_i^{gb} = \ln(\tau^{gb}\omega)$. The δD^j give the strength and the D_u^j give the unrelaxed compliances of each relaxation mechanism. Cole (1995) presents the complete development of the model. The transients in both relaxations are governed by

$$\frac{2}{\pi}\tan^{-1}\exp\left[\alpha^d \ln(\tau\omega_t)\right] \qquad [2]$$

with the appropriate values of the peak broadening term α^j and relaxation time τ. In the last expression, $\tau = 1/\omega$ (ω is the angular driving frequency). Time enters the expression explicitly by setting $\omega_t = t^{-1}$. The data were found to obey time-temperature superposition and are well represented by a single activation energy and a distribution in relaxation times. The strength of the dominant dislocation relaxation is a function of the mobile dislocation density on the basal plane Δ, an orientation factor Ω, a microstructural restoring stress K and the Burgers vector b:

$$\delta D^d = \frac{\Delta\Omega b^2}{K}. \qquad [3]$$

Analysis of the laboratory results from cores of the thin ice (0.3 m) obtained during the Fall of 1993 indicates a significant alignment effect on the dynamic compliance. To quantify the alignment effects, the fabrics of those specimens are being examined to determine the orientation factor, which in turn indicates the proportion of shear stress carried by the basal planes. The field cores are being examined over the range of relatively high temperatures observed in the field. Interestingly, the observed temperature dependence is in line with the predictions of the model (which was based on results for $T \leq$ -10°C) for the effective modulus as indicated in Figure 9.

The orientation effects found in the field specimens are currently being incorporated into the anelastic straining model, with an emphasis on developing a quantitative relationship between fabric and compliance. Work is also under way to incorporate this model into the finite element analysis of the in-situ experiments being developed by Prof. Dempsey's group at Clarkson.

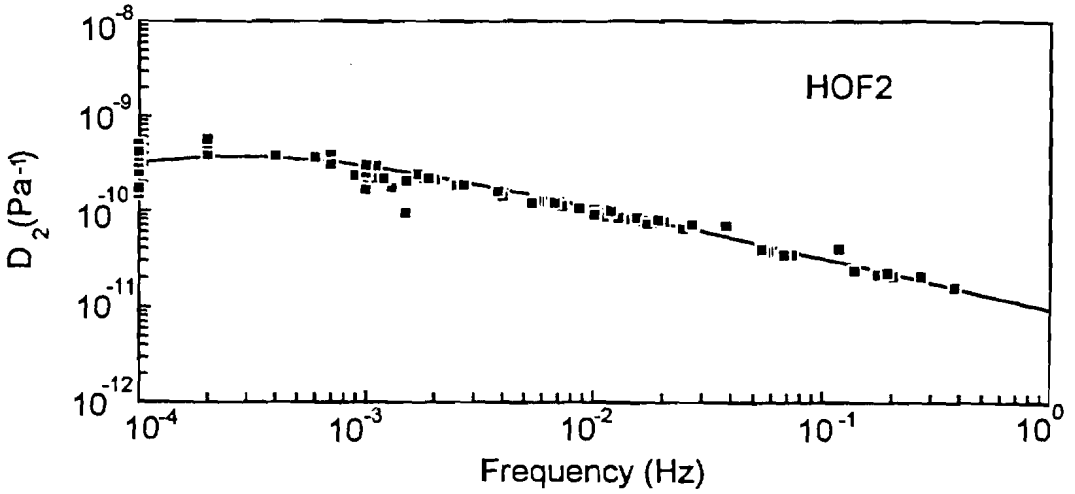

Figure 7. Broad compliance peak observed in laboratory-grown saline ice. Curve is the model prediction.

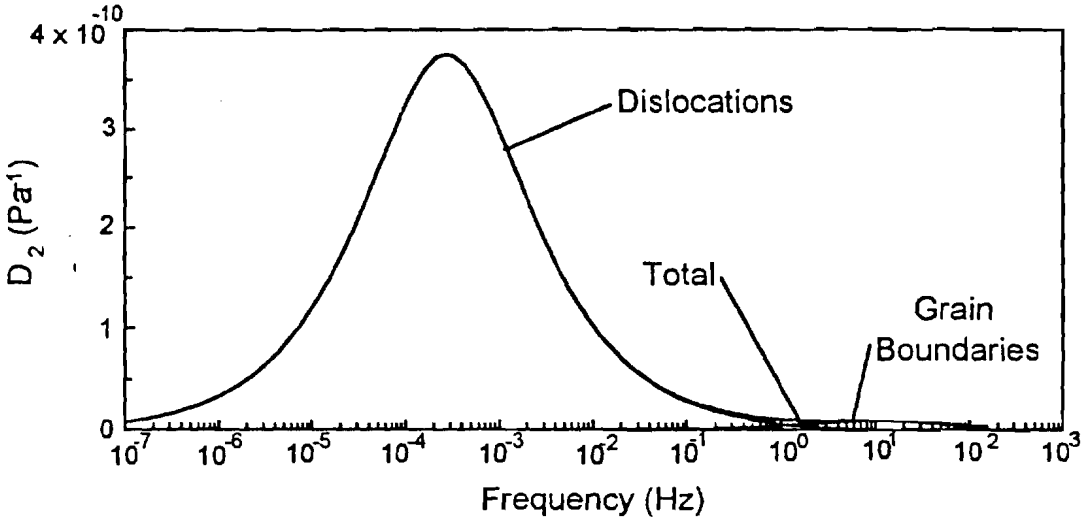

Figure 8. Model predictions of the dislocation and grain boundary peaks in terms of loss compliance, calculated for -10°C.

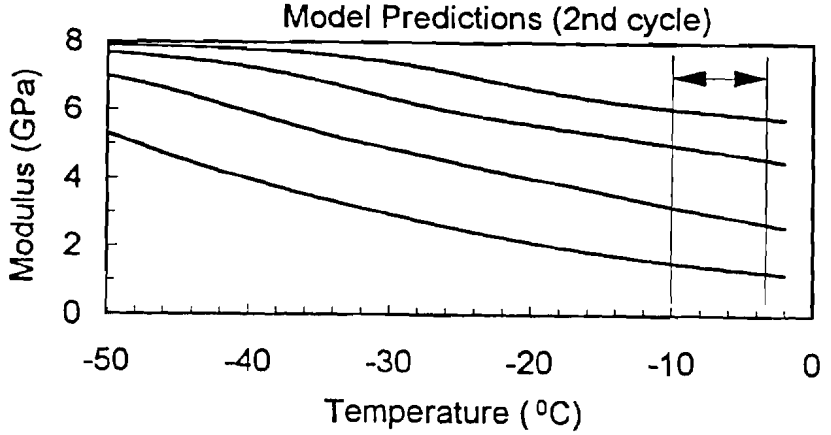

Figure 9. Model predictions of the effective modulus.

Analysis and Publication Plans

The laboratory experiments and analysis of the cores from the March, 1994 and May, 1994, field trips will continue as planned during the remainder of FY95. On the basis of these findings, the anelastic straining model will be extended to include alignment effects and the temperature dependence for $T \geq -10°C$ will be verified. The creep and creep recovery data will be analyzed and the observed viscous effects will be modeled. Radial deformation measurements have been included in the experiments on the field cores and those data will be incorporated into the analysis as well. The acoustic emissions observations from the May, 1994, trip will be analyzed and interfaced with the in-situ load/deformation readings made by Dempsey's group. As of this writing, the anelastic straining model is being implemented in the finite element code that has been developed by Dempsey's group to analyze the in-situ specimens. The analysis will ascertain the role of anelasticity in the time-dependent effects observed in the fracture experiments. Extensive interaction will continue with Prof. Dempsey on this and related matters as attention focuses on the improvement of the small-scale models and their extension to the large-scale in-situ result from the Barrow Experiments. Reports with the following titles will be authored jointly with Prof. Dempsey's group:

In-situ cyclic loading response of sea ice I: Scale effects, and II: Comparison of laboratory-scale predictions with large-scale observations.

Interactions with Profs. Shapiro and Weeks (University of Alaska, Fairbanks) on the topics of fabric, physical properties and drainage network characterization will continue as will interactions with Profs. Schapery and Rodin (University of Texas, Austin) regarding various aspects of the constitutive modeling of sea ice.

Additionally, as there is a good deal of interest in the sea ice community in the physical properties characterization, micrography and brine drainage network observations, these will be accumulated and analyzed in a separate CRREL Report tentatively titled:

Observations on the physical properties, microstructure and brine drainage networks in first-year sea ice through a growth season.

Other papers related to the P.I.'s sea ice mechanics work include:

Cole, D.M. (1995) A model for the anelastic straining of saline ice. Phil. Mag. A, In Press.

Cole, D.M. and G.D. Durell (1995) Cyclic loading of saline ice. Phil. Mag. A, In Press.

Cole, D.M. and G.D. Durell (1995) The cyclic loading of saline ice. CRREL Report In Press.

Cole, D.M. and G. D. Durell (1995) The effect of C-axis alignment on the constitutive behavior of sea ice at low strains. To be presented at the ASME Joint Applied Mechanics and Materials Summer Meeting, UCLA, June 28-30.

R.M. Adamson, C. Byers, D.M. Cole, J. P. Dempsey, O.V. Gluschenkov, V. Petrenko, L.H. Shapiro and W. Weeks (1995) Joint sea ice experiments at Barrow, Alaska. To be presented at the ASME Joint Applied Mechanics and Materials Summer Meeting, UCLA, June 28-30.

Cole, D.M. (1994) The effect of temperature and microstructure on the constitutive behavior of ice at low strains. Proceedings of the IAHR 12th Int'l. Ice Symp., Trondheim, Norway, Vol. 3, pp. 1051-1058.

Cole, D.M. (1993) The effect of creep on the constitutive behavior of saline ice at low strains. In Ice Mechanics 1993, Proc. 1st Joint Mechanics Meeting of ASME, ASCE and SES, Charlottesville, VA, June 6-9, AMD-Vol. 163, pp. 261-272.

Cole, D.M. (1990) Cyclic loading of saline ice: Initial experimental results. Proc. 9th Intl. Conf. on Offshore Mechanics and Arctic Engineering, Vol. IV, pp. 265-271.

Crack Nucleation Mechanisms in Columnar Ice--Recent Developments

V. Gupta (co-PI), R.C. Picu, J. Bergström, and H. J. Frost (PI)

**Thayer School of Engineering, Dartmouth College,
Hanover, New Hampshire 03755**

Scope of Work

Interest has been generated in the mechanical properties of saline ice because of a variety of engineering challenges which involve the interaction between sea ice and man-made structures. Oil exploration in the northern seas requires the design of off-shore platforms for waters subject to ice cover. This requires estimation of forces induced by moving ice sheets and ice bergs against stationary structures; these forces in turn depend on the details of the deformation mechanisms within ice. Similar problems are encountered in designing ice-breaking ships and submarines operating under the ice covers. Of particular interest is the impact of ice sheets at moderate and high velocities, where ice essentially deforms in a *brittle* manner. Within the brittle regime, a variety of mechanisms are possible. At the point of impact, the ice may undergo local crushing which involves the nucleation of several in-plane and out-of-plane cracks, followed by a progressive damage through crack-to-crack interaction, and an ultimate failure through the extrusion of the fragmented ice particles from the edges. Sometimes an additional mechanism is observed in which the ice floe splits through the propagation of a through-thickness crack. Finally, if the ice-sheet thickness is large enough, the failure can be through the propagation of an in-plane crack which eventually turns towards the ice surface, forming an ice spall. Thus, to estimate ice loads from fundamental considerations, it is important to understand the mechanisms associated with crack nucleation, crack propagation and crack-to-crack interaction.

Through a combined experimental and numerical modeling program, we have studied various mechanisms that are responsible for nucleating cracks in both saline and freshwater columnar ice. Since our deformation-based models require the input of fundamental material properties like the cleavage strengths and the fracture toughness of ice crystals, we have obtained them independently by devising separate experiments. Finally, we have shown how the fundamental work on crack nucleation can be applied to develop a mechanism-based failure model for the splitting of ice floes during their interaction with structures at relatively moderate velocities. The predicted failure pressures compare quite well to those measured in basin studies. Thus, one of the future aims of this study should be to develop a failure model for more widely encountered ice-crushing process that occurs during the high velocity edge indentation of the ice sheets by structures. The results obtained so far provide a quantitative prediction of the forces required to nucleate the first set of cracks in such a crushing process.

Below, we provide recent results of our model and experimental studies as related to the process of crack nucleation; measurement of fracture toughness and cleavage strengths; and finally the results from our floe-splitting model.

Findings to date

1. Crack Nucleation in the Brittle Regime

At temperatures close to its melting point, polycrystalline ice Ih shows two kinds of behavior under compressive loading. At strain rates lower than 10^{-4} s^{-1} and under uniaxial

compression, the overall stress-strain behavior is ductile with failure strains as high as 10%. At higher strain rates, the behavior is brittle with a sharp termination of its linear stress-strain curve at the peak. The failure stress increases with an increase in the confinement ratio and decreases with an increase in the temperature and grain size.

Crack nucleation in columnar ice has been investigated in both brittle and ductile regimes and several mechanisms have been proposed to explain the phenomenon. Although the behavior in the ductile regime has been convincingly demonstrated, the mechanisms in the brittle regime had remained a mystery prior to the start of our work. At these high strain rates the dislocation pile-up mechanism cannot be invoked, and twinning which is a common deformation mechanism in hexagonal materials is not observed in ice. Cole (1988) suggested the possibility of crack nucleation due to the elastic anisotropy of the grains--a conclusion, he arrived without obtaining the details of the important singular stresses at the triple grain junctions. As shown by us elsewhere (Picu and Gupta, 1995a,b &1994a), such calculations cannot explain crack nucleation observations in columnar freshwater or saline ice. The observations of several investigators on crack nucleation at high strain rates were also analyzed by Shyam Sunder and Wu (1990). They formulated the crack nucleation problem as a growth of a pre-existing precursor crack of almost 10 to 20% of the grain boundary length. Although the stresses were calculated with due consideration to elastic anisotropy, the stress at the precursor tip was concentrated with an exponent of -0.5 since the assumed precursor lengths were much beyond the range of the singular stress field at the triple junction. In such cases, nucleation of the precursor itself under the singular stress field of the triple junction (with a singularity exponent other than -0.5) becomes the correct nucleation problem, which was not attempted by these authors. Further, in their study the assumed precursor sizes are so large (1 mm-2 mm) that they should be easily visible in a freshwater ice sample. As discussed later here, our observations do not support the presence of such large precursors. Thus, the correct formulation should explore the energetics of the nucleation process under the singular stress field of a grain triple junction, rather than a pre-supposed crack-like singularity exponent of -0.5 which results when the precursor is assumed to be a fully-formed crack.

With above in mind, Picu *et al.* (1994) determined the stress concentrations at triple junctions by assuming the grains to be isotropic but with moduli corresponding to extreme values in an ice crystal. The corresponding energy release rate values for crack nucleation were computed numerically in a polycrystal with symmetric grain boundary orientations. The resulting values were much smaller that the fracture toughness of ice, even when the difference in the elastic constants of the neighboring grains was assumed to be unrealistically high. Also, the difference between the energy release rate and the fracture toughness was too large to be overcome by thermal activation (Frost and Gupta, 1993).

Since the above calculations were limited to isotropic material idealization, a separate study that included the elastic anisotropy of the grains was attempted by Picu and Gupta (1994b). However, such considerations of the elastic anisotropy and realistic grain junction geometries did not lead to energetically favorable conditions for crack nucleation. Thus, in freshwater columnar ice, other mechanisms for crack nucleation needs to be established. Since the mechanistic effects of the brine pocket shape, size and distribution can be all smeared into an effective homogeneous orthotropic grain, the same analysis was used by Picu and Gupta (1994b) to see if cracks can nucleate in saline ice due to elastic anisotropy of grains. This, too, turned out to be negative. Thus, the earlier conclusion of Picu *et al.* (1994) where cracks were shown to nucleate from the brine pocket surface under the influence of the internal brine pressure remains unaltered. In that work, we calculated the magnitudes of the stress concentration coefficients for several particular cases (using infinite arrays of hexagonal grains, with three brine pockets symmetrically arrayed around each triple junction) by the finite element technique. From these calculations it was clear that the internal pressure in brine pockets that results due to the partial freezing of the brine

is the key determinant of the levels of stress concentration achieved. Approximate calculations of the energy release rate for crack nucleation suggested that it was more favorable for the cracks to nucleate from the brine pocket surface than from the triple grain junctions. Furthermore, the favored cracking path should be between brine pockets and nearby triple junctions. This is consistent with observations of star-shaped systems of brine drainage channels with the center of the star coinciding with the triple point.

In the absence of stresses due to brine pockets, the inherent elastic anisotropy of ice is not sufficient to nucleate cracks in purely two-dimensional models, such as perfectly columnar grains in plane strain (Picu and Gupta, 1994b). Calculated nucleation energies are far beyond available thermal activation energies. Therefore some additional stress concentrating effects are required, such as irregularities in the third dimension (e.g. jogs in column boundaries) or inclusions (e.g. brine pockets or dirt particles). Although three dimensional irregularities and dirt particles may sometimes be important, we should not neglect the kinetic processes described above. Experiments on columnar fresh-water ice, loaded perpendicular to the columns, provide evidence that crack nucleation is associated with grain boundaries in a manner consistent with grain boundary sliding. The stress concentrations associated with elastic anisotropy can be relaxed by grain boundary sliding (Picu and Gupta, 1995a&b). This sliding, in turn, produces its own stress concentration fields. That is, the stress concentration fields due to elastic anisotropy are progressively rearranged as the boundary sliding proceeds, until the final result contains the stronger singularities associated with shear cracking. These important developments are summarized below. We first provide experimental evidence for grain boundary sliding-induced boundary decohesions at -10°C even though the strain rate of loading (10^{-3} to 10^{-2} s^{-1}) yields an overall brittle response from the polycrystal. This is followed by a fracture mechanics-based model to explain the crack nucleation stress.

Experimental Procedure

Experiments were conducted on columnar freshwater ice polycrystals grown from de-gased water. The ice puck was sliced in 15.5 x 15.5 x 2.5 cm^3 plates with columns running perpendicular to the largest face and traversing the entire thickness of the plate. The grain size in a typical sample varied from 8 mm to 12 mm. The samples were equilibrated at -10°C for a week before carrying out the tests.

The tests were performed using a multi-axial MTS testing machine (MATS). This is a servo-hydraulic system with six actuators providing three orthogonal axes of loading which is located in a cold room maintained at -10 ± 0.2°C for our experiments. Samples were pulse loaded under biaxial compression with the two loading axes normal to the column axes, at strain rates of 10^{-3} s^{-1} and 10^{-2} s^{-1}. For both strain rates, tests were conducted with confinement ratios varying between 0 and 0.4. Samples were observed for spotting damage between two successive pulse loadings, which were spaced about 2 to 3 minutes apart.

Experimental Observations

Evidence for boundary sliding at strain rates near 10^{-3} s^{-1} have been provided by internal friction experiments. Since the amplitude of the stress cycle in these tests is very low (~ 0.1 MPa), no damage is induced in the material. At higher loads, however, localized boundary decohesions become possible. A set of micrographs showing a typical grain boundary sliding and decohesion pattern is shown in Fig. 1. This set corresponds to the deformation at a strain rate of 10^{-2} s^{-1} and a confinement ratio of 0.4. Figures 1 (a) to 1 (d) correspond to principal load steps of 1.5 MPa, 1.8 MPa, 2.1 MPa and 2.5 MPa, respectively. The two facets marked ABCD and EFGH are oriented at about 50° to the

major loading axis and traverse all the way through the sample thickness. The triple junction lines edging these facets are marked by AD and BC, and EH and FG, respectively. The lines AB, CD, EF and GH lie on the largest faces of the sample, also carrying the c-axis of the grains. The unloaded samples were perfectly transparent, except, at times, some boundaries were visible due to the reflection of light from the boundary grooves located on the surface. As the sample was loaded between 1.0 MPa and 1.3 MPa, a localized boundary opaqueness corresponding to boundary decohesion was observed, which upon subsequent loading, progressed transversally from the specimen surface. Figure 1 (a) shows one of the first slided and decohered grain boundary at a stress level of 1.5 MPa. These separations should be due to the stress concentrations at asperties arising from the boundary waviness, upon boundary sliding- a mechanism proposed by Raj and Ashby (1982). Under increasing shear parallel to the line GH, the relative motion of the grains across the boundary increases, which then should result in material separation at crests and troughs of the waviness parallel to the line EH. The initiation of such decohesions on the surface of the sample is also consistent with the prevalent plane stress-state there.

Upon further loading, the number of decohesions on the boundary increase without necessarily coalescing to form a fully-cracked grain boundary. However, their presence on the boundary facet imply an increase in the shear compliance of the boundary leading to an additional relative displacement of the two grains under the local shear stress. When the accumulated displacement is high enough, the grain boundary which has an overall mode II crack-type behavior leads to the nucleation of mode-I wings at its tips. This, we believe, is the mechanism of crack nucleation from the triple junctions. The sequence of such events under increasing load is captured in Figure 1, with the final crack nucleation events depicted in Fig. 1 (d). Two typical but different behaviors of the boundaries that lead to the nucleation of cracks are illustrated in Fig. 1 (d). If the intrinsic strength of the boundary is high, the boundary decoheres locally and the spot-like features do not coalesce; sometime even when the entire sample has failed. Nevertheless, there is a local increase in the shear compliance of the boundary, which results in the nucleation of cracks from the triple junctions. This behavior is illustrated by the facet EFGH with cracks nucleating along EH and FG. On the other hand, a smaller strength of the boundary leads to the formation of a fully-decohered grain boundary which then behaves as a frictional mode II crack. Obviously, in this case the accumulated relative displacements are higher than the previous case and leads to longer lengths of the nucleated cracks. This behavior is depicted by the facet ABCD with larger nucleated cracks at its end.

An observation which supports the thesis advanced in the companion paper is the nucleation of the crack along the junction line AD. Fig. 1 (b) shows no evidence of any crack while there are several localized decohesions along the facet. At a principal stress level of about 2 MPa, corresponding presumably to a critical sliding displacement, a crack nucleated from the junction AD, as shown by an arrow in Fig. 1 (c).

The intermittently decohered region of the boundary is both thermodynamically and mechanically different than the fully-formed facet cracks. First, the decohered spots were never observed to propagate individually out of their planes. Thus, they do not contribute to the overall damage of the sample in contrast to the fully formed cracks which propagate and interact with others to form the terminal failure. Further, when the cracked samples were annealed for 24 hours at -10°C, all decohesion spots healed-up completely with only the fully-formed cracks remaining. For this reason, here the word "nucleation" refers to the formation of fully-formed cracks, although thermodynamically, the stress level at which the decohesion pockets are nucleated should be considered as the nucleation stress. Since the nucleation stress reported by other investigators in the ice mechanics field always refers to the fully-formed cracks, here we shall also comply with the same standard and leave the issue of whether these decohesion pockets can be considered as nucleated cracks to a later correspondence.

Experimental Data and the Model

Figure 2 synthesizes the experimental data. The principal stress range in which boundary sliding-induced localized decohesions and subsequent wing cracks from the triple junctions were observed are shown by thin and thick lines, respectively. Data-set for experiments done at strain rates of 10^{-3} s^{-1} and 10^{-2} s^{-1} are shown in the figure. The stress required for crack nucleation is seen to increase with the confinement ratio since nucleation may be produced only by the in-plane sliding of the grains. The stress level required for grain boundary sliding and decohesion remains almost constant with the confinement ratio. The two events of grain boundary decohesion and crack nucleation cannot be separated at confinements smaller than 10% when the amplitude of the pulse loading is increased in increments of 0.3 MPa. However, at higher confinement ratios (> 20%) when the in-plane shear stress increment is much smaller than the one at low R for the same increment of the principal load, the occurrence of the two events could be separated. As expected, the boundary decohesions occur much before the crack nucleation. The viscous character of the boundary is further supported by an increase of the average boundary decohesion stress from 1 MPa to 1.3 MPa as the strain rate is increased from 10^{-3} s^{-1} and 10^{-2} s^{-1}.

In the light of above considerations, the grain boundary is modeled as a mode II crack having a shear resistance τ_b, which in turn, is independent of the stress-state and only a function of the strain rate $\dot{\varepsilon}$ and temperature T. If the applied shear stress τ_{appl} is smaller than τ_b, the boundary behaves as a healed crack and transmits fully the tractions, otherwise, the boundary is free to slide. The condition for crack nucleation at 70.5° to a mode-II crack can be readily provided as

$$K_{Ic} = \frac{2}{\sqrt{3}}(\tau_{appl} - \tau_b)\sqrt{\pi a}, \tag{1}$$

where $2a$ is now taken as the grain boundary length which can be approximated as the grain size d, and K_{Ic} is the fracture toughness of ice. The shear stress τ_{appl} required to nucleate cracks can be written from eqn (1) as

$$\tau_{appl} = \tau_b + \sqrt{\frac{3}{2\pi}} K_{Ic} d^{-1/2}. \tag{2}$$

For an applied compressive stress Σ along the principal axis of loading with a confinement ratio R, τ_{appl} can be computed numerically along a grain boundary AB oriented at an angle α with respect to the major axis of loading. For grain boundaries oriented at 45° to the major axis of loading, the nucleation stress Σ_{nucl} becomes

$$\Sigma_{nucl} = \frac{2}{\eta(1-R)}\left[\tau_b(\dot{\varepsilon},T) + A(\dot{\varepsilon},T)d^{-1/2}\right], \tag{3}$$

where

$$A(\dot{\varepsilon},T) = \sqrt{\frac{3}{2\pi}} K_{Ic}(\dot{\varepsilon},T). \tag{4}$$

and η is a constant for a given α and becomes unity for an isotropic material. As shown in Picu and Gupta (1995b), η changes marginally with R and ranges between 0.78 and 0.88 for different possible orientations of the principal anisotropy axes of the plane orthotropic grains, at $\alpha = 45^{\circ}$ and $R = 0$. Equation (3) indicates a Hall-Petch-type dependence of the nucleation stress on the grain size and includes the effect of the strain rate and temperature through the sliding resistance τ_b and the critical stress intensity factor K_{Ic}.

Taking τ_b for the boundary to be 0.18 MPa at -10°C and a strain rate of 10^{-3} s^{-1}, eqn (3) becomes

$$\Sigma_{nucl}[MPa] = \frac{2.5}{1-R}\left(0.18 + 0.76 d^{-1/2}[mm]\right). \qquad (5)$$

In the above, we have taken a fracture toughness value equal to 35 kPa $m^{-1/2}$. The predictions given by eqn (5) are plotted as a curve in Fig. 2 for a grain size equal to 10 mm used in our experiments. Equation (5) describes the experimental data well and gives credence to the boundary sliding mechanism as the source for crack nucleation. Further, for typical grain sizes corresponding to 3 mm and 10 mm, relative shear displacements in the range of 0.2 μm to 0.7 μm were calculated for reaching a K_{Ic} value of 35 kPa $m^{-1/2}$. These displacements are plausible for such large grain sizes.

2. Measurement of Fracture Toughness and Cleavage Strengths in Ice Crystals

We have measured the cleavage strengths of ice crystals along the basal and prismatic planes by adopting a laser spallation experiment, developed recently to measure the tensile strength of thin film interfaces. In this experiment, a laser-produced compression stress pulse is made to propagate normal to the cleavage plane of an ice crystal, which upon reflection into a tensile pulse from the crystal's free surface and leads to the spallation of the planes, given a sufficiently high stress pulse amplitude. Figure 3 shows a schematic of this setup, where the ice crystal is housed in an environmental chamber cooled by a pre-cooled nitrogen gas. Hitherto unreported average cleavage strength values of 1 GPa for the basal planes, and that of 1.3 GPa for the prismatic planes were obtained at -10°C (Gupta and Tian, 1994).

The fracture toughness or work of fracture of ice crystals is another important parameter that provides a measure of the overall mechanical behavior for ice. To measure this designed a double-cantilever-beam geometry apparatus to study the growth of cracks in both single crystals and bicrystals of ice. The cracks were opened by a wedge, the motion of which was carefully controlled by a fine-pitch micrometer screw driven by a DC motor (Fig. 4). The critical crack opening displacement (CCOD) was related to the fracture toughness by a numerical model (Gupta et al. 1992; Chernuschenko, 1995). Following Gupta et al. 1992, where the CCOD were related to fracture toughness via a simple beam bending equation, Chernuschenko (1995) used a numerical model that included anisotropy, and crack tip creep relaxations while relating the CCOD to the fracture toughness. However, the experimental setup was essentially the same as used previously. The new results throw some light on the various inelastic dissipative mechanisms at the crack tip, but the earlier results obtained by Gupta et al. (1992) provide values that are relatively free of such artifacts. Fracture toughness values ranging from 1 to 5 J/m^2 were obtained in our earlier work, whereas the new work reports values anywhere between 3 and 35 J/m^2, which clearly show a rather large influence of creep-related deformations. An attempt was

also made by Chernuschenko (1995) to quantify the magnitude of such inelastic dissipations as a function of strain rate and temperature.

3. *Splitting-floe Model*

The approach of calculating stress singularities at junctions between materials with different elastic properties has also been applied to the question of the size effect in indentation experiments. (Gupta and Picu, 1993 & 1994) The microcracked, triangular-shaped zone underneath the indenter (Fig. 5a) has a lower effective elastic modulus than the uncracked region beyond. At the tip of that zone is a stress singularity, analogous to the singularities discussed above. The load required to nucleate and propagate cracks from the tip of the microcracked zone should scale with indenter size according to the exponent which describes the strength of the singularity. Figure 5b shows the comparison of the model results with the failure pressures obtained in basin experiments.

Analysis and Publication Plan

Most of the papers dealing with crack nucleation in the brittle regime, measurement of cleavage strength and splitting-floe model are in already in press, and listed below. Few ideas are still under development. First, the idea of grain boundary sliding is applied to unravel the intrinsic mechanism for nucleating the column splitting cracks, as observed widely in the biaxial across-column loading of columnar ice at confinement ratios larger than 20%. Under such high confinements, we have confirmed the out-of-plane sliding of the grains, which then provides the necessary local tensile stress pockets for nucleating such cracks. These results are in preparation (Picu et al., 1995).

The fundamental problem of the formation of the terminal shear fault due to the coalescence of several in-plane and grain boundary cracks has also been attempted. This problem is akin to the formation of shear faults in laboratory-scale freshwater and saline ice samples, and also in rocks under both uniaxial and biaxial compression under moderate confinements. The currently used failure models assume the entire volume of the material to be flooded with cracks, contrary to what is observed in the samples where cracking is concentrated on or near a fault plane. Also, there is no evolution of the progressive damage in such models. Our model overcomes this shortcoming, and is based on experimental observations that provide details of the progressive damage process. The damage starts in the form of isolated cracking events, which then tend to cluster at certain locations under an increasing load. The sites for such clusters are essentially defined by the distribution of the weak grain boundaries or those with highly stressed orientations under the given loading. The stresses become concentrated by the increased compliance of the clustered crack region, and leads to increased probability of further cracking in its vicinity. Once the nucleus attains a critical size (at one of the clusters), it spreads laterally under decreasing stress to constitute the overall failure. The failure sites for the first set of cracks are defined by the crack nucleation model already developed under the current program. Next, by using the concept of *stress enhancement factors* sites where the next cracking event is most likely under an increment of further loading is determined. The stress enhancement factor essentially describes the increased probability of fracture by combining the standard stress intensity factor near the existing crack or cluster of cracks with the statistical distribution of the weak grain boundaries or those with highly stressed orientations under the given loading. This then defines the progressive growth of the nucleus or crack cluster at a certain location within the sample. At every increment of the loading, the stability of this cluster itself is checked. Once the failure condition for a given cluster length is satisfied, all lengths larger than the critical should grow much in the same sprit as the growth of a single crack under a critical stress. This work is still in progress, and is taking the shape of two manuscripts (Bergstrom and Gupta, 1995a&b).

Finally we have found that the failure mechanisms in compression experiments done under many pulse increment loadings is largely dependent on the number of increments before the final failure stress, (Bergstrom and Gupta, 1995c). If the failure is achieved in two increments, the damage is quite minimal and mostly along concentrated along a shear band. In contrast, many increments leave a sample flooded with cracks throughout its volume! This occurs due to the local sliding of the grain boundaries even in the brittle regime, as discussed in details earlier. Thus, this observation puts into jeopardy the whole philosophy of compression experiments done under pulse loading, and the mechanisms associated with these as well.

References

Cole, D. M., 1988, "Crack Nucleation in Polycrystalline Ice," Cold Reg. Sci. Tech., Vol. 15, pp. 79-87.

Raj, R., and Ashby, M. F., 1982, "On Grain Boundary Sliding and Diffusional Creep," *Acta Metall.*, Vol. 30, pp. 1113-1127.

Shyam Sunder, S., and Wu, M. S., 1990, "Crack Nucleation Due to Elastic Anisotropy in Polycrystalline Ice," Cold Reg. Sci. Technol., Vol. 18, pp. 29-47.

References and Recent Publications

Journal Publications

Gupta, V. and Tian, X., 1994, "Measurement of Cleavage Strength in Freshwater Ice Crystals by a Laser Spallation Technique", Journal of Offshore Mechanics and Arctic Engineering, **116**, pp. 35-42.

Gupta, V. and R.C. Picu, 1994 "Size Effect in Indentation Experiments," Acta Metallurgica et Materialia, in press.

Picu, R.C., V. Gupta and H.J. Frost, 1994 "Crack Nucleation Mechanism in Saline Ice", Journal of Geophysical Research - Solid Earth, **99**, pp. 11775-11786.

Picu, R.C and Gupta, V., 1994b, "Singularities at Grain Triple Junctions in Two-Dimensional Polycrystals with Cubic and Orthotropic Grains", submitted to Journal of Applied Mechanics.

Picu, R.C. and Gupta, V., 1995a, "Observations of Crack Nucleation in Columnar Ice due to Grain Boundary Sliding", Acta Metallurgica et Materialia, in press.

Picu, R.C. and Gupta, V., 1995b, "Crack Nucleation in Columnar Ice due to Elastic Anisotropy and Grain Boundary Sliding", Acta Metallurgica et Materialia, in press.

Picu, R.C. and Gupta, V., 1995c, "Stress singularities at triple junctions with freely sliding grains," submitted to International Journal of Solids and Structures.

Journal Papers in Preparation

Picu, C. R., Bergstrom, J. and Gupta, V., 1995, "Nucleation of splitting cracks in columnar ice."

Bergstrom, J. and Gupta, V., 1995a, "A progressive damage model for shear faulting in brittle solids under compression loading I. Applications to rocks."

Bergstrom, J. and Gupta, V., 1995b, "A progressive damage model for shear faulting in brittle solids under compression loading I. Applications to columnar freshwater ice with experimental evidence."

Bergstrom, J. and Gupta, V., 1995c, "Comments on cracking in freshwater ice subjected to many load increments."

Chernuschenko, M. A. and Frost, H. J., 1995, "Fracture toughness measurements in ice single crystals in double-cantilever beam geometry with the wedge-loaded crack."

Conference Papers

Picu, R.C. and V. Gupta, 1994a, "Crack nucleation in polycrystalline columnar ice due to anisotropic grains," Proc. IAHR Ice Symposium, Trondheim, Norway.

Frost, H.J. and Gupta, V., 1993, "Crack Nucleation Mechanisms and Fracture Toughness Measurements in Freshwater Ice", in *Ice Mechanics - 1993* -, edited by J.P. Dempsey, Z.P. Bazant, Y.D.S. Rajapakse, and S. Shyam Sunder, Proceedings of the Ice Mechanics Symposium, First Joint ASCE-EMD, ASME-AMD SES Meeting, June 6-9, 1993, Charlottesville, Virginia, pp. 235-250

Gupta, V. and Picu, R.C., 1993, "Size-Effect in Indentation-Induced Splitting Floe Experiments", *Proceedings of the Offshore Mechanics and Arctic Engineering Conference*, Glasgow Scotland, June 20-24, 1993, Vol. 4, pp. 29-34.

Gupta, V., Ruhl, J., Kuehn, G. and Martinez, D., 1992, "Preliminary Investigations of the Measurement of Fracture Toughness on Freshwater Ice Crystals and in Bi-crystals", *IAHR 92 Proceedings of the 11th International Symposium on Ice* held at Banff, Alberta, June 15-19, Vol. 3, pp. 1408-1419

Thesis

Chernuschenko, M. A., 1995, "Fracture toughness measurements in ice single crystals in double-cantilever beam geometry with the wedge-loaded crack." MS Thesis, Thayer School of Engineering, Dartmouth College, Hanover, New Hampshire, USA, February, 1995.

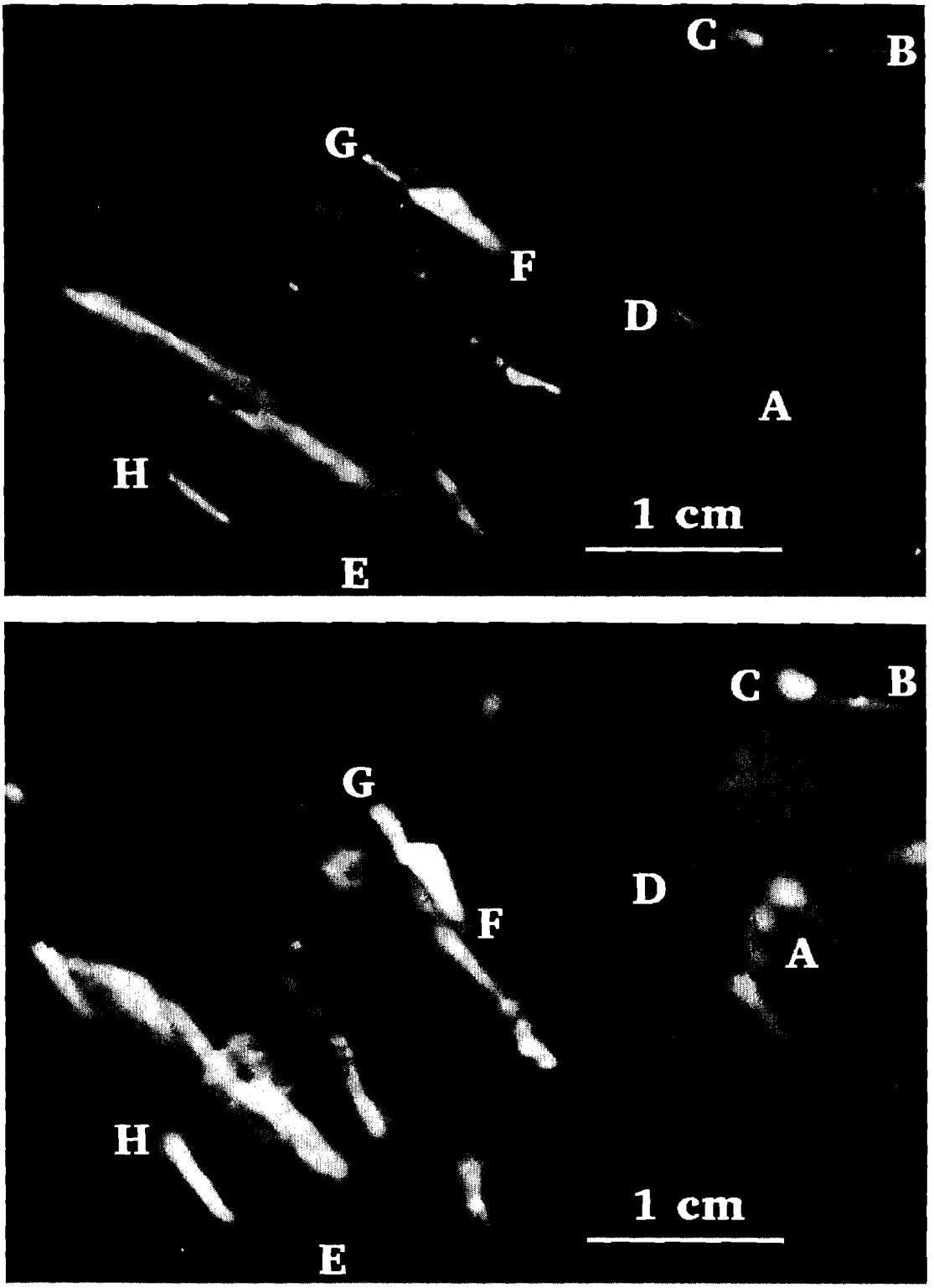

Figure 1

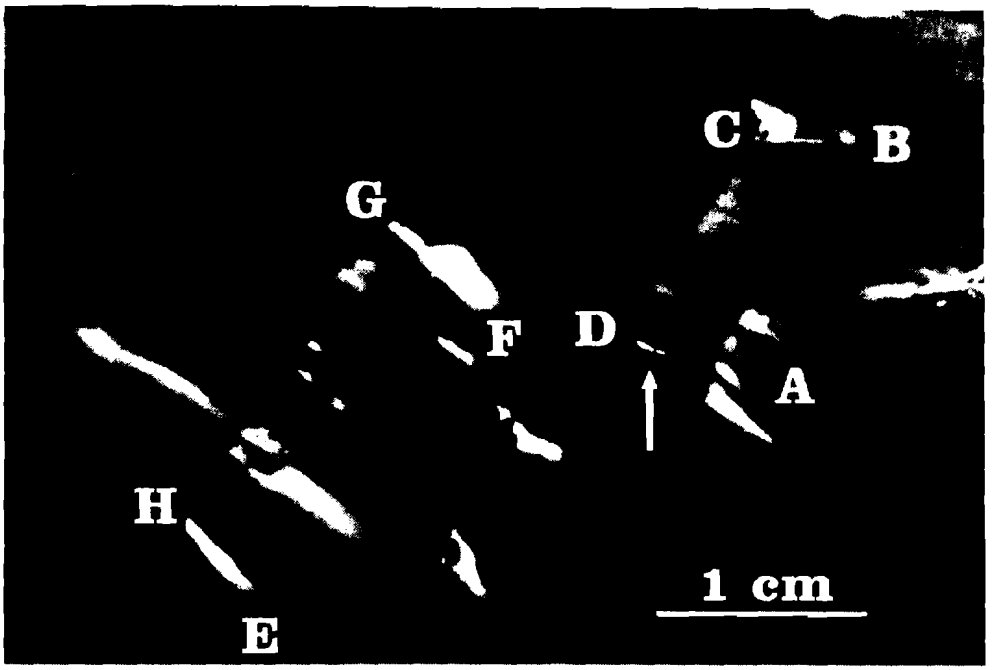

c

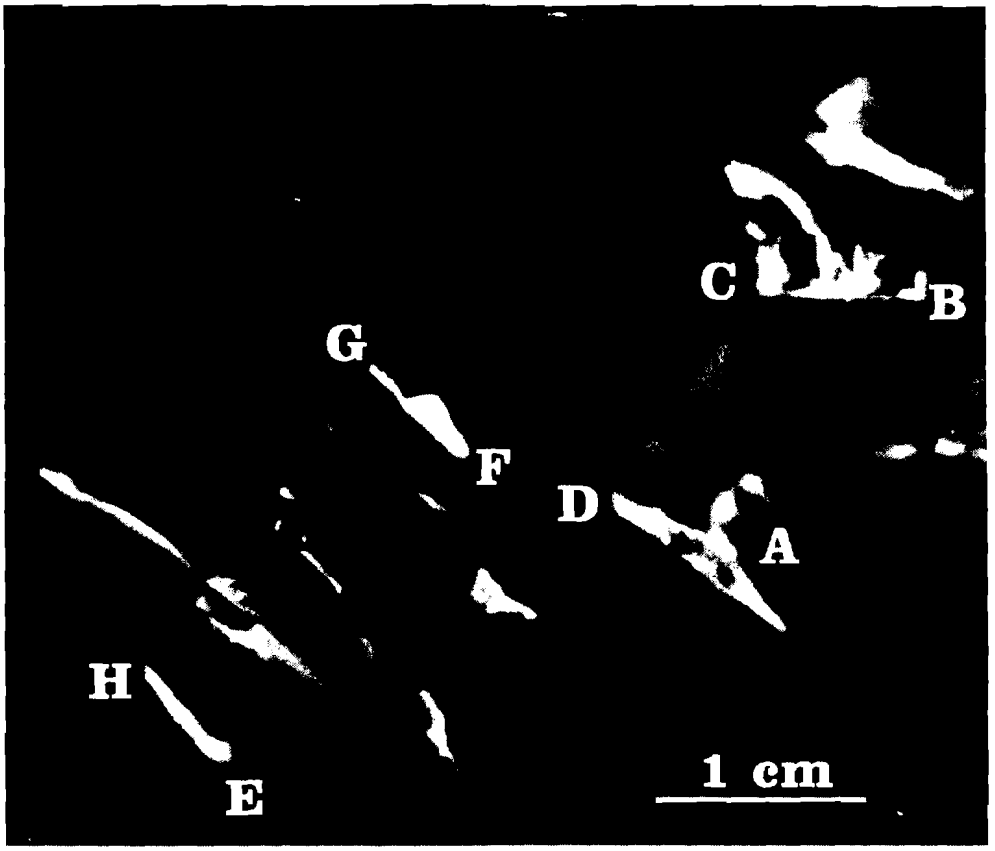

d

Figure 1

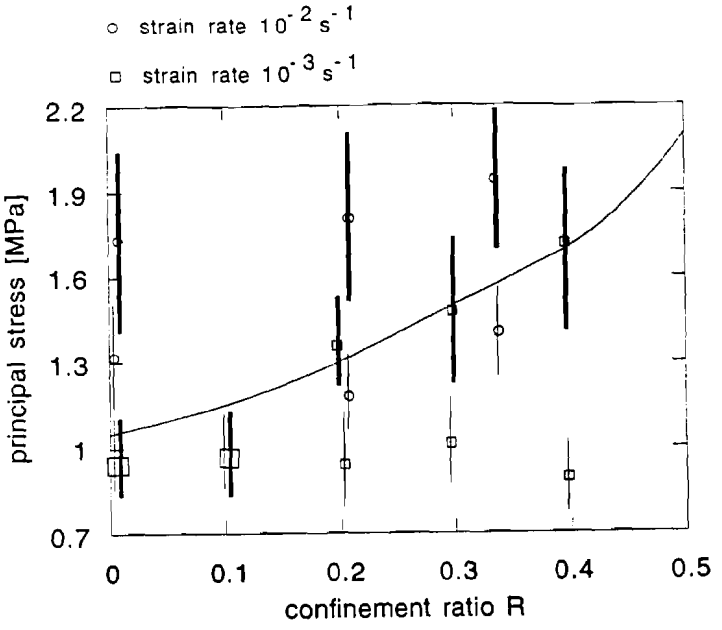

Figure 2

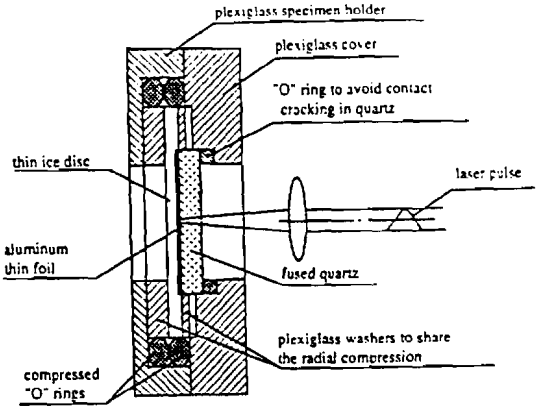

Figure 3

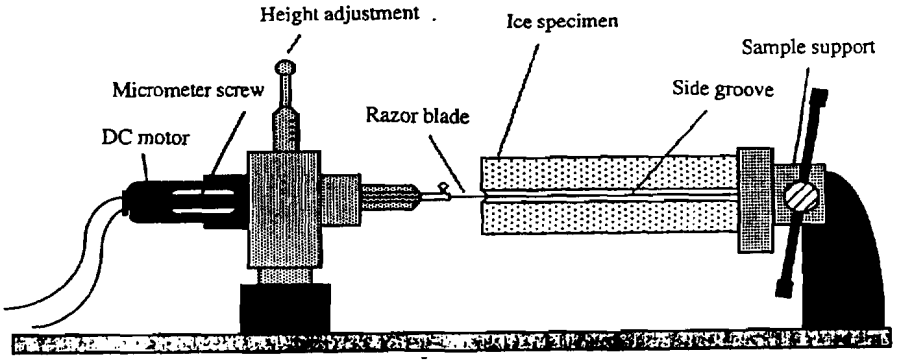

Figure 4

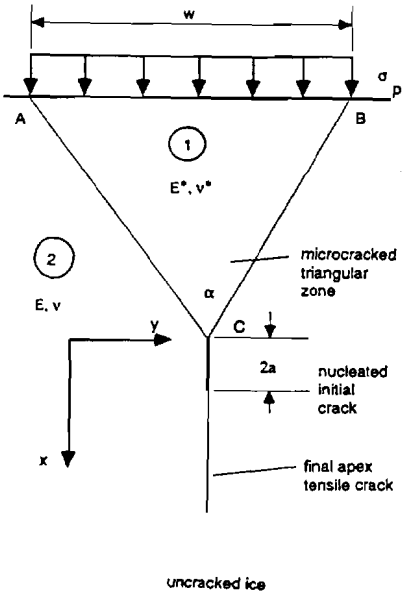

Figure 5a

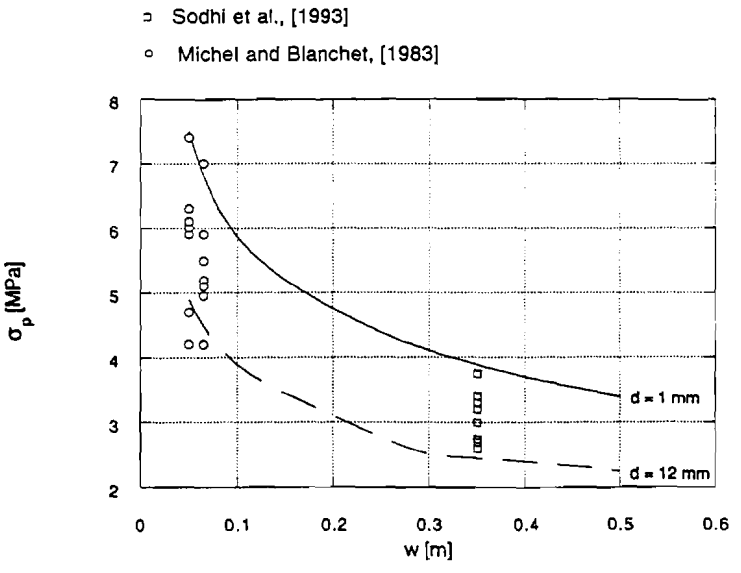

Figure 5b

Compressive Failure of Columnar Saline Ice under Multiaxial Loading

Erland M. Schulson (P.I.), Thayer School of Engineering, Dartmouth College, Hanover, New Hampshire 03755

Scope of Experiments

Sheets of undeformed first-year Arctic ice are generally comprised of columnar-shaped grains whose long axes are oriented in the vertical plane and whose crystallographic c-axes are confined within a few degrees to the horizontal plane. In some locations the c-axes are aligned (Cherepanov 1971, Weeks and Gow 1980), whereas in others they are random within the plane of the sheet. In both cases the sheet is expected to exhibit anisotropic mechanical behavior. Failure under multiaxial loading is thus expected to depend upon the loading path.

This work addresses the compressive failure of unaligned or S2 columnar saline ice deformed under biaxial loading. The major stress (σ_{11}) was applied across the columns and the minor stress was applied proportionally either across the columns (σ_{22}) or along the columns (σ_{33}), Figure 1. The temperature was varied from -40 to -5°C and the strain rate ($\dot{\varepsilon}_{11}$), from 10^{-6} to 10^{-1} s^{-1}. The objectives were to establish the compressive failure envelopes for both ductile (low strain rate) and brittle (high strain rate) failure and to elucidate the underlying failure mechanisms.

The experiments were performed in the Ice Research Laboratory (IRL) at Dartmouth College. The ice was grown under simulated natural conditions; its characteristics, Table 1, were similar to those of first-year sea ice. Both plates (159 x 159 x 38 mm) and cubes (159 mm) were tested. Loading was applied at constant strain rate ($\dot{\varepsilon}_{11}$) using IRL's true multiaxial testing system (MATS). MATS is a six-actuator, servohydraulic device situated in its own cold-room controlled to within 0.2°C. Data were recorded using an IBM AT.

Table 1: Ice Characteristics

Grain Size	6 ± 2mm
Pore Dia.	0.1 - 0.3 mm
Platelet spacings	0.5 - 1mm
Porosity	4 - 5%
Salinity	4.3 ± 0.7 ppt

Findings to Date

Brittle-Ductile Transition-- Two kinds of behavior were observed. At high strain rates the ice is macroscopically brittle and collapses after shortening less than about 0.4 % along the direction of the higher load. At low strain rates the material is macroscopically ductile and does not collapse after shortening by about 3 %, at which point the tests were manually terminated. Figure 2 defines the two regimes for the case of across-column loading at -10°C. Note that the transition strain rate $\dot{\varepsilon}_{11,t}$ although difficult to specify to

better than a factor of two or so, first increases and then decreases with increasing confining stress.

The transition strain rate decreases by about an order of magnitude upon decreasing the temperature from -10 to -40°C.

Compressive Strength Versus Along-Column Confining Stress-- Within the scatter in the data, the compressive failure strength in both the brittle and the ductile regimes is not significantly affected by the along-column confining stress, Figure 3.

Compressive Strength Versus Across-Column Confining Stress-- Confinement across the columns has a large effect on both the brittle and the ductile strength. Figure 4 illustrates this point through a series of failure envelopes. (A more expanded view of the envelopes with all the data has been submitted for publication.)

Consider brittle behavior, denoted by a B (Fig. 4). Although scattered, the brittle strength first increases and then decreases with increasing confining stress. The increase and the decrease, respectively, may be described by the relationships:

$$\sigma_{11,f}^{(b)} = \sigma_{u,1}^{(b)} + k_1 \sigma_{22} \qquad (1)$$

and

$$\sigma_{11,f}^{(b)} = k_2 - \sigma_{22} \qquad (2)$$

where $\sigma_{u,1}^{(b)}$ is the uniaxial across-column brittle compressive strength and k_1 and k_2 are constants, Table 2. Under lower confinement, the strength increases with increasing hydrostatic stress, as seen by rotating the envelopes 45° clock-wise. Friction within the ice is thus important here, and so the envelopes can then be viewed as truncated Coulombic envelopes. Failure occurs by splitting along the loading direction under zero confinement, by macroscopic shear faulting in the loading plane under lower confinement where strengthening occurs, and by spalling out of the loading plane under higher confinement where weakening occurs, Figure 5.

Table 2: Values for the constants in equations (1) and (2)

T (°C)	$\sigma_{u,1}^{(b)}$ (MPa)	k_1	k_2 (MPa)
-10	3.5	3.1	16
-40	6.5	4.8	16

Next consider ductile behavior, denoted D (Fig.4). Again the data are scattered, although less so under lower confinement. Unlike the brittle strength, the ductile compressive strength increases over the whole range of across-column confining stress. The failure envelope is semi-elliptical in shape and expands with increasing strain rate and with decreasing temperature. The envelopes shown were drawn not by connecting the points, but by applying Hill's (1950) criterion for the yielding of plastically orthotropic materials; namely:

$$\sigma_{11}^{\ 2} + \sigma_{22}^{\ 2} - \sigma_{11}\sigma_{22}\left(2 - \left(\frac{\sigma_{u,1}^{(d)}}{\sigma_{u,3}^{(d)}}\right)^2\right) = \left(\sigma_{u,1}^{(d)}\right)^2 \qquad (3)$$

where $\sigma_{u,1}^{(d)}$ and $\sigma_{u,3}^{(d)}$, respectively, are the across-column and the along-column uniaxial compressive strengths measured under the appropriate conditions. That the data seem to conform to Hill's criterion implies that the hydrostatic component of the stress state does not significantly affect ductile compressive failure. It implies also that the biaxial strength under lower and under higher confining stress, respectively, is governed by the across-column and by the along-column uniaxial strength. The conformity to Hill's criterion implies further that the rate and the thermal sensitivities of the lower and the higher confinement strengths are set by the sensitivities of the uniaxial strengths. The last point has been established through separate analysis.

Strain Vector Normality and the Ductile Failure Surface-- Insight into the full 3-D ductile failure surface can be obtained from the inelastic normal strains ($d\varepsilon_{11}$, $d\varepsilon_{22}$ and $d\varepsilon_{33}$) and from the concept of strain vector normality. The concept assumes that inelastic deformation is non-dilatant and that the "strain vector" is everywhere perpendicular to the failure surface which itself is everywhere convex around the origin. The inelastic deformation of ice is not strictly non-dilatant, because the material cracks internally, even when macroscopically ductile. Nevertheless, the approach shows that the projections of the measured inelastic strain components onto the X_1-X_2 plane are more or less in accord with the idea. Figure 6 shows one example to illustrate this point. Analysis along this line is in progress. At this juncture suffice it to note that the ratios of inelastic strains predicted from the associated flow rule for plastically orthotropic material are given by the relationships:

$$\frac{d\varepsilon_{33}^{p}}{d\varepsilon_{11}^{p}} = \frac{2R_{31} - 1}{2\left(\sigma_{u,3}^{(d)} / \sigma_{u,1}^{(d)}\right)^2 - R_{31}} \qquad (4)$$

and

$$\frac{d\varepsilon_{22}^{p}}{d\varepsilon_{11}^{p}} = \frac{2\left(\frac{\sigma_{u,3}^{(d)}}{\sigma_{u,1}^{(d)}}\right)^2 (R_{21} - 1) + 1}{2\frac{\sigma_{u,3}^{(d)\,2}}{\sigma_{u,1}^{(d)}}(1 - R_{21}) + R_{21}} \qquad (5)$$

where R_{31} and R_{21} are the ratios of the minor to major stresses along and across the columns, respectively. Figure 7 shows that the values predicted from these relationships are in reasonable agreement with the measurements made in these experiments.

Analysis and Discussion

Brittle-Ductile Transition-- The transition is important because it marks the point where the compressive strength of the ice reaches its maximum value.

A phenomenological interpretation is that the transition occurs when the ductile failure strength equals the brittle strength. As Figure 8 shows schematically, the ductile strength increases with increasing rate, but the brittle strength is relatively rate independent. A small confining stress raises both strengths, but raises the brittle strength more, and so

the transition strain rate increases. A large confining stress raises the ductile strength further, but lowers the brittle strength. The transition strain rate thus decreases once the confining stress reaches a critical level, R_{21c}. By incorporating the appropriate dependencies of the two strengths on strain rate and on across-column confining stress, it can be shown that under low confinement ($R_{21}<R_{21c}$)

$$\dot{\varepsilon}_{11,t} = \frac{B\sigma_{u,1}^{(b)^n}\left(1+R_{21}{}^2-2R_{21}+C^2R_{21}\right)^{n/2}}{\left(1-k_1R_{21}\right)^n}\ ; \qquad (6)$$

under high confinement ($R_{21}>R_{21c}$)

$$\dot{\varepsilon}_{11,t} = \frac{Bk_2^n\left(1+R_{21}{}^2-2R_{21}+C^2R_{21}\right)^{n/2}}{\left(1+k_1R_{21}\right)^n}\ . \qquad (7)$$

B and n are constants (derived from the present experiments) that relate the failure strength to the strain rate, C is the ratio of the across-column to the along-column uniaxial ductile compressive strength, and the other parameters have the meaning given above. Figure 9 compares the transitions rates calculated from equations (6) and (7), using the parametric values in Table 3, with those observed in the experiments.

Table 3: Parametric values at -10°C used to compute $\dot{\varepsilon}_{11,t}$ from equations (6) and (7).

Parameter	Value	Reference
$\sigma_{u,1}^{(b)}$	3.5 MPa	Smith and Schulson (1994)
k_1	3.1	Smith and Schulson (1994)
k_2	16 MPa	Smith and Schulson (1994)
n	3.2	present work
B	$1.9\cdot10^{-5}$ $MPa^{-3.2}s^{-1}$	present work
C	0.3	present work

A physical interpretation is that the transition from brittle to ductile behavior occurs when crack growth is suppressed owing to crack tip creep. It is imagined that during deformation a competition develops between the building up and the relaxation of tensile stresses at crack tips. When the deformation becomes slow enough the competition tilts in favor of stress relaxation. Assuming that frictional crack sliding and wing cracking are important elements in brittle compressive failure, it can be argued that the confining stress impedes sliding by both raising the stress normal to the sliding plane and lowering the effective shear stress in the sliding plane. The result is that the confining stress lowers the mode-I stress intensity factor associated with the wing cracks and so lowers the rate of stress build-up at the crack tip. Confined across the columns thus raises the transition strain rate. It can then be shown that under low confinement ($R_{21}<R_{21c}$)

$$\dot{\varepsilon}_{11,t} = \frac{1.2B'K_{IC}^{\ 3}}{fd^{1.5}\left\{\left(1+\mu^2\right)^{0.5} - \mu - R_{21}\left[\mu + \left(1+\mu^2\right)^{0.5}\right]\right\}} \qquad (8)$$

and under high confinement ($R_{21}>R_{21c}$)

$$\dot{\varepsilon}_{11,t} = \frac{0.3B'K_{IC}^{\ 3}}{fd^{1.5}Sin\psi[Cos\psi - \mu Sin\psi]} \qquad (9)$$

where B' is the creep constant in the power law creep expression, K_{Ic} is the fracture toughness, μ is the kinetic coefficient of friction, d is the sliding crack size (set by the microstructural size), f is the ratio of the size of the crack tip creep zone to the size of the parent sliding crack when creep blunting first suppresses crack growth, and ψ is the angle between σ_{11} and the sliding plane under high confinement; $R_{21C} = (1-\mu)/(1+\mu)$. Figure 9 compares the transition strain rate obtained using equations (8) and (9) with those observed, using the parametric values listed in Table 4.

Table 4: Parametric values at -10°C for equations (8) and (9).

Parameter	Value	Reference
B'	$5.1 \cdot 10^{-6}$ MPa^{-3} s^{-1}	Sanderson (1988)
K_{IC}	0.1 MPa·m$^{1/2}$	Dempsey (1991)
μ	0.5	Jones et al. (1991)
d	$6 \cdot 10^{-3}$ m	present work
f	0.015	Batto and Schulson (1993)
ψ	15°	present work

To a first approximation it appears that both the phenomenological and the physical descriptions capture the order of magnitude of the transition strain rate as well as the effect of the across-column confining stress.

Failure Strength-- Brittle compressive failure is a complicated process that involves the nucleation, growth and interaction of internal cracks. While many details remain to be determined, what seems to happen is something like the following, Figure 10: Within virgin material cracks nucleate early in the deformation history and continue to nucleate as the stress rises, thereby producing a field of cracks. Within the field some cracks are suitably inclined for sliding on planes parallel to the long axes of the columnar grains under low degrees of across-column confinement. In so doing, they develop out-of-plane extensions or wings along σ_{11}. The wings help to link up the cracks and thus help to generate the macroscopic fault that eventually causes the ice to collapse. An increase in the across-column confiniment impedes the sliding, thereby changing the failure mode from splitting to shear faulting. When high enough, the confinement suppresses in-plane

sliding altogether, changing the failure mode from shear faulting to cracking/spalling across the columns.

Which step in the process governs the failure stress is not clear. If it is assumed that frictional sliding is important right up to the point of collapse, then the dependence of the brittle failure stress on the confining stress can be accounted for within the context of wing crack mechanics. Accordingly, it can be shown that for $R_{21}<R_{21c}$

$$\sigma_{11,f}^{(b)} = \frac{\sigma_{u,1}^{(b)}(1-\mu)}{(1-R_{21})(1-\mu)-2R_{21}\mu} \qquad (10)$$

That this result is reasonable can be seen upon comparing equation (10) with (1) and noting that at -10°C the calculated phenomenological constant $k_1=(1+\mu)/(1-\mu)= R_{21c}^{-1}=(1+0.5)/(1-0.5)=3.0$ vs the measured value (Table 2) of 3.1. For $R_{21}>R_{21c}$ a Hertzian kind of mechanism can explain the reduction in the failure strength with increasing confining stress, but the mechanism is questionable because the extent of the contact stresses (across the surface of cracked grain boundaries) is probably too small to drive crack growth. More work is needed to clarify the failure process in the high-confinement regime.

The ductile failure strength appears to be governed by a combination of crystallographic slip and microstructural restorative processes such as dynamic recrystallization. Considerable evidence for the latter process has been obtained during the course of this study.

Relevance to the Failure of an Ice Sheet

While the observations reported here were made in the laboratory on small pieces of ice without a thermal gradient, it is interesting to consider whether the failure modes reflect in some way the failure of a floating ice sheet. For instance, could some leads be the geophysical equivalent of the in-loading-plane shear faults? Could some pressure ridges in thick ice be the geophysical equivalent of the out-of-loading-plane spalling? In other words, is there in the field as there is in the laboratory a transition from in-plane to out-of-plane brittle compressive failure as the degree of across-column confining stress increases beyond a critical level? If there is, and if the frictional sliding mechanism operates, then one could account for the in-field failure stresses being lower than the failure stresses measured in the laboratory (100 to 400 kPa, Tucker and Perovich 1992, vs. 3 to 10 MPa). The sliding mechanism dictates that the failure stress scales as (sliding crack length)$^{-1/2}$. This implies that cracks need only be as long as a few meters to account for the difference in strength;

i.e. field strength = (ratio of lab crack to field crack length)$^{1/2}$ x (lab strength)
$=(6\times10^{-3}\text{m}/3\text{m})^{1/2}$ x (3 to 10 MPa)
= 0.1 to 0.4 MPa.

Cracks as long as a few meters could be developed by the linking up of shorter cracks that formed during the early stages of deformation. That the global strain rate of an ice sheet may be only around 1 %/day (10^{-7} s^{-1}) does not mean that macroscopically brittle behavior will not be seen in the field, for the ductile-brittle transition strain rate as modelled on the sliding crack basis scales as (sliding crack length)$^{-3/2}$. This implies again that sliding cracks need only be as long as a few meters to impart brittle failure.

References:

Batto, R.A. and E.M. Schulson, On the ductile-to-brittle transition in ice under compression, *Acta Metallurgica et Materialia.*, 41, pp. 2219-2225, 1993.

Cherepanov, N.V., Spatial arrangement of sea ice crystal structure, *Prob. Arkt. i Antarkt.*, 38, pp. 176-181, 1971.

Dempsey, J.P., "Ice-Structure Interactions," ed. by S. J. Jones, R. F. Mckenn, J. Tillotson and I. J. Jordaan, 109, Springer, Berlin (1991).

Hill, R., *The Mathematical Theory of Plasticity*, Oxford U. P., New York (1950).

Jones, D.E., F.E. Kennedy, and E.M. Schulson, The kinetic friction of saline ice against itself at low sliding velocities, *Annals of Glaciology*, 15, pp. 242-246, 1991.

Sanderson, T.J.O., *Ice Mechanics Risks to Offshore Structures*, p. 82, Graham and Trotman, London, Dordrecht, Boston, 1988.

Smith, T.R. and E.M. Schulson, Brittle compressive failure of salt-water columnar ice under biaxial loading, *J. Glaciology*, 40(135), pp. 265-276, 1994.

Tucker, W.B. III and Perovich, D.K., Stress measurements in drifting pack ice, *Cold Regions Science and Technology*, 20, pp. 119-139, 1992.

Weeks, W. F. and A.J. Gow, Crystal alignments in the fast ice of Arctic Alaska, *J. Geophys. Res.* 84, pp. 1137-1146, 1980.

Publications from this work

Journal Articles

"The Fracture of Ice on Scales Large and Small: Arctic Leads and Wing Cracks," E.M. Schulson and W.D. Hibler, III, J. Glac., 37 (1991), 319-322

"Effect of Confining Stress on the Brittle Indentation Failure of Columnar Ice," J. Grape and E.M. Schulson, J. ISOPE, 2 (1992), 212-221

"The Brittle Compressive Failure of Fresh-Water Columnar Ice Under Biaxial Loading," T.R. Smith and E.M. Schulson, Acta Met. et Mater., 41 (1993), 153-163

"Ductile Ice", E.M.Schulson and G.A.Kuehn, Phil. Mag. Lett., 67 (1993), 151-157

"The Compressive Strength of Ice Cubes of Different Sizes", G.A.Kuehn, E.M.Schulson, D.E.Jones and J.Zhang, J.Offshore Mech. and Arctic Eng. (ASME),12 (1993), 142-148

"On the Ductile to Brittle Transition in Ice under Compression", R.A.Batto and E.M.Schulson, Acta Met. et Mater. , 41 (1993), 2219-2225

"The Cracking of Ice During Rapid Unloading", M.L.Couture and E.M.Schulson, Phil. Mag. Lett., 69 (1994), 9-14

"The Brittle Compressive Failure of Columnar Salt-Water Ice Under Biaxial Loading", T.R.Smith and E.M.Schulson, J. Glaciology , 40 (1994) 265-276

"The Mechanical Properties of Saline Ice Under Uniaxial Compression", G.A.Kuehn and E.M.Schulson, Annals of Glaciology, 19 (1994) 39-48

"Preliminary Observations of the Brittle Compressive Failure of Columnar Saline Ice Under Triaxial Loading", E.T.Gratz and E.M.Schulson, Annals of Glaciology, 19 (1994) 33-38

"Ductile Saline Ice", G.A. Kuehn and E.M.Schulson, J. Glaciology, 40, (1994) 566-568

"The Failure of Fresh-Water Granular Ice Under Multiaxial Compressive Loading", J. Weiss and E.M. Schulson, Acta Metall. et Mater. (in press)

"The Brittle-to-Ductile Transition and Ductile Failure Envelopes of Orthotropic Ice Under Biaxial Compression", E.M. Schulson and S.E. Buck, Acta Metall. et Mater. (in press)

"The Failure of Columnar Saline Ice Under Biaxial Compression: Failure Envelopes and the Brittle-to-Ductile Transition", E. M. Schulson and O.Y. Nickolayev, (in preparation)

Conference Proceedings

"The Ductile to Brittle Transition in Ice: Size Effects," E.M. Schulson and J. Zhang, Proc. 6th Inter. Special Conf. on Cold Reg. Eng., Hanover, N.H., ed. by D.S. Sodhi, ASCE, N.Y. (1991), 554-568

"The Brittle Compressive Failure of Freshwater Columnar Ice Under Biaxial Loading," T.R. Smith and E.M. Schulson, Proc. 10th Internat. Conf. OMAE Stavanger, Norway, ed. by O.A. Ayorinde et al., ASME, N.Y. 4 (1991), 207-214

"The Compressive Strength of Ice Cubes of Different Sizes," G.A. Kuehn, E.M. Schulson, D.E. Jones and J. Zhang, Proc. 11th OMAE, Calgary, (1992), 349-356

"The Brittle Compressive Failure of Columnar Ice Under Biaxial Loading," E.M. Schulson and T.R. Smith, Proc. IAHR '92, Banff, (1992), 1047-1064

"A Preliminary Investigation of the Ductile-Brittle Transition in Columnar S2 Ice under Compression," R. Batto and E.M. Schulson, Proc. IAHR '92, Banff, (1992), 1021-1034

"Failure Envelopes and the Ductile to Brittle Transition in Columnar Saline Ice Under Biaxial Loading", O.Y. Nickolayev and E.M. Schulson, Proc. of First Joint ASCE-EMD, ASME-AMD, SES Meeting, Ice Mechanics, Virginia, 6-9 June 1993, 61-70

"Ductile to Brittle Transition in Ice Under Compression: Grain Size Effect", R.A. Batto and E.M. Schulson, Proc. of First Joint ASCE-EMD, ASME-AMD, SES Meeting, Ice Mechanics, Virginia, 6-9 June 1993, 229-234

"Failure Envelopes and the Ductile-Brittle Transition in S2 Columnar Freshwater and Saline Ice Under Biaxial Loading", S.E. Buck, O.Y. Nickolayev and E.M. Schulson, Proc. IAHR Symp. on Ice Mechanics, Trondheim, 1 (1994) 454-463

"The Failure of Fresh-Water Granular Ice Under Multiaxial Compressive Loading", J. Weiss and E.M. Schulson, Proc. IAHR Symp. on Ice Mechanics, Trondheim, 1 (1994) 495-504

"A Failure Surface for the Brittle Compressure Failure of Orthotropic (Columnar) Saline Ice Under Triaxial Loading", E.T. Katz and E.M. Schulson (in preparation for ASME Ice Mechanics '95)

"Ductile Deformation of Columnar Saline Ice Under Triaxial Compressive Loading", J. Melton and E.M. Schulson (in preparation for OMAE '95)

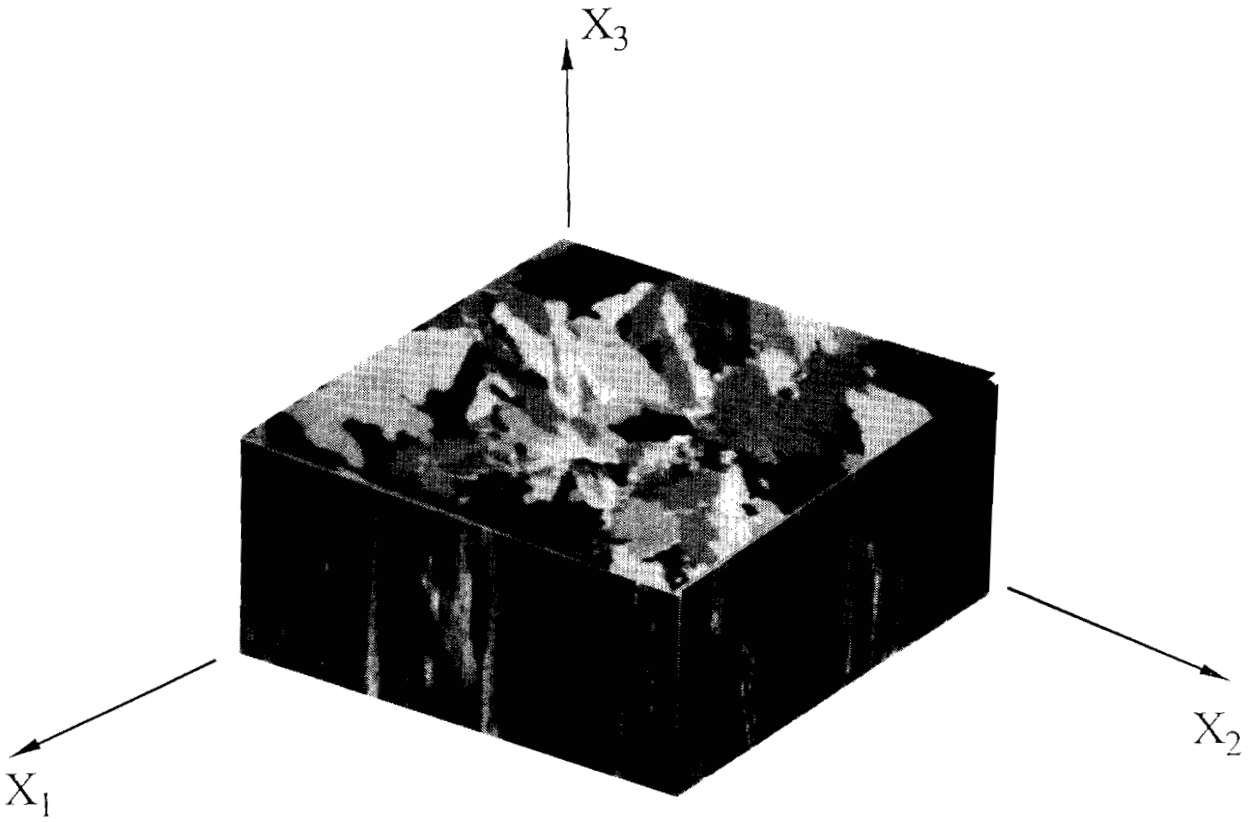

Figure 1: Columnar saline ice

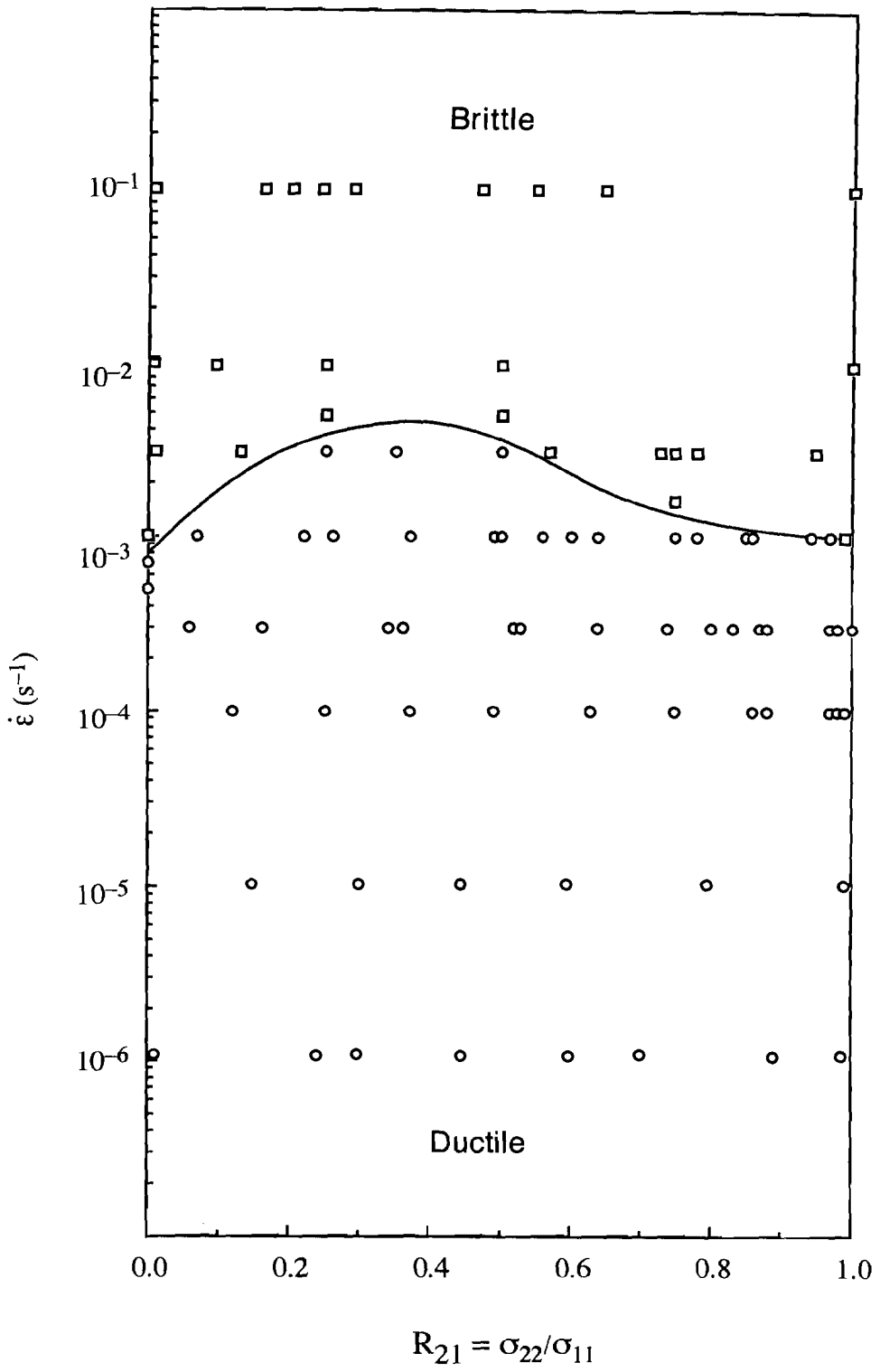

Figure 2: Ductile/brittle transition under across-column confinement

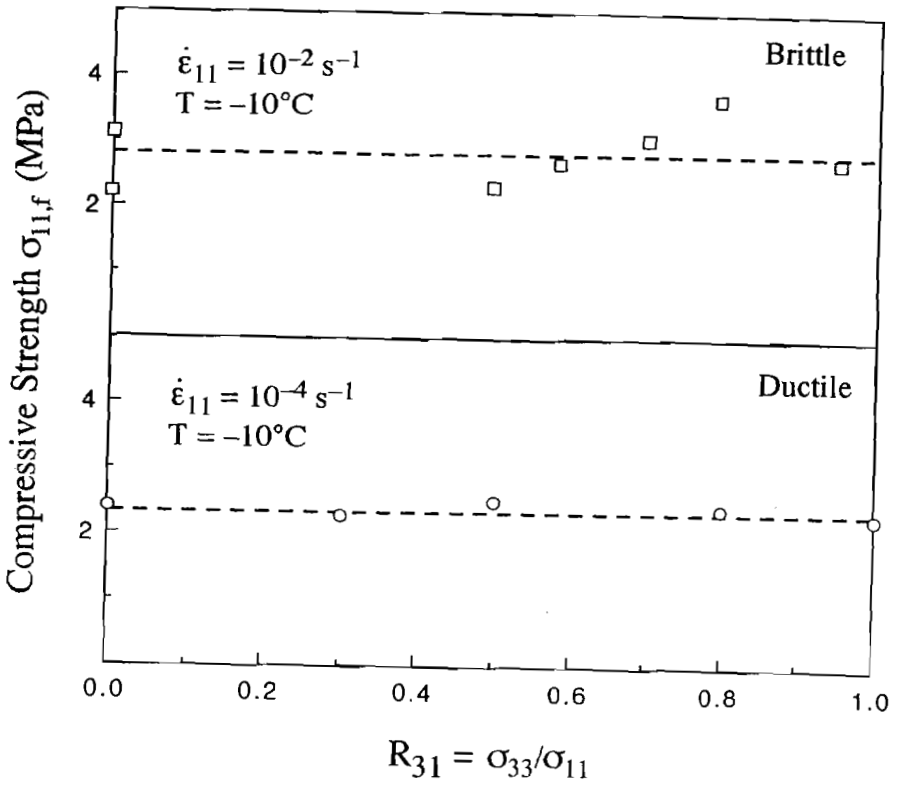

Figure 3: Compressive strength under along-column confining stress

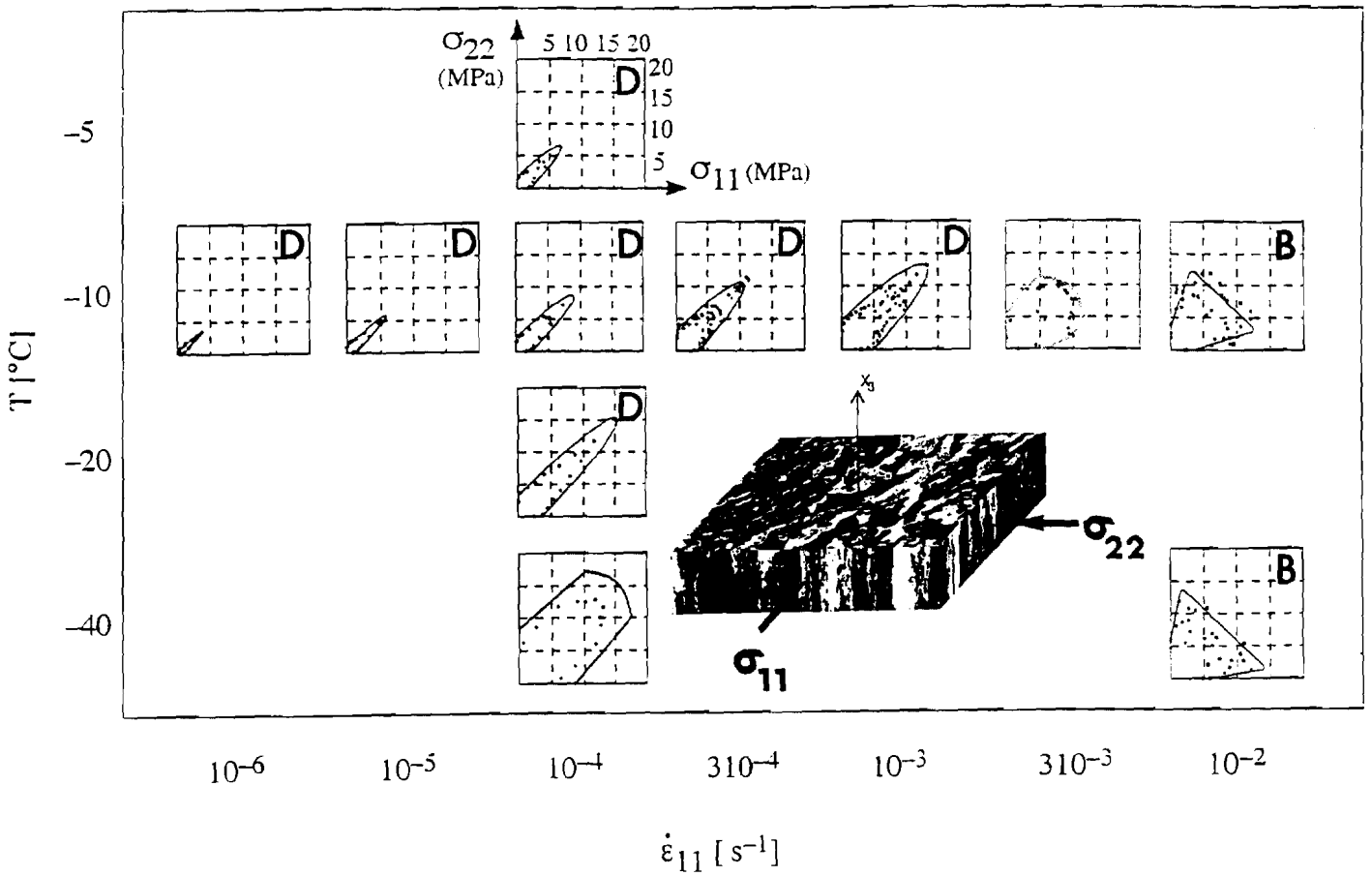

Figure 4: Compressive failure envelopes (D = ductile; B = brittle)

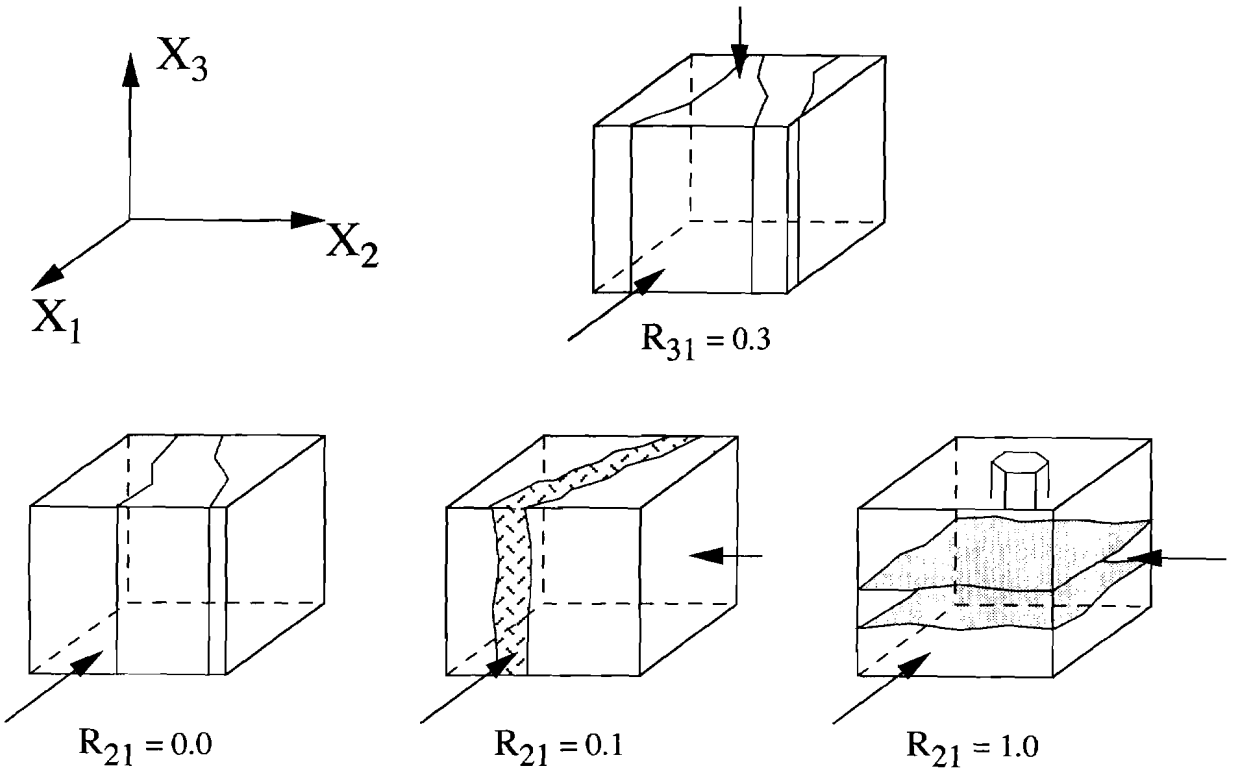

Figure 5: Schematic sketch of failure modes.

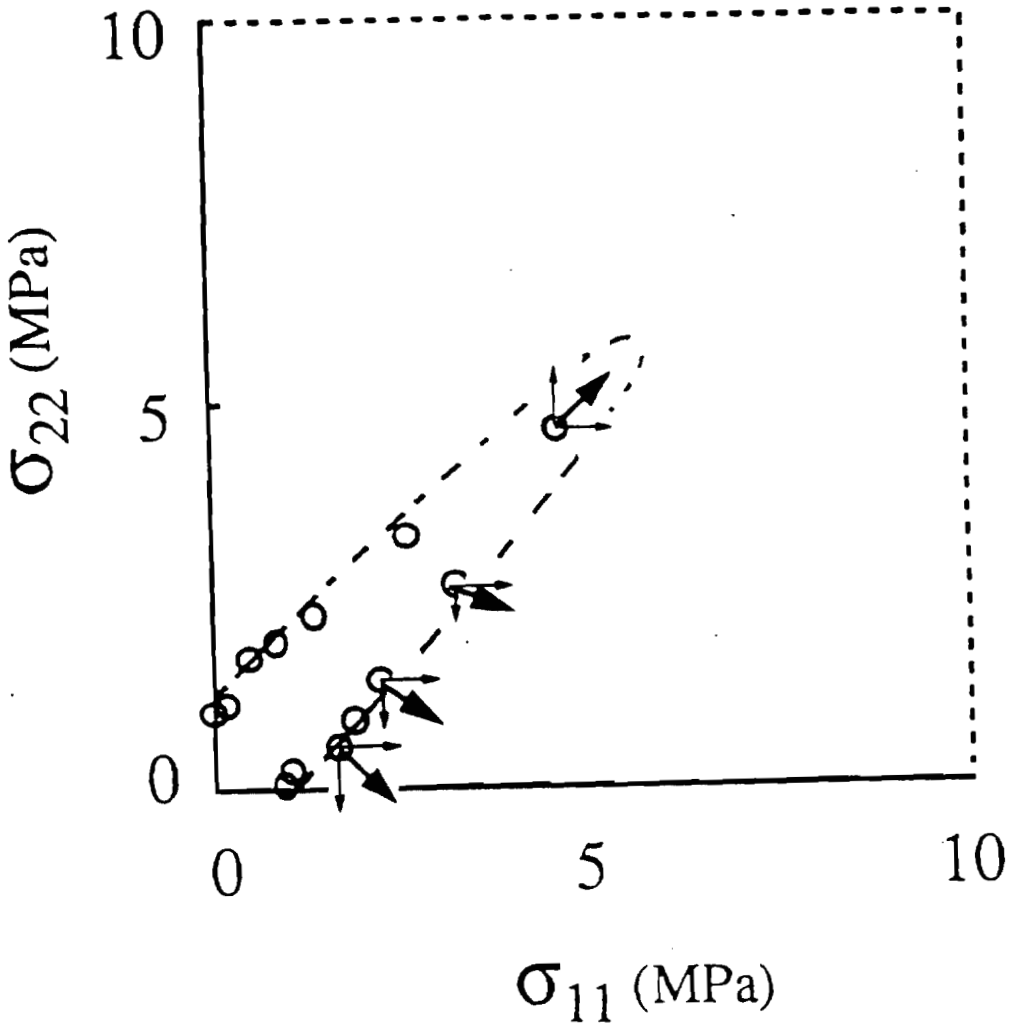

Figure 6: Inelastic strain components and strain vector projected onto X_1 - X_2 plane (-10°C; 10^{-5} s^{-1})

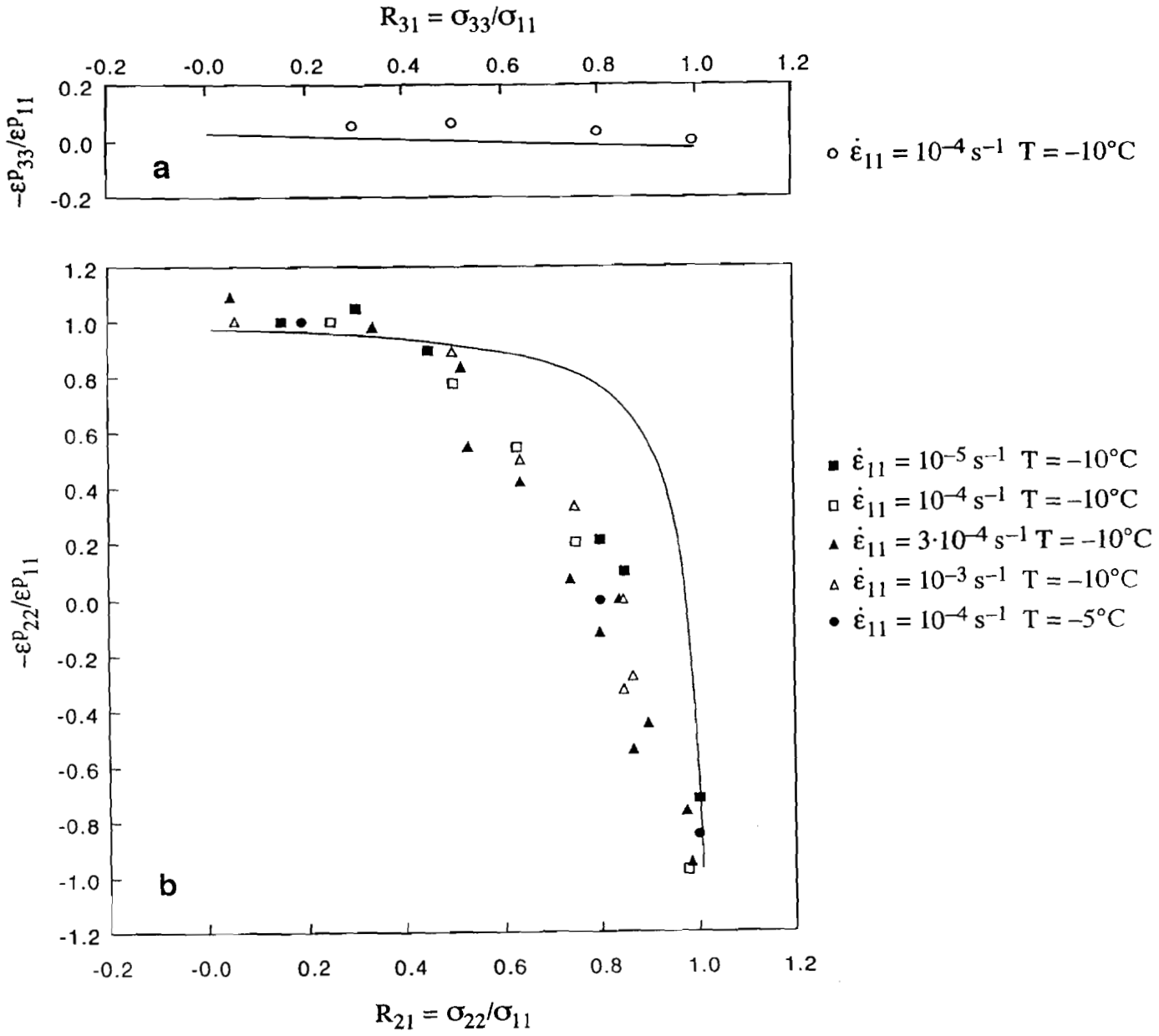

Figure 7: Measured vs. calculated (curve) inelastic strain ratios.

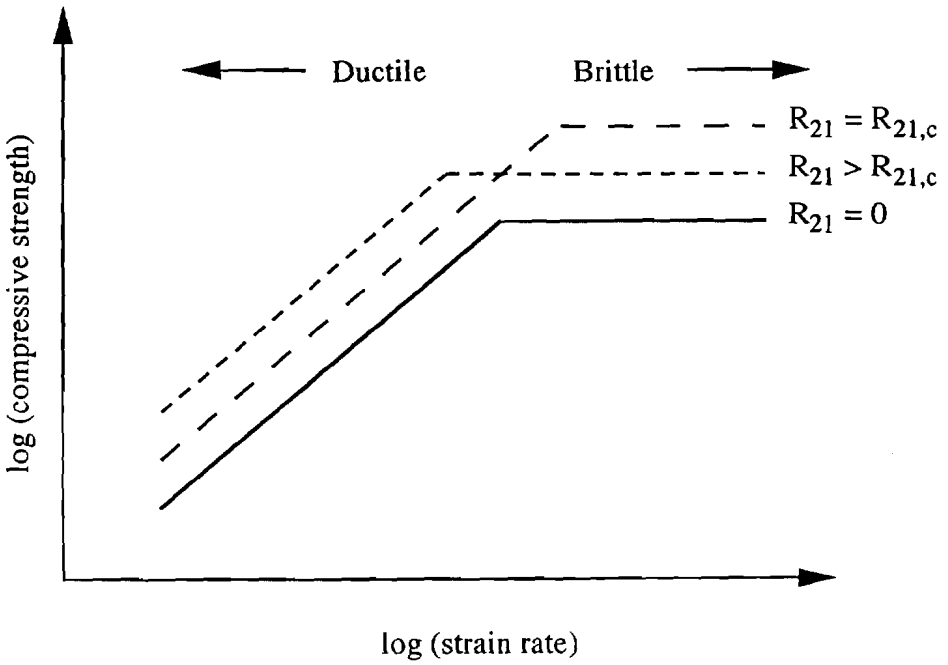

Figure 8: Schematic sketch showing effect of across-column confining stress on ductile/brittle transition, marked by intersection of ductile/brittle strengths.

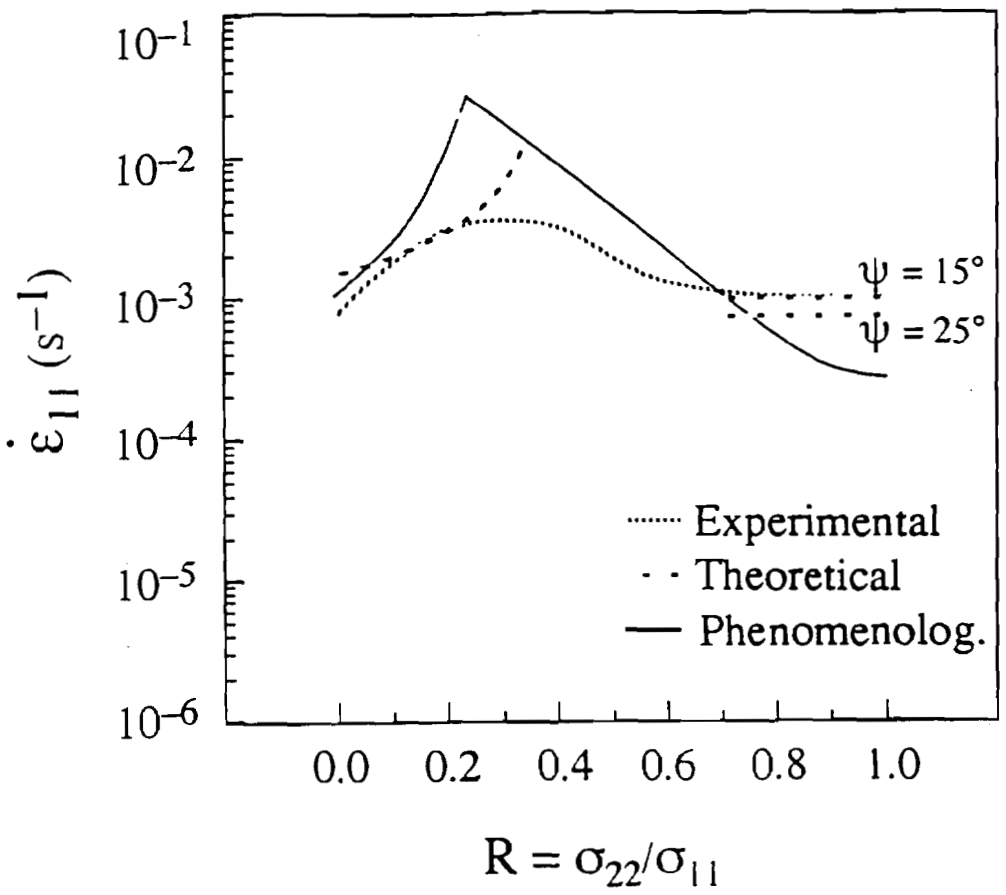

Figure 9: Comparison of calculated and observed transition strain rate under across-column confinement.

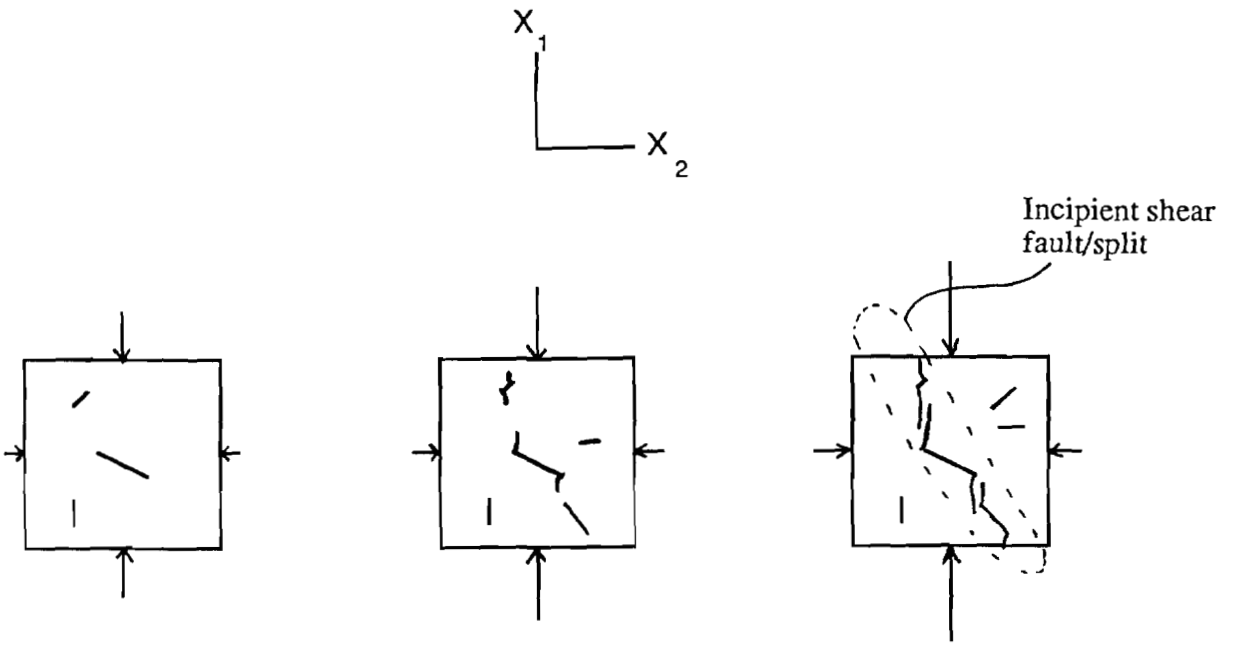

Figure 10: Schematic sketch of the evolution through crack sliding and wing cracking of brittle compressive failure via splitting and shear faulting.

Studies of the Influence of Fabric and Structure on the Flexural Strength of Sea Ice and, of the Consolidation of First-Year Pressure Ridges.

Drs. Lewis H. Shapiro, Wilford F. Weeks and William D. Harrison, Geophysical Institute, University of Alaska Fairbanks

Scope of Model and/or Data Set

During the Sea Ice Mechanics Advanced Research Initiative we have done independent and cooperative studies with other groups into (1) the relationships between the growth history, fabric, and structure of first-year sea ice and some of its physical and mechanical properties, and (2) the consolidation of first-year pressure ridges. Descriptions are given in the following sections.

Influence of Fabric and Structure on the Flexural Strength of Sea Ice -- We did four series of tests to determine the flexural strength of small plates (0.05 m x 0.15 m x 0.15 m) and beams (0.05 m x 0.05 m x 0.15 m) of first-year sea ice to study how the strength changes as the c-axis anisotropy develops and the grain size increases with depth in the ice sheet. We generally took samples through the uppermost 0.8 m of the ice sheet which were aligned with respect to the dominant c-axis orientation. For bending, the "weak" direction of the ice corresponds to loading such that the tensile stress in the outer fiber of the sample is applied parallel to the dominant c-axis direction and thus normal to the platelet boundaries. Conversely, tension normal to the c-axes gives loading in the "strong" direction. The sampling scheme and test geometry are shown in Figure 1. In our tests, the loads were always applied rapidly enough that the sample response could be taken to be elastic and failure was by brittle fracture. Further, all the tests were done in 4-point bending, which provides a uniform bending moment over the sample and allows failure to occur at the weakest point (as opposed to 3-point bending which forces the sample to fail at a particular point). This proved to be important, because it led us to learn of the influence of brine drainage networks on the strength of the samples. These features are networks of closely-spaced drainage tubes covering areas up to about 0.005 m^2. They have been described in the literature, but their role in determining any of the properties of first-year sea ice has not previously been investigated.

The data set available for analysis consists of the results of about 300 tests on plate samples and 250 beams from the same sample blocks, plus a comparable number of tests on beams from prior work. Descriptions of the ice, the test temperature, and the fabric as a function of depth are available for each series of tests and for each individual test we recorded data the on load and displacement with time, and measured the sample salinity. In addition, we recorded the location of the fracture surface relative to the load points and its relationship to the ice fabric and structure, and described structural features visible on the surface that indicate its character and the possible point of origin of the fracture.

Consolidation of First Year Pressure Ridges -- We studied the consolidation of first-year pressure ridges in shallow water off the Chukchi Sea coast near Barrow during the winters of 1992-93 and 1993-94. In early December of 1992, a ridge formed on a shoal in 6 m of water about 0.5 km offshore. The ice thickness at the time was 0.6 m. About one week later, we installed two thermistor strings through the ridge about 10 meters apart along a line normal to the ridge line. One string was placed near the crest of the ridge and the other was shoreward. In both strings the

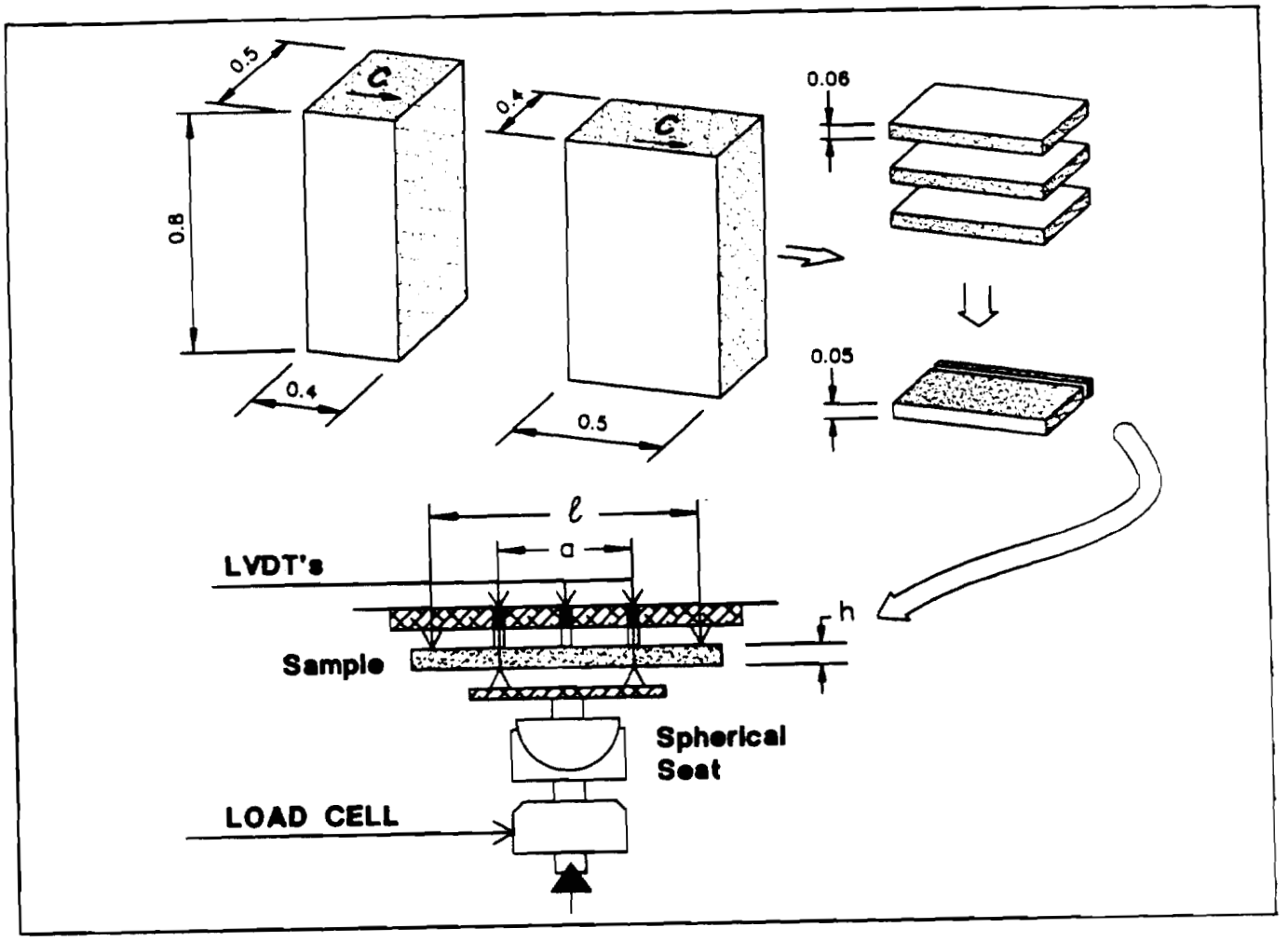

Figure 1. Sample preparation scheme and test geometry for determining the flexural strength of oriented plates and beams in 4-point bending.

thermistors were 0.3 m apart with the highest set 0.6 m above the ice surface. At the time the thermistors were installed the depth to the first void in the ridge was just over 1 m at both sites. Data were recorded every two hours from the time of installation through the end of May, 1993 but, unfortunately, the record of the first 10 days was lost.

In early March we established a profile through the ridge by drilling and logging along a line parallel to that on which the thermistors were installed but about 10 meters from it. We chose the location to avoid disturbing the temperature field near the thermistors. Subsequently, we re-profiled the same line in early May to record changes in the depth of consolidation, and we profiled the line between the thermistor strings at the end of May when they were removed from the ice. We also collected cores through the ridge at that time which were split, described and photographed.

At the time we profiled the ridge in early March and May, we also deployed an ROV under the ice to make observations of the ridge keel. The data obtained (in the form of video tapes) was useful in assessing the state of the ice, and identifying potential problems with the thermistor strings that could have affected the interpretation of the data.

In the 1993-94 winter there were no ridges in the area suitable for study until mid-February when a line of ridges formed in a wide refrozen lead about 1 km from shore where the water is 10 m deep. The lead ice that piled up to make the ridge was approximately 0.25 m thick, and the ridge apparently formed along the lead boundary where the older ice was 0.7 m thick. We installed the thermistor strings at a suitable site on the ridge on 24 February, about 1 week after it formed, and recorded data every two hours until the sensors were removed on 5 May. The ROV was deployed in early April, but operating conditions and damage to the vehicle limited the amount of data obtained. A more successful deployment was made when the thermistors were recovered, and the area was also profiled at that time.

Cooperative Studies -- For the 1993-94 winter we developed a cooperative program with J. P Dempsey (Clarkson Univ.), D. Cole (USACRREL) and V. Petrenko (Dartmouth Univ.) to share logistics and, where possible, coordinate a series of field studies involving (1) in-situ flexure and fracture tests on the full thickness of the ice sheet, (2) sampling for small-scale laboratory tests to determine constitutive laws, (3) monitoring electromagnetic emissions during the in-situ fracture tests, and (4) conducting the flexural strength measurements described above. We planned and conducted field programs in November, March and May to examine young ice, cold Winter ice, and thick ice as it warmed in Spring. The details of the individual parts of the program are described by the investigators named above. Our role involved the following activities:

(1) arranging for logistics including support personnel, field equipment, shelters, heat, power, and transportation,
(2) designing, constructing and operating a self-propelled chain saw capable of cutting smooth, straight slots through ice over 2 m thick,
(3) suppling flatjacks and bottled gas for loading in-situ tests,
(4) doing extensive ice characterization work including fabric studies, collection of ice thickness, temperature and salinity data through the winter to document the growth history, and descriptive work on brine drainage networks.

In addition we conducted two sets of small-scale experiments to supplement other experiments done by J.P Dempsey. The first were a series of 32 fracture toughness and flexural strength measurements on semi-circular bend specimens prepared from 0.2 m diameter cores that had earlier been split in flexure tests. The second consisted of about 60 4-point bending tests on plates of the size noted above, but oriented to fail in the same plane relative to fabric as the in-situ tests. The results thus provide a range of measurements for comparison and analysis.

Findings to Date

Influence of Fabric and Structure on the Flexural Strength of Sea Ice -- We believe that our data support the conclusion that the influence of c-axis fabric on the flexural strength of first-year ice enters appears abruptly at some depth where the intensity of orientation reaches some critical value. During our work, this depth of transition varied form less than 0.1 m up to about 0.4 m, depending on the growth history. Above the transition the ice is essentially isotropic, but below it, the directional dependence of the strength is clearly evident. The transition is so abrupt that test specimens prepared from above the transition in the upper part of the columnar ice zone of the ice sheet show no difference in strength with loading direction, even though the dominant c-axis direction is already apparent in thin sections from that zone. The effect appears within a depth interval of about 0.08 m, the typical increment between our sample plates or beams, across which the spread of c-axis orientations has narrowed. It is shown by an increase in the strength measured for loading in the "strong" direction, while there is no change in the values for the "weak" direction, other than a gradual decrease in flexural strength with depth as the c-axis alignment becomes stronger and the grain size increases. A plot of the data from a set of experiments done in November, 1993 that illustrates some of these conclusions is shown in Figure 2. The details are given in the caption. The logical interpretation is that as the c-axes become oriented, samples in the strong direction lose a weak failure mechanism that is still operative in the weak direction. Examination of the fracture surfaces indicates that the mechanism in question is separation across platelet boundaries which obviously cannot occur when the alignment is complete enough so that there are no suitably oriented surfaces. Our work has also demonstrated the importance of brine drainage networks on the results of laboratory scale tests of the flexural strength of first-year sea ice. Depending on their size relative to that of the samples, and their arrangement with respect to the loading direction, they can be the weakest elements in the samples.

The results of our experiments have allowed us to establish a range of flexural strengths and an associated hierarchy of failure mechanisms for our samples (including both beams and plates) in the temperature range from about -10 to -20°C. Samples from the slush ice zone and upper columnar zone above the depth where the c-axis orientation is well-established are, on average, the strongest , although the range of values is large (0.4 to about 1 MPa). With the anisotropy established, samples loaded in the weak direction that included brine drainage networks large enough to dominate the strength had an upper limit of about 0.4 MP. In the absence of large drainage features, the upper limit approaches 0.5 MP with a tendency for the strength to decrease with depth as the crystal size increases. In cases where the point of crack initiation could be inferred from the presence of plumose structures on the fracture surface, the indication was that the point of origin was the intersection of an individual brine drainage tube with the tensile surface of the sample. For the strong direction, the lowest strengths are within the range of values for the weak direction, and occur in samples with large brine

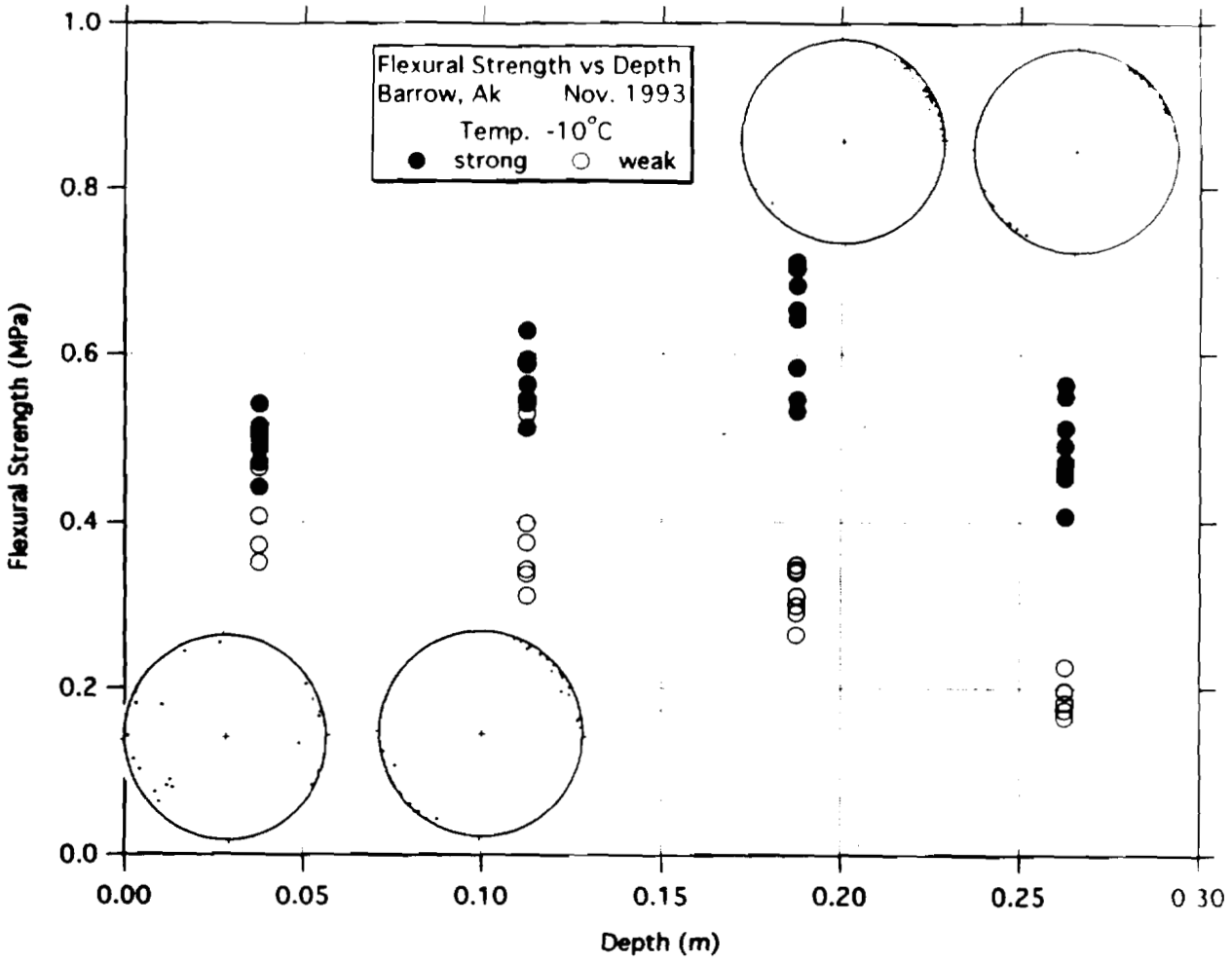

Figure 2. Flexural strength vs depth for a test series run in November, 1993. At the time of the tests, the ice was only 0.3 m thick but had well-developed brine drainage networks. The slush ice layer was under 0.1 m thick and the c-axis alignment developed rapidly with depth as shown in the fabric diagrams in the figure. They were made from thin sections taken at depths of (from left to right across the figure) 0.01, 0.1, 0.2 and 0.28 m.

drainage networks. Flexural strengths reached about 0.7 MPa in samples in the strong direction that lacked large drainage networks. In these cases, the fractures apparently involved smaller clusters or single drainage tubes. A few samples in the strong orientation reached flexural strengths of greater than 0.8 MPa, and in those, we were unable to infer any information about the origin of the fractures. Thus, our results show that, in fact, the flexural strength of the samples in which the c-axes are strongly aligned is determined by an interplay between the brine drainage networks and the crystal structure of the ice.

As noted above, all of our experiments were done in 4-point bending in which a uniform bending moment is applied over a relatively large sample, in contrast to the single stress point of 3-point bending. Our data indicate the value of this approach for studies of an anisotropic, inhomogeneous material such as first-year sea ice. For example, when we were able to measure the displacement of the tensile surface at the load points and the center of the sample, we found that the data usually show that the locus of maximum displacement shifted during the test. Further, some preliminary work suggests that the pattern of changing displacement rates may indicate where along the sample the fracture will form. Thus, the 4-point loading does in fact permit the sample to fail at its weakest point, which is desirable, given the characteristics of the material. However, since the deformation pattern is more complicated than for 3-point bending, unless the sample bends to a smooth arc with its maximum displacement at the center, determination of variables other than the load and loading rate can be uncertain.

Consolidation of First Year Pressure Ridges -- Representative temperature profiles taken by the two thermistor strings deployed in the 1992-93 winter are shown in Figure 3. They clearly show the advance of the freezing front through the ridge. Note that the zero depth is the ice surface at the string rather than sea level, so the differences between the near-surface sections of the profiles probably reflect differences in snow cover and freeboard.

To date, most of our analysis has been done on the temperature data from the 1992-93 winter and has been directed toward using it to estimate the volume of ice that froze within the ridge after its formation, since that is the process that "consolidates" the ridge. We have identified three modes of formation of new ice. First, some freezing should take place shortly after the ridge formed because in the ridging process cold blocks of ice are pushed down into contact with sea water at the freezing point. When the ridge we studied in the 1992-93 season was formed, the air temperature was about -20°C. Assuming this was the surface temperature of the ice and that the temperature gradient through the ice varied linearly, gives an average ice temperature of about -11°C. Using this value and accounting for the sensible and latent heats of ice we calculated that for the temperature to equalize to the melting point throughout the blocks, a volume of ice equivalent to about 6% of the submerged blocks would be formed. Some of the new ice would freeze between the submerged blocks and provide the initial strength of the ridge.

The temperature profiles show a relatively well-delineated freezing front, defined by the freezing temperature of normal seawater and by a discontinuity in the temperature gradient, propagating down through the ridge (Figure 3), and freezing at that interface is the second mode of ice formation. If we were considering fresh water, then the freezing front would correspond to the ice-water interface, and the volume above the front would be solid ice. However, because of the presence of salt in this system, as the front passes a given depth, only about 30% of the liquid at the interface is transformed into ice. In the freezing of a sea ice sheet, the

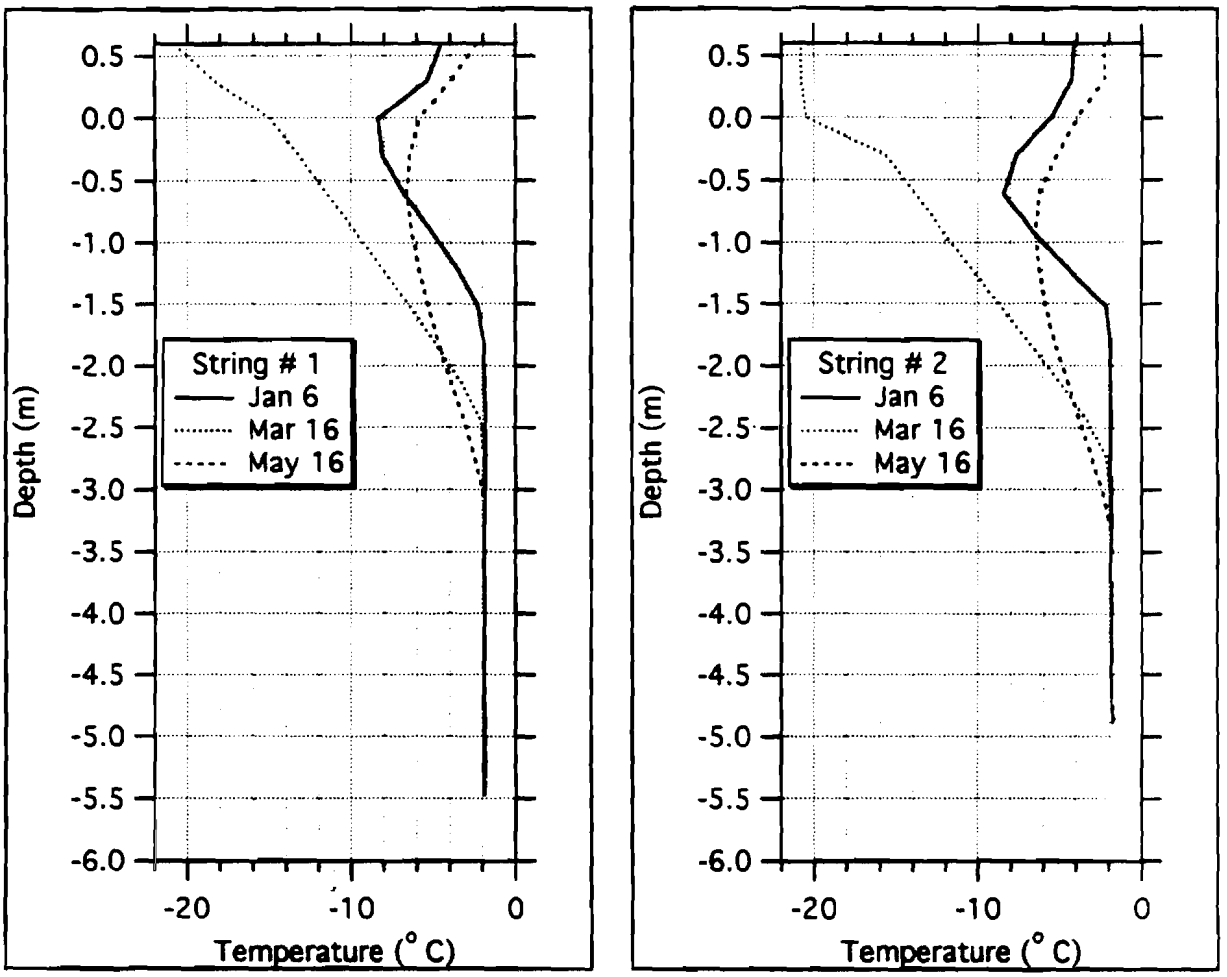

Figure 3. Sample temperature profiles from the 1992-93 experiment. The zero depth is the ice surface at the location of the thermistor string.

remaining liquid is simply the highly saline brine that is rejected at the freezing front. Some of the brine produced that way certainly drains out of the ridge as well, leaving solid ice behind. However, brines can also be trapped or ponded in isolated volumes between blocks of the ridge. They are only partially transformed to ice in the third mode of ice formation which occurs after the freezing front has passed and the temperature drops. How much additional ice is formed in that stage depends on the temperature and the salinity of the trapped brine. Also, how that ice is partitioned between growth from the block surfaces and isolated grains floating in a more concentrated brine is an important consideration, since only the former can contribute to increasing the strength of the consolidated ridge. We have not yet considered the details of that question. It is of interest that during our drilling and profiling we entered several "voids" from which we were able to remove large quantities of slush without advancing the drill. This implies that these voids were at least partially filled with slush, rather than sea water. However, there was a reduction in the number of voids encountered in the upper part of the ridge between profiling in March and May, suggesting that at least some of the voids were able to drain and solidify. Drilling also indicated that the depth of consolidation at the end of the growth season reached to about twice the thickness of the adjacent level ice.

The video tapes of the ROV observations have been scanned, but no detailed analyses have been done yet. However, the observations showed that the ridge had shifted, damaging the tubes in which the thermistor strings were installed and destroying the bottom one or two thermistors in each string. In addition, we found that the lower part of the shoreward thermistor string only passed through a small section of a single block of ice where the ridge ended abruptly.

Cooperative Studies -- We have completed the preparation of data collected during our cooperative studies will make it available to our co-workers as needed.

Analysis and Publication Plans

We have made progress in the analysis of the data regarding the influence of fabric and structure on the flexural strength of first-year sea ice to the extent that we feel confident of the conclusions presented above. Additional work with the data will involve (1) completion of the analytical study of the relationship between fabric and strength, (2) the establishment of relationships between the results and the variables used in the experiments (i.e., peak load in terms of rate effects, salinity and temperature) and possibly statistical analysis of the results to facilitate comparison with data from other sources. We also plan to do an analysis of the 4-point bending test as it applies to inhomogeneous media. We are interested in the conditions and instrumentation required to give data from which material properties can be determined, given that the deformation is irregular as described above. Such an analysis would also be useful for examining the relationship between displacement rates and the location of the fracture surface as noted above.

The ridge consolidation study has been concentrated on analysis of the thermistor data collected in the 1992-93 winter. That effort will be extended to the 1994 data, as well as to analytical work to improve our estimates of ice production. Also, we plan to do additional work on integrating the profiling and ROV observational data with the results of the analysis of temperature data.

We anticipate that there will be additional studies involving the data gathered during the cooperative studies during 1993-94, and these will develop as our colleagues continue with their analyses.

Previously, we published the following paper:

Shapiro, L. H. and W. F. Weeks, 1993, "The Influence of Crystallographic and Structural Properties on the Flexural Strength of Small Sea Ice Beams," in Dempsey, J.P., Z.P.Bazant, Y.D.S. Rajapakse and S. Shyam Sunder, eds., "Ice Mechanics -1993, Proc. 1st Joint Mechanics Meeting of ASME, ASCE, SES, Charlottesville, VA, June 6-9, 1993 , pp. 177-188.

At present, we are preparing the following two papers for presentation at the ASME Joint Applied Mechanics and Materials Summer Meeting, June 28-30, 1995 at UCLA

Cole, D.M., L. H. Shapiro, Adamson, R. M., C. Byers, J.P. Dempsey, O.V. Gluschenkov, V. Petrenko, and W.F. Weeks (in prep) In-situ and laboratory measurements of the physical and mechanical properties of first-year sea ice

Shapiro, L. H. and W. F. Weeks (In prep) Controls on the flexural strength of small plates and beams of first-year

The analysis of the small-scale test data described above will be presented in at least one journal article to integrate the earlier work. In addition, we anticipate that some of the ridge consolidation data will be developed into an M.S. thesis and organized into one or more journal articles by our student, Naomi Fischer.

5. ICE STRESS, ICE STRAIN, AND ICE CONDITIONS

Papers included in this section are the following:

"Sea Ice Mechanics Research," by Dr. Max Coon (P.I.), Mr. Skip Echert, and Dr. Stu Knoke of Northwest Research Associates, Inc.

"SIMI GPS Position and CTD Cast Data," by Ms. Suzanne O'Hara and Mr. Jose Ardai Jr. of Lamont Doherty Earth Observatory of Columbia University

"Regional and Floe-Floe Deformation," by Jim Overland (P.I.) and Sigrid Salo of the Pacific Marine Environmental Laboratory and S. Li and L. McNutt of the University of Alaska

"Pack Ice Stresses and their Relationship to Regional Deformation," Jacqueline A. Richter-Menge (P.I.), Bruce C. Elder, Walter B. Tucker III, and Dr. Donald K. Perovich of the U.S. Army Cold Regions Research and Engineering Laboratory

Sea Ice Mechanics Research

Dr. Max Coon (P.I.), Mr. Skip Echert, and Dr. Stu Knoke of Northwest Research Associates (NWRA).

Scope of Model and/or Data Set

The NWRA team performed a variety of experiments during the SIMI field program: ice-stress measurements, controlled-load and noise-generation tests, ice-on-ice friction tests, ridge-strength tests, and a multiyear floe evolution study.

Ice-Stress Measurements -- NWRA successfully deployed flatjack, fluid-filled stress sensors with an automatic pressurization-check feature in an autonomous station configuration. We installed these sea-ice-stress "buoys" at four sites; each buoy measured ice stress in four directions, from which we will derive the ice-stress state in the horizontal plane. A ridging event buried the first buoy, installed near Mt. Curtin at the West SIMI Ice Camp (Map 2, E7), after one month. The second buoy, installed about two miles north of West Camp on Floe 4 (Map 1, E4), operated continuously for over nine months. The crack that flooded portions of the West Camp disabled the third buoy after three months (Map 2, F5), but we repaired it and operated it for an additional three weeks at the East Camp (Map 4, C6). Table 1 lists the operational lifetime of the four buoy installations and the number of thermistors used to measure ice temperatures. The buoys wrote ice stress to an internal storage module at five-minute intervals and transmitted ten-minute data through the Argos satellite relay system. The buoys also stored and transmitted temperature readings from the higher (colder) two thermistors on the same schedule but stored and transmitted the lower (warmer) thermistor readings and a battery voltage every six hours.

Table 1. Ice-stress buoys

Buoy number	Test site	Start date	End date	Number of thermistors
1	Mt. Curtin	29 Oct. 93	4 Dec. 93	4
2	Floe 4	31 Oct. 93	3 Aug. 94	4
3	Lake Andy	22 Nov. 93	25 Feb. 94	8
4	East camp runway	1 Apr. 94	23 Apr. 94	8

In support of the sea-ice-stress buoys, NWRA performed various other ice-stress sensor experiments at 22 locations near the two ice camps:

- Individual stress sensor measurements,
- "High-data-rate" stress tests with data collection rates to 4 Hz,
- "Sensor/ice contact" tests to check contact between the sensor and the ice,

- "Inclusion" tests to calibrate the response of the stress gauge to the ice stress produced by an air jack a few decimeters away, and
- Comparison tests with other types of ice-stress and strain sensors.

We installed and tested individual stress gauges at the 22 locations listed in Table 2. Dataloggers generally collected this stress and temperature data at five-minute intervals. The two winter-over sites also collected temperature data hourly. The first site (Map 2, F4) tested the installation of a stress gauge in the low, flat, multiyear hummocks in the early autumn. The second site (Map 2, F5) tested the freeze-in of gauges installed at various depths in autumn first-year ice; the lowest was half in the water at installation. The sensors at the third site (Map 2, F5) were installed identically to the stress sensors on the buoys to obtain inclusion test data to support the interpretation of the buoy data. The fourth site (Map 2, F4) again tested the installation of stress gauges in the low flat hummocks of multiyear ice in the autumn. The fifth site (Map 2, E3) was used for the comparison tests in the West camp runway ice. The sixth site (Map 2, E5 and F5) studied the horizontal and vertical variation of ice stress in a large area of flat first-year ice, Lake Andy. (We hypothesize that Lake Andy had been a large, bottomless melt pond during the previous summer.) The seventh site (Map 2, F4) studied the local variations of ice stress near a hummock. The final site (Map 4, C6) was installed for inclusion test data to support the nearby stress buoy.

Table 2. Individual ice-stress gauge sites

Site number	Test site	Start date	End date	Number of stress gauges	Number of thermistors
1	Study area	23 Sept. 93	27 Sept. 93	1	0
2	Lake Andy	27 Sept. 93	16 Nov. 94	5	0
3	Lake Andy	15 Nov. 93	28 Nov. 94	3	2
4	Study area	17 Nov. 93	21 Nov. 93	2	2
5	West camp runway	18 Nov. 93	26 Nov. 93	2	2
6	Lake Andy	29 Nov. 93	27 Feb. 94	4	2
7	Study area	30 Nov. 93	17 Mar. 94	3	2
8	East camp runway	5 Apr. 94	23 Apr. 94	2	0

"High-data-rate" is a relative term; we use it to mean data rates of one to four readings per second as compared to our standard interval of five minutes. We performed high-data-rate tests with one to four stress sensors at a time, looking for stress signals we otherwise would have missed due to sampling rate. We also obtained ice-stress data at one-second intervals for six 15-hour periods and at 1/4-second intervals for one three-hour period.

Two methods were used to evaluate stress sensor installations: sensor/ice contact tests and inclusion tests. Turning a screw-plunger assembly added additional fluid to each ice-stress sensor to assure good contact with the surrounding ice. The additional fluid caused

either an abrupt increase in fluid pressure in the sensor or no response at all. The stress buoys performed these tests automatically on a schedule, which proved useful for timing the melt-out in the spring. Each stress sensor received one or more sensor/ice contact tests; the response varied with season, ice temperature, and ice type. If the sensor showed an increase of at least 50 kPa during the test, we considered the sensor to be in good contact with the ice. Sensors that failed the test also failed to respond to air jack stress and natural ice stress.

Air jacks were used to perform inclusion tests, which were stress sensor response tests at geophysical stress levels (0 to 300 kPa) and geophysical loading rates (1 to 100 kPa/min.). We used a square, flat, air jack about 0.6 meter on a side to apply pressure to ice containing one or two sensors. We performed "square-wave" tests, for which we adjusted the air jack pressure in an on-off cycle, and "ramp" tests, for which we adjusted the pressure in a slow-increase, slow-decrease pattern. The square-wave test was a quick gauge calibration, but the ramp test simulated realistic loading rates based on our prior field data. We measured the stress-sensor inclusion factor on 20 sensor installations. Both 15-cm and 20-cm diameter sensors were tested using square-wave and ramp tests. On the square-wave tests, the air jack pressure was varied from 20 kPa to 200 kPa above ambient; on the ramp tests, the air jack pressure was 100 to 200 kPa above ambient. The square-wave tests typically had a cycle period of a minute, while each up and down ramp test took from one to three hours.

In cooperation with Jackie Richter-Menge from the Cold Regions Research and Engineering Laboratory (CRREL) and Dr. Peter Wadhams from the Scott Polar Institute (SPI), we performed a test series to provide a head-to-head comparison of the CRREL three-wire stress sensor with the NWRA flatjack sensor and of the SPI strain gauge with the NWRA flatjack sensor. We ran a set of square-wave tests and a ramp test. In each, the air jack pressure was varied from ambient to about 60 kPa above ambient, and the resulting stress and strain sensor readings were recorded.

Controlled-Load and Noise-Generation Tests -- NWRA, working with Dr. Robert Pritchard of IceCasting, Inc. (ICI), performed over 30 controlled-load tow tests and 40 other tests to generate various types of the noise representing potential Arctic acoustic sources. These tests were performed at the Football Field (Map 4, D6), East Pond (Map 4, C6), South Camp (about 18 km south of East Camp), and the IOS site (Map 4, B6). Dr. Henrik Schmidt's group from MIT/WHOI and/or Dr. David Farmer's group from the Institute for Ocean Sciences recorded the acoustic signals generated by many of these tests with hydrophones and/or geophones. The tow tests consisted of towing a block of ice on partially submerged ice to simulate rafting, on snow-covered or bare ice to simulate over-ride, and under young ice to simulate under-ride. On each of the tow tests, the tow load was usually recorded at 16 Hz and showed irregular slip-stick oscillations. We also measured the tow speed, the block dimensions and weight, and the snow thickness so that we could calculate the minimum and maximum sliding friction coefficient.

The other tests included dropping blocks onto ice, flopping blocks onto snow-covered or bare ice, tipping blocks into water, tipping blocks underwater to float up, releasing blocks underwater to bounce on the bottom of the ice, and breaking cantilever beams. Table 3 lists these acoustic experiments.

Table 3. Acoustic Source Tests

Block Motion	Number of Tests	Number of Unique Blocks Used for Test Series
Flop onto bare ice	5	5
Flop onto snow	7	5
Drop	10	9
Splash	2	2
Underwater flop	2	2
Underwater bounce	7	2
Cantilever beam	3	3

Ice-on-Ice Friction Tests -- During April 1993, NWRA ran a series of tests to measure the ice-on-ice friction coefficients on "natural" cracks generated in the sea ice near Resolute, NWT. These tests were conducted in conjunction with Dr. John Dempsey of Clarkson University, who conducted sea-ice fracture and ice characterization tests. All of these tests were performed in the 1.8-meter thick, first-year sea ice in Allen Bay. The test parameters are listed in Table 4.

Table 4. Test Parameters for Ice-on-Ice Friction Tests

Normal air pressure (kPa)	Number of tests	Total face displacement (mm)
40	7	13-65
200	8	41-54
400	4	38-93
Varied 15-170	2	77-89

Ridge-Strength Tests -- NWRA ran strength tests on first-year ridged ice using the air jack to simultaneously load the ice and measure the displacement. In November, we obtained underwater video and one inflation sequence of the air jack in the keel at the bog site (Map 2, H5). In April, we characterized the sail and keel geometry of a ridge formed from first-year ice, inflated the air jack in four slots, and recorded the acoustic emissions during the air-jack tests at our ridge site (Map 4, A4). The ridge configuration in the vicinity of the four air-jack slots was characterized by drilling 12 holes and through observations with an underwater camera (but no video tape). Dr. Robert Pritchard recorded the noise using Dr. David Farmer's hydrophone equipment.

Multiyear Floe Evolution Study -- We studied the evolution of a 60-by-60-meter area of multiyear ice near the SIMI West Camp by measuring ice thickness, snow cover, ice temperature, ice salinity, and ice stress (Map 2, F4). Our dataloggers recorded ice temperatures at three depths at four sites every hour from September 1993 to March 1994. We measured ice salinities from core samples taken in September. We also made aligned ice-stress measurements at three sites from November 1993 to March 1994. Ice thickness and snow cover were measured in September and March at nine locations in the study area. We obtained underwater video of the bottom of the ice in September through four holes in the ice using an underwater camera mounted on a pole. Also, U.S. Coast Guard divers from the USCGC Polar Star took underwater videos of the underside of the ice in September with a hand-held camera.

Findings to Date

Ice-stress Measurements -- NWRA buoys measured comparable ice-stress events lasting three to nine days in December (days 350-358), February (days 33-35), and April (days 91-95), as can be seen in Figure 1. Figure 1 shows six-hour samples of the stress-sensor oil-pressure data transmitted via Argos satellite for the full life of the buoy, including spikes resulting from the auto-pressurization cycles. There were no major stress events after mid-May, and the ice apparently melted away from the sensors in early July, totally relieving all residual ice stress around the sensors.

We found comparable stress in the first-year ice on opposite sides of a hummock but much lower stresses in the hummock itself. Some hummocks were strong ice (the stress gauges responded as though they were in lake ice), but others were very soft or porous ice since the stress gauges did not respond to sensor/ice contact tests or inclusion tests. We also found significant stress variations across the length of Lake Andy, a large area of first-year ice surrounded by multiyear ice. We hypothesize that a slip-stick ice motion event caused the most interesting signal which we recorded during the high-data-rate tests (Figure 2). From the inclusion tests, we found that, at these load values and load rates, the sensor response is significantly lower than prior laboratory measurements indicate, implying that ice-stress levels may be two to five times more than the measured sensor fluid pressure.

Controlled-load and Noise-generation Tests -- Blocks of ice sliding over or under flat ice generally exhibited slip-stick behavior with large fluctuations in the sliding friction, as illustrated for the tow load history in Figure 3. Figure 3 shows the first 12 seconds of Test 8-13, a dry over-ride test; the signal almost immediately settles into a repetitive slip-stick pattern. The load fluctuations on the ramp-ups are caused by cable oscillations since the ice block was stationary during those times. The ice-deformation mechanisms that generated more acoustic noise were blocks dropping or flopping onto bare ice, blocks sliding over snow-covered ice, and blocks falling into the water. Quiet ice-deformation mechanisms included blocks sliding or bumping underwater, rafting (lubricated by water), and blocks dropping or flopping onto snow-covered ice.

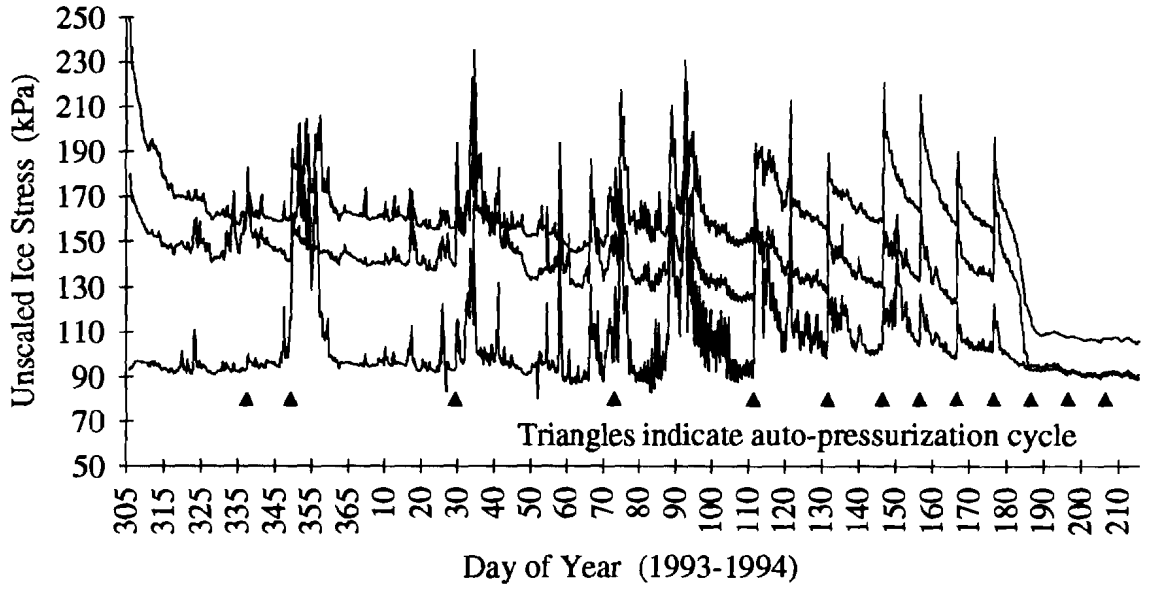

Figure 1. Ice-stress Buoy 2 (Floe 4) data via Argos, Nov. 1, 93 - Aug. 3, 94

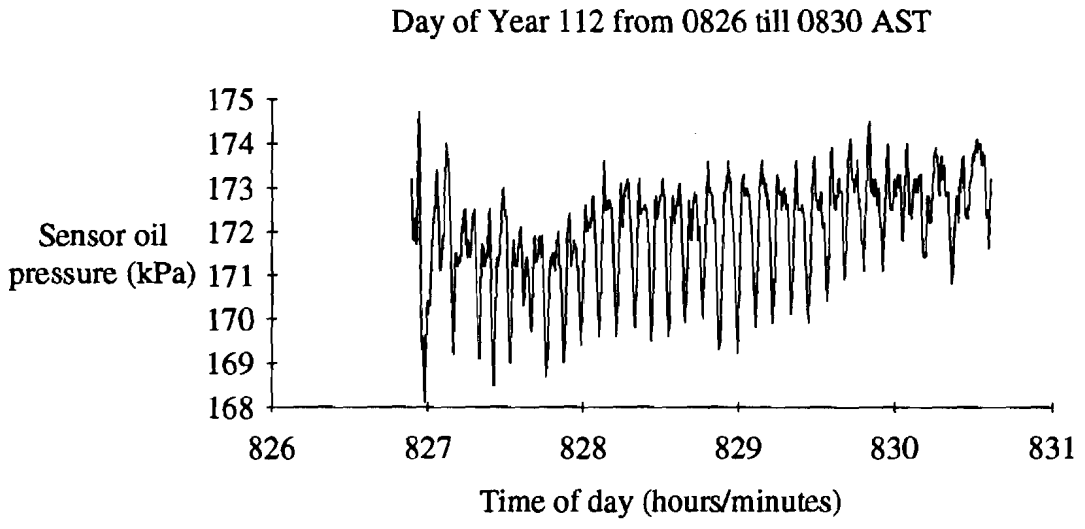

Figure 2. Ice-stress signal recorded near East Camp

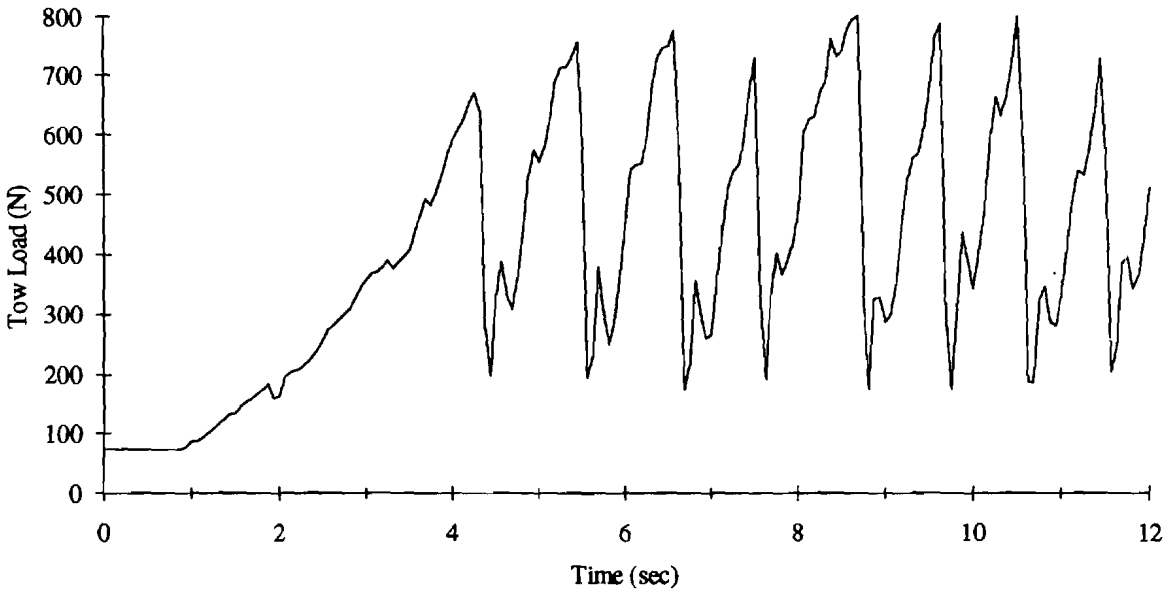

Figure 3. Tow load time series from an over-ride test (Test 8-13)

Ice-on-Ice Friction Tests -- In the configuration tested at Resolute, the shear force to cause shear motion along a fresh crack was surprisingly steady and smooth, except for the initial start-up motion. This may have resulted from having an air jack provide the normal force and a hydraulic jack provide the shear force. These dynamics are very different from an ice block being pulled with a winch. The measured coefficients of friction of natural cracks in first-year sea ice are consistent with the friction angle of pack ice calculated from ice-stress measurements made during the CEAREX program.

Ridge-strength Tests -- The strength of the fused ice in the ridge was highly variable, ranging from essentially solid ice near the surface to loose pieces floating underwater at or near their melting point temperature. Figure 4 shows an intermediate case of air jack pressure versus time. We interpret the down steps during the long rise as ice-to-ice contacts breaking and slipping. We stopped the displacement of the air jack when it had reached maximum stroke. We caused the large down step at the end by releasing the pressure in the air jack. These tests suggested that a better test of ridge keel strength would require a larger volume displacement, on the order of 8 cubic meters or more.

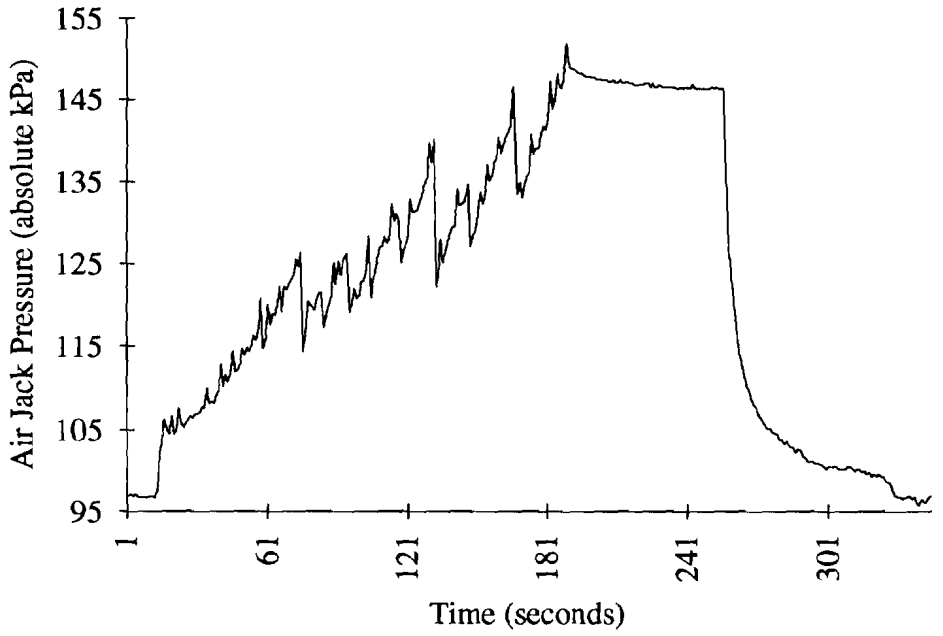

Figure 4. Air jack pressure versus time for one ridge test (results were highly variable).

Multiyear Floe Evolution Study -- In September, the study area consisted of hummocks and melt ponds covered with 20 cm of saline first-year ice. The multiyear ice had a highly porous bottom layer with a rough, lumpy appearance. The five separate melt ponds in the study area were small (two to ten meters across) and the surrounding hummocks protected their first-year ice from ice deformations. Some of the melt ponds had about 40 cm of salt water beneath the first-year ice and about 50 cm of multiyear ice beneath the water; others had nothing but water beneath the first-year ice. Before the first snowfall, the area looked like a huge slice of Swiss Cheese; melt ponds were the holes. The underside of the study area ice also had a unique appearance, with large flat areas of first-year ice separated by lumpy, steep-walled keels. By spring, the melt pond ice was about 1.2 meters thick with 0.5 to 1.5 meters of snow cover, but two- to four-meter keels still separated the flat ice segments. The multiyear ice underlying the salty melt ponds had also grown, about 10 cm.

Analysis and Publication Plans

Our first priority has been to document our SIMI test results in the above categories. We plan to analyze all field data collected during SIMI, including the data from the ice friction experiments conducted at Resolute earlier in 1993. We plan to publish papers and make presentations at the AGU, Oceans, ISOPE, and OTC Conferences. The following is a list of titles for potential papers and/or presentations resulting from our SIMI work:

- Interpretation of inclusion factor tests on flat-jack ice-stress sensors
- Estimates of first-year ridge strength from field measurements
- Acoustic emission of simple motions of sea-ice blocks
- In-situ measurements of ice-on-ice sliding friction
- Analysis of long-term sea-ice-stress measurements
- Validation of an oriented pack ice constitutive law with SAR, GPS, and sea-ice-stress measurements
- Performance comparison of two ice-stress sensors and an ice strain sensor
- Jay's Fingers -- a documented example of the rafting of very thick sea ice
- Chaotic dynamics of the slip-stick behavior of moving blocks of sea ice

Following is a list of our recent publications resulting from the SIMI program and relevant publications on models and equipment used during the SIMI program:

"The Sea Ice Mechanics Initiative (SIMI)," M. D. Coon, G. S. Knoke, and D. C. Echert, in *Proceedings of the 1994 Offshore Technology Conference*, Houston, TX, May 2-5, 1994.

"Contemporaneous Field Measurements of Pack Ice Stress and Ice Strain Measurements from SAR Imagery," M. D. Coon, G. S. Knoke, D. C. Echert, and H. L. Stern, in *Proceedings of OCEANS 93 Conference*, Victoria, B.C. Canada, October 18-21.

"Phenomenological Constitutive Model for Columnar Ice," M. D. Coon and G. S. Knoke, in *ISOPE-93 Singapore: The 3rd International Offshore and Polar Engineering Conference*, Singapore, June, 1993.

"Pack Ice Anisotropic Constitutive Model," M. D. Coon, D. C. Echert, and G. S. Knoke, in *IAHR 92, Proceedings of the 11th International Ice Symposium*, Banff, Alberta, June 15-19, 1992.

"Arctic Ice Stress Measurements," P. A. Lau and G. S. Knoke, in *Proceedings of OCEANS'91 Conference*, Honolulu, October, 1991."

SIMI GPS Position and CTD Cast Data

Ms. Suzanne O'Hara and Mr. Jose Ardai Jr. of Lamont Doherty Earth Observatory of Columbia University.

Scope of Model and/or Data Set

Lamont personnel set up and operated a logging system during the fall and spring SIMI Ice Camps. This system recorded GPS position, electronically logged weather data (fall camp only) and served as an electronic log book for hand entered weather data.
In addition, 13 CTD stations were taken in the fall, with 15 accomplished in the spring.

GPS Position -- GPS position was logged at the fall camp every two seconds from September 27 to December 9. This data is available in 12 hour, 1 hour, 15 and 10 minute subsampled form as well as the 2 second data set. Data gaps and their explanations are available in a file. Data for the spring camp is in the same formats, with different file formats due to two camps running simultaneously. As with the fall data, gaps are available in a file format.

Weather Data -- Temperature, barometric pressure, and wind conditions were recorded manually during all three camp occupations. In addition a 15 day period of half-hourly data was recorded at the end of the fall drift. This electronically recorded data has been plotted along with the hand recorded values and found to agree well.

CTD Data -- Thirteen CTD stations were taken in the fall by LDEO workers, using a Seabird Seacat Model 19 CTD loaned by Dr. Jamie Morison of the University of Washington. Maximum depth reached during these casts was 370 decibars. These stations were taken in the building assigned to the Scripps group. The same unit was returned to the Ice Camps in the spring, but due to a cracked conductivity cell, the data is only useable for temperature and depth. The two stations taken at West Camp were located next to the Morison data buoy and serve as a calibration for sensors installed on the buoy. The additional thirteen stations at East Camp were taken through the hydrohole originally used for the MIT Autonomous Vehicle deployment. Maximum depth was 535 decibars, with most casts to 460 decibars.

Table 1 CTD positions-Fall Camp

ctd#	date & time	lat	long	max db
1	16/11/93 20:30	75 06.70N	142 39.40W	370
2	18/11/93 04:30	75 05.19N	142 45.32W	369
3	19/11/93 02:38	75 03.74N	142 37.75W	369
4	19/11/93 21:22	75 06.37N	142 18.55W	344
5	21/11/93 06:12	75 03.48N	141 23.72W	369
6	22/11/93 06:03	75 08.80N	141 14.21W	369
7	23/11/93 06:40	75 10.45N	140 51.55W	370
8	24/11/93 05:38	75 08.12N	140 49.82W	366
9	25/11/93 22:40	75 03.90N	140 15.50W	372
10	27/11/93 06:20	74 59.75N	139 58.22W	372
11	28/11/93 06:08	74 57.86N	139 44.63W	371
12	29/11/93 03:12	74 53.90N	139 17.76W	363
13	30/11/93 03:03	74 51.62N	138 55.92W	361

Table 2 CTD positions-Spring Camps

ctd#	date & time	lat	long	max db	camp
1	31/03/94 20:27	74 11.29N	153 49.76W	535	W
2	01/04/94 23:54	74 11.55N	153 51.26W	274	W
3	06/04/94 17:18	73 04.00N	149 12.12W	433	E
4	12/04/94 00:16	73 01.20N	149 32.10W	363	E
5	13/04/94 01:02	73 01.19W	149 32.19W	469	E
6	13/04/94 22:49	73 01.45W	149 32.57W	453	E
7	15/04/94 04:29	73 00.63N	149 37.48W	453	E
8	16/04/94 19:39	73 00.09N	149 36.62W	464	E
9	19/04/94 01:26	73 00.27N	149 33.25W	459	E
10	19/04/94 23:15	73 00.48N	149 32.77W	460	E
11	21/04/94 05:18	73 00.47N	149 33.09W	417	E
12	22/04/94 17:14	73 00.59N	149 53.06W	458	E
13	23/04/94 22:31	73 00.77W	150 06.35W	462	E
14	25/04/94 06:22	73 01.41N	150 10.42W	453	E
15	25/04/94 19:33	73 01.21N	150 10.11W	481	E

Accuracy of Data GPS- Since the receivers used are standard civilian units, and differential coverage was not available, it is estimated that recorded position will lie within a 30 meter circle. This has been seen from use of the same units in other locations. Additionally, occasional variations of up to 100 meters may occur from other causes.
Weather- Temperature is estimated to be accurate to 1 degree C based on post calibration of the thermometer used along with the CRREL electronic unit that was checked before the start of the Fall experiment. Barometric pressure was taken from calibrated aircraft barometers that should be good to better than .01 inches of mercury. Comparison with incoming aircraft did not reveal any discrepancies.
CTD- As the CTD unit had been calibrated prior to the use in the fall, and again after the fall and before the spring, the accuracy should be essentially at manufacturer's specifications. It is felt that observed parameters can be used to +/- 2 db in pressure, +/- .002 degrees C in temperature, and +/- .003 in PSU. Again, this must be noted that the salinity measurements in the Spring Camps are missing due to a cracked conductivity cell.

Findings to Date

GPS Data- From Fig. 1, the relative magnitudes of the various camps can be seen. Both the Fall camp and the Spring West Camp are seen to have a greater response in the NW-SE direction than the Spring East Camp shows. The overall drift vector of the Fall and Spring West Camps is to the WSW however, and this compares favorably with the Spring East Camp. Several fine scale features can be seen in both Figure 2, Fall Camp Drift and Figure 3, Spring East Camp Drift. Notably, the course reversals and circular motions observed on Oct. 1, Oct. 12, Nov. 23, and Nov. 31. Some of the circular radii were within the floe boundaries in the case of Nov. 23. The Spring East Camp had a 14 day period bounded by a 3 nautical mile circle, as well at the end of the project on April 25, a sharp course reversal.

CTD Data- The mixed layer depths are roughly comparable between the Fall data and that collected in the spring. Depths ranged from a high of around 25 to a maximum of 45 observed in the Spring Camps. There is a strong locational difference between the two profiles taken at the Spring West camp in support of the Morison Buoy and those taken at the East Camp. The West Camp traces reach 0 degrees C at a depth just below the mixed layer (50 db) and the same depth is fully .9 degrees colder at the East Camp. In addition, the first trace at the East Camp shows a large intrusion of warm water below 100 db that could be associated with the large movement seen in the preceding days. See figures 4 and 5 for station locations.

Analysis and Publication Plans

The data described is available in the form of data reports, previously published after the Fall experiment and recently collated into a Spring report. The data is available via ftp, e-mail or can be provided on several different media for further analysis. Several platform types can be supported such as UNIX, DOS or Macintosh.

figure 1

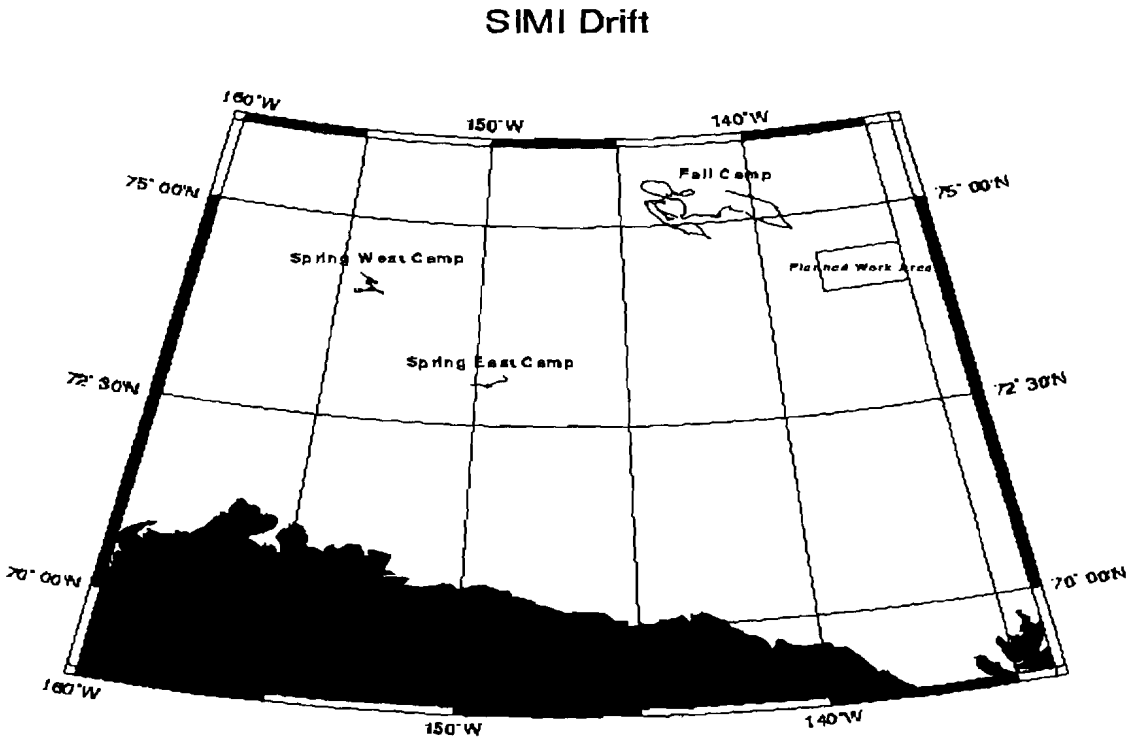

SIMI Ice Camp Drift

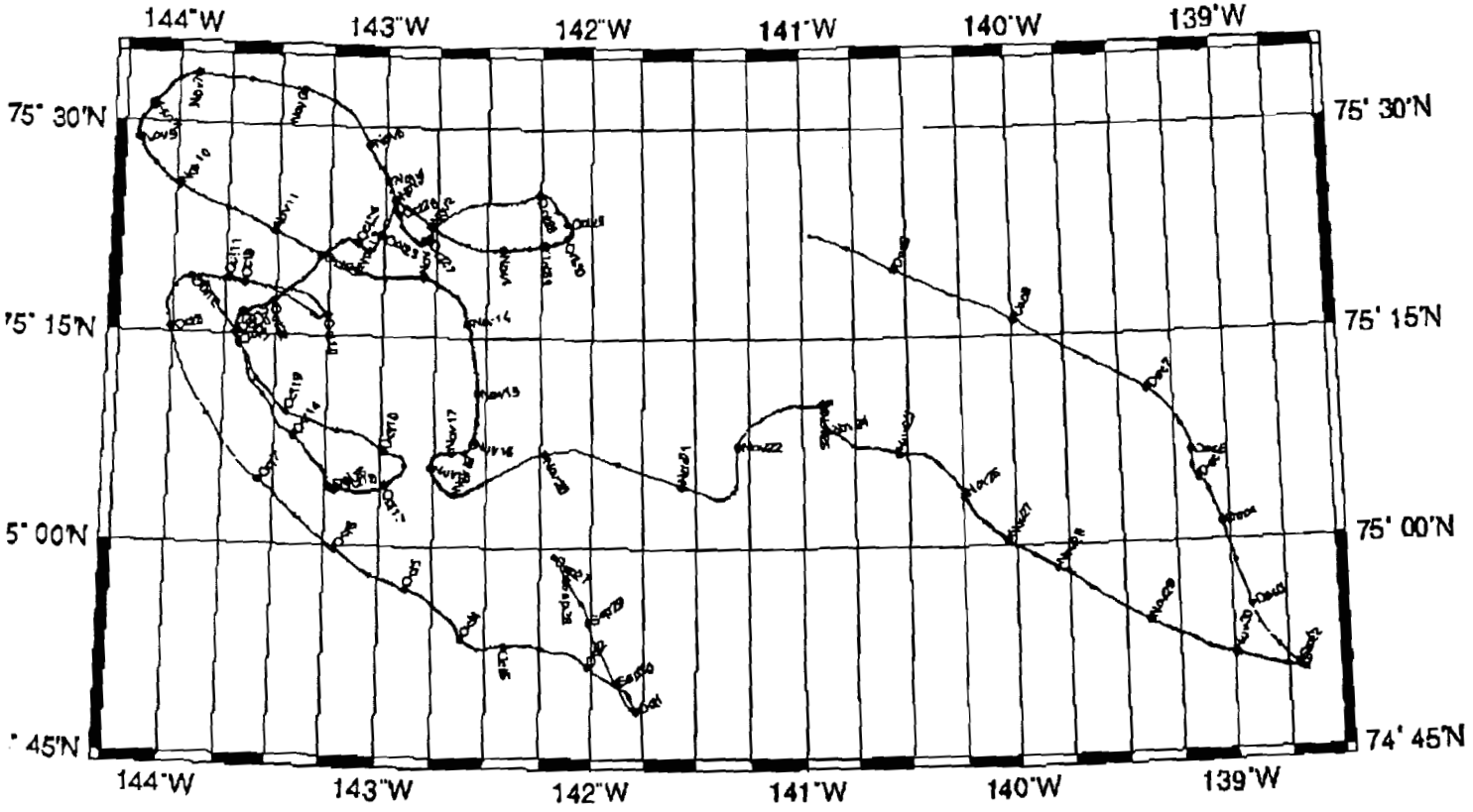

figure 2

figure 3

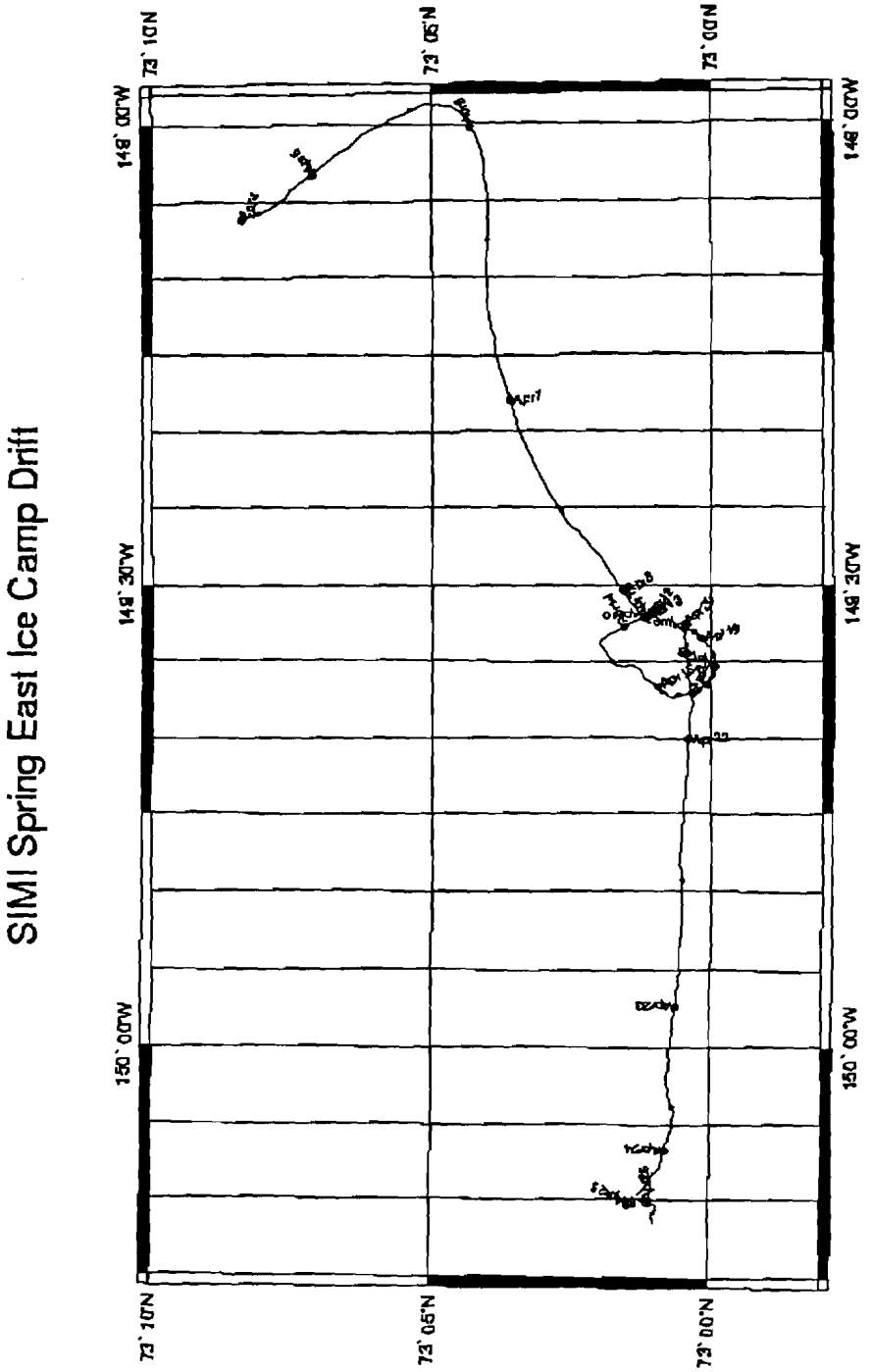
SIMI Spring East Ice Camp Drift
73° 10'N
73° 05'N
73° 00'N
148° 00'W
148° 30'W
149° 00'W
149° 30'W
150° 00'W

figure 4

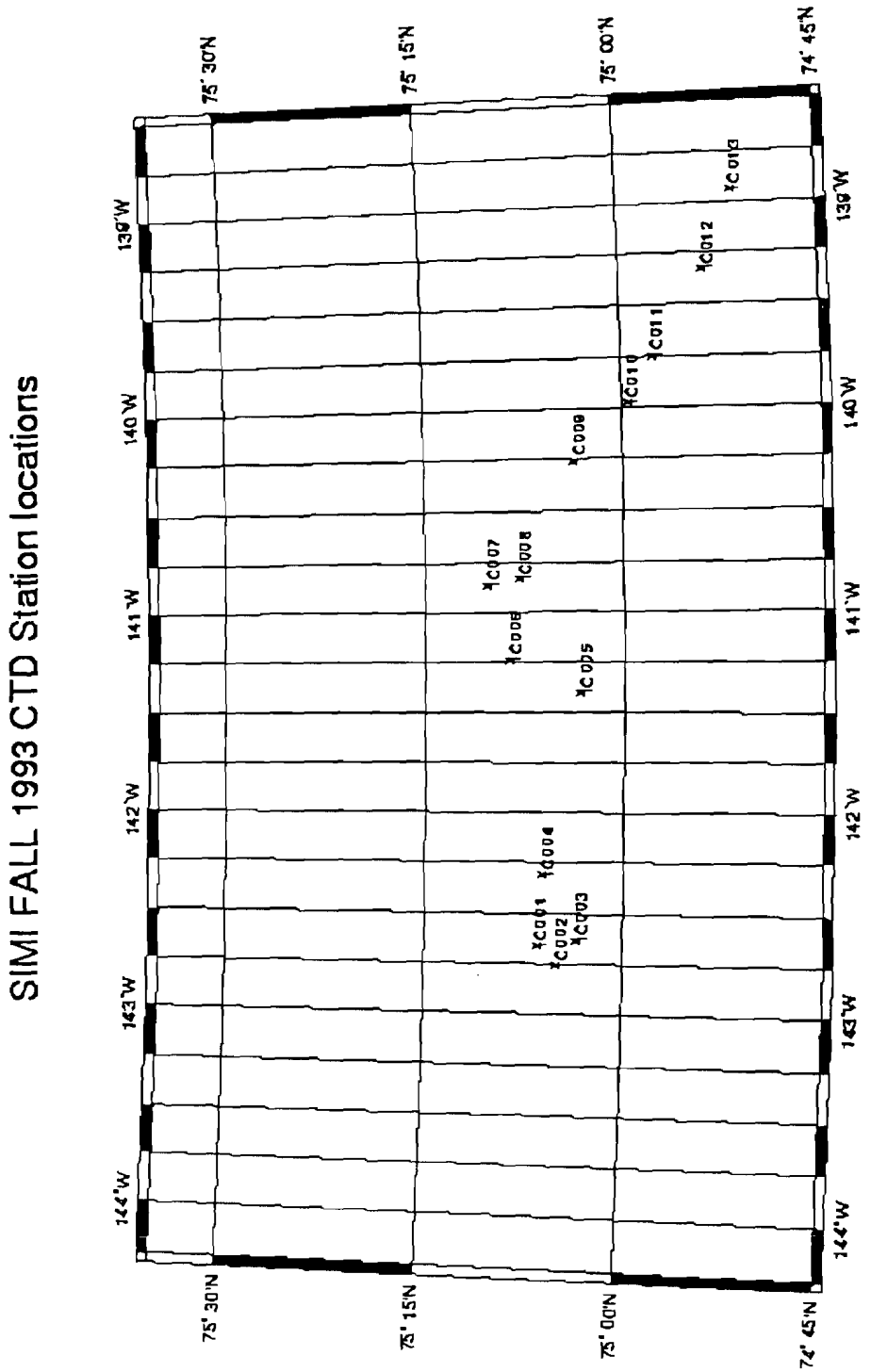
SIMI FALL 1993 CTD Station locations
75° 30'N
75° 15'N
75° 00'N
74° 45'N
139°W
140°W
141°W
142°W
143°W
144°W
C001
C002
C003
C004
C005
C006
C007
C008
C009
C010
C011
C012
C013

figure 5

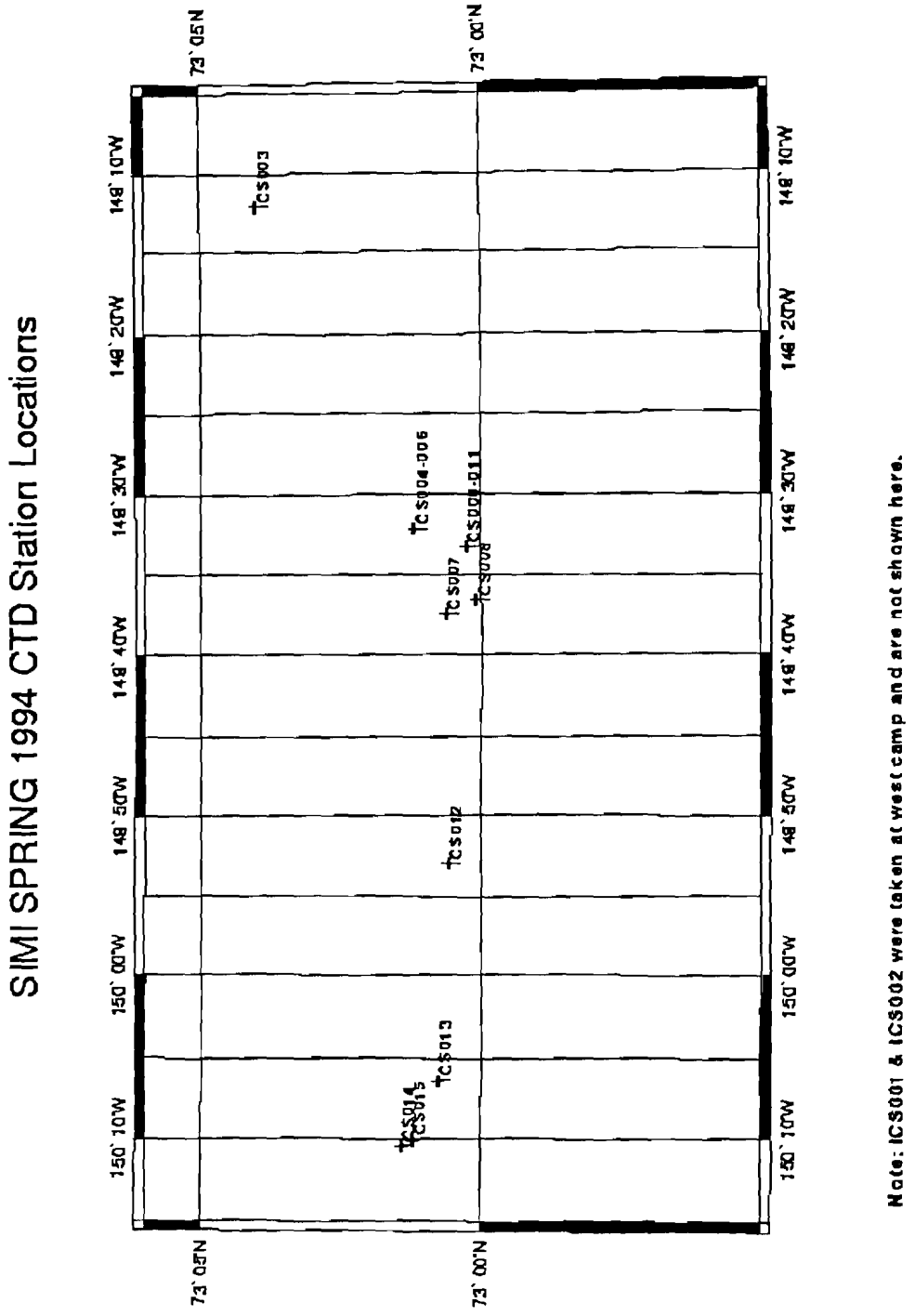
SIMI SPRING 1994 CTD Station Locations
73° 05'N
73° 00'N
148° 10'W
148° 20'W
148° 30'W
148° 40'W
148° 50'W
149° 00'W
149° 10'W
ICS003
ICS004-006
ICS007
ICS008-011
ICS012
ICS013
ICS014
ICS015
Note: ICS001 & ICS002 were taken at west camp and are not shown here.

Regional and Floe-Floe Deformation

Jim Overland (P.I.), and Sigrid Salo, Pacific Marine Environmental Laboratory (PMEL); Coordinated Investigators: S. Li, and L. McNutt, University of Alaska.

Scope of Data Set

In late September 1993, we deployed thirteen ARGOS buoys; one at the SIMI main campand the other twelve in two circles (hexagons) centered at the main camp (Figure 1). The radii of the two circles (hexagons) were approximately 5 and 10 km. We set out an additional seven buoys at the spring SIMI camp (Figure 2). Each of the ARGOS buoys used the GPS system to determine their positions once per hour. The buoys all established their position at the same time to increase the chance that they would all use the same group of satellites for a given fix. When buoys did use the same satellites, their positions had the same "dither", which subtracted out when we calculated the distance and direction between them. The positions, a code for the identity of the satellites used to obtain the most recent position, and the previous two hours' positions were transmitted to us using the ARGOS system. We also obtained the ARGOS positions as a check on the GPS positions, and to fill in missing GPS positions. The ARGOS positions are only accurate to $\pm$300m, but were useful when a buoy was unable to determine a GPS position for several days at a time. GPS positioning is a great improvement over ARGOS positioning to obtain relative motions; on plots of both one-day and three-day relative displacements, buoys with ARGOS fixes appear noisy relative to the pattern calculated from the GPS fixes.

Time series of positions were obtained from GPS positions and from ARGOS positions for GPS gaps longer than 5 hours. We despiked the data by calculating the standard deviation of the buoy displacement per unit time and removing positions whose change was greater than 6 times that value. We then used an Akima cubic spline to obtain an hourly time series of positions. Each position in the final product was coded to indicate if it was derived from GPS or ARGOS positions or extrapolated during a gap. Time series of distances and directions from the SIMI main camp to each of the buoys in the array were obtained from the original unsplined data, using only those positions where both buoys used the same satellites or all but one of the same satellites. The data were despiked and splined in the same manner as the position data.

Figure 1 and 2 also presents a timeline for each of the buoys we set out at the SIMI camps. Each buoy is identified by both its floe number (1-12), and by its ARGOS number. All the buoys except 20727, at site 11 in the northeast, lasted at least through April 1994, although most have gaps of several days to several weeks in their records. Many of the shorter gaps were GPS gaps; we do have ARGOS data during their duration. The longer gaps were caused by foxes who chewed off the ARGOS (transmitting) antennas, and we do not have ARGOS positions to fill them.

SIMI main camp remained near its original position during October and November 1993, but moved 16° of longitude westward in December 1993 and January 1994 (Figure 3). Its displacement was a minimum in February-April 1994, and increased again in May when it moved another 5° west. During the summer the SIMI main camp moved to the northeast and then in the fall to the southeast. The SIMI camp was slightly northeast of its position one year earlier, when its ARGOS buoy stopped transmitting in late October 1994. The SIMI spring camp moved generally westward during its occupation (Figure 2).

1

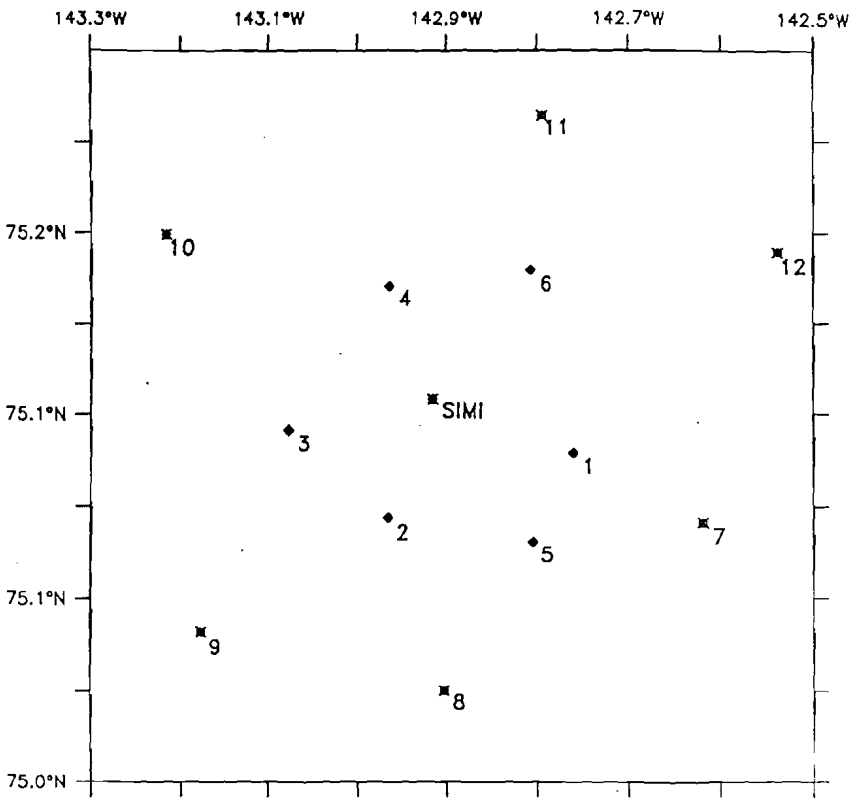

Autumn SIMI ARGOS Buoys and Timeline

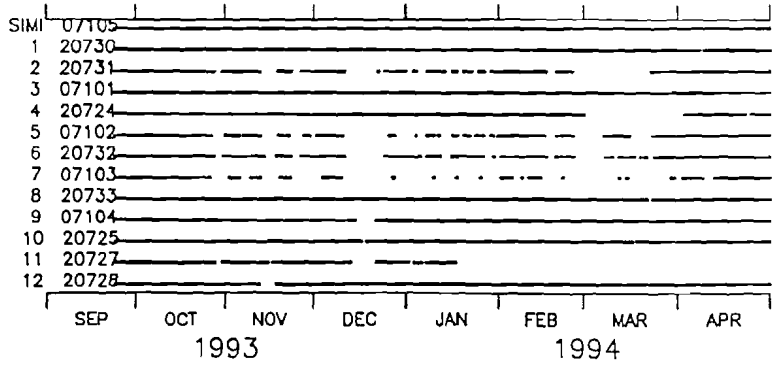

2

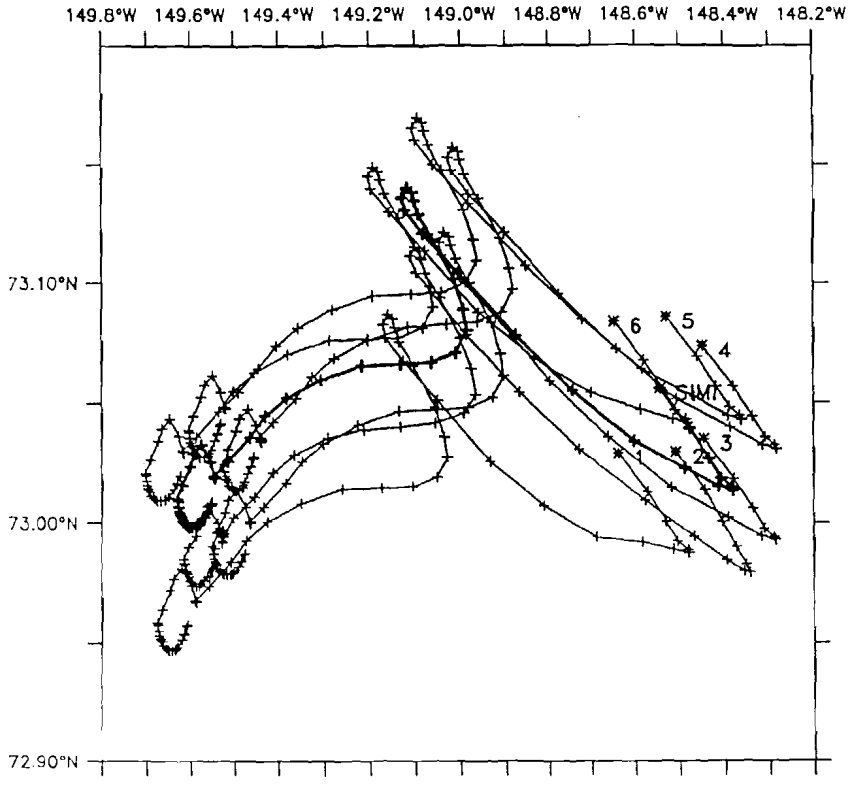

Spring SIMI ARGOS Buoys and Timeline

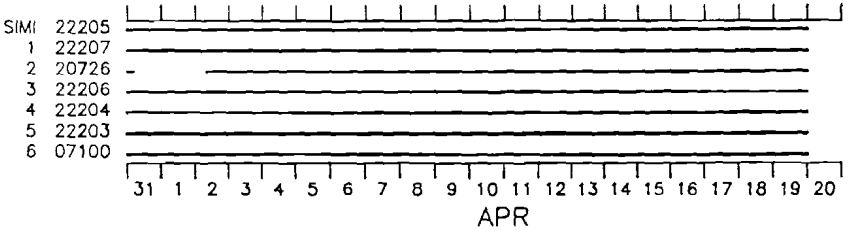

3

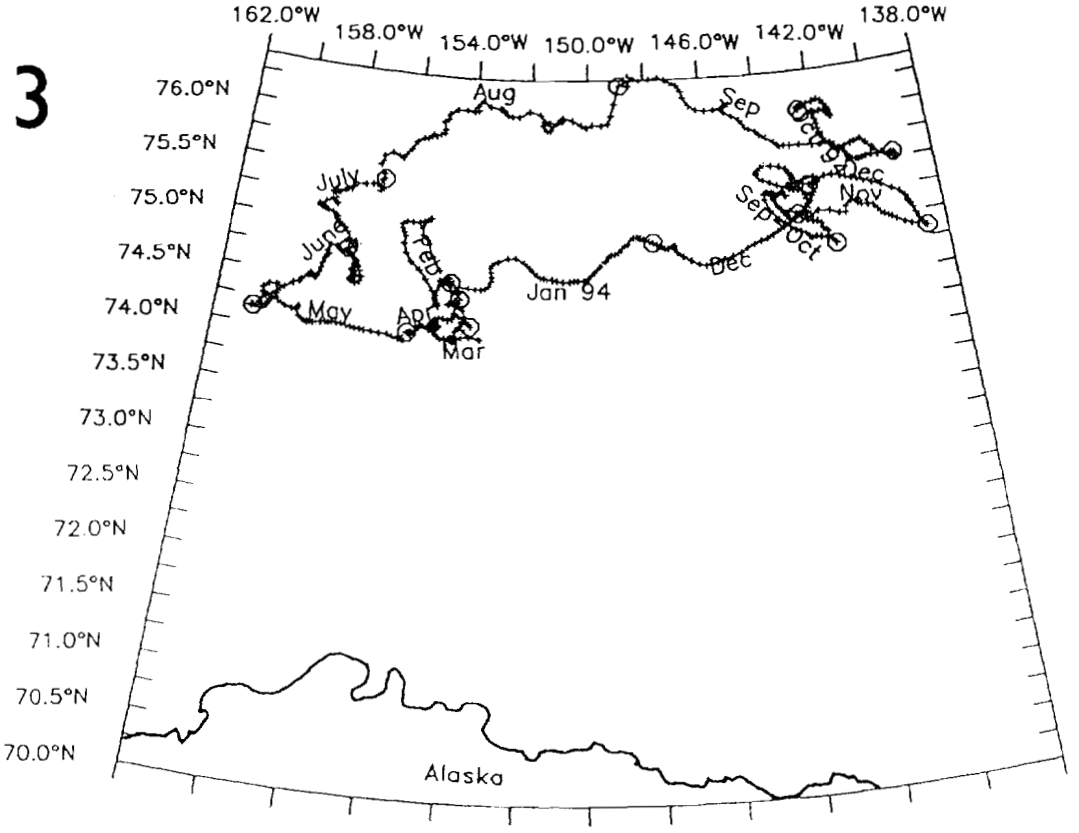

SIMI Ice Camp Drift, Sept 1993–Oct 1994

4

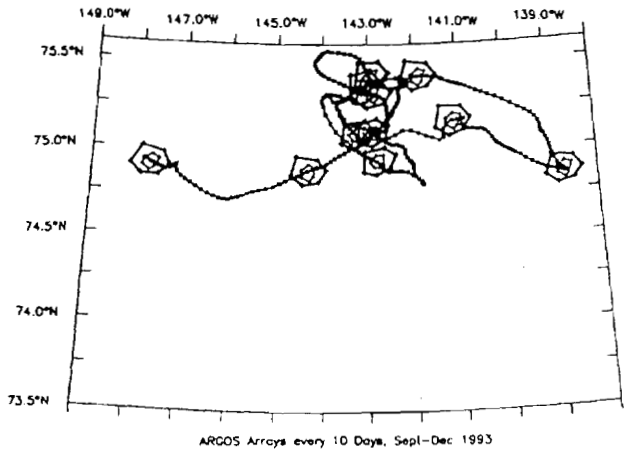

ARGOS Arrays every 10 Days, Sept–Dec 1993

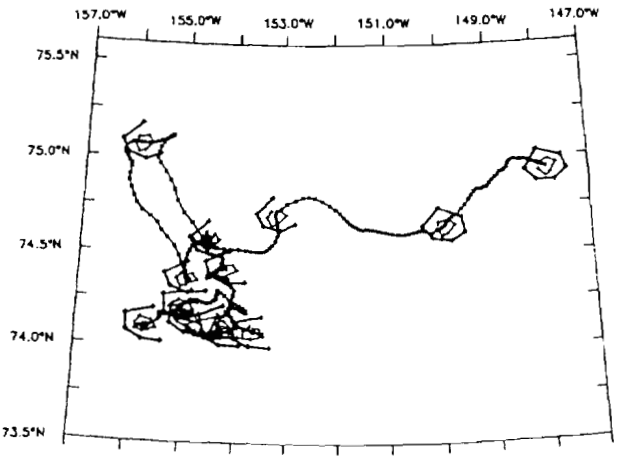

ARGOS Arrays every 10 Days, Jan–Apr 1994

There was little persistent change in the shape of the hexagons formed by the buoy arrays, especially during the first three months, although the arrays did steadily rotate clockwards (Figure 4). The outer hexagon was sometimes flattened in the direction toward which the array was moving, as in October 1993 (~74.8°N, 142.5°W), but later recovered its form. There was more distortion and rotation of the array in February-April, but except for the fact that each buoy was some 80° clockwise of its original position relative to main camp, the array was still recognizable.

Although we collected weather data at the SIMI main camps, the cable from the weather station tower to the ARGOS transmitter was destroyed by foxes in early December and not repaired until late March. We therefore have data only for the first several months and final weeks of the main SIMI experiment. The pressures and winds displayed in Figure 5 are derived from the NMC pressure grids using our METLIB programs. In the top two plots, METLIB data are plotted as a solid line and station data as a dashed line. The METLIB and station pressures match quite well, although we haven't done a statistical comparison. The METLIB winds are not identical to the SIMI camp winds primarily because they represent regional rather than local winds.

Findings to Data

The idea that sea ice behaves as a plastic on regional scales (> 5 km) is over 20 years old (Karlsson, 1972). The concept of a yield surface was well established in sea-ice models of the AIDJEX [*Pritchard*, 1980] and post-AIDJEX periods [*Hibler*, 1979]. A difficulty was the lack of computer capabilities to actually resolve the physics on their appropriate regional scales in the models; grid length were of order 120 km so that mathematical resolution, i.e., the ability to resolve the underlying equations for plastic flow, is limited to $4\Delta X$ or almost 500 km, much larger than the scale of regional stress characteristics and shearing motions O(10-40 km). Note that we are still referring to a continuum model.

A second limitation was *in situ* measurements. The Arctic buoy array provides basin scale ice motion and meteorological information, but it resolves only larger-scale, mostly wind-driven motions [*Colony and Rigor*, 1993]. The SAR is an opportunity to resolve ice motions and thus deformations on a sub-regional scale O(10 km). Its limitations are a 3-day repeat orbit and that there is not complete spatial coverage. However, a major use for SAR data is to verify sea-ice dynamics assumptions through case studies of deformation events.

Our intent is to compare SAR derived ice motions with deformation information obtained from the array of 13 drifting buoys with GPS positioning placed within a 20 km region, 500 km north of Alaska (Figure 1). We wish to understand whether the underlying plastic hypotheses for modeling sea ice are valid, in particular that under compression sea ice yields first in shear (*Marco and Thompson*, 1977; *Pritchard*, 1991). We also note that the deformation in the wind field is not large enough to cause significant deformation in the ice pack, that given the strength of the pack, coastal geometry is important over distances as great as 500+ km (*Overland, et.al.*, 1995). We note that modern generation computers are capable of 10-20 km resolution, so that simulations that resolve the full plastic behavior of sea ice are possible (*Coon, et.al.*, 1992).

5

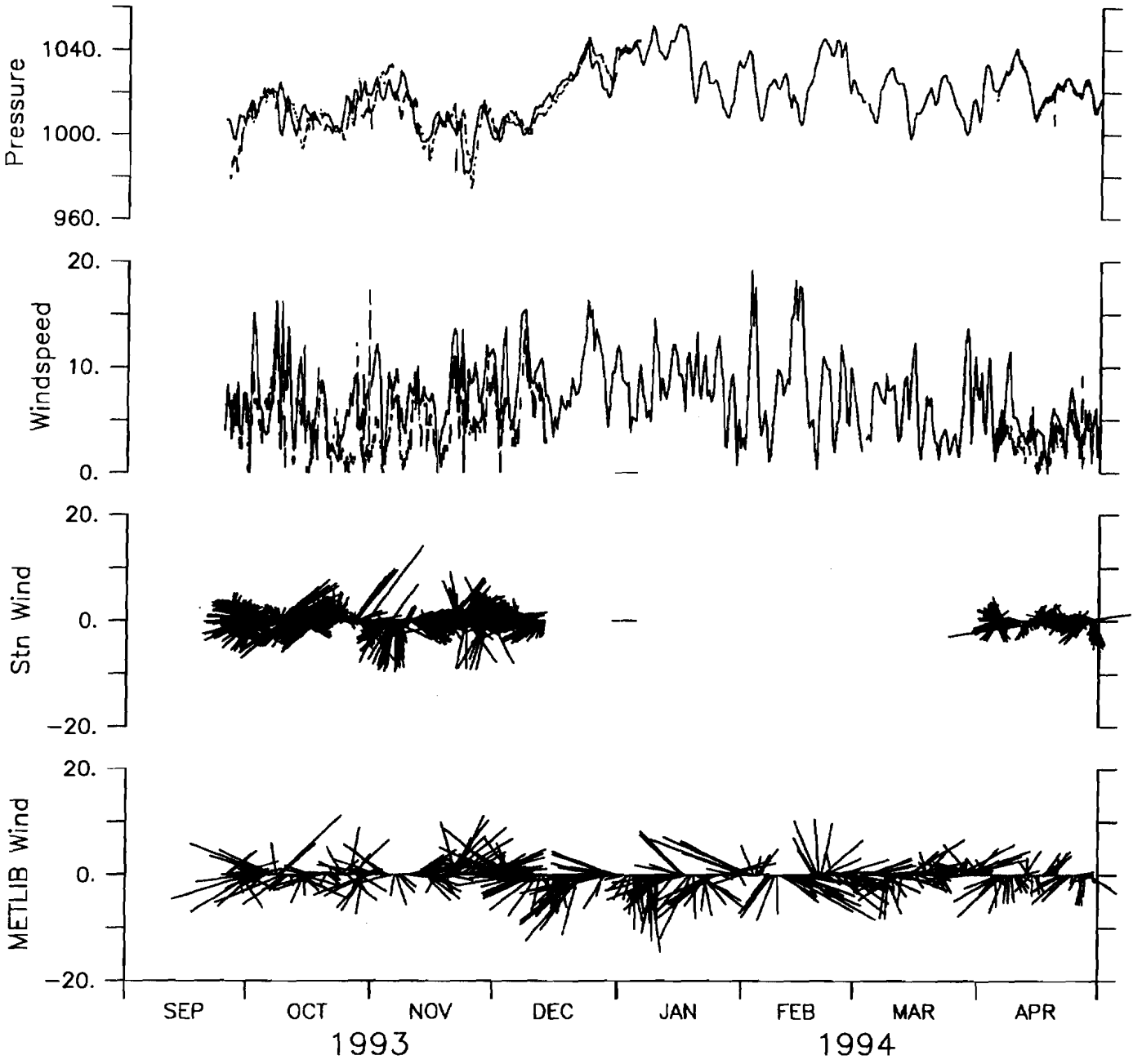

Pressure,Windspeed, and Windsticks, SIMI camp

Time series of the *in situ* SIMI buoy array extends from September 1993 through the spring and summer, 1994. SAR-derived deformation data is analyzed for the winter season, Day 22 to Day 74 in 1994, when the satellite was in a fixed orbit with a three day repeat (*Kwok, et.al.*, 1990; *Li, et.al.*, 1995). The SIMI project was fortunate that the ice camp moved under the satellite track in the middle of January 1994 and remained there through April.

Early fall 1993 was one of the minimum ice extents for the previous 20 years in the Beaufort Sea with 450 km of open water north of Alaska (Figure 6a). There was small and almost continuous shear and divergence during fall freeze-up in October, followed by nearly solid body motion until the first of February (Figure 6b) when large episodic events began and continued through April. This behavior is shown by the buoy displacements relative to main camp (Figure 7). The displacements varied in October and then were nearly constant until the end of January. According to these Joint Ice Center analyses, the Beaufort Sea did not have first year medium ice (70-120 cm) extending to the Alaskan coast until the end of January. We believe that large deformation and stress events were not possible until the ice strength had increased between the camp and shore, such that the coastal boundary participated in establishing the internal stress field (*Overland, et.al.*, 1995).

The first major event near the camp began about Day 32 with convergence with southerly winds against the perennial ice pack to the north of the SIMI camp, followed by slight divergence with northerly winds; with continued northerly winds the region of the ice from the camp to the shore converged and probably failed due to shear after Day 38. This behavior is shown both in the three day relative displacements in the buoy array (Figure 8) and in the SAR data (Figure 9). On Figure 8, the thickest arrow in the center is camp displacement, all other arrows are displacements relative to camp. The thinnest arrows are from ARGOS fixes, which are less consistent with the other buoys on the Day 38-41 figure. There was a second major event near Day 70. Results suggest a plastic nature of Beaufort Sea ice and the importance of coastal boundaries in establishing large values of shear deformation and the propagation of stress characteristics into the interior ice pack (*Pritchard*, 1988; *Erlingsson*, 1991).

Colony, R.L., and I.G. Rigor, 1993: *International Arctic buoy program data report for 1 January 1992-31 December 1992*. Tech. Memo. APL-UWTM 29-93, Seattle, WA, 215 pp.

Coon, M.D., D.C. Echert, and T.S. Knoke, 1992: Pack ice anisotropic constitutive model. IAHR Ice Symposium, Banff, Alberta, pp. 1118-1196.

Erlingsson, B., 1991: The propagation of characteristics in sea-ice deformation fields. *Annals of Glaciology, 15*, 73-80.

Hibler, W.D., III, 1979: A dynamic thermodynamic sea ice model. *J. Phys. Oceanogr., 9*, 815-846.

Karlsson, T., 1972: A viscoelastic-plastic material model for drifting sea ice. In: *SEA-ICE: Proceedings of an International Conference*, National Research Council, Reykjavik, Iceland, R.r. 1972-4, pp. 188-195.

Kwok, R., J.C. Curlander, R. McConnell, and S.S. Pang, 1990: An ice-motion tracking system at the Alaska SAR Facility. *IEEE Journal of Oceanic Engineering, 15*, 44-54.

Li, S., Z. Cheng, and W.F. Weeks, 1995: A grid based algorithm for the extraction of intermediate-scale sea ice deformation descriptors from SAR ice motion products. *Int. J. Remote Sensing*, in press.

Marco, J., and R. Thompson, 1977: Rectilinear leads and internal motions in the ice pack of the western Arctic Ocean. *J. Geophys. Res., 82*, 979-987.

6

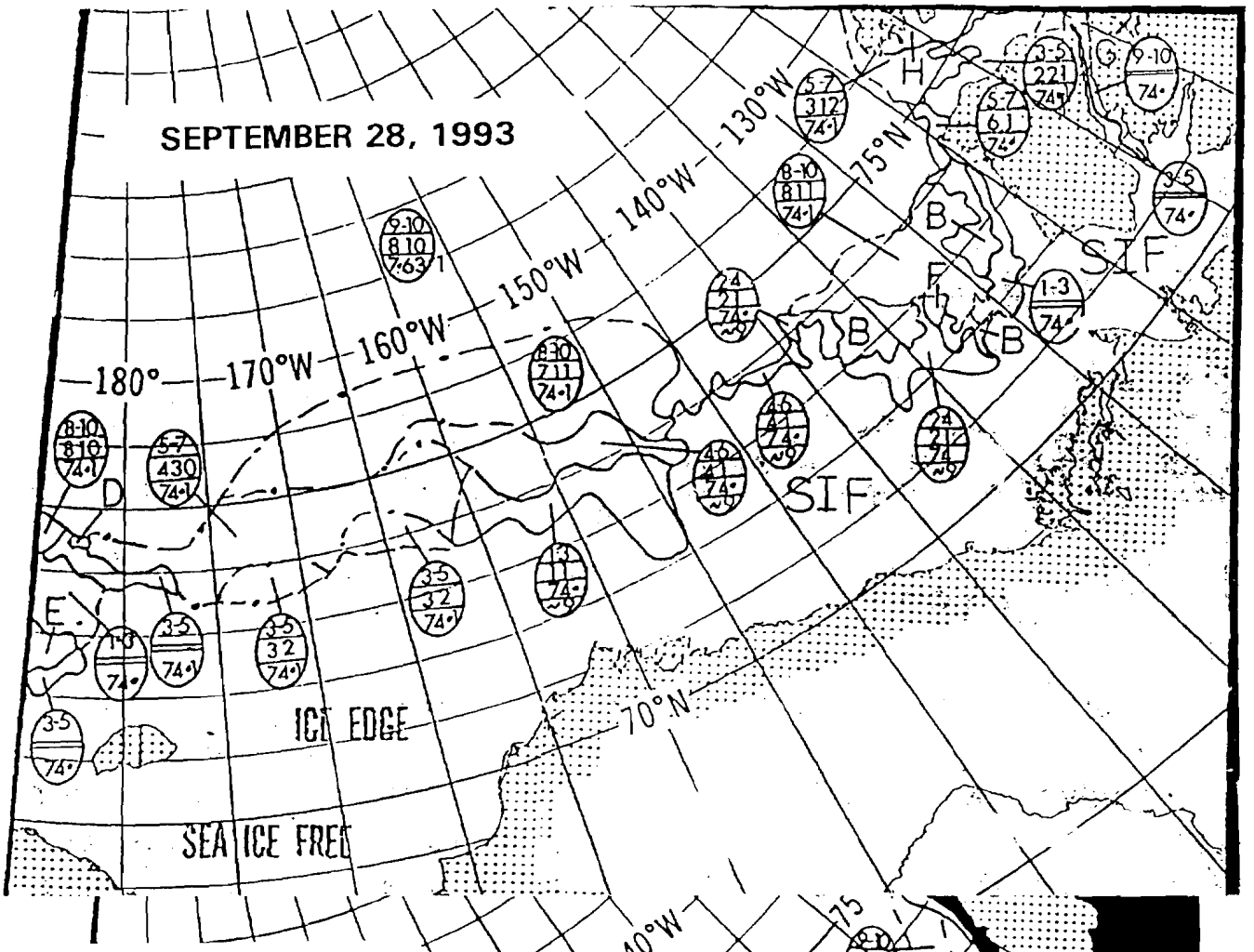

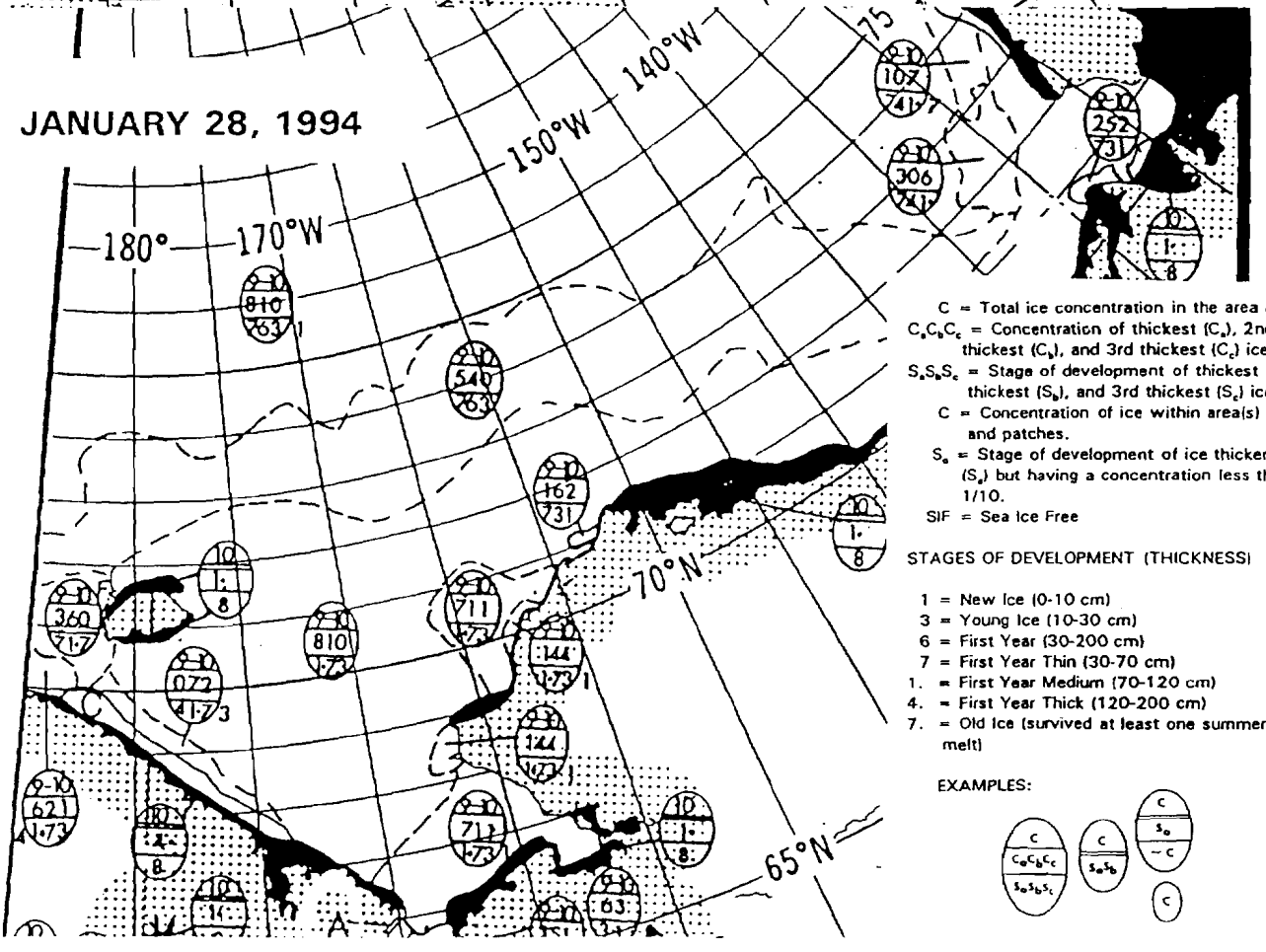

C = Total ice concentration in the area in tenths.

$C_aC_bC_c$ = Concentration of thickest (C_a), 2nd thickest (C_b), and 3rd thickest (C_c) ice

$S_aS_bS_c$ = Stage of development of thickest (S_a), 2nd thickest (S_b), and 3rd thickest (S_c) ice.

C = Concentration of ice within area(s) of strips and patches.

S_a = Stage of development of ice thicker than (S_c) but having a concentration less than 1/10.

SIF = Sea Ice Free

STAGES OF DEVELOPMENT (THICKNESS)

1 = New Ice (0-10 cm)
3 = Young Ice (10-30 cm)
6 = First Year (30-200 cm)
7 = First Year Thin (30-70 cm)
1. = First Year Medium (70-120 cm)
4. = First Year Thick (120-200 cm)
7. = Old Ice (survived at least one summer's melt)

EXAMPLES:

7

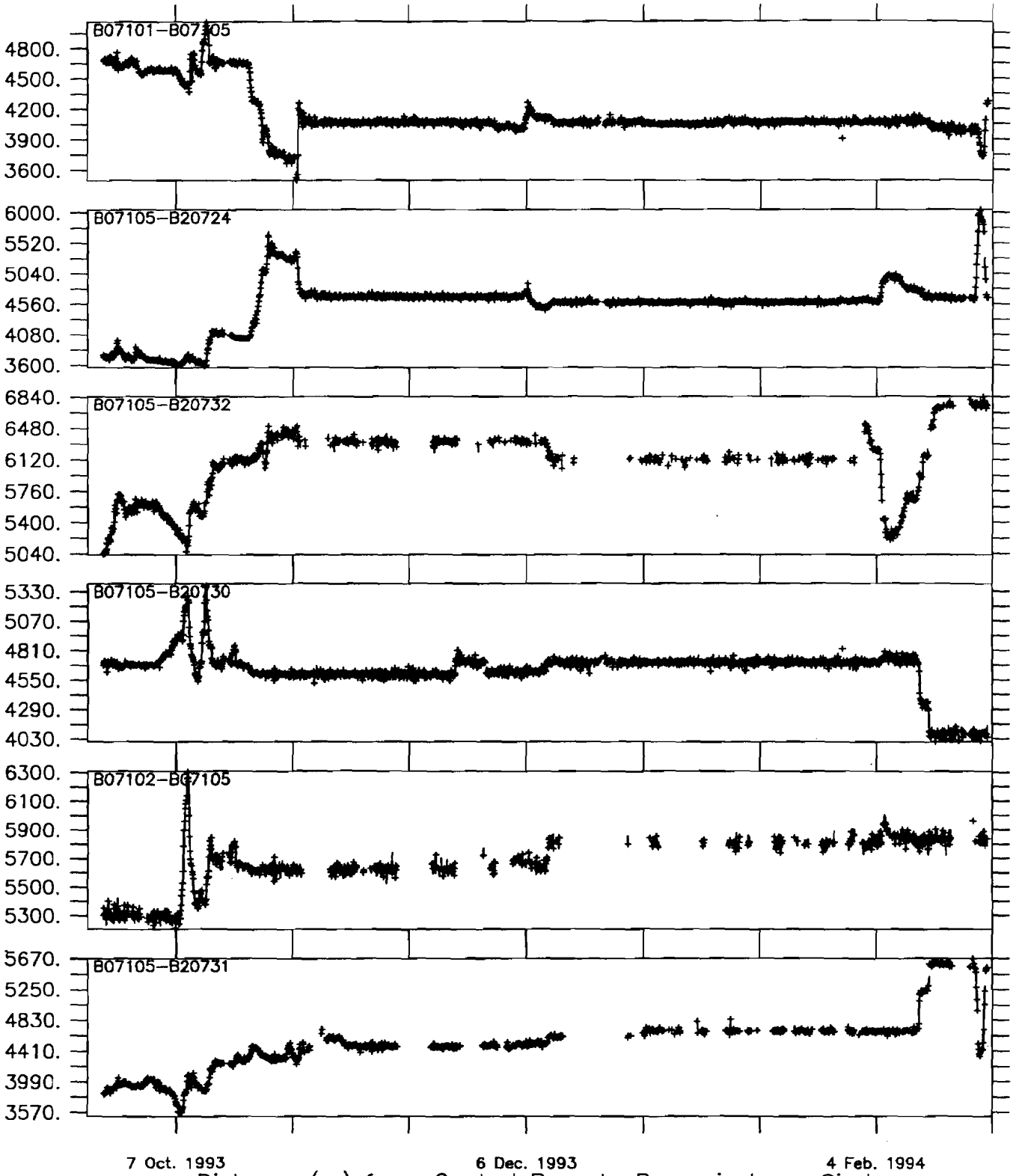

Distance (m) from Central Buoy to Buoys in Inner Circle

8

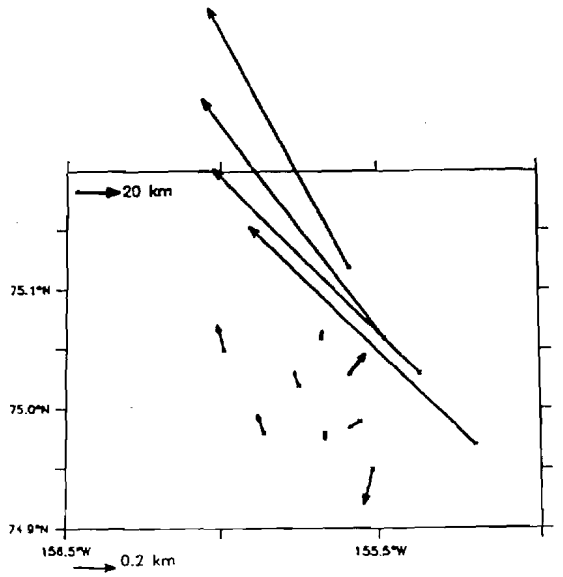

9403500–9403800 relative

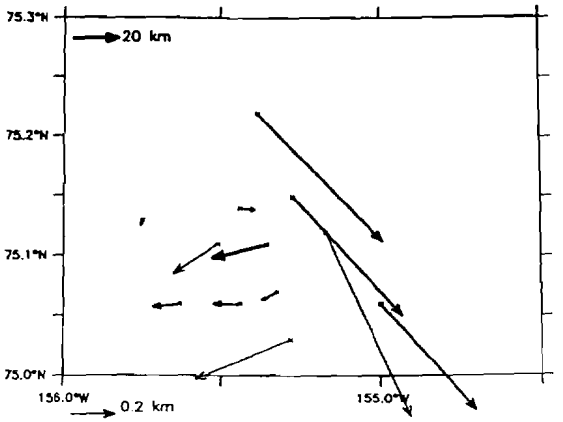

9403800–9404100 relative

9

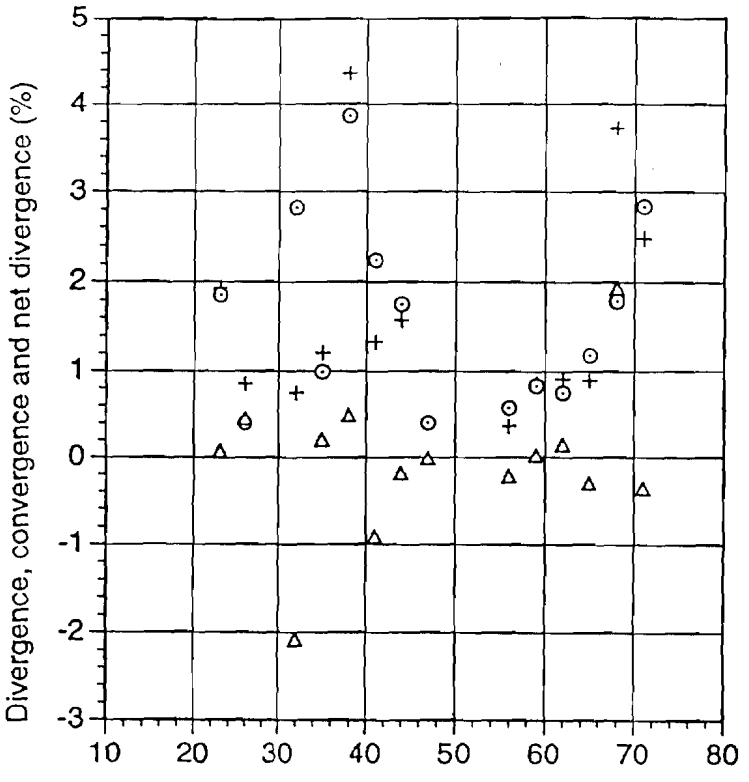

Swath Averaged Divergence, Convergence and Net Divergence

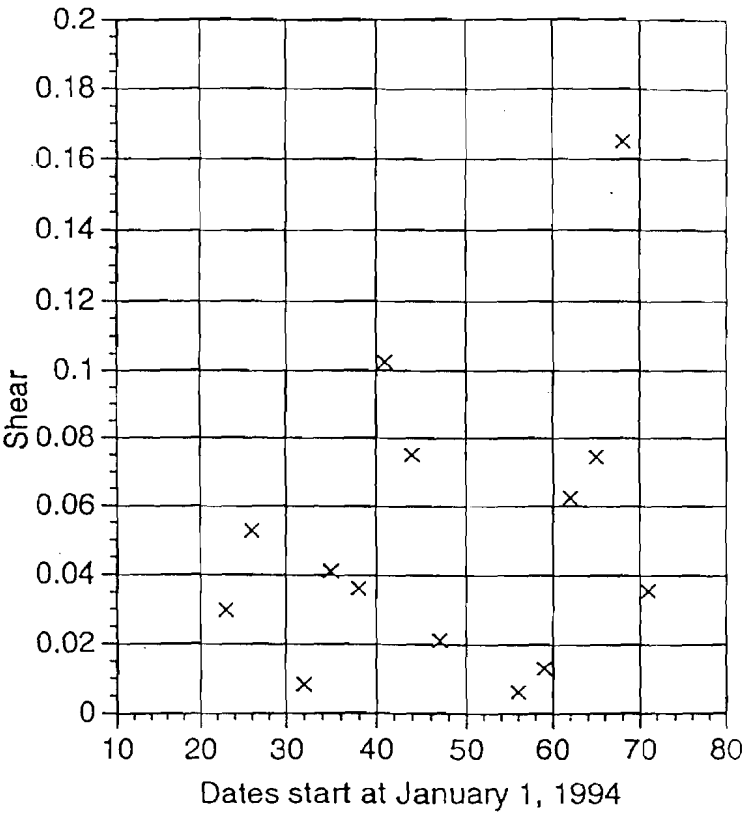

Shear near the Camp Site

Overland, J.E., B.A. Walter, T.B. Curtin, and P. Turet, 1995: Hierarchy and sea-ice mechanics: A case study from the Beaufort Sea. *J. Geophys. Res., 100*, in press.
Pritchard, R.S., 1980: Simulation of nearshore winter ice dynamics in the Beaufort Sea. In: *Sea Ice Processes and Models*, R.S. Pritchard ed., University of Washington Press, pp. 49-61.
Pritchard, R.S., 1988: Mathematical characteristics of sea ice dynamics models. *J. Geophys. Res., 93*, 15,609-15,618.
Pritchard, R.S., 1991: Large-scale lead patterns in sea ice. *Proceedings of the First Soviet-American Workshop on ice mechanics and its applications.*

Analysis and Publication Plans

We plan to compare regional atmospheric forcing to floe-floe deformation based on the buoys and regional deformation based on SAR observations. We take an event orient approach.

We plan to submit a paper to *JGR-Oceans* by early summer; "The seasonal cycle of ice deformation in the Beaufort Sea". We will also provide data support to J. Richter-Menge and work with the M. Coon group on "Validation of an oriented pack ice constitutive law with SAR, GPS and sea-ice stress measurements".

A list of recent publications relevant to SIMI are:

Overland, J.E., B.A. Walter, T.B. Curtin, and P. Turet, 1995: Hierarchy and sea-ice mechanics: A case study from the Beaufort Sea. *J. Geophys. Res., 100*, in press.
Overland, J.E., P. Turet, and A.H. Oort, 1995: Regional variations of moist static energy flux into the Arctic. *J. of Climate, 8*, in press.
Menge-Richter, J.A., and J.E. Overland, 1994: Relating arctic pack ice stress and strain at the 10 km scale. WCRP Conference on the Dynamics of the Arctic Climate System, Göteborg, Sweden, November 7-10, 1994.
Overland, J.E., and R. Colony, 1994: Geostrophic drag coefficients for the central Arctic derived from Soviet drifting station data. *Tellus, 46A*, 75-85.
Walter, B.A., and J.E. Overland, 1993: The response of lead patterns in the Beaufort Sea to storm-scale wind forcing. *Annals of Glaciology, 17*, 219-226.
Overland, J.E., B.A. Walter, and K.L. Davidson, 1992: Sea-ice deformation in the Beaufort Sea. Third Conference on Polar Meteorology and Oceanography, American Meteorological Society, Portland, OR, September 29 - October 2, 1992.

Pack Ice Stresses and their Relationship to Regional Deformation

Jacqueline A. Richter-Menge (P.I.), Bruce C. Elder, Walter B. Tucker III and Dr. Donald K. Perovich of the US Army Cold Regions Research and Engineering Laboratory (CRREL).

Scope of Model and/or Data Set

The overall goal of our research is to improve our understanding of the processes and forces involved in the deformation of sea ice. Towards that end, our objective in this program is to collect and analyze measurements of pack ice stress and couple them with ice deformation measurements and environmental forcing observations. Combined, these data sets can be used to directly obtain a large-scale ice rheology. Such a rheology is a central element of large-scale sea ice dynamic-thermodynamic models. This will lead to a more accurate assessment of the heat, mass and momentum balance of the Arctic ice pack, which is a critical component for examining the role of sea ice in global climate change. Another important application for this research is the determination of design ice forces for offshore structures and vessels.

The measurements we collected during the Sea Ice Mechanics Initiative (SIMI) main field experiment will provide insight on:

- the horizontal distribution of ice stress in a multi-year floe and its dependency on boundary and load conditions
- the relationship between the stress distribution in floes and the local strain field
- the large-scale rheology of sea ice
- the extent and magnitude of thermally-induced ice stresses

Instrumentation and data collection

In situ ice stresses were measured using the cylindrical, vibrating wire sensors described in Cox and Johnson (1983). The sensor consists of a stiff steel cylinder that is 25 cm long, 6 cm in diameter and has a wall thickness of 1.6 cm. The magnitude and direction of the principal stresses in the plane of the wires, which coincides with the horizontal plane of the ice, are determined from measurements of the radial deformation of the cylinder. Inside the cylinder three tensioned wires, separated by 60°, cross the diameter. Deformation is determined by plucking these wires with a magnet/coil assembly and measuring changes in the resonant frequency of each wire. Extensive calibration tests done on these sensors indicate an accuracy of better than 15% for principal stress magnitude and 5° for the direction. The sensors are also instrumented with an internal thermistor to measure the gauge temperature. This allows the stress data to be corrected for temperature effects.

Installation of the sensors in the ice is straightforward. A hole is cored through the ice sheet and the sensor is suspended in the void, locating the wire set at the

depth where stress measurements are desired. The orientation of the wire set, relative to a given datum, is also established and recorded so that the data on the direction of the principal stresses can be used effectively. Once the sensor is in place, the hole is backfilled with water, which freezes the sensor into the ice sheet. The fact that the sensor has frozen in completely is easily determined from the measured stresses. As the water freezes and expands, the sensor records a rapid and significant increase in pressure. These stresses then dissipate, typically within 48 hours. Accurate in situ stresses can be measured once the freeze-in stresses have attenuated.

All of our measurements were recorded and stored on site using battery powered dataloggers. In situ ice stresses were measured at 5 minutes intervals and the thermistor readings were recorded on the hour.

Equipment installation and recovery

A total of 35 sensors were deployed to measure in situ ice stresses. A summary of our deployment and recovery sequence is provided in Table 1. All but 6 of the

Table 1. Summary of instrument deployment and recovery.

Site Number	Location	Start date	End date	Number of stress gauges	Number of thermistors
1	Remote floes 1-6 (Map 1)	22 Sep 93	22 Mar 94	6	0
2	Harbor (Map 2, F1)	24 Sep 93	21 Mar 94	7	0
		25 Nov 93	21 Mar 94	1	
3	Bog (Map 2, H5)	27 Sep 93	30 Sep 93	7	0
		9 Oct 93	2 Dec 93	7	
		2 Dec 93	26 Mar 94	1	
4	Old Frontier (Map 2, A5)	28 Sep 93	3 Oct 93	7	0
		1 Dec 93	20 Mar 94	1	
4a	Frontier (Map 2, B5)	3 Oct 93	20 Mar 94	7	0
5	Center (Map 2, D4)	23 Sep 93	3 Apr 94	1	48
		29 Nov 93	3 Apr 94	2	
6	NWRA study site (Map 2, F4)	22 Nov 93	26 Nov 93	1	0
7	CRREL site (Map 2, E3)	16 Nov 93	25 Mar 94	2	28

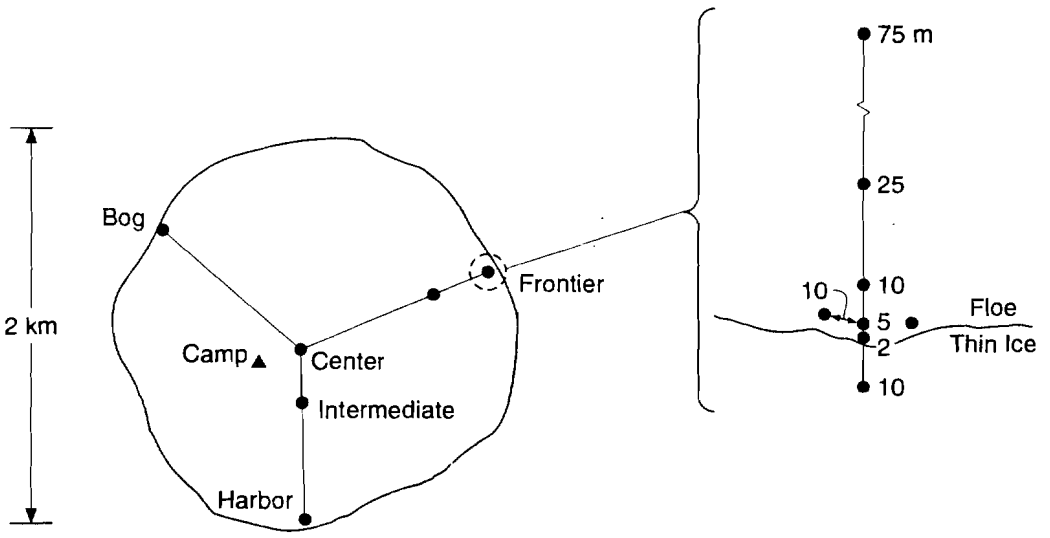

Figure 1. Stress sensor layout on center floe.

sensors were located on the central floe, shown in Map 1, which also served as the location for the SIMI West base camp. A majority of these sensors were installed during the first visit to the floe in late September 1993. During this phase of the deployment 7 sensors were located at each of the three edge sites: Harbor (Map 2, F1), Bog (Map 2, H5), and Old Frontier (Map 2, A5). At the Center site (Map 2, D4) a single sensor was installed along with a thermistor string that extended through the thickness of the floe. All of the stress sensors were located near the top surface of the floe at a constant depth below the water surface. The layout of the sensor groups, shown schematically in Figure 1, was designed to provide information on the attenuation of stresses from the edge of the floe to the center and the distribution of stresses along the boundary. Using the Center site as a point of reference, the edge sites were located 120° apart.

As a result of extensive ice deformation early in the measurement period, the sensors at the Bog and Old Frontier sites were moved. The sensors at the Bog site were moved back less than 50 m, to the new floe edge. The sensors at the Old Frontier site were moved back behind a continuous crack that had formed approximately 400 m from the original floe edge (Map 2, B5). This site was designated Frontier.

During the initial installation period, we also deployed sensors on 6 floes around the center floe. This part of our program was done in collaboration with Jim Overland, from NOAA Pacific Marine Environmental Laboratory (PMEL). The goal was to obtain coincident measurements of stress and deformation on a regional scale. The stress and deformation array consisted of two 6-buoy rings,

with position buoys placed in the center of multi-year floes spaced relatively evenly around each ring (Map 1). The rings were located at a 5 and 10 km radius from the center floe. A position buoy was also located on the center floe at the Center site. Positions of the of the buoys were measured using the Global Positioning System (GPS) and ARGOS. The stress sensors were coincidentally located with the position buoys on the inner ring (Map 1, Floes 1-6). As part of this effort PMEL also established a station on the center floe to measure winds, temperature and currents.

Additional installations took place in November 1993. In an effort to determine the ice stresses being transmitted to the central multi-year floe we deployed sensors in the thin ice immediately adjacent to the floe at the Bog and Harbor sites (Figure 1). Another sensor was deployed at the edge of the Old Frontier site.

In collaboration with Peter Stein, from Scientific Solutions, Inc., a new site was established near the runway (Map 2, E3) along the leg that ran from the Harbor to the Center site. Two sensors were deployed, one near the top and one near the bottom surface of the floe, in conjunction with a thermistor string that extended through the thickness of the floe. The objective was to monitor the stress and acoustic activity in the ice during thermal loading. The thermal load was applied to the ice by removing the snow cover over a 3 x 3 m area during a period when there was a significant and rapid drop in the air temperature. This site also provided us with an additional point for our investigation on the attenuation of stresses in the floe.

During the November phase of the field program we also participated in a joint effort with Max Coon, from Northwest Research Associates (NWRA), and Peter Wadhams, from the Scott Polar Research Institute (SPRI), to compare the stress measured by two different stress sensors and their relationship to measured small-scale strain. Stress was applied to the ice by an air-driven pneumatic flat jack. Both square wave and ramp loads of about 60 kPa above the ambient stress were applied. This test took place at the NWRA study area located on Map 2 at F4. Testing began after we established that our sensors had frozen in and the associated stresses had dissipated. Our measurements indicated that this process took 2-3 days. The loading tests were conducted over a two-day period.

Upon completion of the joint NWRA-CRREL-SPRI experiment, our sensor was removed from the ice and installed at the Center site at mid-depth. A third sensor was also installed at the Center site, near the bottom of the floe. Together these sensors provide data on the vertical distribution of stresses in the ice.

Prior to leaving the field in early December, a significant deformation event occurred, again, at the Bog site. Due to time constraints and equipment damage we were unable to redeploy the site a third time. One sensor was left operating near the new edge of the floe.

Our instruments successfully collected data until the end of March 1994, when we returned to the main SIMI camp to retrieve our equipment. The Center site was left operating after our departure in hopes that the sensors could be recovered during a cruise that took place that summer. Unfortunately, the ship track did not allow for this.

Findings to Date

Our data analysis efforts have been primarily focused on the center floe. The time history of in situ stresses over the six-month sampling period have been established for the Frontier, Harbor and Center sites. Qualitative comparisons of the stress records from these sites have been done. They suggest that at the edge sites, Frontier and Harbor, events of relatively high stress often occurred at the same time. While the signatures of the individual events were strikingly similar at these sites, the magnitude of the peak stresses were consistently higher at the Frontier site. Stresses measured at a 5-meter site at the Frontier, shown in Figure 2a, are representative of the stress time histories measured at the edge sites. From the beginning of the measurement period until Julian Day 320, the stress records showed little activity, with the exception of one isolated, 4-5 day event which started on Day 303. After Day 320 the presence of stress was relatively continuous. We believe that this transition marks the point at which the pack became consolidated and, therefore, began to respond to ice motion as a continuum.

A number of significant compressive stress events, with a magnitude of 100 kPa or more, were observed throughout the December-March period. The magnitude of these events are consistent with pack ice stress measurements reported in other studies (Tucker and Perovich, 1992; Comfort et al., 1992). While a quantitative determination of the characteristics of the stress events remains to be done, it appears they occurred on an average frequency of approximately 10 days. Their duration varied from 2 to 10 days. The maximum stress measured was 400 kPa. It occurred during an event in early December (Julian Day 332) at the Frontier site. The significant and rapid divergence of the major and minor principal stresses that is apparent in Figure 2a from Day 347 to 357 illustrates another characteristic of the stress records. Typically during period of low stress the direction of the principal stress varies widely. When the stress begins to increase, marking the beginning of a significant stress event, the direction becomes much more stable and pronounced.

We believe that the relatively high stresses marking these events represent a combined thermal and dynamic loading. This is suggested by the coincidence of significant changes in the sensor temperature (Figure 2b) and with the time of the events (Figure 2a). The high frequency signature of the stress is indicative of the dynamic, ice motion component.

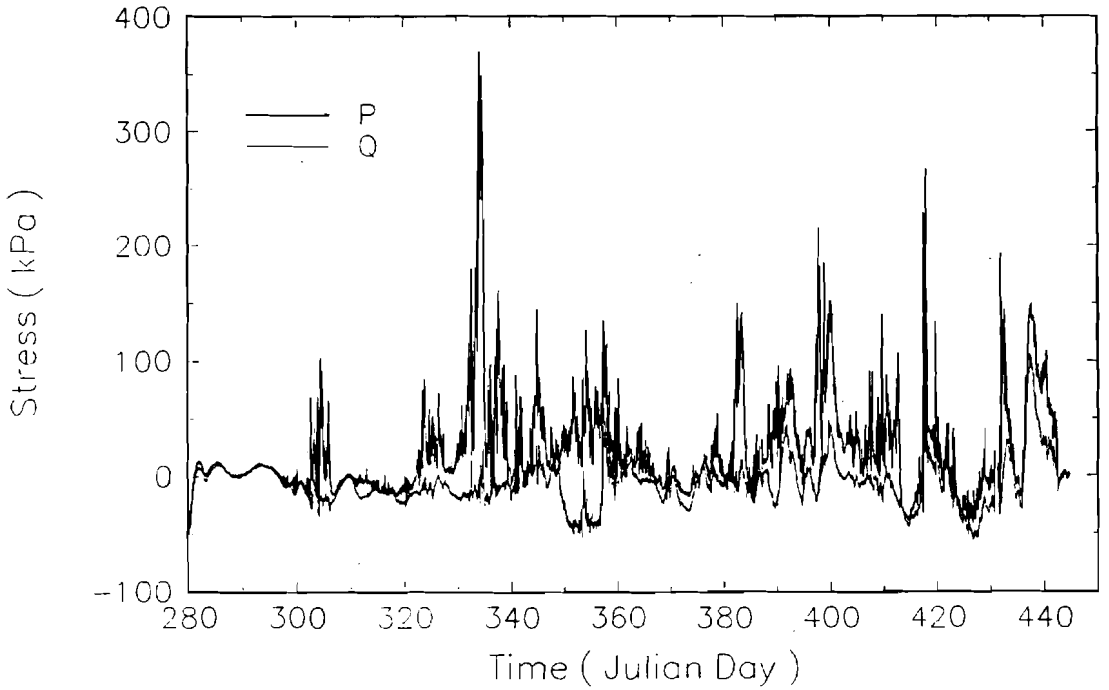

a. In situ ice stresses. P and Q are the major and minor principal stresses. Positive stresses are compressive.

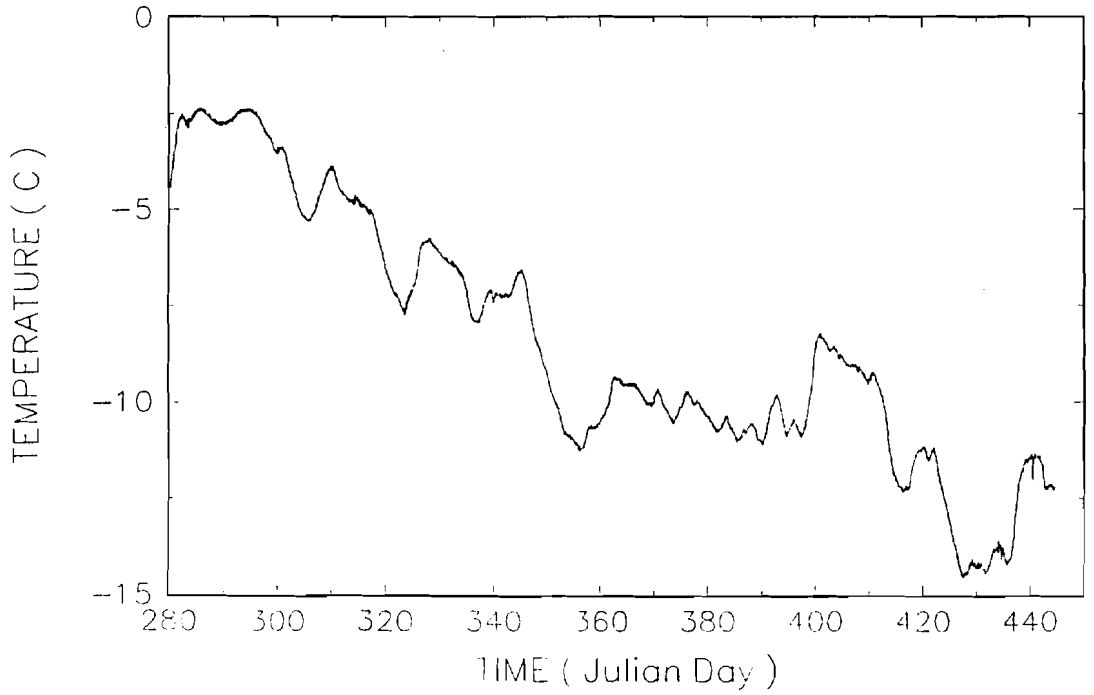

b. Sensor temperature, which corresponds to the ice temperature at a depth of 20 cm.

Figure 2. Time history, from 7 Oct 93 to 20 March 94, of in situ ice stress and sensor temperature at a site located near the edge of the main floe.

Another indication of the fact that the periods of relatively high stress are caused, in part, by ice dynamics is the correspondence we observe between the time of stress events and ice motion at the 10 km scale. Periods of ice motion were determined from data collected by the PMEL position buoys. For each of the 12 instrumented floes, shown on Map 1, a line was drawn from the middle of the center floe to the location of the position buoy. Cumulative changes in the length of these lines were determined using the relationship $(L-L_o)/L_o$, where L_o is the original line length and L is the line length at the time of measurement. A change

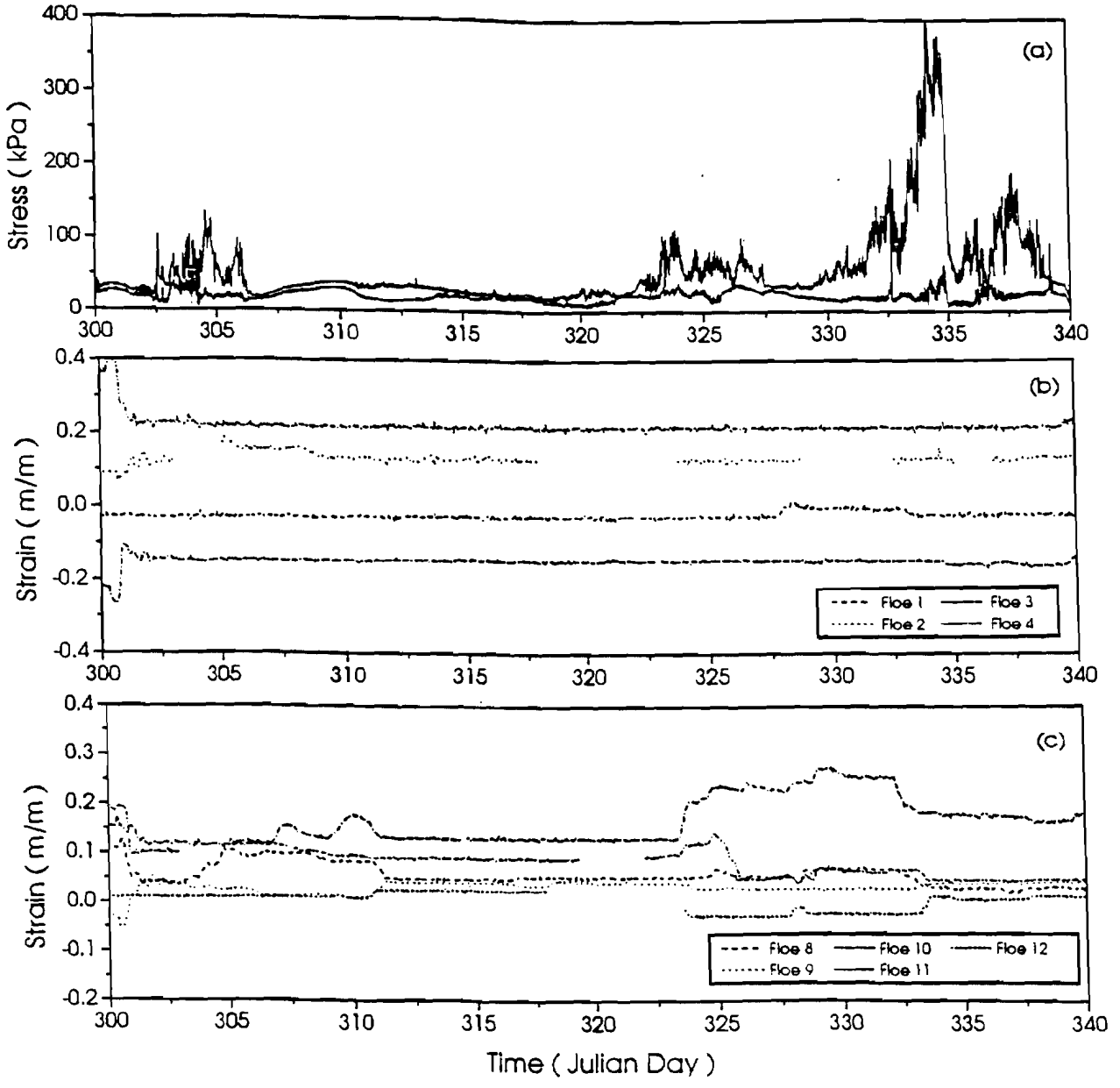

Figure 3. In situ ice stress at the edge of the center floe (a) and cumulative strain measurements from floes in the 5 km inner ring (b) and 10 km outer ring (c).

in any of the line lengths indicated ice motion, or 1-dimensional ice strain. Representative results from our initial analysis are shown in Figure 3. For consistency, the ice stress data is from the same sensor used in Figure 2. The period we have chosen to show, from Julian Day 300 to 340, is marked by significant stress events at its beginning and end, encompassing a relatively inactive period. Two sets of strains are presented: those measured from floes in the 5 km inner ring (Figure 3b) and those in the larger 10 km outer ring (Figure 3c). Correspondence between periods of ice motion and ice stress can be seen when comparing Figures 3a and 3c. Interestingly, the major stress events that are evident in Figure 3a are not at all apparent in the strain measurements from the buoys lying on the 5 km ring. This was typical of our results and is consistent with the suggestion of a number of investigators (Hibler, 1977; Thorndike, 1987; Overland et al., in press) that the 10 km scale is the lower boundary for considering the ice pack as a continuum. At smaller scales, the ice exhibits a behavior that is better explained as aggregate.

Comparison between the stresses at the Center site and the edge sites, Frontier and Harbor, indicate that there is a significant amount of attenuation in stress from the edge to the center of the floe. There is a good correspondence between the time and period of significant stress events measured at these sites. The magnitude of the stress during these events is an order of magnitude lower at the center of the floe than at the edges.

Analysis and Publication Plans

Analysis of our SIMI field data will continue with a focus on characterizing the pack ice stress. Specifically, we will quantify the frequency and magnitude of the pack ice stresses and their relationship to ice strain on this regional scale. Cross-correlation techniques will be applied to the stress and deformation data to confirm the scale effects, examine lead and lag functions, and establish the role of local meteorology. Much of this work will be done in collaboration with Jim Overland, PMEL. We will also use the data from the center floe to study the process of stress distribution in an ice floe; for instance, attenuation, boundary effects, and impact of variations in ice thickness.

We also plan to continue collaborative efforts initiated in the field with Peter Stein, Scientific Solutions, Inc., to investigate the role of thermal loading in the development of ice stresses and with Max Coon, NWRA, to compare the performance of our in situ stress sensors.

The following is a list of titles of publications that we plan to present at conferences and in journals:

- Characteristics of pack ice stresses
- Stress distribution in a multi-year floe
- Pack ice stresses and their relationship to ice strain on a regional scale

- The role of thermal loads in determining ice stress and fracture
- Performance comparison of two ice stress sensors and an ice strain sensor

Recent publications resulting from the SIMI program and relevant publications on models and equipment used during the SIMI program are:

"Relating Arctic pack ice stress and strain at the 10km scale," J.A. Richter-Menge, J.A., B.C. Elder, J.E. Overland and S. Salo, in *Proceedings of Conference on the Dynamics of the Arctic Climate System*, World Climate Research Programme, Goteborg, Sweden, 7-10 November, 1994.

"The tensile strength of first-year sea ice," J.A. Richter-Menge and K.F. Jones *Journal of Glaciology*, 39(133), pp. 609-618, 1993.

"Stress measurements in drifting pack ice,", W.B. Tucker III and D.K. Perovich, *Cold Regions Science and Technology*, 20, 119-139, 1992.

"Observations of stresses in Arctic pack ice," D.K. Perovich, K.F. Jones, and W.B. Tucker III, in *Proceedings of the 11th IAHR International Ice Symposium*, Vol. 2, 979-990, 1992.

"On the relationship between local stresses and strains in Arctic pack ice," W.B. Tucker III, D.K. Perovich, M.A. Hopkins, and W.D. Hibler III, *Annals of Glaciology*, 15, 265-270, 1991.

"Field Observations of stresses in young ice," D.K. Perovich and W.B. Tucker III, in *Proceedings of 10th International Conference on Offshore Mechanics and Arctic Engineering*, Vol. IV, 191-198, 1991.

References

Comfort, G., R. Ritch and R.M.W. Frederking (1992). "Pack ice stress measurements," in *Proceedings ASME Offshore Mechanics and Arctic Engineering Symposium*, Vol. IV, 245-253.

Cox, G.F.N. and J.B. Johnson (1983). "Stress measurements in ice," *Cold Regions Research and Engineering Laboratory*, CRREL Report 83-23, 31 pp.

Hibler, W.D. III (1977). "A viscous sea ice law as a stochastic average of plasticity," *J. Geophys. Res.*, 82: 3932-3938.

Overland, J.E., B.A. Walter, T.B. Curtin and P. Turet (in press). "Hierarchy and sea-ice mechanics: A case study from the Beaufort Sea," *J. Geophys. Res.*

Thorndike, A.S. (1987). "A random discontinuous model of sea ice motion," *J. Geophys. Res.*, 92(C6): 6515-6520.

Tucker, W.B. III and D.K. Perovich (1992). "Stress measurements in drifting pack ice," *Cold Regions Science and Technology*, 20, 119-139.

Tucker, W.B. III, D.K. Perovich, M.A. Hopkins and W.D. Hibler III (1991) "On the relationship between local stresses and strains in the Arctic pack ice," *Ann. Glaciol.*, 15:265-270.

6. MODELING

Papers included in this section are the following:

"Physically Based Constitutive Modeling of Ice," by Prof. Jerome Connor (P.I.), Mr. Alex Elvin, Mr. Dongho Choi, and Mr. Jinkoo Kim of the Massachusetts Institute of Technology and Dr. S. Shyam-Sunder (P.I.) of the National Institute of Standards and Technology

"Numerical Simulation of Arctic Pressure Ridging," by Dr. Mark A. Hopkins (P.I.) of the U.S. Army Cold Regions Research and Engineering Laboratory

"Sea Ice Mechanics Related to Thermally-Induced Stresses and Fracturing of Pack Ice," by Dr. James K. Lewis of Ocean Physics Res. & Dev. and Dr. Peter J. Stein of Scientific Solutions, Inc.

"Measurements of Crack Velocity in Sea Ice Using Electromagnetic Techniques," by Dr. Victor Petrenko (P.I.) and Mr. Oleg Gluschenkov of the Thayer School of Engineering, Dartmouth College

"Constitutive Equations and Fracture Models for Sea Ice," by Dr. Gregory Rodin (co-P.I.), Dr. Richard Shapery (co-P.I.), Mr. Khaled Abdel-Tawab, and Ms. Lu Wang of the University of Texas

"Physically Based Constitutive Modeling of Ice: Damage and Failure," by Mao S. Wu (P.I.), J. Niu, Y. Zhang, and H. Zhou of the Department of Engineering Mechanics, University of Nebraska-Lincoln

Papers with additional information on modeling in Section 2, Acoustics:

"Sea Ice Failure Mechanisms," by Robert S. Pritchard of IceCasting, Inc.

"Seismo-Acoustic Remote Sensing of Ice-Mechanical Processes in the Arctic," by Henrik Schmidt, Arthur B. Baggeroer, and Ira Dyer of the Massachusetts Institute of Technology and Keith von der Heydt and Edward K. Scheer of Woods Hole Oceanographic Institution

Papers with additional information on modeling in Section 4, Ice Properties:

"Crack Nucleation Mechanisms in Columnar Ice -- Recent Developments," V. Gupta (co-P.I.), R.C. Picu, J. Bergström, and H.J. Frost (co-P.I.) of The Thayer School of Engineering, Dartmouth College

Physically Based Constitutive Modeling of Ice

Prof. Jerome Connor (P.I.), Dr. S. Shyam Sunder (P.I.), Mr. Alex Elvin,
Mr. Dongho Choi, Mr. Jinkoo Kim.

Scope of Model and/or Data Set

RESEARCH OBJECTIVES

This research effort is concerned with understanding and modeling the mechanical behavior of ice for loading rates and dimensional scales representative of ice- structure interaction events. In particular, the focus is to develop a modeling strategy which is (i) based on fundamental understanding of the underlying physical mechanisms governing the deformation and failure of polycrystalline ice, (ii) capable of dealing with the evolution of cracking, and (iii) is computationally possible for full scale as well as heterogeneous micro- mechanical scales. It is well known that the behavior of ice is ductile and/ or brittle depending on temperature and loading rate. Separate modeling strategies are employed to capture the brittle and ductile regimes. Details are presented below.

MODELING METHODOLOGY– Brittle Behavior

In this section the loading rate is assumed to be fast enough and temperature low enough so that the behavior is predominantly linear elastic. At least three different scales have been defined in order to help understand the processes leading to, and the brittle failure of, polycrystalline ice. Each scale defines a level of resolution, and uses as input the information from the previous scale (see Fig. 1). In what follows each of these scales will be described and the modeling approach presented.

Scale Level I– A Few Grains

The modeling at the scale of a few grains attempts to explain the cause of microcracking that is observed in polycrystalline ice. Recent work (Picu, Gupta and Frost (1993), and Elvin and Shyam Sunder (1994)) has shown that the elastic anisotropy mechanism acting alone is not strong enough to produce microcracking observed in polycrystalline ice. Even if stress concentrators like air bubbles are included, the microcracks that result are too short when compared with experiments and the stresses required to nucleate these cracks are unrealisticly high (see Elvin and Shyam Sunder (1994) for details). Therefore some additional mechanism has to be present in order to induce microcracking observed in ice at the high loading rates.

Grain boundary sliding has been studied as a possible mechanism of microcracking in polycrystalline ice in (see Elvin and Shyam Sunder, 1994, Elvin and Shyam Sunder, 1995 and Elvin, 1995).The mechanism involves the relative slip of neighboring grains, i.e. neighboring grains are not rigidly connected to each other but grain boundary slip is allowed. This slip might be due to: (i) elastic effects such as a compliant grain boundary layer, or (ii) viscous behavior of the grain boundary– several investigators report a liquid like layer present on the grain boundary at temperatures higher then $-10°C$.

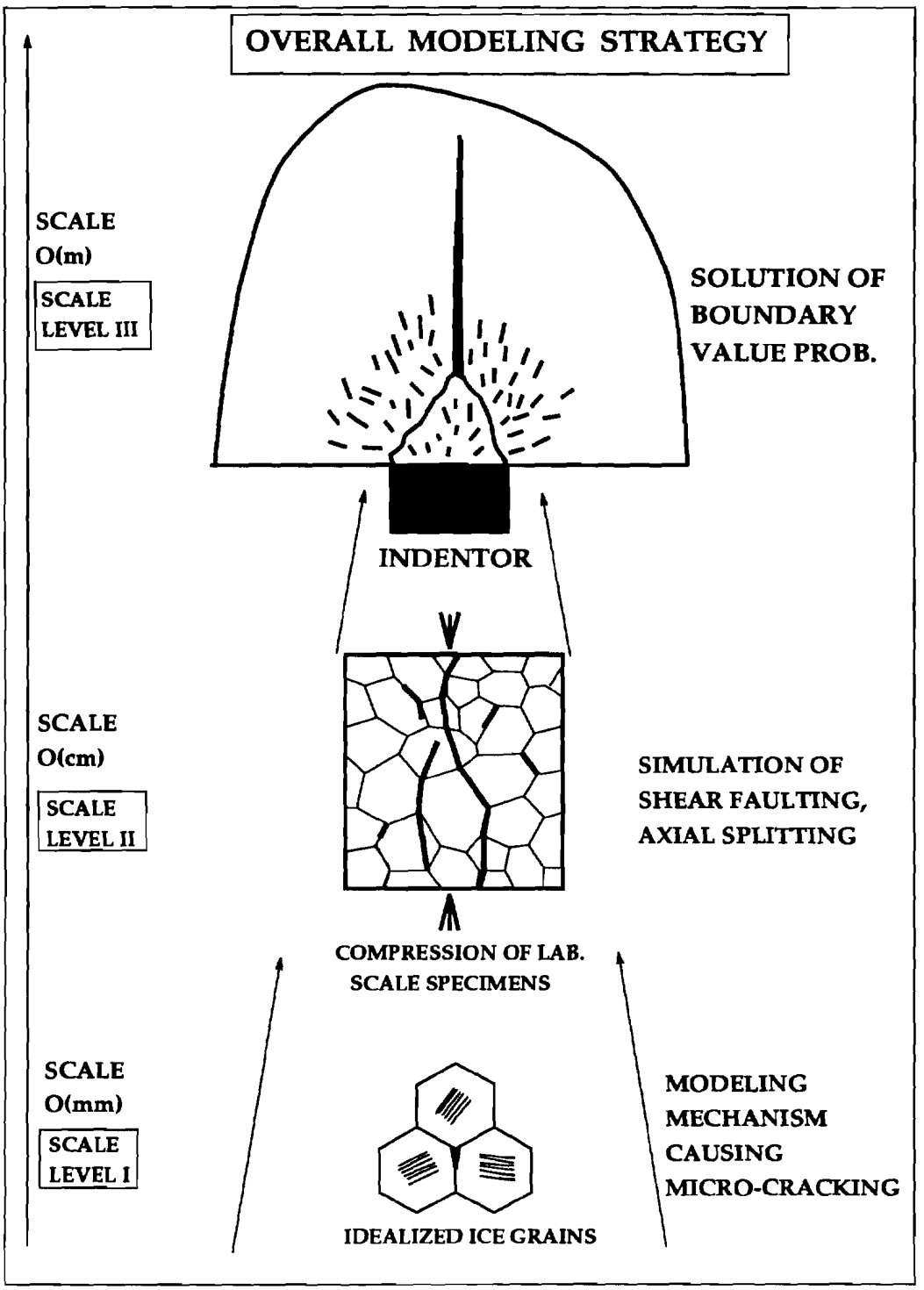

Figure 1: Global modeling strategy– Scale Level I, Scale Level II, and Scale Level III

The model of Scale Level I considers an unit cell consisting of three grains with *free* grain boundary sliding. Material effects such as grain anisotropy, shape, orientation and size on microcracking is studied. The finite element method is used to solve the unit cell model.

Scale Level II – Microcmechanical Modeling of the Representative Area Element

This scale level models an ensemble of randomly shaped polgynoal grains. The primary goal is to study the accumulation of microcracks. Two modeling approaches have been taken. The first model is based on the work of Wu, Shyam Sunder and co- workers– refered to as the discrete cracking model (DCM); the second approach deals with continuous microcracking processes, refered to as continuous cracking model (CCM).

The DCM approach assumes the existence of precursors at grain triple points. The microstructural stress field due to the elastic mismatch between neighboring grains is analyzed; different levels of accuracy in the analysis is considered. Precursors nucleate into microcracks of a pre- specified length when the maximum principal stress criterion is satisfied. Global failure is considered to occur when the stress field at the tip of one or more of the nucleated cracks satisfies the maximum principal stress criterion. The effects of strain rate and temperature are considered by using appropriate friction coefficients and fracture toughneses.

On the other hand the CCM approaches aims to track the nucleation, growth and coalescense of pre-existing defects into microcracks, and the subsequent coalescence of microcracks. This dynamic process of crack growth requires an accurate analysis of stresses in the heterogeneous medium, and a procedure for predicting the paths of the cracks. Approximate criteria such as the strength criterion (e.g. $\sigma \geq \sigma_c$) or plasticity like criteria (e.g. Mohr-Coulomb 'yield' surface) are possible candidates. However, these criterion lack the physical basis. Work is required to develop a comprehensive fracture criterion for crack nucleation, and path prediction. An important difference is that CCM does not require precursors; at any point in time there is a population of microcracks all differing in length. The underlying driving mechanism in CCM is assumed to be grain boundary sliding.

A critical issue for Scale Level II analyses is the choice of the number of grains contained in the representative volume element (or in the case of planar conditions a representative area element- RAE). To this end, numerical simulations of compression of polycrystalline ice samples with different number of grains has been performed. Two limiting cases have been considered: (i) a rigid grain boundary zone where no slip is allowed between grains, an (ii) free slip between grains.

Scale Level III – Mesoscale – Homogeneous Ice

On a scale containing a set of RAE, or on the global scale, materials can be considered as homogeneous. If the deformation causes no cracks, then modeling the ice on the mesoscale (a set of RAE) by substituting the polycrystal aggregate with an equivalent homogeneous material would produce accurate results. However, as soon

as microcracks form, leading to shear faulting/ axial splitting on the scale of the RAE, the appropriateness of a homogeneous material model becomes questionable. The failure process starts on the scale of a few grains (Scale Level I); microcracks grow and accumulate within the RAE (Scale Level II) and as soon as shear faulting or axial splitting occurs in the RAE the cracks become 'visible' on the mesoscale (Scale Level III). There are two types of cracks that are possible; Mode I cracks or cracks due to axial splitting on Level II and Mode II cracks which are shear faults on Level II.

The aim at this scale is to bridge the homogeneous material response and the zone around the local failure which has to be modeled as a heterogeneous aggregate (Level II). The challenge in Level III is the formulation of this heterogeneous to homogeneous transition. Figure 2 shows the heterogeneous, homogeneous, and transition zone for in plane indentation of a floating ice sheet.

MODELING METHODOLOGY– Ductile Behavior

In most engineering problems, ice exists at homologous temperatures exceeding 0.9. At these high temperatures, the creep of ice cannot be completely suppressed even at relatively high loading rates (strain rates exceeding $10^{-3}s^{-1}$) where creep and damage coexist. During ice- structure interaction in the ductile to brittle transition, ice is subjected to a non- monotonic vibratory loading as segments of the ice sheet crack. Experimental data on the cyclic behavior of ice, both under pure compression and reversed stress conditions, is starting to accumulate in the literature. The objective of this research is to develop a physically based constitutive model for ductile behavior capable to predict ice response both under monotonic and cyclic loading.

A physically-based constitutive creep theory is being developed in the continuum mechanics framework using the theory of internal state variables. Two internal state variables are employed to represent isotropic and kinematic hardening. Isotropic hardening is associated with dislocation structures which are induced by external loads; kinematic hardening is due to creep anisotropy of ice crystals. The motions of dislocations are described by using "average" internal stresses resulting from hardeing processes and temperature dependent dislocation drag. In polycrystalline ice, internal stresses are distributed due to variation in basal plane orientation. New evolution equations for the two internal state variables are proposed to describe creep anisotropy and the changes in the microstructures associated with the evolution of dislocation density.

At relatively small anelastic strains, the effects of the internal stresses and their distributions are taken into account by distributing relaxation times. Evidence for this distribution is provided from the data of Cole (1993). Our model uses the Gaussian distribution of relaxation times, to account for the measured loss compliance. The model parameters are obtained from the experiments of Cole (1993).

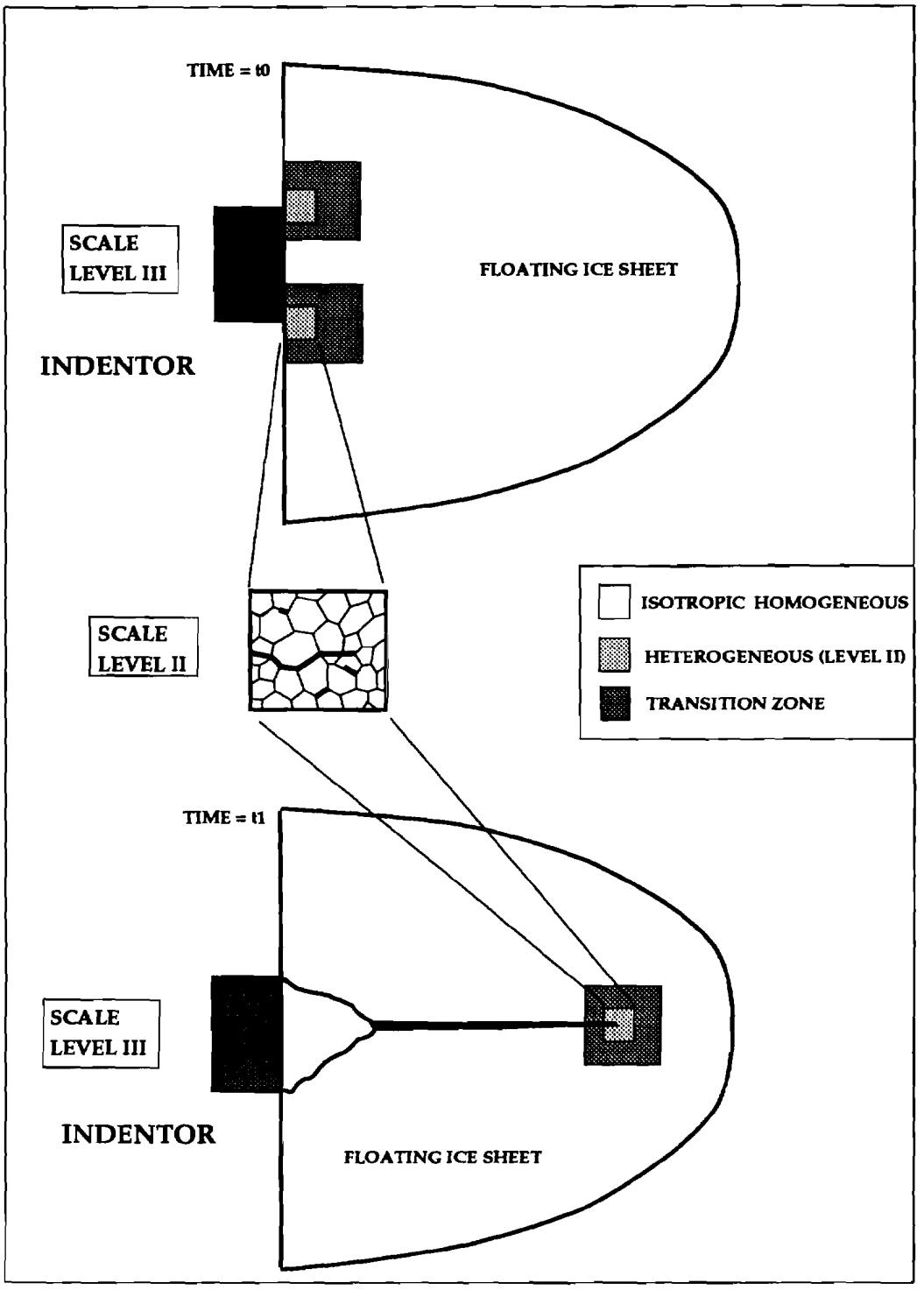

Figure 2: Homogeneous, heterogeneous and transition zone in Scale Level III

Findings to Date

Brittle Behavior

Scale Level I– A Few Grains

- If no grain sliding takes place, and only the elastic anisotropy mechanism operates, the stresses required for microcrack nucleation and growth are unrealisticly high compared to experiments; the resulting microcracks are also too short.

- Simulations show that by allowing grain boundary sliding, a defect originating at the triple point grows stably, reaches a critical length and then propagates unstably to the neighboring triple point. This is shown in Fig. 3 where the stress Σ required to propagate a microcrack is plotted versus the microcrack length l. The microcrack is located along the grain facet (of length a). The variation of the grain anisotropy, given by the parameter ζ, is also shown. Note, first the stress increases (stable crack growth). reaches a peak and then decreases (unstable crack growth). Thus microcracks as long as the facet length can be realized.

- With grain boundary sliding, the origin of the defect is not critical; examples of a defect could be an air bubble or a decohesion pocket.

- The stress causing microcrack growth is found to be inversely proportional to the square root of the grain size.

- The results agree qualitatively with experimental data; as expected, the assumption of *free* grain boundary sliding causes an under prediction of microcrack nucleation stresses.

These results are documented in:
(1) Elvin, A., and Shyam Sunder, S. (1994) Microcracking Due to Grain Boundary Sliding in Polycrystalline Ice Under Uniaxial Compression, *Submitted to Acta Metallurgica et Materialia*
(2) Elvin, A., and Shyam Sunder, S. (1995) Microcracking Due to Grain Boundary Sliding in Polycrystalline Ice Under Compression, *To Appear in Ice Mechanics -'95, ASME- AMD*, June 28-30 1995, UCLA.
(3) Elvin, A., (1995) Microcracking Due to Grain Boundary Sliding in Polycrystalline Ice Under Biaxial Compression, *In Preparation*

Scale Level II – Microcmechanical Modeling of the RAE

- The RAE was found to contain 230 grains from direct finite element simulations. The probabilistic distribution of stress components at the grain centers is approximately Gaussian in nature. The average computed homogenized Young's modulus and Poisson ratio at $-16°C$ is: 9.58 GPa and 0.33- with no grain boundary sliding; 7.83 GPa and 0.45- with free grain boundary sliding.

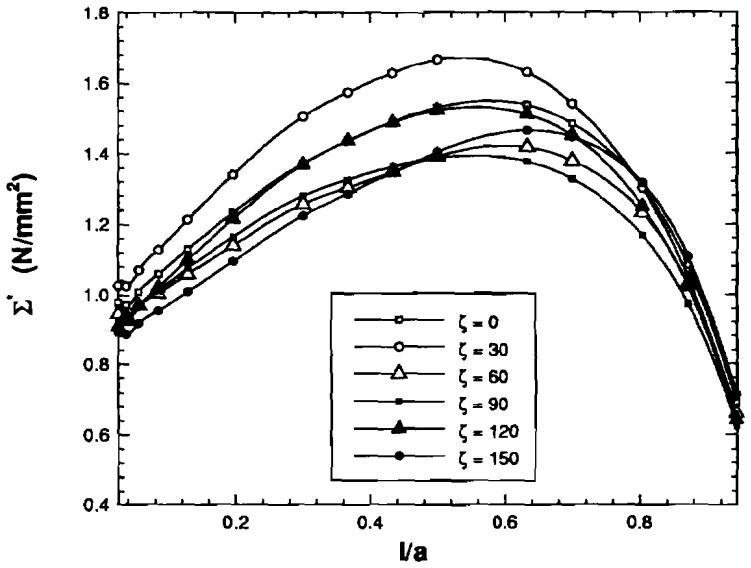

Figure 3: Variation of applied compressive stress, Σ^* with normalized microcrack lengths for various grain orientations; after Elvin and Shyam Sunder (1994).

- Failure stress predicted by the DCM model is in good agreement with experimental data for various grain sizes, strain rates and temperatures- see Fig. 4.
- The probabilistic distribution of failure stress and compliance caused by a statistical variation of the grain size, precursor length and crystalographical orientation was generated by the DCM approach. The 10 to 90th percentile of the distribution function of the calculated failure stress captures most of the scatter in experimental data. The 10 to 90th percentile of the compliance show that the range of distribution increases when the microstructural parameters are more scattered and skewed. The damage accumulation in the columnar $S3$ ice can be predicted by applying the non-uniform distribution of the $c-axes$ orientation.
- The effect of specimen size on the failure stress of polycrystalline ice was examined using a DCM approach. The failure stress is found to be inversely proportional to the square root of the grain size. Using different grain geometries having the same mean grain size, leads to a scatter in the calculated failure stress. The critical crack density at the calculated failure increases with decreasing specimen size.

These results and the details of the models used, are documented in:
(1) Elvin, A., (1995) Number of Grains Required to Homogenize Elastic Properties of Polycrystalline Ice, *Submitted to Mechanics of Materials.*
(2) Shyam Sunder, S., Kim, J., and Connor, J.J., (1995) Prediction of Brittle Failure Strength of Ice Using a Microstructural Model, *In Preparation.*

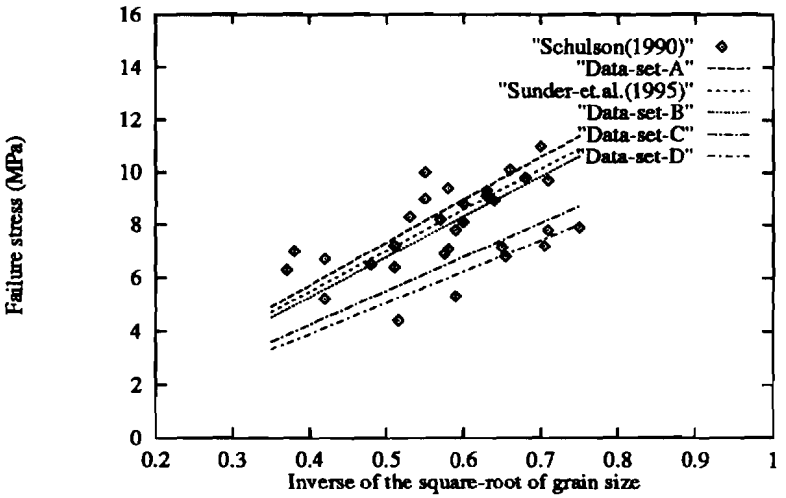

Figure 4: Calculated failure stress for four different grain geometries (A, B, C, D) versus $d^{-0.5}$; experimental data of Schulson (1990) also shown

(3) Shyam Sunder, S., Kim, J., and Connor, J.J., (1995) Statistical Effects on the Evolution of Elastic Moduli and the Fracture Stress of Ice, *In Preparation.*
(4) Kim, J., and Connor, J.J., (1995) Modeling of Brittle Failure of Ice and Specimen Size Effect, *In Preparation.*

Ductile Behavior

Creep Response Under Cyclic Loading

A model for relatively low anelastic strains, on the order of 10^{-4}, and for cyclic loading has been developed. The model predictions are compared with the cyclic experiments of Cole (1990) in Fig. 5. The following stress levels are considered: 0.6 , 0.8 and 1.0 MPa, at the loading frequencies of 0.01, 0.1 and 1 Hz. The comparison shows that the model adquately predicts the frequency dependence at low strains where no significant changes are observed in the microstructures.

The normalized data generated from the constant stress experiments of Mellor and Cole (1982), when plotted as strain rate versus time, shows considerable scatter. It is believed that the scatter is due to microcracking, and furthermore this mechanism enhances the creep rate during the primary creep. A more comprehensive creep model which incorporates the effects of microcracking, needs to be developed.

(1) Choi, D.H., and Connor, J.J. (1995) Constitutive Model of Transient Creep Model in Polycrystalline Ice Under Cyclic Loading, *In Preparation.*
(2) Choi, D.H., and Connor, J.J. (1995) Physically-Based Constitutive Model of Transient Creep model in Polycrystalline Ice, *In Preparation.*

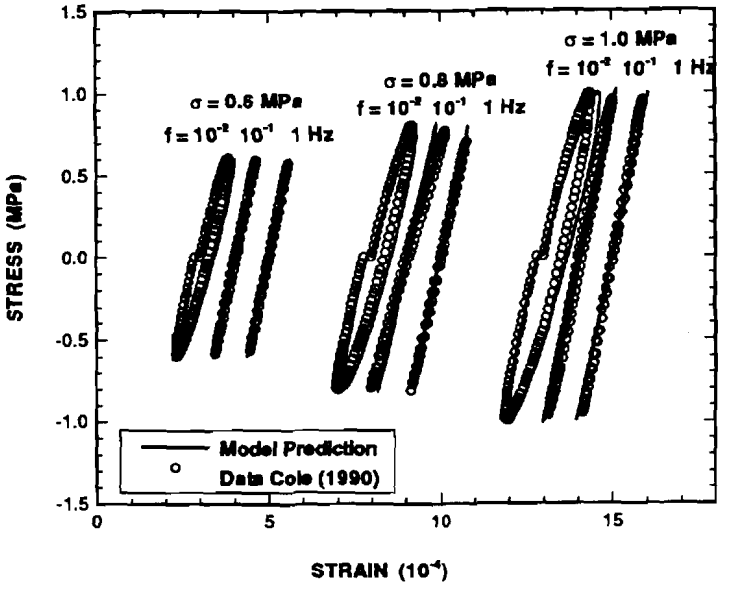

Figure 5: Stress strain response of polycrystalline ice under cyclic loading at various stress levels and frequencies; experimental data of Cole (1990) and model predictions are plotted.

Analysis and Publication Plans

This section describes our future modeling plans. The main emphasis in the brittle behavior regime will be on Scale Levels II and III.

Brittle Behavior

Scale Level I – A Few Grains

- More accurate modeling of grain- grain interaction. Improve on the assumption of *free* grain boundary sliding.
- Simulate microcracking with new model and compare predicted results with experimental data,qualitatively.

Scale Level II – Microcmechanical Modeling of the RAE

- Develop a fracture mechanics based crack propagation criterion– crack path analysis.
- Validate the crack path analysis.
- Simulate microcrack growth and coalescence; the aim is to predict shear band formation and axial splitting.

Scale Level III

Micro- to Macro- Scopic transition zone to analyzed multiscaled boundary value

problems. Theoretical formulation and computational procedures.

Ductile Behavior

- A physically-based creep model which accounts for damage will be developed. The evolution equations associated with generation and movement of dislocations and microcracking will be developed. Particular emphasis will be placed on the influence of microcracking on creep.
- Extensive numerical simulations will be carried out to provide a comparison with experimental data.
- Once a valid constitutive theory has been established a computational algorithm will be developed and applied to a set of boundary value problems.

Numerical Simulation of Arctic Pressure Ridging

Dr. Mark A. Hopkins (P.I.) USACRREL

Scope of Model

The goals of this project have been to construct a realistic computer model of the pressure ridging process and to use the model to develop a better understanding of the mechanics and energetics of the ridging process. The ridging model is based on a concept of ridge growth in which an intact sheet of thin ice is driven against a thick ice floe. The key assumption is that the ice sheet breaks in flexure. The brief description of the ridging model that follows is excerpted from Hopkins (1994).

Structure of the Model -- The pressure ridging model is based on the discrete element technique in which a computer program is used to explicitly model the dynamics of a system of discrete blocks. The important features of the ridging model are: a dynamic linear viscous-elastic model of a floating ice sheet; flexural failure (including buckling) of the ice sheets; blocks broken from the parent sheet at points where tensile stress exceeds strength; secondary flexural breakage of rubble blocks; inelastic contacts between rubble blocks; frictional sliding contacts between blocks; separate friction coefficients for submerged and above water contacts; buoyancy of the ice sheets and rubble; and water drag.

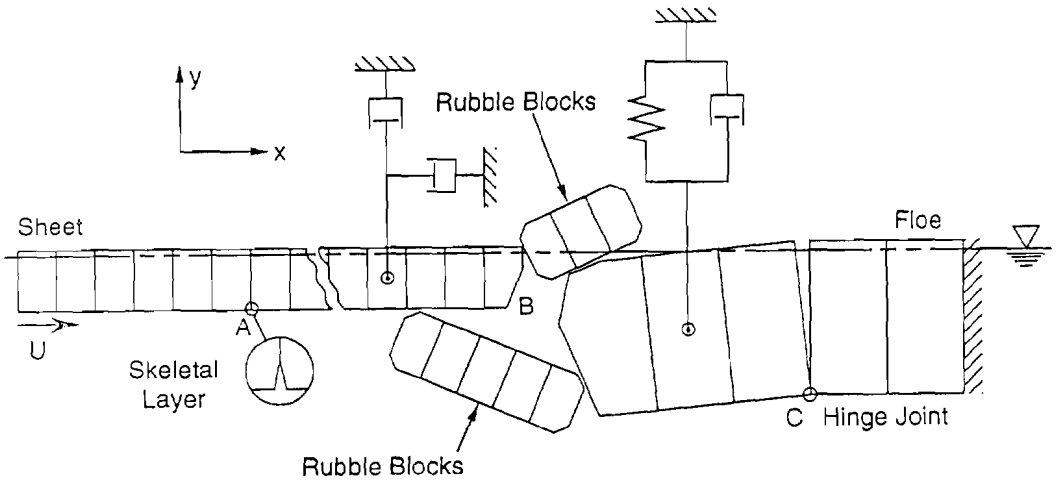

Figure 1: Discretization of the floe and lead ice sheet into uniform rectangular blocks; showing the boundary conditions on the lead ice sheet and floe. A skeletal layer is modeled by terminating the viscous elastic joint between adjacent blocks (point A). The tip of the sheet is bevelled (point B) to facilitate override. The pin joint (point C) constrains the motion of a broken floe.

The general structure of the model is shown in Figure 1. The thin ice sheet and rubble blocks, broken from the sheet, are composed of single rows of uniform, rectangular blocks that are attached to neighboring blocks by viscous-elastic joints. Relative displacements between adjacent blocks create forces and moments, internal to the sheet and rubble blocks, that act on the individual, component blocks. The internal forces on the component blocks are added to external forces exerted by the surrounding ice rubble, gravity, and buoyancy. When the tensile stress in a joint at either surface of the sheet or a rubble block exceeds the specified strength, the joint is broken. The block created by the fracture becomes part of the rubble and is added to the ridge structure.

Temperature and salinity gradients are present in an ice sheet because the top surface is exposed to air and the bottom surface is submerged. These gradients produce a variation in the stiffness and tensile strength through the sheet. This variation is qualitatively modeled by using an elastic modulus that varies linearly through the sheet and separate values of the tensile strength at the top and bottom surfaces. In addition, there is a weak layer of extremely saline ice, several centimeters thick, at the bottom surface of an ice sheet. The saline layer is modeled by terminating the viscous-elastic joint between the rectangular blocks several centimeters above the bottom surface as shown at A in Figure 1.

Contact forces between rubble blocks, between rubble and sheet, or between sheet and floe use a different force model that supports no tensile force. Two blocks are defined to be in contact if the polygons defining their shapes intersect. The force between two intersecting blocks is calculated in a local coordinate frame with axes normal and tangential to a contact surface connecting the intersection points. The force acts at the centroid of the area of intersection. A viscous-elastic normal force model is used with a Coulomb friction, tangential force model. The internal forces and moments at each joint in the ice sheet and rubble blocks and the external, contact forces between blocks are calculated at each time step. Equations of motion, derived from a Taylor series expansion about the current time, are used to find the updated positions and velocities.

Experiments on Ridging Energetics --Each experiment begins with a thin sheet of intact lead ice pushed at a constant speed against a thick floe. A random variation (±1%) in the elastic modulus at each joint in the thin ice sheet was used to create unique outcomes in experiments using the same initial configuration of ice and parameters. This small variation was sufficient to produce the chaos inherent in the ridging process causing the experiments to diverge noticeably by the time several blocks had been broken from the parent sheet. The results of sets of seven or more experiments, using the same parameters, were averaged to remove the large variability between individual ridges. The range of parameters used in the experiments are listed in Table 1.

Table 1. Parameters used in the ridging simulations.

Parameter	Value
floe thickness	2 m
ice sheet thickness	20,25,30,35,40,45,50,60 cm
ice sheet speed	6.25,25 cm/s
elastic modulus	100 MPa
ice tensile strength (top)	700 kPa
ice tensile strength (bot)	350 kPa
ρ_i (ice density)	920 kg/m^3
ρ_w (water density)	1000 kg/m^3
above water friction	0.4,0.6,0.8.1.0
under water friction	0.3,0.6

Experiments on the Evolution of the Average Ridge Profile -- A second goal of the project has been to model the evolution of the average pressure ridge profile. Average ridge profiles were constructed by sampling ridge profiles (see Figure 3) at uniform intervals during individual experiments. Each profile was partitioned into 25-cm-wide vertical sections. The maximum elevation and draft of ice in each section was calculated. The difference or thickness in each section was averaged by section and time over 200 experiments. The evolution of the average profile was measured in terms of the volume (thickness times length) of ice pushed into the ridge. The average ridge profile defines the change in the local ice thickness distribution in an area surrounding a single pressure ridge.

Modeling Ice Pile-Up on an Inclined Ramp -- Ice pile-up or ride-up occurs when an intact ice sheet is pushed up an inclined surface such as a beach, river bank, or offshore structure. The forces exerted by the ice are of interest in the design of protective structures. Physical experiments were performed in the 36 m by 9 m refrigerated basin at the CRREL Ice Engineering Facility. An intact sheet of urea doped ice was pushed against an inclined ramp moving with constant speed. The ramp, shown in Figure 2, was suspended from a movable carriage by load cells. Slots were cut in the ice sheet, ahead of the ramp, leaving a 25 m long strip of ice slightly narrower than the 120 cm width of the ramp. The end of the ice sheet opposite the ramp was left attached. Walls, 30 cm in height, attached to the sides and upper end of the ramp were used to confine the ice pile. Following each experiment, a grid placed above the pile was used to measure the three-dimensional relief of the top surface of the pile. The experiments were designed to measure the forces exerted by the ice on the ramp, the total energy expended, and the potential energy of the final pile. By comparing the potential energy in the final pile to the total energy expended, a measure of the energy dissipation was obtained.

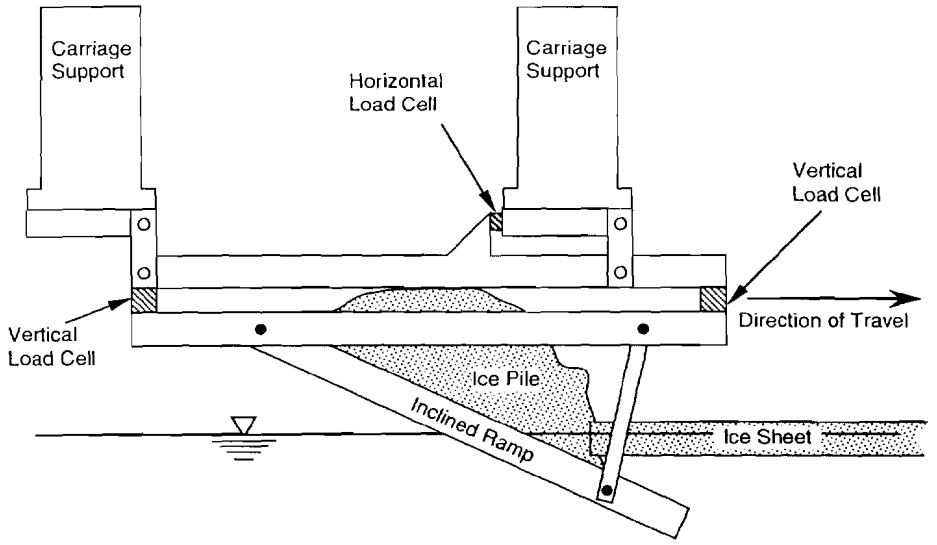

Figure 2. Diagram of the experimental apparatus consisting of a moving, inclined ramp and a stationary ice sheet.

The experiments used 1% urea doped model ice. The dimensions and material properties of the ice sheet and the dimensions of the ramp used in the experiments are listed in Table 2.

Table 2. Dimensions and properties of the ice sheet and ramp.

Parameter	Value
ice sheet width	120 cm
ice sheet thickness	4 cm
ice sheet speed	10 cm/s
characteristic length	50 cm
ice tensile strength (top)	100 kPa
ice tensile strength (bot)	50 kPa
ρ_i (ice density)	920 kg/m^3
ρ_w (water density)	1000 kg/m^3
ramp slope	25.6°

An analogous set of numerical experiments or simulations, using a discrete element computer model based on the ridging model described above, are in progress. The apparatus dimensions, ice dimensions, and ice properties used in the numerical experiments were taken from the physical experiments.

Findings to Date

Experiments on Ridging Energetics -- The energetics of the pressure ridging process depend on various parameters such as the speed, thickness and

modulus of the ice sheet and the coefficient of friction between blocks. The sensitivity of the ridging simulation to these various parameters is discussed in Hopkins (1994). The results of experiments using the numerical ridging model have shown that the ridging process can be divided into four phases. The first phase begins with an intact sheet of relatively thin ice impacting a floe and ends when the maximum sail volume is reached. In the second phase the ridge keel maintains a triangular shape, deepening and growing in the leadward direction. The second phase, shown in Figure 3, ends when the maximum keel depth is reached. In the third phase the direction of growth is leadward creating a rubble field of more or less uniform thickness. The third phase ends when the supply of thin ice is exhausted. The fourth phase is the compression of the rubble field between floes.

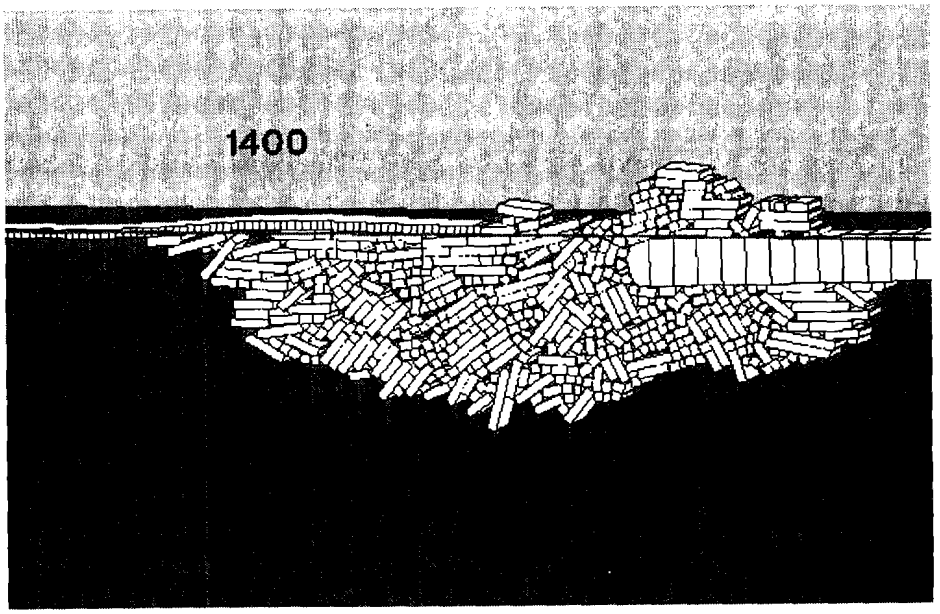

Figure 3. A snapshot from a ridging simulation. The ridge in the snapshot is in the second stage of growth in which the sail has reached its maximum size, but the keel is still growing.

Experiments with the computer model (Hopkins, 1994) show that friction between ice blocks controls the shape of the average ridge profile. The underwater friction coefficient controls the slope of the keel through its effect on the angle of repose of the ice rubble. The above-water friction coefficient controls the volume of the ridge sail through its effect on the force resisting the motion of the ice sheet. Since the sail building force is limited by the strength of the ice sheet, increasing the friction coefficient, in turn, increases the sail building force resulting in a smaller sail and larger keel for a given ice volume.

The experiments show that the average ridge profile and energetics during the first stage are a function of the volume of ridged ice. This is defined as the length of lead ice pushed into the ridge multiplied by its thickness. The total energy consumed in the ridging experiments with ice of various thicknesses as a

function of the volume of ridged ice (Hopkins, 1994) is shown in Figure 4.

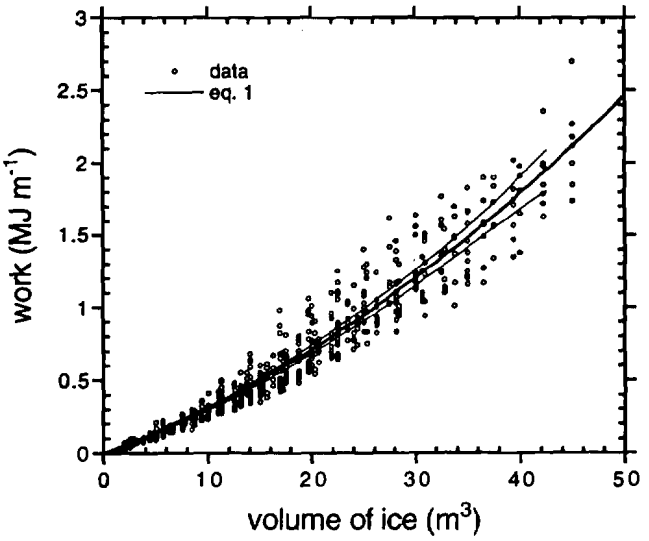

Figure 4: Total energy consumption (megajoules per meter) versus volume of ridged ice. The data points are from sets of seven experiments with ice of six thicknesses. Equation (1) is plotted within a 95% confidence interval.

The equation plotted in the figure is

$$W = V\,(463.9\,V + 26126) \tag{1}$$

where W is energy consumption in joules per meter and V is the volume of ridged ice in cubic meters per meter. This equation was obtained from the results of experiments with ice of 20-45 cm thickness using a least squares regression. The equation applies to the first stage of ridging, the period before the ridge sail reaches its maximum volume. The ratio of the rate of energy expended in ridging to the rate of increase in potential energy of the ridge structure is important in finite difference models of the Arctic Basin for determining the large-scale strength of the ice pack. An expression for this ratio, derived from the results of the numerical experiments (Hopkins, 1994), is

$$\Delta W/\Delta PE = (927.8\,V + 26126)/(61.8\,V + 2107) \tag{2}$$

that ranges from an initial value of 12.4 to 14 at 50 cubic meters of ridged ice.

More recent experiments have studied ridge formation from initiation well into the second stage in lead ice from 30 to 60 cm thick. A plot of the average energy consumed versus the volume of ridged ice obtained in these experiments is shown in Figure 5.

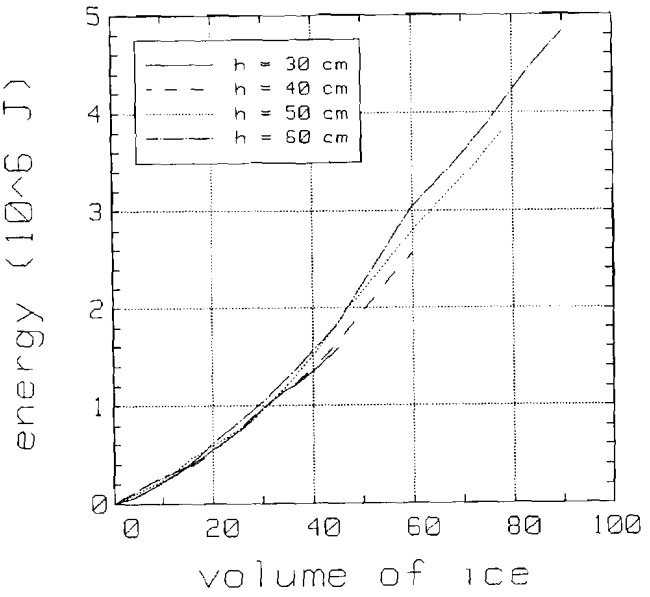

Figure 5: Total energy consumption (megajoules per meter) versus volume of ridged ice. The data points are from sets of ten experiments with ice of four thicknesses.

These results are noteworthy because they show the transition from the first stage to the second stage for the various ice thicknesses. The sail building force increases with the height of the sail. As the sail grows, a point is reached where the strength of the lead ice sheet is insufficient to transmit the sail building force. Subsequent growth, directed into the ridge keel, requires less energy. The transition point depends on the strength of the sheet that, in turn, depends on thickness.

Experiments on the Evolution of the Average Ridge Profile -- The change in the ice thickness distribution in an area of the ice pack undergoing compression is a function of the changes in the thickness distribution in the areas surrounding each individual pressure ridge. The results of 200 individual ridging simulations were averaged to obtain the function shown in Figure 6.

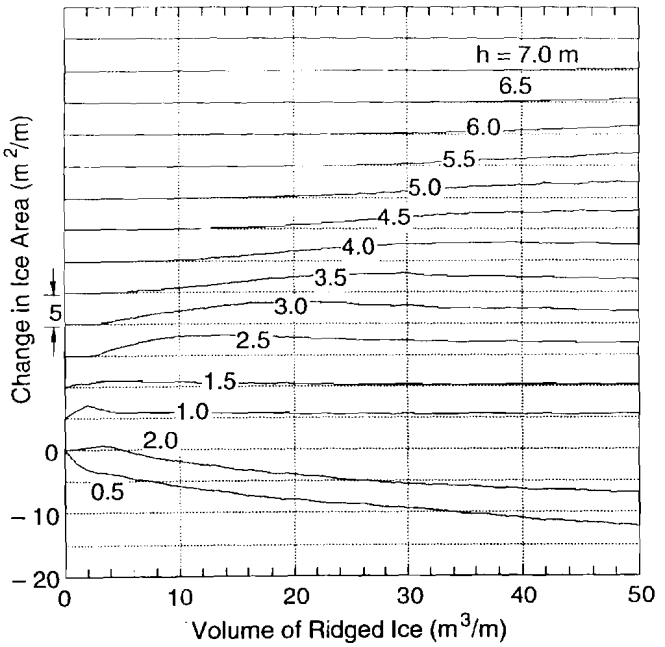

Figure 6: Change in area of ice in each thickness category in the area surrounding a single pressure ridge (from Hopkins, in review).

The bottom line in the figure shows the area of thin ice (h=0.5±0.25-m) indirectly destroyed by rubble piled beneath the sheet. This corresponds to the area of the ridge to the left of the floe in Figure 3. The lower of the 2 m lines shows the area of floe ice (h=2±0.25-m) indirectly destroyed by rubble piled on and under the floe. The lines above 0 are lines of creation. Each line is offset +5-m^2 from the previous line for clarity. For example, at a point where the volume of ridged ice is 20 m^3, about 3.5 m^2 of 3 m ice and 2 m^2 of 4 m ice have been created. The maximum thickness when the volume is 20 m^3 is 5 m. Note that 2 m ice is destroyed on the floe side and created on the lead side. Figure 6 does not include the area of thin ice that was converted into rubble. By specifying the change in the area of ice in each thickness category, the figure constitutes an empirical transfer function or data table that can be used to determine the discrete change in the local thickness distribution at a point in the ridging process.

Modeling Ice Pile-Up on an Inclined Ramp -- Twelve experiments were performed in the CRREL ice basin (Hopkins, 1995). The experiments were generally terminated by the premature failure of the attached end of the ice sheet. The forces measured in the experiment are shown in Figure 7. The vertical force shows the weight of the accumulating ice rubble supported by the ramp. The graph of the horizontal force exhibits several periods of gradual increase and precipitous decrease. The periods of gradual increase correspond to periods when the sheet is pushed smoothly onto the pile forming on the ramp. The preciptous drops mark the end of these periods caused by buckling of the sheet.

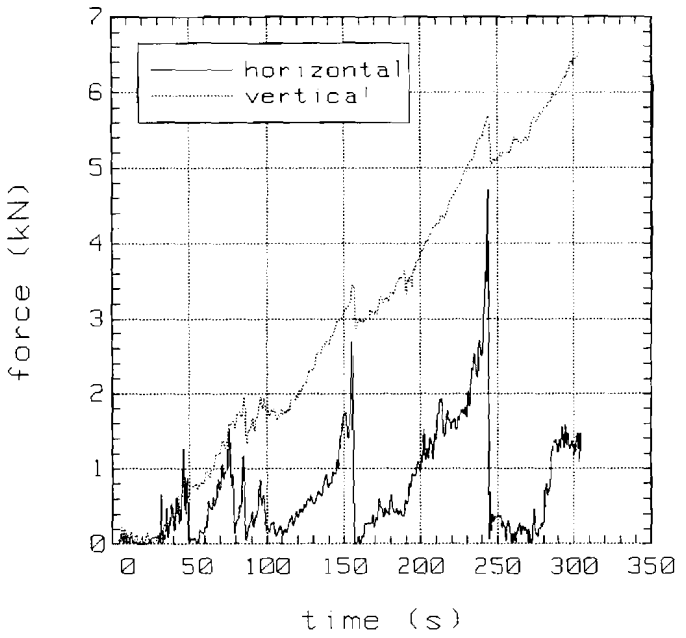

Figure 7. Force versus time from experiment #1 in Table 3.

The energy expended in creating the pile was calculated by integrating the product of the horizontal force and the carriage velocity over the duration of the experiment. The calculation of the potential energy was based on measurements of the rubble profile using a 10 cm x 10 cm grid laid over the pile. The rubble profile and the vertical force were used to calculate the rubble density ρ_i that includes porosity. The rubble density was then used to calculate the potential energy of the rubble in each cell defined by the grid. The results of all twelve experiments are shown in Table 3.

Table 3: The results of twelve ice pile-up experiments.

#	duration	weight	ρ_i	Work	PE	W/PE
1	265 s	6544 N	729 kg/m^3	19736 J	2790 J	7.1
2	110	2368	779	6446	661	9.8
3	145	3410	728	9316	1007	9.3
4	220	4782	788	12646	1806	7.0
5	75	2038	544	3011	692	4.4
6	105	2970	809	5410	767	7.1
7	137	3578	754	9158	1015	9.0
8	200	5473	731	13210	2046	6.5
9	130	3306	708	7869	1038	7.6
10	275	6500	753	14028	2280	6.2
11	215	5666	795	10520	1788	5.9
12	175	3719	790	8743	978	8.9

The average value for the ratio of work to potential energy in Table 2 is 7.4. The companion numerical experiments are in progress and will be reported in the near future.

Analysis and Publication Plans

Immediate plans are to finish the experiments on the energetics of the second and third stages of pressure ridging. The following publication will describe that work:

Hopkins, M.A., On the four stages of pressure ridging, in preparation.

Recent Publications resulting from the SIMI program:

Hopkins, M.A., On the mesoscale interaction of floes and lead ice, submitted to the *J. Geophys. Res.*

Hopkins, M.A., The ice pile-up problem: A comparison between experiments and simulations, proceedings of the ASME Applied Mechanics Conference, Los Angeles, CA, June 28-30, 1995.

Hopkins, M.A., and J.M. Stanley, The Energetics of Ice Pile-Up: Physical Experiments, proceedings of the 10th ASCE Engineering Mechanics Conference, Boulder, CO, May 21-24, 1995.

Hopkins, M.A., The effects of individual ridging events on the ice thickness distribution in the Arctic ice pack, submitted to *J. Cold Regions Science and Technology.*

Hopkins, M.A., On the ridging of an intact sheet of lead ice, *J. Geophys. Res.*, 99, C8, 16351-16360, 1994.

Hopkins, M.A., The numerical simulation of systems of multitudinous polygonal blocks, United States Army Corps of Engineers Cold Regions Research and Engineering Laboratory (USACRREL) Report 92-22, 1992.

Hopkins, M., A Discussion of the Numerical Modeling of Sea Ice Ridging, proceedings of the 9th Conference of the ASCE Engineering Mechanics Division, eds. L.D. Lutes and J.M. Niedzwecki, College Station, TX, May 24-27, 1992.

Sea Ice Mechanics Related To Thermally-Induced Stresses And Fracturing In Pack Ice

Dr. James K. Lewis, Ocean Physics Res. & Dev., 207 S. Seashore Av., Long Beach, MS. 39560; Dr. Peter J. Stein, Scientific Solutions Inc., 18 Clinton Dr., Hollis, NH. 03049.

Scope of Modeling and Data Sets

Data Sets: Three data sets have been generated specifically for the studying thermally-induced stresses and fracturing in sea ice. The first data were collected at Resolute Bay, Canada, on first-year ice. The data include snow thickness distribution, longwave and shortwave radiation, wind speed, and air temperature, and have been combined with ice salinity and porosity data collected by Dr. W. Tucker. The data were discussed in Lewis et al. (*J. Geophys. Res.*, C8, 16361-16371, 1994). The second data set was collected during the fall 1994 SIMI experiment on multi-year ice. The data collected were snow thickness distribution and longwave and shortwave radiation. These have been combined with a version of the wind speed and air temperature data collected by Dr. J. Overland and ice salinity and porosity data collected by Ms. J. Richter-Menge. In addition to the above, we have put together data collected during the CEAREX experiment to run test simulations. These include snow thickness distribution, longwave and shortwave radiation, wind speed, air temperature, under-ice noise variations, and ice salinity and porosity. These data have been described by Lewis (*Cold Reg. Sci. Tech.*, 21, 337-348, 1993; *J. Acoust. Soc. Amer.*, 95, 1378-1385, 1994).

Modeling: Modeling activities have included the development of an enhanced thermodynamic model for sea ice coupled with a ice stress model driven by thermally-induced strain rates. Enhancements of the thermodynamic model are based on the work of Wade (Ph.D. thesis, Univ. Alaska, Fairbanks, 1993). The features of the thermodynamic model are outlined in Fig. 1. The model is driven by observed atmospheric variables.

The thermally-induced strain rates drive the stress model through a non-linear rheology relating stress at a given location in the ice to thermally-induced strains, mechanically-transmitted strains, and the give of the ice under stress (creep). The specifics of the thermal stress model are discussed in Lewis (in press, *J. Geophys. Res.*) along with a conceptual model of how existing cracks impact the stress state of the ice under the assumption that typical floes are too large to bend or twist in response to spatially varying strain rates. The features of the stress model are outlined in Fig. 2. Of

For a given snow cover:

1) Set surface heat fluxes, albedo, and emissivity.

2) Calculate specific heats and thermal conductivities for each vertical level

   i) Functions of ice level temperature, salinity, brine volume, and density.

3) Calculate new vertical profile of temperature

   i) Calculated implicitly.

   ii) Based on a set under-ice water temperature.

4) Calculate the change in ice thickness.

   i) Based on melting/freezing due to net heat flux at ice-water interface.

5) Calculate new vertical profile of salinity.

   i) Brine expulsion if an ice layer is being cooled.

   ii) Gravity drainage if the vertical profile of brine volume is unstable.

Fig. 1. Basic features of the thermodynamic model.

particular interest is our attempt to specify the relative quantity of fractures and stress relief as the tensile yield strength of the ice is exceeded. Fracturing and stress relief are now formulated to be proportional to the amount of existing cracks. This allows us to simulate first-year and multi-year ice using the same model by differentiating the two ice types based on the extent of existing cracks. With first-year ice, the fractional coverage of existing cracks would be small, leading to less fracturing, less stress relief, and greater tensile stresses. This is in accordance with observations.

Findings to Date

Thermal Forcing - The thermal forcing as deduced from the three sets of observations indicate very similar conditions between the fall CEAREX forcing, the fall SIMI forcing, and the spring Resolute forcing. All three data sets include the passage of cold fronts and gradual warming after the fronts. The magnitudes of the net heat losses between the three data sets are similar, but the response of the stresses within the ice floes were considerably different between the CEAREX and SIMI multi-year ice and the Resolute first-year ice. An analysis of the data and other observations (Lewis, et al., *J. Geophys. Res.*, C8, 16361-16371, 1994) imply that first year floes have a much higher fracture toughness in tension than multi-year floes. The direct corollary to the above statement is that first year floes are considerably less flawed than multi-year floes.

1) Calculate spatially-weighted strain rate.

i) Weighted by effective elastic moduli

a) Elastic moduli functions of temperatures, porosities, and overall strain rates.

ii) Spatially-weighted strain rate is modified by fractional coverage of existing cracks for each vertical level.

2) Calculate new vertical profile of stress for a given snow cover.

i) Creep is a function of stress, temperature, and porosity.

ii) Elastic moduli is a function of temperature, porosity, and overall strain rate.

iii) Iterate to a solution.

3) Determine any fracturing during time step for a given vertical level and snow cover.

i) Tensile yield strength is a function of temperature and salinity.

ii) Estimate relative number of fractures.

a) Modify by fractional coverage of existing cracks to get net number of fractures.

iii) Estimate stress relief.

a) Function of net number of fractures and amount the initially-calculated stress exceeded the tensile yield strength.

iv) Estimate under-ice noise.

a) Function of net number of fractures and location of fractures in the vertical.

4) After stress relief, readjust stresses such that the spatial average is zero.

Fig. 2. Basic features of the thermal stress model.

Since existing cracks appear to be a critical factor, theoretical and modeling activities have concentrated on how a rheology should quantify the extent of existing cracks in the ice and how they impact the overall strain rate within a floe.

Thermal Stress Modeling - The sea ice rheology based on thermally-induced strain rate information represents the ice as a spring that is forced by strains which result from thermal and mechanical processes. The equation relating stress and strain rates is

$$\sigma_t = E' (\epsilon_t - \zeta_t - \gamma)$$

where σ_t is the time rate of change of stress, E' is the effective elastic modulus, ϵ_t is the thermally-induced strain rate, ζ_t is a mechanically-induced strain rate, and γ is the strain rate as a result of the viscous creep of a material under stress. The ζ_t term reflects strain transmitted throughout the ice as a result of the floe being too large to bend or twist in response to spatial variations of strain rates. For ice of thickness H, variations in the snow cover result in both laterally as well as vertically varying strain rates. These are accounted for in the model by specifying the mechanically-induced strain rate in the x direction (relative to a fixed coordinate system on the floe) as

$$\zeta_t = \int_{-L}^{L} [\int_{o}^{H} E' (\epsilon_t - \gamma)(1 - 2N)\, dz]\, dy / \int_{-L}^{L} \int_{o}^{H} E'\, dz\, dy.$$

where 2L is the extent of the horizontal variations of the snow cover thickness and N is the fractional coverage of the cracks (whether continuous or not) in the horizontal at a depth z in the ice. The stress in the y direction is calculated as above except the integrals are with respect to z and x. Explicit in the above expression is the assumption that the ice under all thicknesses of snow cover have the same relative fraction of existing cracks, namely N.

As N increases, the stress in between existing cracks will be enhanced (Lewis, in press, *J. Geophys. Res.*, 1995). For young, nearly flawless ice floes, N will tend to be small. As a result, there would be little stress enhancement due to existing cracks. Thus, we would expect such floes to require greater levels of tensile stresses to induce fracturing than floes which are more flawed (e.g., older floes).

Before we can use the above expressions to model the stress state of a flawed ice floe, we must first specify a fracturing paradigm. This is required since any fracture results in some reduction of the stress that caused the fracture. Our fracturing paradigm specifies the tensile yield strength of the ice σ_{ten} as a function of the salinity and temperature of the ice at a given vertical level and snow cover. Based on the assumption of no bending or twisting, we assume the any stress enhancement at the tips of a flaw extends horizontally only 10% of that predicted for a theoretical elliptical flaw in an infinite ice sheet. For a crack with a horizontal extent of R, this becomes R/10 on either side of the crack. Assuming that the ice will fracture a distance of R/10 on both sides of an existing crack allows us to estimate a relative number of fractures at a given vertical level for a given time step:

$$\text{Relative Number of Fractures} = \sigma_e \times N/0.833.$$

where σ_e is the yield strength exceedence, $\sigma - \sigma_{ten}$ where σ is the predicted tensile stress. If there are enough existing cracks to cover 83.3% of an ice layer (N = 0.833), an episode of tensile fracturing would increase the extent of the cracks by 20% (10% on each side), and, under our assumptions, this would extend the existing cracks to a fractional coverage of 100%. Thus, N = 0.833 would result in the maximum number of fractures. As N becomes smaller, fracturing at the tips of existing cracks still occurs (as long as the predicted σ exceeds σ_{ten}), but the relative amount reduces linearly with N. The dependence on σ_e accounts for the fact that more individual fractures could occur during a given time step larger rates of increases in tension.

Studies indicate that stress relief during fracturing should be based on the degree to which the model-predicted stress exceeds the tensile yield strength of the ice (Lewis, *J. Acoust. Soc. Am.*, 95 (3), 1378-1385, 1994). Simulations based on the CEAREX observations suggest a reduction of the calculated tensile stress σ due to stress relief of

$$(\sigma - \sigma_{ten}) \times 6.5\ 10^{-6} \times N/0.833$$

where σ is in Pascals. Thus, if the forcing is significant for a given time step ($\sigma - \sigma_{ten}$ large), a larger amount of fracturing should occur, and the stress relief is greater. In addition, the stress relief has to be dependent on the amount of existing cracks, and thus N/0.833 is included in the above expression. With these two expressions for fracturing and stress relief, we can simulate first-year and multi-year ice using the same thermal stress model by differentiating the two ice types based on the extent of existing cracks.

This technology was used to simulate thermally-induced stresses during CEAREX. Fig. 3 shows the observed and model-predicted stresses near the center of the main multi-year CEAREX ice floe. The observed stresses can be predicted relatively well assuming that the top third of the floe has N = 70%, the middle third has N = 80%, and the bottom third has N = 50%. Using the same variables, the stresses during the fall SIMI experiment were simulated, and these are shown in Fig. 4.

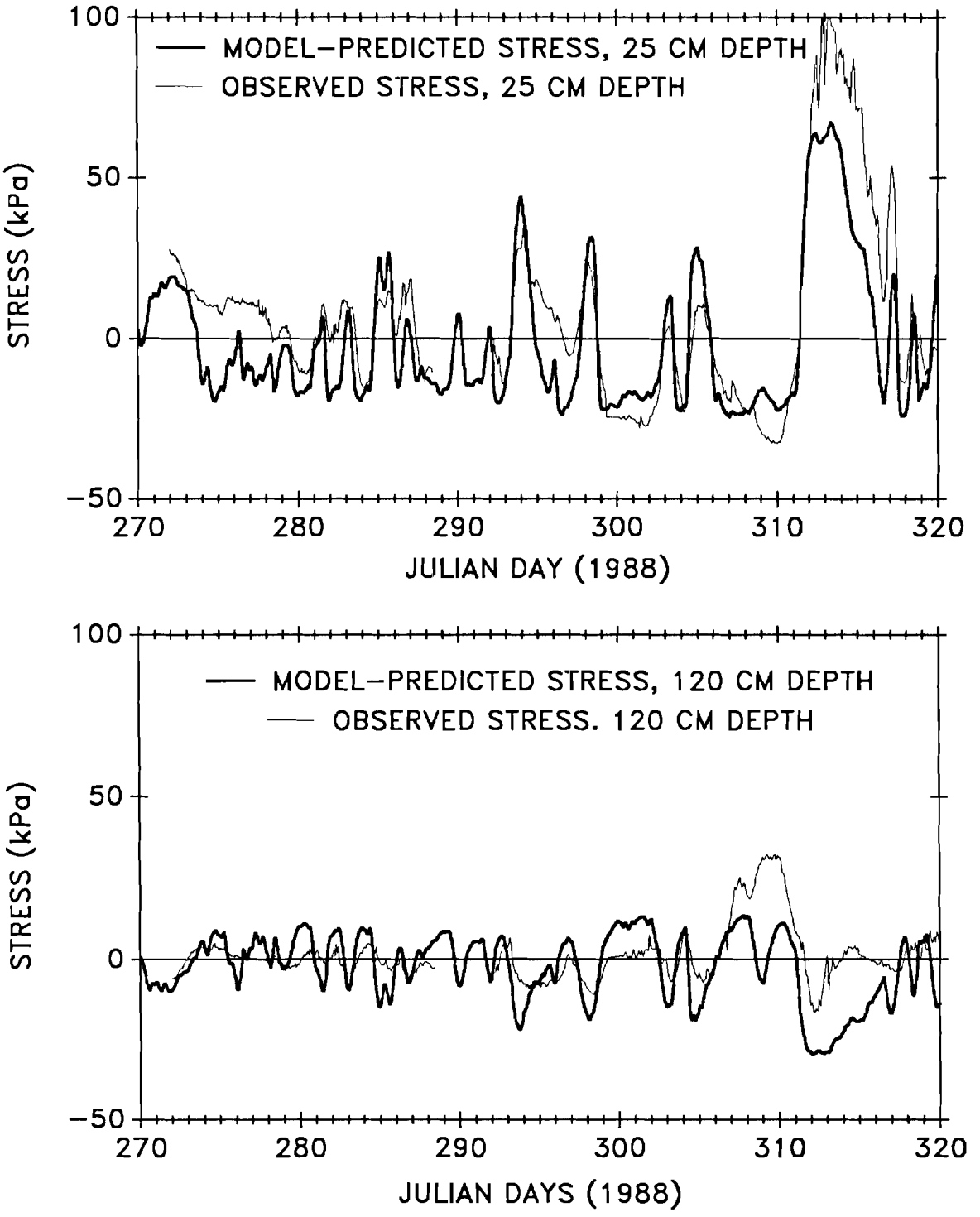

Fig. 3. observed and model-predicted stress during CEAREX.

Analysis and Publication Plans

We plan to use observed under-ice noise data to refine the thermal stress/fracturing model. Noise variations at 500-1000 Hz should correspond well to thermally-induced fracturing. We will study how the acoustic energy propagates through the ice down and through the water column. It is already known that, for a given frequency and ice thickness, fractures at certain depths within a floe generate little sound in the water column. This information will be used to refine the formulation of fracturing and stress relief when the tensile yield strength is exceeded. This work will lead to studies of under-ice noise variations as a means of studying and monitoring climate variations.

The following is a list of publications resulting from the SIMI program:

"A model for thermally-induced stresses in multi-year sea ice". J. K. Lewis, *Cold Reg. Sci. Tech.*, 21, 337-348 (1993).

"Relating Arctic ambient noise to thermally-induced fracturing of the ice pack". J. K. Lewis, *J. Acoust. Soc. Am.*, 95 (3), 1378-1385 (1994).

"Observations and modeling of thermally-induced stresses in first-year sea ice". J. K. Lewis, W. W. Tucker and P. J. Stein, *J. Geophys. Res.*, 99(C8), 16361-16371 (1994).

"A conceptual model of the impact of flaws on the stress state of sea ice". J. K. Lewis, in press, *J. Geophys. Res.* (1995).

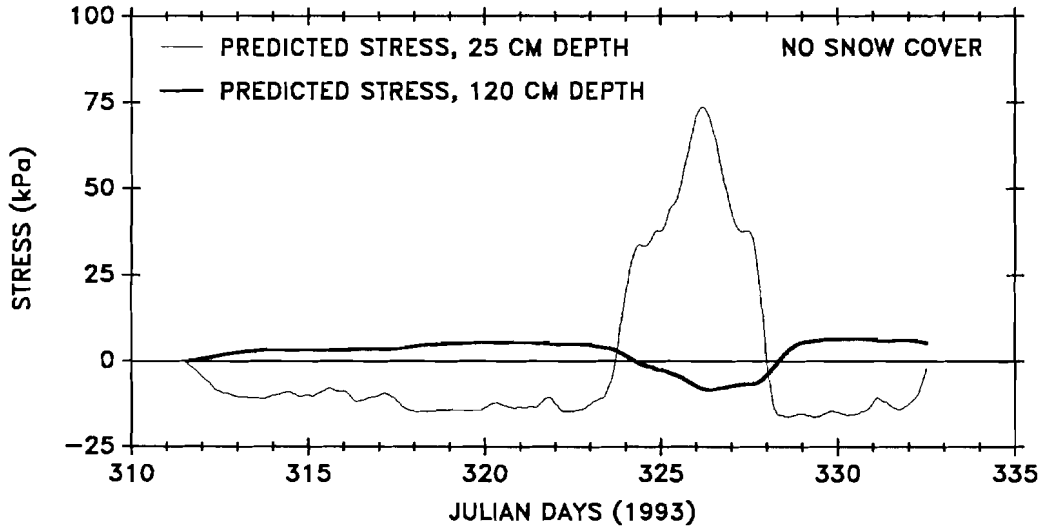

Fig. 4. Model-predicted stresses during the fall SIMI experiment.

resistance method and by using the natural electromagnetic emission from cracks. The experiments were performed on square plate samples. The samples had been isolated from the surrounding ice sheet and were kept from refreezing during the tests. To cut these full-thickness samples a sled-mounted, motor-driven saw was used, although a ditchwitch was hired to cut the largest sample. The sample size varied from 0.5 m to 30 m on a side. The loading system was developed by John Dempsey and Robert Adamson (Clarkson University, Potsdam, N.Y.) and employed a computer-controlled flatjack loaded with nitrogen gas. The flatjack was inserted into a precrack with a length of about 1/3 of the sample length. The loading time was varied from a few seconds to tens of minutes. The details of the mechanical setup will be published elsewhere[9].

The sea ice at the site was strongly aligned and had a columnar structure[10]. The ice thickness in November was 0.3–0.35 meter and in March 1.36 meters. The temperature profile ranged from –1.8°C at the ice bottom down to –7.2 to –10.2°C at the ice surface in November and –17 to –31.2°C at the surface in March. Even at the coldest air temperature, –42°C, the floating ice was quite wet throughout its thickness and contained many liquid inclusions: brine pockets and brine channels. This explained the high electrical conductivity of the ice, $\sigma \approx 3 \cdot 10^{-2}\ (\Omega m)^{-1}$. Because of the high conductivity, the resistance method was used to determine crack velocities in these samples. For the smaller samples (1.0 m × 0.6 m × 0.1 m) that were cooled down to the air temperature, –35°C, crack velocities were determined by means of the natural electromagnetic emission.

Resistance Method -- The idea that crack velocity can be determined by measuring changes in the impedance induced by cracks was first applied by Carlsson[11] to study fast cracks in metals. Later this method was referred to as the "autoresistance method"[8,12]. The ideology of the method is very simple. A propagating crack changes the electrical resistance of the sample and the resistance is recorded as a function of time. The crack length can then be recovered from the electrical data using a calibration curve of resistance versus crack length. The calibration requires either theoretical analysis of electrical boundary conditions of the sample or experimental modeling.

To detect changes in the sample resistance a bridge type circuit was used, see Figures 1 and 2. The resistance signals were stored in a digital oscilloscope (Tektronix 2431L) and in a computer. The 200-MHz oscilloscope is capable of continuously recording 4084 points of a signal with high time resolution of up to 10 ns. The acquisition board DAS 16F (Metrabyte) together with an IBM-compatible computer can continuously record a signal at the acquisition rate of 4 kHz for more than 1.5 hours; therefore the computer-based acquisition system was used in recording responses from multiple cracks and microcracks.

The equipment was calibrated in a set of experiments in which ice was replaced with a poorly conducting liquid, sea water was substituted with metallic foil, and a crack was simulated by a dielectric plate. Once the calibration curve is obtained the crack length can be recreated as a function of time. The designed computer code performs this routine automatically.

Electromagnetic Emission Method -- In natural polycrystalline ice there is an intrinsic electric field due to the nonuniform distribution of impurity ions[5]. In freshwater ice the concentration of impurities has a maximum at each grain boundary and the intrinsic electric field oscillates spatially from grain to grain[7]. In natural sea ice the salinity concentration changes vertically; this produces a more uniform intrinsic electric field. As a crack crosses

Measurements of Crack Velocity in Sea Ice Using Electromagnetic Techniques

Dr. Victor Petrenko (P.I.) and Mr. Oleg Gluschenkov, Thayer School of Engineering, Dartmouth College, Hanover, NH 03755

Scope of Model and Data Set

To study crack dynamics in sea ice, high time-resolution measurements of ice electrical resistance and electromagnetic emissions from cracks were used. The sample dimensions ranged from 0.05 to 30 meters. In laboratory-grown freshwater ice, crack velocities varied from a few hundred to 1000 meters per second (m/s) while in natural sea ice, crack velocity was very low, about 10 m/s. This remarkable difference in crack velocities is likely due to the dynamic resistance of unfrozen water in brine pockets and channels and to the high ductility of sea ice. It was found that cracks propagate in ice discontinuously owing to the strong interaction with such microstructural elements as liquid inclusions and grain boundaries. The high sensitivity of the method used allowed us to detect nucleation of the very first microcracks.

Previous Results -- Geophysical ice is a very complex material. It may have a granular or columnar polycrystalline structure, in which single crystals may be oriented along a particular direction (aligned columnar ice)[1,2]. In addition, saline sea ice is saturated with liquid inclusions, so-called brine pockets and brine channels. The overall content of the brine in a sea ice sheet is a function of ice temperature and salinity[1,2].

The first report on the velocity of unstable cracks in freshwater ice was published by Sato and Wakahama[3] in 1992. According to their paper, the terminal velocity of unstable cracks in freshwater ice is about 1100 m/s. In 1987 Parson *et al.*[4] published the results of field measurements in which they claimed that the average velocity of an unstable crack in saline ice is only 20 m/s. To resolve this controversy new, inexpensive and reliable methods for crack velocity measurements are needed. These methods should be equally reliable under field and laboratory conditions.

In 1992 Petrenko[5] proposed the use of natural and stimulated electromagnetic emission from cracks in ice as the method for crack velocity determination. Fifolt *et al.*[6] used this idea to measure the velocity of ice cracks in the laboratory. Later, Gluschenkov and Petrenko[7] applied this method to estimate the velocities of natural thermocracks in lake ice. According to these studies, the velocity of cracks in ice varied from several hundred to 1000 m/s.

This report presents the results of field experiments on sea ice near Barrow, Alaska during the winter of 1993-94. Crack velocities were detected by measuring natural electromagnetic emission and ice impedance. The determination of crack velocity by measuring the change in the sample impedance induced by a crack is known as the autoimpedance method[8]. These methods, coupled with a high-speed data acquisition system and an advanced noise filtering system, enabled us to monitor small changes in the crack velocity and to detect the appearance of microcracks under cyclic loading. We found that: 1) crack velocities in natural sea ice are indeed very low, only 10 m/s; 2) cracks likely propagate in sea ice with numerous jumps and stops, as if they strongly interact with microstructural features.

Ice Samples -- Two sets of field experiments were conducted at Barrow, Alaska in November, 1993 and March, 1994. The crack velocities in saline ice were measured by the

prepolarized ice, an electromagnetic field is generated (electromagnetic emission) at frequency *f:*

$$f = \frac{v}{d} \tag{1}$$

where *d* is either an average grain size or a crack length for the uniform intrinsic field and *v* is the crack velocity. After crack arrest the electromagnetic emission decays with the ice dielectric relaxation time[5–7]. Such electromagnetic emission, measured either locally with contacts attached to ice or remotely with a dipole antenna, can be used to determine *v* if one knows the average grain size of ice or the crack length. This technique is suitable for ice with low conductivity, such as freshwater ice or saline ice at temperatures below –30°C, which behaves mainly as a dielectric.

The electromagnetic emission was captured by a 6-meter dipole antenna connected to a preamplifier, Figure 3. All electromagnetic emission signals captured from cracks were stored in the oscilloscope. The ice samples were cut from the sea ice sheet and cooled in the air for about 24 hours, down to the ambient temperature of –35°C. The cracks were produced in three-point bend geometry. The crack planes were perpendicular to the intrinsic electric field originating from the salinity gradient in the ice.

Findings to Date

The methods described above allowed us to monitor a crack each time it appeared. All the signals of the same nature were very similar. A typical "autoresistance" signal from a final through crack (Figure 4) has two distinctive areas: the crack propagation area and the area affected by the conducting sea water. It is clear that the part of the signal associated with a propagating crack is not affected by the conducting sea water, which enters the crack later. A typical electromagnetic emission signal (Figure 5) shows the region of crack propagation and the relaxation of the signal after crack arrest, as was predicted[13] and observed in the laboratory[6].

The "autoresistance" signals have been converted to crack length versus time curves by using the experimental calibration method described above. The crack length versus time profile (Figure 6) is similar (except for absolute values) to those that were calculated for double cantilever beam specimens[14]. The high resolution of the resistance method allows us to distinguish oscillations in the velocity at a small scale (see the insert in Figure 6). Figure 7 depicts the spectra of both electrical noise and crack velocity. It is clear that the velocity oscillations are caused by natural factors and not by electrical noise. These velocity oscillations are likely due to an interaction between the moving crack and the ice microstructure. However, there may be another explanation for the oscillations: the electrical conductivity of sea ice is discontinuous due to the existence of brine inclusions, and this discontinuity may produce the signal oscillations when a crack passes by. According to Weeks and Ackley[1], the distance between brine pockets is about 1 mm. Then for a crack velocity of 10 m/s, oscillations on this scale should be about 10 MHz, which is far beyond the frequency range of Figure 7.

The average crack velocities are summarized in Table I. These velocities are extremely low: 10–20 m/s. This is only 0.0024–0.0048 from the longitudinal sound velocity in ice, $v_s \approx$ 4200 m/s[15]. The maximum crack velocities measured in other materials appear to be between 0.1 and $0.5 \cdot v_s$[14,16]. Only in very cold ice samples were the crack velocities comparable with crack velocity measured in freshwater ice[6,7]. Possible explanations of this

Table I. *Crack velocities in first-year sea ice, Barrow, Alaska, November 1993, March 1994.*

Sample size, m	Temperature at the ice surface °C	Crack orientation	Loading time, s	Type of measurement	Crack velocity, m/s
1.5×1.5×1.4	–19.7	∥ to (0001)	250	Resistance	8.18
3.0×3.0×1.4	–22.3	∥ to (0001)	830	Resistance	11.97
3.0×1.4×1.4	–22.3	⊥ to (0001)	540	Resistance	8.86
3.0×3.0×1.4	–20.6	∥ to (0001)	7	Resistance	17.1
2.0×2.0×1.4	–25.3	∥ to (0001)	1200	Resistance	16.1
2.0×1.1×1.4	–25.3	⊥ to (0001)	1300	Resistance	15.55
30×30×1.4	–31.2	∥ to (0001)	250	Resistance	7.5
0.5×0.5×1.4	–31.2	∥ to (0001)	300	Resistance	3.38
2.4×2.4×0.3	–7.4	∥ to (0001)	N/A	Resistance	9.3
2.4×2.4×0.3	–7.4	∥ to (0001)	N/A	Resistance	9.2
0.7×0.4×0.1	–35 (uniform)	⊥ to (0001)	1	EME	220
1.0×0.6×0.1	–35 (uniform)	⊥ to (0001)	1	EME	285

EME = electromagnetic emission; N/A = not available.

fact may be either freezing of all brine inclusions in the ice at temperatures below the water/salt eutectic temperature, –22°C, or a decrease in plasticity of saline ice at such a low temperature.

Analysis and Publication Plans

The previous work on crack velocity in sea ice by Parsons *et al.*[4] attributed the low crack velocities to the existence of a large plastic process zone around a crack tip in saline ice. The authors argued that the plastic zone in saline ice is three orders of magnitude higher than in other tested materials; therefore they expected a very low crack velocity. It is possible that the plasticity can play a certain role in the phenomenon, but how big is its influence? We think that such an influence cannot be cardinal because cracks in warm freshwater ice, which is a bit less plastic than its sea counterpart, behave in an absolutely ordinary manner. The terminal crack velocity in this ice is about 0.28 of the sound velocity[3,6].

We propose another possible explanation of very low crack velocity in sea ice: the dynamic effect of liquid inclusions on a rapidly moving crack. The fact that resistance of brittle solids to the propagation of cracks can be strongly influenced by microstructure and by the use of various reinforcements is well known. For instance, the incorporation of small ductile metal particles into a brittle ceramic considerably increases its fracture toughness[17]. The effect produced by a liquid on a static crack has been considered by M. Kachanov[18]. He pointed out that the liquid can cause a significant toughening effect.

First-year sea ice contains many liquid inclusions. They are so-called brine pockets and brine drainage channels[1,2]. Under slow, stable crack propagation the brine has almost no effect on crack resistance[19]. However, in our opinion, an unstable, rapidly moving crack may be very sensitive to the liquid inclusions since the bulk tensile strength of liquids is extremely high. For example, the theoretical value for water lies in the range of 0.1–1 GPa[20] while the tensile strength of ice ranges from 0.7 to 1.5 MPa[21]. This makes it unlikely that a crack can disrupt liquid by destroying its intrinsic cohesion. To propagate further the crack instead moves the entire liquid inclusion from its path. This produces large inertia effects and crack suspension. During the collision a crack and a liquid inclusion act on each other with high-impulse forces. These forces produce a high negative pressure inside the liquid. The pressure will be the same at each moment in time in the whole liquid inclusion if the velocity of sound in the liquid is much higher than the crack velocity. Thus we have a shielding or cohesive zone ahead of the crack tip with characteristic length r_o (liquid particle diameter), and impulse pressure P. The impulse pressure P can be roughly evaluated as $\rho_f v^2$, where ρ_f is the density of the liquid and v is the crack velocity. In this case the increase in crack resistance ΔR due to the liquid inclusions is given by: [22]

$$\Delta R \approx f \rho_f v^2 \cdot r_o \qquad (2)$$

where f is the area fraction of the liquid inclusions along the crack plane. The area fraction of reinforcements along the crack plane, f, can be approximated with the average brine volume, v_b, if brine pockets and brine drainage channels are primarily aligned along the crack surface. The value of v_b varies from 0.02 at the surface of ice to 0.12 at the bottom[23,24]; we shall use $f = 0.02$. The average diameter of brine pockets is 0.1–0.3 mm, whereas the average diameter of brine drainage channels is 1.0–10 mm[1,2]; let us take r_o = 0.3 mm. Then ρ_f is the density of brine $\cong 10^3$ kg/m^3. Letting ΔR be equal to the static critical energy release rate $G_c \approx 1$ J/m[19] we can obtain the crack velocity $v = 13$ m/s. This rough estimation shows the importance of considering the liquid inclusions.

At present, however, we do not have an exact answer to the question: what mechanisms control crack velocity in saline ice? The arguments in favor of a particular specific mechanism require much more experimental data and theoretical modeling.

In the near future we are planning a joint data analysis with John Dempsey and David Cole.

Publication plans:

1. Gluschenkov, O. and Petrenko, V. (1995). An investigation into the interaction between propagating cracks and microstructure of ice. Application of electrical methods to crack dynamics. Proceedings of the Fall Meeting of MRS, Boston, MA, November-December 1994 (In press).
2. Petrenko, V. F. and Gluschenkov, O. V. (1995). Crack velocity in freshwater and saline ice. *Journal of Geophysical Research.*

Following is a list of our resent publications resulting from the SIMI program:

1. Gluschenkov, O.V. and V.F. Petrenko (1993) Remote sensing of damage in ice using electromagnetic emission from cracks: theoretical background and preliminary experimental results. In *Ice Mechanics*, edited by J. P. Dempsey *et al.* New York: American Society of Mechanical Engineers, pp. 97–112.

2. Fifolt, D.A., V.F. Petrenko and E.M. Schulson (1993) A preliminary study of electromagnetic emissions from cracks in ice. *Phil. Mag. B*, **67**, pp. 289–99.

3. Petrenko,V.F. (1993) On the nature of electrical polarization of materials caused by cracks. Application to ice electromagnetic emission, *Phil. Mag. B*, **67**, p. 301–315.

4. Petrenko, V.F. and Schulson, E.M. (1993) Action of electric fields on the plastic deformation of pure and doped ice single crystals. *Philosophical Magazine,* **A 67**(1): 173–85.
5. Petrenko, V. F. (1993). Electromagnetic emission from cracks in ice. *Bulletin of American Physical Society,* **38**(1), p. 791.

References

1. W.F. Weeks and S.F. Ackley, U.S. Army Cold Regions Research and Engineering Laboratory (CRREL) Monograph 82-1 (1982).
2. J. Schwarz and W.F. Weeks, *J. Glaciol.* **19**(81), 499–530 (1977).
3. A. Sato and G. Wakahama, in *Physics and Chemistry of Ice*, edited by N. Maeno and T. Hondoh. Hokkaido University Press, pp. 476–80 (1992).
4. B.L. Parson, J.B. Snellen, and B. Hill, *Cold Regions Science and Tech* **13**, 233–38 (1987).
5. V.F. Petrenko, *IAHR 92: Proc. of the 11th Int. Symposium on Ice*, Vol. 2, pp.1140–1154 (1992).
6. D.A. Fifolt, V.F. Petrenko, and E.M. Schulson, *Phil. Mag. B*, **67**(3), 289–99 (1993).
7. O.V. Gluschenkov and V.F. Petrenko, in *Ice Mechanics*, edited by J.P. Dempsey *et al.* New York: American Society of Mechanical Engineers, pp. 97–112 (1993).
8. R.J. Weimer and H.C. Rogers, in *Fast Fracture and Crack Arrest*, edited by G.T. Hahn and M.F. Kanninen. ASTM STP 627, pp. 359–71 (1977).
9. R.M. Adamson, J.P. Dempsey, and S.V. Mulmute, in *Ice Mechanics—1995*, edited by J.P. Dempsey *et al.* New York: American Society of Mechanical Engineers, in press (1995).
10. D.M. Cole and G.D. Durrel, in *Ice Mechanics—1995*, edited by J.P. Dempsey *et al.* New York: American Society of Mechanical Engineers, in press (1995).
11. J. Carlsson, *Transactions of the Royal Institute of Technology* **189**, Mechanical Engineering, Vol. 6, 2–55 (1962).
12. J. Congleton and B.K. Denton, in *Fast Fracture and Crack Arrest*, edited by G.T. Hahn and M.F. Kanninen. ASTM STP 627, pp. 336–58 (1977).
13. V.F. Petrenko, *Phil. Mag. B*, **67**(3), 301–15 (1993).
14. M.F. Kanninen and C.H. Popelar, *Advanced Fracture Mechanics*. New York: Oxford Press (1985).
15. P.V. Hobbs, *Ice Physics*. Oxford, England: Clarendon Press (1974).
16. D. Broek, *Elementary Engineering Fracture Mechanics*, Dordrecht: Martinus Nijhoff (1986).
17. A.G. Evans, *J. Am. Ceram. Soc.* **73**, 187–206 (1990).
18. M. Kachanov, *Advances in Applied Mechanics* **30**, 259–440 (1994).
19. S.A. Sabol and E.M. Schulson, *J. Glaciol.* **35** (120), 191–2 (1989).
20. D.H. Trevena, *Cavitation and Tension in Liquids*. Bristol: Adam Hilger (1987).
21. E.M. Schulson, P.N. Lim and R.W. Lee, *Phil. Mag.*, **49**, 353 (1984); 1585 (1993).
22. B.R. Lawn, *Fracture of Brittle Solids*. Cambridge, England: University Press (1993).
23. G.F.N. Cox and W.F. Weeks, *J. Glaciol.* **29** (102), 306–16 (1983).
24. A. Kovacs, R.M. Morey, G.F.N. Cox, and N.C. Valleau, U.S. Army Cold Regions Research and Engineering Laboratory (CRREL) Report 87-6 (1987).

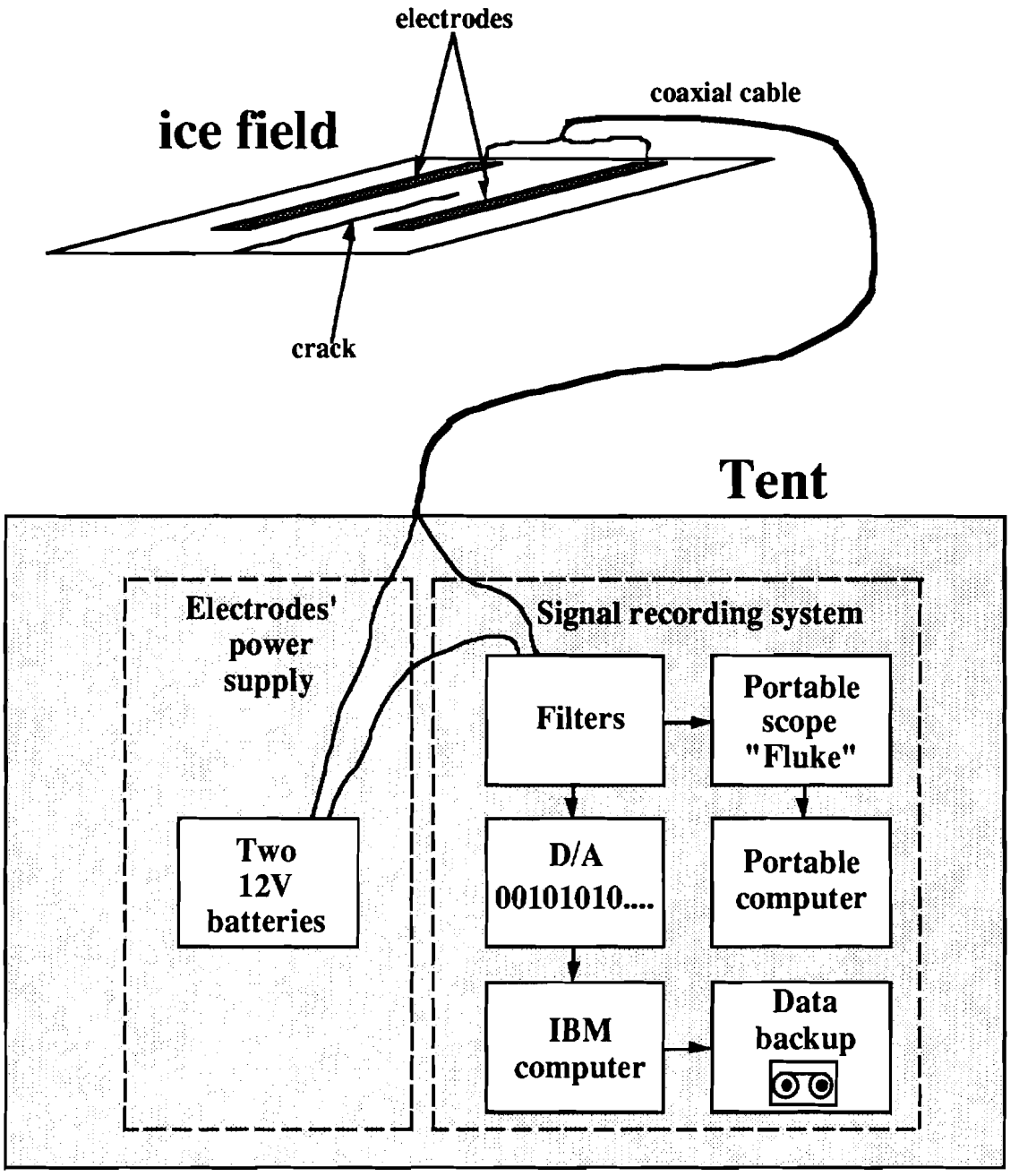

Figure 1. *Schematics of the field experiment, resistance method; Alaska, 1993–1994.*

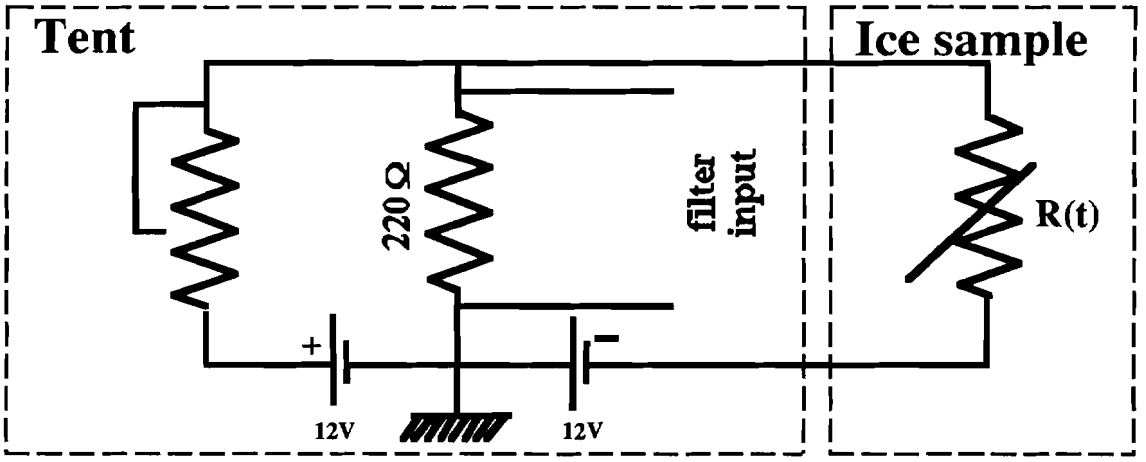

Figure 2. *Bridge circuit for ice resistance measurements.*

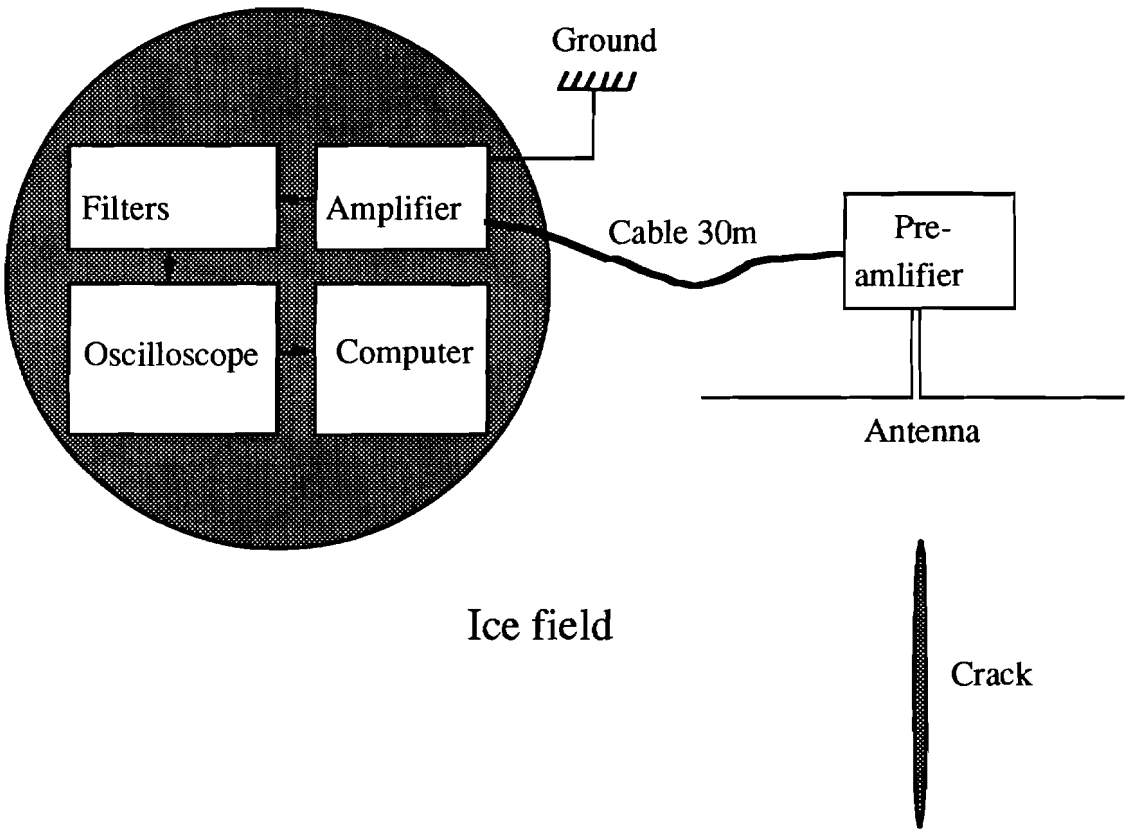

Figure 3. *Schematic of signal detection system used in remote sensing of electromagnetic emission from cracks in a sea ice sheet.*

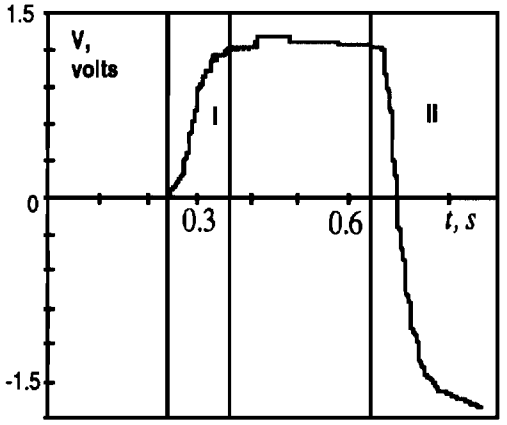

Figure 4. *Typical "resistance" signal from a long crack. Area I corresponds to the crack propagation; area II shows the effect of sea water, a conductor, penetration into the crack.*

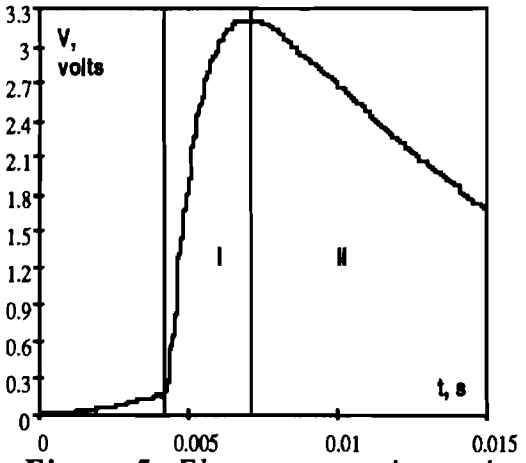

Figure 5. *Electromagnetic emission from a crack in sea ice. The crack was 60 cm long and 10 cm wide. Area I shows the crack propagation and area II corresponds to the relaxation of electromagnetic fields generated by the crack after crack arrest.*

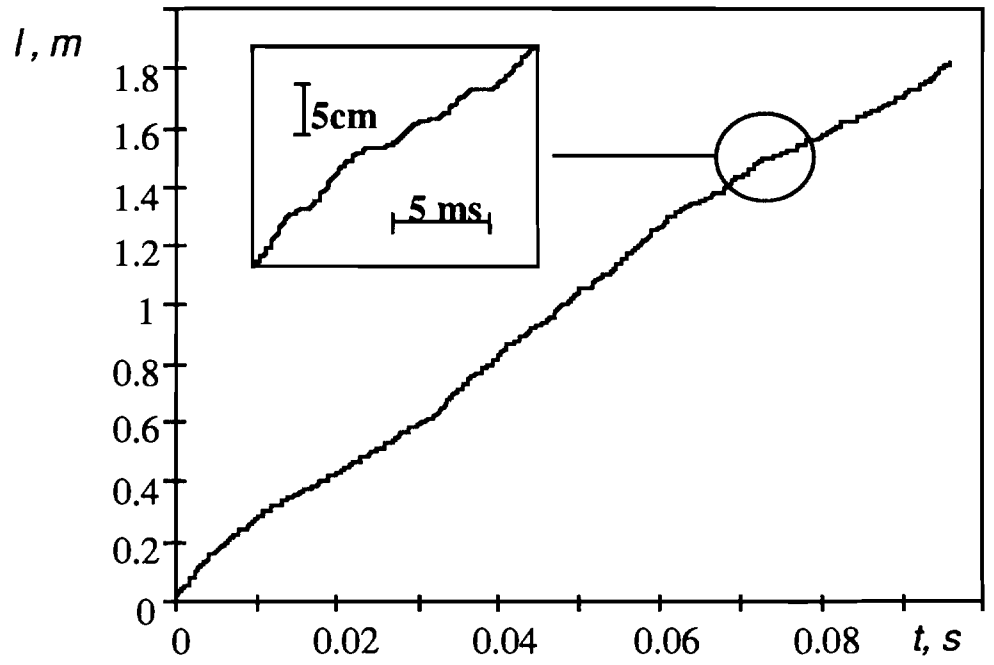

Figure 6. *Crack length vs. time for the 4th sample in Table I. The value **l** is the length of the unstable part of the crack. The acquisition rate is 10 kHz.*

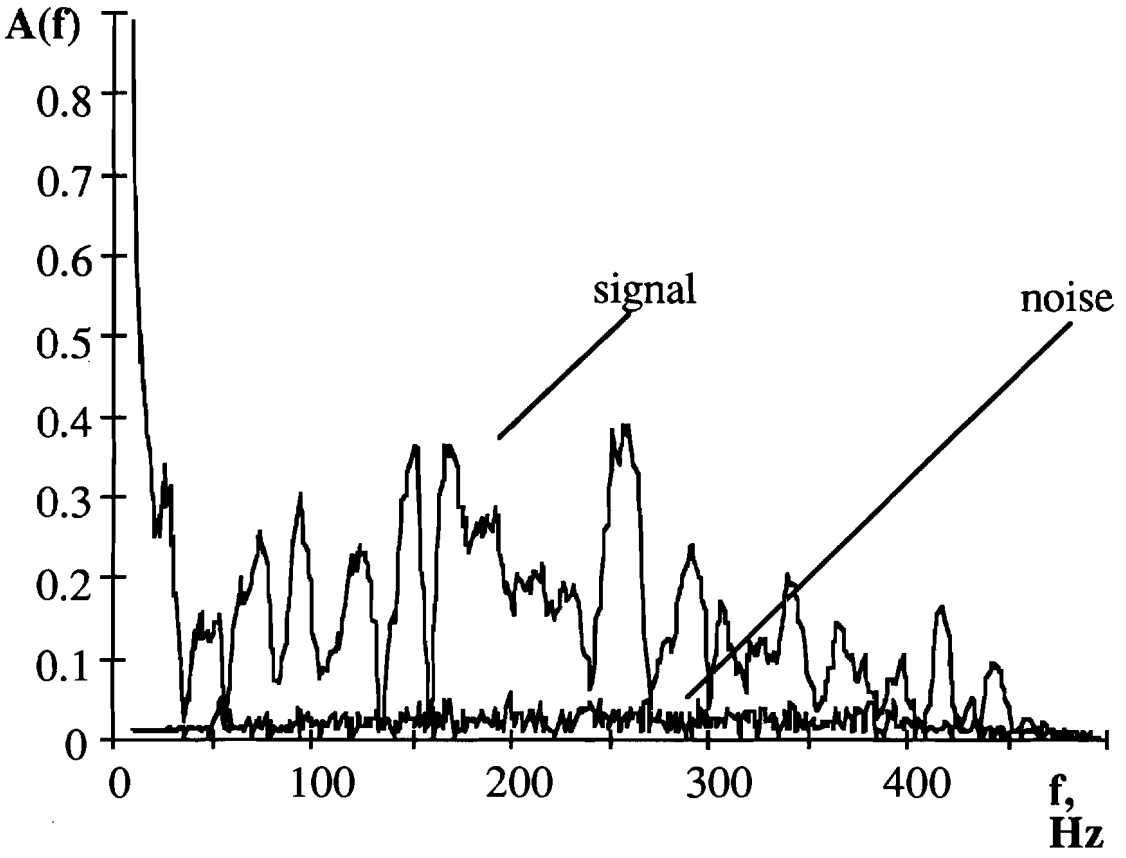

Figure 7. *Fourier amplitudes electrical noise and crack velocity signal for the 2nd sample in Table I.*

Constitutive Equations and Fracture Models for Sea Ice

Co-PI's: Dr. Gregory Rodin and Dr. Richard Schapery
Graduate Students: Mr. Khaled Abdel-Tawab and Ms. Lu Wang

Scope of Model

The research is concerned with the development of mathematical models for sea ice that describe its deformation and fracture behavior. This summary of work-to-date is divided into two parts: (1) linear elastic and viscoelastic deformation behavior of columnar polycrystals and (2) nonlinear and fracture behavior of polycrystals. Each part is discussed separately under major headings for the report.

1. Linear Deformation Behavior

Elastic Model: Elastic moduli and local crystal stresses for columnar, polycrystalline sea ice have been predicted in terms of single crystal properties using an analytical, averaging approach called the self-consistent method. In this method, the number of grains or crystals is assumed to be large, so that the polycrystal behaves as a homogeneous continuum. Anisotropic properties of the polycrystal are predicted explicitly in terms of the distribution of c-axis orientations. Although an existing method of analysis is used, its implementation for anisotropic sea ice has required a considerable amount of new development because earlier work has been limited to isotropic ice. For comparison, upper and lower bounds on elastic constants were found by standard energy-based bounding methods. These results for elastic behavior provide the equations needed to predict viscoelastic behavior.

Figure 1 is a schematic of columnar ice, in which the c-axis for all crystals is in the horizontal plane. The coordinate systems for the polycrystals (x-y-z) and each crystal (x_1, x_2, x_3) are shown in Fig 2; note that the x-axis is the column axis, and thus would be a vertical axis in Fig 1. We have developed equations for anisotropic columnar ice and the special case of transversely isotropic (S2) ice, both in terms of single crystal properties.

Anisotropic columnar ice is a monoclinic material, in which the column axis is the axis of symmetry. Referring to Fig 2, the stress-strain equations for the polycrystalline aggregate may be written in terms of moduli L_{ij},

$$
\begin{aligned}
\sigma_x &= L_{11}\epsilon_x + L_{12}\epsilon_y + L_{13}\epsilon_z + L_{14}\gamma_{yz} \\
\sigma_y &= L_{12}\epsilon_x + L_{22}\epsilon_y + L_{23}\epsilon_z + L_{24}\gamma_{yz} \\
\sigma_z &= L_{13}\epsilon_x + L_{23}\epsilon_y + L_{33}\epsilon_z + L_{34}\gamma_{yz} \\
\tau_{yz} &= L_{14}\epsilon_x + L_{24}\epsilon_y + L_{34}\epsilon_z + L_{44}\gamma_{yz} \\
\tau_{xz} &= L_{55}\gamma_{xz} + L_{56}\gamma_{xy} \\
\tau_{xy} &= L_{56}\gamma_{xz} + L_{66}\gamma_{xy}
\end{aligned} \tag{1}
$$

or in the inverse form using compliances $M_{ij} = [L_{ij}]^{-1}$,

$$
\begin{aligned}
\epsilon_x &= M_{11}\sigma_x + M_{12}\sigma_y + M_{13}\sigma_z + M_{14}\tau_{yz} \\
\epsilon_y &= M_{12}\sigma_x + M_{22}\sigma_y + M_{23}\sigma_z + M_{24}\tau_{yz} \\
\epsilon_z &= M_{13}\sigma_x + M_{23}\sigma_y + M_{33}\sigma_z + M_{34}\tau_{yz} \\
\gamma_{yz} &= M_{14}\sigma_x + M_{24}\sigma_y + M_{34}\sigma_z + M_{44}\tau_{yz} \\
\gamma_{xz} &= M_{55}\tau_{xz} + M_{56}\tau_{xy} \\
\gamma_{xy} &= M_{56}\tau_{xz} + M_{66}\tau_{xy}
\end{aligned} \tag{2}
$$

Observe that there are thirteen independent elastic constants.

For comparison with experimental results, it is helpful to relate the compliances to the so-called engineering constants consisting of Young's' moduli, Poisson's ratios and shear moduli. Specifically, the Young's modulus E_x and two Poisson's ratios ν_{xy} and ν_{xz}, which are defined using loading in only the x direction, are obtained from Eq (2) after setting $\sigma_y = \sigma_z = \tau_{yz} = 0$; thus

$$
\begin{aligned}
E_x &\equiv \frac{\sigma_x}{\epsilon_x} = \frac{1}{M_{11}} \\
\nu_{xy} &\equiv -\frac{\epsilon_y}{\epsilon_x} = -\frac{M_{12}}{M_{11}} \\
\nu_{xz} &\equiv -\frac{\epsilon_z}{\epsilon_x} = -\frac{M_{13}}{M_{11}}
\end{aligned} \tag{3}
$$

The Young's modulus E_y and Poisson's ratios ν_{yx} and ν_{yz} are defined similarly using loading in only the y direction, while the Young's modulus E_z and Poisson's ratios ν_{zx} and ν_{zy} are defined for loading in only the z direction. The shear modulus G_{xy} is defined by applying shear stress τ_{xy} only,

$$
G_{xy} \equiv \frac{\tau_{xy}}{\gamma_{xy}} = \frac{1}{M_{66}} \tag{4}
$$

and G_{xz} and G_{yz} are defined similarly.

Employing the x_i coordinate system in Fig 2, the stress-strain equations for a single, hexagonal crystal are

$$\begin{aligned}
\sigma_1 &= C_{11}\epsilon_1 + C_{12}\epsilon_2 + C_{13}\epsilon_3 \\
\sigma_2 &= C_{12}\epsilon_1 + C_{11}\epsilon_2 + C_{13}\epsilon_3 \\
\sigma_3 &= C_{13}\epsilon_1 + C_{13}\epsilon_2 + C_{33}\epsilon_3 \\
\tau_{23} &= C_{44}\gamma_{23} \\
\tau_{13} &= C_{44}\gamma_{13} \\
\tau_{12} &= C_{66}\gamma_{12}
\end{aligned} \tag{5}$$

where $C_{66} = (C_{11} - C_{12})/2$.

A crystal or grain, with the elastic constants in Eq (5), is assumed to be a circular cylinder with its axis parallel to the x-axis. Each one is assumed to be embedded in an infinitely large, monoclinic continuum whose elastic moduli are initially unknown, but they are those of the polycrystal. The moduli in Eq (1) are then predicted from a set of equations that result when the volume average of the stresses in all crystals is equated to the stresses applied to a macroscopically homogeneous polycrystal. This approach is called the *self-consistent method.* The equations employed in this analysis have also been used to predict average stresses in each crystal as a function of c-axis orientation. When extended to viscoelastic behavior these stresses provide, for example, an indication of how creep behavior influences the stresses and thus the tendency for microcracking.

Viscoelastic Model: Creep of single crystals of freshwater ice occurs most readily along basal planes. This behavior is accentuated for sea (saline) ice because of the concentration of brine pockets on basal planes. This observation has been used in extending the elastic polycrystal model to linear viscoelastic behavior by means of the elastic-viscoelastic correspondence principle. Starting with elastic solutions and creep properties assigned only to shearing along the basal plane for each individual crystal, a mathematical model for polycrystal response to arbitrary applied stress histories has been developed. It has been used to predict strain response to constant stress (creep), constant stress rate and cyclic (sinusoidal) stressing.

The constitutive equations for viscoelastic behavior are similar to the elastic equations, except convolution integrals appear. For example, to characterize creep on the basal plane, the fourth equation in Eq (5) becomes

$$\tau_{23} = \int_{-\infty}^{t} C_{44}(t - t')\frac{d\gamma_{23}}{dt'}dt' \tag{6}$$

where $C_{44}(t)$ is a (time-dependent) shear relaxation modulus; it is equal to τ_{23}/γ_{23} when γ_{23} is applied at $t = 0$ and then held constant. For comparison with experi-

mental behavior, the inverse form of Eq (6) is better,

$$\gamma_{23} = \int_{-\infty}^{t} D_{44}(t-\tau)\frac{d\tau_{23}}{dt'}dt' \tag{7}$$

in which $D_{44}(t)$ is a creep compliance; it is equal to γ_{23}/τ_{23} when τ_{23} is applied at $t = 0$ and held constant thereafter. If all significant single-crystal creep is due to basal-plane shearing, then one uses an equation identical to Eq (6) or (7) to relate τ_{13} and γ_{13}, while all other stresses and strains for the single crystal are related using the elastic constants.

Extension of Eqs (1) and (2) to viscoelastic behavior using the elastic-viscoelastic correspondence principle leads to a representation in which convolution integrals (in terms of thirteen relaxation moduli or creep compliances) appear in place of the thirteen elastic constants. In general, all thirteen are affected by basal-plane creep, but only some are significantly affected. With the convolution integrals, response to arbitrary stress or strain input histories may be easily predicted.

2. Nonlinear and Fracture Behavior

Brittle Fracture: In brittle fracture tests, ice behavior may be significantly affected by coarse grains whose diameter usually exceeds 1 mm. Namely, crack growth observed in the lab should be viewed as a sequence of increments which involve single crystals rather than continuous propagation through a quasi-homogeneous body, as it is done with conventional materials. Central to our approach is the classical formalism of Eshelby and Rice which allows us to properly identify thermodynamic forces consistent with Griffith's fracture criterion.

Creep Model: In many experiments ice undergoes primary creep. This phenomenon has been modeled in the linear range using the viscoelastic model described above, and in the nonlinear range using the concept of back stress. Although the mathematical structure of equations is simmilar to that proposed by Ashby and Duval, our interpretation is based on the Bailey-Orowan concept rather than the notion that the deformation is controlled by a non-basal slip system(s). The nonlinear model was compared with experiments reported in the literature, and implemented as a user-defined subroutine in the finite element program ABAQUS. In addition to primary creep, we are in the process of developing a model for tertiary creep microcracking. This model reflects experimental results of Gold and Zaretsky.

Inelastic Fracture Model: Using the aforementioned creep models in ABAQUS, we have studied the rate-dependence of the apparent fracture toughness and crack tip creep zones. To this end, we considered specimens subjected to a remote stress field

defined by the opening-mode stress intensity factor, K_I, as well as laboratory specimens used by Dempsey and co-workers.

Findings To-Date

1. Linear Deformation Behavior

Elastic Model: Predictions for both granular (isotropic) and anisotropic columnar ice have been completed. Emphasis has been on developing and applying the theory for anisotropic columnar ice, which is a commonly occurring form of sea ice. In this case the c-axis is in the plane of the ice sheet. Considering several different distributions of c-axis orientations, all anisotropic moduli have been predicted as a function of the basal plane shear modulus, C_{44}. The range of C_{44} extends from its value for elastic, freshwater ice to zero. This range is needed in order to predict viscoelastic behavior of saline ice, allowing for extensive creep and other significant amounts of softening due to brine pockets. Figure 3 illustrates the effect of C_{44} on the in-plane Young's modulus (E_y or E_z) for transversely isotropic (S2) ice.

Average stresses within individual crystals have been found. Consider, as an example, S2 ice subjected to a uniaxial compressive stress σ_y. When C_{44} is very small the maximum local compressive and tensile stresses are $-1.5 \mid \sigma_y \mid$ and $0.5 \mid \sigma_y \mid$, respectively. They act in the y-z plane and are parallel to and perpendicular to the y-axis, respectively; the latter stress may cause microcracks whose planes are parallel to the applied stress direction.

Viscoelastic Model: Starting with elastic solutions and creep properties assigned only to shearing along the basal plane for each individual crystal, a mathematical model for polycrystal response to arbitrary applied stress histories has been developed, as discussed above.

Creep data for S2 saline ice loaded uniaxially in the isotropic plane were provided by David Cole, and they were used to check the theoretical model. The experimental strain exhibits power law, primary creep behavior, $\epsilon \sim t^n$. By curve-fitting the data the exponent was found to be approximately 0.5, as shown in Fig 4. This value of the exponent is predicted by our model when the basal plane exhibits simple viscous creep. Namely, if the single crystal creep compliance is of the form $D_{44} = D_1 t$, then the polycrystal creep obeys a power law with $n \simeq 0.5$. Mechanical interactions between individual crystals within a polycrystal convert the single-crystal viscous creep to viscoelastic creep ($n < 1$) for the polycrystal.

The value of $n = 0.5$ is for S2 ice. For other types of columnar ice the predicted exponent is different. Figure 5 shows the exponent for a class of orthotropic, columnar ice, which illustrates one set of results obtained. A discrete distribution of c-axis

orientations was used to illustrate their effect. Specifically, an equal number of c-axes are oriented in the y-z plane at 0^0 and $\pm\theta^0$, relative to the y-axis. When $\theta = 60^0$, the polycrystal behaves as S2 ice, with $n \simeq 0.5$. The several different curves are for different amounts of creep and brine, as defined by basal plane shear modulus, C_{44} divided by that for elastic, freshwater ice; this ratio is designated in Figure 5 as "Normalized C_{44}." Observe that the exponent is relatively insensitive to the amount of creep and brine, but is sensitive to the c-axis orientation distribution.

2. Nonlinear and Fracture Behavior

Brittle Fracture: At this point, we have developed a good understanding of how coarse grains influence the induced crack tip fields. Our findings are summarized as follows:

- In general, there are two singular elastic crack tip fields. The first one is the outer standard field derived from classical elasticity. The second field is inside the grain containing the crack tip, and it is consistent with the anisotropy of this grain.
- Only the inner, anisotropic singular field is consistent with Griffith's fracture criterion.
- The intensity of the anisotropic field is essentially controlled by the grain containing the crack tip.
- To determine the intensity of the anisotropic field it is sufficient to analyze a homogeneous anisotropic specimen whose elasticity tensor coincides with that of the grain containing the crack tip.
- The apparent fracture energy is a strong function of the orientation of the grain containing the crack tip. It may vary by a factor of four from specimen to specimen.
- Under a broad range of loading conditions, all of the above findings are relevant to structural ceramics, not just ice.

Inelastic Fracture Models: We have carried out a series of computations in which we have determined the loading rate effect on the apparent fracture toughness. Representative results are shown in Figure 6 in the form of a function $K_{IQ}(\dot{K}_I)$ at $T = -10$C. In addition, we have found that the crack tip nonlinear creep zones are significantly larger than those predicted by Riedel and Rice, and appear to be in agreement with those observed in fracture experiments by Dempsey and co-workers. Furthermore, it appears that a typical fracture toughness test performed in the laboratory satisfies small-scale creep conditions for fresh-water ice but not for saline ice.

Analysis and Publication Plans

At this point, we have developed an analytical/computational infrastructure which allows us to coordinate our effort with the laboratory and field experimental activities of David Cole at CRREL and John Dempsey at Clarkson. Appropriate arrangements for the joint effort have been made. Assisted by the laboratory and field results, the existing models will be further verified and refined, as necessary, and then used to design more definitive experiments, so that it will be possible to establish improved guidelines for constitutive and fracture testing of ice. Also, as additional experimental results become available, single crystal models will be improved and a realistic analysis for ice plates with property gradients will be developed.

Two papers are in preparation for the Ice Mechanics-95 Symposium at the ASME-AMD-MD Summer Conference, June 28-30, 1995, UCLA:

"Prediction of Elastic and Viscoelastic Properties of Anisotropic Columnar Ice," L. Wang and R. A. Schapery.

"Inelastic Effects in Crack Growth of Fresh-Water and Saline Ice," K. Abdel-Tawab and G. J. Rodin.

Following is a list of our publications resulting from the SIMI program:

"Viscoelastic Deformation Behavior of Ice Based on Micromechanical Models," R. A. Schapery, in *Ice Mechanics*, ASME Publication AMD-Vol. 163, 1993, pp. 15-33.

"Stress Transmission in Polycrystals With Frictionless Grain Boundaries," G. J. Rodin, *J. Applied Mechanics*, 1995 (in press).

"The Role of Grain Structure in Brittle and Semi-Brittle Fracture of Polycrystals," K. Abdel-Tawab and G. J. Rodin, submitted to *Acta Metallurgica Et Materialia*, 1994.

"On the Relevance of Linear Elastic Fracture Mechanics to Ice," K. Abdel-Tawab and G. J. Rodin, *Int. J. Fracture*, Vol. 62, 1993, pp. 171-181.

"An Interpretation of the Fracture Toughness Test Results on Ice,"K. Abdel-Tawab and G. J. Rodin, in *Ice Mechanics*, ASME Publication AMD-Vol. 163, 1993, pp. 49-59.

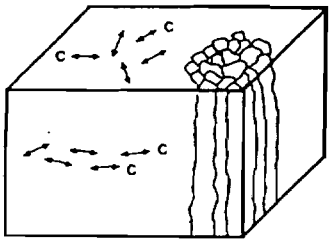

Fig. 1 Columnar ice structure

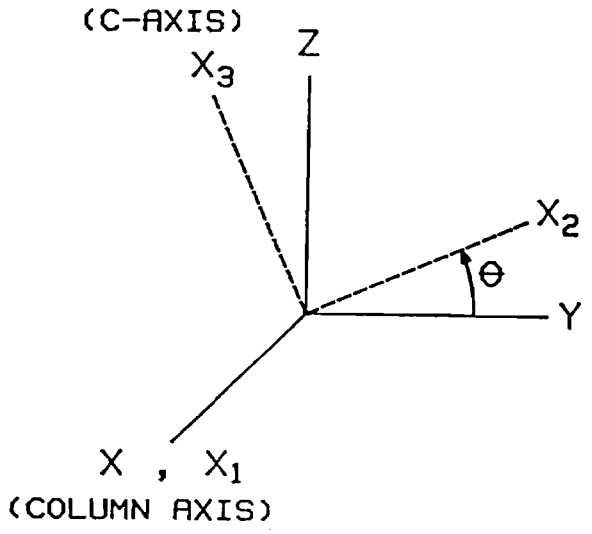

Fig. 2 Coordinate axes. The x-axis is the thickness or vertical direction in Fig. 1.

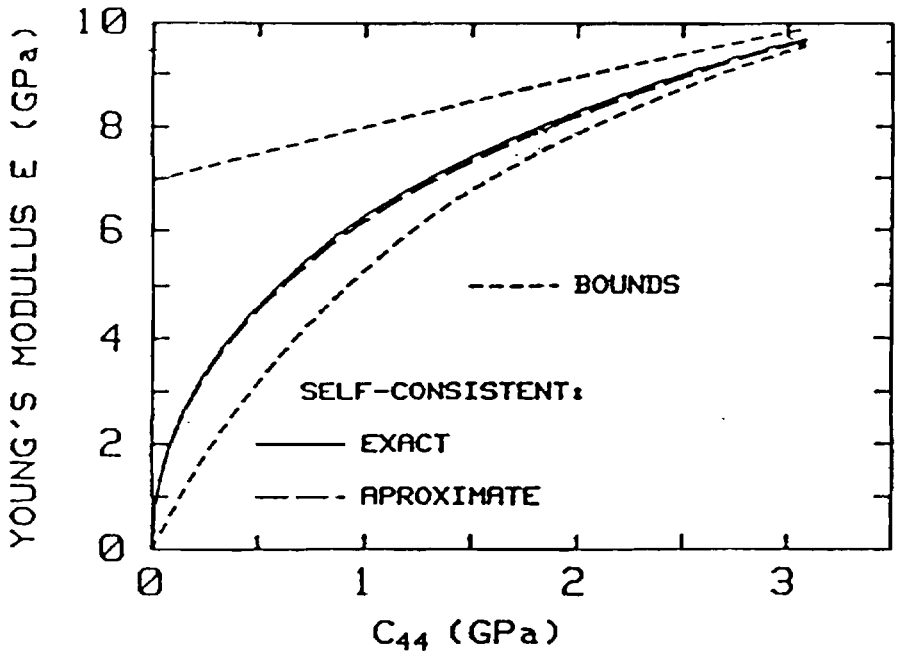

Fig. 3 In-plane Young's modulus for S2 ice.

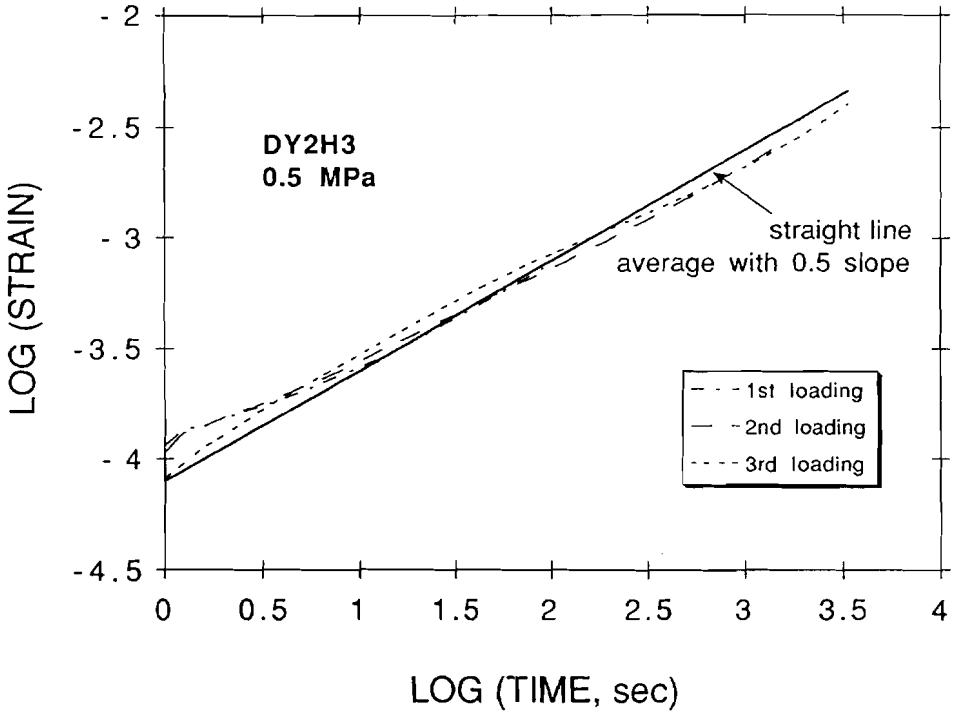

Fig. 4 Creep curves for specimens subjected to repeated constant load, from S2 saline ice data provided by David Cole. All curves have been shifted to a common time origin.

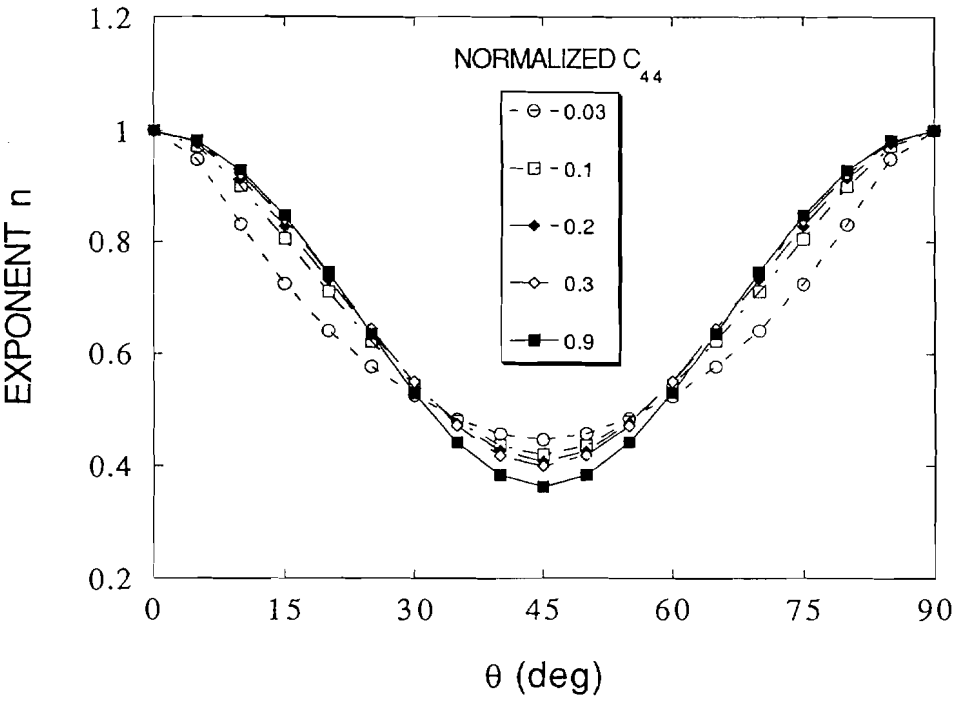

Fig. 5 Creep exponent for in-plane, uniaxial loading of columnar ice having $0/+\theta/-\theta/$ c-axis orientations.

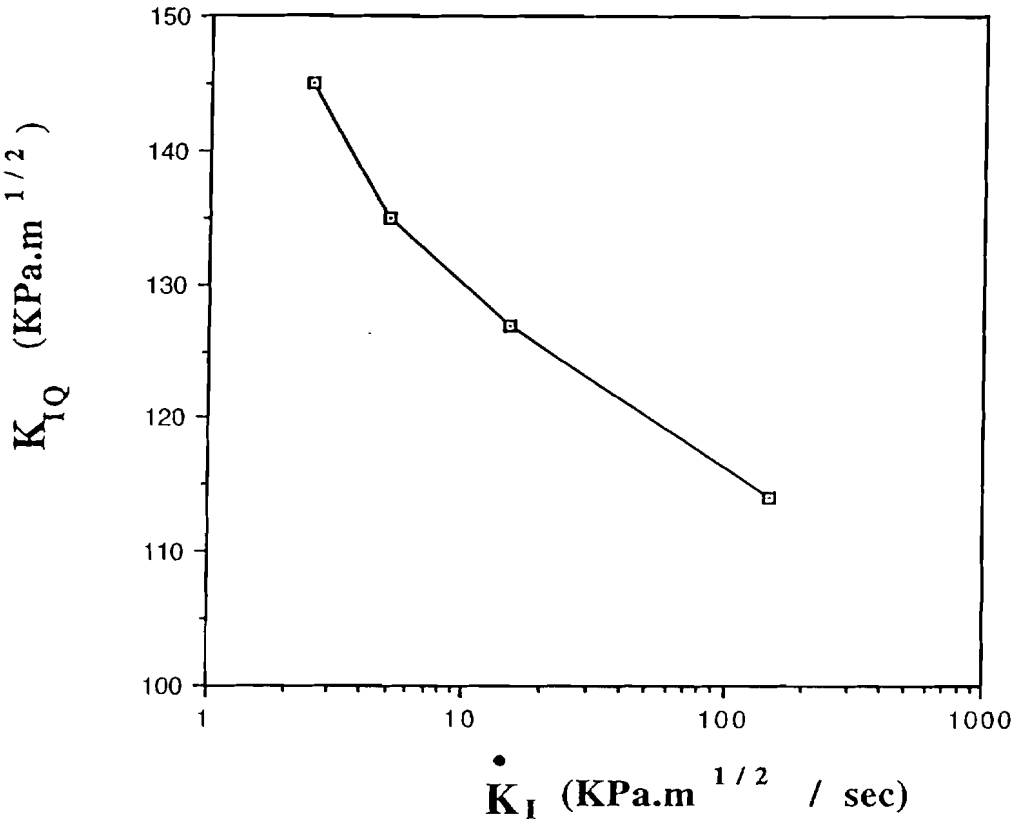

Fig. 6 Fracture toughness vs. applied stress intensity factor rate

Physically-Based Constitutive Modeling of Ice: Damage and Failure

Mao S. Wu (P.I.), and J. Niu, Y. Zhang, H. Zhou (Research Assistants), Department of Engineering Mechanics, University of Nebraska-Lincoln

Scope of Model

The focus of this research is to develop physically-based theories of damage and failure in the ductile-to-brittle transition domain in which ice realizes its maximum strength. The approach consists of a multi-scale hierarchy whereby brittle behavior is studied at the crystal (10^{-3} to 10^{-2} meter) and the specimen (10^{-1} to 1 meter) scale. See Figure 1. This provides a basis for predicting the behavior at the field scale.

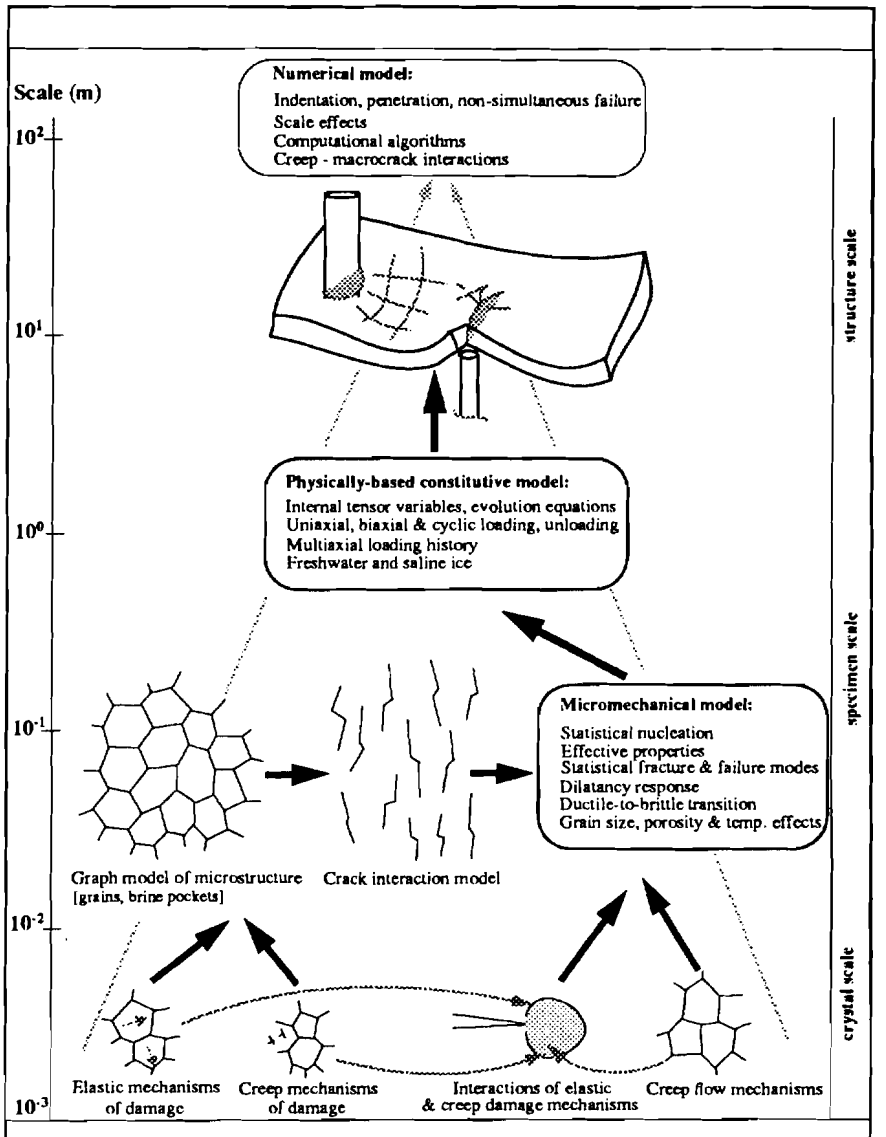

Figure 1. Physically-based constitutive modeling of ice: hierarchical methodology

The fundamental problems of failure prediction include: (a) modeling of the statistical material heterogeneities (grain and brine pocket sizes, shapes, orientations) which can critically determine failure, (b) insufficient knowledge of the physical mechanisms of material behavior at various scales and under complex loading conditions, and (c) the challenge of developing theoretical and computational methods to describe the physical mechanisms, their interactions, the damage produced, the effective properties, and the ultimate failure. To overcome these difficulties, the heterogeneity of the microstructure is captured by using a *graph model*. The damage and failure of the specimen are then predicted using three models which describe (a) *crack nucleation* (sub-crystal and crystal scales), (b) *crack interactions* (crystal scale), and (c) *effective properties* and *failure* (specimen scale). These models are identified in Figure 1.

Domain of Model Applicability -- The models are applicable for the following conditions: plane strain, temperatures between 0 and -50°C, ductile-to-brittle transition, and uniaxial or biaxial loading. The material investigated is S2 ice, i.e., the crystals have random in-plane *c*-axes. The grain size range is 1 to 10 mm.

Mathematical Model of Microstructure -- A two-dimensional graph model of 'Voronoi' polygons (grains) suffices for the type of analysis attempted (see Figure 2). The model is generated by distributing randomly a set of grain nuclei in a plane and following the rule that each interior point of any polygon is closer to the associated nucleus than all other nuclei. In sea ice, a network of pressurized brine pockets of circular can be superimposed on the grains. A random number generator assigns each crystal the orientation of its *c*-axis.

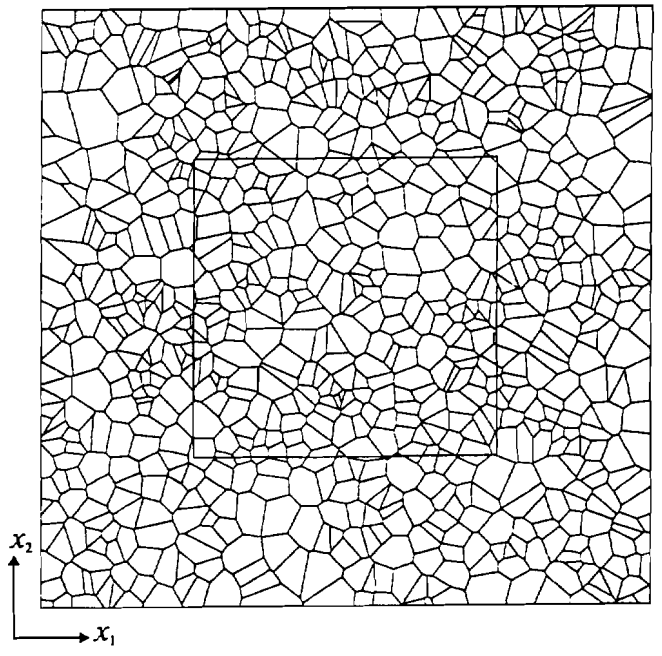

Figure 2. Voronoi polygons used to analyze statistical nucleation and failure in S2 ice

Crack Nucleation Model -- A major theoretical task is to estimate the stress concentrations due to various possible physical mechanisms. It is then possible to obtain a comparative study of the most probable mechanisms for nucleating cracks in ice. Three possible mechanisms that have been investigated: (a) elastic anisotropy and thermal expansion anisotropy of the grains, (b) pile-ups of grain boundary dislocations (GBDs) at triple points, and (c) the presence of brine pockets. All three mechanisms are related to the microscale heterogeneities: grains, dislocation groups and brine pockets.

Due to the elastic or thermal expansion anisotropy, each grain in general deforms differently from its neighbors in a polycrystalline matrix (Figure 3). The misfit between grains thereby generates stress concentrations and possibly stress singularities at grain corners. In the model, these stress concentrations are estimated using the Eshelby technique, and crack nucleation is determined using linear elastic fracture mechanics (Wu and Niu, 1994).

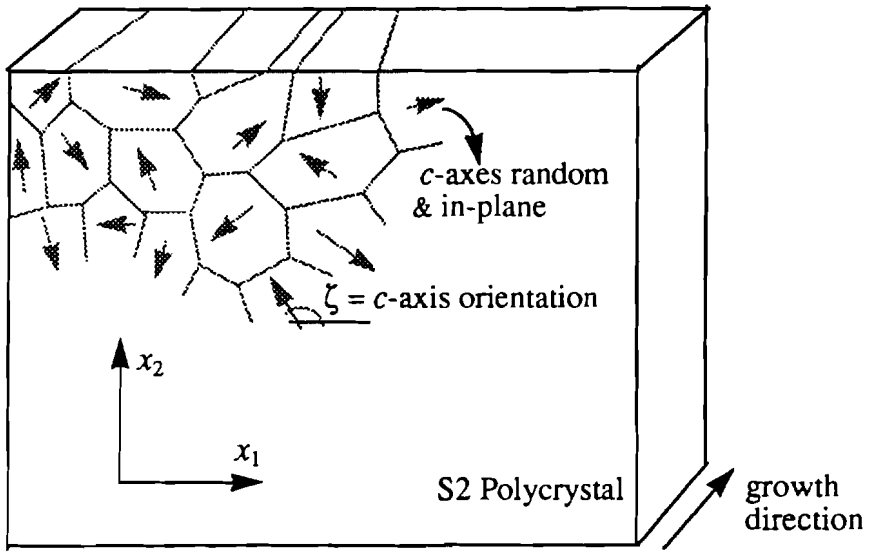

Figure 3. Crack nucleation: thermal expansion or elastic anisotropy between randomly oriented grains generates stress concentrations in the polycrystalline S2 matrix

The GBD pile-up mechanism is examined by analyzing the interactions between three pile-up groups on the grain boundaries around triple points (Figure 4). This mechanism is associated with grain boundary sliding. The nucleation criterion is formulated in terms of the energy of the dislocation groups and the energy of a crack wedged open by dislocations. The nucleation of small cracks where none existed before is examined using this model (Wu and Niu, 1994, 1995c). The stability of the nucleated cracks is also studied.

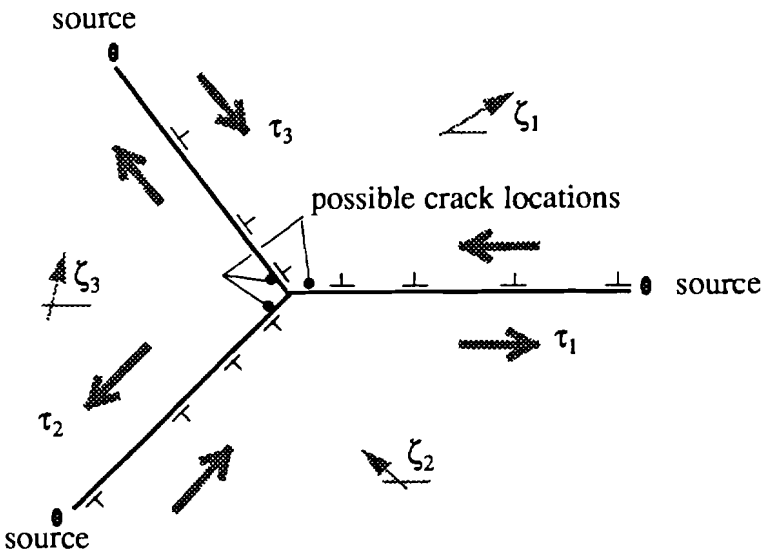

Figure 4. Crack nucleation: model of the pile-up of grain boundary dislocations around a triple point

Because of their shapes and the pressurized brine in them, brine pockets are sources of stress concentrations, which can be estimated by solving a system of integral equations. Stress concentrations due to the elastic anisotropy (or thermal expansion anisotropy) mechanism are also present. The two physical mechanisms are analyzed simultaneously (Figure 5). Crack nucleation initiating from the brine pocket surfaces is predicted using linear elastic fracture mechanics (Wu and Zhang, 1995).

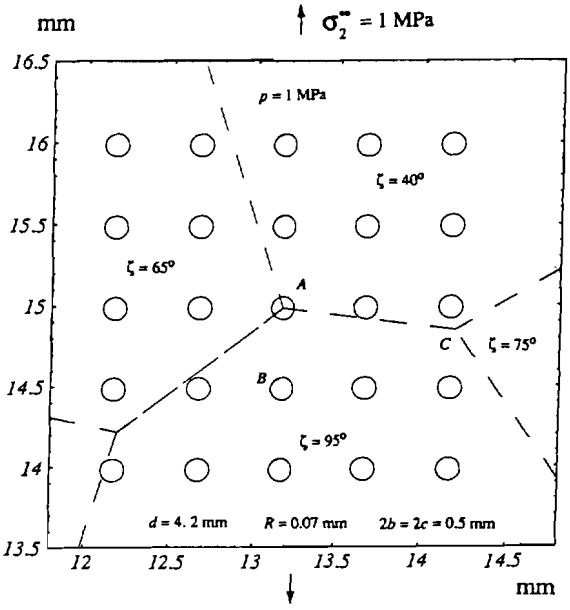

Figure 5. Crack nucleation: model of two heterogeneities (brine pockets and grains) in sea ice

Crack Interaction Model -- In general, the nucleated cracks do not immediately cause failure in compression. To predict crack instability leading to specimen fracture, it is necessary to compute the interactions between cracks. Two difficulties arise: the presence of kinked cracks in compression (i.e., complicated crack geometry), and the calculations of the stress intensity factors of interacting cracks with arbitrary locations and orientations. A kinked crack consists of a parent crack capable of undergoing frictional sliding and a pair of branched cracks. A simplified model in which a kinked crack is replaced by a straight crack loaded by two point forces is adopted, and a model of crack interactions based on the superposition of crack tractions is developed (see Figure 6, and Wu and Niu, 1995a).

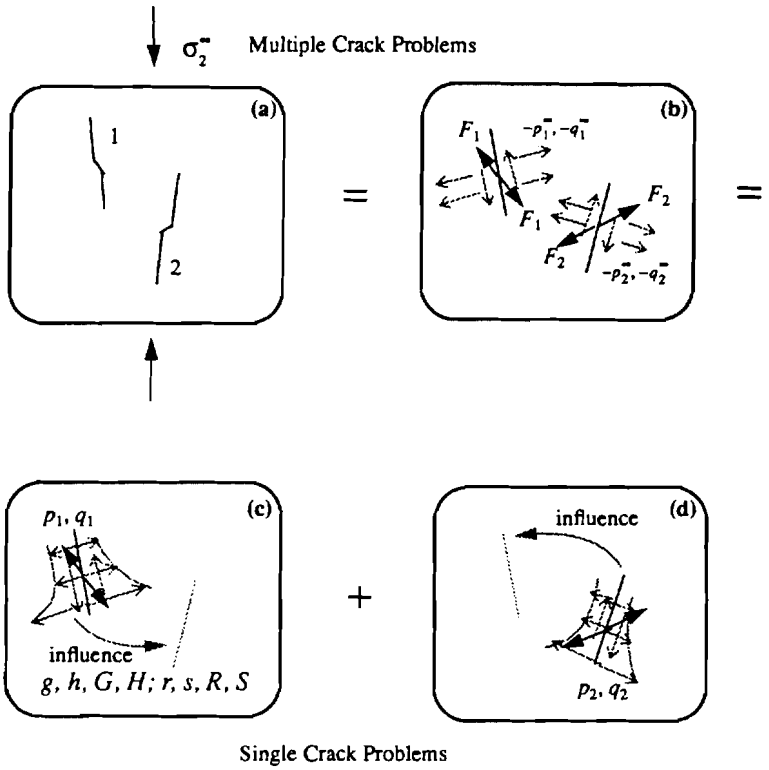

Figure 6. Superposition scheme for analyzing crack interactions. (a) Multiple cracks, (b) Equivalent problem, (c) Single cracks with point forces and crack tractions

Model of Effective Properties and Failure -- The elastic properties of interest are the effective compliance components of the damaged specimen, since they can be used to calculate the constitutive behavior of the damaged ice. In the model formulation, the effective compliance is computed directly from the crack opening displacements of the interacting cracks in a material rendered anisotropic by the cracks. Other models of effective compliance such as the non-interacting and self-consistent models are available, as used in Wu (1993, 1994). Finally, the failure of the specimen is determined by applying the maximum mode I stress intensity factor criterion to all crack tips. The computation of the stress intensity factors is based on the crack interaction model described above.

Significant Results

The significant model results can be divided into three groups: crack nucleation, damage accumulation and its influence on effective properties, and complete failure.

Crack Nucleation -- For Voronoi polygons with no brine pockets, the stress concentrations on grain boundaries due to elastic or thermal expansion anisotropy are found to obey Gaussian distributions. The maximum amplitude on the grain boundary a thousandth of the grain boundary length from the triple point is ~ 0.5 MPa when the remote stress is 1 MPa. The small amplitude is due to the small elastic anisotropy of ice crystals. For thermal expansion anisotropy, the maximum amplitude is ~ 8 MPa for a rapid temperature change of -20°C. In reality, the temperature change occurs over time and stress relaxations occur so that the results for thermal expansion anisotropy are overestimated.

The small stress concentrations due to the anisotropy mechanisms can generate cracks if they are assumed to act on pre-existing crack precursors. Based on a comparative study, the GBD pile-up mechanism emerges as a more dominant mechanism. In fact, under compression the pile-up mechanism can generate very small stable cracks (~ 0.002 of the mean grain size) as well as unstable cracks which propagate until they meet the next triple points to become boundary cracks. *No* pre-existing precursors are assumed. The length of the stable cracks obeys a Gamma-type distribution with a long tail (Figure 7). The mean and standard deviation of the distribution depend significantly on the mean grain size and the applied stress amplitude. Furthermore, the ability of the model to predict the crack location distribution is critical to failure prediction since the crack locations determine important phenomena such as damage localization and crack interactions.

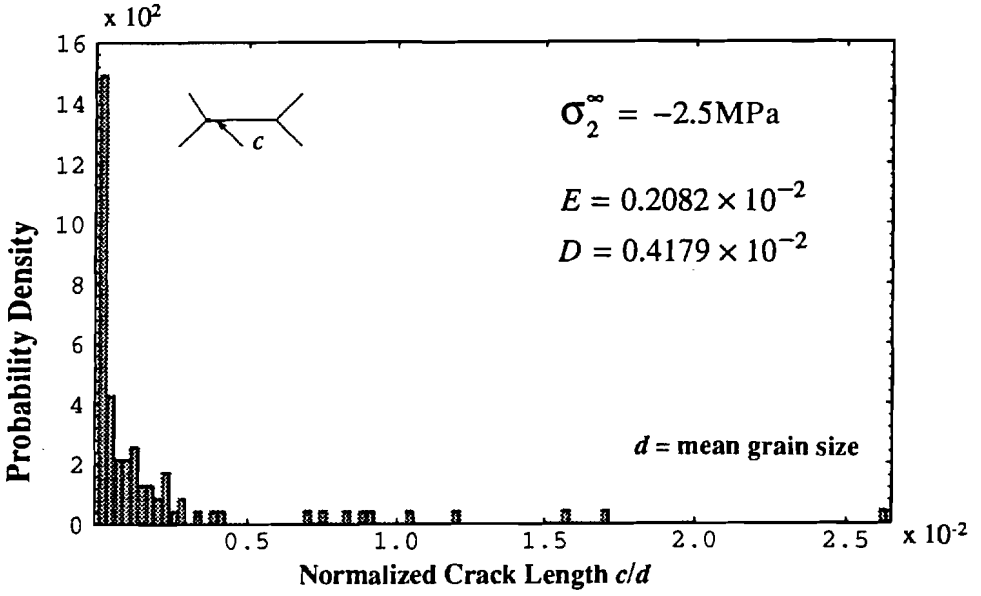

Figure 7. Probability density of the length of stable cracks (pile-up mechanism)

The models have also been employed to study crack nucleation in sea ice under uniaxial tension. Since the first cracks in tension generally lead to the failure of the specimen, nucleation defines failure in tension. For this reason, the model results for sea ice are presented subsequently when the results for failure are described.

Damage Accumulation and Effective Compliance -- Damage accumulation can be measured by a scalar quantity, i.e., the crack density, which is defined as the sum of the squares of all crack lengths divided by the area of the microstructure under consideration. Figure 8 shows the evolution of the crack density with the applied uniaxial compression for four different realizations of the random microstructure. An important result is the dependence of the evolution curves on the microstructure - the crack density may reach its saturation value without the microstructure failing (microstructures I, II, III) or with failure occurring almost immediately (microstructure IV). Thus, a scalar critical crack density is not a good failure descriptor. The existence of a saturation value is due to the exhaustion of sites at which nucleation can occur easily. The dependence on the mean grain size is such that crack nucleation in the case of the smaller grain size occurs at a larger stress level and the corresponding saturation crack density is maintained to a larger value of the failure stress.

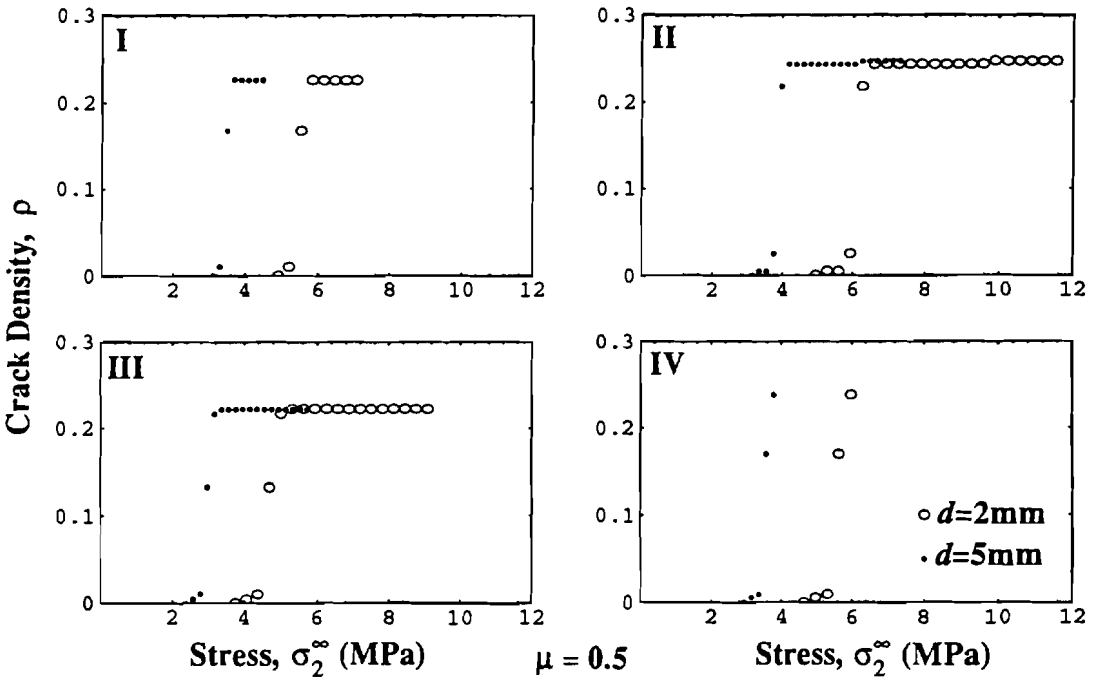

Figure 8. Crack density evolution with applied compression for four microstructures

Furthermore, numerical simulations show that the effective compliance is a strong function of the crack orientation distributions, and is strongly anisotropic in the case where all the cracks are approximately aligned with the compressive axis of loading. This implies that

the scalar crack density defined above is not sufficient to characterize damage accumulation completely. The effective compliance is a relatively weak function of the microstructural randomness. This is because the compliance is a globally averaged quantity, and the effects of the different microstructures of nominally identical specimens are smoothed in the constitutive response. The dependence becomes very significant for the failure stress, however, as shown below.

Failure Stress -- The failure stress or strength is dependent on many factors, e.g., biaxiality, temperature, and mean grain size. The model predictions of the strength dependence on these factors are in good agreement with experimental data. In particular, the dependence of the compressive strength on the randomness of the microstructure (for S2 ice) is shown in Figure 9. It is noted that failure initiates locally and is therefore a strong function of the local heterogeneity. This is reflected in the rather large strength variations (up to 100%) of the four microstructures at temperatures between 0 and -50°C.

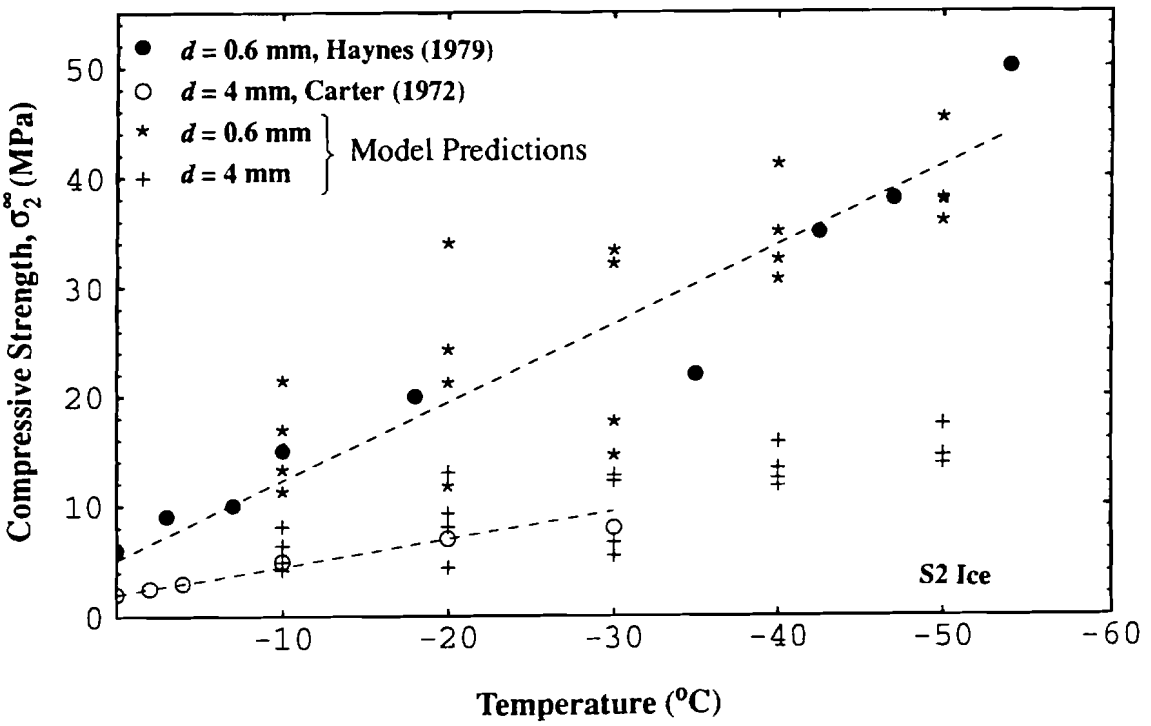

Figure 9. Dependence of uniaxial compressive strength on microstructure and temperature

As a final example, the tensile strength of the Alaskan Beaufort sea ice is predicted using a microstructure containing pressurized brine pockets. The tensile strength, approximately equal to the nucleation stress, is predicted to be a non-linearly decreasing function of porosity, i.e., it decreases from ~ 0.8 MPa at 20 ppt porosity to 0.2 MPa at 60 ppt porosity. The

predictions agree well with available experimental results (Figure 10). A detailed investigation of the stress fields reveals that brine pockets at triple points do not necessarily give rise to larger circumferential stress than brine pockets within grains. Considering only the elastic anisotropy mechanism, the preferred sites for crack nucleation appear to be on the brine pocket surfaces rather than at the triple points (without brine pockets). This is due to the weak elastic anisotropy and the strong effect of pressure within brine pockets (0.8 - 3 MPa). The relative importance of the dislocation pile-up mechanism in comparison to the brine pocket mechanism, however, remains to be investigated.

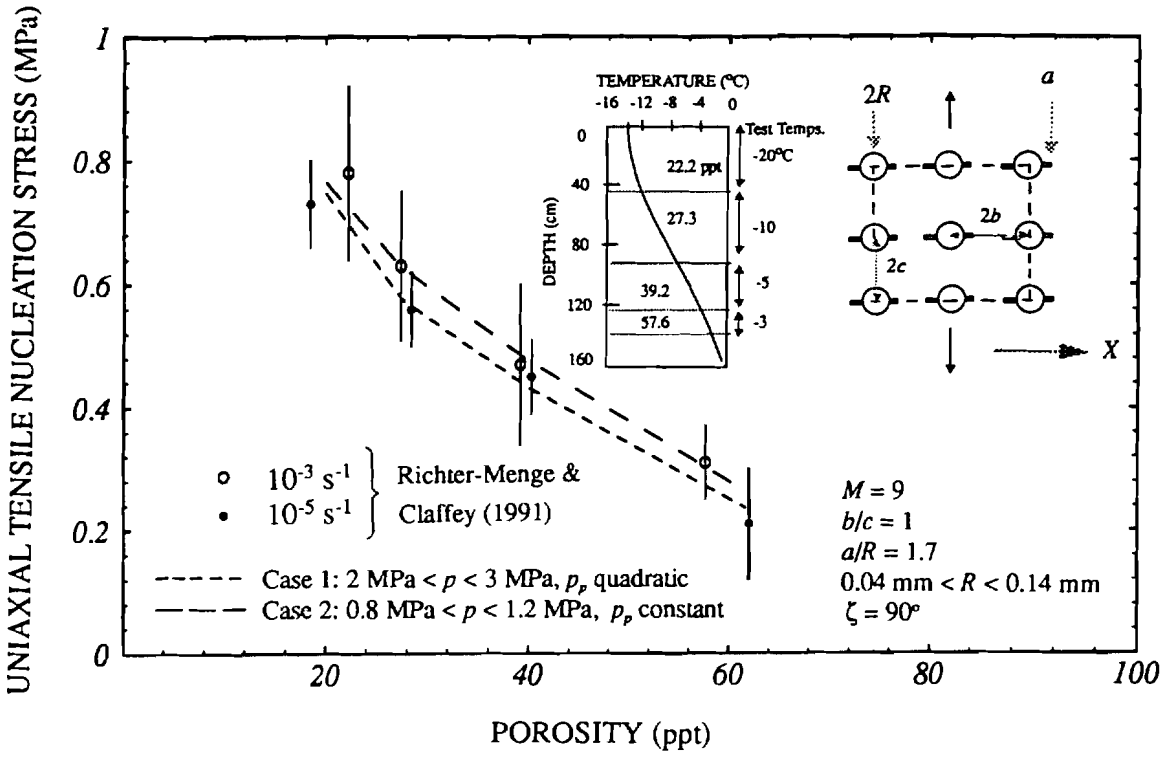

Figure 10. Dependence of the tensile strength on the porosity of Alaskan Beaufort sea ice

Summary

The damage and failure models outlined in this paper possess the following salient features: (a) a consistent hierarchical approach linking the dislocation scale to the macroscopic (laboratory specimen) scale is feasible, i.e., the computational results derived from this linkage are consistent with test data obtained on the specimen scale, (b) the models are physically-based, i.e., the physical mechanisms responsible for the failure phenomena are integrated in the model formulation and all material parameters have definite physical meaning, and (c) the material heterogeneities are taken into account explicitly so that statistical results are obtained naturally.

Analysis and Publication Plans

Model Development -- Further development is needed to solve the following fundamental problems of damage and failure prediction at the sub-crystal, crystal, and specimen scales:
(a) Dislocation group interactions and grain boundary sliding,
(b) Interactions of brine pockets containing surface flaws,
(c) Interactions of arbitrarily oriented and located kinked cracks with long or short parent cracks in an anisotropic porous medium, and
(d) Failure criterion based on the synthesis of developed models.
Detailed comparison of model predictions with test data at various scales will be carried out in collaboration with SIMI investigators at the Massachusetts Institute of Technology.

Planned Future Publications --

(1) Analysis of the interactions of grain boundary dislocation groups by a discrete approach.
(2) Wedge crack formation in polycrystals by continuum and discrete dislocation modeling.
(3) Interaction of brine pockets containing surface flaws.
(4) Effects of kinked crack interactions on stress intensity factors and effective elastic compliance.
(5) Micromechanical prediction of the failure of sea ice in compression and tension.

Recent Journal Publications (resulting from the SIMI program)

(1) Wu, M.S. (1993). Effective moduli of finite anisotropic media with cracks. *Mechanics of Materials*, 15:139-158.
(2) Wu, M.S. (1994). Material anisotropy effects on stress intensity factors and the effective elastic compliance. *Engineering Fracture Mechanics*, 48(2): 177-198.
(3) Wu, M.S. and Niu, J. (1994). A theoretical investigation into the nucleation of stable precursors in polycrystalline ice. *International Journal of Fracture*, 68: 151-181.
(4) Wu, M.S. and Niu, J. (1995a). Micromechanical prediction of the compressive failure of ice: model development. *Mechanics of Materials*, In Press, 24p.
(5) Wu, M.S. and Niu, J. (1995b). Micromechanical prediction of the compressive failure of ice: numerical simulations, *Mechanics of Materials*, In Press, 26p.
(6) Wu, M.S. and Niu, J. (1995c). A theoretical analysis of crack nucleation due to grain boundary dislocation pile-ups in a random ice microstructure. *Philosophical Magazine A*, In Press, 24p.
(7) Wu, M.S. and Zhang, Y. (1995). Crack nucleation in saline ice with interacting inhomogeneities. *Cold Regions Science and Technology*, In Press, 45p.

Conference papers: Winter Annual Meeting of ASME (1992), ASCE-ASME-SES Meeting (1993), U.S. National Congress of Applied Mechanics (1994), Society of Engineering Science Meeting (1994).

APPENDIX A

Reprint

Air-Ice-Ocean Interaction: Lead Dynamics, Ice Mechanics, Ice Acoustics
(Sea Ice Mechanics Workshop, Airlie, VA, 1990)

Air-Ice-Ocean Interaction

Lead Dynamics Ice Mechanics Ice Acoustics

Office of Naval Research

Sea Ice Mechanics Workshop,12-14 November 1990, Airlie, Virginia

SEA ICE MECHANICS WORKSHOP

PROCEEDINGS

November 12-14, 1990

Thomas B. Curtin (Editor)

OFFICE OF NAVAL RESEARCH

April 1991

4/5/91
1-0803-91/A

TABLE OF CONTENTS

3/8/95
1-0803-91/G

INTRODUCTION

Beginning in fiscal year 1992, the Office of Naval Research (Arctic Sciences, Solid Mechanics and Ocean Technology Programs) will undertake a five-year duration Accelerated Research Initiative (ARI) focused on sea ice mechanics. Objectives are to understand stress-strain behavior of sea ice on scales from 1 cm to 1 km and establish constitutive equations related to observed continuum behavior, to determine the scales and mechanisms governing modes of failure and develop modeling approaches to predict intermediate scale behavior based on small scale properties, and to understand the interaction of sea ice failure mechanisms with macroscale stress fields as the basis for predicting peak loads on structures. To help ascertain the state of the art and foster initial interdisciplinary interaction, a workshop was convened in November 1990 at Airlie, Virginia. Sea ice mechanics was examined from different perspectives, both methodological (theoretical modeling, laboratory experiments, field observations) and behavioral (material, structural and acoustical aspects). The following Workshop Proceedings document outlines limits of current understanding, prioritizes research issues, and documents innovative methods of approach.

Within the Arctic Ocean and high latitude marginal seas, work done on the ice by wind and current can be transferred by ice stress to distant locations, where it is dissipated in local regions by rafting, ridging, rubbling and leading. Geophysical scale (10 - 100 km) continuum models simulate daily displacements to within about 3 km/day, but are currently unable to reproduce locally realistic ice conditions and stresses. The effectiveness of new generation high resolution numerical models will depend critically on improved understanding of subgrid mechanical processes and their scale dependence.

The unusual deformation and strength properties of natural sea ice are related to two major characteristics. Ice is a solid which is close to its melting point, thus exhibiting creep and temperature dependent strength. Also, ice is a highly flawed, anisotropic material through which cracks can propagate easily. Understanding of ice mechanics on a laboratory scale has advanced considerably over the past two decades. Difficulties remain in moving from the knowledge of small-scale ice properties to prediction of how ice behaves on a larger scale. Currently, there are no generally accepted and reliable methods for accurately predicting ridge/lead formation or ice loads on structures. Current understanding is limited first, because of the complex material nature of ice and second, because of the many additional ways it can fail as the scale increases.

Ice is a creeping, ductile material at low stress, yet an extremely brittle material at high stress. Behavior is dependent on the rate of deformation, the deformation history and temperature. Ice strength seems to be scale dependent: average compressive stresses at failure under small-scale laboratory conditions are of order 10 MPa, whereas measured average stresses during full-scale interaction with a

3/8/95
1-0803-91/F

structure are less than 1 MPa. When a stress is applied to ice a combination of responses is observed: an instantaneous elastic response together with a time-dependent creep. For stresses in the range 1-5 MPa, deformation due to creep exceeds initial elastic deformation after 5-200 s depending on temperature. For higher or more persistent stresses, the ice may crack by brittle fracture rather than deform by ductile creep. Distinguishing between brittle and ductile behavior is critical. Although both are forms of failure in the sense that the ice responds irreversibly to stress, they are distinct processes with different scaling that must be addressed by different formalisms: continuum mechanics and fracture mechanics.

The continuum behavior of granular and columnar ice (the two principal crystal arrangements occurring naturally) has been described by uniaxial constitutive laws through the stages of transient creep, but long-term and oscillatory creep effects are not well understood. Also not understood and of fundamental importance are the spatial scales and stress conditions over which continuum mechanics is applicable and for which a multidimensional constitutive law can be determined and applied. For example, at geophysical scales of order 100 km, a continuum visco-plastic rheology has been used, ad hoc, based on matching results with observed overall ice thickness distributions. The net effect on geophysical scales clearly involves fracture modes at intermediate and localized scales. Laws applicable between the laboratory and geophysical scale extremes need to be derived based on an understanding of the intermediate scale physics.

In the fracture mechanics of ice, crack nucleation and crack propagation under complex thermomechanical loading are mechanisms that are poorly understood. Fracture is propagation controlled if an applied load induces the nucleation of stable micro-cracks. After nucleation the ice may contain many cracks with an associated increase in ductility, but failure cannot occur until they propagate further under an increase in load. Fracture is nucleation controlled if an applied load results in cracks unstable enough to propagate the moment they nucleate. Under tensile loading, the operative controlling mechanism depends on the size of the cracks when they nucleate. If, however, flaws already exist, as is the case in nature, and are longer than a few grain diameters, these pre-existing flaws may control ice failure. The stress required for failure decreases strongly with the size of the flaw. Tensile strength is expected to have a pronounced scale effect if governed by the profligation of the existing cracks. Real sea ice will contain a distribution of crack lengths, and the ultimate failure strength may be controlled by the largest nucleated flaw formed under tension. Mechanisms that regulate both the transition to and the type of fracture include nonuniform contact at surfaces, stress rate limitation, and flaw size distribution. The stability of crack growth is also dependent on the way in which the driving force for crack growth (the energy release rate) varies with crack size. Addressing the fundamental question concerning the transition from continuum to discrete mechanics requires improved understanding of the scale interaction physics.

Questions framed by this Initiative are summarized below. In Sections following, details are explored and priorities recommended.

- What is the intermediate scale (1 cm - 1 km) mechanical behavior of sea ice?
- How does the mechanical behavior of small homogenous specimens of sea ice relate to behavior on larger scales in nature? Scale dependent constitutive relationships?
- What is the role of multiaxial stresses on the mechanical behavior and the scaling laws of sea ice?
- How is the mechanical behavior in both the ductile and brittle regimes affected by small-scale microstructure, temperature, salinity, and porosity?
- Does microcrack nucleation and/or propagation affect intermediate scale events such as ridging?
- Over what range of scales is ice fracture behavior similar?
- What combined stress states lead to the initiation of rafting, ridging, and rubbling?
- What are the associated combinations of failure modes?
- How can realistic ice loading on structures be calculated and predicted using homogenization and hierarchical failure techniques?
- What determines the morphology of surface (top and bottom) roughness?
- What is the distribution of block size and orientation resulting from failure events?

SECTION 1
METHODOLOGICAL PERSPECTIVE

1.1 THEORETICAL MODELING

Limits of Current Understanding

The deformation behavior of laboratory specimens of freshwater ice without microcracking under uniaxial loading is well understood with respect to relationships between stress, strain, strain rate, temperature, and grain size. Although a considerable amount of data exists in the microcracking range, there is little agreement on the mathematical description of behavior. For uniaxial and multiaxial stress states for all types of ice, the limits of linear viscoelastic behavior and the creep compliances necessary to fully characterize the linear viscoelastic behavior have not been established.

Freshwater ice under certain laboratory conditions appears to exhibit simple behavior in the relationship between time and temperature (i.e., it obeys time-temperature superposition). However, the limits of this behavior are unknown. The time-temperature superposition in its common formulation is not applicable to saline ice since it allows similar superposition mechanisms for both increases and reductions in temperature. Phase equilibria versus temperature and stress and the nonequilibrium diffusion can only be described by thermodynamic coordinates. The mechanisms of autohesion/healing and sticktion are not well established and environmental and loading transients have not been considered for sea ice. Diffusion and dislocation motion probably dominate nonlinear viscoelastic behavior. Grain growth can be modeled using a function of time, surface, and diffusion constants to account for the movement of atoms across grain boundaries. Diffusion movements increase exponentially with temperature; consequently, grain growth increases at higher temperatures and at higher stresses due to lower effective activation energy. This grain growth process, however, is irreversible. The diffusion and recrystallization processes are influenced by multiphase boundaries that result in nonlinear viscoelastic anisotropies. These effects, particularly autohesion/healing, become especially important in crack tip process zones. The microstructure dynamics must be related to environment and loading history and present values. A direct correspondence between nonlinear viscoelastic mechanical behavior and microstructure has not yet been established. The recrystallization, local damage, and crack dynamics must be theoretically and experimentally related to environment and loading transients. The importance of recrystallization and grain growth during deformation remains to be clearly established.

At larger scales (1-100 meters), two of the most important phenomena are crushing of ice on ice or ice on a structure and the formation and growth of ridges. Fracturing, lead opening, and crushing appear to be governed by mechanisms which vary with size of the crushed zone and time scale. The

3/8/95
1-0803-91/F

ability to scale up and incorporate laboratory measured properties in the theoretical models is needed. There is a need for modelling the formation and growth of multiyear ridges. Such ridges apply maximum force to Arctic structures and are a dominant Arctic feature, second in size to ice islands. Our present understanding of ice-structure and ice-ice interaction is largely based on limited plasticity models. These are known to overestimate initial fracture mechanisms but to underestimate ride up and clearing forces.

Further understanding is needed of the velocity dependence of crushing (which led to partial liquefaction failure of the Molikpaq sand core) and of the interaction of ice pieces which are already broken during clearing. For example, the clearing and ride up of broken ice typically leads to larger forces than an initial failure. It is necessary to determine the role of multimode failure, non-simultaneous failure, aggregate behavior, ridge formation and crushing mechanisms on the scale of 1-100m. Models of failure mechanisms should include initial fracture, secondary fracture and clearing of fractured ice pieces.

Priority Research Issues

The following is a prioritized list of research issues:

(1) Formulate the size and distribution of structural (1-100 meters) inhomogeneities in sea ice and the crack tip zone as a function of scale.

(2) Formulate the crack/flaw/porosity distribution as a function of time in sea ice, including location, crack size, and crack orientation. Focus is on both pre-existing flaws as well as the evolution of microcracking under stress and temperature variations. Develop appropriately scaled models of friction, adhesion, and healing.

(3) Mathematically characterize deformation behavior of sea ice and establish the three-dimensional effective elastic modulus tensor including its spatial and temporal variability. Formulate effective moduli for characteristic strain rate/time regimes.

(4) Formulate the crack/flaw distribution in laboratory specimens of ice undergoing multiaxial deformation. This includes location analysis, crack size and crack orientation under complex loading histories.

(5) Formulate micromechanical models of constitutive behavior (including the relationship between single crystal and polycrystalline behavior):

   (a) Undamaged: creep mechanisms, recrystallization,

   (b) Damage and failure: crack nucleation, initiation, propagation

State-of-the-Art Methods

State-of-the-art methods for modeling deformation and structural phenomena include the finite-element method, the discrete-element method and analytical modeling techniques from solid mechanics, e.g., visco-elasticity, plasticity with limit analysis, and rigid body dynamics with simplified interaction models. Present finite element techniques are capable of modeling both 2-D and 3-D ice behavior up to and including the initial fracture. Once the ice is broken it must be viewed as a granular material that has a very different behavior. In this phase, ice must be modeled using discrete element techniques. Presently, both 2-D and 3-D discrete element models are available but require further development before they can become reliable predictive tools. Improvements appear possible in all of these methods, particularly in the inclusion of more refined material behavior formulations. For example, discrete element models could include crushing behavior and fracture mechanics criteria. Finite-element models need to include rotation for ridge building studies and material flow for crushing studies. Better methods of handling multiple fractures also are needed.

A fundamental advance will be the inclusion of inhomogeneity, since failure seems to be governed by local weakness and occurs progressively. Inclusion of inhomogeneity should provide a scale effect. Stochastic models of inhomogeneity are necessary, supported by robust laboratory and field data. Other new approaches include granular flow theory applied to crushed material, energy-based formulations, and thermodynamic models.

Tomographic imaging using an array of acoustic sources and receivers is an emerging tool for mapping the 3-D field of ice properties. Methods exist to invert for compressional and shear speeds in ice, Poisson's ratios, and elastic parameters. Theoretical research is required to extend these methods to characterize effective structural inhomogeneities, flaw distribution, and cracking activity under load.

Current knowledge, research needs and methods in theoretical modeling are summarized in Table 1.1-1.

TABLE 1.1-1. THEORETICAL MODELING OF SEA ICE

KNOWN	• DUCTILE BEHAVIOR GOVERNED BY DISLOCATION MECHANICS • BRITTLE BEHAVIOR GOVERNED BY CRACK MECHANICS • CRACKING A NECESSARY BUT NOT SUFFICIENT CONDITION FOR DUCTILE TO BRITTLE TRANSITION • THERMAL/MECHANICAL HISTORY MODIFIES INTERNAL STRUCTURE
RESEARCH NEEDS	• PHYSICALLY BASED CONSTITUTIVE RELATIONSHIPS • UNDERSTAND AND QUANTIFY SIZE EFFECT(S) • CRACK INTERACTION MECHANICS ON SCALES SMALL AND LARGE
STATE-OF-THE-ART METHODS	• FINITE ELEMENT • DISCRETE ELEMENT • TOMOGRAPHIC IMAGING

3/8/95
1-0803-91/F

1.2 LABORATORY EXPERIMENTS

Limits of Current Understanding

First-year columnar ice is the most commonly encountered ice structure type in the Arctic region. To develop an understanding of the laboratory-scale processes that influence failure in the field, the mechanical properties of this ice type must be used as a foundation. The mechanical property work that has been done to date is incomplete. Further, the work that has been done with saline ice has focused on obtaining the stress-strain behavior of the ice without trying to determine the processes responsible for the behavior. Much of what is known about the micromechanical processes of failure in ice has been derived from tests on lab-grown, freshwater granular ice. This ice type differs significantly from columnar saline ice in characteristics ranging from grain size to void system. As a result, these two ice types show different stress-strain behavior under similar loading conditions outside of the brittle regime. Building on the experience with fresh water ice, future testing programs should focus more specifically on the mechanisms responsible for deformation in columnar saline ice to assure applicability to field scenarios.

The majority of small-scale property tests that have been done on columnar saline ice have involved uniaxial compressive stress states. While investigations on the behavior of the ice under this loading condition provide significant insight into failure mechanisms, field measurements indicate that this stress state is rarely observed. Instead, multiaxial states of stress including both compression and tension are present as the ice sheet crushes, bends, buckles and fractures. Mechanical property test programs should reflect this variety of load states.

Typical strain rates of the pack ice under natural conditions range from 10^{-7} to 10^{-4} and s^{-1}. At these rates the ice undergoes the transition from ductile to nearly brittle behavior. The transitional behavior of the ice combines ductile and brittle deformation mechanisms to varying degrees. One approach to modeling this combined behavior is to first establish separate models for flow and crack mechanisms. To do this, strain rates for the mechanical property tests should be extended up to 10^{-1} s^{-1} in order to reach the fully brittle regime of columnar saline ice for small specimens. (Evidence suggests that the transition strain rate is lower for large floes.) Once models have been developed to explain the flow and crack mechanisms, it may be possible to synthesize the models appropriately to explain the combined models of failure, for example, by examining the stress relaxation rate through creep at crack tips. The extension to higher strain rates also addresses the issue of engineering design loads since ice achieves its maximum strength in the brittle region.

Investigations to determine and model the behavior of ice at the 1 meter scale using information from the 10 centimeter scale mechanical property tests should be given strong consideration. This is an important intermediate step toward understanding the applicability of small-scale failure processes to

deformation in the field. Samples at this scale can have both temperature and stress gradients and, therefore, will be more representative of ice in the field. Based on this information, models can be developed that use the small-scale physical and deformational properties to describe the meter-scale behavior.

Microcracks form in the 10 centimeter scale mechanical property samples, leading to failure, and macrocracks exist throughout the ice in the field, possibly reducing the strength of the ice. Linear elastic or time dependent fracture mechanics can be used to help understand the role these flaws play in the failure of the ice. Sample preparation is still an area of investigation as is the question of size effect. Processes involved in crack tip deformation need to be addressed.

The uniaxial compressive failure stress measures from small-scale lab samples is apparently higher than the global failure stress measured in an ice sheet under compression. This relationship, known as the pressure-area effect, is poorly understood. Indeed, Russian literature suggests little or no effect of size on the strength of sea ice. Investigations in the laboratory to define the mechanisms responsible for this phenomenon are necessary.

Priority Research Issues

The following is a prioritized list of research issues:

(1) Determine dominant deformation mechanisms in columnar, saline ice in the ductile and brittle regime;

(2) Characterize transition from brittle to ductile behavior in columnar, saline ice;

(3) Determine the principal failure surfaces for columnar saline ice under multiaxial loading;

(4) Determine 10 centimeter scale physical and deformational properties relevant to 1 meter scale behavior;

(5) Establish the mechanisms responsible for the pressure-area size effect.

State-of-the-Art Methods

Coldroom and material testing systems are available at a number of locations around the country for both the 10 centimeter and 1 meter scale work. These include University of Iowa, NOSC Arctic Submarine Laboratory, MIT, Exxon, Dartmouth, CRREL, and Clarkson University. CRREL and NOSC have facilities that enable scale model work to be done. This capability is also available at Memorial University in Newfoundland. True multiaxial testing capabilities exist at Dartmouth College. Cooperative efforts utilizing these facilities should be encouraged.

Multiaxial tests should be utilized to develop an understanding of ice behavior under the complex loading states found in the field. Cyclic loading tests designed to identify deformational mechanisms are an important step in developing micromechanical models. This test technique can also be used for understanding the influence of load path on the behavior of the ice.

Mechanical property tests should be relevant to model requirements and results should be made available to the community expeditiously. This permits those without testing facilities to develop realistic models, and allows for consistency checks among data sets. Accurate and precise data sets against which hypothesis-based models can be tested are recommended, as are models based on physical insight that can guide and focus laboratory experiences and field observations. Field programs are logistically challenging and expansive. Equipment and techniques for measuring the behavior of ice in the field should be tested initially in the lab.

Current knowledge, research needs and methods in laboratory experimentation are summarized in Table 1.2-1.

TABLE 1.2-1. LABORATORY EXPERIMENTS

KNOWN	• TENSILE AND COMPRESSIVE STRESS-STRAIN CURVES UNDER UNIAXIAL LOADING • UNIAXIAL COMPRESSIVE FAILURE STRENGTHS AND MODES IN BOTH DUCTILE AND BRITTLE REGIMES • SIZE AFFECTS BRITTLE COMPRESSIVE STRENGTH BUT NOT DUCTILE COMPRESSIVE STRENGTH • FRACTURE TOUGHNESS
RESEARCH NEEDS	• STRESS-STRAIN BEHAVIOR AND FAILURE MODES UNDER MULTIAXIAL LOADING; DEFORMATION MECHANISMS • FAILURE SURFACES FOR BOTH DUCTILE AND BRITTLE REGIMES; FAILURE MECHANISMS • ESTABLISH WHICH PROPERTIES AFFECTED BY SCALE; SCALING LAW(S) AND ORIGIN(S) • CRACK NUCLEATION AND PROPAGATION MECHANISMS
STATE-OF-THE-ART METHODS	• MULTIAXIAL MONOTONIC AND CYCLIC LOADING SYSTEM IN WHICH ANY RATIO OF THE THREE PRINCIPAL STRESSES CAN BE OBTAINED AND CONTROLLED DURING PROPORTIONAL OR CONSTANT LOADING IN ANY OCTANT OF PRINCIPAL STRESS SPACE TO TEMPERATURES FROM 0 TO 50°C • PRESSURE CELLS • UNIAXIAL LOADING SYSTEMS • CYCLIC LOADING UNDER REVERSED TENSION AND COMPRESSION • LARGE-SCALE TEST BASINS

3/8/95
1-0803-91/F

1.3 FIELD OBSERVATIONS

Limits of Current Understanding

The loading, deformation field, and ice properties that affect sea ice behavior in the field and the stress distribution through a floe under loading are essential. Small-scale (1-10 m) mechanical properties that affect structural scale (1 km) behavior must be understood. Ice fails in blocks that are the order of 10 m. Ridges, rafts and leads are the order of 1 km. Breaking blocks, whether by splitting, rafting, bending, or other mechanisms constitute the small-scale mechanisms that constitute ridging, rafting, and leading. Nothing is known about multidimensional effects (shear), lead initiation, or the source of finger rafting. Ice floes behave as thin visco-elastic shells loaded in two dimensions by compression, shear, and bending. As loads are applied by neighboring floes, the ice crushes at local contact points, buckles as a plate, and bends and cracks. Local imbalance allows ice blocks to pile up and down, to raft and ridge; continued loading consumes the floe. Other processes are important: friction is an essential part of rafting and ridging. This friction includes sliding over a smooth surface, or pushing an ice sheet through a rubble pile.

Understanding ice behavior on laboratory scales (10 cm) has advanced, but little is known about how the laboratory scale properties affect processes such as cracking, crushing, bending, and buckling, and breaking of ice floes. Even less is known about how the laboratory properties affect structural scale processes such as ridging, rafting, and leading. The number of failure modes appears to increase with scale. The distribution in time and space of oriented ice (first year ice with c-axis aligned in the horizontal plane) can produce strong anisotropy, control crack propagation, and affect other properties. Is the c-axis orientation important in ridging? Failure to account for anisotropy could lead to misinterpretation of data.

Controlled-load tests must be carefully designed, (e.g., petroleum industry indentation tests show identical failure loads when applied stress is absolutely uniform, but reduced failure loads when the stress is less well controlled). Thus, failure by a different mechanism may look like a scale effect. This result suggests that scale effects could be caused by non-uniform loading, rather than material flaw distributions or other material defects. Controlled-load tests should be designed to give insight into in-situ geophysical behavior.

Fractures are intermittent and of finite length. They are not always visible. Crack distributions that are important in defining ice behavior must be measured. These ruptures are similar to those in the earth's crust. Therefore, fault plane analysis and seismic techniques can be applied to ice. Stress fields that induce cracking have not been sampled adequately. Natural failures, such as ridging, are seldom

measured. Rupture speeds are unknown. Elastic wave (acoustic) radiation is diagnostic of ice failure mechanisms should be further exploited.

A recommended objective of the field program is to document crack propagation in-situ. Observations should be made before, during, and after the event. A valuable test is to generate a crack in the field. Does the presence of cracks induced by thermal or mechanical forcing weaken the ice to large scale loading? What are the cracking processes as a function of space and time? When determining ice condition, the origin of a crack, whether initiated by thermal or mechanical forcing, may be unimportant compared to its presence.

Priority Research Issues

The following is a prioritized list of research issues:

(1) Relate 1 km behavior to the failure mechanisms that occur on 1-10 m; relate 1-10 m behavior to the laboratory scale behavior measured by new testing methods where stress state can be prescribed and controlled on scales of 10 cm -1 m. Based on the 1 m scale material behavior, describe the large-scale aggregate behavior of the failure mechanisms in a constitutive law.

(2) Measure the spatial distribution of stress, the stress field where a rupture occurs, through a floe, and across a ridge. The resultant force acting on geophysical scales (greater than 1 km) should be estimated from the stress measurements distributed over several floes on the structural scale.

(3) Determine the flaw distributions on scale of 10 meters that affect and control formation of ridges, rafts and leads. Understand the degree to which these processes are controlled by thickness variations, property gradients, and pre-existing distribution of cracks.

(4) Measure elastic properties within the ice (scales of 1 m to 1 km) and as the ice fails and deforms.

(5) Determine geophysical applied loads and the distribution of deformations including the effects of shearing and uniaxial deformations. Characterize the structural scale in terms of elastic, viscous, and/or plastic behavior. Understand what controls the existing floe size distribution.

(6) Determine the time scale over which ridges consolidate, the under-ice geometry in the shear zone., and what happens to water that melts off a multiyear floe and percolates downward.

(7) Load ice to failure in controlled-loading tests under known stress and strain rate conditions.

(8) Determine the maximum load that can be transmitted through a floe as a function of its thickness. Stress concentrations produced by thickness variability can dominate the failure stress, and be more important than the choice of mechanical property or stress-strain law. Thickness profiles of multiyear floes are needed to determine the range of thickness variations.

(9) Determine the behavior of ice under an isolated failure mechanism such as cracking of a floe and bending, crushing, or buckling of a beam. How is this behavior related to structural scale behavior (1 km) such as ridging, rafting, or leading?

State-of-the-Art Methods

Two types of field experiments are described. The first type requires deployment of a field camp in an area where formation of a ridge is likely based on regional wind fields. Stress sensors and devices to measure relative position must be deployed in the vicinity of this event prior to its occurence. This experiment is called an in-situ field program. The second type requires that forcing be supplied or augmented. The test geometry and loading are chosen. This type is called a controlled-load experiment. Both the in-situ and controlled-loading experiments are necessary. In-situ tests are of higher priority.

In-situ Field Program

The objective is to understand sea ice constitutive behavior on 1 km length scales where processes such as ridging, rafting, and leading control response. Measurements are needed to estimate large-scale applied loads, and the resulting deformations. Geophysical-scale loads from wind and current will help define the applied load. Arrays of stress sensors embedded strategically around several floes will help define the stress field. Deformations should be estimated frequently in time at discrete locations around the region boundary using acoustic, GPS, Del Norte, laser, or other equipment. Deformation fields (continuous spatial coverage) can be estimated several times daily over the experimental area using satellite remote sensing capabilities (ERS-1, JRS-1, RADARSAT) that are scheduled to be available by 1994, or using camera, radar, or other sensors tethered above the area. Ice conditions throughout the area should be measured: ice thickness, morphology, structure, flaw distributions, mechanical properties, temperature, and failure surfaces.

Controlled-Loading Experiments

The objective is to understand the processes that contribute to the formation of ridges, rafts, and leads. Ridging, rafting, and leading are composed of smaller-scale processes such as floe splitting, plate bending and breaking, crushing, buckling, and sliding of sheets and blocks across each other. A set of experiments needs to be performed to relate the forces required to activate these smaller processes to the resulting deformations. Each such process should be tested separately by designing the full-scale specimen and the loading pattern. The acoustic radiation patterns emitted by each process should also be measured along with the deformation, and associated ice conditions. Two specific tests have been identified: in-situ fracture generation, and breaking a cantilever beam (vertical bending and horizontal crushing/buckling). These processes are known to be important in the formation of leads, rafts, and ridges, with horizontal loading of the beam expected to actually form a small ridge.

The location of a field test should be dictated by the likelihood of encountering a desired loading state, deformation, and ice morphology. Ideally, the area should be acoustically quiet until desired events occur. The edge of the shear zone offers some advantages because of the likely deformation, but the disadvantage is that extreme deformations would destroy the experiment (and possibly the experimenters). Acoustic techniques would work best if the ambient conditions were quiet during controlled-loading tests. Shallow water complicates interpretation of emitted radiation signatures. Some balance must be achieved between these contradictory needs. The region should contain a variety of first and multiyear ice, and ridges. Deformations must be likely. Attempts to isolate thermal cracking in different areas are recommended. The field test location should be chosen so that loading and morphology can be measured.

Several types of stress gauges are available to embed in the ice , sampling on length scales of 20 cm. These gauges have been field tested in several programs, including CEAREX. Geophones, which have been more useful than hydrophones, can locate and follow a crack. Seismic models can provide estimated of local forces and moments by measuring acoustic signatures.

Understanding failure modes of ice on structural scales requires characterizing the ice condition, which includes determining the three dimensional field of elastic modulus, its spatial and temporal variability, and the size and distribution of inhomogeneities and defects. These can be estimated by acoustic tomography. Two dimensional distributions have been successfully obtained in the field, and attempts will be made in 1992 to obtain three dimensional fields. Acoustic tomography might also be useful to determine the distribution of flaws prior to and during an experiment. The distribution of Lamb wave speed can be estimated over 10-100m scales. Limitations arise because ice bottom topography controls results over 500 m scales. Topographic techniques could help determine flexural rigidity of flawed ice.

Forward and back scattering from underside of ice will soon be measured using GUTS (Geodesic Underice Tramway system). It provides a precisely locatable stable platform under the ice spanning a range of .5 x 1 km, and can transport acoustic optical, and other sensors for mapping fields. For example, thickness of first and multiyear ice can be measured by high frequency (40--80 kHz) upward-looking sonar. Survey ranges can be extended using autonomous underwater vehicle technology. Large-scale deformation surrounding a field experiment can be estimated with acoustic tracking ranges, GPS and Del Norte. Advantages and disadvantages of the different technologies should be assessed, including accuracy, cost, maximum range, power requirements, and deployment limitations.

SECTION 2
BEHAVIORAL PERSPECTIVE

2.1 MATERIAL ASPECTS

Limits of Current Understanding

Understanding of the micromechanics of sea ice is based on progress made in the micromechanics of freshwater ice with the added complexity of brine inclusions and associated microstructure. Physically-based models must be developed to address deformation and failure process under an extraordinarily wide range of environmental and loading conditions. The mechanisms responsible for the processes of creep, creep rupture, void growth and coalescence, crack nucleation and propagation, thermal cracking, brittle tensile and compressive failure, the ductile-to-brittle transition, as well as cyclic loading and fatigue effects must be understood. Although much can be gained by continuing the examination of these processes under simple stress states, it will be necessary to investigate multiaxial loading effects in order to properly generalize the findings.

The process of developing a physically-based understanding of the mechanical behavior of sea ice consists of three fundamental steps: observing and quantifying the microstructure, observing and quantifying changes in microstructure as a consequence of deformation, and the associated model development. The objective of this process is to allow the prediction of mechanical behavior given physical characteristics, thermal regime and loading conditions. As it is generally not possible to account for all contributing mechanisms, it is common to center micromechanical models on the dominant mechanism. The stress, time and temperature dependencies of specific deformational mechanisms are of interest, especially as the microstructure and flaw characteristics affect their operation. It is therefore of interest to perform experiments that isolate specific deformation mechanisms as much as possible. The ranges of operation of specific mechanisms must be established in terms of applied stress or strain rate and temperature.

Physical Properties Characterization. Since extreme variations in microstructure exist in sea ice, the spatial coherence of relevant properties must be established. The pertinent properties are grain size, shape and orientation, platelet spacing, salinity, bulk density, and pore size and shape. Spatial coherence in some properties is likely related to thickness. Temporal coherence must also be considered since sea ice microstructure is a strong function of its thermal history. Temporal coherence in properties tends to be related to seasonal cycling.

3/8/95
1-0803-91/F

Microstructural Changes. Since no comprehensive study of the microstructural changes in sea ice resulting from deformation has been made, the experimental work should focus on making direct observations of the dominant deformation and failure mechanisms. Of greatest concern are the mechanisms operating in the following regimes of behavior:

(1) The upper end of the creep regime (approximately, strain rates of 10^{-7} to 10^{-4} s^{-1}) - mechanisms of viscous flow and tensile creep rupture.

(2) The ductile-to-brittle transition, crack nucleation and/or propagation processes, combined flow and fracture processes.

(3) The brittle regime, brittle fracture processes in direct tension and compression, and flexure.

In addition, there is uncertainty regarding the physical processes underlying the attenuation of low frequency stress waves and thermal expansion of a large floating plate.

If dislocation-based processes are determined to be important in flatscale deformation and fracture processes, than it will be necessary to more fully understand the rate and temperature dependencies of the dislocation contribution to straining. The behavior dislocation both within isolated grains and within polycrystalline aggregates may be of interest. The role of grain boundary sliding may also need to be addressed

In all regimes, attention should be paid to the complete strength or creep curve: deformational processes and the accumulation of microstructural damage should be tracked up to and well beyond failure. The limits of operation of specific mechanisms and processes should also be explored and clearly identified.

The stress states of interest include direct tension and compression under uniaxial and multiaxial conditions, cyclic axial loading, bending and plate loading. As many of the relevant deformational processes are intimately related to fracture-based phenomena, consideration must be given to crack nucleation processes in the transitional and brittle regimes, fracture initiation and propagation processes as well as the processes of crack tip blunting and healing. These processes must be carefully assessed with regard to their operation in the sea ice microstructure.

Micromechanical Model Development. A long-term objective is the development of a set of physically-based, micromechanical models of sea ice behavior for use in formulations of large-scale mechanics problems. Thus, a heavy emphasis will be placed on developing mathematical models that correctly embody the underlying physics of the various deformational processes. To facilitate the use and extension of such models, every effort should be made to link the observed mechanical properties of the ice with its physical characteristics.

Models for sea ice should decompose strain into elastic, anelastic and viscous components and include a mechanism to account for accumulated damage in a rational manner. The models must

address ice behavior at low strains (where the pre-failure stress-strain behavior is of interest), and high-strain cases (where a failure criterion is required and post-peak stress-strain behavior is of interest).

As a continuing need exists for reliable estimates of the effective modulus of sea ice under a variety of conditions, physically-based modeling of this quantity is another area of concern. The modeling effort should also address the effects of bi- and triaxial stress states on the operation of specific deformation mechanisms and on failure mode.

Sea and Freshwater Ice Studies. The study of the mechanical properties of freshwater ice as an indicator of sea ice behavior has proved useful and this practice will undoubtedly continue. However, as a consequence of the vast differences in microstructure, great care should be taken in extending freshwater-based models to sea ice behavior. Validation of models should rely not only on predictions of peak strength, for example, but also on descriptions of the complete stress-strain or strain-time behavior. Special emphasis should be placed on the effect of the unique flaw structure of sea ice and on the role of brine as it affects the temperature dependence of the mechanical properties through its effect on phase composition.

Scale Issues. The links between micromechanical processes to be studied and larger-scale processes should be reasonably well established. Some attention must necessarily be paid to identifying the micromechanical processes of greatest interest. Large-scale phenomena requiring little or no micromechanical input should be identified as well. Highest priority will be given to studies concerned with micromechanical processes having the broadest range of application to the large-scale problems.

The fact that an additional and complex flaw population emerges when consideration passes from the laboratory scale to the field scale must be taken into account. Flaw structure must be well documented in naturally-occurring ice and such information must be assimilated in the modeling process. As a consequence, it will be especially important to document the microstructure of the material with respect to the characteristics of interest to the micromechanical experimentation and modeling efforts. It is important that the microstructurally-oriented observations be made on specimens having the widest possible range in size, allowing an assessment of scale effects on specific deformation mechanisms. The usefulness of micromechanical models should be demonstrated by their ability to bridge scale or specimen size gaps of approximately one order of magnitude. The complexities of the larger-scale problems will dictate the use of probabilistic approaches to extend micromechanical models to large scales.

Priority Research Issues

The following is a prioritized list of research issues:

(1) Identify the set of micromechanical processes having the broadest range of application to large-scale problems.

(2) Determine the spatial and temporal coherence of critical sea ice properties.

(3) Identify microstructural changes resulting from dominant deformation and failure mechanisms.

(4) Link observed mechanical properties with physical characteristics.

(5) Develop a physically-based model of the effective elastic modulus.

(6) Determine the role of brine in the temperature dependence of mechanical properties building on the work of Peyton.

State-of-the-Art Methods

To address the need for detailed characterizations, some effort must focus on the development of techniques to map microstructural properties to the precision necessary to test hypotheses. The use of computer-based image processors to analyze thin sections and provide statistical representations of complex microstructural distributions in the field should be explored. Physical processes in question should be well documented through the use of thin sections or SEM micrographs where applicable. Also, techniques such as acoustic emission monitoring should be carefully assessed both as a means to monitor microstructural damage during straining and as a vehicle to link laboratory observations with large-scale behavior.

Current knowledge, research needs and methods in material aspects are summarized in Table 2.1-1.

TABLE 2.1-1. MATERIAL ASPECTS

KNOWN	• MECHANICAL PROPERTIES CONTROLLED BY MICROSTRUCTURE WHEN STRESS STATE, TEMPERATURE AND STRAIN RATE FIXED • GENERAL MICROSTRUCTURE CHARACTERISTICS OF SEA ICE; BRINE POCKETS DISTINGUISH FROM FRESH-WATER ICE • MICROSTRUCTURE DEPENDENT UPON THERMAL HISTORY
RESEARCH NEEDS	• QUANTIFY EFFECT OF THERMAL HISTORY ON BRINE POCKET ARRAY • QUANTIFY EFFECT OF DEFORMATION (UNIAXIAL AND MULTIAXIAL) ON MICRORACKING
STATE-OF-THE-ART METHODS	• OPTICAL MICROSCOPY • ENVIRONMENTAL SCANNING ELECTRON MICROSCOPY • UNIAXIAL AND MULTIAXIAL LOADING SYSTEMS (TABLE 1.2)

3/8/95
1-0803-91/F

2.2 STRUCTURAL ASPECTS

Limits of Current Understanding

Sea ice structural aspects are taken to cover the scale of 1m to 1 km and to involve a single ice floe and floe-floe interaction. A number of physical processes occur naturally in the ice cover. The most prominent ones are (not ordered by importance):

(1) A large single crack initiating, propagating, opening,

(2) Crushing of one floe against another,

(3) Compression pressure ridge formation, growth, consolidation, and degradation,

(4) Shear pressure ridge formation, growth, consolidation, and degradation,

(5) Rubble field formation, and

(6) Seabed gouging.

Understanding these processes will help us understand relative motion of the ice on a geophysical scale. In addition, the processes should help us understand problems associated with man-made structures in the offshore ice environment. Some of these man-made structures are:

(1) Vertical sided bottom founded,

(2) Sloping sided bottom founded,

(3) Floating structures such as ships,

(4) Anchored floating structures,

(5) Submarines,

(6) Pipelines, and

(7) Man-made gravel islands.

There is some experience with ships and submarines in the Beaufort Sea, but there is little experience beyond the landfast ice zone for fixed offshore structures with vertical or sloping sides. Some experience exists for gravel islands and vertical sided structures in the land fast ice zone.

There are ice properties that can be measured on a small sample such as failure surfaces under multiaxial loading that may help understand and predict the larger-scale physical processes that have been observed. These include tensile or flexural strength, friction, and crushing strength. Care should be taken when applying the small sample properties to full scale. In some cases, small-scale properties can be used directly, while in other cases (for example, the crushing strength), a careful interpretation of the small-scale tests is required. Current thinking on the crushing strength is that it represents a failure load for the specific boundary conditions, and it is not a property of the ice. This is not to say that a crushing strength test of ice is not useful. It obviously reflects a strength property, but its relation to the total load on any particular sample, whether small or large, is not well understood. It is currently thought

that the nonuniformity of contact in both time and space may explain why the crushing strength on large structures in the field is lower than that for small samples. When the structure or loading device is flexible rather than rigid, dynamic interaction can occur which makes the interpretation of the crushing strength more difficult. The following failure processes are known to be of importance for ice-structure interaction.

(1) Crushing, which can cause fluctuating loads,

(2) Bending on a sloping surface,

(3) Clearing of the broken ice on a sloping structure,

(4) Rubble formation around structures, particularly gravel islands, and

(5) Ice gouging of the seabed which requires pipelines and well heads to be buried.

In order to predict the ice forces correctly, the ice type, failure mode and the structure must be considered together. The oil industry has two main concerns with regard to ice in the Arctic: (1) designing an offshore fixed structure to withstand the ice, and (2) transporting the oil by pipeline or tanker. When the ice is severe, pipeline is the preferred method. Recent emphasis has been on developing statistical methods to calculate the return period for ice loads. In the past, theories were developed to predict the ice loads for different ice features and failure modes against various structures. Improvement to existing theories and development of new theories are currently being considered. However, a major limitation is predicting changing ice distributions and properties sufficiently well so that extreme situations can be confidently identified.

Summary Limits: Theoretical Modeling

- Computation methods available for ice sheet, ridge, and rubble loads on vertical and conical structures and vessels are based on idealized geometry and failure patterns.
- Models available for ice-ice interactions (spring and dashpot, 1D deformation) are overly simplistic.
- Deterministic and statistical models available for ice-soil interaction (ice gouging) are unrealistic.
- Ice properties and ice-interaction tests conducted in laboratories and ice test basins do not adequately address scale effects.

Summary Limits: Field Experiments

- Aerial/satellite data on ice coverage, floe dimensions, sail heights exist; lack ice floe/ridge thickness data.
- Buoy data on ice motion exist; need better spatial resolution.

- Existing ice forecasting models are coarse resolution with poor ocean dynamics and ad hoc rheologies.
- Mechanical and physical properties of different ice types have been measured in the field; need more sensitive tests to better determine key ice properties.
- Many structures have been designed, built, and successfully operated n a wide variety of ice environments; the structure designs have been mostly conservative.
- Ice pressure and forces have been measured on various structures, e.g., Hans Island, Molikpaq, Baltic Sea lighthouse; the measured loads have been considerably less than those predicted by analytical, numerical, and empirical models.

Priority Research Issues

The following is a prioritized list of research issues:

(1) Refine and verify ice-ice interaction models ("weak link" properties).

(2) Determine scale and velocity effects on ice crushing pressure.

(3) Assess effects of end conditions and multiaxial stress state (residual stress) on the ice failure mode.

(4) Understand non-simultaneous, multimodal failure (bending, splitting, spalling, and flaking); full-scale ice loads.

(5) Measure ridge formation processes (large-scale ice flexural strength, ice-ice friction, evolution of keel and sail shapes, keel consolidation and structure, shear ridge).

(6) Measure lead formation processes, floe splitting (crack nucleation/propagation).

(7) Quantify floe-floe interaction (hydrostatic/hydrodynamic stability, thermal cracking, rafting, ridge formation).

(8) Determine vertical penetration failure criteria.

State-of-the-Art Methods

- Discrete Element Method for ridge formation (2D and 3D), ice-structure interaction, and vertical penetration.
- Finite Element Method for ice-structure interaction, floe-floe interaction, and lead opening.
- Damage constitutive model for ice-structure interaction.
- Multiyear ridge formation predictive model.
- Standard set of test data to calibrate and compare various theories.

- State-of-the-art surveys of the available data and models.
- Segmented indenter, instrumented by multiple load cells, to achieve nonperfect contact, non-simultaneous failure, to asses end effects and scale/size effects on ice crushing.
- Geometrically similar fracture tests of different sizes to assess scale effects on ice fracture.
- Coordinated indentation and triaxial tests of continuous crushing (at high speeds) to investigate the velocity effects on ice pressure.
- Better planning, instrumenting, and reporting of field tests.
- Large-scale ice floe splitting tests (residual stresses).
- Acoustic emission measurement, tomographic imaging, remote sensing of ice thickness, and better resolution satellite images.
- Large-scale cantilever beam tests of compressive and flexural strength.

Consider the difficulties in obtaining the ice thickness, an extremely important item. Obtaining ice thickness by drilling holes through the ice is costly because it is labor intensive. Consequently, relatively few ice features have been measured. Measuring the surface elevation by laser is accurate but the ice thickness cannot be predicted from buoyancy because of the snow cover depth and the bending resistance of the ice. Impulse radar does not work for broken ice and requires special interpretation. The electromagnetic induction method has a large footprint and thus does not work for local features such as ridges. Ice keel profiles obtained by upward looking sonar from submarines has provided the best overall ice thickness estimates in the Arctic, but the type of ice feature is not identified. Single beam sonars cannot determine the thickness, horizontal size, and type of ice feature simultaneously.

With the planned use of SAR from satellites, much more information on the position and horizontal size of ice features will become available in the near future. From the position data at various time increments, the motion of the ice can be obtained.

The ideal ice data collection system would include identifying the large ice features and determining the position, horizontal size, and thickness. If the thickness varies considerably within an ice feature, it would be desirable to produce a contour map of the feature. For example, contour maps of icebergs have been made from aerial photographs. Since most of the ice is below the water, measurement of the ice surface from below is the preferred method. Upward looking sonar simultaneous with side scan sonar has been used to obtain horizontal area and ice thickness profiles from a submarine. Other transducers could be used from submarines to obtain a more complete description of the ice features. Autonomous underwater vehicles could also be used, particularly on the continental shelf. In addition to obtaining ice feature data, information on ice gouges on the seabed could be obtained simultaneously.

In general, adequate determination of regional ice cover is a major effort. In order to reduce the cost to any one organization, the task should be shared by all interested parties, such as government, oil industry, universities, and research institutes.

2.3 ACOUSTICAL ASPECTS

Limits of Understanding

Ridges, rafts, and other similar features of pack ice of the central Arctic are culminations of accumulated ice fracture, which takes place either internally or at the boundaries of an ice sheet. Fractures accumulate (net of production over healing). The fundamental acoustics approach to understanding sea ice mechanics must entail observations of ice fracture processes. Work to date demonstrates the feasibility of measuring individual ice fractures by their acoustic radiation, and via inversion, the feasibility of determining relevant ice mechanical properties. Acoustic radiation is defined to include not only the stress wave (pressure) radiated into the sea water below, but also the kinematic field (displacement, velocity, acceleration) of the various elastic waves radiated into the ice.

Acoustic observation of ice fractures is analogous to observation of earthquakes. Much of the science of earthquake seismology can therefore guide such work in sea ice mechanics. For example, efforts to date on acoustic observation of ice fractures have yielded estimates (via inversion) of ice moment (basically the antilog of the popular Richter Scale), fault area, rupture speed, stress drop across arrested ruptures and, for cases in which ice sheet deformation accompanies rupture, as mostly it must, ice force. In one important aspect the approach suggested goes beyond earthquake seismology. For sea ice, source motion can be observed simultaneously, or nearly simultaneously, with the radiation field. This step is central to verification of models connecting radiation to source and hence ice mechanical properties. The ice can also be continuously monitored with auxiliary wave sources to assess accumulated damage via changes in relevant modulii.

The particular form of acoustic research suggested can also be compared to laboratory scale materials research, in which microfracture is measured (acoustic emission) prior to major failure of the sample. Similarly, the overall objective is the determination of those material properties of sea ice, in its natural environment and with its complicated shapes and arrangements, that pertain to ultimate large-scale failure such as ridge-building. Microfractures are also present in sea ice, possibly related to grain boundary slips, but intermediate scale fractures (the order of 1m to 10m in length) are the major focus, because these are the immediate predecessors of large-scale failure.

Priority Research Issues

The following is a prioritized list of research issues:

(1) Observe naturally-occurring ice fractures.

(2) Study artificially-induced ice fractures.

(3) Determine the relationship between large-scale deformation and ice fracture (constitutive law).

(4) Clarify the connection between aggregated noise and environmental forcing.

(5) Determine the properties of elastic waves in heterogeneous ice with non-ideal boundaries.

Issues are outlined in Tables 2.3-1 through 2.3-5. Each summarizes the limits of current understanding (under the heading: **KNOWN**), the high priority new knowledge to be obtained (under the heading: **NEEDS, QUESTIONS, HYPOTHESES**), and state-of-the-art approaches to obtaining the new knowledge (under the heading: **METHODS**).

Table 1 outlines the research setting and approach for acoustic observation of ice fractures. Three field techniques deserve additional comment:

(1) Tomographic and other NDT approaches for real-time close-in observation of an individual fracture are in early development, will require preliminary field testing, and will come into full use in the coming years.

(2) Sensor channels need to be increased in number and capacity relative to the past. (CEAREX 89 had about 50 channels with bandwidths up to 2 khz, but not all simultaneously this wide.) Significant increase in capacity is feasible.

(3) Since fractures are known to cluster in space and time, it is feasible to consider fast deployment of a sensor-suite for close-in observation of individual fractures. Real-time location of these hot spots is feasible, in much the same way that real-time monitoring of drifting sensor locations is now being done in the Arctic.

Research Issue (1) is central to the overall acoustics research thrust, and is basic to sea ice mechanics as studied in the field. Other acoustics research issues, notably (5), need to be adopted for confident prosecution of it. Each requires, as will be seen, relatively modest field equipment beyond that for (1), and therefore each has high benefit/cost ratio.

Models for source motion, and its radiation into ice or through ice into water, should be checked for confident reduction of remote acoustic measurements to ice mechanics properties. Hence the research Issue (2) outlined in Table 2. Once the sensor arrays are established as in (1), and non-intrusive techniques developed for inducing and close-in observing of fractures, the research objectives can be addressed efficiently. Laboratory research on material failure suggests both poor and acceptable methods for inducing fracture. It is essential therefore to translate carefully from lab to field scale, perhaps via intermediate scales in a tank, lake, and/or preliminary Arctic field test.

It is known in both earthquake seismology and fracture mechanics that large-scale deformation relates to fracture accumulation. Simply put, the more the damage (net of fracture production over

healing), the greater the deformation. The relationship between the two is the constitutive law, a sea ice mechanics formulation of high interest (Table 3). Deformation sensors over a scale of several kilometers or more would be employed, and could be acoustic or electromagnetic. Airborne remote sensing would be a valuable qualitative assist, but the large number of images required for quantitative evaluation is a challenging proposition.

Large-scale deformation should be obtained in a long-time series, for comparison with long-time accumulation of fracture. The latter would be obtained from addressing Issue (1) via the number density of fractures, and the ice deformation area. Healing, as caused by refreezing, could be obtained via thermal flux measurements and/or monitoring of elastic modulii (5).

Research Issue (4) seeks to clarify the cross-correlation between aggregated noise (e.g., 5-minute or longer averages of ice fracture radiation at a single hydrophone) and environment forcing (e.g., heat flux). Both are typically long-time series (at least many days) and frequently entail multiple forcing (e.g., wind stress and heat flux) and/or material changes via accumulated damage. Cross correlations are often surprisingly low because, it is hypothesized, these complexities are not accounted for. Data to achieve the desired clarification would be acquired in the course of other research elements in the suggested acoustics program, but the data reduction and interpretation would follow different paths.

All research described requires knowledge of the ice with all its complexities. These include, but are not limited to, nonuniform thickness, flaws associated with prior fractures or partially consolidated blocks, and modulus profile with depth. Further, such complexities can change, sometimes dramatically, even over the relatively short time span of a typical field experiment. Issue (5) addresses this concern. In essence, the idea is to study the relatively small area being researched via fracture mechanics, first to obtain independent descriptions of complexities such as underside roughness, second to verify elastic wave propagation models incorporating such complexities, and third to continuously monitor such waves to sense changes in flaw-modified elastic modulii and/or heterogeneity length scales.

State-of-the-Art Methods

A field program in pack ice typical of the central Arctic is necessary. As the research evolves, a preliminary field test in the Arctic (or with lake ice) will likely be useful. Finally, a high degree of collaboration will be essential among those researching materials, structure, and acoustics aspects from theoretical, laboratory, and field perspectives. Indeed, a proper study of sea ice mechanics could not be done without acoustical observations of fractures as a coordinated and highly integrated effort in the total program.

TABLE 2.3-1. OBSERVATIONS OF NATURALLY OCCURRING ICE FRACTURES

KNOWN	• INDIVIDUAL FRACTURES CAN BE LOCATED IN SPACE AND TIME WITH ARRAYS OF GEOPHONES AND/OR HYDROPHONES • FRACTURE MOMENT, LENGTH SCALE, STRESS DROP, KNOWN TO FIRST ORDER • DEFORMATION FORCE, CREEP-AFFECTED ICE STRENGTH, KNOWN TO FIRST ORDER
NEEDS, QUESTIONS, HYPOTHESES	• RUPTURE SPEED, DIRECTION, RADIATION PATTERN, NOT RESOLVED BY PREVIOUS MEASUREMENTS REMOTE FROM FRACTURE • MEASUREMENTS AT FRACTURE SITE FOR SLIP DISPLACMENT, AND TO CONFIRM LENGTH SCALE, DIRECTION, ETC., NEEDED • COMPLEXITIES OF RADIATIVE TRANSMISSION WITHIN AND THROUGH THE ICE NEED TO BE ACCOUNTED FOR • CAN ACTIVE MEANS (E.G., TOMOGRAPHY OR NDT) DELINEATE CRACK UNDER STUDY (IN NEAR-REAL TIME)?
METHODS	• AN ORDER-OF-MAGNITUDE INCREASE IN SENSOR CHANNEL CAPACITY IS NEEDED • USE MAN-MADE SOURCES TO CHECK RADIATION PATH MODELS AND TO RESOLVE COMPLEXITIES • USE FULL SUITE OF ENVIRONMENTAL AND ICE STRESS SENSORS • DEVELOP AND USE A FAST-DEPLOYMENT SENSOR SUITE TO OBSERVE INDIVIDUAL FRACTURES IN NEAR REAL-TIME

3/8/95
1-0803-91/F

TABLE 2.3-2. STUDY OF ARTIFICIALLY INDUCED FRACTURES

KNOWN	• METHODS TO AVOID
NEEDS, QUESTIONS, HYPOTHESES	• CREATE A FRACTURE AT A GIVEN PLACE AND TIME TO CHECK SOURCE MODELS, RADIATION PATHS, RUPTURE SPEEDS, AND ASSOCIATED ELECTROMAGNETIC RADIATION
METHODS	• OPTICAL ACCELEROMETER, STRAIN ETC. ARRAYS TO DENSELY POPULATE SOURCE REGION, FOR NON-INTRUSIVE MEASUREMENT OF SOURCE PROPERTIES • DEVELOP TECHNIQUES IN PRELIMINARY FIELD, LAKE, OR TANK TEST

3/8/95
1-0803-91/F

TABLE 2.3-3. DETERMINATION OF THE CONNNECTION BETWEEN DEFORMATION AND FRACTURE (CONSTITUTIVE LAW)

KNOWN	• NO CONNECTION IN PACK ICE AT LOW FREQUENCIES (BUT THIS IS THE REGIME OF UNLOADING RATHER THAN FRACTURE MOTIONS) • NO CONNECTION IN MIZ AT LOW AND MID FREQUENCIES (BUT THIS IS THE REGIME OF FREE DRIFT)
NEEDS, QUESTIONS, HYPOTHESES	• AT MID-FREQUENCIES (FRACTURE REGIME), AND IN PACK ICE, IS THERE A CLOSE LINK BETWEEN FRACTURE ACCUMULATION AND STRUCTURE-SCALE DEFORMATION? (IN ANALOGY WITH EARTHQUAKE SEISMOLOGY, THERE COULD BE)
METHODS	• MEASURE DEFORMATION ON STRUCTURE SCALE (FEW KM) • DETERMINE NUMBER DENSITY OF FRACTURES (NUMBER/UNIT TIME/FREQ. BAND) • WEIGHT LATTER BY FRACTURE MOMENT, AGGREGATE, AND COMPARE WITH DEFORMATION

3/8/95
1-0803-91/F

TABLE 2.3-4. CLARIFICATION OF THE CONNECTION BETWEEN AGGREGATED NOISE AND ENVIRONMENTAL FORCING

KNOWN	• CONNECTION OF AGGREGATED NOISE TO GLOBAL FORCING KNOWN AT LEAST TO FIRST ORDER VIA CROSS-CORRELATION WHICH, AT BEST, IS BETWEEN 0.6 AND 1.0
NEEDS, QUESTIONS, HYPOTHESES	• MULTIPLE FORCING EFFECTS NOT YET ACCOUNTED FOR • MATERIAL PROPERTY CHANGES UNDER RAPIDLY REPEATED OR CONTINUOUS FORCING NOT YET ACCOUNTED FOR
METHODS	• SEGREGATE NOISE VIA FRACTURE TYPES, SOURCE PROPERTIES, AND DRIVING STRESS FIELD • DETERMINE NUMBER DENSITY FOR EACH • AGGREGATE NOISE FOR EACH STRESS FORCING FUNCTION AND CORRELATE • MONITOR MATERIAL PROPERTIES VIA ELASTIC WAVES • USE FULL SUITE OF ENVIRONMENT AND STRESS SENSORS

3/8/95
1-0803-91/F

TABLE 2.3-5. DETERMINATION OF THE PROPERTIES OF ELASTIC WAVES IN HETEROGENEOUS ICE WITH NON-IDEAL BOUNDARIES

KNOWN	• WAVE CHARACTERISTICS FOR HOMOGENEOUS ISOTROPIC ICE OF UNIFORM THICKNESS KNOWN • WAVE CALCULATION CODES FOR REALISTIC ICE CONFIGURATIONS AVAILABLE
NEEDS, QUESTIONS, HYPOTHESES	• WAVE CHARACTERISTICS FOR SEA ICE WITH ALL ITS RELEVANT COMPLEXITIES MUST BE DETERMINED • ELASTIC MATERIAL PROPERTIES (E.G., FLAW-AFFECTED YOUNG'S MODULUS) FOR SEA ICE CAN BE OBTAINED BY INVERSION • WAVE CODES CAN BE RUN, BUT WE NEED INPUTS DESCRIBING REAL ICE
METHODS	• STUDY SMALL AREA [0(1KM^2)] FOR DETAILED INVENTORY OF RELEVANT COMPLEXITIES (E.G., UNDERSIDE PROPERTIES, ICE HETEROGENEITIES) • MEASURE ELASTIC WAVES TO GET MODULII, WAVE/WAVE AND WAVE/FLAW SCATTERING, AND HETEROGENEITY LENGTH SCALES

3/8/95
1-0803-91/F

SECTION 3
SYNTHESIS AND PROSPECTUS

A number of central themes emerge from the methodological and behavioral cross-cuts. In general, these themes identify needs for further understanding of size effects, rate effects, gradient effects and failure modes.

A major question in understanding and predicting the mechanical behavior of Arctic sea ice involves the effect of size on the dynamics. The notion that the scale of a specimen alone influences the operative physics has fundamental implications. The prime example is the pressure versus contact area relationship, suggesting a decrease in strength with an increase in size. There was consensus that obtaining a comprehensive quantitative relationship spanning from microscale to structural scale behavior is too ambitious on a five-year horizon; however, establishing the linkage between a few scales (e.g., centimeters to meters, meters to tens of meters) is achievable and should be pursued.

Theoretical modeling is essential in relating behavior across scales and developing parameterizations. Improved models are required for both continuum and fracture behavior. Continuum and fracture models should be linked where possible. Small-scale laboratory experiments are required to link micromechanical properties with physical behavior and to identify mechanisms that may be important across scale. Intermediate scale laboratory tests under carefully controlled conditions can provide a crucial link between small and large scales. There was consensus on the need to establish the critical scales at which microscale processes become measurably important to larger scale behavior.

Brittle or ductile sea ice behavior depends to a large extent on loading rates, which in nature typically range from 10**-7 to 10**-4 s**-1. Continuum behavior at different rates, particularly at larger scales, needs further investigation. Rate effects on fracture need to be quantified.

While it is well known that temperature can determine elastic or viscous plastic behavior under isothermal conditions, the behavior of sea ice with realistic temperature gradients, as in the Arctic, remains to be characterized. The effects of temperature on fracture need to be resolved. Porosity, salinity and microcrack distribution are important at small and medium scales. Gradients in these properties, in addition to those in thickness, degree of ridge consolidation and macroflaw distribution at larger scales, need to be ordered and quantified in the effects on the governing mechanics.

Coherent and economical field tests designed to definitively relate forcing and response under the range and limits of conditions in nature are essential. Controlled loading tests in the field are necessary to understand large-scale behavior. In-situ ice properties and stresses can be monitored to some extent with current technology. Methods for more complete spatial mapping of these fields are needed. Techniques to measure three dimensional flaw generation and distribution within full scale floes need development.

3/8/95
1-0803-91/F

The roles of mixed mode and non-simultaneous failure in reducing large-scale loads needs to be understood, as well as the important mechanisms in the initiation of long fractures (leads) in pack ice. The relative importance of bending, buckling, crushing and crack nucleation/propagation in overall failure needs to be determined. Factors causing ice of the same thickness to ridge in some cases and raft (including finger rafting) in others need to be determined. Thermal stresses may be as important as mechanical stresses in preconditioning the ice for the propagation of cracks. The role of existing flaws and the residual stress state in the generation and propagation of long fractures requires study.

Figure 3-1 is a schematic framework useful in synthesizing the main issues. Relations suggesting intra-scale research are depicted horizontally, while possible inter-scale studies are depicted vertically and diagonally. The transition from laboratory to floe scales is best addressed within a hypothesis-testing framework. One hypothesis is that the behavior of samples under tensile stress and the distribution of this stress is most important in floe-scale cracking processes. Therefore, these stress conditions should be examined experimentally and parameterized in larger scale relationships that can be tested in floe experiments.

Bridging the gap in understanding of ice processes from floe to regional scales may come from relating floe measurements to a viable statistical measure of the structure of regional scale distributions of ice. The measurements of environmental forcing and regional strain, for instance, can be related to average pack ice forces measured on the floe. Careful study of the relationships, particularly during deformation, should lead to improved regional constitutive laws. Also, fracture models developed for a single floe may be applicable to a collection of floes. Thus, selected geophysical parameters obtained from aerial or satellite imagery of a region combined with environmental forcing, will produce time dependent theoretical and numerical models that can predict with improving degrees of skill the spatial distribution of new leads and ridges.

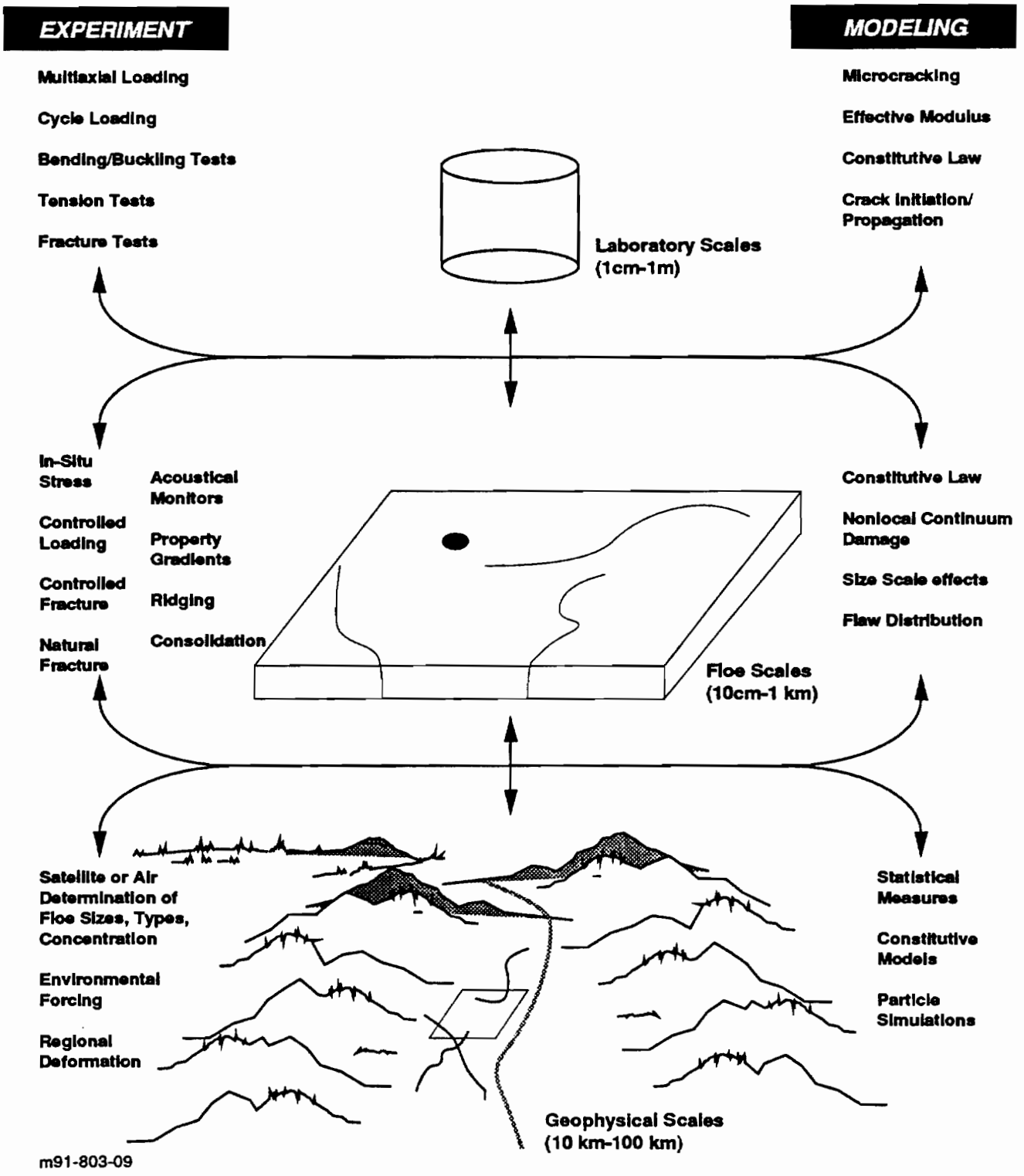

Figure 3-1. Schematic Framework Depicting Intra-Scale (Horizontal) and Inter-Scale (Vertical) Research Issues.

APPENDIX A

ACKNOWLEDGMENTS

Appreciation is extended to all workshop participants for freely contributing their insight and enthusiasm to the proceedings. Particular thanks are due to the Overview Speakers (Appendix B) who provided essential initial perspective, and the Working Group and Prospectus Leaders (Appendix B) who led the discussions, synthesized input in real time and later created the main body of this document through several iterations. In addition to the Working Group Leaders, E. Schulson and T. Ewart provided valuable comments on draft versions of the text. My colleagues in this endeavor, S. Ramberg and Y. Rajapakse, have provided continuous and critical support. M. Coon and J. Pierce have assisted greatly in the logistics, editing and distribution. N. Crawford designed and produced the cover.

3/8/95
1-0803-91/F

APPENDIX B

Reprint

Sea Ice Mechanics Initiative (SIMI) Summary Plan, FY94-95
(Workshop, Sidney, B.C., 1993)

SEA ICE MECHANICS INITIATIVE (SIMI)

SUMMARY PLAN
FY94-95

24 AUGUST 1993

Contents

1 GOALS

- Understand sea ice constitutive laws and fracture mechanics over the full range of geophysical scales and determine the scaled responses to applied external forces

- Develop physically-based constitutive and fracture models

OBJECTIVES

- Relate the regional and local stress distributions to the deformation of a cluster of floes within the ice pack

- Relate the stress distribution in an individual floe to its mechanical property distribution and boundary conditions

- Relate the oscillating flexural strain field associated with propagating gravity waves and wind forcing to the existing stress field in a floe

- Determine the force - deformation relationship in the ridging process and its relation to larger scale constitutive laws

- Determine the evolution of properties in a recently formed ridge through the consolidation process

- Determine the distribution, magnitude and character of seismic events associated with the ridging process

- Determine the magnitude of thermal stress relief from individual cracks, how often they occur, what their dimensions are, and how well they can be characterized from seismic and acoustic signatures

- Correlate ice seismicity with the macroscopic strain field and seismic mode conversion with irregularities in the ice

- Relate physical and mechanical properties of first year ice to its growth history

- Relate physical properties and size of first year ice to its fracture mode and constitutive behavior

- Combine in-situ size-effect fracture and flexure experiments with cyclic loading and creep recovery experiments to determine deformation, fracture and failure behavior to validate theoretical models

- Evaluate the scale effect over the range 10 cm to 10 m using both field and laboratory measurements linked to theoretical fracture, constitutive and property models

- Evaluate the nonlinear ice growth model of Cox et al. thereby providing forecasting capability for areas where only the freeze-over date and meteorological conditions are known

2 MODELING

2.1 SUMMARY

100 KM SCALE (PACK)

- Coupled air-ice-ocean (Overland)
- Fracture characteristics (Pritchard)
- Deformation characteristics (Erlingsson)

10 KM SCALE (FLOE CLUSTER)

- Granular media rheology (Hibler)
- Anisotropic constitutive law (Coon, et al.)

1 KM SCALE (FLOE, RIDGE, LEAD)

- Ridge building energetics (Hopkins)
- Fracture mechanics, size effects (Bazant)

1-100 M SCALE (MACROCRACK)

- Thermal fracture (Bazant, Lewis)
- Physically-based constitutive laws (Sunder, Wu, Schapery)

- Fracture mechanics, size effects (Rodin, Sunder)

1 CM - 1 M SCALE (MICROCRACK-CRYSTAL)

- Ductile-brittle transition, failure surfaces (Schulson)
- Crack nucleation (Frost, Gupta)

2.2 PACK - FLOE SCALE

Coon, et al. [1992] introduced a method for incorporating the behavior of individual leading, rafting, and ridging events into the large-scale constitutive behavior of pack ice. The concept is that the large-scale stress state must lie within all of the yield surfaces that describe failure of individually resolved ice features. Ice conditions are described in terms of an oriented thickness distribution including the thickness of ice in leads. In resolving behavior on scales from one to hundreds of kilometers, processes of leading, rafting and ridging that describe and control the behavior of sea ice are explicitly considered. Previous models [e.g., Coon, et al., 1974] are applicable only over scales large enough that the multiplicity of ice features give rise to an isotropic response.

SIMI includes nested arrays of drifting buoys to measure deformation on different scales. The large, pack scale Arctic buoy array, with resolution of order tens of kilometers, is not useful for locating individual events [*Overland, et al.*, 1992]. However, diagnostic simulations will be very valuable for setting the large scale forcing fields and boundary conditions. The floe cluster array will be deployed at roughly 3 km intervals over a uniform grid 15 to 20 km on a side, allowing the deformation of individual events to be tracked. Stress gages will measure forces associated with failures. At different times leads will form and deform at different locations and in different orientations. Subsets of the buoy array will measure lead motion.

An anisotropic model enables measurements of stress, deformation, and ice conditions associated with individual leading, rafting, and ridging events to be used as components of a large-scale model. During SIMI, these variables will be measured during specific events. At times, isolated events with length scales of order 100 m will likely occur within the floe cluster array while the remainder of the array will be nearly rigid. Such events will be described by observations on the scale of 3 to 15 km by the deformation of the array and by direct ground observations. Airborne imagery of the region near the end of October will help identify earlier events and provide a baseline for comparison in spring. Ice motion vectors will be derived from SAR and AVHRR imagery. To minimize the effect of GPS position errors, the deformation gradient between sets of buoys will be estimated. The

spatial fields of dilatation and shearing (or their mean square sum) will then be plotted to identify the likely locations of events. Ice conditions in the vicinity of events (thickness, block sizes, keel profiles, surface texture and physical properties) will be measured whenever possible by a visiting ground party. These measurements will be valid long after the event occurred. In some cases the event may be still active so that ice conditions at the onset of failure will be directly observed. In other cases, they will have to be inferred. During winter, buoy data will be analyzed periodically. It is essential that all winter data be analyzed before the spring experiment begins, so that earlier events can be located and revisited. During spring, data will be analyzed continuously, so that events can be visited as quickly as possible, hopefully while still active. Real time beamforming on ambient noise sources using a large aperture acoustic array will help identify events expeditiously. Stress gages installed over the widest possible distance around the camp will provide an estimate of the stress state and forces existing at the time of failure. The relationship between the stress applied in the ice surrounding the event and the resulting deformation will define the constitutive behavior.

Incorporating an anisotropic constitutive law into an ice dynamics code [*e.g., Coon,* 1980; *Pritchard*, 1980] requires closure assumptions such as elasticity so that a viable numerical method can be used to solve realistic boundary value problems. It must be coupled with a momentum balance equation and with sub-models for forcing by wind and current. As a first step, existing ice dynamics codes will be modified to use new anisotropic constitutive laws and oriented thickness distributions.

The performance of the ice dynamics model will be determined by simulating ice behavior during SIMI and comparing the model output with observations. The model will be forced by winds, currents and boundary motions. Ice motion, deformation, stress, and ice condition will be calculated with grid spacing 10 km. It is essential that all data necessary to force the model and measure model performance be identified and obtained. Questions include: How many Argos buoys are needed along the model boundary? Do any of the large domain boundary buoys need GPS accuracy? Are additional buoys needed in the interior of the region? Do any buoys need current meters or anemometers?

Finite element [*e.g., Pritchard, et al.*, 1983] and discrete element models will address individual events such as the initiation and continuation of leading, rafting, and ridging under a broad range of applied loads. Results will be compared directly with observations. These studies will help define the anisotropic yield surface and flow rule of the constitutive law. In addition, ridge building force data are useful in industry for estimating ice loads on offshore structures. Existing data are plotted with theoretical estimates in Figure 1 [Wang, personal communication]. The combined set is inadequate to clearly determine the magnitude of ridge building forces for engineering calculations. Effort during SIMI will be directed toward improved determinations of ridge building forces. A complete ice dynamics

model is useful for a range of practical problems: e.g., climate dynamics, offshore platform design, and environmental hazard analysis.

2.3 CRACK - CRYSTAL SCALE

Modeling on smaller scales is focused on fracture mechanics and constitutive relations particular to saline ice. The relationship of crack and crystal scale processes to floe and pack behavior is a major question to be addressed.

A constitutive model is being developed (Schapery and Rodin) for viscoelastic polycrystaline behavior of saline ice which accounts for grain-to-grain interactions and the in-situ behavior of individual grains. Overall anisotropy of the polycrystal is related to the distribution function for the c-axis orientations. A fracture model is being formulated that explicitly accounts for the polycrystalline structure of ice ahead of the crack tip. The mechanical property data and microstructural observations will provide essential information for model development and validation. Optimum plate aspect ratios for field tests will first be examined through finite element analysis.

The time series of basic physical properties that will be required to both analyze the large scale full thickness tests and to bridge the gap between these tests, the smaller scale field tests and the laboratory tests will be obtained by investigators from the University of Alaska/Fairbanks. Changes in the ice thickness, salinity, and temperature will both be measured and modeled (Cox, et al.). Detailed vertical variations in the ice fabric will be determined by thin section analysis. Included will be a numerical characterization, both vertically and horizontally, of the spatial distribution of brine drainage channels, features that have recently been shown to be important in controlling the strength of sea ice but are, as yet, not included in any body of theory.

The modeling program at Clarkson will link to the planned field experiments by

(1) quantitatively validating the appropriate constitutive models in order to understand the near-tip processes and relaxation processes. In this context, the effectiveness of the currently available size effect laws will be determined in terms of their predictions for fracture energy and process zone size;

(2) quantitatively verifying a process zone model for fracture in saline ice at any scale by linking the experimentally determined P - COD information with an analytical treatment of the process zone.

An elastic strain model for saline ice currently under development at CRREL will be extended to include warmer temperatures and the microstructures indicated in the field

experiments. In all cases the precise microstructure will provide the critical link between the observed mechanical properties and the physical properties.

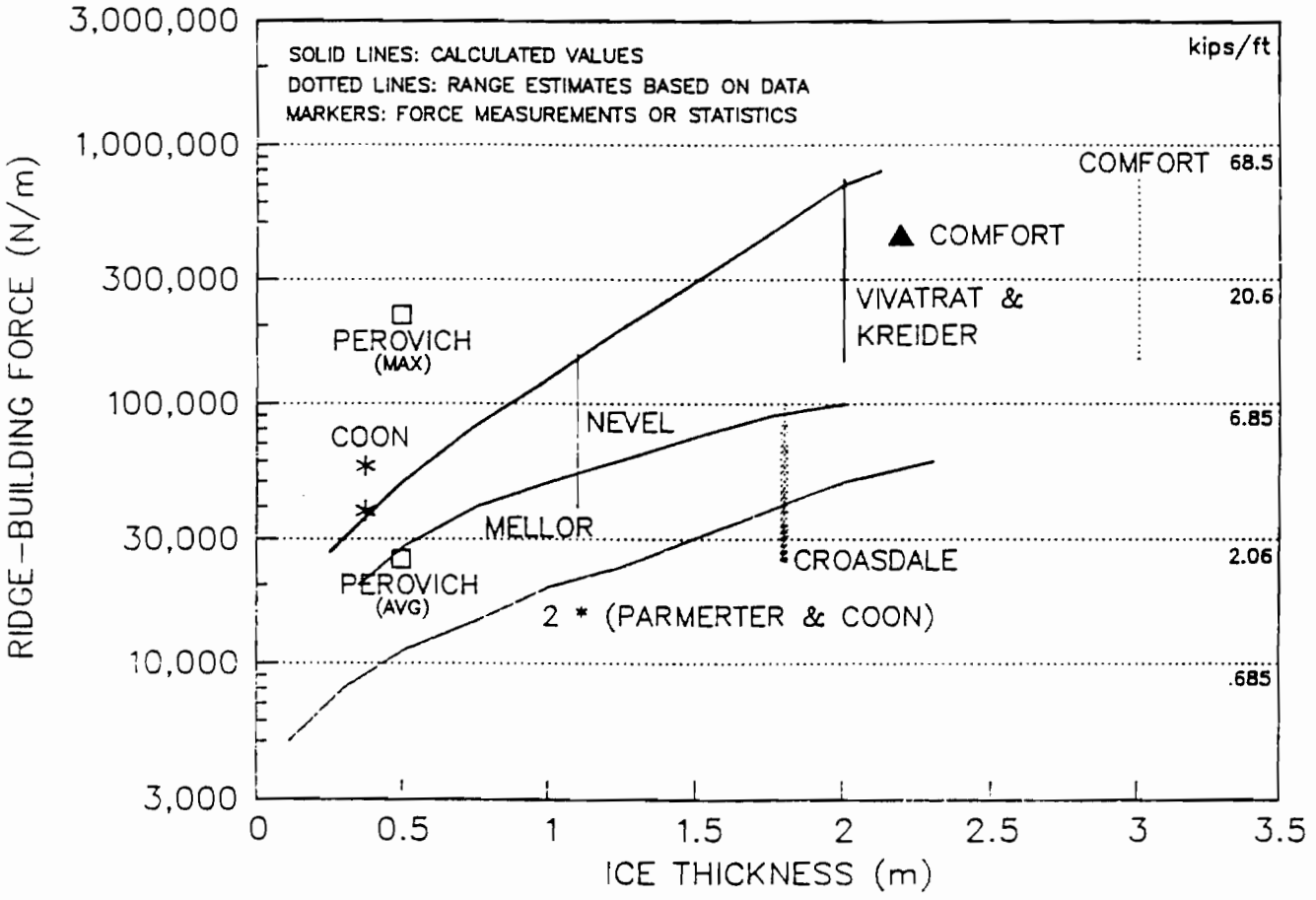

Figure 2.2-1. Calculated and measured ridge-building forces (Wang).

3 MEASUREMENTS

3.1 SUMMARY: SPATIAL DISTRIBUTION AND TIME SCHEDULE

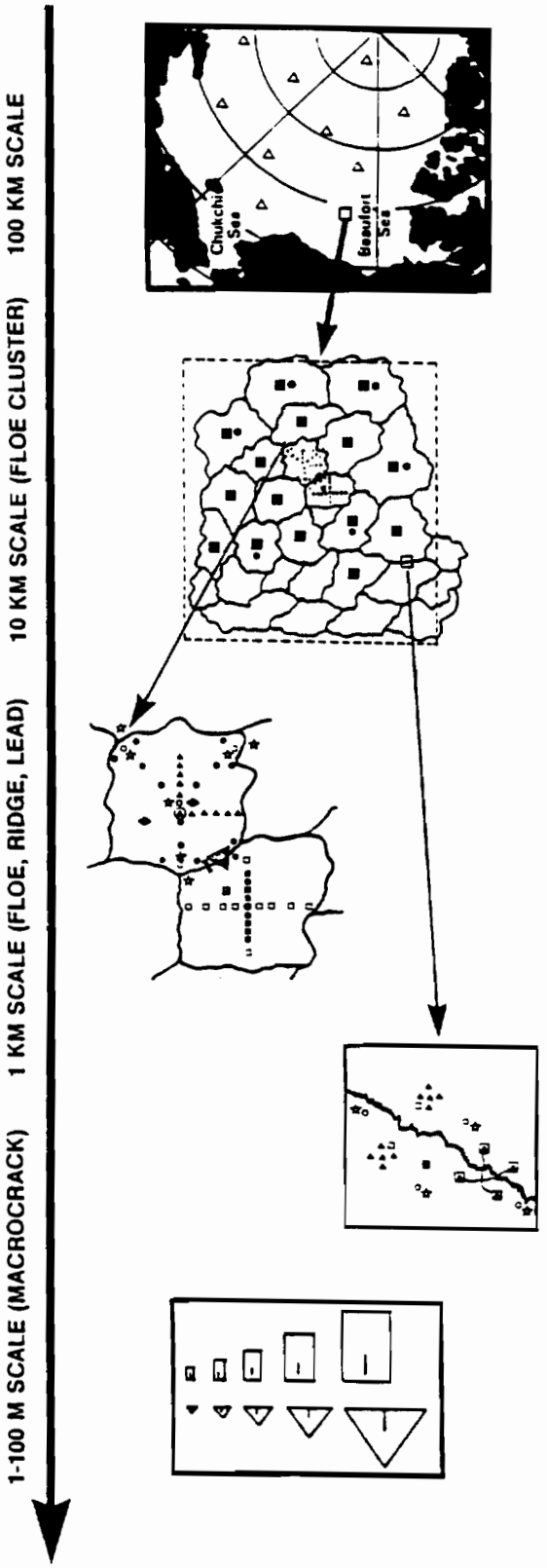

FORCING

MECHANICAL
- Regional surface winds (NOGAPS, NMC/Overland)
- Regional surface currents (GPS buoy array/Overland)

THERMODYNAMIC
- ● Surface temperature (ARGOS buoy array/Benner)

DEFORMATION/FRACTURE
- ● Point strain field (ARGOS buoy array/Benner)
- Image strain field (satellite AVHRR, SSMI, SAR/Fetterer, Kwok)

PROPERTIES
- Thickness distribution (low frequency acoustics/Mikhalevsky)

FORCING

MECHANICAL
- ● Stress on floes (GPS buoy array/Coon, Richter-Menge)

THERMODYNAMIC
- ■ Surface temperature (15 element GPS buoy array/Overland, Pease)

DEFORMATION/FRACTURE
- Image strain field (satellite SAR/ASF)
- Image strain field (satellite AVHRR, SSMI/Fetterer, Rothrock)
- ■ Point strain field (15 element GPS buoy array/Overland, Pease)
- Image strain field (sequential images/RC Helo, Twin Otter)
- Seismicity mapping, ridging localization (hydrophone array/Baggeroer, Schmic

PROPERTIES
- Thickness distribution (AUV/Bellingham, Catipovic, Stewart; submarine/Tucker
- Ridge event distribution (SAR/ASF, AVHRR, buoys/Overland, Coon)
- Ice type distribution (SAR/ASF)

FORCING

MECHANICAL
- ◆ Wind, ocean stress (main floe station/Overland)
- ●■ Ice stress array (24-30 stress sensors/Richter-Menge, Coon)

THERMODYNAMIC
- ◆ Surface temperature, radiation (main floe station/Overland, Lewis)

DEFORMATION/FRACTURE
- ☆ Strain, tilt, acceleration (sensor clusters/Wadhams)
- ■ Ridging event detection, localization (hydrophone array/Baggeroer, Schmidt)

PROPERTIES
- Morphology, ridge-lead distribution (main floe survey/Tucker)
- Thickness distribution (AUV/Bellingham, Stewart; submarine/Tucker)
- Ridge event distribution (SAR/ASF, AVHRR, buoys/Overland, Coon)

1 KM SCALE (FLOE, RIDGE, LEAD)

1-100 M SCALE (MACROCRACK)

1 CM - 1 M SCALE (CRYSTAL-MICROCRACK)

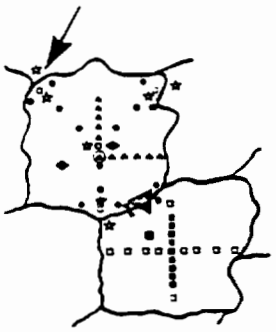

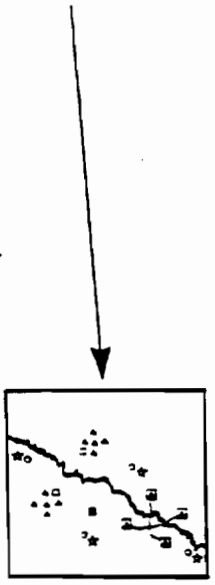

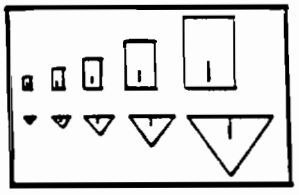

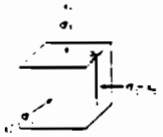

FORCING

MECHANICAL

Controlled loads (stress gage array/Coon, Pritchard)

THERMODYNAMIC

- Ice temperature profiles (thermistor arrays/Tucker)

DEFORMATION/FRACTURE

- Event localization and magnitude (hydrophone, geophone arrays/Baggeroer; Stein, Santos; Farmer)
- Ridging event seismo-acoustic inversion (geophone, hydrophone arrays/Schmidt, Farmer)
- Ridging deformation (high resolution GPS, stress sensors, tilt-strain meters and borehole jack/Coon, Pritchard)
- Fracture energy, failure modes (first-year ice controlled load/Dempsey, CANMAR)
- Fracture energy distribution (first-year ice controlled load-acoustic, seismic response; borehole jack, hydrophone, geophone arrays/Coon, Pritchard, Baggeroer)

PROPERTIES

- Seasonal evolution of elastic and shear wave properties and fissures on flat ice (controlled impulse source/Stein)
- Seasonal evolution of elastic and shear wave properties, fissures in ridged ice, crack event localization, failure mode detection (acoustic tomography/Rajan)
- Seasonal evolution of ridge elastic, structural properties (conng, thermistor arrays/Coon, Tucker, Weeks)
- Seismo-acoustic scattering from ridges (pencil beam and explosive sources, hydrophone and geophone arrays/Ewart, Baggeroer, Schmidt)
- Block friction (in-situ tests/Coon)

FORCING

MECHANICAL

- Regional surface winds (NWS/Shapiro)
- Experiments under controlled loads

THERMODYNAMIC

- Surface temperature (NWS/Shapiro)

DEFORMATION/FRACTURE

- Flexure, fracture related to microstructure (in-situ samples/Weeks, Shapiro, Dempsey)
- Flexure, fracture related to microstructure (pit-pond tests/Richter-Menge, Dempsey)
- Fracture related to microstructure (testing machine/Dempsey)
- Low strain rate creep (testing machine/Richter-Menge)
- Internal friction, anelasticity (cyclic loading/Cole)
- Multiaxial compressive strength (pit-pond, testing machine/Richter-Menge, Schulson)
- 3-D failure surfaces (testing machine/Schulson)

PROPERTIES

- Microstructure linked with growth conditions (in-situ samples/Weeks, Shapiro)

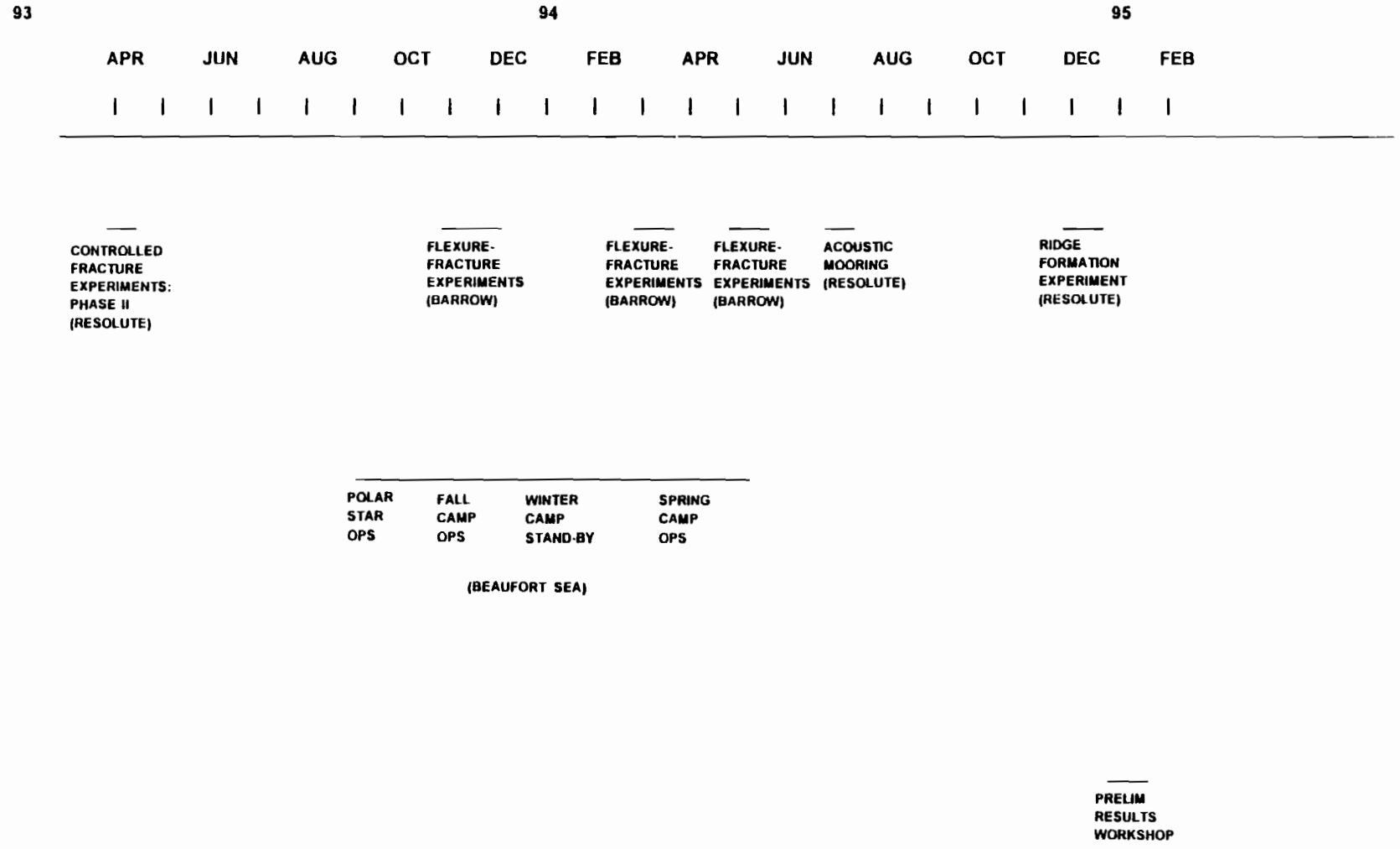
93
94
95
APR
JUN
AUG
OCT
DEC
FEB
APR
JUN
AUG
OCT
DEC
FEB
CONTROLLED FRACTURE EXPERIMENTS: PHASE II (RESOLUTE)
FLEXURE-FRACTURE EXPERIMENTS (BARROW)
FLEXURE-FRACTURE EXPERIMENTS (BARROW)
FLEXURE-FRACTURE EXPERIMENTS (BARROW)
ACOUSTIC MOORING (RESOLUTE)
RIDGE FORMATION EXPERIMENT (RESOLUTE)
POLAR STAR OPS
FALL CAMP OPS
WINTER CAMP STAND-BY
SPRING CAMP OPS
(BEAUFORT SEA)
PRELIM RESULTS WORKSHOP

3.2 DETAILS

100 KM SCALE (PACK)

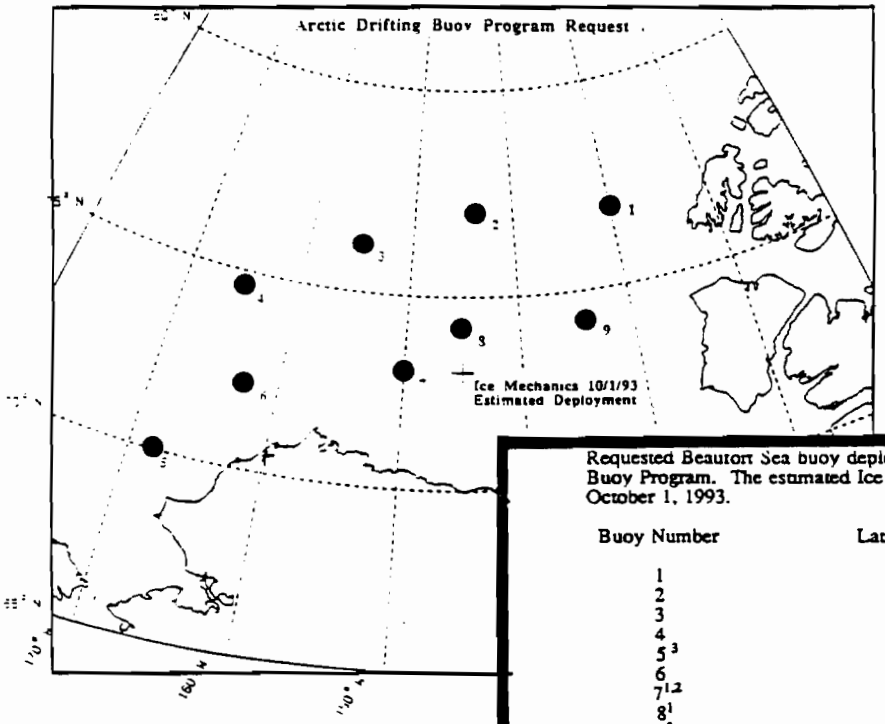

Requested Beaufort Sea buoy deployments for early autumn 1993 by Arctic Drifting Buoy Program. The estimated Ice Mechanics deployment site is 73°N, 144°W by October 1, 1993.

Buoy Number	Latitude (°N)	Longitude (°W)
1	77°00'	130°00'
2	77°00'	144°00'
3	76°00'	155°00'
4	74°20'	165°00'
5[3]	70°00'	168°00'
6	72°00'	162°30'
7[1,2]	73°00'	150°00'
8[1]	74°00'	145°00'
9[2]	74°00'	134°00'

[1]We offer to deploy buoys #7 and 8 by helicopter during the Ice Mechanics buoy deploymnet period (late September 1993).

[2]Alternative 1: drop buoy #9 and shift buoy #7 to 74°N, 137°W.

[3]Alternative 2: drop buoy #5.

FORCING

MECHANICAL

- Regional surface winds (NOGAPS, NMC/Overland)
- Regional surface currents (GPS buoy array/Overland)

THERMODYNAMIC

- Surface temperature (ARGOS buoy array/Benner)

DEFORMATION/FRACTURE

- Point strain field (ARGOS buoy array/Benner)
- Image strain field (satellite AVHRR, SSMI, SAR/Fetterer, Kwok)

PROPERTIES

- Thickness distribution (low frequency acoustics/Mikhalevsky)

Sea Ice Motion and Strains from AVHRR

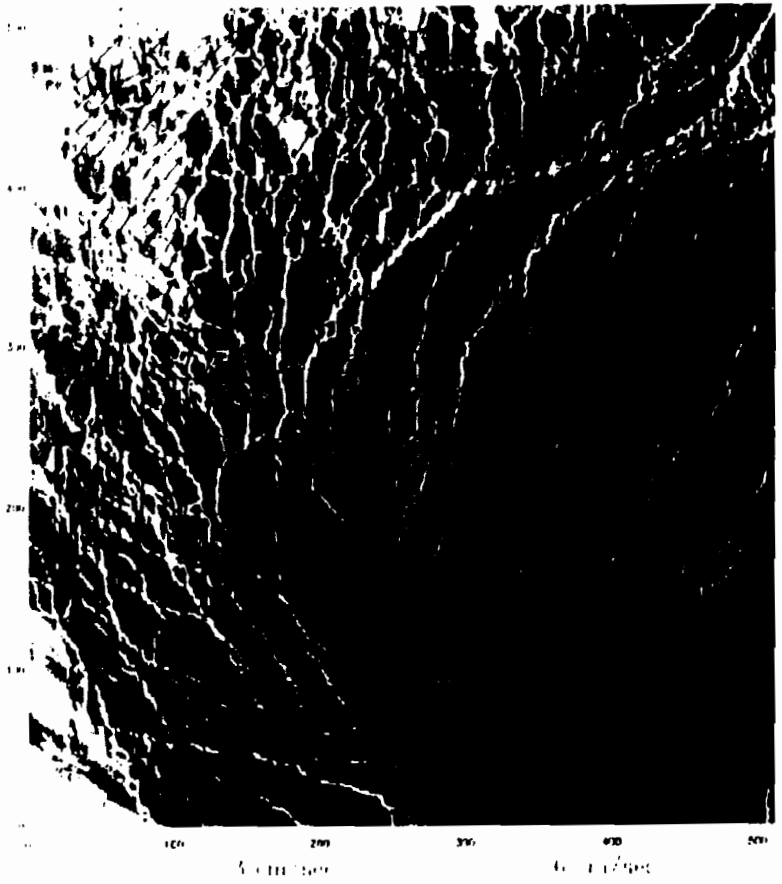

Channel-1 Image on April 8 1992
and Motion Vectors

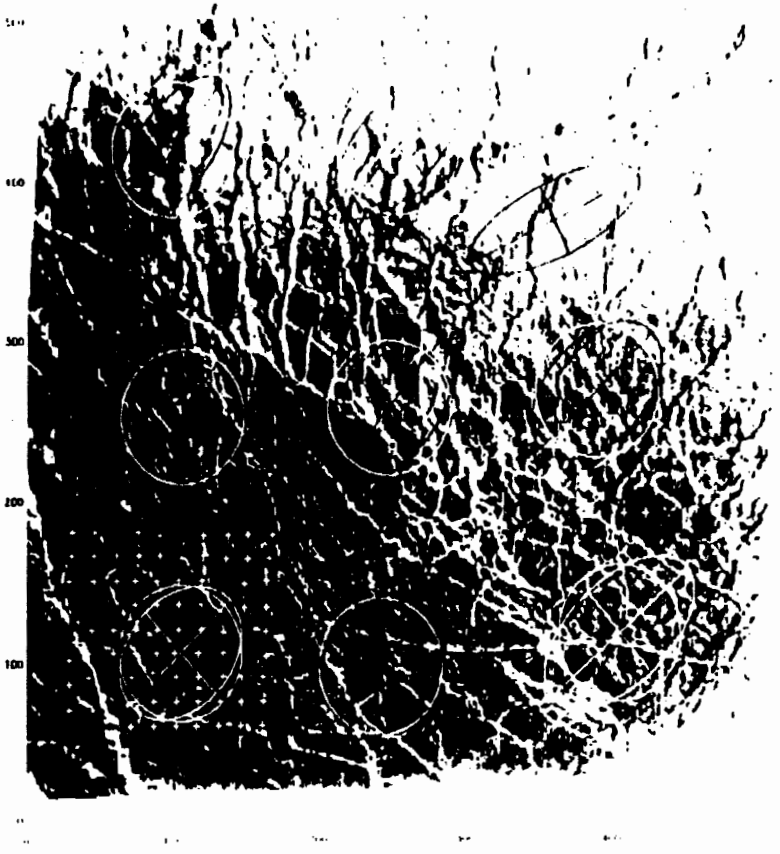

Difference Image April 16 - April 8
(remapped) and Strain Ellipses

Figure 3.2-1. Example of motion and strain fields derived from AVHRR (Rothrock).

10 KM SCALE (FLOE CLUSTER)

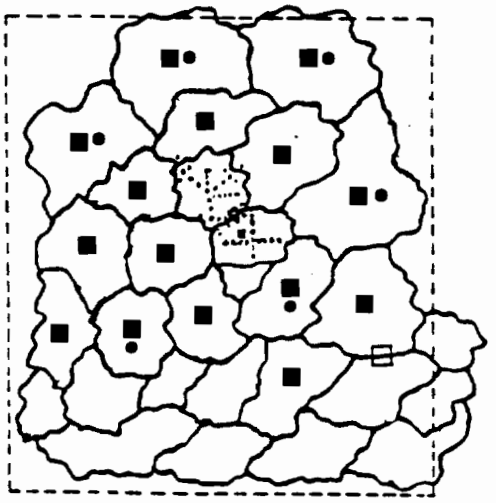

FORCING

MECHANICAL

- Stress on floes (GPS buoy array/Coon, Tucker)

THERMODYNAMIC

- Surface temperature (15 element GPS buoy array/Overland, Pease)

DEFORMATION/FRACTURE

- Image strain field (satellite SAR/ASF)
- Image strain field (satellite AVHRR, SSMI/Fetterer, Rothrock)
- Point strain field (15 element GPS buoy array/Overland, Pease)
- Image strain field (sequential video/RP Helo, Twin Otter)

PROPERTIES

- Thickness distribution (AUV/Bellingham, Stewart; submarine/Tucker)
- Ridge event distribution (SAR/ASF; AVHRR, buoys/Overland, Coon)
- Ice type distribution (SAR/ASF)

1 KM SCALE (FLOE, RIDGE, LEAD)

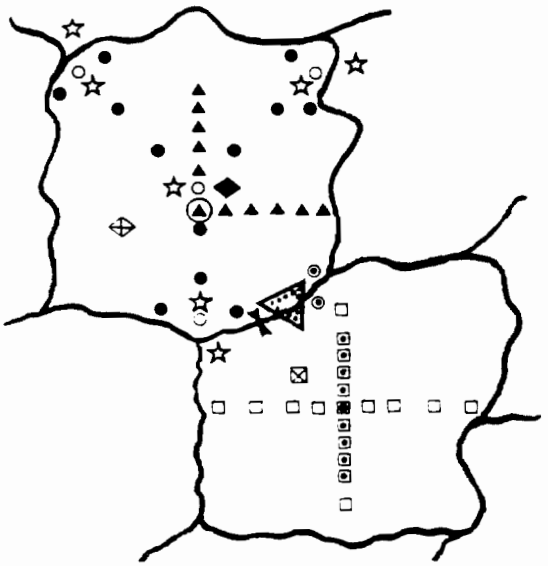

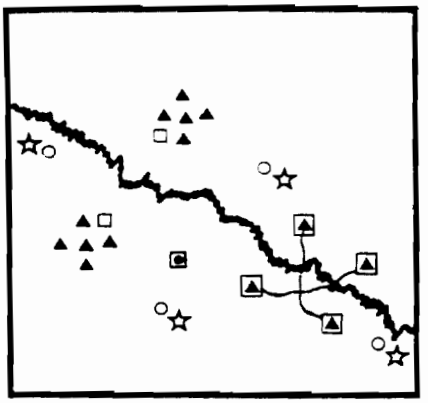

FORCING

MECHANICAL

- ◆ Wind, ocean stress (main floe station/Overland)
- ○● Ice stress array (24-30 stress sensors/Tucker, Coon)

THERMODYNAMIC

- ◆ Surface temperature, radiation (main floe station/Overland, Lewis)

DEFORMATION/FRACTURE

- ☆ Strain, tilt, acceleration (sensor clusters/Wadhams)
- □⊡■ Event localization and magnitude (hydrophone array/Baggeroer)

PROPERTIES

Morphology, ridge-lead distribution (main floe survey/Tucker)
Thickness distribution (AUV/Bellingham, Stewart; submarine/Tucker)
Ridge event distribution (SAR/ASF; AVHRR, buoys/Overland, Coon)

1-100 M SCALE (MACROCRACK)

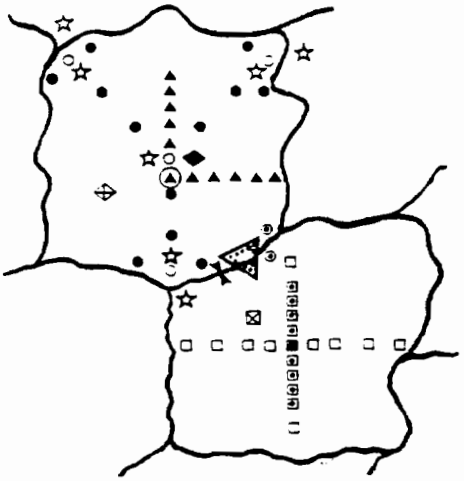

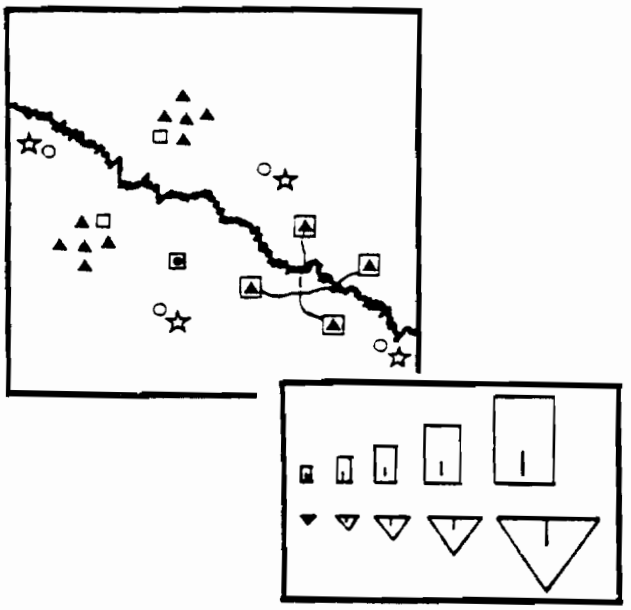

FORCING

MECHANICAL

Controlled loads (stress gage array/Coon, Pritchard)

THERMODYNAMIC

⊙ Ice temperature profiles (thermistor arrays/Tucker)

DEFORMATION/FRACTURE

□⊡■ Event localization and magnitude (hydrophone, geophone arrays/Baggeroer; Stein, Santos; Farmer)

□▲▣ Ridging event acoustic/seismic energy partitioning (geophone, hydrophone arrays/Schmidt, Fricke; Farmer)

Ridging deformation (high resolution GPS or laser-microwave stress sensors, tilt-strain meters and borehole jack/Coon, Pritchard)

Fracture energy, failure modes (first-year ice controlled load/Dempsey, CANMAR)

Fracture energy distribution (first-year ice controlled load-acoustic, seismic response: borehole jack, hydrophone, geophone arrays/Coon, Pritchard, Baggeroer)

PROPERTIES

Seasonal evolution of elastic and shear wave properties and fissures on flat ice (controlled impulse source/Stein)

Seasonal evolution of elastic and shear wave properties, fissures on ridged ice (acoustic tomography/Rajan)

⊙ Seasonal evolution of ridge elastic, structural properties (coring, thermistor arrays/Coon, Tucker, Weeks?)

⊠ Acoustic surface scattering function from ridges (pencil beam source, hydrophone arrays/Ewart, Baggeroer)

Block friction (in-situ tests/Coon)

1 CM - 1 M SCALE (CRYSTAL-MICROCRACK)

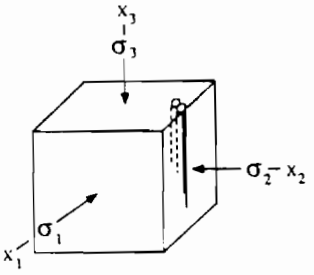

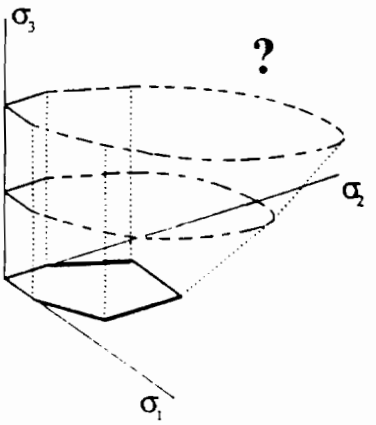

FORCING

MECHANICAL
- All experiments under controlled loads

THERMODYNAMIC
- ??

DEFORMATION/FRACTURE

- Flexure, fracture related to microstructure (in-situ samples/Weeks, Shapiro, Dempsey)
- Flexure, fracture related to microstructure (pit-pond tests/Richter-Menge, Dempsey)
- Fracture related to microstructure (testing machine/Dempsey)
- Low strain rate creep (testing machine/Richter-Menge)
- Internal friction, anelasticity (cyclic loading/Cole)
- Multiaxial compressive strength (pit-pond, testing machine/Richter-Menge, Schulson)
- 3-D failure surfaces (testing machine/Schulson)

PROPERTIES

- Microstructure linked with growth conditions (in-situ samples/Weeks, Shapiro)

To sample the seasonal evolution of the physical properties controlling the mechanical properties, the measurements include three sets of experiments at Barrow, each for approximately 10 days:

Mid- to late November: Experiments will be performed on young sea ice with thickness in the range 45 to 60 cm. In addition to salinity, grain size and thermal profile variability, c-axis aligned ice is expected at Barrow (usually at a depth of about 30 cm) providing important natural microstructure. Large temperature gradients through the ice sheet are possible at this thickness if the air temperature is cold. The test pods that will be cut at this time will also establish new ice areas that can be utilized in the following two field trips.

Mid- to late March: Experiments will be conducted on typical winter ice sheets with thickness about 1.5 m, depending on temperature history and snow cover. "Normal" winter salinity and temperature profiles are expected.

Early to Mid-May: During this period the ice sheet will be reaching its maximum thickness (about 1.75 m) and starting to deteriorate. Temperature profiles are expected to show near-surface warming; brine drainage systems will be enlarging and the salinity will decrease. These changes will combine to alter the physical and mechanical properties of the ice.

Each set will involve a large scale in-situ (full ice thickness) matrix of experiments and complementary small scale (partial thickness) matrix:

In-Situ (Full Thickness) Test Matrix

Test Type	Size	#	Loading
FRACTURE (Square Plate)	0.5m×0.5m	2	For each test: Cyclic loading, creep recovery, monotonic, vary rate monotonic, set rate, fracture
	1.5m×1.5m	2	
	4.5m×4.5m	2	
FLEXURE (Keyhole Geometry)	1m×1m	2	cyclic loading, creep recovery, monotonic, varying rate monotonic, set rate, split
	4m×4m	2	

Small-Scale (Partial Thickness) Test Matrix

Test Type	Size	=	Loading
FRACTURE			For each test: as much of
1. Square Plate	0.5m×0.5m	2	Cyclic loading, creep
2. SCB	0.2m (core diameter)	2 (at each depth)	recovery, monotonic, vary rate monotonic, set rate, fracture
FLEXURE			
Keyhole Geometry	0.5m×0.5m	2	Cyclic loading, creep recovery, monotonic, vary rate monotonic, set rate, fracture

Appropriately sized in-situ flexure (keyhole specimen) and fracture (square plate geometry) tests will be performed (Figure 3.2.5-1). The procedures that will be used for the plate tests were tested in 1993 at Resolute and were very successful. A computer controlled flatjack loading system will stress the ice

along preset load paths including controlled unloading; both load and deformation will be recorded. These experiments will be repeated during each of the three field trips. Issues include the effects of size, geometrical orientation relative to c-axis alignment, rate, load, and path (monotonic, cyclic and creep recovery: Figure 3.2.5-2):

Cyclic: A minimum of two cycles of a sinusoidally varying load will be applied to each of the 3 m x 3 m flexure and fracture in-situ specimens. The deformation will be monitored during the load cycling and the recovery period after the load drops to zero. The loading frequency will range between 0.001 Hz and 1 Hz. Each frequency will be run at an intermediate load level and a range of load levels will be applied at selected frequencies.

Creep Recovery: A minimum of three cycles of a sinusoidally varying load will be applied to each of the 3 m x 3 m flexure and fracture in-situ specimens. Unlike the above cyclic experiments, each cycle will be progressively longer, with a progressively longer unloaded period. For example, the three load/unload cycle time durations may be chosen to be $\Delta t/3\Delta t$, $2\Delta t/6t$ and $4\Delta t/12\Delta t$, with Δt = 5 minutes.

Following fracture tests, samples will be examined to document the crack path relative to the microstructure to determine the source of crack initiation (e.g., individual brine pockets or brine drainage channels and networks) and whether crack propagation is controlled by grain boundaries or sub-grain features. At issue is a useful fracture parameter for predicting crack initiation, growth and propagation extent.

The ice at the test site will be monitored throughout the year (bi-weekly) to provide a record of changes in thickness, snow cover, temperature and salinity profiles, grain size, fabric, geometry and distribution of brine drainage networks. Photomicrography in a nearby cold room will be used for microstructural characterization. Local meteorological data is available from the NWS or the NOAA clean air monitoring station in the vicinity. The combined data sets will be used to test and expand the Cox et al. model that predicts ice thickness, salinity, temperature and brine volume profiles from the thermal forcing.

3.3 INSTRUMENTATION

New or modified hardware and software being implemented for the field measurements include the following. Collaboration is beneficial and encouraged.

1) Base camp time-position computer network (O'Hara)
2) Regional (1-10KM) imaging (Pacific RPV)
3) Automated hammer blow source (Stein)
4) High capacity data logging system (Stein, Santos)
5) Radio LAN telemetry (VonderHeydt)
6) Real time beamformer (VonDerHeydt)
7) Dual bore hole in-situ profiler (Maffione, Zaneveld)
8) Auto-cal stress sensors (Coon)

(1) Description of Base Camp Time-Position Computer Network

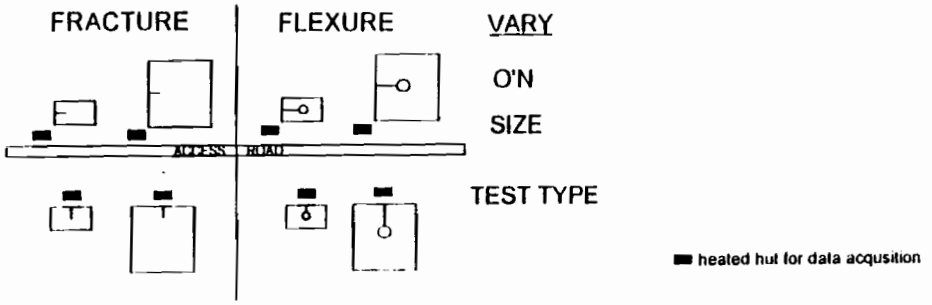

Figure 3.2.5-1. In-situ, full thickness, large scale tests.

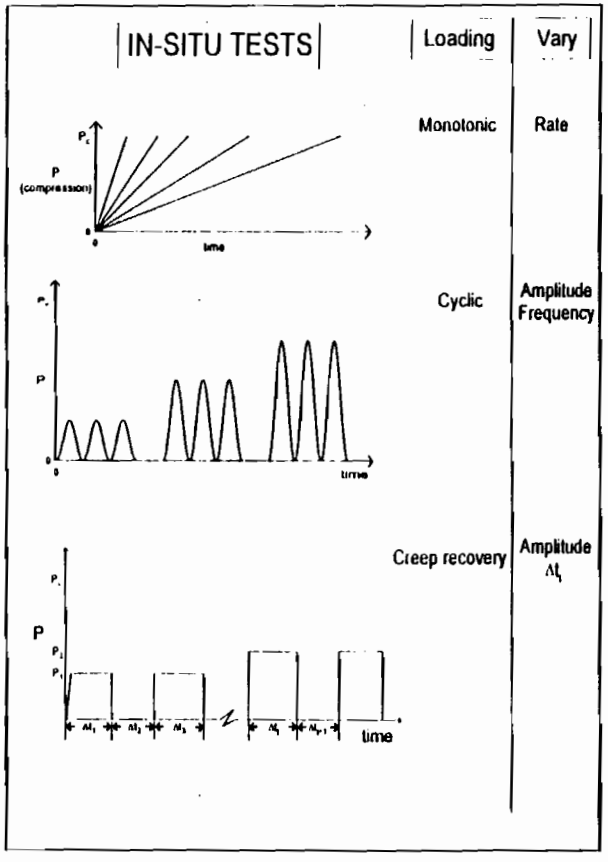

Figure 3.2.5-2. Loading paths for in-situ tests.

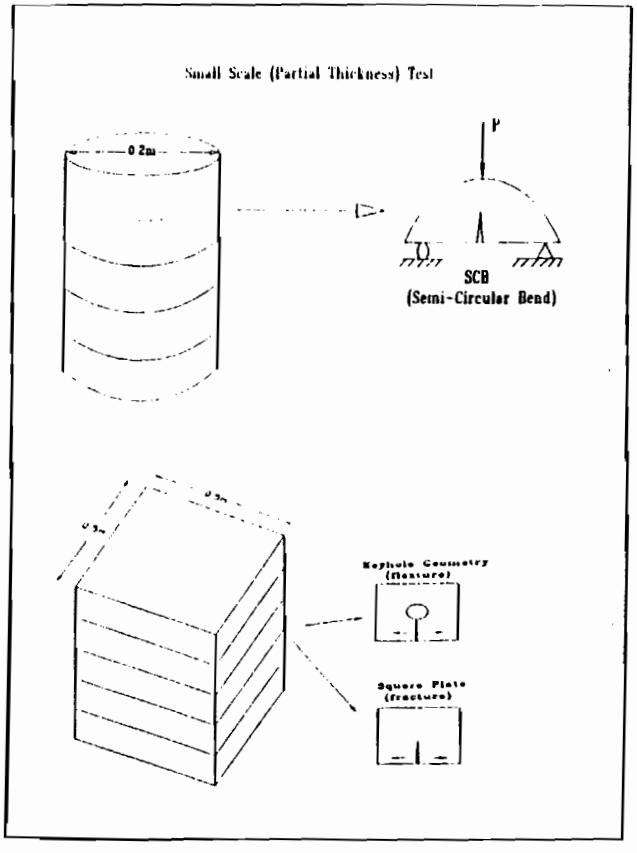

Figure 3.2.5-3. Partial thickness, small scale tests.

Computer networking capability will be available at the main campsite using the computer acquired for GPS logging as a system server. Jay Ardai and Suzanne O'Hara will provide thin Ethernet cable to each hut that requests it. Individuals must supply the necessary connectors and internal cards (e.g., com standard card) to connect their computer to the system as well as their machine specific software. We will be running pctip with telnet (NCSA) and ftp for data and email transfer. Users can also bring their own terminal emulate software and make temporary connections to the server through the serial ports. This should allow all users to connect to the hard disk to store or back up data. A special directory will be set up to allow the exchange of data between groups. Raw real-time navigation will be available at any time and processed navigation files with longitude, latitude and time fields will be available daily. There will also be general purpose plotting and other software programs for use on the SUN Unix computer. The ability to make email or data transfers of other types out of the camp may be limited by the communications method selected. Anyone interested in taking advantage of this system please contact either Jay or Suzanne so that they can prepare the necessary software and hardware for the particular application.

System hardware:
Sun SPARCstation ipx computer
1.5 GB hard disk
4mm DAT drive (for backups or data storage)
1.44 MB floppy drive (includes ability to read/write dos floppies)
10 serial ports (at least 2 dedicated to logging data), 1 parallel port

Points of contact:
email: jay@lamont.ldeo.columbia.edu, sohara@lamont.ldeo.columbia.edu
telemail (Omnet): j.ardai
phone: Suzanne O'Hara - 914-365-8381, Jay Ardai - 914-365-8436
mail: Lamont-Doherty Earth Observatory, Route 9w, Palisades, NY 10964

References

Coon, M. D., Maykut, G. A., Pritchard, R. S., Rothrock, D. A., and Thorndike, A. S. (1974) "Modeling the Pack Ice as an Elastic-Plastic Material," AIDJEX Bulletin No. 24, University of Washington, Seattle, WA., pp. 1-106.

Coon, M. D. (1980) "A Review of AIDJEX Modeling," in *Sea Ice Processes and Models*, (ed) R. S. Pritchard, University of Washington Press, Seattle, WA, pp. 12-27.

Coon, M. D., Echert, D. C., and Knoke, G. S. (1992) "Pack Ice Anisotropic Constitutive Model," in Proceedings of *IAHR Ice Symposium 1992*, Banff, Alberta.

Overland, J. E., Walter, B. A., and Davidson, K. L. (1992) "Sea Ice Deformation in the Beaufort Sea," in *Proceedings of Third Conference on Polar Meteorology and Oceanography*, Am. Meteorological Society, Portland, OR, 29 September - 2 October, 1992, pp. 64-67.

Pritchard, R. S. (1980) "A Simulation of Near Shore Winter Ice Dynamics in the Beaufort Sea," in *Sea Ice Processes and Models*, (ed) R. S. Pritchard, University of Washington Press, Seattle, WA, pp. 49-61.

Pritchard, R. S., Rutland, C. J., and Knoke, G. S. (1983) "Dynamics of the Sea Ice Cover," Proprietary Report to Shell Development Company, RTD Report No. 278, Flow Industries, Kent, WA.